AB INITIO THREE-DIMENSIONAL ATOM-DIATOM REACTION CROSS SECTIONS USING HYPERSPHERICAL COORDINATES AND VARIATIONAL SURFACE FUNCTIONS

Thesis by

Steven Andrew Cuccaro

In Partial Fulfillment of the Requirements

for the Degree of

Doctor of Philosophy

California Institute of Technology

Pasadena, California

1991

(Defended December 11, 1990)

ACKNOWLEDGEMENTS

There are many people that I want to thank for their help and encouragement, since any project of the magnitude of a doctoral thesis could not succeed without the support of friends and colleagues during the course of the work. First on this list has to be my thesis advisor, Aron Kuppermann. The initial conception for the work I have done originated with him, and he has always taken great interest in my research as it developed in ways both expected and unanticipated, offering advice but never taking over. I especially wish to thank him for the ample computational resources which have made the completion of this work possible.

Among my colleagues and friends, special mention must go to Paul Hipes, with whom I have collaborated since my arrival at Caltech. His assistance in the early years of my stay here were invaluable, and his friendship still is. I also want to thank my coworkers Diane Zirin, Joseph Wong, Mark Wu and Zhengwei Peng for the insights that they have provided me and for the pleasure of working with them. On the experimental side of the group, Kerry Walzl, Jim Garvey, and Maria Giorgi have all been close friends, and I also want to thank Jerry Winniczek, Mary Rodgers and Isaak Xavier for the good times (and bad) that I've shared with them. Finally, outside of the Kuppermann group, Terry Coley, Bob Scheid and Dan Zirin deserve special mention; they have all made my life better by being part of it.

Most of all I want to thank my family for their constant love, prayers and support over the last seven years. My sister Pat has always managed to keep me smiling despite all else, and has helped me both in work and in life in ways that she probably isn't even aware of. Above all, I want to thank my mother, Frances Cuccaro, who has had to put up with my idiosyncracies and has still managed to keep caring for me and working hard to make my life easier, even when her own situation was difficult. It is no exaggeration to say that I wouldn't be where I am now if it weren't for her help; this thesis is dedicated to her, with love.

ABSTRACT

This thesis discusses the development of a symmetrized hyperspherical coordinate technique for the calculation of accurated differential cross sections in the reactive collision of an atom with a diatomic molecule in three-dimensional space. The hyperspherical methodology has the advantage that all regions of configuration space are treated equivalently; this allows the reduction of the reactive scattering problem to an equivalent inelastic scattering problem, which is both computationally simpler and more straightforward conceptually.

The hyperspherical methodology is discussed in detail, including the expansion of the scattering wavefunction in terms of a basis of local hyperspherical surface functions and the calculation of this basis set. The methods are applied to the $H + H_2$ system (using the LSTH potential energy surface) and used to calculate scattering matrices and partial wave cross sections for this reaction up to a total energy of 1.6 eV. The results presented here include the geometric phase effect due to the conical intersection of the H_3 system, along with a set of results which do not include this effect for comparison with the previous work in the field.

TABLE OF CONTENTS

I. INTRODUCTION

This thesis is composed of a set of four papers, two of which are already in the literature. The individual papers are meant to stand alone, and may be read more or less independently. Since each paper will have an introduction discussing the motivation of and the background for the paper, this material will not be repeated here; instead, this introduction will give a summary of the intent of each paper and an overview of the results to establish the unifying theme of the thesis, which is the calculation from first principles of the differential cross sections for atom-diatom scattering by hyperspherical coordinate methods.

Chapter two details the calculation of local hyperspherical surface functions using a variational basis set and symmetrized hyperspherical coordinates. The formal expansion of the wavefunction in the surface functions is given in order to determine the matrix functions needed for the eventual scattering matrix and cross section calculations. The construction of a basis set for expansion of the surface functions consisting of products of analytic functions and a numerically determined function is discussed, and the matrix functions are expanded in this basis set. The formalism is designed to take advantage of permutation symmetry if two or all three atoms are indistinguishable, in order to reduce the numerical effort required to solve the surface function problem as well as the subsequent scattering matrix calculation. A series of surface function contour plots are presented and analyzed.

The third chapter gives the formalism for the calculation of differential and integral cross sections from the surface function information given by the methods of chapter 2. The formal expression of the wavefunction in terms of the surface functions is discussed in more detail, as are the means of solution of the coupled differential equations which arise from this expansion. The resulting calculated wavefunction expression is compared with the physical asympotic behavior of the wavefunction to determine the scattering matrix for the system, which in turn is

used in the cross section calculation. Finally, we apply the methods to the H + H_2 system to examine the behavior of the transition probabilities, scattering resonances and cross sections; we also introduce corrections for the presence of the H_3 conical intersection which alter the expected physical behaviors dramatically.

Chapter four is a reprint of the first publication using the hyperspherical method with variational surface functions, applied to the $J = 0$ partial wave of the H + H_2 system. Comparison was made to previous independent calculations and the results were shown to be very similar, thus validating the method. Chapter five is a reprint of the subsequent paper reporting results for the $J = 1$ partial wave of both parities; in this paper, we also reported the existence of a selection rule for the resonances of the H_3 system depending on the permutation symmetry and parity of the partial wave and explained this rule in terms of a simple model for the resonant state.

II. COMPUTATION OF SURFACE FUNCTIONS FOR 3D ATOM-DIATOM SCATTERING CALCULATIONS USING SYMMETRIZED HYPERSPHERICAL COORDINATES[†]

Steven A. Cuccaro[¶] and Aron Kuppermann

Arthur Amos Noyes Laboratory of Chemical Physics,
Division of Chemistry and Chemical Engineering,[‡]
California Institute of Technology,
Pasadena, California 91125

(Received)

Abstract

We present a method for calculation of accurate five-dimensional surface functions which may be used to expand the total six-dimensional wavefunction of a three particle system, yielding a set of coupled equations in the remaining variable. The results of application of this method to the $H+H_2$ system are discussed.

1. INTRODUCTION

In the last five years there have been great advances in the field of quantum reactive scattering for atom-diatom systems. Prior to 1986, the only converged exact three-dimensional calculations that had been performed were done on the $H + H_2 \rightarrow H_2 + H$ reaction. In 1975, Kuppermann and Schatz[1,2] reported converged integral and differential cross sections for a range of energies up to 0.7 eV above the ground state energy of H_2, using the Porter-Karplus potential energy surface (PK2).[3] These were the only accurate converged differential cross sections published until 1989.[4–7] Also in 1975, Elkowitz and Wyatt[8,9] published integral cross section calculations for that reaction which were performed with minor approximations. These integral cross section calculations were repeated in 1978 by Walker, Stechel and Light[10] on the more accurate LSTH potential energy surface.[11] The long delay in the production of new results in the field was caused by the difficulty in application of the methods used in these early calculations to other systems, for reasons of increased computational effort associated with the loss of the symmetry of the three identical atoms; in addition, the methods failed at higher energies for the H + H_2 reaction for the same reason. Beginning in 1986 with the publication by Kuppermann and Hipes[12,13] of $J = 0$ partial wave results for the H + H_2 reaction up to energies of 1.6 eV above threshold using symmetrized hyperspherical coordinates, a surge of publications has occurred. There are now converged calculations for the systems H + H_2 and D + H_2,[4–7,12–35] F + H_2, F + D_2 and F + HD,[36–44] O + H_2,[45,46] H + HBr,[47] and Cl + HCl.[19,48]

These calculations are of three basic types: the propagation methods of Kuppermann *et al.*,[12–15] Pack *et al.*,[16–18,36,37] Schatz,[19,48] Linderberg *et al.*,[20] and Launay and Le Dorneuf,[21] all involving some form of hyperspherical coordinates; the variational methods used by Manolopoulos and Wyatt,[4,32,33,42–44] Miller,[5,6,30,31] and the Truhlar and Kouri groups,[7,22–29,38–41,45–47] using Jacobi coordinates; and

the recent work of Webster and Light[34,35] using a "natural collision coordinate"[49] method related to the methods of the early work[1,2,8-10].

Variational methods[4-7,22-35,38-47] were developed based on several scattering variational principles, which involve expansions of the scattering wavefunction in terms of basis functions for the reactants and products, expressed in terms of the Jacobi coordinates of the arrangement channel. The couplings between these basis sets are evaluated through multi-dimensional exchange integrals,[50] which leads to a system of linear equations that must be solved to obtain the scattering matrix for the three-particle system. These methods are very powerful but have the disadvantage that a new set of integrals must be calculated for each new total energy of the system; furthermore, they are very memory intensive.

The propagation method calculations,[12-21,36,37,48] on the other hand, are based on an expression of the problem in terms of a hyperspherical coordinate system, which describes the degrees of freedom of the system of particles in terms of a single distance variable (the hyperradius) and five hyperangles. In these methods the Schrödinger equation is solved for fixed hyperradius to obtain "surface functions" in the hyperangles, so called since they are defined on the surface of a hypersphere; the hyperradius is treated as the generalized collision coordinate for the system. When these surface functions are substituted back into the Schrödinger equation, the result is a system of coupled second order linear differential equations in the hyperradius which may be solved by any of several well known numerical techniques. The surface functions are independent of the total energy of the system, and thus if scattering calculations at many energies are desired the time spent in evaluating the surface functions becomes unimportant. A further advantage of these methods is that the hyperspherical coordinates are the most practical way to describe the wavefunctions in cases where a heavy-light-heavy mass combination results in a large overlap between reactant and product channels[51,52] and for the case of collision-induced dissociation.[53,54]

There is more than one possible set of hyperspherical coordinates which may be used for these propagation calculations. The coordinates introduced by Delves[55] (currently in use by Schatz[19,48]) and by Whitten and Smith[56] both share the disadvantage that certain configurations of the system may be described by more than one set of internal coordinates (*i.e.*, the coordinates on which the potential depends), so that there is not a 1 to 1 mapping of the configurations of the system and the description of the system in the coordinates. In addition, the transformation of the three internal coordinates of the system from a set based on one arrangement channel to another is not orthogonal. Kuppermann[57] developed a set of symmetrized hyperspherical coordinates (SHC) which does not have this undesirable characteristic, and suggested that these coordinates would be an appropriate system for study of reactive scattering problems;[57,58] they are currently in use by this group[12–15]. Other sets of symmetrized hyperspherical coordinates have been designed so as to treat all three arrangement channels in equivalent ways; these have been proposed by Johnson[59] (based on the Smith–Whitten coordinates), Mead[60] (used by Linderberg *et al.*[20]), and Pack and Parker.[16–18,36,37]

In this paper and one to follow, we report the results of our work on the $H + H_2$ system. This paper will be concerned with the determination of surface functions using the SHC system of coordinates and their properties; a subsequent paper will describe the use of these surface functions in the calculation of scattering matrices and differential cross sections. Section 2 will describe a general formalism for the calculation of surface functions from a variational basis set. In section 3, we will discuss the implementation of the formalism in a computational algorithm, and in section 4 the results of these calculations will be presented. Section 5 will be a summary of the main points of this paper.

2. FORMALISM OF VARIATIONAL SURFACE FUNCTIONS

2.1 Symmetrized Hyperspherical Coordinate System

The symmetrized hyperspherical coordinate (SHC) system that we have chosen to use for the three-body problem has been described previously,[12,13,57,58] so only a brief description is necessary here. Let $A_\alpha, A_\beta, A_\gamma$ be the atoms of a triatomic system with masses $m_\alpha, m_\beta, m_\gamma$, respectively, defined in the following manner: for a system of type ABC (three distinguishable atoms) A_α = A, A_β = B, and A_γ = C; for a system of type AB_2 (two identical atoms) A_α = A, and A_β and A_γ are each assigned to one of the two B atoms; and in an A_3 system all are A atoms. In addition, let λ, ν, κ be an arbitrary cyclic permutation of α, β, γ. There are three sets of body-fixed Jacobi coordinates $(\mathbf{R}'_\lambda, \mathbf{r}'_\lambda)$ for this system, where $\mathbf{r}'_\lambda$ is the vector from atom A_ν to atom A_κ and $\mathbf{R}'_\lambda$ is the vector from the center of mass of $\{A_\nu, A_\kappa\}$ to the atom A_λ. The index λ can be any of the values α, β or γ. The body-fixed $\mathbf{z}_\lambda$ axis is taken to be in the same direction as the vector $\mathbf{R}'_\lambda$, and the body-fixed $\mathbf{y}$ axis in the direction defined by $\mathbf{R}'_\lambda \times \mathbf{r}'_\lambda$. The center of mass of the triatomic system lies on the vector $\mathbf{R}'_\lambda$, which is specified by its length R'_λ and two spherical polar angles θ_λ and ϕ_λ with respect to the space-fixed $\mathbf{Z}$ axis. The vector $\mathbf{r}'_\lambda$ is specified by its length r'_λ and two body-fixed angles: the angle γ_λ (in the range 0 to π) between $\mathbf{R}'_\lambda$ and $\mathbf{r}'_\lambda$, and the angle ψ_λ, between the half-plane containing $\mathbf{Z}$ and $\mathbf{R}'_\lambda$ and the half-plane containing $\mathbf{R}'_\lambda$ and $\mathbf{r}'_\lambda$, in the range 0 to 2π and measured counterclockwise from the positive $\mathbf{R}'_\lambda$ direction from the first to the second of these half-planes. These relationships are diagrammed in figure 2.1.

The angles $\theta_\lambda, \phi_\lambda$, and ψ_λ determine the orientation of the triatomic plane in space and will be referred to as the Euler angles of the system.[61] This set of coordinates is best used to describe the system when the A_λ atom is distant from the diatom $A_\nu A_\kappa$, and will therefore be referred to as the λ arrangement channel

coordinates. For a given choice of the λ, ν and κ cyclic permutation, we may similarly define coordinates $(\mathbf{R}'_\nu, \mathbf{r}'_\nu)$ and $(\mathbf{R}'_\kappa, \mathbf{r}'_\kappa)$ for the ν and κ arrangement channels, respectively. The Euler angles in the ν or κ coordinate system may be expressed as functions of all 6 variables in the λ coordinate system. We will use the λ set of coordinates in the discussion to follow, whenever it is not necessary to specify a particular arrangement channel; however, since λ may stand for any of the three indices α, β or γ, this choice is general, and the equations in ν and κ coordinates may be obtained from those in λ coordinates by replacing the indices $\{\lambda, \nu, \kappa\}$ in each equation by the appropriate cyclic permutation.

The wavefunction Ψ of the system $A_\lambda, A_\nu, A_\kappa$ is the solution, subject to appropriate boundary conditions, of the Schrödinger equation $\hat{H}_\lambda \Psi = E\Psi$, which we require to be single-valued, continuous and differentiable (*i.e.*, well-behaved). The hamiltonian $\hat{H}_\lambda$ for the system in the λ set of coordinates is

$$\hat{H}_\lambda = \frac{-\hbar^2}{2\mu_{\lambda,\nu\kappa}} \nabla^2_{\mathbf{R}'_\lambda} - \frac{\hbar^2}{2\mu_{\nu\kappa}} \nabla^2_{\mathbf{r}'_\lambda} + V'_\lambda(R'_\lambda, r'_\lambda, \gamma_\lambda) \tag{2.1.1}$$

in which the reduced masses are

$$\mu_{\lambda,\nu\kappa} = \frac{m_\lambda(m_\nu + m_\kappa)}{m_\lambda + m_\nu + m_\kappa} \; ; \quad \mu_{\nu\kappa} = \frac{m_\nu m_\kappa}{m_\nu + m_\kappa}. \tag{2.1.2}$$

The Born-Oppenheimer potential energy surface V'_λ depends on the interatomic distances R'_λ and r'_λ and on the angle $\gamma_\lambda = \arccos \frac{(\mathbf{R}'_\lambda \cdot \mathbf{r}'_\lambda)}{R'_\lambda r'_\lambda}$. To simplify the hamiltonian (2.1.1), we scale the position vectors as

$$\mathbf{R}_\lambda = \left(\frac{\mu_{\lambda,\nu\kappa}}{\mu}\right)^{\frac{1}{2}} \mathbf{R}'_\lambda; \quad \mathbf{r}_\lambda = \left(\frac{\mu_{\nu\kappa}}{\mu}\right)^{\frac{1}{2}} \mathbf{r}'_\lambda \tag{2.1.3}$$

where

$$\mu = \left(\frac{m_\lambda m_\nu m_\kappa}{m_\lambda + m_\nu + m_\kappa}\right)^{\frac{1}{2}} = \left(\frac{m_\alpha m_\beta m_\gamma}{m_\alpha + m_\beta + m_\gamma}\right)^{\frac{1}{2}} \tag{2.1.4}$$

The new lengths of the vectors will be denoted by R_λ and r_λ, respectively; since mass-scaling of the vectors does not affect their angular coordinates, θ_λ, ϕ_λ, γ_λ and ψ_λ are unchanged. In this Delves' mass-scaled coordinate system,[55,62] μ is a single

reduced mass which is independent of λ and common to both $\mathbf{R}_\lambda$ and $\mathbf{r}_\lambda$, and the hamiltonian takes the form

$$\hat{H}_\lambda = \frac{-\hbar^2}{2\mu}(\nabla^2_{\mathbf{R}_\lambda} + \nabla^2_{\mathbf{r}_\lambda}) + V_\lambda(R_\lambda, r_\lambda, \gamma_\lambda). \tag{2.1.5}$$

Their use has the further benefit that the transformation matrix relating the coordinate systems $(\mathbf{R}_\lambda, \mathbf{r}_\lambda)$ and $(\mathbf{R}_\nu, \mathbf{r}_\nu)$ is orthogonal.[62]

The λ SHC for this system are obtained by conversion from the two distance variables r_λ and R_λ to a (hyper-)radius ρ and an additional angle ω_λ:[57]

$$\rho = (r_\lambda^2 + R_\lambda^2)^{\frac{1}{2}}; \quad \omega_\lambda = 2\arctan\frac{r_\lambda}{R_\lambda}; \quad 0 \le \omega_\lambda \le \pi \tag{2.1.6}$$

(The remaining four angles are unchanged.) In this coordinate system the hamiltonian is expressed as

$$\hat{H}_\lambda = \hat{T}(\rho) + \hat{h}_\lambda(\zeta_\lambda; \rho) \tag{2.1.7}$$

where we have defined the quantity ζ_λ to represent all five hyperangles in the λ SHC: $\{\theta_\lambda, \phi_\lambda, \psi_\lambda, \gamma_\lambda, \omega_\lambda\}$. The hyperradial kinetic energy operator $\hat{T}(\rho)$ has the form

$$\hat{T}(\rho) = -\frac{\hbar^2}{2\mu}\rho^{-5}\frac{\partial}{\partial\rho}\rho^5\frac{\partial}{\partial\rho} = -\frac{\hbar^2}{2\mu}\rho^{-\frac{5}{2}}\frac{\partial^2}{\partial\rho^2}\rho^{\frac{5}{2}} + \frac{15\hbar^2}{8\mu\rho^2} \tag{2.1.8}$$

and the surface hamiltonian $\hat{h}_\lambda(\zeta_\lambda; \rho)$ is

$$\hat{h}_\lambda(\zeta_\lambda; \rho) = \frac{\hat{\Lambda}^2(\zeta_\lambda)}{2\mu\rho^2} + V(\rho, \omega_\lambda, \gamma_\lambda) \tag{2.1.9}$$

This system has several advantages: the hyperradius ρ is independent of the arrangement channel in which the SHC are defined; the operators for hyperradius and hyperangles may be separated, and thus an expansion for the wavefunction in terms of a basis set made up of products of functions of ζ_λ (parameterized by ρ) and functions of ρ may be used; and ω_ν and γ_ν are functions of ω_λ and γ_λ only, making conversion between different arrangement channel SHC relatively easy.

The generalized or grand canonical angular momentum operator $\hat{\Lambda}^2$ is defined by

$$\hat{\Lambda}^2(\zeta_\lambda) = \hat{L}^2_\lambda(\omega_\lambda) + \frac{\hat{\ell}^2_\lambda(\theta_\lambda, \phi_\lambda, \psi_\lambda, \gamma_\lambda)}{\cos^2(\frac{\omega_\lambda}{2})} + \frac{\hat{\jmath}^2_\lambda(\psi_\lambda, \gamma_\lambda)}{\sin^2(\frac{\omega_\lambda}{2})}, \tag{2.1.10}$$

where $\hat{\ell}^2_\lambda$ and $\hat{\jmath}^2_\lambda$ are the angular momentum operators associated with the vectors $\mathbf{R}_\lambda$ and $\mathbf{r}_\lambda$, respectively, and

$$\hat{L}^2_\lambda(\omega_\lambda) = \frac{-4\hbar^2}{\sin\omega_\lambda}\left[\frac{\partial^2}{\partial\omega^2_\lambda} + 1\right]\sin\omega_\lambda \tag{2.1.11}$$

is a non-physical angular momentum operator associated with the hyperangle ω_λ. In this system of coordinates, the operator $\hat{\Lambda}^2$ has second order poles for $\omega_\lambda = 0$ (corresponding in physical space to atoms A_ν and A_λ coinciding) and $\omega_\lambda = \pi$ (corresponding to A_λ located on the center of mass of the system); in scalar products involving eigenfunctions of $\hat{H}_\lambda$ the effect of these poles is exactly cancelled by the effect of the ω_λ-dependent factor in the volume element, which in these coordinates is $d\vartheta = d\vartheta_\rho d\vartheta^\lambda_1 d\vartheta^\lambda_2$, with

$$d\vartheta_\rho = \frac{1}{8}\rho^5 d\rho; \quad d\vartheta^\lambda_1 = \sin\theta_\lambda d\theta_\lambda d\phi_\lambda d\psi_\lambda; \quad d\vartheta^\lambda_2 = \sin^2\omega_\lambda \sin\gamma_\lambda d\omega_\lambda d\gamma_\lambda \tag{2.1.12}$$

Therefore, the presence of the poles will cause no difficulty when determining the expectation value of this operator. This issue is further discussed in section 2.6.

2.2 Permutation Symmetry, Angular Momentum and Inversion Parity

To simplify the solution of the problem in cases where some of the atoms A_λ are identical, we can apply group theory for the permutation symmetry P_p of the system.[63] There are three possibilities for three atoms, namely that all three atoms are distinguishable ($p = 1$), that one atom differs from the other two ($p = 2$), or that all three are indistinguishable ($p = 3$). In each of these cases there is a set of permutation operations which commutes with the hamiltonian. For P_1, the only symmetry operation is the identity E, while in the P_2 case there are two, the identity operation E and the interchange of the two identical particles A. There are six operations for P_3, corresponding to the identity E, three two-particle interchanges (A, B, C) and two three-particle interchanges (D, F). Each of these permutations can be described by transformations $R \in (E,A,B,C,D,F)$ which act on the coordinates of the system; in addition, each R has associated to it an operator $\hat{O}_R$ which acts on functions of the coordinates, such that

$$\hat{O}_R F(\mathbf{x}) = F(R^{-1}\mathbf{x}) \tag{2.2.1}$$

where the inverse of the transformations (E,A,B,C,D,F) are (E,A,B,C,F,D), respectively. The transformations R and the permutations which generate them are defined in table 2.1. Application of the symmetry operators $\hat{O}_R$ to a general function $F(\rho, \zeta_\lambda)$ (in a system which has that particular symmetry operation) yields the following results:

$$\hat{O}_E F(\rho, \zeta_\lambda) = F(\rho, \zeta_\lambda) \tag{2.2.2}$$

$$\begin{aligned}
\hat{O}_A F(\rho, \zeta_\alpha) &= F(\rho, \theta_\alpha, \phi_\alpha, \pi + \psi_\alpha, \pi - \gamma_\alpha, \omega_\alpha) \\
\hat{O}_A F(\rho, \zeta_\beta) &= F(\rho, \theta_\gamma, \phi_\gamma, \pi + \psi_\gamma, \pi - \gamma_\gamma, \omega_\gamma) \\
\hat{O}_A F(\rho, \zeta_\gamma) &= F(\rho, \theta_\beta, \phi_\beta, \pi + \psi_\beta, \pi - \gamma_\beta, \omega_\beta)
\end{aligned} \tag{2.2.3}$$

$$\begin{aligned}
\hat{O}_B F(\rho, \zeta_\alpha) &= F(\rho, \theta_\gamma, \phi_\gamma, \pi + \psi_\gamma, \pi - \gamma_\gamma, \omega_\gamma) \\
\hat{O}_B F(\rho, \zeta_\beta) &= F(\rho, \theta_\beta, \phi_\beta, \pi + \psi_\beta, \pi - \gamma_\beta, \omega_\beta) \\
\hat{O}_B F(\rho, \zeta_\gamma) &= F(\rho, \theta_\alpha, \phi_\alpha, \pi + \psi_\alpha, \pi - \gamma_\alpha, \omega_\alpha)
\end{aligned} \tag{2.2.4}$$

$$\begin{aligned}
\hat{O}_C F(\rho,\zeta_\alpha) &= F(\rho,\theta_\beta,\phi_\beta,\pi+\psi_\beta,\pi-\gamma_\beta,\omega_\beta) \\
\hat{O}_C F(\rho,\zeta_\beta) &= F(\rho,\theta_\alpha,\phi_\alpha,\pi+\psi_\alpha,\pi-\gamma_\alpha,\omega_\alpha) \\
\hat{O}_C F(\rho,\zeta_\gamma) &= F(\rho,\theta_\gamma,\phi_\gamma,\pi+\psi_\gamma,\pi-\gamma_\gamma,\omega_\gamma)
\end{aligned} \tag{2.2.5}$$

$$\hat{O}_D F(\rho,\zeta_\lambda) = F(\rho,\zeta_\nu) \tag{2.2.6}$$

$$\hat{O}_F F(\rho,\zeta_\lambda) = F(\rho,\zeta_\kappa) \tag{2.2.7}$$

By examination of the group tables[63] for the groups P_p, we can see that each of these permutation symmetry groups is isomorphic with one of the crystallographic point groups: P_1 with C_1, P_2 with C_s, and P_3 with C_{3v}. (This also allows us to identify the two-particle interchange operations with reflections through a symmetry plane, and the three particle interchanges with rotations by $\frac{\pi}{3}$ about a symmetry axis.) Accordingly, we will use the symbols for the irreducible representations (IR) of these point groups to denote those of the permutation groups. The projection operators $\hat{P}^\Gamma_{ik}$ for the IR Γ of each of these groups are linear combinations of the symmetry operations for the group, and (in notation slightly modified from that of Hamermesh[64]) are given by

$$\hat{P}^\Gamma_{ik} = \frac{n_\Gamma}{g} \sum_R \left[d^\Gamma_{ki}(R)\right]^* \hat{O}_R \tag{2.2.8}$$

in which n_Γ is the dimension of the IR labeled by Γ, $g = \sum_\Gamma (n_\Gamma)^2$ is equal to the total number of symmetry operations of the group, the indices i and k fall in the range $[1, n_\Gamma]$, and the coefficients d^Γ_{ki} for each operation R form a unitary matrix $\mathbf{d}^\Gamma$ given in table 2.1. For irreducible representations which are not degenerate (the A_1 and A_2 IR in P_3 and all representations in the P_1 and P_2 groups) the matrices $\mathbf{d}^\Gamma(R)$ are one-dimensional and equal to the character for the operation R and the IR Γ. The two-dimensional representations of the E IR in P_3 are arbitrary in the sense that any unitary transformation of these matrices is a valid representation of E; we have chosen the representation in which one of the E symmetry functions

($k = 1$) is even and the other ($k = 2$) is odd with respect to interchange of the atoms A_β and A_γ.

The projection operators defined above have the following properties when applied to a general function $F(\rho, \zeta_\lambda)$:

$$F^\Gamma_{ik}(\rho, \zeta_\lambda) = \hat{P}^\Gamma_{ik}(\zeta_\lambda) F(\rho, \zeta_\lambda), \tag{2.2.9}$$

$$\hat{P}^\Gamma_{ik}(\zeta_\lambda) F^{\Gamma'}_{i'k'}(\rho, \zeta_\lambda) = \delta^{\Gamma k}_{\Gamma' i'} F^\Gamma_{ik'}(\rho, \zeta_\lambda), \tag{2.2.10}$$

$$F(\rho, \zeta_\lambda) = \sum_\Gamma \sum_{k=1}^{n_\Gamma} F^\Gamma_{kk}(\rho, \zeta_\lambda), \tag{2.2.11}$$

$$\langle F^\Gamma_{ik} | F^{\Gamma'}_{i'k'} \rangle = \delta^{\Gamma' k'}_{\Gamma k} \langle F^\Gamma_{ik} | F^\Gamma_{i'k} \rangle. \tag{2.2.12}$$

(In (2.2.12) and elsewhere, the bra-ket notation will be used exclusively to denote integration over ζ_λ with volume element $d\vartheta_1^\lambda d\vartheta_2^\lambda$.) From equation (2.2.11), we find that $F(\rho, \zeta_\lambda)$ is composed solely of the functions $F^\Gamma_{kk}(\rho, \zeta_\lambda)$, and from (2.2.10) that the operators $\hat{P}^\Gamma_{kk}$ all have the eigenvalue 1. We will not need the operators $\hat{P}^\Gamma_{ik}$ with $i \neq k$ for our purposes; as a consequence, the eigenfunctions of $\hat{P}^\Gamma_{kk}$ will be labeled Γ_k.

The hamiltonian operator (2.1.7) commutes with several other important operators, due to the isotropicity of space. These are the total angular momentum operator $\hat{J}^2$, the projection of the total angular momentum onto a space-fixed axis (such as $\hat{J}_z$ for the **Z** axis), and the operator $\hat{I}$ for inversion through the center of mass. The inversion operator has eigenvalues of ± 1, while the angular momentum operators have an infinite number of eigenvalues.

2.3 Partial Wave Expansion of the 6D Wavefunction

Since the hamiltonian operator (2.1.7) commutes with all the operators of section 2.2, we can expand the wavefunction of the system in terms of eigenfunctions of these operators, also well-behaved:

$$\Psi(\rho,\zeta_\lambda)=\sum_{J=0}^{\infty}\sum_{M=-J}^{J}C_\lambda^{JM}\sum_{\Pi=0}^{1}\sum_{\Gamma}\sum_{k=1}^{n_\Gamma}\Psi^{JM\Pi\Gamma_k}(\rho,\zeta_\lambda) \tag{2.3.1}$$

The partial wave functions $\Psi^{JM\Pi\Gamma_k}(\rho,\zeta_\lambda)$ simultaneously satisfy the equations

$$\hat{H}_\lambda(\rho,\zeta_\lambda)\Psi^{JM\Pi\Gamma_k}(\rho,\zeta_\lambda)=E\Psi^{JM\Pi\Gamma_k}(\rho,\zeta_\lambda) \tag{2.3.2}$$

$$\hat{J}^2(\theta_\lambda,\phi_\lambda,\psi_\lambda)\Psi^{JM\Pi\Gamma_k}(\rho,\zeta_\lambda)=\hbar^2J(J+1)\Psi^{JM\Pi\Gamma_k}(\rho,\zeta_\lambda) \tag{2.3.3}$$

$$\hat{J}_z(\phi_\lambda)\Psi^{JM\Pi\Gamma_k}(\rho,\zeta_\lambda)=\hbar M\Psi^{JM\Pi\Gamma_k}(\rho,\zeta_\lambda) \tag{2.3.4}$$

$$\hat{\mathcal{I}}(\theta_\lambda,\phi_\lambda,\psi_\lambda)\Psi^{JM\Pi\Gamma_k}(\rho,\zeta_\lambda)=(-1)^\Pi\Psi^{JM\Pi\Gamma_k}(\rho,\zeta_\lambda) \tag{2.3.5}$$

$$\hat{P}_{ii}^{\Gamma'}(\zeta_\lambda)\Psi^{JM\Pi\Gamma_k}(\rho,\zeta_\lambda)=\delta_\Gamma^{\Gamma'}\delta_i^k\Psi^{JM\Pi\Gamma_k}(\rho,\zeta_\lambda) \tag{2.3.6}$$

which define the quantum numbers J, M and Π of the total angular momentum of the system, its projection on the space-fixed OZ axis, and the inversion parity, respectively.

2.4 Expansion of the Partial Waves in Terms of Surface Functions

We now define local hyperspherical surface functions (LHSF) $\Phi_n^{JM\Pi\Gamma_k}$ to be well-behaved solutions to the Schrödinger equation for the five-dimensional hamiltonian defined by equation (2.1.9), which resulted from omitting from $\hat{H}_\lambda$ the radial kinetic energy operator (2.1.8). This operator commutes with the same set of operators as the full six-dimensional hamiltonian operator, and therefore we also define the LHSF to have the appropriate permutation symmetry behavior and to be simultaneous eigenfunctions of $\hat{J}^2$, $\hat{J}_z$ and $\hat{\mathcal{I}}$. This yields the set of equations

$$\hat{h}_\lambda(\rho,\zeta_\lambda)\Phi_n^{JM\Pi\Gamma_k}(\zeta_\lambda,\rho) = \epsilon_n^{J\Pi\Gamma}(\rho)\Phi_n^{JM\Pi\Gamma_k}(\zeta_\lambda,\rho) \tag{2.4.1}$$

$$\hat{J}^2(\theta_\lambda,\phi_\lambda,\psi_\lambda)\Phi_n^{JM\Pi\Gamma_k}(\zeta_\lambda,\rho) = \hbar^2 J(J+1)\Phi_n^{JM\Pi\Gamma_k}(\zeta_\lambda,\rho) \tag{2.4.2}$$

$$\hat{J}_z(\phi_\lambda)\Phi_n^{JM\Pi\Gamma_k}(\zeta_\lambda,\rho) = \hbar M\Phi_n^{JM\Pi\Gamma_k}(\zeta_\lambda,\rho) \tag{2.4.3}$$

$$\hat{\mathcal{I}}(\theta_\lambda,\phi_\lambda,\psi_\lambda)\Phi_n^{JM\Pi\Gamma_k}(\zeta_\lambda,\rho) = (-1)^\Pi\Phi_n^{JM\Pi\Gamma_k}(\zeta_\lambda,\rho) \tag{2.4.4}$$

$$\hat{P}_{ii}^{\Gamma'}(\zeta_\lambda)\Phi_n^{JM\Pi\Gamma_k}(\zeta_\lambda,\rho) = \delta_\Gamma^{\Gamma'}\delta_i^k\Phi_n^{JM\Pi\Gamma_k}(\zeta_\lambda,\rho) \tag{2.4.5}$$

The index n arises from the quantization of the energies of the LHSF, which follows from the finite bounds on the values of the 5 hyperangles. The LHSF energies are shown in appendices B and C to be independent of the quantum number M and the index k and therefore will not carry these labels.

The five-dimensional LHSF are an excellent basis set for expansion of the six-dimensional scattering wavefunction $\Psi^{JM\Pi\Gamma_k}$, since they contain much of the effect of the kinetic energy operators and of the potential energy function, and also because of the separability of the hyperradial part of the hamiltonian from the hyperangular part. The $\Psi^{JM\Pi\Gamma_k}$ are therefore expressed as:

$$\Psi^{JM\Pi\Gamma_k}(\rho,\zeta_\lambda) = \rho^{-\frac{5}{2}}\sum_n b_n^{J\Pi\Gamma}(\rho;\bar{\rho})\Phi_n^{JM\Pi\Gamma_k}(\zeta_\lambda;\bar{\rho}). \tag{2.4.6}$$

Although n spans a denumerably infinite but discrete set of surface functions, in practice it must be truncated at a finite number, determined by appropriate convergence criteria on the final scattering matrices; this will be discussed further in the

second half of this thesis. To solve for these coefficients, the $\Phi_n^{JM\Pi\Gamma_k}$ are determined at a set of discrete values of $\bar{\rho}$. (When we need to distinguish between different values of $\bar{\rho}$, we will label them as $\bar{\rho}_i$, with $i = 0$ for the smallest value of $\bar{\rho}$ and increasing with ρ.) Substituting (2.4.6) into the (time-independent) Schrödinger equation corresponding to the hamiltonian defined by (2.1.7) and using (2.4.1), the coefficients are found to satisfy

$$\left\{-\frac{\hbar^2}{2\mu}\frac{d^2}{d\rho^2}+\frac{15\hbar^2}{8\mu\rho^2}+\left(\frac{\bar{\rho}}{\rho}\right)^2\epsilon_n^{J\Pi\Gamma}(\bar{\rho})-E\right\}b_n^{J\Pi\Gamma}(\rho;\bar{\rho}) + \sum_{n'} b_{n'}^{J\Pi\Gamma}(\rho;\bar{\rho})[\boldsymbol{\mathcal{I}}^{J\Pi\Gamma}]_n^{n'}(\rho;\bar{\rho}) = 0 \tag{2.4.7}$$

in which the interaction matrix $\boldsymbol{\mathcal{I}}^{J\Pi\Gamma}$, which is a measure of the coupling of the LHSF functions by the potential, or equivalently of the change in the wavefunction as a function of ρ from the values at $\rho = \bar{\rho}$, is defined by

$$[\boldsymbol{\mathcal{I}}^{J\Pi\Gamma}]_n^{n'}(\rho;\bar{\rho}) = \left\langle \Phi_n^{JM\Pi\Gamma_k}(\zeta_\lambda;\bar{\rho}) \,\middle|\, \bar{V}(\rho,\omega_\lambda,\gamma_\lambda;\bar{\rho}) \,\middle|\, \Phi_{n'}^{JM\Pi\Gamma_k}(\zeta_\lambda;\bar{\rho})\right\rangle. \tag{2.4.8}$$

As is shown in appendices B and C, these matrices are independent of the quantum number M and index k. The potential of interaction $\bar{V}(\rho,\omega_\lambda,\gamma_\lambda;\bar{\rho})$ is defined as

$$\bar{V}(\rho,\omega_\lambda,\gamma_\lambda;\bar{\rho}) = V(\rho,\omega_\lambda,\gamma_\lambda) - \left(\frac{\bar{\rho}}{\rho}\right)^2 V(\bar{\rho},\omega_\lambda,\gamma_\lambda). \tag{2.4.9}$$

Since we will expand the six-dimensional wavefunction in terms of a finite number of LHSF, the expansion (2.4.6) will become inaccurate for sufficiently large values of $|\rho - \bar{\rho}_i|$, as some of the coupling is with functions excluded from the truncated LHSF basis. Accordingly, the coefficients $b(\rho;\bar{\rho}_i)$ are calculated as a function of ρ in a region near $\bar{\rho}_i$ corresponding to a hyperspherical shell. It is therefore necessary for determination of the scattering wavefunction at all ρ to smoothly match the wave function calculated for each shell across the boundary $\rho = \rho_{i,i+1}$ of adjacent hyperspherical shells. This is accomplished by imposing the conditions

$$b_n^{J\Pi\Gamma}(\rho_{i,i+1};\bar{\rho}_{i+1}) = \sum_{n'} b_{n'}^{J\Pi\Gamma}(\rho_{i,i+1};\bar{\rho}_i)[\boldsymbol{\mathcal{O}}^{J\Pi\Gamma}]_n^{n'}(\bar{\rho}_{i+1},\bar{\rho}_i); \tag{2.4.10}$$

$$\left(\frac{\partial b_n^{J\Pi\Gamma}(\rho;\bar{\rho}_{i+1})}{\partial\rho}\right)_{\rho\to\rho_{i,i+1}^{(+)}} = \sum_{n'}\left(\frac{\partial b_{n'}^{J\Pi\Gamma}(\rho;\bar{\rho}_i)}{\partial\rho}\right)_{\rho\to\rho_{i,i+1}^{(-)}} [\mathcal{O}^{J\Pi\Gamma}]_n^{n'}(\bar{\rho}_{i+1},\bar{\rho}_i); \tag{2.4.11}$$

in which the overlap matrices $\mathcal{O}^{J\Pi\Gamma}$ are defined by

$$[\mathcal{O}^{J\Pi\Gamma}]_n^{n'}(\bar{\rho}_{i+1},\bar{\rho}_i) = \left\langle \Phi_n^{JM\Pi\Gamma_k}(\zeta_\lambda;\bar{\rho}_{i+1}) \,\middle|\, \Phi_{n'}^{JM\Pi\Gamma_k}(\zeta_\lambda;\bar{\rho}_i)\right\rangle. \tag{2.4.12}$$

These matrices are also independent of M and k. Since all terms in the defining equations for the coefficients $b_n^{J\Pi\Gamma}(\rho;\bar{\rho})$ are independent of M and k, these coefficients are also independent of M and k and have been labelled accordingly.

2.5 Expansion of LHSF in Analytic Functions - 2D Surface Functions

We calculate the LHSF by expanding the functions in terms of a basis set of functions with the same permutation symmetry and J, M and Π quantum numbers. The basis set which we chose to use for this expansion is derived from an expansion of the LHSF in terms of analytic functions in four of the five hyperangles, which yields coupled equations for the coefficients of these expansions, which are functions of the remaining angle. The numerical solutions of these equations are not easy to obtain; however, the form of these equations suggests approximate solutions which can be used in the construction of a basis set for an accurate variational calclulation of the LHSF.

A set of two-dimensional surface functions $\psi_{n\Omega}^{J\Pi\Gamma_k}(\omega_\lambda,\gamma_\lambda;\bar{\rho})$ independent of the orientation of the system in space are defined by expansion of the LHSF in terms of Wigner rotation matrices $D_{M\Omega}^J(\phi_\lambda,\theta_\lambda,\psi_\lambda)$:[65]

$$\Phi_n^{JM\Pi\Gamma_k}(\zeta_\lambda;\bar{\rho}) = \sum_{\Omega=0}^{J} D_{M\Omega}^{J\Pi}(\phi_\lambda,\theta_\lambda,\psi_\lambda)\psi_{n\Omega}^{J\Pi\Gamma_k}(\omega_\lambda,\gamma_\lambda;\bar{\rho}). \tag{2.5.1}$$

Here we have used a parity-symmetrized Wigner matrix, which is defined as

$$D_{M\Omega}^{J\Pi} = \left(\frac{2J+1}{32\pi^2}\right)^{\frac{1}{2}} [D_{M\Omega}^J + (-1)^{J+\Pi+\Omega} D_{M,-\Omega}^J]; \quad \Omega \geq 0 \tag{2.5.2}$$

this function is even (odd) with respect to inversion of the system through its center of mass for $\Pi = 0(1)$, and in the case of $\Omega = 0$ is zero when $J + \Pi$ is odd. The functions $D^{J\Pi}_{M\Omega}$ form an orthogonal set with normalization

$$\int D^{J'\Pi'*}_{M'\Omega'}(\phi_\lambda, \theta_\lambda, \psi_\lambda) D^{J\Pi}_{M\Omega}(\phi_\lambda, \theta_\lambda, \psi_\lambda) d\vartheta_1^\lambda = \frac{1}{2}\delta^{J'\Pi'M'\Omega'}_{J\Pi M\Omega}\left[1 + (-1)^{J+\Pi}\delta^\Omega_0\right] \quad (2.5.3)$$

This normalization was chosen to simplify the form of the equations to follow. Replacement of (2.5.3) into (2.4.1) gives

$$\begin{aligned}\hat{h}_\lambda \sum_{\Omega=0}^{J} D^{J\Pi}_{M\Omega}(\phi_\lambda, \theta_\lambda, \psi_\lambda)\psi^{J\Pi\Gamma_k}_{n\Omega}(\omega_\lambda, \gamma_\lambda; \bar{\rho}) \\ = \epsilon^{J\Pi\Gamma}_n \sum_{\Omega=0}^{J} D^{J\Pi}_{M\Omega}(\phi_\lambda, \theta_\lambda, \psi_\lambda)\psi^{J\Pi\Gamma_k}_{n\Omega}(\omega_\lambda, \gamma_\lambda; \bar{\rho})\end{aligned} \quad (2.5.4)$$

Multiplication of both sides of (2.5.4) by $D^{J\Pi*}_{M\Omega'}(\phi_\lambda, \theta_\lambda, \psi_\lambda)$ and integration over the three Euler angles yields an equation coupling the $\psi^{J\Pi\Gamma_k}_{n\Omega}$ in Ω:[2]

$$\begin{aligned}\hat{h}^\Omega_0(\omega_\lambda, \gamma_\lambda; \bar{\rho})\psi^{J\Pi\Gamma_k}_{n\Omega}(\omega_\lambda, \gamma_\lambda; \bar{\rho}) + C^{J\Pi\Omega}_- \hat{h}^\Omega_-(\gamma_\lambda; \bar{\rho}, \omega_\lambda)\psi^{J\Pi\Gamma_k}_{n(\Omega-1)}(\omega_\lambda, \gamma_\lambda; \bar{\rho}) \\ + \hat{h}^\Omega_+(\gamma_\lambda; \bar{\rho}, \omega_\lambda)\psi^{J\Pi\Gamma_k}_{n(\Omega+1)}(\omega_\lambda, \gamma_\lambda; \bar{\rho}) = 0; \quad \Omega \geq \Omega_{\min}\end{aligned} \quad (2.5.5)$$

a common factor of $\frac{1}{2}(1 + (-1)^{J+\Pi}\delta^0_\Omega)$ has been removed, which gives values of $\Omega_{\min} = 0$ for $J + \Pi$ even and 1 for $J + \Pi$ odd. The operators in this equation are

$$\begin{aligned}\hat{h}^\Omega_0(\omega_\lambda, \gamma_\lambda; \bar{\rho}) = \frac{1}{2\mu\bar{\rho}^2}\Bigg\{ \frac{\hbar^2}{\cos^2\frac{\omega_\lambda}{2}}\left[J(J+1) - 2\Omega^2 + \frac{\Omega^2}{\sin^2\gamma_\lambda} - \left(\frac{\partial^2}{\partial\gamma_\lambda{}^2} + \cot\gamma_\lambda\frac{\partial}{\partial\gamma_\lambda}\right)\right] \\ + \frac{\hbar^2}{\sin^2\frac{\omega_\lambda}{2}}\left[\frac{\Omega^2}{\sin^2\gamma_\lambda} - \left(\frac{\partial^2}{\partial\gamma_\lambda{}^2} + \cot\gamma_\lambda\frac{\partial}{\partial\gamma_\lambda}\right)\right] + \hat{L}^2_\lambda(\omega_\lambda)\Bigg\} \\ + V(\bar{\rho}, \omega_\lambda, \gamma_\lambda) - \epsilon^{J\Pi\Gamma}_n(\bar{\rho})\end{aligned} \quad (2.5.6)$$

and

$$\hat{h}^\Omega_\pm(\gamma_\lambda; \bar{\rho}, \omega_\lambda) = \frac{\hbar^2\xi_\pm(J, \Omega)}{2\mu\bar{\rho}^2\cos^2\frac{\omega_\lambda}{2}}\left[(\Omega \pm 1)\cot\gamma_\lambda \pm \frac{\partial}{\partial\gamma_\lambda}\right] \quad (2.5.7)$$

with $\Omega \geq 0$,

$$C^{J\Pi\Omega}_- = (1 - \delta^\Omega_0)(1 + (-1)^{J+\Pi}\delta^\Omega_1) \quad (2.5.8)$$

and

$$\xi_{\pm}(i,k) = [i(i+1) - k(k\pm 1)]^{\frac{1}{2}} \tag{2.5.9}$$

with $i \geq k$ integers. From equations (2.5.7) through (2.5.9), we see that $\hat{h}^J_+ = 0$ and $C^{J\Pi 0}_- = 0$, which restricts the coupling to terms with $\Omega \in [0, J]$.

2.6 Boundary conditions for the $\psi^{J\Pi\Gamma_k}_{n\Omega}$

Certain boundary conditions for the $\psi^{J\Pi\Gamma_k}_{n\Omega}$ will result from the conditions of single-valuedness and differentiability on the $\Phi^{JM\Pi\Gamma_k}_n$. These are imposed when $\gamma_\lambda = \{0, \pi\}$, which correspond to collinear configurations of the system, and are $\psi^{J\Pi\Gamma_k}_{n\Omega}(\omega_\lambda, \gamma_\lambda = \{0,\pi\}; \bar{\rho}) = 0$ for $\Omega \neq 0$ and $\frac{\partial}{\partial \gamma_\lambda}\left[\psi^{J\Pi\Gamma_k}_{n\Omega}(\omega_\lambda, \gamma_\lambda; \bar{\rho})\right]\big|_{\gamma_\lambda = \{0,\pi\}} = 0$ for $\Omega = 0$. These conditions derive from the invariance of the LHSF with respect to the angle ψ_λ, which is indeterminate in the collinear configurations. There is a special case when $\mathbf{R}_\lambda = \mathbf{0}$ (*i.e.*, A_λ coincides with the center of mass of $\{A_\nu, A_\kappa\}$) and $\omega_\lambda = \pi$. For this case, all four angles θ_λ, ϕ_λ, ψ_λ and γ_λ are indeterminate, while in the ν and κ SHC coordinate systems only the angles ψ_ν and ψ_κ, respectively, become indeterminate. For this configuration it is possible for the $\psi^{J\Pi\Gamma_k}_{n\Omega}$ to be multi-valued and still result in single-valued $\Phi^{JM\Pi\Gamma_k}_n$. The form of this behavior can be determined by comparison of the expansion (2.5.1) with a similar expansion in a space-fixed hyperspherical coordinate system

$$\Phi^{JM\Pi\Gamma_k}_n(\zeta_\lambda; \bar{\rho}) = \sum_{\ell=0}^{\infty}\sum_{j=0}^{\infty}\left[\frac{1+(-1)^{j+\ell+\Pi}}{2}\right]\mathcal{Y}^{JM}_{j\ell}(\theta_{\mathbf{r}_\lambda}, \phi_{\mathbf{r}_\lambda}; \theta_\lambda, \phi_\lambda)\varphi^{J\Gamma_k}_{nj\ell}(\omega_\lambda; \bar{\rho}) \tag{2.6.1}$$

in which the angles $\theta_{\mathbf{r}_\lambda}$ and $\phi_{\mathbf{r}_\lambda}$ are the spherical polar coordinates of the $\mathbf{r}_\lambda$ vector with respect to the space-fixed $\mathbf{Z}$ axis and $\mathcal{Y}^{JM}_{j\ell}$ is the Arthurs-Dalgarno function,[66] for which $(-1)^{\ell+j} = (-1)^{\Pi}$ (leading in equation (2.6.1) to the term in square brackets). The boundary conditions on the function $\varphi^{J\Gamma_k}_{nj\ell}$ which follow from the well-behavedness of the LHSF are that when $\omega_\lambda = 0$ (and $\mathbf{r}_\lambda = \mathbf{0}$) $\varphi^{J\Gamma_k}_{nj\ell} = 0$ unless $j = 0$ and $\ell = J$, and at $\omega_\lambda = \pi$ (and $\mathbf{R}_\lambda = \mathbf{0}$) $\varphi^{J\Gamma_k}_{nj\ell} = 0$ unless $j = J$ and $\ell = 0$.

We will use the relationship[2]

$$D^{J}_{M\Omega'}(\phi_\lambda,\theta_\lambda,0)Y^{\Omega'}_{j}(\gamma_\lambda,\psi_\lambda) = (-1)^{j+\Omega'}\left(\frac{4\pi}{2J+1}\right)^{\frac{1}{2}}\sum_{\ell} C(Jj\ell;\Omega',-\Omega',0)\mathcal{Y}^{JM}_{j\ell}(\theta_{r_\lambda},\phi_{r_\lambda};\theta_\lambda,\phi_\lambda) \tag{2.6.2}$$

where $C(Jj\ell;\Omega',-\Omega',0)$ is a Clebsch-Gordon coefficient[67] and $Y^{\Omega}_{j}(\gamma_\lambda,\psi_\lambda)$ a spherical harmonic. Multiplication of both sides of this equation by $C(Jj\ell;\Omega,-\Omega,0)$, summing over Ω and using the orthogonality properties of the Clebsch-Gordon coefficients yields

$$\mathcal{Y}^{JM}_{j\ell}(\theta_{r_\lambda},\phi_{r_\lambda};\theta_\lambda,\phi_\lambda) = \left(\frac{2J+1}{8\pi^2}\right)^{\frac{1}{2}}\sum_{\Omega}(-1)^{j-\Omega}C(Jj\ell;\Omega,-\Omega,0)D^{J}_{M\Omega}(\phi_\lambda,\theta_\lambda,\psi_\lambda)\mathcal{P}^{\Omega}_{j}(\cos\gamma_\lambda) \tag{2.6.3}$$

where $\mathcal{P}^{\Omega}_{j}$ is a normalized associated Legendre function. Substitution of (2.6.3) into (2.6.1), multiplication by $D^{J\Pi*}_{M\Omega'}$ and integrating over the Euler angles yields the relation

$$\psi^{J\Pi\Gamma_k}_{n\Omega}(\omega_\lambda,\gamma_\lambda;\bar{\rho}) = \sum_{j\ell}(-1)^{j-\Omega}\left(\frac{1+(-1)^{j+\ell+\Pi}}{2}\right)C(Jj\ell;\Omega-\Omega 0)\mathcal{P}^{\Omega}_{j}(\cos\gamma_\lambda)\varphi^{J\Gamma_k}_{nj\ell}(\omega_\lambda;\bar{\rho}) \tag{2.6.4}$$

At $\omega_\lambda = \{0,\pi\}$ this reduces to

$$\begin{aligned}\psi^{J\Pi\Gamma_k}_{n\Omega}(0,\gamma_\lambda;\bar{\rho}) &= \left(\frac{1+(-1)^{J+\Pi}}{2}\right)\delta^{0}_{\Omega}\varphi^{J\Gamma_k}_{n0J}(0;\bar{\rho})\\ \psi^{J\Pi\Gamma_k}_{n\Omega}(\pi,\gamma_\lambda;\bar{\rho}) &= \left(\frac{1+(-1)^{J+\Pi}}{2\sqrt{2J+1}}\right)\mathcal{P}^{\Omega}_{J}(\cos\gamma_\lambda)\varphi^{J\Gamma_k}_{nJ0}(\pi;\bar{\rho})\end{aligned} \tag{2.6.5}$$

From this relationship we can see that at $\omega_\lambda = \pi$ the γ_λ dependence of the $\psi^{J\Pi\Gamma_k}_{n\Omega}$ is that of an associated Legendre function if the sum of J and Π is even; if this sum is odd, the function goes to zero.

2.7 Expansion of LHSF in Analytic Functions - 1D Surface Functions

It is useful to factor the $\psi_{n\Omega}^{J\Pi\Gamma_k}$ further into separate terms in ω_λ and γ_λ. The form of the operator $\hat{j}_\lambda^2$ and the boundary conditions on the $\psi_{n\Omega}^{J\Pi\Gamma_k}$ make the associated Legendre functions a good basis set for this factorization. Therefore, we expand these functions as

$$\psi_{n\Omega}^{J\Pi\Gamma_k}(\omega_\lambda,\gamma_\lambda;\bar{\rho}) = \sum_{j=\Omega}^{\infty} \mathcal{P}_j^{\Omega}(\cos\gamma_\lambda)\frac{\phi_{nj\Omega}^{J\Pi\Gamma_k}(\omega_\lambda;\bar{\rho})}{\sin\omega_\lambda}, \tag{2.7.1}$$

where the coefficients $\phi_{nj\Omega}^{J\Pi\Gamma_k}(\omega_\lambda;\bar{\rho})$ are called one-dimensional surface functions. Substitution of this expansion into equation (2.5.5), multiplication by $\mathcal{P}_{j'}^{\Omega'}(\cos\gamma_\lambda)$ and integration over γ_λ leads to the equation satisfied by these functions:

$$\begin{aligned}
&\frac{\hbar^2}{2\mu\bar{\rho}^2}\left(\left\{-4\left(\frac{\partial^2}{\partial\omega_\lambda^2}+1\right)+\frac{\left[J(J+1)-2\Omega^2\right]}{\cos^2\frac{\omega_\lambda}{2}}+\frac{4j(j+1)}{\sin^2\omega_\lambda}\right\}\phi_{nj\Omega}^{J\Pi\Gamma_k}(\omega_\lambda;\bar{\rho})\right.\\
&\left.-\frac{\hbar^2}{\cos^2\frac{\omega_\lambda}{2}}\left\{\xi_+(J,\Omega)\xi_+(j,\Omega)\phi_{nj,\Omega+1}^{J\Pi\Gamma_k}(\omega_\lambda;\bar{\rho})+\xi_-(J,\Omega)\xi_-(j,\Omega)\phi_{nj|\Omega-1|}^{J\Pi\Gamma_k}(\omega_\lambda;\bar{\rho})\right\}\right)\\
&\qquad+\sum_{\bar{\jmath}=\Omega}^{\infty}V_{j\bar{\jmath}}^{\Omega}(\bar{\rho},\omega_\lambda)\phi_{n\bar{\jmath}\Omega}^{J\Pi\Gamma_k}(\omega_\lambda;\bar{\rho})=\epsilon_n^{J\Pi\Gamma}(\bar{\rho})\phi_{nj\Omega}^{J\Pi\Gamma_k}(\omega_\lambda;\bar{\rho}).
\end{aligned} \tag{2.7.2}$$

where the term $V_{j\bar{\jmath}}^{\Omega}$ is given by

$$V_{j\bar{\jmath}}^{\Omega}(\bar{\rho},\omega_\lambda)=\int_0^\pi \mathcal{P}_j^{\Omega}(\cos\gamma_\lambda)V(\bar{\rho},\omega_\lambda,\gamma_\lambda)\mathcal{P}_{\bar{\jmath}}^{\Omega}(\cos\gamma_\lambda)\sin\gamma_\lambda d\gamma_\lambda. \tag{2.7.3}$$

The multiplicative factor $(\sin\omega_\lambda)^{-1}$ has been introduced into (2.7.1) because of the form of equation (2.1.11). The presence of this term forces the boundary conditions $\phi_{nj\Omega}^{J\Pi\Gamma_k}(\omega_\lambda=\{0,\pi\};\bar{\rho})=0$ for equation (2.7.2) in order that the $\Phi_n^{JM\Pi\Gamma_k}$ not diverge at $\omega_\lambda=0,\pi$; in fact, the condition on the $\phi_{nj\Omega}^{J\Pi\Gamma_k}$ to ensure single-valuedness of the LHSF is that they approach zero as $\omega_\lambda\to\{0,\pi\}$ as fast or faster than $\sin\omega_\lambda$. Examination of equation (2.6.5) gives the further conditions

$$\begin{aligned}
\lim_{\omega_\lambda\to 0}\frac{\phi_{nj\Omega}^{J\Pi\Gamma_k}(\omega_\lambda;\bar{\rho})}{\sin\omega_\lambda}&=0 \qquad \Omega\neq 0\\
\lim_{\omega_\lambda\to\pi}\frac{\phi_{nj\Omega}^{J\Pi\Gamma_k}(\omega_\lambda;\bar{\rho})}{\sin\omega_\lambda}&=0 \qquad j\neq J
\end{aligned} \tag{2.7.4}$$

It is important to note that for equation (2.7.2) to be valid, the functions $\phi_{nj\Omega}^{J\Pi\Gamma_k}$ with $\Omega = 0$ must be defined to be identically equal to zero when $J + \Pi$ is odd. The set of equations (2.5.1), (2.7.1), and (2.7.2) are equivalent to equation (2.4.1).

2.8 Basis Set for Expansion of the LHSF

The variational basis set that we have chosen to use to expand the surface functions was suggested by the expansion equation (2.7.1) and by equation (2.7.2). We define functions $t_{vj\Omega}^{J\lambda}(\omega_\lambda;\bar{\rho})$ with associated eigenvalues $e_{vj\Omega}^{J\lambda}(\bar{\rho})$ which satisfy the latter after the Ω and j coupling is removed:

$$\left(-\frac{2\hbar^2}{\mu\bar{\rho}^2}\left\{\frac{\partial^2}{\partial\omega_\lambda^2}+1-\frac{[J(J+1)-2\Omega^2]}{4\cos^2\frac{\omega_\lambda}{2}}-\frac{j(j+1)}{\sin^2\omega_\lambda}\right\}+V_{jj}^{\Omega}(\rho,\omega_\lambda)\right)t_{vj\Omega}^{J\lambda}(\omega_\lambda;\rho)$$
$$= e_{vj\Omega}^{J\lambda}(\rho)t_{vj\Omega}^{J\lambda}(\omega_\lambda;\rho). \tag{2.8.1}$$

These functions are defined to be normalized as

$$\int_0^\pi d\omega_\lambda t_{v'j\Omega}^{J\lambda}(\omega_\lambda;\rho)t_{vj\Omega}^{J\lambda}(\omega_\lambda;\rho)=\delta_v^{v'} \tag{2.8.1a}$$

and are required to satisfy the same boundary conditions as the $\phi_{nj\Omega}^{J\Pi\Gamma_k}$: $t_{vj\Omega}^{J\lambda}(0;\bar{\rho}) = t_{vj\Omega}^{J\lambda}(\pi;\bar{\rho}) = 0$. We now define a five-dimensional variational basis set by

$$\mathrm{F}_{\lambda vj\Omega}^{JM\Pi}(\zeta_\lambda;\bar{\rho}) = D_{M\Omega}^{J\Pi}(\phi_\lambda,\theta_\lambda,\psi_\lambda)\mathcal{P}_j^{\Omega}(\cos\gamma_\lambda)f_{vj\Omega}^{J\lambda}(\omega_\lambda;\bar{\rho}), \tag{2.8.2}$$

where for notational convenience we have introduced the function

$$f_{vj\Omega}^{J\lambda}(\omega_\lambda;\bar{\rho}) = \frac{t_{vj\Omega}^{J\lambda}(\omega_\lambda;\bar{\rho})}{\sin\omega_\lambda} \tag{2.8.3}$$

We desire this five-dimensional basis set to be continuous and differentiable everywhere. From equation (2.6.5), we know that to satisfy this condition, it is necessary that $f_{vj\Omega}^{J\lambda} = 0$ at $\omega_\lambda = 0$ except when $j = \Omega = 0$ and that it be zero at $\omega_\lambda = \pi$ except when $J = j = \Omega = 0$; for these exceptions either the function or its derivative with respect to ω_λ must be zero. These conditions are automatically fulfilled in the

numerical calculation of the $t^{J\lambda}_{vj\Omega}$. When the effective potential does not diverge, *i.e.*, when the potential is finite and $j = 0$ (for $\omega_\lambda = 0$) or $J = j = \Omega = 0$ (for $\omega_\lambda = \pi$), the fact that a general three-body potential $V(\bar{\rho}, \omega_\lambda, \gamma_\lambda)$ has local extrema for collinear configurations, which set includes the configurations with $\omega_\lambda = 0$ and π, implies that the effective potential will have zero derivative in the region of the endpoints; in this local region, the $t^{J\lambda}_{vj\Omega}$ behave as solutions of a second-order linear differential equation with constant coefficients, *i.e.*, as $C \sin K_{0,\pi}\omega_\lambda + D \cos K_{0,\pi}\omega_\lambda$ where

$$\begin{aligned} K_0 &= \sqrt{1 - \frac{1}{4}[J(J+1) - 2\Omega^2] - \frac{\mu\rho^2}{2\hbar^2}\left[V^{\Omega}_{jj}(\rho, 0) - e^{J\lambda}_{vj\Omega}(\rho)\right]} \\ K_\pi &= \sqrt{1 - \frac{\mu\rho^2}{2\hbar^2}\left[V^{\Omega}_{jj}(\rho, \pi) - e^{J\lambda}_{vj\Omega}(\rho)\right]} \end{aligned} \tag{2.8.4}$$

With the boundary conditions that $t^{J\lambda}_{vj\Omega} = 0$ when $\omega_\lambda = 0, \pi$, we find that near $\omega_\lambda = 0$, $t^{J\lambda}_{vj\Omega}$ behaves as $\sin K_0 \omega_\lambda$ and that near $\omega_\lambda = \pi$ it behaves as $\sin K_\pi(\pi - \omega_\lambda)$ for real K; for imaginary K it behaves as $\sinh |K| \omega_\lambda$ near $\omega_\lambda = 0$ and as $\sinh |K|(\pi - \omega_\lambda)$ near $\omega_\lambda = \pi$. From this result, it can be seen that $f^{J\lambda}_{vj\Omega}$ will limit to a constant value with zero derivative when $\omega_\lambda = \{0, \pi\}$. When the effective potential of equation (2.8.1) diverges at these values of ω_λ due to divergence of the terms depending on $\csc^2 \omega_\lambda$ and $\sec^2 \frac{\omega_\lambda}{2}$, it is growing quadratically as $\omega_\lambda \to 0$ or π, and in these regions the $t^{J\lambda}_{vj\Omega}$ will go to zero as $e^{-c\omega_\lambda{}^2}$ as ω_λ approaches zero or as $e^{-c(\pi-\omega_\lambda)^2}$ as ω_λ approaches π. Consequently, under these conditions the $f^{J\lambda}_{vj\Omega}$ will go to zero.

Since this basis set is concentrated in the λ arrangement channel region when $\bar{\rho}$ is sufficiently large, accurate representation of the LHSF probability density concentrated in the ν and κ channels may require a large number of terms at such values of $\bar{\rho}$. In addition, the condition that the 5D basis be single-valued is overly restrictive for $\omega_\lambda = \pi$, at which value these criteria are not met by the two-dimensional surface functions of equation (2.5.1) when $J > 0, J + \Pi$ even. As a result, a more efficient basis set is constructed by taking the union of the basis sets $\mathrm{F}^{JM\Pi}_{\lambda vj\Omega}, \mathrm{F}^{JM\Pi}_{\nu vj\Omega}$ and $\mathrm{F}^{JM\Pi}_{\kappa vj\Omega}$; this basis will then be able to well represent the surface functions in all

channels. (It should be noted that the functions $F^{JM\Pi}_{\nu vj\Omega}$ and $F^{JM\Pi}_{\kappa vj\Omega}$ with $\Omega = 0$ and general J are not forced to zero at $\omega_\lambda = \pi$, unlike the $F^{JM\Pi}_{\lambda vj\Omega}$ functions.) Furthermore, for systems with P_2 or P_3 permutation symmetry, the functions in one of a set of indistinguishable channels can be generated from the functions in another by application of the permutation operators $\hat{O}_R$ of equation (2.2.1), and accordingly we can construct symmetrized basis sets which belong to the irreducible representations of that symmetry group. We will refer to the symmetrized basis sets as "primitives" to distinguish between them and the unsymmetrized basis sets $F^{JM\Pi}_{\lambda vj\Omega}$.

We define the index τ in the symmetrized primitives $F^{JM\Pi\Gamma_k}_{\tau vj\Omega}$ to distinguish between different types of primitives in the P_2 permutation group. It will denote a set of indistinguishable arrangement channels, so that for a system with P_3 permutation symmetry it takes on only one value: A (since all three arrangement channels have the same asymptotic form of A + A_2). As a consequence, there is only one type of primitive contributing to each irreducible representation, and the τ label is not really necessary for the P_3 group. For the P_1 group, there is a single IR and all primitive functions contribute to it, in a direct union of the three arrangement channel basis sets into a larger basis; as the primitives in each channel form a different type of contributing basis set, the τ values A, B and C give no new information, corresponding to the arrangement channel labels α, β and γ. However, in the P_2 group, τ takes on one of the two values A and B, corresponding to the A + B_2 channel and either of the AB + B channels, respectively; thus there will be two types of primitives contributing to each of the two IR, the A+B_2 type (with even or odd exchange symmetry depending on Γ) and the appropriate even or odd linear combination of the unsymmetrized functions from the two AB + B channels, and the τ index is needed to distinguish between these sets of primitives. It is the union of the sets of primitives with different τ values that form the complete primitive basis set for our calculation.

The results of application of the various permutation operations $\hat{O}_R$ to the basis

functions is given in table 2.2 for each permutation symmetry P_p. The factors $(-1)^j$ appear in this table since the functions $\mathrm{F}^{JM\Pi}_{\lambda v j \Omega}$ have certain symmetries with respect to the changes in the angular variables caused by the two-particle permutations (2.2.3) through (2.2.5); these derive from the properties of the Wigner rotation functions and the associated Legendre functions:

$$D^{J\Pi}_{M\Omega}(\phi_\lambda, \theta_\lambda, \pi + \psi_\lambda) = (-1)^\Omega D^{J\Pi}_{M\Omega}(\phi_\lambda, \theta_\lambda, \psi_\lambda) \tag{2.8.5}$$

$$\mathcal{P}^\Omega_j\big(\cos(\pi - \gamma_\lambda)\big) = (-1)^{j+\Omega}\mathcal{P}^\Omega_j(\cos\gamma_\lambda) \tag{2.8.6}$$

The symmetrized primitives are obtained by taking the appropriate linear combinations of these functions as defined in equation (2.2.8) for the IR Γ_k; the general form for the primitives is therefore

$$\mathrm{F}^{JM\Pi\Gamma_k}_{\tau v j \Omega}(\zeta_{\bar\lambda}; \bar\rho) = \sum_\lambda c^{\Gamma_k}_{\tau\lambda j}\mathrm{F}^{JM\Pi}_{\lambda v j \Omega}(\zeta_\lambda[\zeta_{\bar\lambda}]; \bar\rho), \tag{2.8.7}$$

where $\bar\lambda$ is fixed and can be chosen to be α arbitrarily, and the constants $c^{\Gamma_k}_{\tau\lambda j}$ (given in table 2.3) are easily determined from the functions of table 2.2 and the $\mathbf{d}^\Gamma$ matrix elements in table 2.1.

The normalization for the τ =B coefficients of the P_2 group and all coefficients of the P_3 group has been changed from that which is produced by the projection operators. This has been done in order to simplify properties of the scattering formalism to be discussed in the second paper in this series and to remove trivial dependence of the integral matrices on k; with a different choice, the matrices for different k would be related by similarity transforms; our choice makes the matrices identical. As a consequence, we need only use one value of k in our calculations to obtain all the information necessary for scattering calculations in the E symmetry.

There is a subtlety in the definition of the primitives for the E symmetries of P_3 which should be mentioned. Since the E IR matrices are defined to make the functions generated from the permutation operator either even or odd with respect to the atoms labelled β and γ, a basis set generated from an unsymmetrized basis

function in the α channel coordinates will be incomplete; the α channel function already has symmetry with respect to this interchange, and consequently there will be no representation of functions with the opposite symmetry in the basis set so generated. (This precludes the use of the character table for projecting the E symmetry part of the unsymmetrized function, as is suggested in Hamermesh[64], since the character table is independent of arrangement channel and therefore will not generate the opposite symmetry functions for any choice of initial coordinates.) The basis set for this case and for the P_2 case with $\tau = \mathrm{B}$ were generated from the β channel function; the functions generated from the γ channel are the same except for an (unimportant) factor of $(-1)^j$ multiplying the primitives.

For certain Γ and τ, the coefficients $c^{\Gamma_k}_{\tau\lambda j}$ are zero for all even j or all odd j, and thus some of the primitive functions as defined by equation (2.8.7) also are zero; it will therefore be useful to define the rectangular matrix

$$\left[\mathbf{C}^{\Gamma_k}\right]^{\lambda v' j' \Omega'}_{\tau v j \Omega} = \delta^{v j \Omega}_{v' j' \Omega'} c^{\Gamma_k}_{\tau\lambda j} \tag{2.8.8}$$

and express (2.8.7) as

$$\mathrm{F}^{JM\Pi\Gamma_k}_{\tau v j \Omega}(\zeta_{\bar{\lambda}}; \bar{\rho}) = \sum_{\lambda v' j' \Omega'} C^{\Gamma_k \lambda v' j' \Omega'}_{\tau v j \Omega} \mathrm{F}^{JM\Pi}_{\lambda v' j' \Omega'}(\zeta_\lambda[\zeta_{\bar{\lambda}}]; \bar{\rho}), \tag{2.8.9}$$

where the range of values of j is not required to be the same as that of j', and thus eliminate these functions.

The five-dimensional LHSF are now expanded in terms of these primitives:

$$\Phi^{JM\Pi\Gamma_k}_n(\zeta_\lambda; \bar{\rho}) = \sum_{\tau v j \Omega} a^{J\Pi\Gamma}_{\tau v j \Omega n}(\bar{\rho}) \mathrm{F}^{JM\Pi\Gamma_k}_{\tau v j \Omega}(\zeta_\lambda; \bar{\rho}) \tag{2.8.10}$$

The primitive basis set is not orthogonal, since the variational basis sets with different λ overlap; therefore, calculation of the $a^{J\Pi\Gamma}_{\tau v j \Omega m}$ coefficients requires the determination of overlap integrals for the variational basis set as well as integrals involving the hamiltonian. The generalized eigenvalue equation which results is

$$\mathbf{H}^{J\Pi\Gamma}(\bar{\rho})\mathbf{a}^{J\Pi\Gamma}(\bar{\rho}) = \mathbf{M}^{J\Pi\Gamma}(\bar{\rho})\mathbf{a}^{J\Pi\Gamma}(\bar{\rho})\mathbf{E}^{J\Pi\Gamma}(\bar{\rho}) \tag{2.8.11}$$

in which

$$\left[\mathbf{H}^{J\Pi\Gamma}(\bar{\rho})\right]_{\tau v j\Omega}^{\tau' v' j'\Omega'} = \left\langle \mathrm{F}_{\tau v j\Omega}^{JM\Pi\Gamma_k}(\zeta_\lambda;\bar{\rho}) \mid \hat{h}_\lambda \mid \mathrm{F}_{\tau' v' j'\Omega'}^{JM\Pi\Gamma_k}(\zeta_\lambda;\bar{\rho})\right\rangle \tag{2.8.12}$$

$$\left[\mathbf{a}^{J\Pi\Gamma}(\bar{\rho})\right]_{n}^{\tau' v' j'\Omega'} = a_{\tau' v' j'\Omega' n}^{J\Pi\Gamma} \tag{2.8.13}$$

$$\left[\mathrm{M}^{J\Pi\Gamma}(\bar{\rho})\right]_{\tau v j\Omega}^{\tau' v' j'\Omega'} = \left\langle \mathrm{F}_{\tau v j\Omega}^{JM\Pi\Gamma_k}(\zeta_\lambda;\bar{\rho}) \mid \mathrm{F}_{\tau' v' j'\Omega'}^{JM\Pi\Gamma_k}(\zeta_\lambda;\bar{\rho})\right\rangle \tag{2.8.14}$$

$$\left[\mathbf{E}^{J\Pi\Gamma}(\bar{\rho})\right]_{n'}^{n} = \delta_{n}^{n'}\epsilon_{n}^{J\Pi\Gamma}(\bar{\rho}) \tag{2.8.15}$$

The interaction and overlap matrices of equations (2.4.8) and (2.4.12) can also be expressed in terms of the primitive basis set integrals. Substitution of equation (2.8.10) into these equations yields

$$\boldsymbol{\mathcal{I}}^{J\Pi\Gamma}(\rho;\bar{\rho}) = \tilde{\mathbf{a}}^{J\Pi\Gamma}(\bar{\rho})(\boldsymbol{\mathcal{I}}p)^{J\Pi\Gamma}(\rho;\bar{\rho})\mathbf{a}^{J\Pi\Gamma}(\bar{\rho}) \tag{2.8.16}$$

$$\boldsymbol{\mathcal{O}}^{J\Pi\Gamma}(\bar{\rho}_{i+1},\bar{\rho}_i) = \tilde{\mathbf{a}}^{J\Pi\Gamma}(\bar{\rho}_{i+1})(\boldsymbol{\mathcal{O}}p)^{J\Pi\Gamma}(\bar{\rho}_{i+1},\bar{\rho}_i)\mathbf{a}^{J\Pi\Gamma}(\bar{\rho}_i) \tag{2.8.17}$$

where

$$[(\boldsymbol{\mathcal{I}}p)^{J\Pi\Gamma}]_{\tau v j\Omega}^{\tau' v' j'\Omega'}(\rho;\bar{\rho}) = \left\langle \mathrm{F}_{\tau v j\Omega}^{JM\Pi\Gamma_k}(\zeta_\lambda;\bar{\rho}) \mid \bar{V}(\rho,\omega_\lambda,\gamma_\lambda;\bar{\rho}) \mid \mathrm{F}_{\tau' v' j'\Omega'}^{JM\Pi\Gamma_k}(\zeta_\lambda;\bar{\rho})\right\rangle \tag{2.8.18}$$

$$[(\boldsymbol{\mathcal{O}}p)^{J\Pi\Gamma}]_{\tau v j\Omega}^{\tau' v' j'\Omega'}(\bar{\rho}_{i+1},\bar{\rho}) = \left\langle \mathrm{F}_{\tau v j\Omega}^{JM\Pi\Gamma_k}(\zeta_\lambda;\bar{\rho}_{i+1}) \mid \mathrm{F}_{\tau' v' j'\Omega'}^{JM\Pi\Gamma_k}(\zeta_\lambda;\bar{\rho}_{i+1})\right\rangle \tag{2.8.19}$$

2.9 Calculation of Surface Functions and Propagation Matrices

The quadrature for the matrices of integrals in equation (2.8.11), (2.8.16) and (2.8.17) are the most CPU intensive part of the surface function calculation. It has proven to be most efficient to calculate matrices of integrals of the non-symmetrized functions $\mathrm{F}^{JM\Pi}_{\lambda v j\Omega}$ as if the three particles were distinguishable and use the coefficients $c^{\Gamma_k}_{\tau\lambda j}$ to assemble the desired irreducible representation matrices. The integration is performed in two parts, of which the first is integration involving a λ channel basis function $\mathrm{F}^{JM\Pi}_{\lambda v' j'\Omega'}$ with the result of an operation on another λ channel basis function $\mathrm{F}^{JM\Pi}_{\lambda v j\Omega}$, which we will refer to as $\lambda\lambda$ integrals, and the second the integration of a ν channel basis function $\mathrm{F}^{JM\Pi}_{\nu v' j'\Omega'}$ with the result of an operation on the λ channel basis functions $\mathrm{F}^{JM\Pi}_{\lambda v j\Omega}$, which are known as $\nu\lambda$ integrals. (The operations referred to are the 5D hamiltonian for the **H** matrix, the potential function $\bar{V}$ for the $\boldsymbol{\mathcal{I}}$ matrix, and **I** for the **M** and $\boldsymbol{\mathcal{O}}$ matrices. It is true in general that the matrix of integrals $\lambda\nu$, where the operation is performed on the ν channel basis functions, is the transpose of the $\nu\lambda$ integral matrix, since all these operators are Hermitian and the integrals are real (see Appendix B), so it is not necessary to explicitly calculate these integrals; the $\lambda\lambda$ matrix of integrals is symmetric by the same reasoning.) In the general case where there is no permutation symmetry, it is necessary to let λ take on all values $\{\alpha,\beta,\gamma\}$ to determine the full set of integrals for the calculation. When there are indistinguishable channels in the system, it is sufficient to calculate integrals within and between all distinguishable channels. In the P_2 case, the $\gamma\gamma$ integral matrix will be the same as the $\beta\beta$ matrix; in addition, formally expressing the integral of the functions $F^{J\Pi\Gamma=A'}_{\tau=\mathrm{A}\ v j\Omega}$ and $F^{J\Pi\Gamma=A''}_{\tau=\mathrm{B}\ v' j'\Omega'}$ (which is zero by symmetry) and the integral of the functions $F^{J\Pi\Gamma=A''}_{\tau=\mathrm{A}\ v j\Omega}$ and $F^{J\Pi\Gamma=A'}_{\tau=\mathrm{B}\ v' j'\Omega'}$ in terms of the $\lambda\lambda$ and $\nu\lambda$ type integrals leads to the result that

$$\langle \mathrm{F}^{JM\Pi}_{\alpha v j\Omega} | \mathrm{F}^{JM\Pi}_{\beta v' j'\Omega'} \rangle = (-1)^{j+j'} \langle \mathrm{F}^{JM\Pi}_{\alpha v j\Omega} | \mathrm{F}^{JM\Pi}_{\gamma v' j'\Omega'} \rangle; \quad P_p, p \in [2,3] \tag{2.9.1}$$

therefore, λ will need to take on only the two values α and β to fully determine all necessary integrals. The threefold symmetry of the P_3 case allows us to generate

from (2.9.1) the stronger relationships

$$\langle \mathrm{F}^{JM\Pi}_{\lambda v j\Omega} | \mathrm{F}^{JM\Pi}_{\nu v' j'\Omega'} \rangle = (-1)^{j+j'} \langle \mathrm{F}^{JM\Pi}_{\lambda v j\Omega} | \mathrm{F}^{JM\Pi}_{\kappa v' j'\Omega'} \rangle$$

$$P_p, p = 3 \qquad (2.9.2)$$

$$\langle \mathrm{F}^{JM\Pi}_{\lambda v j\Omega} | \mathrm{F}^{JM\Pi}_{\nu v' j'\Omega'} \rangle = (-1)^{j+j'} \langle \mathrm{F}^{JM\Pi}_{\nu v j\Omega} | \mathrm{F}^{JM\Pi}_{\lambda v' j'\Omega'} \rangle;$$

thus in this case, a single value of λ suffices to determine the full set of integrals.

The IR integral matrices may be determined from these distinguishable particle matrices in the following manner: we substitute equation (2.8.9) into equation (2.8.14) to yield

$$\left[\mathrm{M}^{J\Pi\Gamma_k}(\bar{\rho})\right]^{\tau' v' j'\Omega'}_{\tau v j\Omega} = \sum_{\bar{\lambda}\bar{v}\bar{j}\bar{\Omega}} \sum_{\bar{\lambda}'\bar{v}'\bar{j}'\bar{\Omega}'} (C^{\Gamma_k})^{\bar{\lambda}\bar{v}\bar{j}\bar{\Omega}}_{\tau v j\Omega} (C^{\Gamma_k})^{\bar{\lambda}'\bar{v}'\bar{j}'\bar{\Omega}'}_{\tau' v' j'\Omega'} \times \left\langle \mathrm{F}^{JM\Pi}_{\bar{\lambda}\bar{v}\bar{j}\bar{\Omega}}(\zeta_{\bar{\lambda}}; \bar{\rho}) \,\middle|\, \mathrm{F}^{JM\Pi}_{\bar{\lambda}'\bar{v}'\bar{j}'\bar{\Omega}'}(\zeta_{\bar{\lambda}'}; \bar{\rho}) \right\rangle \qquad (2.9.3)$$

If the distinguishable particle matrices $\mathrm{M}_{\lambda\lambda}$ and $\mathrm{M}_{\nu\lambda}$ are joined to form a matrix $(\mathrm{M}d)$ which has α, β and γ as part of the row and column indices:

$$\mathrm{M}d = \begin{bmatrix} \mathrm{M}_{\alpha\alpha} & \mathrm{M}_{\alpha\beta} & \mathrm{M}_{\alpha\gamma} \\ \mathrm{M}_{\beta\alpha} & \mathrm{M}_{\beta\beta} & \mathrm{M}_{\beta\gamma} \\ \mathrm{M}_{\gamma\alpha} & \mathrm{M}_{\gamma\beta} & \mathrm{M}_{\gamma\gamma} \end{bmatrix} \qquad (2.9.4)$$

this expression may be written in matrix form as

$$\mathrm{M}^{J\Pi\Gamma_k}(\bar{\rho}) = \tilde{\mathbf{C}}^{\Gamma_k} (\mathrm{M}d)^{J\Pi}(\bar{\rho}) \mathbf{C}^{\Gamma_k} \qquad (2.9.5)$$

Similar expressions may be written for all of the IR integral matrices; an example for the E symmetry of the P_3 permutation group is given in Appendix C.

The $\lambda\lambda$ integrals are relatively simple to calculate, as the integration over the angles $\theta_\lambda, \phi_\lambda, \psi_\lambda$ and γ_λ can be done analytically; the results of these integrations (which are performed explicitly in Appendix B) are

$$\begin{aligned}\left[\mathbf{M}^{J\Pi}_{\lambda\lambda}(\bar{\rho})\right]^{v'j'\Omega'}_{vj\Omega} &= \left\langle \mathrm{F}^{JM\Pi}_{\lambda vj\Omega}(\zeta_\lambda;\bar{\rho}) \mid \mathrm{F}^{JM\Pi}_{\lambda v'j'\Omega'}(\zeta_\lambda;\bar{\rho})\right\rangle \\ &= \frac{1}{2}\delta^{v'j'\Omega'}_{v\ j\ \Omega}\left[1+(-1)^{J+\Pi}\delta^{\Omega}_{0}\right]\end{aligned} \tag{2.9.6}$$

$$\begin{aligned}\left[\mathbf{H}^{J\Pi}_{\lambda\lambda}(\bar{\rho})\right]^{v'j'\Omega'}_{vj\Omega} &= \left\langle \mathrm{F}^{JM\Pi}_{\lambda vj\Omega}(\zeta_\lambda;\bar{\rho}) \mid \hat{h}_\lambda \mid \mathrm{F}^{JM\Pi}_{\lambda v'j'\Omega'}(\zeta_\lambda;\bar{\rho})\right\rangle \\ &= \frac{1}{2}\Bigg[\delta^{\Omega}_{\Omega'}\left(1+(-1)^{J+\Pi}\delta^{\Omega}_{0}\right)\Bigg(\delta^{v\ j}_{v'\ j'}e^{J\lambda}_{vj\Omega}(\bar{\rho}) + \\ &\quad (1-\delta^{j}_{j'})\int_0^{\pi}\sin^2\omega_\lambda d\omega_\lambda V^{\Omega}_{j'j}(\bar{\rho},\omega_\lambda)f^{J\lambda}_{vj\Omega}(\omega_\lambda;\bar{\rho})f^{J\lambda}_{v'j'\Omega}(\omega_\lambda;\bar{\rho})\Bigg) \\ &\quad -\frac{\hbar^2}{2\mu\rho^2}\delta^{j}_{j'}\Bigg(\delta^{\Omega'}_{\Omega-1}\xi_+(J,\Omega')\xi_+(j,\Omega')\int_0^{\pi}\sin^2\omega_\lambda\sec^2\frac{\omega_\lambda}{2}d\omega_\lambda\times \\ &\qquad f^{J\lambda}_{v'j\Omega'}(\omega_\lambda;\bar{\rho})f^{J\lambda}_{v'j(\Omega'+1)}(\omega_\lambda;\bar{\rho}) \\ &\quad +\left(\delta^{\Omega'}_{\Omega+1}+(-1)^{J+\Pi}\delta^{\Omega'}_{1-\Omega}\right)\xi_-(J,\Omega')\xi_-(j,\Omega')\int_0^{\pi}\sin^2\omega_\lambda\sec^2\frac{\omega_\lambda}{2}d\omega_\lambda\times \\ &\qquad f^{J\lambda}_{v'j\Omega'}(\omega_\lambda;\bar{\rho})f^{J\lambda}_{vj|\Omega'-1|}(\omega_\lambda;\bar{\rho})\Bigg)\Bigg]\end{aligned} \tag{2.9.7}$$

Each of the integrals of (2.9.7) is one-dimensional, and the corresponding numerical quadrature can be performed with a very small amount of computer time when compared to the two-dimensional numerical quadratures considered below.

For the $\nu\lambda$ integration, only the integral over the three Euler angles $(\theta_\lambda, \phi_\lambda, \psi_\lambda)$ is analytic, and the integration over ω_λ and γ_λ must be performed numerically. The equations for the $\nu\lambda$ integral matrices are

$$\begin{aligned}\left[\mathbf{M}^{J\Pi}_{\nu\lambda}\right]^{v'j'\Omega'}_{vj\Omega} &= \left\langle \mathrm{F}^{JM\Pi}_{\nu vj\Omega}\left(\zeta_\nu[\zeta_\lambda];\bar{\rho}\right) \mid \mathrm{F}^{JM\Pi}_{\lambda v'j'\Omega'}(\zeta_\lambda;\bar{\rho})\right\rangle \\ &= \int\int d\vartheta^{\lambda}_{2}\mathcal{P}^{\Omega'}_{j'}(\cos\gamma_\lambda)\mathcal{P}^{\Omega}_{j}\left(\cos\gamma_\nu[\omega_\lambda,\gamma_\lambda]\right)\times \\ &\quad f^{J\lambda}_{v'j'\Omega'}(\omega_\lambda;\bar{\rho})f^{J\nu}_{vj\Omega}[\omega_\nu(\omega_\lambda,\gamma_\lambda);\bar{\rho}]d^{J\Pi}_{\Omega'\Omega}[\Delta_{\nu\lambda}(\omega_\lambda,\gamma_\lambda)]\end{aligned} \tag{2.9.8}$$

$$[\mathbf{H}^{J\Pi}_{\nu\lambda}]^{v'j'\Omega'}_{vj\Omega} = \langle \mathrm{F}^{JM\Pi}_{\nu vj\Omega}(\zeta_\nu[\zeta_\lambda];\bar{\rho}) \mid \hat{h}_\lambda \mid \mathrm{F}^{JM\Pi}_{\lambda v'j'\Omega'}(\zeta_\lambda;\bar{\rho})\rangle$$

$$= \int\int d\vartheta_2^\lambda \mathcal{P}_j^\Omega(\cos\gamma_\nu[\omega_\lambda,\gamma_\lambda])\, f^{J\lambda}_{v'j'\Omega'}(\omega_\lambda;\bar{\rho}) f^{J\nu}_{vj\Omega}[\omega_\nu(\omega_\lambda,\gamma_\lambda);\bar{\rho}]\times$$

$$\Big\{\mathcal{P}_{j'}^{\Omega'}(\cos\gamma_\lambda)\big[V(\bar{\rho},\omega_\lambda,\gamma_\lambda) + e^{J\lambda}_{v'j'\Omega'}('rb) - V^\Omega_{jj}(\bar{\rho},\omega_\lambda)\big] d^{J\Pi}_{\Omega'\Omega}(\Delta_{\nu\lambda}[\omega_\lambda,\gamma_\lambda]$$

$$- \frac{\hbar^2 \sec^2\frac{\omega_\lambda}{2}}{2\mu\bar{\rho}^2}\Big[\xi_+(J,\Omega')\xi_+(j,\Omega')\mathcal{P}_{j'}^{\Omega'+1}(\cos\gamma_\lambda) d^{J\Pi}_{\Omega'+1,\Omega}(\Delta_{\nu\lambda}[\omega_\lambda,\gamma_\lambda$$

$$+ \xi_-(J,\Omega')\xi_-(j,\Omega')\mathcal{P}_{j'}^{\Omega'-1}(\cos\gamma_\lambda) d^{J\Pi}_{\Omega'-1,\Omega}(\Delta_{\nu\lambda}[\omega_\lambda,\gamma_\lambda])\Big]\Big\} \qquad (2$$

where the parity $\mathbf{d}^{J\Pi}$ matrix is the result of the integration over the Euler ang

$$\int D^{J\Pi *}_{M\Omega}(\phi_\nu,\theta_\nu,\psi_\nu) D^{J\Pi}_{M\Omega'}(\phi_\lambda,\theta_\lambda,\psi_\lambda) d\vartheta_1^\lambda = d^{J\Pi}_{\Omega'\Omega}(\Delta_{\nu\lambda}[\omega_\lambda,\gamma_\lambda])$$

$$= \frac{1}{2}\left(d^J_{\Omega',\Omega}(\Delta_{\nu\lambda}[\omega_\lambda,\gamma_\lambda]) + (-1)^{J+\Pi+\Omega'} d^J_{-\Omega',\Omega}(\Delta_{\nu\lambda}[\omega_\lambda,\gamma_\lambda])\right) \qquad (2.9$$

and the $d^J_{\Omega'\Omega}$ are as defined by Davydov.[65] $\Delta_{\nu\lambda}$ is the angle (in the 0 to π ra between the $\mathbf{R}_\lambda$ and $\mathbf{R}_\nu$ axes which is expressed in $\omega_\lambda,\gamma_\lambda$ coordinates as[2]

$$\cos\Delta_{\nu\lambda}(\omega_\lambda,\gamma_\lambda) = \frac{\mathbf{R}_\nu\cdot\mathbf{R}_\lambda}{R_\nu R_\lambda}$$

$$= -\sec\frac{\omega_\nu(\omega_\lambda,\gamma_\lambda)}{2}\left[\cos\beta_{\nu\lambda}\cos\frac{\omega_\lambda}{2} + \sin\beta_{\nu\lambda}\sin\frac{\omega_\lambda}{2}\cos\gamma_\lambda\right] \qquad (2.9.1$$

where the angle $\beta_{\nu\lambda}$ is dependent only on the masses of the three atoms:

$$\tan\beta_{\nu\lambda} = \left(\frac{m_\kappa(m_\lambda+m_\nu+m_\kappa)}{m_\nu m_\lambda}\right)^{\frac{1}{2}}, \quad 0\le\beta_{\nu\lambda}\le\frac{\pi}{2} \qquad (2.9$$

For sufficiently large values of $\bar{\rho}$ and for total energies significantly below system's dissociation energy into three isolated atoms (which will be the case in thesis; generalization to higher energies is however possible), the overlap bet functions in the λ channel and the ν channel may be taken to be zero, due to limited extent in ω_λ and ω_ν of $f^{J\lambda}_{vj\Omega}$ and $f^{J\nu}_{v'j'\Omega'}$, respectively; thus in these

the $\nu\lambda$ integrals vanish, which greatly reduces the numerical work necessary for the LHSF calculation. In systems with P_1 or P_2 symmetry, the overlap between one pair of channels may vanish before that of a different pair, and this is taken into account as well.

Once the necessary integrals have been calculated, the $a^{J\Pi\Gamma_n^k}_{vj\Omega n}$ coefficients are determined by a generalized eigenvalue-eigenvector procedure. Since our primitive basis set is not an orthogonal set and is overcomplete[68], the matrix $\mathbf{M}^{J\Pi\Gamma}$ is formally nonnegative definite if in (2.8.9) a complete (*i.e.*, infinite) set of $\mathrm{F}^{JM\Pi}_{\lambda v'j'\Omega'}$ is included for each λ; if these sets are truncated, then $\mathbf{M}^{J\Pi\Gamma}$ is formally positive definite. However, with the introduction of errors stemming from the finite accuracy of the computer operations (including error) and of the numerical algorithms used, it is possible to obtain negative eigenvalues for this matrix. The standard methods of solving generalized eigenvalue problems, which assume a positive definite M matrix, will therefore not be applicable. We have therefore developed a method to find the eigenvalues of the system when the M matrix is not positive definite, which will be described in the next section.

The integrals which make up the primitive basis set form of the interaction and overlap matrices (defined in equations (2.8.18) and (2.8.19), respectively) are calculated in the same way, *i.e.*, the unsymmetrized $\lambda\lambda$ and $\nu\lambda$ forms are calculated and then linearly combined to give the primitive basis set form. The integrals for the interaction matrix have the form

$$\begin{aligned}\left[(\mathcal{I}p)^{J\Pi}_{\lambda\lambda}(\rho;\bar{\rho})\right]^{v'j'\Omega'}_{vj\Omega} &= \left\langle \mathrm{F}^{JM\Pi}_{\lambda vj\Omega}(\zeta_\lambda;\bar{\rho}) \mid \bar{V}(\rho,\omega_\lambda,\gamma_\lambda;\bar{\rho}) \mid \mathrm{F}^{JM\Pi}_{\lambda v'j'\Omega'}(\zeta_\lambda;\bar{\rho})\right\rangle \\ &= \delta^{\Omega'}_{\Omega}\frac{1+(-1)^{J+\Pi}\delta^{\Omega}_{0}}{2}\int_0^{\pi}\sin^2\omega_\lambda d\omega_\lambda f^{J\lambda}_{vj\Omega}(\omega_\lambda;\bar{\rho})f^{J\lambda}_{v'j'\Omega}(\omega_\lambda;\bar{\rho})\times \\ &\quad \left(V^{\Omega}_{jj'}(\rho,\omega_\lambda)-\left(\frac{\bar{\rho}}{\rho}\right)^2 V^{\Omega}_{jj'}(\bar{\rho},\omega_\lambda)\right)\end{aligned} \tag{2.9.13}$$

$$\begin{aligned}\left[(\mathcal{I}p)^{J\Pi}_{\nu\lambda}(\rho;\bar{\rho})\right]^{v'j'\Omega'}_{vj\Omega} &= \left\langle \mathrm{F}^{JM\Pi}_{\nu vj\Omega}(\zeta_\nu[\zeta_\lambda];\bar{\rho}) \mid \bar{V}(\rho,\omega_\lambda,\gamma_\lambda;\bar{\rho}) \mid \mathrm{F}^{JM\Pi}_{\lambda v'j'\Omega'}(\zeta_\lambda;\bar{\rho})\right\rangle \\ &= \int\int d\vartheta_2^\lambda \mathcal{P}^{\Omega'}_{j'}(\cos\gamma_\lambda)\mathcal{P}^{\Omega}_{j}\left(\cos\gamma_\nu[\omega_\lambda,\gamma_\lambda]\right)\bar{V}(\rho,\omega_\lambda,\gamma_\lambda;\bar{\rho})\times \\ &\quad f^{J\lambda}_{v'j'\Omega'}(\omega_\lambda;\bar{\rho}) f^{J\nu}_{vj\Omega}(\omega_\nu[\omega_\lambda,\gamma_\lambda];\bar{\rho}) d^{J\Pi}_{\Omega'\Omega}(\Delta_{\nu\lambda}[\omega_\lambda,\gamma_\lambda])\end{aligned} \tag{2.9.14}$$

and for the overlap matrix the form

$$\begin{aligned}\left[(\mathcal{O}p)^{J\Pi}_{\lambda\lambda}(\bar{\rho}_{i+1};\bar{\rho}_i)\right]^{v'j'\Omega'}_{vj\Omega} &= \left\langle \mathrm{F}^{JM\Pi}_{\lambda vj\Omega}(\zeta_\lambda;\bar{\rho}_{i+1}) \mid \mathrm{F}^{JM\Pi}_{\lambda v'j'\Omega'}(\zeta_\lambda;\bar{\rho}_i)\right\rangle \\ &= \frac{1}{2}\delta^{j'\Omega'}_{j\Omega}\left(1+(-1)^{J+\Pi}\delta^{\Omega}_{0}\right)\int_0^\pi \sin^2\omega_\lambda d\omega_\lambda f^{J\lambda}_{vj\Omega}(\omega_\lambda;\bar{\rho}_{i+1}) f^{J\lambda}_{v'j\Omega}(\omega_\lambda;\bar{\rho}_i)\end{aligned} \tag{2.9.15}$$

$$\begin{aligned}\left[(\mathcal{O}p)^{J\Pi}_{\nu\lambda}(\bar{\rho}_{i+1};\bar{\rho}_i)\right]^{v'j'\Omega'}_{vj\Omega} &= \left\langle \mathrm{F}^{JM\Pi}_{\nu vj\Omega}(\zeta_\nu[\zeta_\lambda];\bar{\rho}_{i+1}) \mid \mathrm{F}^{JM\Pi}_{\lambda v'j'\Omega'}(\zeta_\lambda;\bar{\rho}_i)\right\rangle \\ &= \int\int d\vartheta_2^\lambda d^{J\Pi}_{\Omega'\Omega}(\Delta_{\nu\lambda}[\omega_\lambda,\gamma_\lambda])\mathcal{P}^{\Omega'}_{j'}(\cos\gamma_\lambda)\mathcal{P}^{\Omega}_{j}\left(\cos\gamma_\nu[\omega_\lambda,\gamma_\lambda]\right) \\ &\quad \times f^{J\lambda}_{v'j'\Omega'}(\omega_\lambda;\bar{\rho}_i) f^{J\nu}_{vj\Omega}(\omega_\nu[\omega_\lambda,\gamma_\lambda];\bar{\rho}_{i+1})\end{aligned} \tag{2.9.16}$$

2.10 Solution of the Generalized Eigenvalue Problem for the LHSF

The matrices in the initial statement of the symmetric generalized eigenvalue problem (2.8.11) are square matrices of dimension N. We first determine the eigenvalues and eigenvectors of the real, positive-definite symmetric overlap matrix $\mathbf{M}$:

$$\mathbf{MX} = \mathbf{X\Lambda} \tag{2.10.1}$$

The eigenvector matrix $\mathbf{X}$ is orthogonal, and the eigenvalue matrix $\mathbf{\Lambda}$ is diagonal with positive real diagonal elements ordered such that $[\mathbf{\Lambda}]_{ii} \geq [\mathbf{\Lambda}]_{jj}$ for $i < j$. We thus have

$$\mathbf{Ha} = \mathbf{X\Lambda X}^{\mathrm{T}}\mathbf{aE}. \tag{2.10.2}$$

If we were to multiply both sides of the equation from the left by $\bar{\mathbf{X}}^{\mathrm{T}}$ where $\bar{\mathbf{X}} = \mathbf{X\Lambda}^{-\frac{1}{2}}$, and defining the matrix $\mathbf{c}$ by $\mathbf{c} = \bar{\mathbf{X}}^{-1}\mathbf{a}$, we could recast the equation in the form

$$\bar{\mathbf{H}}\mathbf{c} = \mathbf{cE} \tag{2.10.3}$$

in which

$$\bar{\mathbf{H}} = \bar{\mathbf{X}}^{\mathrm{T}}\mathbf{H}\bar{\mathbf{X}}. \tag{2.10.4}$$

The new hamlitonian matrix $\bar{\mathbf{H}}$ is thus the original $\mathbf{H}$ matrix expressed in terms of a new orthogonal basis set $\bar{F}$, related to the original basis F by

$$|\bar{F}_j\rangle = \sum_i \bar{X}_{ij}|F_i\rangle. \tag{2.10.5}$$

This new symmetric eigenvalue problem in $\bar{\mathbf{H}}$, which will have the same eigenvector matrix $\mathbf{E}$ as the original problem, can be solved in the same way as for the M matrix eigenvalues. Finally, the eigenvector matrix $\mathbf{a}$ of the generalized eigenvalue problem is determined from the eigenvector matrix $\mathbf{c}$ of (2.10.3), $\mathbf{\Lambda}$ and $\mathbf{X}$:

$$\mathbf{a} = \bar{\mathbf{X}}\mathbf{c} = \mathbf{X}\mathbf{\Lambda}^{-\frac{1}{2}}\mathbf{c}. \tag{2.10.6}$$

The method for determination of $\mathbf{a}$ and $\mathbf{E}$ as described above will fail if the matrix $\mathbf{M}$ has negative or very small positive eigenvalues; since (as noted in section 2.7) $\mathbf{M}$ is formally positive definite, a negative eigenvalue is indication that the error in that eigenvalue is of the same order of magnitude as or larger than the correct value, and therefore the error in the associated eigenvector is likely to be quite large. The eigenvectors associated with small positive eigenvalues will also suffer from this condition. Use of the error-containing eigenvectors in the calculation can result in obtaining incorrect LHSF energies, since the effect of multiplication of $\mathbf{H}$ by the inverse of the eigenvalues of $\mathbf{M}$ is to disproportionately weight the error-containing terms. This difficulty is resolved by reducing the dimensionality of the calculation: we remove a sufficient number of eigenvectors of the $\mathbf{M}$ matrix with negative or small positive eigenvalues such that the problem does not occur. This is equivalent to dropping the corresponding functions from the basis $\bar{F}$. This dimensionality reduction results in a square diagonal matrix $\mathbf{\Lambda}'$ which is the N' by N' upper left hand corner of $\mathbf{\Lambda}$ (where $N' < N$), and in a rectangular matrix $\bar{\mathbf{X}}'$ of dimension N by N'. These matrices are used as above to define the matrix $\bar{\mathbf{H}}'$, which is the N' by

N' upper left hand corner of $\bar{\mathbf{H}}$. The new symmetric eigenvalue problem is solved to generate the matrices $\mathbf{c}'$ and $\mathbf{E}'$, and the eigenvector matrix $\mathbf{a}'$ is calculated from $\mathbf{a}' = \bar{\mathbf{X}}'\mathbf{c}'$.

The fact that an orthogonal basis set derived from the primitives as above is the basis set actually used to determine the surface functions means that addition of a function to the primitive basis set does not necessarily improve the quality of the surface functions generated. A strict variational principle does not apply in this case, since the orthogonal basis set $\bar{F}$ obtained before the new primitive was added is not usually a subset of the orthogonal basis set obtained after its addition. In practice, we have found that addition of one function to an N function primitive basis set which yields a set of N' orthogonal functions will cause all surface function eigenvalues to decrease as expected if the new set of $N + 1$ primitives is still made to yield only N' orthogonal functions, since the resulting N' function orthogonal basis set will be a better set for expansion of the surface functions; however, if the new set is allowed to have $N' + 1$ orthogonal functions, some surface function eigenvalues will decrease while others increase. Although the variational principle does not strictly apply for addition of new primitives, the trend observed as more primitives are added is for the calculated surface functions and their eigenvalues to converge to their true values, so the method as described remains valid.

2.11 Characterization and Elimination of Linear Dependence

The success of the method for solution of the generalized eigenvalue problem described in section 2.8 depends on the selection of the number of orthogonal basis functions to be retained. The best value for this parameter is basis-set dependent; if too many are kept, spurious eigenvalues of the generalized eigenvalue problem may result, while if too few are used, the resulting eigenvalues and eigenvectors are not as converged as possible with the basis set chosen. Obviously, the first of these two possibilities results in more serious errors, and it is better to err by removing more functions than necessary. For low values of J, calculation of the integrals which make up the matrices for the generalized eigenvalue problem is much more CPU-intensive than the diagonalization routines; we therefore save all the matrices of integrals in the primitive basis set in disc-stored files to allow recalculation of the LHSF and the matrices involving integrals of the LHSF if the convergence criterion chosen turns out to be inadequate.

The current choice of convergence criterion is to examine the change in the eigenvalues of the surface functions with addition of new orthogonal basis set functions $\bar{F}_i$. An estimate of a reasonable value for this parameter can be obtained for individual values of $\bar{\rho}$ by examination of the behavior of the LHSF eigenvalues *vs.* the number of linearly independent functions $\bar{F}_i$ used in their calculation. Up to a certain number of these functions (ordered by decreasing magnitude of the eigenvalues Λ_{ii} of the M matrix), the eigenvalues converge towards their correct levels; after this number is reached, the functions $\bar{F}_i$ subsequently added are composed almost entirely of error in the original basis, and spurious eigenvalues are introduced. This induces error in all the eigenvalues, and the effect is easily visible when the eigenvalues are plotted against the number of $\bar{F}_i$ used. In figure 2.2, an example for the $J = 3, \Pi = 1$ A_1 symmetry is given. At the left of the figure, the lowest eigenvalues are already converged, but some of the higher energy eigenvalues are still converging. As a basis set size of 230 is reached, a rippling pattern begins to

appear as a spurious eigenvalue enters the plot and proceeds to decrease in energy as the basis set size increases. At the largest basis set size plotted (which is also the last basis with only positive eigenvalues) the incorrect eigenvalue is the lowest in energy, and another spurious eigenvalue has appeared at higher energy.

A time-consuming but failsafe method of insuring the absence of difficulties due to linear dependence is to generate plots of the LHSF eigenvalues *vs.* number of $\bar{F}_i$ of the type of figure 2.2 for all values of $\bar{\rho}$ and all symmetries, and choosing by visual observation of these plots the correct number of orthogonal functions to keep for each symmetry and $\bar{\rho}$. This also assures that the functions obtained from the basis set are the best possible, since convergence of the energies towards their true values becomes obvious. (For the example given, between 220 and 235 functions would be a good choice for a calculation up to approximately 2.0 eV; a higher energy calculation may require a larger basis set for the LHSF calculation.)

Alternatively, a method which uses the convergence of the eigenvalues as orthogonal basis functions are added may be applied to testing for the presence of spurious eigenvalues. When using this method, the criterion for convergence must be strict enough to ensure good surface functions while preventing the presence of spurious functions. We examine the lowest N_e eigenvalues (with N_e a program parameter) for the characteristic feature of a spurious eigenvalue, which is the large negative change in its magnitude as the basis set size increases. This will cause the following condition to hold for the set of eigenvalues which it crosses as it decreases:

$$|e(j,n) - e(j,n+1)| > |e(j-1,n) - e(j,n+1)| \qquad (2.11.1)$$

where $e(j,n)$ is the j^{th} LHSF eigenvalue when a total of n orthonormal basis functions are included in the set. If the eigenvalue that changes falls below more than one (formerly lower) eigenvalue, the relation in (2.11.1) will hold for a series of values of j, and the total difference in the changing eigenvalue will be measured between the largest and smallest j values: $\Delta e = e(j_{min}, n+1) - e(j_{max}, n)$. Since some change is to be expected as the LHSF converge towards their true eigenvalues,

and this change may result in the crossing of states, another program parameter is set to the maximum change in a single surface function energy attributable to convergence (usually between 5 and 10% of the value of the function); any larger change is assumed to be due to error caused by the effects of linear dependence. In practice, this convergence criterion has sometimes been inadequate at elimination of the spurious eigenvalue problem, and it has been necessary to recalculate the LHSF at a few values of $\bar{\rho}$ in these cases to obtain good results; however, it yields good LHSF at most values of $\bar{\rho}$, and with improvement will make plots of the type of figure 2.2 unnecessary.

A large part of the problems caused by linear dependence are due to "missing" functions in the basis set, particularly in the regions of configuration space where the arrangement channels are nearly separated and each primitive function is a good approximation to a corresponding LHSF. In this case, if a primitive corresponding to a relatively low-energy LHSF is not in the basis set, a function composed of small pieces of the other primitives will be formed as a substitute. This composite function is poorly converged at best; in addition, it is unstable in the sense that addition to the orthonormal basis set of a function which is mostly error can cause this eigenvalue to change drastically, falling below the true "missing" eigenvalue and becoming spurious. In the near-separated channels region, the problem can be ameliorated by including the primitive which corresponds to the missing LHSF; this process can be repeated until all functions below an arbitrary selected number or energy are good. In the interior regions, it is less obvious what primitives correspond to a particular LHSF, but by the same token there will be a better representation of the LHSF by the other primitives, so the problem will not be as severe.

In practice, we have been able to obtain accurate surface eigenfunctions and eigenvalues using a combination of these methods for every case attempted so far (which has been for the H_3 system and partial waves $J = 0, 1, 2,$ and 3). After some experience is developed, the procedure is fairly straightforward and workable, since

the surface functions are independent of the total energy E for which the scattering calculation is performed.

2.12 Selection of the Primitive Basis Set

The basis set for expansion of the LHSF at each value of $\bar{\rho}$ is chosen in the following fashion. First, a large LHSF calculation is done for a select number of values of $\bar{\rho}$. The primitives for this calculation are not selected in any particularly intelligent way, but enough are included so that one can reasonably expect that an adequate number of good surface functions will be present. Linear dependence is eliminated by examination of the eigenvalue-*vs.*-number of orthogonal functions plots mentioned in section 2.8 and illustrated in figure 2.2, and selecting the proper number to use. At this point, we evaluate the matrix

$$\hat{\mathbf{a}} = \mathbf{X}\mathbf{c} \tag{2.12.1}$$

from the matrices $\mathbf{X}$ and $\mathbf{c}$ determined in the course of calculating the coefficient matrix $\mathbf{a}$ of equation (2.10.6). The omission of the diagonal weighting function $\mathbf{\Lambda}^{-\frac{1}{2}}$ reduces the contribution of primitives which effectively cancel by eliminating the scaling effect of the inverse square root of the (small) eigenvalue, and therefore permits one to see the unscaled contributions to the surface function. This is important since the result of cancellation of a set of primitives can contain a large amount of error, which is magnified by the $\mathbf{\Lambda}^{-\frac{1}{2}}$ weighting. In addition, the $\hat{\mathbf{a}}$ matrix is orthogonal, which makes it possible to determine the contribution of each primitive to the surface function easily. Examination of these coefficient matrices then allows one to pick the "most important" primitives for the calculation of the LHSF at that value of $\bar{\rho}$, and this set of primitives is then used for a range of $\bar{\rho}$ about the original value.

It has also become apparent that certain primitives with most of their probability density at large ω_λ do not contribute significantly to the LHSF calculation, but may be selected by the coefficient checking program when an important primitive

is missing from the calculation (this occurs most frequently at large values of $\bar{\rho}$, when the primitives more closely approximate the LHSF). This situation can result in the introduction of subtle linear dependence difficulties which in the absence of these primitives would be obviously due to the missing function. These primitives can be eliminated from the calculation *a priori* by examination of the probability density function of the primitives, and coefficient checking on this reduced basis set will yield more accurate information on the important primitives in the calculation.

A possible choice for a variational basis set for the calculation is to expand the LHSF in terms of a complete (or nearly complete) set of primitives defined in a single channel and which are symmetrized in parity only. This basis set would have the advantage of being orthogonal, and therefore would need no time-consuming $\nu\lambda$ integrations as are required by the primitives involving all three arrangement channels. Unfortunately, as defined above this basis set would not be able to accurately represent the LHSF in the region near $\omega = \pi$ without a very large number of functions; a basis set of the type with a Wigner rotation matrix in the λ coordinate Euler angles multiplying a function of the other two hyperangles which could represent the LHSF well in this region would necessarily be multivalued at $\omega = \pi$. In addition, the basis set would not represent the parts of the LHSF in the ν and κ channels very well, especially as the channels begin to separate. Tests performed for $H+H_2$ in the $J = 0$ partial wave, where any difficulties with $\omega = \pi$ would not occur, reveal that the large number of basis functions required for this method to begin to approach the accuracy of the method using primitives in all three arrangement channels causes the time required for the larger eigenvalue problem to more than exceed the time saved by avoidance of the $\nu\lambda$ integration. Accordingly, this method was tried and discarded.

3. CALCULATION ALGORITHM

3.1 General Discussion

A well-optimized algorithm for the calculation of the LHSF is necessary due to the large amount of numerical effort needed for the two-dimensional integrals. The two-dimensional quadratures may be performed by any sufficiently efficient means; for simplicity of programming, we chose to do the integration on n_ω evenly spaced grid points in the angle ω_λ using Simpson's Rule and using n_γ point Gauss-Legendre quadrature in the angle γ_λ (taking advantage of the behavior of the associated Legendre function in the λ channel). The terms needed for each integrand are the 1D primitives $t^J_{vj\Omega}$ and associated Legendre polynomials $\mathcal{P}^\Omega_j$ in both the λ and ν channels, and the $d^{J\Pi}_{\Omega'\Omega}(\Delta_{\nu\lambda})$ functions which remain from the integration over the Euler angles. For the P_3 symmetry, these functions are sufficient to specify the integrals involving the symmetrized primitives, since the values for the $\nu\lambda$ integrations are the same as those for the $\kappa\nu$ and $\lambda\kappa$ integrations by symmetry; if the system does not have P_3 symmetry, it will also be necessary to calculate the functions in the κ channel and the values of the $\mathbf{d}^{J\Pi}$ matrix for angles $\Delta_{\kappa\lambda}$ and $\Delta_{\nu\kappa}$ for these latter integrals. In the λ channel, the function $t^J_{vj\Omega}$ is known at all n_ω ω_λ points and the $\mathcal{P}^\Omega_j$ at all n_γ γ_λ points, which is a relatively small number of points; in the ν channel, however, these functions must be known at all ω_ν and γ_ν points, and since these variables are non-separable functions of ω_λ and γ_λ, values for these functions must be stored for all $n_\omega n_\gamma$ grid points. In addition, the angle $\Delta_{\nu\lambda}$ depends on both ω_λ and γ_λ and therefore must also be calculated for the entire grid. To obtain the values of the $t^J_{vj\Omega}$ functions on all the ω_ν grid points, a cubic spline interpolant at these points was calculated from the known values on the (evenly-spaced) ω_λ grid. For the $\mathcal{P}^{\Omega'}_{j'}$ and the $d^{J\Pi}_{\Omega'\Omega}$, either this method or direct calculation of the values at the grid points could be used. It was found that, in general, direct calculation was

faster for the $\mathcal{P}_j^{\Omega}$ while interpolation from an evenly-spaced $\Delta_{\nu\lambda}$ grid was faster for the $d^{J\Pi}_{\Omega'\Omega}$.

If the amount of memory needed by the program were not a constraint, the most efficient method would be to calculate the ρ-independent functions $\mathcal{P}_{j'}^{\Omega'}(\gamma_\nu)$ and $d^{J\Pi}_{\Omega'\Omega}(\Delta_{\nu\lambda})$ at the beginning of the program for all necessary grid points and read these values as necessary. Unfortunately, this would use a substantial amount of memory (for $H+H_2$ at the current grid size, greater than $(J+1)$ Mwords). Our calculation was programmed initially for a CRAY X-MP/48 on which we had convenient access to 3 MWords of memory. Therefore, these functions were redetermined in each integration along with the $t^J_{v'j'\Omega'}(\omega_\nu;\bar{\rho})$. To minimize this duplicated effort, the algorithm was constructed so as to perform these calculations once per set of integrals. The primitive basis set was organized so that the outermost loop involved Ω' (and thus this value changed least frequently); the succeeding loops were over the values of j', v', Ω, j and finally v. (For vectorization, the three primed indices and the three unprimed indices were combined into one index each, without affecting the ordering described.) The $d^{J\Pi}_{\Omega'\Omega}$ are determined each time Ω' changes, the $\mathcal{P}_{j'}^{\Omega'}$ each time either Ω' or j' changes, and the $t^J_{v'j'\Omega'}$ when any of the three primed parameters change.

3.2 Integration Algorithm

Having minimized the overhead in this fashion, the calculation of the integrand is performed so as to maximize the vectorization of the integration. The description which follows will be for the simplest case, which is the calculation of the M and $\mathcal{O}$ matrices; generalization to the calculation of the H and $\mathcal{I}$ matrices is given subsequently. The value of J is fixed, while the matrices for both values of Π are calculated simultaneously.

As mentioned above, when the value of Ω' changes, the matrix of little d values is calculated by interpolation from a set of values known on an evenly spaced grid in $\Delta_{\nu\lambda}$. The interpolation is done for values of Ω ranging from $-J$ to J; the result is a matrix

$$\mathrm{ltld(iw,ig,io)} \equiv d^{J}_{\Omega',\mathrm{io}}\left(\Delta_{\nu\lambda}\left(\omega_\lambda(\mathrm{iw}),\gamma_\lambda(\mathrm{ig})\right)\right) \tag{3.2.1}$$

in which the indices iw, ig and io have ranges

$$\mathrm{iw} \in [1,n_\omega], \quad \mathrm{ig} \in [1,n_\gamma], \quad \mathrm{io} \in [-J,J] \tag{3.2.2}$$

(For simplicity of notation, we will not label the matrices with the appropriate quantum numbers; the values of these indices will be apparent from the construction of the matrix.) The volume element is included in this matrix since the matrix changes less frequently than others in the calculation.

$$\mathrm{dwt(iw,ig,io)} = \mathrm{ltld(iw,ig,io)} * \frac{\sin(\omega_\lambda(\mathrm{iw}))}{\sin(\omega_\nu(\mathrm{iw,ig}))} * \mathrm{d}(\cos\gamma_\lambda(\mathrm{ig})) * \mathrm{d}\omega_\lambda(\mathrm{iw}) \tag{3.2.3}$$

Similarly, whenever the value of either Ω' or j' is changed, the values of the associated Legendre polynomials in the ν coordinates is calculated:

$$\mathrm{pnu(iw,ig)} \equiv \mathcal{P}^{\Omega'}_{j'}(\cos\gamma_\nu(\mathrm{iw,ig})) \tag{3.2.4}$$

In the (implicit) loop over v' the $t^{J}_{v'j'|\Omega'|}$ term is calculated and multiplied by the result of the previous step:

$$\mathrm{prim(iw,ig)} = \mathrm{pnu(iw,ig)} * t^{J}_{v'j'|\Omega'|}(\omega_\lambda(\mathrm{iw});\bar{\rho}) \tag{3.2.5}$$

Finally, a working array involving these functions and the little d functions is formed:

$$\text{work1}(\text{ig},\text{iw},\text{io}) = \text{dwt}(\text{iw},\text{ig},\text{io}) * \text{prim}(\text{iw},\text{ig}) \tag{3.2.6}$$

this array will be referred to as the ν primitive matrix, and has implicit dependence on v', j' and Ω'.

The integration over ω_λ is performed by a matrix times vector subroutine which is very efficient on the CRAY architecture; the vector is the λ channel primitive $t^J_{vj|\Omega|}$ and the matrices are the submatrices of the ν primitive matrix which has $\Omega' = \pm\Omega$:

$$\text{scr1}(\text{ig}) = \sum_{\text{iw}} \text{work1}(\text{ig},\text{iw},\Omega) * t^J_{vj|\Omega|}(\omega_\lambda(\text{iw});\bar{\rho}) \tag{3.2.7}$$

$$\text{scr2}(\text{ig}) = \sum_{\text{iw}} \text{work1}(\text{ig},\text{iw},-\Omega) * t^J_{vj|\Omega|}(\omega_\lambda(\text{iw});\bar{\rho}) \tag{3.2.8}$$

The integration in γ_λ is completed by taking the dot product of the resulting vector with the function $\mathcal{P}^\Omega_j$:

$$\text{tpos} = \sum_{\text{ig}} \text{scr1}(\text{ig}) * \mathcal{P}^\Omega_j(\cos\gamma_\lambda(\text{ig})) \tag{3.2.9}$$

$$\text{tneg} = (-1)^\Omega \sum_{\text{ig}} \text{scr2}(\text{ig}) * \mathcal{P}^\Omega_j(\cos\gamma_\lambda(\text{ig})) \tag{3.2.10}$$

The matrix element for $J + \Pi$ even is given by

$$\text{ele1} = \frac{1}{2}(\text{tpos} + \text{tneg}) \tag{3.2.11}$$

and for $J + \Pi$ odd by

$$\text{ele2} = \frac{1}{2}(\text{tpos} - \text{tneg}); \tag{3.2.12}$$

there is implicit dependence of this final answer on all six indices $vj\Omega$ and $v'j'\Omega'$.

Essentially the same algorithm is used in the calculation of the $\mathcal{I}$ matrix; the only difference is the replacement of equation (3.2.3) with a similar equation which includes the interaction potential function:

$$\begin{aligned}\text{dwt}(\text{iw},\text{ig},\text{io}) =& \text{ltld}(\text{iw},\text{ig},\text{io}) * \frac{\sin(\omega_\lambda(\text{iw}))}{\sin(\omega_\nu(\text{iw},\text{ig}))} * \text{d}(\cos\gamma_\lambda(\text{ig})) * \text{d}\omega_\lambda(\text{iw}) \\ & * \bar{V}(\rho,\omega_\lambda(\text{iw}),\gamma_\lambda(\text{ig});\bar{\rho})\end{aligned} \tag{3.2.13}$$

The **H** matrix is more difficult. The function in the λ channel is operated on by the hamiltonian, and the integration must be broken up into three pieces to account for the Ω coupling introduced by the action of this operator. The term diagonal in Ω is multiplied by a function which contains the potential as well as some terms dependent on v, j and Ω. This integration is therefore broken into two parts. Along with the matrix of equation (3.2.6), two additional working arrays are needed, one including the potential energy function and the other a factor of $\frac{1}{2}\sec^2\frac{\omega_\lambda}{2}$:

$$\text{work2(ig,iw,io)} = \text{work1(ig,iw,io)} * V(\bar{\rho}, \omega_\lambda(\text{iw}), \gamma_\lambda(\text{ig})) \tag{3.2.14}$$

$$\text{work3(ig,iw,io)} = \text{work1(ig,iw,io)} / (1 + \cos\omega_\lambda(\text{iw})) \tag{3.2.15}$$

We also define the array

$$\text{g(iw)} = \left(e^{J\lambda}_{vj\Omega}(\bar{\rho}) - V^{\Omega}_{jj}(\bar{\rho}, \omega_\lambda(\text{iw}))\right) * t^{J}_{vj|\Omega|}(\omega_\lambda(\text{iw})) \tag{3.2.16}$$

The integrals for $\Omega' = \pm\Omega$ are determined by summing successive matrix times vector routine calls, as

$$\text{scr1(ig)} = \sum_{\text{iw}} \text{work2(ig,iw,}\Omega) * t^{J}_{vj|\Omega|}(\omega_\lambda(\text{iw});\bar{\rho}) + \sum_{\text{iw}} \text{work1(ig,iw,}\Omega) * \text{g(iw)} \tag{3.2.17}$$

$$\text{scr2(ig)} = \sum_{\text{iw}} \text{work2(ig,iw,}-\Omega) * t^{J}_{vj|\Omega|}(\omega_\lambda(\text{iw});\bar{\rho}) + \sum_{\text{iw}} \text{work1(ig,iw,}-\Omega) * \text{g(iw)} \tag{3.2.18}$$

The Ω coupling caused by the hamiltonian requires the following integrals:

$$\text{scr3(ig)} = \sum_{\text{iw}} \text{work3(ig,iw,}\Omega - 1) * t^{J}_{vj|\Omega|}(\omega_\lambda(\text{iw});\bar{\rho}) \tag{3.2.19}$$

$$\text{scr4(ig)} = \sum_{\text{iw}} \text{work3(ig,iw,}1 - \Omega) * t^{J}_{vj|\Omega|}(\omega_\lambda(\text{iw});\bar{\rho}) \tag{3.2.20}$$

$$\text{scr5(ig)} = \sum_{\text{iw}} \text{work3(ig,iw,}\Omega + 1) * t^{J}_{vj|\Omega|}(\omega_\lambda(\text{iw});\bar{\rho}) \tag{3.2.21}$$

$$\text{scr6(ig)} = \sum_{\text{iw}} \text{work3(ig,iw,}-\Omega - 1) * t^{J}_{vj|\Omega|}(\omega_\lambda(\text{iw});\bar{\rho}) \tag{3.2.22}$$

After weighting by the factors given in equation (2.9.9), a dot product of these arrays generates the hamiltonian matrix elements equivalent to tpos and tneg above:

$$\begin{aligned}\text{tpos} = \sum_{\text{ig}} &\text{scr1(ig)} * \mathcal{P}_{\text{j}}^{\Omega}(\cos\gamma_\lambda(\text{ig})) + \text{scr3(ig)} * \mathcal{P}_{\text{j}}^{\Omega-1}(\cos\gamma_\lambda(\text{ig})) \\ &+ \text{scr5(ig)} * \mathcal{P}_{\text{j}}^{\Omega+1}(\cos\gamma_\lambda(\text{ig}))\end{aligned} \tag{3.2.23}$$

$$\begin{aligned}\text{tneg} = \sum_{\text{ig}} &\text{scr2(ig)} * \mathcal{P}_{\text{j}}^{\Omega}(\cos\gamma_\lambda(\text{ig})) + \text{scr4(ig)} * \mathcal{P}_{\text{j}}^{\Omega-1}(\cos\gamma_\lambda(\text{ig})) \\ &+ \text{scr6(ig)} * \mathcal{P}_{\text{j}}^{\Omega+1}(\cos\gamma_\lambda(\text{ig}))\end{aligned} \tag{3.2.24}$$

and the parity matrix elements are generated as in equations (3.2.11) and (3.2.12).

A simple means of reducing the numerical effort in the integration is based on the limited extent of the $t^J_{v j\Omega}$ in ω_λ. These functions are often very small (less than 10^{-15} in amplitude) in two ranges of values of ω_λ near the points $\omega_\lambda = 0$ and $\omega_\lambda = \pi$, respectively; the extent of these ranges depends on the values of all four indices of the function. The grid points with values of ω_λ in these regions are excluded from the integration including this one-dimensional primitive, as their contribution to the total integral would be negligible. This can substantially reduce the size of the integration grid with concommittant savings in computation.

In the asymptotic region, where the $\nu\lambda$ integrals are assumed to be zero, we may *a priori* restrict the integration range in ω_λ; for the primitives to have zero overlap with functions in the other channels, the $f^J_{v j\Omega}(\omega_\lambda;\bar{\rho})$ must be zero beyond certain surfaces dividing the asymptotic arrangement channels (for $H+H_2$, the surface dividing the λ channel from the ν and κ channels is determined by symmetry to be $\omega_\lambda = \frac{\pi}{3}$). At the largest value of $\bar{\rho}$ for which the $\nu\lambda$ integrals are calculated explicitly, the maximum value of r_λ in the outer region, $r_\lambda^{\max}$, is defined as the value of r_λ on the dividing surface for this value of $\bar{\rho}$, and the number of ω_λ points (n_ω) is set to the number of ω_λ points on the current grid corresponding to r_λ values less than this maximum value. The value of $\bar{\rho}$ which is chosen for this purpose is an empirical parameter determined by convergence of the resulting scattering matrices. For all subsequent $\bar{\rho}_i$, the range of the ω_λ variable is determined by the value of

ω_λ corresponding to $r_\lambda^{\max}$ for this value of $\bar{\rho}_i$; this insures that the range of the λ and the ν primitives does not overlap. This procedure results in a ω_λ grid which changes with $\bar{\rho}$, and accordingly when calculating the overlap between two sets of surface functions, the $f^J_{v_j\Omega}(\omega_\lambda;\bar{\rho})$ functions at one value of $\bar{\rho}$ must be interpolated onto the grid of the other; this is done by a cubic spline fit. A special routine was written to handle the calculation of the overlap between LHSF at the transition between the interior and exterior regions, where the interior functions span the full range of ω_λ but the exterior functions have a limited range of ω_λ and are calculated on a different ω_λ grid.

4. RESULTS AND DISCUSSION

4.1 General Comments

Unless otherwise noted, all results reported here were calculated for the system $H+H_2$ on the LSTH potential energy surface, with a grid of 451 evenly spaced ω_λ points and 96 Gauss-Legendre quadrature points in the γ_λ direction. The LHSF program was run for 51 values of $\bar{\rho}$, evenly spaced by 0.2 bohr, in the inclusive range [2.0 bohr, 12.0 bohr]. The last inner region value of $\bar{\rho}$ (where $\nu\lambda$ integrals are calculated) was chosen to be 6.0 bohr; therefore, 21 values of $\bar{\rho}$ were used for the inner region and 30 for the outer region. $\mathcal{I}$ matrices were calculated at four evenly spaced values of ρ for each value of $\bar{\rho}$, and an $\mathcal{O}$ matrix was calculated between each contiguous pair of $\bar{\rho}$ values. The selection of primitives for the calculation of the $J = 0$ through 3 LHSF is given in table 4.1; for $J = 0$ through 2 the choice of quantum numbers (number of values of j and number of vibrations v for each value of j) which determine the primitive basis set is independent of $\bar{\rho}$, but for the $J = 3$ LHSF calculation these numbers were chosen to be different for different ranges of $\bar{\rho}$ to optimize the resulting basis sets in these regions and thus increase the efficiency of the calculation. For each v, j combination, there are $\min(j, J)$ functions in the basis set for $J + \Pi$ odd which are associated to quantum numbers $\Omega \in [1, \min(j, J)]$ and $\min(j, J)+1$ functions for $J+\Pi$ even associated with quantum numbers $\Omega \in [0, \min(j, J)]$; the total size of the basis set in each case is given in table 4.2. The simplifications implied by the P_3 symmetry of this system were taken into account to reduce the computational effort. The calculations were performed on one processor of various CRAY architecture machines; when times and percentages of peak speed are reported, they will be in terms of the values of these quantities when the program is run on a single processor of a CRAY Y-MP/864.

4.2 Convergence of the LHSF

The convergence of the LHSF must be determined with respect to the following quantities: the size of the basis set used, the number of orthonormalized basis functions kept in the calculation, and the number of points in each variable of the integration grid. The method for determining the convergence of the LHSF is to test the convergence of the LHSF energies with respect to these quantities since, as in any eigenvalue problem, the calculated eigenvector is usually accurate to about half the accurate digits of the calculated eigenvalue.

The first two of these quantities have been discussed in terms of the linear dependence difficulties (section 2.9). In the coefficient checking step, a large set of functions is used in a trial LHSF calculation to determine the subset which will be used as the primitive basis set in the production calculation; convergence of the LHSF eigenvalues is assured by comparison of the eigenvalues obtained from this trial calculation with those obtained from the full set of trial primitives. Similarly, the convergence of the LHSF with respect to the number of functions kept after removal of linear dependence can be seen from the plots of the type of figure 2.2 which ensure that there are no remaining linear dependence effects.

Convergence with respect to the integration grid was tested for the system $H+H_2$ on the $J = 0$ partial wave by choosing a fixed large primitive basis set and varying the number of ω_λ and γ_λ points in the grid. A generalized eigenvalue problem was solved for the **H** and **M** matrices obtained from each of these calculations, and the resulting eigenvalues were compared. Naïvely, one would expect that the number of grid points necessary for a good calculation of the LHSF would increase with $\bar{\rho}$, since the range of values of ω_λ and γ_λ which correspond to the configurations where the ν and κ primitives are important becomes smaller as $\bar{\rho}$ increases. However, testing the integration grid at $\rho = 6.0a_0$ (table 4.3) showed that the LHSF energies were practically independent of the density of points in the γ_λ grid. This effect occurs since the $\nu\lambda$ integrals at 6.0 bohr are much smaller than the $\lambda\lambda$ inte-

grals, and the integration over γ_λ is analytic in the latter case. (This also serves as confirmation that the $\nu\lambda$ integrals can be assumed to be zero when ρ is greater than 6.0 bohr.) The energies of the calculated LHSF decrease slightly as the number of ω_λ points decreases. This effect may be explained by the change in the basis set with the integration grid, since the $f^J_{vj\Omega}$ are calculated by a finite difference method on the same grid and accordingly are slightly different when the grid changes; there is no variational principle for this finite difference calculation, and the energies of the primitives are underestimates of the true energy. As the LHSF energies depend on these primitive energies through the hamiltonian matrix **H**, they are also slightly underestimated; however, this effect will not significantly affect our results due to its small magnitude.

We therefore chose to perform our convergence testing of the integration grid at $\bar{\rho} = 3.2$ bohr; this value of $\bar{\rho}$ was chosen as being near the saddle point of the LSTH surface, where one would expect the $\nu\lambda$ overlaps to be large. In comparing the LHSF energies for the various integration grids at 3.2 bohr, it proved to be necessary to take into account the linear dependence effects on the calculation, since the coarser integration grids resulted in more error in the integration and therefore worsened the linear dependence effects described in section 2.9; to achieve results comparable with the finer integration grid calculations, it was necessary to use a smaller basis set of the orthogonal functions derived from diagonalizing the M matrix (see section 2.8). When the linear dependence is removed in such a way as to minimize the deviation between the results for different grids, the results are as shown in table 4.4, with the number of orthogonal functions removed from the transformed basis set for each case included in parenthesis. Since the size of the basis set is effectively reduced by the removal of these functions, the finer grid sizes should give better converged results; however, the deviation between results for the different grids is very small, and seems to depend more on the effect of the change in the calculated $f^J_{vj\Omega}$ functions as the ω_λ grid changes than on the integration grid

itself. Consequently, we conclude that (up to a point) the errors introduced by coarsening the integration grid can be corrected by appropriate linear dependence removal techniques, and that integration grids with point density intermediate to the calculations presented in table 4.4 should give good results.

The result of the previous paragraph was obtained through comparison of the calculation for several different grids. It is, of course, impractical to do this for all $\bar{\rho}$ in a large scale calculation. In addition, in the dense 1001x200 grid the effect of linear dependence is dramatically visible as the occurence of spurious eigenvalues in plots of the LHSF eigenvalue *vs.* the total number of orthogonal functions kept in the basis set (as is also the case for the 451x96 grid we have used in most calculations – see figure 2.2), but in the coarse grids the convergence of the LHSF energies with number of orthogonal basis functions is much slower. As a result, we have chosen a moderately dense grid for the calculation, namely the 451x96 grid.

In our initial $J = 0$ calculation, the choice of 96 γ_λ points in the Gauss-Legendre quadrature was dictated by the available routine for calculating the quadrature points and weights, in which 96 was the maximum number of points available and the next lower number of points was 80. We have since improved the Gauss-Legendre routine to be able to calcuate quadrature points and weights for any order integration. However, by that time most of the production calculations reported in this paper had been performed with 96 points, although a lower number such as 50 is acceptable.

4.3 Timing Data for LHSF Calculation

For $J = 0$ and a basis set of 152 primitive functions, a total of 1949 seconds of CPU time was required for the complete run of the LHSF code on a single CPU of the CRAY Y-MP/864 of the SDSC; the speed for this run was 222.3 Mflops, or about 67% of the rated maximum speed. A breakdown of the time required for each of the several steps in the calculation of the LHSF and the $\mathcal{I}$ and $\mathcal{O}$ matrices is given in table 4.5. The bulk of the computational effort in calculating the necessary matrices for the propagation is in the two-dimensional integration for the calculation of the matrices $\mathbf{H}_{\nu\lambda}$, $\mathbf{M}_{\nu\lambda}$, $\mathcal{I}_{\nu\lambda}$ and $\mathcal{O}_{\nu\lambda}$; these routines, which are only called in the interior region, account for 1629 seconds, or 84% of the computational effort. These routines are highly optimized, running at a speed of 247 Mflops (74% of peak). On average, the calculation of the integrals for the $\mathbf{H}_{\nu\lambda}$ and $\mathbf{M}_{\nu\lambda}$ matrices required 27.4 seconds (excluding the overhead from the calculation of associated Legendre polynomials and spline fitting), while each $\mathcal{I}_{\nu\lambda}$ matrix required 8.26 seconds and each $\mathcal{O}_{\nu\lambda}$ matrix needed 8.4 seconds. Since the $\mathbf{H}_{\nu\lambda}$ and $\mathbf{M}_{\nu\lambda}$ matrices were calculated at 21 values of $\bar{\rho}$ each, the $\mathcal{O}_{\nu\lambda}$ matrix at 20 values of $\bar{\rho}$ plus the additional overlap between the inner and outer regions, and the $\mathcal{I}_{\nu\lambda}$ matrices at 84 values of $\bar{\rho}$, the total time for integration in the evaluation of these matrices was 1459 seconds; this number is more important than the overhead value, as the time needed for the overhead will increase only linearly with basis set size, while the number of integrals increase quadratically. Due to the automatic cutoff of the integration range depending on the magnitudes of the $f^J_{v\bar{j}\Omega}$ in the λ channel, the integration tends to take less time as ρ increases beyond the saddle point of the surface. Aside from approximately 100 seconds of overhead, the remaining computational effort is evenly divided between the one-dimensional $\lambda\lambda$ integration, the primitive calculation, calls to the LSTH potential and the solution of the generalized eigenvalue problem (about 60 seconds total for each).

The time required for a calculation increases approximately as the square of

the number of primitives used in the calculation, due to the dominance of these two-dimensional quadratures. (The factor is somewhat larger due to the matrix diagonalization needed for the LHSF calculation and the various matrix multiplications in the algorithm, as these algorithms scale as the number of functions cubed.) However, there is additional effort involved in the LHSF calculation for $J > 0$ due to the coupling terms in the $\mathbf{H}_{\nu\lambda}$ matrix; for example, with $J = 3$ and 524 primitive functions (used in the range $\rho > 5.5$ bohr), the average time for the calculation of the $\mathbf{H}_{\nu\lambda}$ and $\mathbf{M}_{\nu\lambda}$ matrices taken together is 565.3 seconds, while each $\boldsymbol{\mathcal{I}}_{\nu\lambda}$ matrix required 88.6 seconds and each $\boldsymbol{\mathcal{O}}_{\nu\lambda}$ matrix needed 89.0 seconds on average.

The overall time for the $J = 1$ LHSF run, which had a basis set of 292 primitive functions, was 2.47 hours; the time for the $J = 2$ run was 5.35 hours, and the time for $J = 3$ was 12.6 hours.

4.4 Analysis of LHSF Results – LHSF Eigenvalues vs. ρ

As the LHSF are solutions of the full 6D Schrödinger equation for fixed values of $\bar{\rho}$, the LHSF energies $\epsilon_n^{J\Pi\Gamma}(\rho)$ are a continuous function of ρ. We present several plots of these functions for the LSTH surface in figures 4.1 through 4.3. Although the eigenvalues of the LHSF are determined in order of energy, information on the correlation of the eigenfunctions at $\bar{\rho}_i$ with those at $\bar{\rho}_{i+1}$ is contained in the $\boldsymbol{\mathcal{O}}$ matrices, and this information has been used in order to allow crossing of these curves. Some features are common to all of these functions. At sufficiently large ρ, as the LHSF converge to the diatomic state wavefunctions in each channel, the $\epsilon_n^{J\Pi\Gamma}$ converge to the energy of that diatomic state. For values of $J > 0$, this means that the $\epsilon_n^{J\Pi\Gamma}$ will become degenerate, as the energy of the wavefunction becomes independent of the orientation of the diatom with respect to the relative motion direction and thus on the Ω index; this may be seen in figure 4.3. For sufficiently small ρ, the $\epsilon_n^{J\Pi\Gamma}$ all vary as ρ^{-2} due to the predominance of the kinetic energy term of the hamiltonian over the potential energy V.

Near the saddle point of the LSTH surface (at $\rho = 3.270145a_0$), most of the

sets of $\epsilon_n^{J\Pi\Gamma}$ curves have members with local minima or maxima. This structure in the $\epsilon_n^{J\Pi\Gamma}$ curves has been shown to lead to resonant behavior for that partial wave.[69-72] This will be discussed in detail in a subsequent paper; however, we note that the $J = 0$ A_2 symmetry curves and the $J = 1, \Pi = 0$ A_1 symmetry curves have none of this structure, and there is no resonant behavior found in these partial waves.

A comparison of LHSF energies at selected values of $\bar{\rho}$ from the finite element calculations of Hipes and Kuppermann and from the present work are presented in table 4.6. The energies found by the variational LHSF method tend to be lower than those of the finite element method by up to about 0.01 eV for the $n = 20$ function, but there is substantial agreement between the results of both methods.

4.5 Analysis of LHSF Results – Propagation Matrix Elements

In a certain sense, the behavior of the LHSF is less important than the behavior of the interaction matrices $\boldsymbol{\mathcal{I}}$ and overlap matrices $\boldsymbol{\mathcal{O}}$, since these matrices determine the scattering matrices which are the ultimate goal of the LHSF calculations. The true test of these matrices is in the scattering calculation; however, a comparison of the matrices calculated by the variational LHSF method and the finite element method is possible, and such a comparison was made early in the development of the present method for the $J = 0$ partial wave A_1 irreducible representation of H + H_2 using the PK2[3] potential energy surface for interaction matrices at 2.05 bohr in the 2.0 bohr basis set and at 3.05 bohr in the 3.0 bohr basis set, and for overlap matrices between basis sets at 2.0 and 2.05 bohr and between those at 3.0 and 3.05 bohr. The results are presented in tables 4.7 and 4.8 for the upper left 5 by 5 submatrices of these matrices. The elements of the overlap matrix are unitless, and the interaction matrix elements are made so through scaling by the factor $-\frac{2\mu}{\hbar^2}$, the inverse of which appears in the propagation equation (2.4.7).

The variational basis set for this comparison consisted of only 25 functions, and would not be suitable for a production calculation; nevertheless, the agreement

between the two calculations is fairly good, particularly for the diagonal elements of the matrices. The maximum difference for the 2.05 bohr interaction matrix is 0.08 for an element of size 14.2, which is about half a percent of the value of the element; most of the smaller elements agree to two significant figures. The magnitude of the elements for the 3.05 bohr interaction matrices is smaller than those at 2.05 bohr, since the potential is changing more slowly in this region and the interaction potential of equation (2.4.9) is itself smaller. Once again most elements agree to two digits. Similar agreement exists for the overlap matrix elements.

The interaction matrices are restricted to be symmetric by the P_3 symmetrization algorithm, but no such restriction applies to the overlap matrices. In fact, the range of $(\omega_\lambda, \gamma_\lambda)$ configuration space accessible to the nth surface function at the smaller value of $\bar{\rho}$ is larger than that for the nth surface function at the larger $\bar{\rho}$ value, as with increasing $\bar{\rho}$ the potential approaches that of a separated atom and diatomic molecule. Due to this, the overlap matrix is not symmetric.

4.6 Analysis of LHSF Results – 2D Coefficient Plots

For $J = 0$, the LHSF, which are calculated for fixed values of ρ, are independent of the three Euler angles and therefore are functions of only the two variables ω_λ and γ_λ. Consequently, the behavior of these functions can be examined graphically by means of contour plots of the LHSF in these two variables. The LHSF for larger values of J are dependent on all five angles, and so for purposes of display will be expanded in terms of the parity Wigner functions in the λ coordinate system, as done in equation (2.5.1):

$$\Phi_n^{JM\Pi\Gamma_k}(\zeta_\lambda;\bar{\rho}) = \sum_\Omega D^{J\Pi}_{M\Omega}(\phi_\lambda,\theta_\lambda,\psi_\lambda)\psi_{n\Omega}^{J\Pi\Gamma_k}(\omega_\lambda,\gamma_\lambda;\rho); \qquad (4.6.1)$$

in which the sum over Ω ranges from 0(1) to J for $J+\Pi$ even(odd). We obtain the expression for these $\psi_{n\Omega}^{J\Pi\Gamma_k}$ by equating equations (2.8.10) and (4.6.1), multiplication of both sides of the resulting equation by $D^{J\Pi}_{M\Omega'}$ and integrating over the Euler angles

to yield

$$\psi_{n\Omega}^{J\Pi\Gamma_k}(\omega_\lambda,\gamma_\lambda;\rho) = \sum_{\tau v j\Omega' n} a_{\tau v j\Omega' n}^{J\Pi\Gamma_k} \Big\{ c_{\tau\lambda j}^{\Gamma_k}\delta_\Omega^0 \mathcal{P}_j^{\Omega'}(\cos\gamma_\lambda) f_{vj\Omega'}^{J\lambda}(\omega_\lambda;\rho) + c_{\tau\nu j}^{\Gamma_k}(1+\delta_\Omega^0)^{-1} d_{\Omega\Omega'}^{J\Pi}(\Delta_{\nu\lambda}) \mathcal{P}_j^{\Omega'}(\cos\gamma_\nu) f_{vj\Omega'}^{J\nu}(\omega_\nu;\rho) + c_{\tau\kappa j}^{\Gamma_k}(1+\delta_\Omega^0)^{-1} d_{\Omega'\Omega}^{J\Pi}(\Delta_{\lambda\kappa}) \mathcal{P}_j^{\Omega'}(\cos\gamma_\kappa) f_{vj\Omega'}^{J\kappa}(\omega_\kappa;\rho) \Big\} \tag{4.6.2}$$

For $J = 0$, the parity Wigner function is a constant equal to 1, and the coefficients $\psi_{n\Omega}^{J\Pi\Gamma_k}$ will be identical to the LHSF.

For convenience in examination of the properties of LHSF calculated at higher values of J, where the multiplicity of Ω values leads to several $\psi_{n\Omega}^{J\Pi\Gamma_k}$ contributing to the same LHSF, we will also examine the probability density of the LHSF averaged over the Euler angles: from equation (4.6.1) and the definition of the $D_{M\Omega}^{J\Pi}$, we find that this function $\Theta_n^{J\Pi\{\Gamma_k\otimes\Gamma_k\}}$ has the form

$$\begin{aligned}\Theta_n^{J\Pi\{\Gamma_k\otimes\Gamma_k\}}(\omega_\lambda,\gamma_\lambda;\rho) &= \int\int\int \left|\Phi_n^{JM\Pi\Gamma_k}(\zeta_\lambda;\bar{\rho})\right|^2 d\vartheta_1^\lambda \\ &= \sum_\Omega \frac{1+(-1)^{J+\Pi}\delta_\Omega^0}{2} \left|\psi_{n\Omega}^{J\Pi\Gamma_k}(\omega_\lambda,\gamma_\lambda;\rho)\right|^2\end{aligned} \tag{4.6.3}$$

The coefficients $\psi_{n\Omega}^{J\Pi\Gamma_k}$ will not in general have the full P_3 symmetry properties of the LHSF, *i.e.*, will not transform according to the irreducible representation of P_3, since the parity Wigner does not have these properties. However, the parity Wigner function in λ coordinates is an eigenfunction of the $\nu\kappa$ interchange operation with eigenvalue $(-1)^\Omega$, and therefore these coefficients will retain appropriate symmetry about the plane $\gamma_\lambda = \frac{\pi}{2}$. For the Θ functions of equation (4.6.3), averaging over the rotation of the system yields a function with the symmetry of the direct product $\Gamma_k \otimes \Gamma_k$, which for LHSF belonging to either the A_1 or A_2 irreducible representation will have A_1 symmetry. The E type functions, however, will be a linear combination of functions with A_1 and E symmetry. (The direct product $E \otimes E = A_1 \oplus A_2 \oplus E$ in general. However, the E LHSF are defined in terms

of a plane of symmetry about which the A_2 functions are odd, and the modulus squared of such a function must be even about that plane; as a consequence the coefficient of the A_2 symmetry term in this case is zero.) From equation (4.6.1) and the definition of the $D^{J\Pi}_{M\Omega}$, we find that this function $\Theta_n^{J\Pi\{\Gamma_k\otimes\Gamma_k\}}$ has the form

$$\begin{aligned}\Theta_n^{J\Pi\{\Gamma_k\otimes\Gamma_k\}}(\omega_\lambda,\gamma_\lambda;\rho) &= \int\int\int \left|\Phi_n^{JM\Pi\Gamma_k}(\zeta_\lambda;\bar{\rho})\right|^2 d\vartheta_1^\lambda \\ &= \sum_\Omega \frac{1+(-1)^{J+\Pi}\delta^0_\Omega}{2}\left|\psi_{n\Omega}^{J\Pi\Gamma_k}(\omega_\lambda,\gamma_\lambda;\rho)\right|^2\end{aligned} \tag{4.6.3}$$

Contour plots may be made of the two-dimensional coefficients of the LHSF in the two variables ω_λ and γ_λ. In order to display such plots it is convenient to define a set of axes $O\bar{X}_\lambda\bar{Y}\bar{Z}_\lambda$ and associated coordinates by[57]

$$\bar{X}_\lambda = \rho\sin\omega_\lambda\cos\gamma_\lambda; \quad \bar{Y} = \rho\sin\omega_\lambda\sin\gamma_\lambda \quad \bar{Z}_\lambda = \rho\cos\omega_\lambda \tag{4.6.4}$$

These coordinates define a three-dimensional half-space with $\bar{Y}$ positive. The $\bar{Y}$ axis is independent of the arrangement channel of the SHC and will be depicted as pointing out of the plane of the paper. The $\bar{Z}_\lambda$ axis (corresponding to $\omega_\lambda = 0$) is in the plane of the paper and points upwards and consequently the $\bar{X}_\lambda$ axis is also in this plane and points to the left. The figures will be a representation of the surface of a hemisphere with fixed ρ. The projection used is known as an azimuthal equidistant projection, which has the property that arc lengths measured from the pole of the projection (in this case the $\bar{Y}$ axis) to any point equal the linear distance from the pole to the projection of that point on the map plane (see figure 4.4). The plane of the plot is tangent to the hemispherical surface at the $\bar{Y}$ axis and as such is perpendicular to this axis. The azimuthal angle χ_λ about the $\bar{Y}$ axis is the same on the hemisphere and on the plane of the plot; the angle ξ measured from the $\bar{Y}$ axis on the hemisphere becomes proportional to the radius of the plot, which is $\xi\rho$. These coordinates are expressed in terms of the internal coordinates as

$$\xi = \cos^{-1}(\bar{Y}/\rho) \qquad \chi_\lambda = \tan^{-1}(\bar{X}_\lambda/\bar{Z}_\lambda) \tag{4.6.5}$$

We may use these coordinates to define a cartesian set of axes $\bar{x}$ and $\bar{y}$ with origin at the center of the plot, where $\bar{x}$ increases from left to right and $\bar{y}$ from bottom to top. The definitions are given by

$$\bar{x} = -\rho\xi \sin\chi_\lambda \qquad \bar{y} = \rho\xi \cos\chi_\lambda \tag{4.6.6}$$

Finally, for convenience we will define scaled axes x and y as $x = \bar{x}/\rho$ and $y = \bar{y}/\rho$; this will give ease of comparison when examining LHSF at different $\bar{\rho}$ values. The angle ω_λ increases from 0 to π as y decreases from 1 to -1, and the angle γ_λ increases from 0 to π as x increases from -1 to 1.

For purposes of plotting, an evenly spaced grid of 100 points in each of the x and y directions is generated. The coordinates of these points in terms of an ω/γ grid in each of the three arrangement channels is calculated from the relationships given above, and the functions of equation (4.6.2) are evaluated on these grids, the associated Legendre polynomials and Wigner little d functions by direct calculation and the $f^J_{vj\Omega}$ by cubic spline interpolation from the ω_λ grid of the calculation. Finally, matrix multiplication with the coefficients $a^{JM\Gamma_k}_{\tau vj\Omega',n}$, which were determined in the course of the LHSF calculation, generates the desired functions on the grid. The total time for calculation of the grid and the generation of the functions for $J = 0$, 152 primitives and all symmetries is on the order of 8 seconds on a CRAY Y-MP/864; this time depends mainly on the number of primitives and as such is indirectly dependent on J. The nature of the variational method for determining LHSF causes small fluctuations in the calculated LHSF, due to the incomplete cancellation of the basis set in regions with small probability density. This poses no difficulties in the calculation, but results in some fictitious convoluted nodal patterns in plots of the $\psi^{JM\Gamma_k}_{n\Omega}$, which for this reason are not explicitly shown. The correct nodal lines may easily be inferred from the positions of the low amplitude contours.

We will present plots of the LHSF for three values of $\bar{\rho}$ which correspond to characteristic regions in configuration space. These values are as follows: 2.0 bohr,

which is the beginning value of $\bar{\rho}$ in our LHSF calculation and typifies the case for which the interatomic forces are strong between all three atoms; 3.270145 bohr, which is the saddle point of the LSTH potential energy surface; and 6.0 bohr, which typifies the behavior of the system when one atom is well separated from the others. Plots of the potential energy surface projected in the manner described above at these values of $\bar{\rho}$ are provided in figure 4.5 to aid the discussion of the LHSF characteristics.

4.7 Analysis of LHSF Results – J = 0

In the case $J = 0$ (figures 4.6 through 4.15), the LHSF retain full P_3 symmetry properties due to their independence from the Euler angles. The threefold symmetry of the A_1 and A_2 LHSF is readily apparent from the plots of figures 4.6 through 4.8 (panel (a) for A_1 and panel (d) for A_2), with the A_2 nodal structure along the planes $\gamma = \frac{\pi}{2}$ and the symmetry of the A_1 functions with respect to these planes. There is freedom to choose any symmetry plane for the two degenerate E functions (one of which is symmetric to this plane, the other antisymmetric). The plane $\gamma_\lambda = \frac{\pi}{2}$ has been chosen for convenience, since reflection through this plane is equivalent to interchange of the ν and κ particles, which will give the same symmetry as is found in the $D^{J\Pi}_{M\Omega}$ functions defined in the λ SHC. Comparison of these plots with plots of the $J = 0$ LHSF calculated by Hipes and Kuppermann on the LSTH surface (unpublished) show only minor differences in shape or magnitude of the 10 lowest energy E functions of each of the two calculations; as discussed in section 4.4 and shown in table 4.6, the energies of the LHSF calculated in each method differ by less than 1% for each function examined, to a maximum of 0.04 eV. Given the large difference between the methods used to calculate these LHSF, the closeness of the results validates their correctness and accuracy.

When the energetically accessible part of the potential energy function becomes independent of the γ coordinate in that arrangement channel, the primitive basis set functions become good approximations to the LHSF; since the ω and γ

coordinates are then separable, the associated Legendre functions are the correct solutions for the γ variable part of the Schrödinger equation, and the reference potentials used to calculate the $f^J_{v j \Omega}$ become closely related to the radial potentials (including angular momentum) of the isolated diatom (if ω_λ is sufficiently small such that $\rho \sin \omega_\lambda \approx \rho \omega_\lambda$ is valid over the range of the function, the $f^J_{v j \Omega}$ become the radial functions). Accordingly, the v and j quantum numbers of the primitive basis set become good quantum numbers for the LHSF under these conditions. (For $J > 0$, the set of degenerate LHSF for quantum numbers v and j will be linear combinations of the set of degenerate primitives having these quantum numbers and the full range of values of Ω.) The nodal structure in the γ directions can therefore be correlated with the rotational excitation of the diatom, and the structure in the ω directions (corresponding to the diatomic internuclear distance) with the vibrational excitation.

We will begin by analyzing the $\rho = 6.0$ bohr LHSF of figure 4.6, as this value of ρ is sufficiently large to show some similarity to the separated particle wavefunctions. The LSTH potential energy surface at a hyperradius of 6.0 bohr shows minima for ranges of ω concentrated about the $\bar{Z}$ axes of each arrangement channel, and within this region, the potential is nearly independent of the angle γ. The reason is that at this hyperradius the effect of the isolated atom on the diatom is small and can be treated as a perturbation. Accordingly, the structure of the LHSF at a hyperradius of 6.0 bohr, when examined within a single arrangement channel, is simply related to the wavefunction of a diatomic molecule. The LHSF are confined to a small region of configuration space localized about the $\bar{Z}$ axes of each arrangement channel due to the large classical barrier between arrangement channels, which corresponds to configurations with large distances between all three atoms. The lack of overlap between the localized functions causes the energies of the E functions which are locally symmetric in regions where they have density to be nearly degenerate with the A_1 functions (which are locally symmetric in every

arrangement channel); accordingly, in figure 4.6 the energy of the A_1 function in panel (a) agrees within four significant figures with the degenerate E symmetry functions of panels (b) and (c). Similarly, the locally antisymmetric E functions of panels (e) and (f) have nearly the same energy as the function with A_2 symmetry of panel (d).

The series of excited state E function plots consisting of figures 4.6 (b), 4.6 (e), and panel (c) of figures 4.9 through 4.12 (and the degenerate partner in figures 4.6 (c), 4.6 (f) and panel (f) of 4.9 through 4.12) shows nodal structure in the γ directions which correlates asymptotically to rotational motion of the H_2 diatomic molecule (to be precise, to the nodes of the Legendre polynomials $\mathcal{P}_j^0$ which describe the γ behavior), and at sufficiently high energies nodal structure in the ω directions correlating to vibrational excitation. Specifically, the $n = 1$ functions of 4.6 (b) and (c) correlate to $v = 0, j = 0$, the $n = 2$ states of figure 4.6 (e) and (f) to $v = 0, j = 1$, the $n = 3$ of figures 4.9 (c) and (f) to $v = 0, j = 2$, the $n = 4$ functions of figures 4.10 (c) and (f) to $v = 0, j = 3$, the $n = 9$ functions in figures 4.11 (c) and (f) to $v = 1, j = 0$ and finally the $n = 10$ functions of 4.12 (c) and (f) to $v = 1, j = 1$. The presence or absence of probability density in the λ channel is determined by the symmetry requirements of the E function; the functions even with respect to $\gamma_\lambda = \frac{\pi}{2}$ will have no λ channel density for functions with odd j, and the functions odd with respect to $\gamma_\lambda = \frac{\pi}{2}$ will have no λ channel density for functions with even j.

At the saddle point of the LSTH potential energy surface ($\rho = 3.270145 a_0$), the minima of the surface are in the collinear configurations (which correspond to the limiting circles of each plot), and are located symmetrically between each pair of arrangement channels, in the configuration with one atom on the center of mass of the system, as can be seen on figure 4.5 panel (b). The ground state wavefunctions for all symmetries is isolated in regions near the minimum of the potential; however, the barrier between each of these minima is small and the excited state LHSF

calculated at this value of $\bar{\rho}$ have density over large regions of configuration space. The density of these functions is not confined to a region clearly belonging to a single arrangement channel, but is maximal in the regions between the $\bar{Z}$ axes. The rotational structure of the diatom may still be seen in the excited state LHSF, although shifted to a range centered on a value of ω larger than that for 6.0 bohr; however, the distinction between rotation and vibration in terms of γ and ω nodal patterns is no longer sharp, and the "rotation" of one pair of atoms overlaps strongly with the "rotation" of the other two possible pairs in these functions, particularly for the excited state functions in figures 4.9 through 4.12, panels (b) and (e). In this region of configuration space, the v and j labels of the primitive basis set are not good quantum numbers, and the E symmetry LHSF of both symmetries have density in the λ channel.

At a hyperradius of 2.0 bohr, the LSTH potential energy surface of figure 4.5 (a) has a set of minima near the $\bar{Y}$ axis, and accordingly the probability density of the LHSF at this value of $\bar{\rho}$ are concentrated near the center of the plots. The three atoms interact strongly at this hyperradius, and the nodal behavior shows that the excited states have mixed rotational and vibrational character. The lowest energy A_1 function of figure 4.8 (a) is nodeless, and the lowest energy A_2 function (in figure 4.8 (d)) has three nodal planes; therefore, the ground state E function of figures 4.8 (b) and (c) (with one node) and the first excited state with E symmetry in figures 4.8 (e) and (f) (with two nodes) are intermediate in energy between these two functions, since all of these functions span the same regions of the internal configuration space.

In figures 4.9 through 4.12, the excited state E symmetry functions are given for the three values of $\bar{\rho}$ mentioned above. As expected, the number of nodal lines increases with increasing LHSF energy for each value of $\bar{\rho}$. For $\rho = 2$ bohr, the density of the wavefunction is localized near the $\bar{Y}$ axis, and the small dip in the center of the A_1 function in figure 4.8 (a) corresponds to a local maximum in the

potential shown in figure 4.5 (a). Comparison of the functions at the saddle point and at $\rho = 6$ bohr show the same behavior, and so the flow of probability density into regions of configuration space characterized by relatively low potential energy is clearly visible for each set of plots as ρ changes.

The functions $\Theta_n^{J\Pi\{\Gamma_k \otimes \Gamma_k\}}$ of equation (4.6.3) are given in figures 4.13 through 4.15 for the LHSF which were diagrammed in figures 4.6 through 4.8. There is little information to be gained from these figures for $J = 0$, as they are simply the squares of the functions already plotted in the latter figures, but we present them here for comparison with other values of J.

4.8 Analysis of LHSF Results – J = 1

The $J = 1$, $\Pi = 0$ LHSF coefficients for the lowest energy LHSF (figures 4.16 through 4.18) look very much like the corresponding $J = 0$ LHSF. This occurs because the value of Ω is restricted to $\Omega = 1$, leaving only one term in the expansion, and the Wigner function $D_{M1}^{J=1,\Pi=0}(\phi_\lambda, \theta_\lambda, \psi_\lambda)$ has the property

$$\int D_{M1}^{J=1,\Pi=0*}(\phi_{\lambda'}, \theta_{\lambda'}, \psi_{\lambda'}) D_{M1}^{J=1,\Pi=0}(\phi_\lambda, \theta_\lambda, \psi_\lambda) d\vartheta_1^\lambda = 1/2 \qquad (4.8.1)$$

for all values of λ, λ'. As a consequence, the coefficients for this partial wave also retain the full P_3 symmetry. However, the parity Wigner function has A_2 symmetry (Ω is odd), and therefore the coefficient for the A_1 surface function also has A_2 symmetry so that the product is A_1. Similarly, the A_2 coefficient has A_1 symmetry, and the coefficient for the E function which is symmetric to the plane $\gamma_\lambda = \frac{\pi}{2}$ is antisymmetric to this plane (and vice versa). In accord with the constraints on the two-dimensional surface functions when $J + \Pi$ is odd, the LHSF are zero in the collinear configurations (the outermost circle of the plot). Again, for this case where the LHSF can be expanded in terms of a single Wigner function, the plots of $\Theta_n^{J\Pi\{\Gamma_k \otimes \Gamma_k\}}$ in figures 4.19 through 4.21 give no additional information.

The energies of the $J = 1, \Pi = 0$ functions are higher than those for the corresponding $J = 0$ functions, in particular for the A_1 function, which for this

partial wave may not have $j = 0$ character; in particular, at $\rho = 6.0$ bohr, the A_1 function of figure 4.16 (a) correlates to the asymptotic state $v = 0, j = 2$ (with γ_λ dependence approximately that of the associated Legendre function $\mathcal{P}_2^1$) instead of the $v = 0, j = 0$ correlation displayed by the $J = 0$ A_1 function of figure 4.6 (a). Similarly, the ground state E function for $J = 1, \Pi = 0$ more closely resembles the first excited state E function for $J = 0$ at $\rho = 6.0$ bohr. At this value of ρ, the ground state A_2 functions are still directly comparable, with the $\mathcal{P}_1^0$ γ_λ dependence of the $J = 0$ replaced by dependence on $\mathcal{P}_1^1$; there is an increase in energy with J due to the energy of rotation of the system, partially compensated by the accessability of the $J = 1, \Pi = 0$ function to the minima of the potential. The energies of these functions at the saddle point bears this out; for $\rho = 3.270145$ bohr, the energy of the $J = 1, \Pi = 0$ A_2 function of figure 4.17d is significantly lower than that for the $J = 0$ A_2 function of figure 4.7d. The increase in energy due to the higher total angular momentum is most easily determined from the E functions at $\rho = 2.0$ bohr, where the effect of the Wigner is to make the $k = 1$ density pattern for $J = 1, \Pi = 0$ resemble the $k = 2$ pattern for $J = 0$ and vice versa (see figures 4.15 and 4.21, panels (b) and (c), and so there is no net difference in accessibility to the potential; the increase in energy is about 0.015 eV for this value of ρ. At the larger values of ρ, the $J = 1, \Pi = 0$ functions are bounded away from the collinear configurations by the effect of the angular momentum (with $\Omega = 1$), and as a consequence the difference in energy is much greater.

The $J = 1$, $\Pi = 1$ LHSF coefficients consist of two terms with values of $\Omega = 0$ and $\Omega = 1$. Figures 4.22 through 4.27 display the coefficients for the lowest energy LHSF for each IR. For these functions, the P_2 symmetry about $\gamma_\lambda = \frac{\pi}{2}$ is clear; the $\Omega = 0$ coefficients in panels (a) through (c) preserve the symmetry of the LHSF about this plane, while the $\Omega = 1$ coefficients in panels (d) through (f) reverse the LHSF symmetry, due to the symmetry properties of the parity Wigner.

For the LHSF at 6.0 bohr (figures 4.22 and 4.23), the most striking character-

istic is the resemblance of the $n = 1$ $\Omega = 0$ functions for the A_1 and A_2 symmetries, in figures 4.22 (a) and 4.23 (a) respectively, to the $J = 0$ E functions of figures 4.6 (b) ($n = 1$) and 4.6 (f) ($n = 2$), and of the $n = 1$ $\Omega = 0$ E functions of figure 4.22 (b) and the $n = 2$ $\Omega = 0$ E function of figure 4.23 (c) to the $J = 0$ A_1 and A_2 functions of figures 4.6 (a) and 4.6 (d). The energies of the $J = 1, \Pi = 1$ A_1 and the $n = 1$ E functions are slightly higher than those of the similar $J = 0$ functions, due to the increase in internal energy of the system from the nonzero angular momentum. However, the energies of the $J = 1, \Pi = 1$ A_2 and $n = 2$ E functions are slightly lower than those for the $J = 0$ case; this is attributable to the extra degree of freedom present in the system. Figures 4.22 (f) and 4.23 (d) and (f) show that the $\Omega = 1$ coefficient for these functions is nodeless, and therefore the full LHSF for $J = 1, \Pi = 1$ has density in the minimum region of the potential for these symmetries, while the $J = 0$ LSHF for these symmetries were required to have nodes in this region.

At the saddle point, the A_2 and E LHSF can be nonzero for $\omega_\lambda = \pi$, and because the LHSF are expanded in terms of the parity Wigners in the λ SHC the expansion coefficients are multivalued at this point, being dependent on γ_λ as described in equation (2.9.14). This can be seen in figure 4.25, panels (a), (b), (d), and (e). However, as can be seen in figure 4.29 panels (c) and (d), the square of these surface functions integrated over the Euler angles (the $\Theta_n^{J\Pi\{\Gamma_k \otimes \Gamma_k\}}$ of equation (4.4.3)) has a smooth approach to zero derivative in the limit as ω_λ approaches π, as must be the case for LHSF which are continuous and differentiable everywhere.

At $\bar{\rho} = 2.0$ bohr, the ground state $J = 1, \Pi = 1$ A_1 and A_2 LHSF are closely related; in fact, the functions $\Theta_n^{J\Pi\{\Gamma_k \otimes \Gamma_k\}}$ derived from these LHSF (figure 4.30 panels (a) and (d)) are nearly equal. The coefficients of these functions, given in figure 4.26 (a) and (d) for the A_1 symmetry and figure 4.27 (a) and (d) for A_2 strongly resemble the coefficients for the ground state E LHSF for $J = 0$ (figure 4.8 (b) and (c)); the change from A_1 to A_2 symmetry is accomplished by switching the

coefficients between the $\Omega = 0$ and $\Omega = 1$ Wigner functions and changing the sign of one. Similarly, the ground state E symmetry functions of figure 4.26 panels (b) and (e) and 4.27 (b) and (e) contain coefficients which resemble the $J = 0$ A_1 symmetry LHSF, with the other coefficient resembling the ground state $J = 0$ E function with $k = 2$; the $\Theta_n^{J\Pi\{\Gamma_k \otimes \Gamma_k\}}$ functions associated with the two E symmetry functions closely resemble the similar function for $J = 0$ A_1, and indeed their energies differ by only 0.01 eV. The E function with $k = 1$ has the symmetric piece as the coefficient for the Wigner with $\Omega = 0$, while the $k = 2$ E has it as the coefficient for the $\Omega = 1$ Wigner. The $n = 2$ E function again resembles the $J = 0$ ground state E and the $n = 1$ $J = 1, \Pi = 1$ A_1 and A_2 states; as a consequence, the $n = 2$ E function is nearly degenerate with the latter two functions for this partial wave and ρ.

4.9 Analysis of LHSF Results – J = 2 and 3

The coefficients of the lowest energy $J = 2$ and $J = 3$ LHSF look very similar to those of the $J = 1$, $\Pi = 1$ LHSF; accordingly, we will give only two examples for each of these partial waves, which will be chosen to be the LHSF which display multivalued behavior for the point $\omega_\lambda = \pi$ at the saddle point ($\rho = 3.270145 a_0$). The full complement of $\Theta_n^{J\Pi\{\Gamma_k \otimes \Gamma_k\}}$ functions will still be presented.

Figures 4.31 through 4.36 contain the $J = 2$ $\Theta_n^{J\Pi\{\Gamma_k \otimes \Gamma_k\}}$ results. For $\Pi = 1$ and $\rho = 6.0$ bohr, the energies of the A_1 and $n = 2$ E functions of figure 4.31 are lower than the comparable $J = 1, \Pi = 0$ results of figure 4.19, once again due to greater accessiblilty to the low energy regions of the potential; however, the $J = 2, \Pi = 1$ A_2 and $n = 1$ E have approximately the same range in the internal configuration space as the corresponding $J = 1, \Pi = 0$ functions and accordingly are higher in energy due to the increased angular momentum, by about 0.0014 eV. (The smaller increase in energy from the $J = 1$ to the $J = 2$ E state as compared to the difference between the $n = 1$ $J = 1, \Pi = 1$ E functions and the $n = 1$ $J = 0$ E functions at $\rho = 2.0$ bohr, which was examined previously, is mainly due to the ρ^{-2} factor in the angular momentum terms. The difference in ρ reduces the effect of the

angular momentum terms by a factor of 9.) For $\rho = 3.270145$ bohr, we compare figure 4.32 for the $J = 2, \Pi = 1$ functions with figure 4.20 for the $J = 1, \Pi = 0$ functions. The major difference is for the $n = 1$ A_2 function. For the $J = 1, \Pi = 0$ case, the Wigner function D^{10}_{M1} has the appropriate A_2 exchange symmetry, so the coefficient $\psi^{10A_2}_{11}$ in the internal coordinate space has A_1 symmetry and therefore is nodeless. For $J = 2, \Pi = 1$, the Wigner functions do not have A_2 symmetry, only having symmetry with respect to the $\nu\kappa$ interchange; since each term in the sum of equation (4.6.1) must have A_2 symmetry, the coefficients $\psi^{21A_2}_{1\Omega}$ must build in the exchange symmetry. The $\Omega = 1$ term will therefore have nodes between the λ and ν and λ and κ channels, and the $\Omega = 2$ term will have a node between the ν and κ channels. Consequently, the density of the LHSF between the three channels will be low. Accordingly, the $J = 2, \Pi = 1$ A_2 function is significantly higher in energy than its $J = 1, \Pi = 0$ counterpart. Similarly, since the $J = 1, \Pi = 0$ A_1 coefficients have A_2 symmetry and the nodes which result from the antisymmetric exchange, the $J = 2, \Pi = 1$ A_1 functions, with coefficients which do not have this restriction, have significantly lower energies. The E functions for these two partial waves have similar but not identical patterns, with the $k = 1$ functions for $J = 1, \Pi = 0$ resembling the $k = 2$ functions for $J = 2, \Pi = 1$ and vice versa; the change in the energies for these functions is small. Finally, the $\rho = 2.0$ bohr patterns of figure 4.33 are nearly identical with those for $J = 1, \Pi = 1$ (figure 4.30), since each of these cases has an even and odd coefficient and consequently can access the same regions of internal configuration space; the LHSF energies increase somewhat with the increase in J.

The density patterns for the $J = 2, \Pi = 0$ functions at $\rho = 6.0$ bohr given in figure 4.34 are nearly the same as those in figure 4.28 for $J = 1, \Pi = 1$. The energies of the A_1 and $n = 1$ E functions increases by 0.0018 eV and 0.0016 eV, respectively, while the A_2 and $n = 2$ E function energies increase by only 0.0007 eV and 0.0006 eV, respectively. The additional value of Ω accessible for the $J = 2$ case allows the

functions to spread over a greater region of total configuration space, and this has a larger effect on the functions resembling the $j = 1$ asymptotic functions by lowering the density of the $\Omega = 0$ coefficient, which has an internal node corresponding to the associated Legendre function $\mathcal{P}_1^0$.

At $\rho = 3.270145$ bohr, the A_1 and $n = 1$ E functions of figure 4.35 may access the collinear configurations, while the A_2 and $n = 2$ E functions cannot; this is the opposite of the case in figure 4.29 with $J = 1, \Pi = 1$. The result is that the density of the A_1 function for the $J = 2, \Pi = 0$ case resembles the density for the A_2 function in the $J = 1, \Pi = 1$ partial wave, and vice versa; the patterns for the E functions are similarly exchanged between the $k = 1$ and $k = 2$ functions of the same energy. Accordingly, the A_1 and A_2 energies for the $J = 2, \Pi = 0$ functions are more closely related to those of the $J = 1, \Pi = 1$ A_2 and A_1 functions, respectively, than to those of the same symmetry. The coefficients $\psi_{n\Omega}^{J\Pi\Gamma_k}$ for the $J = 2, \Pi = 0$ A_1 and $n = 1, k = 1$ E functions are included in figure 4.37; the associated Legendre function behavior in the region near $\omega_\lambda = \pi$ is evident.

The $\Theta_n^{J\Pi\{\Gamma_k \otimes \Gamma_k\}}$ functions for $\rho = 2.0$ bohr are given in figure 4.36; the A_2 and E functions closely resemble their $J = 1, \Pi = 1$ counterparts in figure 4.30, while the A_1 function for the $J = 2$ case has significantly lower energy than for the $J = 1$ case. This is due to the accessibility of the $\Omega = 2$ state, in which the A_1 function has most of its density. As might be expected from examination of 4.36a, the coefficients for $\Omega = 0$ and $\Omega = 2$ are nodeless, and the coefficient for $\Omega = 1$, which has a node for $\nu\kappa$ interchange, is small compared to the nodeless coefficients.

Figures 4.38 through 4.43 contain the $J = 3$ $\Theta_n^{J\Pi\{\Gamma_k \otimes \Gamma_k\}}$ functions. The functions at $\rho = 6.0$ bohr in figures 4.38 and 4.41 are essentially the same as those for the $J = 2$ case in figures 4.31 and 4.34, respectively. The lowest energy LHSF in this nearly asymptotic region are associated with j values of 0, 1, and 2, and since the value of Ω is limited by the value of j, the availability of $\Omega = 3$ makes little difference in these cases. For $\rho = 3.270145$, we see from figures 4.39 for $J = 3, \Pi = 0$

and 4.32 for $J = 2, \Pi = 1$ that the functions for these partial waves are nearly the same if the A_2 functions of one partial wave are compared with the A_1 of the other, and similarly if the $k = 1$ E functions of one set are compared with the $k = 2$ E functions of the other. The same holds for the $J = 3, \Pi = 1$ functions of figure 4.42 and the $J = 2, \Pi = 0$ functions of figure 4.35. For half of the functions displayed, there is a small increase in energy with increasing J; however, for the A_2 and $n = 1$ E functions for the $J = 3$ partial wave (compared to the A_1 and $n = 1$ E functions for $J = 2$) there is a decrease in energy.

The $J = 3, \Pi = 0$ $\rho = 2.0$ bohr $\Theta_n^{J\Pi\{\Gamma_k \otimes \Gamma_k\}}$ functions of figure 4.40 are essentially equivalent to the $J = 2, \Pi = 0$ 2.0 bohr functions of figure 4.36, again comparing the A_1 function of one set with the A_2 function of the other and the $k = 1$ E functions of one with the $k = 2$ E functions of the other. The $J = 3, \Pi = 1$ $\rho = 2.0$ bohr functions of figure 4.41 differ from the other partial waves; the A_1 and A_2 functions of this set are nearly degenerate, while the E functions are somewhat higher in energy. The degeneracy of the A_1 and A_2 functions is explained by the addition of the $\Omega = 3$ terms, which give the A_2 function sufficient flexibility in the internal configuration space to access the lower energy regions of the potential. Comparison with the 2.0 bohr $\Theta_n^{J\Pi\{\Gamma_k \otimes \Gamma_k\}}$ functions for the lower values of J shows that the same distinctive pattern occurs for $J = 0$ A_1, $J = 1, \Pi = 0$ A_2, $J = 2, \Pi = 0$ A_1, $J = 3, \Pi = 0$ A_2 and $J = 3, \Pi = 1$ A_1 and A_2; in addition, the $n = 1$ E states for $J \geq 1$ have versions of the pattern which do not have perfect A_1 symmetry. The factor which connects all of these cases together is the ability of the surface function to access the potential with minimal interference from the symmetry-enforced nodal patterns, which comes from the freedom provided by the Ω degeneracy and the nodal structure in the Euler angles.

Figures 4.44 and 4.45 contain the $J = 3, \Pi = 1$ A_2 and $n = 2, k = 2$ E $\psi_{n\Omega}^{J\Pi\Gamma_k}$ functions at $\rho = 3.270145$ bohr, respectively. Once again the coefficients near the point $\omega_\lambda = \pi$ are seen to have the behavior of associated Legendre functions.

4.10 Possible Modifications to Improve Efficiency

As evidenced by the above discussion, the current methodology and algorithm are effective in the calculation of surface functions for use in a scattering calculation. However, there is always room for improvement, and some modifications are already under consideration which may increase the efficiency of the calculation.

There is no requirement that one use the reference potential chosen in (2.7.3) for calculation of the primitive basis set. A different set of one-dimensional primitives $\bar{t}^J_{vj\Omega}$ may be defined to correspond to the solutions of (2.8.1) with the potential function replaced by a different reference potential and the five-dimensional functions which result from this choice used to expand the LHSF. This will introduce additional terms into the equations which define the elements of the hamiltonian matrix **H**, since the previous reference potential was designed to include as large a portion of the surface hamiltonian as possible; however, a reduction in the range of definition of the primitives (accomplished by letting the reference potential go to infinity at some $\omega_\infty < \pi/2$ radians) can compensate for this by reducing the range of integration and consequently the time needed for each integral. A method which involves primitives defined in such a truncated ω_λ range has been developed in our laboratory[74] and results in a factor of 7 increase in speed over the current method in a code optimized for $J = 0$; efforts are currently under way to extend this method to general J.

Another possibility under consideration is a modification in the part of the basis set dependent on γ_λ. The associated Legendre functions currently in use are the correct solutions for a potential which is independent of γ_λ, which is only true when the atom-diatom distance is large (for the H+H_2 system, this does not occur for ρ less than 7 bohr). A better basis set can be derived in a self-consistent manner by determining the one-dimensional ω_λ-dependent $t^J_{vj\Omega}$ functions with lowest energy as above ($v = 1$ by definition), and then averaging the potential energy function $V(\rho, \omega_\lambda, \gamma_\lambda)$ over these primitives to determine a reference potential in the

γ_λ variable:

$$W_j^\Omega(\rho,\gamma_\lambda) = \int_0^\pi \left|t^J_{1j\Omega}(\omega_\lambda)\right|^2 V(\rho,\omega_\lambda,\gamma_\lambda)d\omega_\lambda. \tag{4.10.1}$$

The new γ_λ-dependent terms in the five-dimensional basis set are defined by the differential equation

$$\left(\frac{\partial^2}{\partial{\gamma_\lambda}^2} + \cot\gamma_\lambda\frac{\partial}{\partial\gamma_\lambda} + W_j^\Omega(\rho,\gamma_\lambda) - \frac{\Omega^2}{\sin^2\gamma_\lambda}\right)\mathcal{T}_j^\Omega(\cos\gamma_\lambda;\rho) = E_j^\Omega\mathcal{T}_j^\Omega(\cos\gamma_\lambda;\rho); \tag{4.10.2}$$

this differential equation reduces to that for the associated Legendre functions when the reference potentials W_j^Ω are constant. The new variational primitive basis set, obtained from using this new numerical function in the unsymmetrized basis set in place of the associated Legendre functions, will more closely correspond to the features of the potential, and therefore will be a better approximation to the γ_λ dependence of the LHSF; as a consequence, the size of the γ_λ-basis set needed for convergence (after removal of linear dependence) should be smaller. The most important reason to make this change, which adds additional terms to the two-dimensional integrals and requires numerical solution of the differential equation (4.10.2) and determination of the derivatives of these solutions, is the possibility of reduction of the linear dependence problems of the current choice of basis set. The rationale for assuming that the linear dependence will be decreased is that the primitives will be better approximations to the LHSF, which themselves are linearly independent. A program using this basis set is under development.

5. Summary

We have presented a method for the efficient calculation of local hyperspherical surface functions, and applied this method to the calculation of these functions on the LSTH potential energy surface for the system H + H_2 for partial waves $J = 0$ through $J = 3$. The LHSF so calculated were analyzed in terms of their dependence on the features of the potential and on the effect of increasing angular momentum.

Appendix A. Application of Hamiltonian to Primitive Basis Set

The result of application of the surface function hamiltonian $\hat{h}_\lambda$ to an expansion of the LHSF in terms of Wigner rotation matrices and associated Legendre functions is given in the main text in section 2.5; since this expansion is used not only in development of the formalism for the one-dimensional surface functions $\phi^{J\Pi\Gamma}_{njk}$ but also as an important part of our basis set for expansion, we will derive the results more explicitly here.

The Wigner rotation matrices have the properties[61]

$$\begin{aligned}\hat{J}^2(\theta_\lambda,\phi_\lambda,\psi_\lambda)D^J_{M\Omega}(\phi_\lambda,\theta_\lambda,\psi_\lambda) &= \hbar^2 J(J+1)D^J_{M\Omega}(\phi_\lambda,\theta_\lambda,\psi_\lambda)\\ \hat{J}_Z(\phi_\lambda)D^J_{M\Omega}(\phi_\lambda,\theta_\lambda,\psi_\lambda) &= \hbar M D^J_{M\Omega}(\phi_\lambda,\theta_\lambda,\psi_\lambda)\\ \hat{J}_{z_\lambda}(\psi_\lambda)D^J_{M\Omega}(\phi_\lambda,\theta_\lambda,\psi_\lambda) &= \hbar\Omega D^J_{M\Omega}(\phi_\lambda,\theta_\lambda,\psi_\lambda)\end{aligned} \tag{A.1}$$

and the normalization

$$\int\int\int d\vartheta^\lambda_1 D^{J*}_{M\Omega}(\phi_\lambda,thl,\psi_\lambda)D^J_{M\Omega'}(\phi_\lambda,thl,\psi_\lambda) = \left(\frac{8\pi^2}{2J+1}\right)\delta^\Omega_{\Omega'} \tag{A.2}$$

The normalization of the parity Wigner (2.5.2) follows from this and is given in (2.5.3). The normalized associated Legendre function is defined as[2]

$$\mathcal{P}^\Omega_j(\cos\gamma_\lambda) = \left[\frac{2j+1}{2}\frac{(j-|\Omega|)!}{(j+|\Omega|)!}\right]^{\frac{1}{2}} P^{|\Omega|}_j(\cos\gamma_\lambda)\begin{cases}(-1)^\Omega & \Omega\geq 0\\ 1 & \Omega<0\end{cases} \tag{A.3}$$

$$\int_0^\pi \sin\gamma_\lambda d\gamma_\lambda \mathcal{P}^\Omega_{j'}(\cos\gamma_\lambda)\mathcal{P}^\Omega_j(\cos\gamma_\lambda) = \delta^{j'}_j \tag{A.4}$$

The operator $\hat{j}^2_\lambda$ which appears in the surface hamiltonian is given by[2]

$$\hat{j}^2_\lambda(\gamma_\lambda,\psi_\lambda) = -\hbar^2\left(\frac{\partial^2}{\partial{\gamma_\lambda}^2} + \cot\gamma_\lambda\frac{\partial}{\partial\gamma_\lambda} + \frac{1}{\sin^2\gamma_\lambda}\frac{\partial^2}{\partial\psi^2_\lambda}\right) \tag{A.5}$$

The rotation matrices $D^J_{M\Omega}$ are eigenfunctions of $\frac{\partial}{\partial\psi_\lambda}$ with eigenvalue $\imath\Omega$, and consequently

$$\begin{aligned}\hat{j}^2_\lambda(\gamma_\lambda,\psi_\lambda)D^{J\Pi}_{M\Omega}(\phi_\lambda,\theta_\lambda,\psi_\lambda)\mathcal{P}^\Omega_j(\cos\gamma_\lambda)f^{J\lambda}_{vj\Omega}(\omega_\lambda;\bar{\rho}) &= -\hbar^2 D^{J\Pi}_{M\Omega}(\phi_\lambda,\theta_\lambda,\psi_\lambda)\times\\ \left(\frac{\partial^2}{\partial{\gamma_\lambda}^2} + \cot\gamma_\lambda\frac{\partial}{\partial\gamma_\lambda} - \frac{\Omega^2}{\sin^2\gamma_\lambda}\frac{\partial^2}{\partial\psi^2_\lambda}\right)&\mathcal{P}^\Omega_j(\cos\gamma_\lambda)f^{J\lambda}_{vj\Omega}(\omega_\lambda;\bar{\rho})\end{aligned} \tag{A.6}$$

The associated Legendre functions are in turn eigenfunctions of the operators in γ_λ:

$$\left(\frac{\partial^2}{\partial\gamma_\lambda{}^2}+\cot\gamma_\lambda\frac{\partial}{\partial\gamma_\lambda}-\frac{\Omega^2}{\sin^2\gamma_\lambda}\frac{\partial^2}{\partial\psi_\lambda^2}\right)\mathcal{P}_j^\Omega(\cos\gamma_\lambda)=-j(j+1)\mathcal{P}_j^\Omega(\cos\gamma_\lambda) \qquad (A.7)$$

so the net result is

$$\hat{j}_\lambda^2(\gamma_\lambda,\psi_\lambda)\mathrm{F}_{vj\Omega}^{JM\Pi}=\hbar^2 j(j+1)\mathrm{F}_{vj\Omega}^{JM\Pi} \qquad (A.8)$$

The rotation matrices are not eigenfunctions of the $\hat{\ell}_\lambda^2$ operator; however, this operator may be expressed in terms of a vector sum of the operators $\hat{\mathbf{j}}_\lambda$ and $\hat{\mathbf{J}}$, which in turn may be expressed in terms of raising and lowering angular momentum operators as[2]

$$\hat{\ell}_\lambda^2=\hat{J}^2+\hat{j}_\lambda^2+2\hbar^2\frac{\partial^2}{\partial\psi_\lambda{}^2}-\hat{j}_\lambda^-\hat{J}^+-\hat{j}_\lambda^+\hat{J}^- \qquad (A.9)$$

for which

$$\hat{J}^\pm D_{M\Omega}^J=\hbar\xi_\mp(J,\Omega)D_{M\Omega\mp1}^J \qquad (A.10)$$

$$\hat{j}_\lambda^\pm\mathcal{P}_j^\Omega=\hbar\xi_\mp(j,\Omega)\mathcal{P}_j^{\Omega\mp1} \qquad (A.11)$$

Using equations $(A.1)$ and $(A.9)$ through $(A.11)$, we find that

$$\begin{aligned}\hat{\ell}_\lambda^2 D_{M\Omega}^J\mathcal{P}_j^\Omega f_{vj\Omega}^{J\lambda}=&\\ &\hbar^2\left[J(J+1)+j(j+1)-2\Omega^2\right]D_{M\Omega}^J\mathcal{P}_j^\Omega f_{vj\Omega}^{J\lambda}\\ &-\hbar^2\xi_+(J,\Omega)\xi_+(j,\Omega)D_{M\Omega+1}^J\mathcal{P}_j^{\Omega+1}f_{vj\Omega}^{J\lambda}\\ &-\hbar^2\xi_-(J,\Omega)\xi_-(j,\Omega)D_{M\Omega-1}^J\mathcal{P}_j^{\Omega-1}f_{vj\Omega}^{J\lambda}\end{aligned} \qquad (A.12)$$

To determine the effect on the functions which have parity symmetry, we note from the definition $(A.3)$ that $\mathcal{P}_j^\Omega=(-1)^\Omega\mathcal{P}_j^{-\Omega}$; therefore we may write

$$D_{M\Omega}^{J\Pi}\mathcal{P}_j^\Omega=\left(\frac{2J+1}{32\pi^2}\right)\left(D_{M\Omega}^J\mathcal{P}_j^\Omega+(-1)^{J+\Pi}D_{M-\Omega}^J\mathcal{P}_j^{-\Omega}\right) \qquad (A.13)$$

The parity equation is found by substituting $-\Omega$ for Ω in equation $(A.12)$ and summing with the original expression:

$$\begin{aligned}\hat{\ell}_\lambda^2 D_{M\Omega}^{J\Pi}\mathcal{P}_j^\Omega f_{vj\Omega}^{J\lambda}=&\\ &\hbar^2\left[J(J+1)+j(j+1)-2\Omega^2\right]D_{M\Omega}^{J\Pi}\mathcal{P}_j^\Omega f_{vj\Omega}^{J\lambda}\\ &-\hbar^2\xi_+(J,\Omega)\xi_+(j,\Omega)D_{M\Omega+1}^{J\Pi}\mathcal{P}_j^{\Omega+1}f_{vj\Omega}^{J\lambda}\\ &-\hbar^2\xi_-(J,\Omega)\xi_-(j,\Omega)D_{M\Omega-1}^{J\Pi}\mathcal{P}_j^{\Omega-1}f_{vj\Omega}^{J\lambda}\end{aligned} \qquad (A.14)$$

Appendix B. Derivation of the Form of the Integral Matrices

The overlap integral between two λ channel functions is given by equation (2.9.6) as

$$\left[\mathbf{M}^{J\Pi}_{\lambda\lambda}(\bar{\rho})\right]^{v'j'\Omega'}_{vj\Omega} = \left\langle \mathbf{F}^{JM\Pi}_{\lambda vj\Omega}(\zeta_\lambda;\bar{\rho}) \mid \mathbf{F}^{JM\Pi}_{\lambda v'j'\Omega'}(\zeta_\lambda;\bar{\rho})\right\rangle \tag{B.1}$$

Substitution of equation (2.8.2) yields

$$\left[\mathbf{M}^{J\Pi}_{\lambda\lambda}(\bar{\rho})\right]^{v'j'\Omega'}_{vj\Omega} =$$

$$\left\langle D^{J\Pi}_{M\Omega}(\phi_\lambda,\theta_\lambda,\psi_\lambda)\mathcal{P}^{\Omega}_{j}(\cos\gamma_\lambda) f^{J\lambda}_{vj\Omega}(\omega_\lambda;\bar{\rho}) \middle| D^{J\Pi}_{M\Omega}(\phi_\lambda,\theta_\lambda,\psi_\lambda)\mathcal{P}^{\Omega'}_{j'}(\cos\gamma_\lambda) f^{J\lambda}_{v'j'\Omega'}(\omega_\lambda;\bar{\rho})\right\rangle \tag{B.2}$$

The integration over the Euler angles involves only the $D^{J\Pi}_{M\Omega}$; using the definition of these functions in equation (2.5.2) and the normalization (A.2) of the $D^{J}_{M\Omega}$, we find the result of this integration is as given in equation (2.5.3). Substituting this equation and the expression for the volume element (2.1.12), we find

$$\begin{aligned}\left[\mathbf{M}^{J\Pi}_{\lambda\lambda}(\bar{\rho})\right]^{v'j'\Omega'}_{vj\Omega} = {} & \frac{1}{2}\delta^{\Omega'}_{\Omega}\left(1+(-1)^{J+\Pi}\delta^{0}_{\Omega}\right)\times \\ & \int_0^\pi \sin\gamma_\lambda d\gamma_\lambda \mathcal{P}^{\Omega}_{j'}(\cos\gamma_\lambda)\mathcal{P}^{\Omega}_{j}(\cos\gamma_\lambda)\times \\ & \int_0^\pi \sin^2\omega_\lambda d\omega_\lambda f^{J\lambda}_{v'j'\Omega}(\omega_\lambda;\bar{\rho}) f^{J\lambda}_{vj\Omega}(\omega_\lambda;\bar{\rho})\end{aligned} \tag{B.3}$$

The integration over the γ_λ variable is the normalization integral (A.4) for the normalized associated Legendre functions. Substitution of this equation yields

$$\begin{aligned}\left[\mathbf{M}^{J\Pi}_{\lambda\lambda}(\bar{\rho})\right]^{v'j'\Omega'}_{vj\Omega} = {} & \frac{1}{2}\delta^{j'\Omega'}_{j\ \Omega}\left(1+(-1)^{J+\Pi}\delta^{0}_{\Omega}\right)\times \\ & \int_0^\pi \sin^2\omega_\lambda d\omega_\lambda f^{J\lambda}_{v'j\Omega}(\omega_\lambda;\bar{\rho}) f^{J\lambda}_{vj\Omega}(\omega_\lambda;\bar{\rho})\end{aligned} \tag{B.4}$$

Finally, using equations (2.8.1a) and (2.8.2) we have

$$\int_0^\pi \sin^2\omega_\lambda d\omega_\lambda f^{J\lambda}_{v'j\Omega}(\omega_\lambda;\bar{\rho}) f^{J\lambda}_{vj\Omega}(\omega_\lambda;\bar{\rho}) = \int_0^\pi d\omega_\lambda t^{J\lambda}_{v'j\Omega}(\omega_\lambda;\bar{\rho}) t^{J\lambda}_{vj\Omega}(\omega_\lambda;\bar{\rho}) = \delta^{v'}_{v} \tag{B.5}$$

and substitution of this gives the result

$$\left[\mathbf{M}^{J\Pi}_{\lambda\lambda}(\bar{\rho})\right]^{vj\Omega}_{v'j'\Omega'} = \frac{1}{2}\delta^{v\ j\ \Omega}_{v'j'\Omega'}\left(1+(-1)^{J+\Pi}\delta^{0}_{\Omega}\right) \tag{B.6}$$

The integration for the overlap matrix between primitive basis sets in the λ channel but at different $\bar{\rho}$ is the same except for the final step, where equation $(B.5)$ does not apply. Modification of equation $(B.4)$ to account for the differing values of $\bar{\rho}$ yields

$$\left[\mathcal{O}p^{J\Pi}_{\lambda\lambda}(\bar{\rho}_{i+1};\bar{\rho}_i)\right]^{v'j'\Omega'}_{vj\Omega} = \left\langle \mathrm{F}^{JM\Pi}_{\lambda vj\Omega}(\zeta_\lambda;\bar{\rho}_{i+1}) \mid \mathrm{F}^{JM\Pi}_{\lambda v'j'\Omega'}(\zeta_\lambda;\bar{\rho}_i)\right\rangle$$
$$= \delta^{j'\Omega'}_{j\Omega}\frac{1+(-1)^{J+\Pi}\delta^{\Omega}_{0}}{2}\int_0^\pi \sin^2\omega_\lambda d\omega_\lambda f^{J\lambda}_{vj\Omega}(\omega_\lambda;\bar{\rho}_{i+1})f^{J\lambda}_{v'j\Omega}(\omega_\lambda;\bar{\rho}_i) \tag{B.7}$$

The λ-channel primitive basis set interaction matrices are defined in equation (2.9.13) as

$$\left[(\mathcal{I}p)^{J\Pi}_{\lambda\lambda}(\rho;\bar{\rho})\right]^{v'j'\Omega'}_{vj\Omega} = \left\langle \mathrm{F}^{JM\Pi}_{\lambda vj\Omega}(\zeta_\lambda;\bar{\rho}) \mid \bar{V}(\rho,\omega_\lambda,\gamma_\lambda;\bar{\rho}) \mid \mathrm{F}^{JM\Pi}_{\lambda v'j'\Omega'}(\zeta_\lambda;\bar{\rho})\right\rangle \tag{B.8}$$

The integral over the Euler angles is performed as above, yielding

$$\left[(\mathcal{I}p)^{J\Pi}_{\lambda\lambda}(\rho;\bar{\rho})\right]^{v'j'\Omega'}_{vj\Omega} = \frac{1}{2}\delta^{\Omega'}_{\Omega}\left(1+(-1)^{J+\Pi}\delta^{0}_{\Omega}\right)\times$$
$$\int_0^\pi \sin\gamma_\lambda d\gamma_\lambda \int_0^\pi \sin^2\omega_\lambda d\omega_\lambda \mathcal{P}^{\Omega}_{j'}(\cos\gamma_\lambda)\mathcal{P}^{\Omega}_{j}(\cos\gamma_\lambda)\times \tag{B.9}$$
$$\bar{V}(\rho,\omega_\lambda,\gamma_\lambda;\bar{\rho})f^{J\lambda}_{v'j'\Omega}(\omega_\lambda;\bar{\rho})f^{J\lambda}_{vj\Omega}(\omega_\lambda;\bar{\rho})$$

We perform the integration over γ_λ first; by the definition of equation (2.7.3) and the form of $\bar{V}$ given in equation (2.4.9), we obtain the result

$$\left[(\mathcal{I}p)^{J\Pi}_{\lambda\lambda}(\rho;\bar{\rho})\right]^{v'j'\Omega'}_{vj\Omega} = \delta^{\Omega'}_{\Omega}\frac{1+(-1)^{J+\Pi}\delta^{\Omega}_{0}}{2}\int_0^\pi \sin^2\omega_\lambda d\omega_\lambda f^{J\lambda}_{vj\Omega}(\omega_\lambda;\bar{\rho})f^{J\lambda}_{v'j'\Omega}(\omega_\lambda;\bar{\rho})\times$$
$$\left(V^{\Omega}_{jj'}(\rho,\omega_\lambda) - \left(\frac{\bar{\rho}}{\rho}\right)^2 V^{\Omega}_{jj'}(\bar{\rho},\omega_\lambda)\right) \tag{B.10}$$

The result of application of the surface function hamiltonian $\hat{h}_\lambda$ to a primitive in the λ channel can be derived from the expressions $(A.8)$ and $(A.14)$; substituting these expressions into equation (2.1.10) and the result into equation (2.1.9), we find

that

$$
\begin{aligned}
&\hat{h}_\lambda \mathrm{F}^{JM\Pi}_{\lambda v j\Omega} = \\
&\left\{ \frac{1}{2\mu\rho^2} \left(\hat{L}^2_\lambda(\omega_\lambda) + \frac{\hat{\ell}^2_\lambda(\theta_\lambda,\phi_\lambda,\psi_\lambda,\gamma_\lambda)}{\cos^2(\frac{\omega_\lambda}{2})} + \frac{\hat{\jmath}^2_\lambda(\psi_\lambda,\gamma_\lambda)}{\sin^2(\frac{\omega_\lambda}{2})} \right) + V(\rho,\omega_\lambda,\gamma_\lambda) \right\} \mathrm{F}^{JM\Pi}_{\lambda v j\Omega} = \\
&\left\{ \frac{1}{2\mu\rho^2} \left(\hat{L}^2_\lambda(\omega_\lambda) + \frac{\hbar^2\left[J(J+1)-2\Omega^2\right]}{\cos^2(\frac{\omega_\lambda}{2})} + \frac{4\hbar^2 j(j+1)}{\sin^2(\omega_\lambda)} \right) \right. \\
&\qquad\qquad \left. + V(\rho,\omega_\lambda,\gamma_\lambda) \right\} D^{J\Pi}_{M\Omega} \mathcal{P}^{\Omega}_j f^{J\lambda}_{vj\Omega} \\
&- \frac{\hbar^2 \xi_+(J,\Omega)\xi_+(j,\Omega)}{2\mu\rho^2\cos^2(\frac{\omega_\lambda}{2})} D^{J\Pi}_{M(\Omega+1)} \mathcal{P}^{(\Omega+1)}_j f^{J\lambda}_{vj\Omega} \\
&- \frac{\hbar^2 \xi_-(J,\Omega)\xi_-(j,\Omega)}{2\mu\rho^2\cos^2(\frac{\omega_\lambda}{2})} D^{J\Pi}_{M(\Omega-1)} \mathcal{P}^{(\Omega-1)}_j f^{J\lambda}_{vj\Omega}
\end{aligned}
\tag{B.11}
$$

This may be somewhat simplified by using the differential equation for the $f^{J\lambda}_{vj\Omega}$ functions, which is closely related to equation (2.8.1) for the $t^{J\lambda}_{vj\Omega}$:

$$
\begin{aligned}
&\left(\frac{1}{2\mu\bar{\rho}^2} \left\{ -\hat{L}^2_\lambda(\omega_\lambda) + \frac{\hbar^2\left[J(J+1)-2\Omega^2\right]}{\cos^2\frac{\omega_\lambda}{2}} + \frac{4\hbar^2 j(j+1)}{\sin^2\omega_\lambda} \right\} \right. \\
&\qquad \left. + V^{\Omega}_{jj}(\rho,\omega_\lambda) \right) f^{J\lambda}_{vj\Omega}(\omega_\lambda;\rho) = e^{J\lambda}_{vj\Omega}(\rho) f^{J\lambda}_{vj\Omega}(\omega_\lambda;\rho).
\end{aligned}
\tag{B.12}
$$

Substitution of (B.12) into (B.11) yields

$$
\begin{aligned}
&\hat{h}_\lambda \mathrm{F}^{JM\Pi}_{\lambda v j\Omega} = \\
&\left(e^{J\lambda}_{vj\Omega}(\rho) + V(\rho,\omega_\lambda,\gamma_\lambda) - V^{\Omega}_{jj}(\omega_\lambda;\rho) \right) D^{J\Pi}_{M\Omega} \mathcal{P}^{\Omega}_j f^{J\lambda}_{vj\Omega} \\
&- \frac{\hbar^2 \xi_+(J,\Omega)\xi_+(j,\Omega)}{2\mu\rho^2\cos^2(\frac{\omega_\lambda}{2})} D^{J\Pi}_{M(\Omega+1)} \mathcal{P}^{(\Omega+1)}_j f^{J\lambda}_{vj\Omega} \\
&- \frac{\hbar^2 \xi_-(J,\Omega)\xi_-(j,\Omega)}{2\mu\rho^2\cos^2(\frac{\omega_\lambda}{2})} D^{J\Pi}_{M(\Omega-1)} \mathcal{P}^{(\Omega-1)}_j f^{J\lambda}_{vj\Omega}
\end{aligned}
\tag{B.13}
$$

We multiply this equation by $D^{J\Pi *}_{M\Omega'} \mathcal{P}^{\Omega'}_{j'} f^{J\lambda}_{v'j'\Omega'}$ and integrate; the integral over the

Euler angles is again given by equation (2.5.3), and we have

$$\begin{aligned}
\left[\mathbf{H}^{J\Pi}_{\lambda\lambda}(\bar{\rho})\right]^{vj\Omega}_{v'j'\Omega'} &= \left\langle \mathrm{F}^{JM\Pi}_{\lambda v'j'\Omega'}(\zeta_\lambda;\bar{\rho}) \mid \hat{h}_\lambda \mid \mathrm{F}^{JM\Pi}_{\lambda vj\Omega}(\zeta_\lambda;\bar{\rho})\right\rangle \\
&= \frac{1}{2}\delta^{\Omega}_{\Omega'}(1+(-1)^{J+\Pi}\delta^0_{\Omega'})\int\int d\vartheta_2^\lambda \left(e^{J\lambda}_{vj\Omega}(\rho)+V(\rho,\omega_\lambda,\gamma_\lambda)-V^{\Omega'}_{jj}(\omega_\lambda;\rho)\right)\times \\
&\mathcal{P}^{\Omega'}_j\mathcal{P}^{\Omega'}_{j'}f^{J\lambda}_{vj\Omega'}f^{J\lambda}_{v'j'\Omega'} \\
&-\frac{1}{2}\delta^{\Omega+1}_{\Omega'}(1+(-1)^{J+\Pi}\delta^0_{\Omega'})\int\int d\vartheta_2^\lambda \frac{\hbar^2\xi_+(J,\Omega'-1)\xi_+(j,\Omega'-1)}{2\mu\rho^2\cos^2(\frac{\omega_\lambda}{2})}\times \\
&\mathcal{P}^{\Omega'}_{j'}f^{J\lambda}_{v'j'\Omega'}\mathcal{P}^{\Omega'}_{j}f^{J\lambda}_{vj(\Omega'-1)} \\
&-\frac{1}{2}\delta^{\Omega-1}_{\Omega'}(1+(-1)^{J+\Pi}\delta^0_{\Omega'})\int\int d\vartheta_2^\lambda \frac{\hbar^2\xi_-(J,\Omega'+1)\xi_-(j,\Omega'+1)}{2\mu\rho^2\cos^2(\frac{\omega_\lambda}{2})}\times \\
&\mathcal{P}^{\Omega'}_{j}f^{J\lambda}_{vj(\Omega'+1)}\mathcal{P}^{\Omega'}_{j'}f^{J\lambda}_{v'j'\Omega'}
\end{aligned} \tag{B.14}$$

Performing the γ_λ integration yields

$$\begin{aligned}
\left[\mathbf{H}^{J\Pi}_{\lambda\lambda}(\bar{\rho})\right]^{vj\Omega}_{v'j'\Omega'} &= \delta^{j\Omega}_{j'\Omega'}\frac{1+(-1)^{J+\Pi}\delta^0_{\Omega'}}{2}epr(\rho)\int_0^\pi \sin^2\omega_\lambda d\omega_\lambda f^{J\lambda}_{vj'\Omega'}f^{J\lambda}_{v'j'\Omega'} \\
&+\delta^{j\Omega}_{j'\Omega'}\frac{1+(-1)^{J+\Pi}\delta^0_{\Omega'}}{2}(1-\delta^j_{j'})\int_0^\pi \sin^2\omega_\lambda d\omega_\lambda V^{\Omega'}_{jj}(\omega_\lambda;\rho)f^{J\lambda}_{vj'\Omega'}f^{J\lambda}_{v'j'\Omega'} \\
&-\delta^{j\Omega+1}_{j'\Omega'}\frac{1+(-1)^{J+\Pi}\delta^0_{\Omega'}}{2}\frac{\hbar^2\xi_-(J,\Omega')\xi_-(j,\Omega')}{2\mu\rho^2}\int_0^\pi \sin^2\omega_\lambda d\omega_\lambda \frac{f^{J\lambda}_{v'j'\Omega'}f^{J\lambda}_{vj(\Omega'-1)}}{\cos^2(\frac{\omega_\lambda}{2})} \\
&-\frac{1}{2}\delta^{j\Omega-1}_{j'\Omega'}\frac{1+(-1)^{J+\Pi}\delta^0_{\Omega'}}{2}\frac{\hbar^2\xi_+(J,\Omega')\xi_+(j,\Omega')}{2\mu\rho^2}\int_0^\pi \sin^2\omega_\lambda d\omega_\lambda \frac{f^{J\lambda}_{v'j'\Omega'}f^{J\lambda}_{vj(\Omega'+1)}}{\cos^2(\frac{\omega_\lambda}{2})}
\end{aligned} \tag{B.15}$$

Finally, the integration in the first line of equation (B.15) can be performed, the remaining terms can be reorganized and the primed and unprimed indices interchanged to obtain equation (2.9.7).

The expressions for the $\nu\lambda$ integrals are simpler, since most of the integration is not analytic. The Wigner rotation matrix in the ν arrangement channel coordinates can be related to the matrices in the λ channel through a rotation:[61]

$$D^J_{M\Omega}(\phi_\nu,\theta_\nu,\psi_\nu)=\sum_{\Omega'}D^J_{M\Omega'}(\phi_\lambda,\theta_\lambda,\psi_\lambda)D^J_{\Omega'\Omega}(\theta_1,\theta_2,\theta_3) \tag{B.16}$$

where the rotations are done in the order θ_3 about the $\mathbf{z}_\lambda$ axis, θ_2 about the $\mathbf{y}$ axis and θ_1 about the $\mathbf{z}_\lambda$ axis. Since the two sets of coordinates share a common $\mathbf{y}$ axis,

$\theta_1 = \theta_3 = 0$ and θ_2 is the angle between the $\mathbf{z}_\lambda$ and $\mathbf{z}_\nu$ axes; we may simplify the equation to

$$D^J_{M\Omega}(\phi_\nu, \theta_\nu, \psi_\nu) = \sum_{\Omega'} D^J_{M\Omega'}(\phi_\lambda, \theta_\lambda, \psi_\lambda) d^J_{\Omega'\Omega}(\Delta_{\nu\lambda}) \qquad (B.17)$$

where the angle $\Delta_{\nu\lambda}$ is given in equation (2.9.11). Multiplying both sides of $(B.17)$ by $D^{J*}_{M\Omega''}(\phi_\lambda, \theta_\lambda, \psi_\lambda)$ and performing the analytic integration yields

$$\int d\vartheta_1^\lambda D^{J*}_{M\Omega''}(\phi_\lambda, \theta_\lambda, \psi_\lambda) D^J_{M\Omega}(\phi_\nu, \theta_\nu, \psi_\nu) = \left(\frac{8\pi^2}{2J+1}\right) d^J_{\Omega''\Omega}(\Delta_{\nu\lambda}) \qquad (B.18)$$

The function $d^J_{\Omega'\Omega}$ is real; since the Wigner rotation matrices are the only complex quantities in our basis, we therefore have that all integrals in our formalism are real. The determination of the result with the parity Wigner functions is straightforward, and the result is given in equation (2.9.10).

The form of the $\nu\lambda$ integrals is simple, as there are no orthogonality relations to reduce the integration beyond the integral over the Euler angles; the main effect is to add the function $d^{J\Pi}_{\Omega\Omega'}$ to the integrals over ω_λ and γ_λ, which are not analytic.

We note that the dependence of the integrals on the quantum number M has vanished with the integration over the Wigner rotation matrices. This is as expected from the isotropicity of space.

Appendix C. Construction of Symmetry Integral Matrices

For illustrative purposes, and to demonstrate the independence of the $\mathcal{I}$ and $\mathcal{O}$ matrices from the index k, we will give in explicit form the E matrices for P_3 with $k = 1, 2$. Substitution of equation (2.8.9) into equation (2.9.3) yields

$$\left[\mathrm{M}^{J\Pi E_k}(\bar{\rho})\right]^{\tau' v' j' \Omega'}_{\tau v j \Omega} = \sum_{\bar{\lambda}\bar{\lambda}'} c^{E_k}_{\tau\bar{\lambda}j} c^{E_k}_{\tau'\bar{\lambda}'j'} \left\langle \mathrm{F}^{JM\Pi}_{\bar{\lambda}vj\Omega}(\zeta_{\bar{\lambda}};\bar{\rho}) \mid \mathrm{F}^{JM\Pi}_{\bar{\lambda}'v'j'\Omega'}(\zeta_{\bar{\lambda}'};\bar{\rho}) \right\rangle \qquad (C.1)$$

We will drop the τ and τ' terms as they are equal and may take on only the value A. From the symmetry relations of equation (2.9.2), we can reformulate this equation as

$$\begin{aligned}\left[\mathrm{M}^{J\Pi E_k}(\bar{\rho})\right]^{\tau' v' j' \Omega'}_{\tau v j \Omega} &= \left\langle \mathrm{F}^{JM\Pi}_{\alpha vj\Omega}(\zeta_\alpha;\bar{\rho}) \mid \mathrm{F}^{JM\Pi}_{\alpha v'j'\Omega'}(\zeta_\alpha;\bar{\rho}) \right\rangle \left(\sum_\lambda c^{E_k}_{\lambda j} c^{E_k}_{\lambda j'} \right) \\ &+ \left\langle \mathrm{F}^{JM\Pi}_{\beta vj\Omega}(\zeta_\beta;\bar{\rho}) \mid \mathrm{F}^{JM\Pi}_{\alpha v'j'\Omega'}(\zeta_\alpha;\bar{\rho}) \right\rangle \left(\sum_\lambda c^{E_k}_{\nu j} c^{E_k}_{\lambda j'} + (-1)^{j+j'} c^{E_k}_{\lambda j} c^{E_k}_{\nu j'} \right)\end{aligned} \qquad (C.2)$$

Performing these sums yields

$$\sum_\lambda c^{E_k}_{\lambda j} c^{E_k}_{\lambda j'} = \begin{cases} 1 & j + j' \text{ even} \\ 0 & j + j' \text{ odd} \end{cases} \qquad (C.3)$$

$$\sum_\lambda \left(c^{E_k}_{\nu j} c^{E_k}_{\lambda j'} + (-1)^{j+j'} c^{E_k}_{\lambda j} c^{E_k}_{\nu j'} \right) = \begin{cases} -1 & j + j' \text{ even} \\ (-1)^j \sqrt{3} & j + j' \text{ odd} \end{cases} \qquad (C.4)$$

and we have that the $\mathbf{M}$ matrix is independent of k:

$$\left[\mathrm{M}^{J\Pi E}(\bar{\rho})\right]^{\tau' v' j' \Omega'}_{\tau v j \Omega} = \begin{cases} \left\langle \mathrm{F}^{JM\Pi}_{\alpha vj\Omega}(\zeta_\alpha;\bar{\rho}) \mid \mathrm{F}^{JM\Pi}_{\alpha v'j'\Omega'}(\zeta_\alpha;\bar{\rho}) \right\rangle & \\ \quad - \left\langle \mathrm{F}^{JM\Pi}_{\beta vj\Omega}(\zeta_\beta;\bar{\rho}) \mid \mathrm{F}^{JM\Pi}_{\alpha v'j'\Omega'}(\zeta_\alpha;\bar{\rho}) \right\rangle & j + j' \text{ even} \\ \sqrt{3}(-1)^j \left\langle \mathrm{F}^{JM\Pi}_{\beta vj\Omega}(\zeta_\beta;\bar{\rho}) \mid \mathrm{F}^{JM\Pi}_{\alpha v'j'\Omega'}(\zeta_\alpha;\bar{\rho}) \right\rangle & j + j' \text{ odd} \end{cases} \qquad (C.5)$$

The same algebra with the basis set coefficients applies to the $\mathbf{H}^{J\Pi\Gamma}$, $(\mathcal{I}p)^{J\Pi\Gamma}$ and $(\mathcal{O}p)^{J\Pi\Gamma}$ matrices. It follows from the nature of the generalized eigenvalue problem of equation (2.8.8) that the coefficient matrix $\mathbf{a}^{J\Pi\Gamma}$ and the surface function energy matrix $\mathbf{E}^{J\Pi\Gamma}$ are also independent of k. This results in the $\mathcal{I}^{J\Pi\Gamma}$ and $\mathcal{O}^{J\Pi\Gamma}$ matrices being independent of k and proves the assertion in section 2.4 that the coefficients $b_n^{J\Pi\Gamma}$ do not depend on k.

References

† Work supported in part by DOE grant DE-AS03-83ER and AFAL contract F04611-86-K-0067. One of the authors (SAC) also thanks NSF for a Graduate Fellowship. Most of the calculations were performed on the CRAY X-MP/48, SCS-40 and CRAY Y-MP/864 computers at the NSF San Diego Supercomputing Center.

¶ Work performed in partial fulfillment of the requirements for the Ph.D. degree in Chemistry at the California Institute of Technology.

‡ Contribution number

1. A. Kuppermann and G. C. Schatz, *J. Chem. Phys.* **62**, 2502 (1975).
2. G. C. Schatz and A. Kuppermann, *J. Chem. Phys.* **65**, 4642,4668 (1976).
3. R. N. Porter and M. Karplus, *J. Chem. Phys.* **40**, 1105 (1964).
4. D. E. Manolopoulos and R. E. Wyatt, *Chem. Phys. Lett.* **159**, 123 (1989).
5. J. Z. H. Zhang and W. H. Miller, *J. Chem. Phys.* **91**, 1528 (1989); **92**, 1811 (1990).
6. J. Z. H. Zhang and W. H. Miller, *J. Chem. Phys.* **88**, 4549 (1988); **90**, 7610 (1989); *Chem. Phys. Lett.* **159**, 130 (1989).
7. M. Zhao, D. G. Truhlar, D. W. Schwenke and D. J. Kouri, *J. Phys. Chem.* **94**, 7074 (1990).
8. A. B. Elkowitz and R. E. Wyatt, *J. Chem. Phys.* **62**, 2504 (1975).
9. A. B. Elkowitz and R. E. Wyatt, *J. Chem. Phys.* **63**, 702 (1975).
10. R. B. Walker, E. B. Stechel and J. C. Light, *J. Chem. Phys.* **69**, 2922 (1978).
11. P. Siegbahn and B. Liu, *J. Chem. Phys.* **68**, 2457 (1978); D. G. Truhlar and C. J. Horowitz, *J. Chem. Phys.* **68**, 2466 (1978); **71**, 1514E (1979).
12. A. Kuppermann and P. G. Hipes, *J. Chem. Phys.* **84**, 5962 (1986).
13. P. G. Hipes and A. Kuppermann, *Chem. Phys. Lett.* **133**, 1 (1987).
14. S. A. Cuccaro, P. G. Hipes and A. Kuppermann, *Chem. Phys. Lett.* **154**, 155 (1989); **157**, 440 (1989).
15. Y. M. Wu, S. A. Cuccaro, P. G. Hipes and A. Kuppermann, *Chem. Phys.*

Lett. **168**, 429 (1990).

16. G. A. Parker, R. T. Pack, B. J. Archer and R. B. Walker, *Chem. Phys. Lett.* **137**, 564 (1987).

17. R. T. Pack and G. A. Parker, *J. Chem. Phys.* **87**, 3888 (1987); **90**, 3511 (1989).

18. T. J. Park and J. C. Light, *J. Chem. Phys.* **91**, 974 (1989).

19. G. C. Schatz, *Chem. Phys. Lett.* **150**, 92 (1988).

20. J. Linderberg, *Int. J. Quant. Chem. Symp.* **19**, 467 (1986); J. Linderberg and B. Vessal, *Int. J. Quant. Chem.* **31**, 65 (1987); J. Linderberg, S. B. Padkjaer, Y. Öhrn and B. Vessal, *J. Chem. Phys.* **90**, 6254 (1989).

21. J. M. Launay and M. Le Dorneuf, *Chem. Phys. Lett.* **163**, 178 (1989).

22. J. Z. H. Zhang, D. J. Kouri, K. Haug, D. W. Schwenke, Y. Shima and D. G. Truhlar, *J. Chem. Phys.* **88**, 2492 (1988).

23. M. Mladenovic, M. Zhao, D. G. Truhlar, D. W. Schwenke, Y. Sun and D. J. Kouri, *Chem. Phys. Lett.* **146**, 358 (1988).

24. M. Zhao, M. Mladenovic, D. G. Truhlar, D. W. Schwenke, Y. Sun, D. J. Kouri and N. C. Blais, *J. Am. Chem. Soc.* **111**, 852 (1989).

25. M. Mladenovic, M. Zhao, D. G. Truhlar, D. W. Schwenke, Y. Sun and D. J. Kouri, *J. Phys. Chem.* **92**, 7035 (1988).

26. M. Zhao, M. Mladenovic, D. G. Truhlar, D. W. Schwenke, O. Sharafeddin, Y. Sun and D. J. Kouri, *J. Chem. Phys.* **91**, 5302 (1989).

27. K. Haug, D. W. Schwenke, Y. Shima, D. G. Truhlar, J. Z. H. Zhang and K. J. Kouri, *J. Phys. Chem.* **90**, 6757 (1986).

28. M. Zhao, D. G. Truhlar, Y. Sun, D. J. Kouri and D. W. Schwenke, *Chem. Phys. Lett.* **156**, 281 (1989).

29. N. C. Blais, M. Zhao, M. Mladenovic, D. G. Truhlar, D. W. Schwenke, Y. Sun and D. J. Kouri, *J. Chem. Phys.* **91**, 1038 (1989).

30. J. Z. H. Zhang and W. H. Miller, *Chem. Phys. Lett.* **140**, 329 (1987); **153**,

465 (1988); **159**, 130 (1989).

31. S. M. Auerbach, J. Z. H. Zhang and W. H. Miller, *J. Chem. S. F.* **86**, 1701 (1990).
32. D. E. Manolopoulos and R. E. Wyatt, *Chem. Phys. Lett.* **152**, 23 (1988).
33. D. E. Manolopoulos and R. E. Wyatt, *J. Chem. Phys.* **92**, 810 (1990).
34. F. Webster and J. C. Light, *J. Chem. Phys.* **90**, 265 (1989).
35. F. Webster and J. C. Light, *J. Chem. Phys.* **90**, 300 (1989).
36. J. D. Kress, Z. Bačić, G. A. Parker and R. T. Pack, *Chem. Phys. Lett.* **157**, 585 (1989); **170**, 306 (1990).
37. Z. Bačić, J. D. Kress, G. A. Parker and R. T. Pack, *J. Chem. Phys.* **92**, 2344 (1990).
38. C. Yu, D. J. Kouri, M. Zhao, D. G. Truhlar and D. W. Schwenke, *Chem. Phys. Lett.* **157**, 491 (1989).
39. C. Yu, Y. Sun, D. J. Kouri, P. Halvick, D. G. Truhlar and D. W. Schwenke, *J. Chem. Phys.* **90**, 7608 (1989).
40. C. Yu, D. J. Kouri, M. Zhao, D. G. Truhlar and D. W. Schwenke, *Int. J. Quant. Chem. Symp.* **23**, 45 (1989).
41. M. Zhao, D. G. Truhlar, D. W. Schwenke, C. H. Yu and D. J. Kouri, *J. Phys. Chem.* **94**, 7062 (1990).
42. D. E. Manolopoulos, M. D'Mello and R. E. Wyatt, *J. Chem. Phys.* **93**, 403 (1990).
43. M. D'Mello, D. E. Manolopoulos and R. E. Wyatt, *Chem. Phys. Lett.* **168**, 113 (1990).
44. D. E. Manolopoulos, M. D'Mello, R. E. Wyatt and R. B. Walker, *Chem. Phys. Lett.* **169**, 482 (1990).
45. K. Haug, D. W. Schwenke, D. G. Truhlar, Y. Zhang, J. Z. H. Zhang and D. J. Kouri, *J. Chem. Phys.* **87**, 1892 (1987).
46. J. Z. H. Zhang, Y. Zhang, D. J. Kouri, B. C. Garrett, K. Haug, D. W. Schwenke

and D. G. Truhlar, *Faraday Discuss. Chem. Soc.* **84**, 371 (1987).

47. Y. C. Zhang, J. Z. H. Zhang, D. J. Kouri, K. Haug, D. W. Schwenke and D. G. Truhlar, *Phys. Rev. Lett* **60**, 2367 (1988).

48. G. C. Schatz, *Chem. Phys. Lett.* **151**, 409 (1988); *J. Chem. Phys.* **90**, 3582 (1989).

49. R. A. Marcus, *J. Chem. Phys.* **45**, 4493 (1966).

50. W. H. Miller, *J. Chem. Phys.* **50**, 407 (1969).

51. J. A. Kaye and A. Kuppermann, *Chem. Phys. Lett.* **77**, 573 (1981).

52. J. Manz and J. Römelt, *Chem. Phys. Lett.* **77**, 172 (1981).

53. J. Manz and J. Römelt, *Chem. Phys. Lett.* **81**, 179 (1981).

54. J. A. Kaye and A. Kuppermann, *Chem. Phys. Lett.* **78**, 546 (1981).

55. L. M. Delves, *Nucl. Phys.* **9**, 391 (1958); **20**, 275 (1960).

56. F. T. Smith, *J. Math. Phys.* **3**, 735 (1962); *J. Chem. Phys.* **38**, 1304 (1963); R. C. Whitten and F. T. Smith, *J. Math. Phys.* **9**, 1103 (1968).

57. A. Kuppermann, *Chem. Phys. Lett.* **32**, 374 (1975).

58. R. T. Ling and A. Kuppermann, in: **Electronic and Atomic Collisions, Abstracts of Papers of the 9th International Conference on the Physics of Electronic and Atomic Collisions**, Seattle, Washington, 24–30 July, 1975, Vol. 1, eds. J. Risley and R. Geballe (Univ. Washington Press, Seattle, 1975) pp. 353, 354.

59. B. R. Johnson, *J. Chem. Phys.* **73**, 5051 (1980).

60. C. A. Mead, *Chem. Phys.* **49**, 23 (1980); *J. Chem. Phys.* **72**, 3839 (1980).

61. A. S. Davydov, **Quantum Mechanics**, 2nd edition (Pergamon Press, Oxford, 1976), pp. 167ff.

62. A. Kuppermann, in: **Theoretical chemistry — Theory of scattering: papers in honor of Henry Eyring,** ed. D. Henderson (Academic Press, New York, 1981) Vol. 6, part A, chapter 2, pp. 79–164.

63. M. Hamermesh, **Group Theory and its Application to Physical Prob-**

lems, (Addison-Wesley, Reading, MA, 1962), pp. 182ff.

64. ref. 63, pg. 113.
65. ref. 61, pp. 151–161.
66. A. M. Arthurs and A. Dalgarno, *Proc. R. Soc. London A* **256**, 540 (1960).
67. ref. 61, pg. 171.
68. ref. to overcomplete basis sets.
69. J. Römelt, *Chem. Phys.* **79**, 197 (1983); J. Römelt and E. Pollak, in: **Resonances in Electron Molecule Scattering, van der Waals Complexes and Reactive Chemical Dynamics**, ed. D. G. Truhlar, (Plenum Press, 1984), p. 353.
70. J. Manz, *Comments At. Mol. Phys.* **17**, 91 (1985).
71. A. Kuppermann, in: **Potential Energy Surfaces and Dynamics Calculations**, ed. D. G. Truhlar, (Plenum Press, New York, 1981), pp. 405, 414.
72. J. Macek, *J. Phys. B* **1**, 831 (1968).
73. D. M. Hood and A. Kuppermann, in: **Theory of Chemical Reaction Dynamics** (D. Reidel, Boston, 1986) pp. 193,214.
74. J. K. C. Wong and A. Kuppermann, unpublished results.

Table 2.1: Operations and irreducible representations for P_p

P_1

Operation	Permutation	$\mathbf{d}^A$
$\hat{O}_E$	$\begin{pmatrix} \alpha & \beta & \gamma \\ \alpha & \beta & \gamma \end{pmatrix}$	1

P_2

Operation	Permutation	$\mathbf{d}^{A_1}$	$\mathbf{d}^{A_2}$
$\hat{O}_E$	$\begin{pmatrix} \alpha & \beta & \gamma \\ \alpha & \beta & \gamma \end{pmatrix}$	1	1
$\hat{O}_A$	$\begin{pmatrix} \alpha & \beta & \gamma \\ \alpha & \gamma & \beta \end{pmatrix}$	1	-1

P_3

Operation	Permutation	$\mathbf{d}^{A_1}$	$\mathbf{d}^{A_2}$	$\mathbf{d}^E$
$\hat{O}_E$	$\begin{pmatrix} \alpha & \beta & \gamma \\ \alpha & \beta & \gamma \end{pmatrix}$	1	1	$\begin{pmatrix} 1 & 0 \\ 0 & 1 \end{pmatrix}$
$\hat{O}_A$	$\begin{pmatrix} \alpha & \beta & \gamma \\ \alpha & \gamma & \beta \end{pmatrix}$	1	-1	$\begin{pmatrix} 1 & 0 \\ 0 & -1 \end{pmatrix}$
$\hat{O}_B$	$\begin{pmatrix} \alpha & \beta & \gamma \\ \gamma & \beta & \alpha \end{pmatrix}$	1	-1	$\begin{pmatrix} -\frac{1}{2} & \frac{\sqrt{3}}{2} \\ \frac{\sqrt{3}}{2} & \frac{1}{2} \end{pmatrix}$
$\hat{O}_C$	$\begin{pmatrix} \alpha & \beta & \gamma \\ \beta & \alpha & \gamma \end{pmatrix}$	1	-1	$\begin{pmatrix} -\frac{1}{2} & -\frac{\sqrt{3}}{2} \\ -\frac{\sqrt{3}}{2} & \frac{1}{2} \end{pmatrix}$
$\hat{O}_D$	$\begin{pmatrix} \alpha & \beta & \gamma \\ \gamma & \alpha & \beta \end{pmatrix}$	1	1	$\begin{pmatrix} -\frac{1}{2} & \frac{\sqrt{3}}{2} \\ -\frac{\sqrt{3}}{2} & -\frac{1}{2} \end{pmatrix}$
$\hat{O}_F$	$\begin{pmatrix} \alpha & \beta & \gamma \\ \beta & \gamma & \alpha \end{pmatrix}$	1	1	$\begin{pmatrix} -\frac{1}{2} & -\frac{\sqrt{3}}{2} \\ \frac{\sqrt{3}}{2} & -\frac{1}{2} \end{pmatrix}$

Table 2.2: Results of operations $\hat{O}_R$ on functions for P_p

P_1

R	$\hat{O}_R \mathrm{F}^{JM\Pi}_{\alpha v j \Omega}$	$\hat{O}_R \mathrm{F}^{JM\Pi}_{\beta v j \Omega}$	$\hat{O}_R \mathrm{F}^{JM\Pi}_{\gamma v j \Omega}$
E	$\mathrm{F}^{JM\Pi}_{\alpha v j \Omega}$	$\mathrm{F}^{JM\Pi}_{\beta v j \Omega}$	$\mathrm{F}^{JM\Pi}_{\gamma v j \Omega}$

P_2

R	$\hat{O}_R \mathrm{F}^{JM\Pi}_{\alpha v j \Omega}$	$\hat{O}_R \mathrm{F}^{JM\Pi}_{\beta v j \Omega}$	$\hat{O}_R \mathrm{F}^{JM\Pi}_{\gamma v j \Omega}$
E	$\mathrm{F}^{JM\Pi}_{\alpha v j \Omega}$	$\mathrm{F}^{JM\Pi}_{\beta v j \Omega}$	$\mathrm{F}^{JM\Pi}_{\gamma v j \Omega}$
A	$(-1)^j \mathrm{F}^{JM\Pi}_{\alpha v j \Omega}$	$(-1)^j \mathrm{F}^{JM\Pi}_{\gamma v j \Omega}$	$(-1)^j \mathrm{F}^{JM\Pi}_{\beta v j \Omega}$

P_3

R	$\hat{O}_R \mathrm{F}^{JM\Pi}_{\alpha v j \Omega}$	$\hat{O}_R \mathrm{F}^{JM\Pi}_{\beta v j \Omega}$	$\hat{O}_R \mathrm{F}^{JM\Pi}_{\gamma v j \Omega}$
E	$\mathrm{F}^{JM\Pi}_{\alpha v j \Omega}$	$\mathrm{F}^{JM\Pi}_{\beta v j \Omega}$	$\mathrm{F}^{JM\Pi}_{\gamma v j \Omega}$
A	$(-1)^j \mathrm{F}^{JM\Pi}_{\alpha v j \Omega}$	$(-1)^j \mathrm{F}^{JM\Pi}_{\gamma v j \Omega}$	$(-1)^j \mathrm{F}^{JM\Pi}_{\beta v j \Omega}$
B	$(-1)^j \mathrm{F}^{JM\Pi}_{\gamma v j \Omega}$	$(-1)^j \mathrm{F}^{JM\Pi}_{\beta v j \Omega}$	$(-1)^j \mathrm{F}^{JM\Pi}_{\alpha v j \Omega}$
C	$(-1)^j \mathrm{F}^{JM\Pi}_{\beta v j \Omega}$	$(-1)^j \mathrm{F}^{JM\Pi}_{\alpha v j \Omega}$	$(-1)^j \mathrm{F}^{JM\Pi}_{\gamma v j \Omega}$
D	$\mathrm{F}^{JM\Pi}_{\gamma v j \Omega}$	$\mathrm{F}^{JM\Pi}_{\alpha v j \Omega}$	$\mathrm{F}^{JM\Pi}_{\beta v j \Omega}$
F	$\mathrm{F}^{JM\Pi}_{\beta v j \Omega}$	$\mathrm{F}^{JM\Pi}_{\gamma v j \Omega}$	$\mathrm{F}^{JM\Pi}_{\alpha v j \Omega}$

Table 2.3: Symmetry coefficients $c^{\Gamma_{kk}}_{\tau\lambda j}$ for P_p

P_1

Γ_{kk}	τ	λ		
		α	β	γ
A	A	1	0	0
	B	0	1	0
	C	0	0	1

P_2

Γ_{kk}	τ	λ		
		α	β	γ
A'	A	$\frac{1+(-1)^j}{2}$	0	0
	B	0	$\frac{1}{\sqrt{2}}$	$\frac{(-1)^j}{\sqrt{2}}$
A''	A	$\frac{1-(-1)^j}{2}$	0	0
	B	0	$\frac{1}{\sqrt{2}}$	$-\frac{(-1)^j}{\sqrt{2}}$

P_3

Γ_{kk}	τ	λ		
		α	β	γ
A_1	A	$\frac{1+(-1)^j}{2\sqrt{3}}$	$\frac{1+(-1)^j}{2\sqrt{3}}$	$\frac{1+(-1)^j}{2\sqrt{3}}$
A_2	A	$\frac{1-(-1)^j}{2\sqrt{3}}$	$\frac{1-(-1)^j}{2\sqrt{3}}$	$\frac{1-(-1)^j}{2\sqrt{3}}$
E_{kk}	A	$\frac{c_1}{\sqrt{6}}$	$-\frac{c_1}{2\sqrt{6}}+\frac{c_2}{2\sqrt{2}}$	$-\frac{c_1}{2\sqrt{6}}-\frac{c_2}{2\sqrt{2}}$

$$c_1 = \left[1-(-1)^{j+k}\right] \quad c_2 = \left[(-1)^k+(-1)^j\right]$$

Table 4.1: Number of vibrational states $n_v(j, J, \rho)$ for different ρ, J and $j^{(a)}$

$J = 0, 1, 2$

ρ (bohr)	j																						
	0	1	2	3	4	5	6	7	8	9	10	11	12	13	14	15	16	17	18	19	20	21	22
2.0–12.0	12	12	11	10	10	10	9	9	9	7	6	7	5	6	5	5	4	4	3	4	1	2	1

$J = 3$

ρ (bohr)	j																							
	0	1	2	3	4	5	6	7	8	9	10	11	12	13	14	15	16	17	18	19	20	21	22	23
2.0–2.4	4	7	7	7	7	10	10	10	10	10	10	8	9	6	6	5	5	5	3	3	3	3	3	0
2.6–3.4	2	20	20	20	15	15	13	12	12	12	10	10	8	8	8	7	7	7	5	5	4	4	3	2
3.6–4.4	3	16	16	16	17	15	14	13	12	12	11	10	9	7	7	6	6	5	4	4	3	0	0	0
4.6–5.4	4	8	12	12	13	11	11	12	12	12	9	9	8	8	8	6	6	3	3	2	2	0	0	0
5.6–12.0	7	9	9	10	9	10	9	9	8	8	8	6	6	6	6	5	5	5	3	3	1	1	0	0

(a) The total number of primitives for a given j, J and ρ is $n_v(j, J, \rho)\,[\min(j, J) + 1]$.

Table 4.2: Total number of primitives for each J, Π, Γ and $\rho^{(a)}$

J, Π	ρ (bohr)	Γ		
		A_1	A_2	E
0, 0	2.0–12.0	76	76	152
1, 0	2.0–12.0	64	76	140
1, 1	2.0–12.0	140	152	292
2, 1	2.0–12.0	128	140	268
2, 0	2.0–12.0	204	216	420
3, 0	2.0–2.4	212	208	420
	2.6–3.4	295	326	621
	3.6–4.4	281	280	561
	4.6–5.4	240	233	473
	5.6–12.0	183	198	381
3, 1	2.0–2.4	289	282	571
	2.6–3.4	402	448	850
	3.6–4.4	383	384	767
	4.6–5.4	328	316	644
	5.6–12.0	254	270	524

(a) The numbers are obtained from the formulae

$\sum_j n_v(J, j, \rho)\,[\min(j, J) + 1]$ for $J + \Pi$ even,

$\sum_j n_v(J, j, \rho)\,\min(j, J)$ for $J + \Pi$ odd.

Table 4.3: Convergence tests of $\Phi_n^{JM\Pi\Gamma_k}$ energies (in eV) at $\bar{\rho} = 6.0$ bohr no linear dependence checking; independent of n_γ for $n_\gamma > 50$

$n_\omega = 1001$

n	Γ		
	A_1	A_2	E
1	0.26583	0.28097	0.26583
10	1.0699	1.2016	0.78345
20	1.7277	1.8353	1.2017
40	2.5341	2.6658	1.7673

$n_\omega = 501$

n	Γ		
	A_1	A_2	E
1	0.26574	0.28085	0.26573
10	1.0695	1.2011	0.78297
20	1.7218	1.8343	1.2015
40	2.5320	2.6627	1.7652

$n_\omega = 451$

n	Γ		
	A_1	A_2	E
1	0.26571	0.28080	0.26569
10	1.0694	1.2008	0.78279
20	1.7216	1.8340	1.2014
40	2.5313	2.6617	1.7652

$n_\omega = 301$

n	Γ		
	A_1	A_2	E
1	0.26550	0.28039	0.26543
10	1.0686	1.1971	0.78133
20	1.7198	1.8310	1.2006
40	2.5269	2.6465	1.7617

Table 4.4: Convergence tests of $\Phi_n^{JM\Pi\Gamma_k}$ energies at $\bar{\rho} = 3.2$ bohr

$n_\omega = 1001$, $n_\gamma = 200$

	Γ		
n	$A_1(-5)^a$	$A_2(-11)^a$	$E(-16)^a$
1	0.59317	0.75999	0.59318
10	1.5624	1.8496	1.2259
20	2.2998	2.7748	1.6998
40	3.7150	4.4059	2.5455

$n_\omega = 1001$, $n_\gamma = 50$

	Γ		
n	$A_1(-4)^a$	$A_2(-12)^a$	$E(-16)^a$
1	0.59315	0.75999	0.59318
10	1.5623	1.8469	1.2259
20	2.3000	2.7751	1.6996
40	3.7144	4.4060	2.5455

$n_\omega = 301$, $n_\gamma = 200$

	Γ		
n	$A_1(-12)^a$	$A_2(-20)^a$	$E(-32)^a$
1	0.59315	0.75995	0.59316
10	1.5592	1.8455	1.2255
20	2.2959	2.7693	1.6985
40	3.7147	4.4202	2.5417

$n_\omega = 301$, $n_\gamma = 50$

	Γ		
n	$A_1(-12)^a$	$A_2(-20)^a$	$E(-32)^a$
1	0.59315	0.75995	0.59316
10	1.5609	1.8455	1.2255
20	2.2957	2.7693	1.6985
40	3.7140	4.4199	2.5417

[a] number of functions lost to linear dependence checks

Table 4.5: Breakdown of timing of a $J = 0$ A_1 symmetry calculation

Description of routine	CPU time needed/sec
$\nu\lambda$ integration for $\boldsymbol{\mathcal{I}}$	694
$\nu\lambda$ integration for **H, S**	575
associated Legendre functions ($\nu\lambda$ overhead)	174s
$\nu\lambda$ integration for $\boldsymbol{\mathcal{O}}$	168
calls to potential function	71
solution of $\mathbf{Ha} = \mathbf{MaE}$	54
calculation of 1D primitives	53
spline fitting ($\nu\lambda$ overhead)	45
total $\lambda\lambda$ integration	42
other	90
TOTAL	1949

Table 4.6: Comparison of Surface Function Energies (in eV) for Finite Element (FE) and Variational (V) Methods - $J = 0$

$\bar{\rho}/a_0$	PK2[a]								LSTH[b]							
	A1			A2		E			A1			A2			E		
	n	FE	V	n	V	n	FE	V	n	FE	V	n	FE	V	n	FE	V
2.0	1	3.0031	3.0029	1	3.7612	1	3.1562	3.1558	1	3.1988	3.1987	1	4.0947	4.0937	1	3.3938	3.3935
	5	4.5951	4.5586	5	5.8307	10	5.2093	5.1996	5	4.7962	4.7918	5	6.1193	6.1104	10	5.4317	5.4247
	10	5.8126	5.7980	10	7.1675	20	6.5485	6.5309	10	6.0898	6.0795	10	7.6127	7.5981	20	6.8744	6.8608
	15	6.8547	6.8247	15	8.5371	30	7.7914	7.7361	15	7.2700	7.2574	15	9.1025	9.0699	30	8.1385	8.1159
	20	7.9175	7.8703	20	9.5651	40	8.9223	8.8574	20	8.3031	8.2787	20	10.137	10.088	40	9.3596	9.3065
3.0	1	.61272	.61267	1	.80296	1	.61277	.61272	1	.72438	.72435	1	.96023	.96011	1	.72440	.72437
	5	1.1472	1.1463	5	1.3912	10	1.3210	1.3192	5	1.2819	1.2814	5	1.5368	1.5357	10	1.4473	1.4464
	10	1.6735	1.6679	10	2.0120	20	1.8613	1.8573	10	1.7585	1.7550	10	2.1531	2.1463	20	1.9919	1.9877
	15	2.0847	2.0788	15	2.5986	30	2.3244	2.3082	15	2.2466	2.2432	15	2.7673	2.7604	30	2.4375	2.4328
	20	2.5316	2.5219	20	3.0725	40	2.8049	2.7933	20	2.6695	2.6638	20	3.2483	3.2368	40	2.9494	2.9377
4.0	1	.41158	.41118	1	.41563	1	.41169	.41129	1	.43738	.43713	1	.44677	.44658	1	.43753	.43728
	5	.88557	.88426	5	.89775	10	.89821	.89670	5	.87687	.87631	5	.90314	.90240	10	.90160	.90082
	10	1.2436	1.2413	10	1.3507	20	1.3192	1.3158	10	1.2080	1.2068	10	1.3431	1.3410	20	1.2916	1.2895
	15	1.5936	1.5868	15	1.7777	30	1.6246	1.6193	15	1.5617	1.5583	15	1.7631	1.7583	30	1.6026	1.5994
	20	1.8317	1.8234	20	2.0267	40	1.9527	1.9428	20	1.8025	1.7976	20	1.9981	1.9925	40	1.9166	1.9110
5.0	1	.32308	.32230	1	.33328	1	.32308	.32230	1	.29753	.29702	1	.31150	.31112	1	.29753	.29702
	5	.83267	.82921	5	.83878	10	.84158	.83878	5	.79821	.79600	5	.80894	.80723	10	.80894	.80723
	10	1.1443	1.1394	10	1.2899	20	1.2973	1.2899	10	1.1107	1.1069	10	1.2614	1.2562	20	1.2614	1.2562
	15	1.4603	1.4506	15	1.6199	30	1.6060	1.5974	15	1.4218	1.4149	15	1.5910	1.5821	30	1.5579	1.5526
	20	1.8092	1.7972	20	1.9166	40	1.8322	1.8190	20	1.7572	1.7510	20	1.8734	1.8665	40	1.7837	1.7756

[a] Porter Karplus potential energy surface, ref. 3

[b] Liu-Siegbahn-Truhlar-Horowitz potential energy surface, ref. 11

Table 4.7a: Comparison of $\mathcal{T}$ matrices of FE[a] and V[b] methods
$J = 0$, A_1 symmetry; PK2[c]; $\bar{\rho} = 2.0$ bohr, $\rho = 2.05$ bohr
(upper left 5 by 5 submatrix - elements scaled by $-\frac{2\mu}{\hbar^2}$)

FE

9.532	2.871	−1.913	0.0194	0.0867
2.871	11.97	2.047	3.327	−1.365
−1.913	2.047	12.12	−0.0804	2.752
0.0194	3.327	−0.0804	14.52	3.128
0.0867	−1.365	2.752	3.128	14.18

V

9.533	2.868	−1.913	0.0214	0.0877
2.868	11.97	2.040	3.318	−1.360
−1.913	2.040	12.11	−0.0693	2.749
0.0214	3.318	−0.0693	14.53	3.052
0.0877	−1.360	2.749	3.052	14.26

[a] Finite element surface functions, ref. 12,13.

[b] Variationally determined surface functions, current work, ref. 14,15.

[c] Porter-Karplus potential energy surface, ref. 3.

Table 4.7b: Comparison of $\mathcal{I}$ matrices of FE[a] and V[b] methods
$J = 0$, A_1 symmetry; PK2[c]: $\bar{\rho} = 3.0$ bohr, $\rho = 3.05$ bohr
(upper left 5 by 5 submatrix - elements scaled by $-\frac{2\mu}{\hbar^2}$)

FE

0.8073	−0.5440	0.4775	0.3901	−1.349
−0.5440	0.1741	0.1337	−0.3740	−1.724
0.4775	0.1337	0.2796	0.0910	0.2467
0.3901	−0.3740	0.0910	0.0478	−0.7599
−1.349	−1.724	0.2467	−0.7599	0.5912

V

0.8075	−0.5437	0.4773	0.3877	−1.349
−0.5437	0.1756	0.1339	−0.3759	−1.722
0.4773	0.1339	0.2815	0.0920	0.2463
0.3877	−0.3759	0.0920	0.0479	−0.7594
−1.349	−1.722	0.2462	−0.7594	0.5953

[a] Finite element surface functions, ref. 12,13.

[b] Variationally determined surface functions, current work, ref. 14,15.

[c] Porter-Karplus potential energy surface, ref. 3.

Table 4.8a: Comparison of $\mathcal{O}$ matrices of FE[a] and V[b] methods
$J = 0$, A_1 symmetry; PK2[c]; $\bar{\rho}_i = 2.0$ bohr, $\bar{\rho}_{i+1} = 2.05$ bohr

FE

0.9966	−0.07656	0.02974	3.44×10^{-3}	7.86×10^{-4}
−0.07347	0.9898	0.09507	−0.07531	−0.01108
0.03673	−0.09115	0.9935	0.01294	0.05041
2.44×10^{-3}	0.07448	-2.10×10^{-3}	0.9914	−0.09485
2.00×10^{-3}	0.02247	−0.04631	0.09669	0.9831

V

0.9966	−0.07662	0.02980	3.48×10^{-3}	7.82×10^{-4}
−0.07353	0.9898	0.09504	−0.07550	−0.01116
0.03679	−0.09111	0.9935	0.01280	0.05064
2.41×10^{-3}	0.07468	-1.99×10^{-3}	0.9915	−0.09332
2.01×10^{-3}	0.02244	−0.04636	0.09544	0.9827

[a] Finite element surface functions, ref. 12,13.

[b] Variationally determined surface functions, current work, ref. 14,15.

[c] Porter-Karplus potential energy surface, ref. 3.

Table 4.8b: Comparison of $\mathcal{O}$ matrices of FE[a] and V[b] methods
$J = 0$, A_1 symmetry; PK2[c]; $\bar{\rho}_i = 3.0$ bohr, $\bar{\rho}_{i+1} = 3.05$ bohr

FE

0.9983	−0.03789	0.02290	0.01245	−0.03246
0.03590	0.9961	0.02608	−0.01479	−0.06291
−0.02333	−0.02553	0.9974	3.82×10^{-3}	0.01632
−0.01548	8.32×10^{-3}	-1.37×10^{-3}	−0.9920	−0.1102
0.03590	0.05756	−0.01577	0.1065	0.9771

V

0.9982	−0.03790	0.02293	0.01242	-0.03252
0.03591	0.9961	0.02613	-0.01493	−0.06294
−0.02336	−0.02558	0.9974	3.90×10^{-3}	0.01636
−0.01542	8.49×10^{-3}	-1.46×10^{-3}	−0.9921	−0.1096
0.03598	0.05760	−0.01581	0.1058	0.9771

[a] Finite element surface functions, ref. 12,13.

[b] Variationally determined surface functions, current work, ref. 14,15.

[c] Porter-Karplus potential energy surface, ref. 3.

Figure Captions

Figure 2.1 Relationship between the space-fixed coordinate system (axes **X**, **Y**, **Z**) and the body-fixed λ SHC system (axes $\mathbf{x}_\lambda$, $\mathbf{y}$, $\mathbf{z}_\lambda$). The point labelled **O** is the center of mass of the three-particle system, while the point $G_{A_\nu A_\kappa}$ is the center of mass of the A_ν and A_κ atoms.

Figure 2.2 $J = 3, \Pi = 1, A_1$ LHSF eigenvalues $\epsilon_n^{J\Pi\Gamma}(\rho)$ at $\bar{\rho} = 3.27$ bohr as a function of the number of orthogonal functions derived from the primitive basis set in this region of ρ values (see table 4.1). The eigenvalues are given in eV and are calculated at all integer values of the orthogonal basis set size.

Figure 4.1 $J = 0$ surface function eigenvalues $\epsilon_n^{J\Pi\Gamma}(\rho)$ as a function of ρ. The eigenvalues are calculated every 0.2 bohr and the curves drawn by examination of the overlap matrices $\boldsymbol{\mathcal{O}}$ between basis sets at different $\bar{\rho}$ values. Panel a is for the A_1 irreducible representation, b for the A_2 IR and c for the E IR.

Figure 4.2 $J = 1$ $\Pi = 0$ surface function eigenvalues $\epsilon_n^{J\Pi\Gamma}(\rho)$ as a function of ρ. See the caption for figure 4.1 for details.

Figure 4.3 $J = 1$ $\Pi = 0$ A_2 surface function eigenvalues $\epsilon_n^{J\Pi\Gamma}(\rho)$ as a function of ρ. See the caption for figure 4.1 for details of the plotting.

Figure 4.4 Diagram of projection of constant $\bar{\rho}$ hemisphere in internal coordinate space onto a mapping plane. The arc length $\widehat{\mathbf{EP}}$ on the surface of the hemisphere is equal to the distance **EQ** on the mapping plane. The point labelled **E** (common to both surfaces) is the pole of projection and is the intersection of the hemisphere with the y axis.

Figure 4.5 Projection of the LSTH potential energy surface onto the mapping plane. Panel a is the potential for $\rho = 2.0$ bohr, b for $\rho = 3.270145$ bohr, and c for

$\rho = 6.0$ bohr. The energies are given in eV and the contours spaced 0.5 eV apart.

Figure 4.6 Projection of the $J = 0$ surface functions (or equivalently the functions $\psi_{n\Omega}^{J\Pi\Gamma_k}$ for $J = 0$) at $\rho = 6.0$ bohr onto the mapping plane. Panel a gives the result for the ground state A_1 symmetry function, panel d for the ground state A_2 symmetry function, and panels b and c for the degenerate E ground state functions; in addition, panels e and f give the degenerate E first excited state functions. The contour interval δ defines the spacing of the nodal lines at the values $\pm 0.1 + n\delta$ with n any integer. The solid lines represent positive function values while the dashed lines represent negative function value. The functions of panels b and c transform as row 1 of the E irreducible representation and are even with respect to $\nu\kappa$ interchange, while those of panels e and f transform as row 1 of the E irreducible representation and are odd with $\nu\kappa$ interchange.

Figure 4.7 Same as figure 4.6 except the value of ρ is 3.270145 bohr.

Figure 4.8 Same as figure 4.6 except the value of ρ is 2.0 bohr.

Figure 4.9 $J = 0$ E surface function amplitudes (or equivalently the functions $\psi_{n\Omega}^{J\Pi\Gamma_k}$ for $J = 0$) at three values of ρ for the $n = 3$ level. Dashed lines indicate negative values and solid lines indicate positive values. The spacing of the nodal lines is as in figure 4.6. The left column is the first row of the E representation, which is symmetric to $\nu\kappa$ interchange; the right column is the degenerate second row function of the E representation, which is antisymmetric to $\nu\kappa$ interchange. Panels (a) and (d) show the $n = 3$ degenerate pair at $\rho = 2.0$ bohr, panels (b) and (e) the pair at $\rho = 3.270145$ bohr, and panels (c) and (f) the pair at $\rho = 6.0$ bohr.

Figure 4.10 Same as figure 4.9 except for $n = 4$.

Figure 4.11 Same as figure 4.9 except for $n = 9$.

Figure 4.12 Same as figure 4.9 except for $n = 10$.

Figure 4.13 Projection of the functions $\Theta_n^{J\Pi\{\Gamma_k \otimes \Gamma_k\}}$ for $J = 0$, $\rho = 6.0$ bohr onto the mapping plane. For $J = 0$ these functions are the square of the LHSF function which appeared in the same panel of figure 4.6. Panel a gives the result for $\Gamma = A_1$, $n = 1$, panel d for $\Gamma = A_2$, $n = 1$, panels b and c for $\Gamma = E, k = 1$ and $n = 1, 2$ respectively, and panels e and f for $\Gamma = E, k = 2$ and $n = 1, 2$ respectively. See caption of figure 4.6 for details.

Figure 4.14 Same as figure 4.13 except for $\rho = 3.270145$ bohr; these functions are the squares of the LHSF functions which appeared in the same panel of figure 4.7.

Figure 4.15 Same as figure 4.13 except for $\rho = 2.0$ bohr; these functions are the squares of the LHSF functions which appeared in the same panel of figure 4.8.

Figure 4.16 Projection of the $J = 1$ $\Pi = 0$ functions $\psi_{n\Omega}^{J\Pi\Gamma_k}$ at $\rho = 6.0$ bohr onto the mapping plane. Panel a gives the result for the ground state A_1 symmetry function, panel d for the ground state A_2 symmetry function, and panels b and c for the degenerate E ground state functions; in addition, panels e and f give the degenerate E first excited state functions. The contour interval δ defines the spacing of the nodal lines at the values $\pm 0.1 + n\delta$ with n any integer. The solid lines represent positive function values while the dashed lines represent negative function value. The functions of panels b and c, after multiplication by the Wigner rotation function as in equation (4.6.1), transform as row 1 of the E irreducible representation and are even with respect to $\nu\kappa$ interchange, while those of panels e and f transform as row 1 of the E irreducible representation and are odd with $\nu\kappa$ interchange.

Figure 4.17 Same as figure 4.16 except for $\rho = 3.270145$ bohr.

Figure 4.18 Same as figure 4.16 except for $\rho = 2.0$ bohr.

Figure 4.19 Projection of the functions $\Theta_n^{J\Pi\{\Gamma_k \otimes \Gamma_k\}}$ for $J = 1$, $\Pi = 0$ $\rho = 6.0$ bohr onto the mapping plane. For this partial wave these functions are the square of the coefficient function $\psi_{n\Omega}^{J\Pi\Gamma_k}$ which appeared in the same panel of figure 4.16. Panel a gives the result for $\Gamma = A_1$, $n = 1$, panel d for $\Gamma = A_2$, $n = 1$, panels b and c for $\Gamma = E, k = 1$ and $n = 1, 2$ respectively, and panels e and f for $\Gamma = E, k = 2$ and $n = 1, 2$ respectively.

Figure 4.20 Same as figure 4.19 except for $\rho = 3.270145$ bohr; these functions are the squares of the functions which appeared in the same panel of figure 4.17.

Figure 4.21 Same as figure 4.19 except for $\rho = 2.0$ bohr; these functions are the squares of the functions which appeared in the same panel of figure 4.18.

Figure 4.22 Projection of the $J = 1$ $\Pi = 1$ functions $\psi_{n\Omega}^{J\Pi\Gamma_k}$ at $\rho = 6.0$ bohr onto the mapping plane. The left column gives the $\Omega = 0$ coefficient terms, while the right column contains the $\Omega = 1$ terms. The first row, consisting of panels a and d, is for the lowest energy A_1 symmetry surface function; the coefficients for the ground state E function symmetric with respect to $\nu\kappa$ interchange are given in the second row (panels b and e) and for the first excited state E function with this symmetry in the third row (panels c and f). The contour interval δ defines the spacing of the nodal lines at the values $\pm 0.1 + n\delta$ with n any integer. The solid lines represent positive function values, while the dashed lines represent negative function value.

Figure 4.23 Projection of the $J = 1$ $\Pi = 1$ functions $\psi_{n\Omega}^{J\Pi\Gamma_k}$ at $\rho = 6.0$ bohr onto the mapping plane. The left column gives the $\Omega = 0$ coefficient terms, while the right column contains the $\Omega = 1$ terms. The first row, consisting of panels a and d, is for the lowest energy A_2 symmetry surface function; the coefficients for the

ground state E function antisymmetric with respect to $\nu\kappa$ interchange are given in the second row (panels b and e) and for the first excited state E function with this symmetry in the third row (panels c and f). The contour interval δ defines the spacing of the nodal lines at the values $\pm 0.1 + n\delta$ with n any integer. The solid lines represent positive function values, while the dashed lines represent negative function value.

Figure 4.24 Same as figure 4.22 except for $r = 3.270145$ bohr.

Figure 4.25 Same as figure 4.23 except for $r = 3.270145$ bohr.

Figure 4.26 Same as figure 4.22 except for $r = 2.0$ bohr.

Figure 4.27 Same as figure 4.23 except for $r = 2.0$ bohr.

Figure 4.28 Projection of the functions $\Theta_n^{J\Pi\{\Gamma_k \otimes \Gamma_k\}}$ for $J = 1$, $\Pi = 1$ $\rho = 6.0$ bohr onto the mapping plane. Panel a gives the result for $\Gamma = A_1$, $n = 1$, panel d for $\Gamma = A_2$, $n = 1$, panels b and c for $\Gamma = E, k = 1$ and $n = 1, 2$ respectively, and panels e and f for $\Gamma = E, k = 2$ and $n = 1, 2$ respectively.

Figure 4.29 Same as figure 4.28 except for $r = 3.270145$ bohr.

Figure 4.30 Same as figure 4.28 except for $r = 2.0$ bohr.

Figure 4.31 Projection of the functions $\Theta_n^{J\Pi\{\Gamma_k \otimes \Gamma_k\}}$ for $J = 2$, $\Pi = 1$ $\rho = 6.0$ bohr onto the mapping plane. Panel a gives the result for $\Gamma = A_1$, $n = 1$, panel d for $\Gamma = A_2$, $n = 1$, panels b and c for $\Gamma = E, k = 1$ and $n = 1, 2$ respectively, and panels e and f for $\Gamma = E, k = 2$ and $n = 1, 2$ respectively.

Figure 4.32 Same as figure 4.31 except for $r = 3.270145$ bohr.

Figure 4.33 Same as figure 4.31 except for $r = 2.0$ bohr.

Figure 4.34 Projection of the functions $\Theta_n^{J\Pi\{\Gamma_k \otimes \Gamma_k\}}$ for $J = 2$, $\Pi = 0$ $\rho = 6.0$ bohr onto the mapping plane. Panel a gives the result for $\Gamma = A_1$, $n = 1$, panel d for $\Gamma = A_2$, $n = 1$, panels b and c for $\Gamma = E, k = 1$ and $n = 1, 2$ respectively, and panels e and f for $\Gamma = E, k = 2$ and $n = 1, 2$ respectively.

Figure 4.35 Same as figure 4.34 except for $r = 3.270145$ bohr.

Figure 4.36 Same as figure 4.34 except for $r = 2.0$ bohr.

Figure 4.37 Projection of the $J = 2$ $\Pi = 0$ functions $\psi_{n\Omega}^{J\Pi\Gamma_k}$ with $\Gamma = A_1$, E (with $n = 1, k = 1$) at $\rho = 3.270145$ bohr onto the mapping plane. The A_1 coefficients are presented with $\Omega = 0$ in panel a, $\Omega = 1$ in panel b and $\Omega = 2$ in panel c, and the E with $\Omega = 0$ in panel d, $\Omega = 1$ in panel e and $\Omega = 2$ in panel f. The solid lines represent positive function values, while the dashed lines represent negative function value.

Figure 4.38 Projection of the functions $\Theta_n^{J\Pi\{\Gamma_k \otimes \Gamma_k\}}$ for $J = 3$, $\Pi = 0$ $\rho = 6.0$ bohr onto the mapping plane. Panel a gives the result for $\Gamma = A_1$, $n = 1$, panel d for $\Gamma = A_2$, $n = 1$, panels b and c for $\Gamma = E, k = 1$ and $n = 1, 2$ respectively, and panels e and f for $\Gamma = E, k = 2$ and $n = 1, 2$ respectively.

Figure 4.39 Same as figure 4.38 except for $r = 3.270145$ bohr.

Figure 4.40 Same as figure 4.38 except for $r = 2.0$ bohr.

Figure 4.41 Projection of the functions $\Theta_n^{J\Pi\{\Gamma_k \otimes \Gamma_k\}}$ for $J = 3$, $\Pi = 1$ $\rho = 6.0$ bohr onto the mapping plane. Panel a gives the result for $\Gamma = A_1$, $n = 1$, panel d for $\Gamma = A_2$, $n = 1$, panels b and c for $\Gamma = E, k = 1$ and $n = 1, 2$ respectively, and panels e and f for $\Gamma = E, k = 2$ and $n = 1, 2$ respectively.

Figure 4.42 Same as figure 4.41 except for $r = 3.270145$ bohr.

Figure 4.43 Same as figure 4.41 except for $r = 2.0$ bohr.

Figure 4.44 Projection of the $J = 3$ $\Pi = 1$ coefficients $\psi_{n\Omega}^{J\Pi\Gamma_k}$ with $\Gamma = A_2$, at $\rho = 3.270145$ bohr onto the mapping plane. The coefficients are presented with $\Omega = 0$ in panel a, $\Omega = 1$ in panel b, $\Omega = 2$ in panel c, and $\Omega = 3$ in panel d. The solid lines represent positive function values, while the dashed lines represent negative function value.

Figure 4.45 Projection of the $J = 3$ $\Pi = 1$ coefficients $\psi_{n\Omega}^{J\Pi\Gamma_k}$ with $\Gamma = E$ (with $n = 2, k = 2$) at $\rho = 3.270145$ bohr onto the mapping plane. The coefficients are presented with $\Omega = 0$ in panel a, $\Omega = 1$ in panel b, $\Omega = 2$ in panel c, and $\Omega = 3$ in panel d. The solid lines represent positive function values, while the dashed lines represent negative function value.

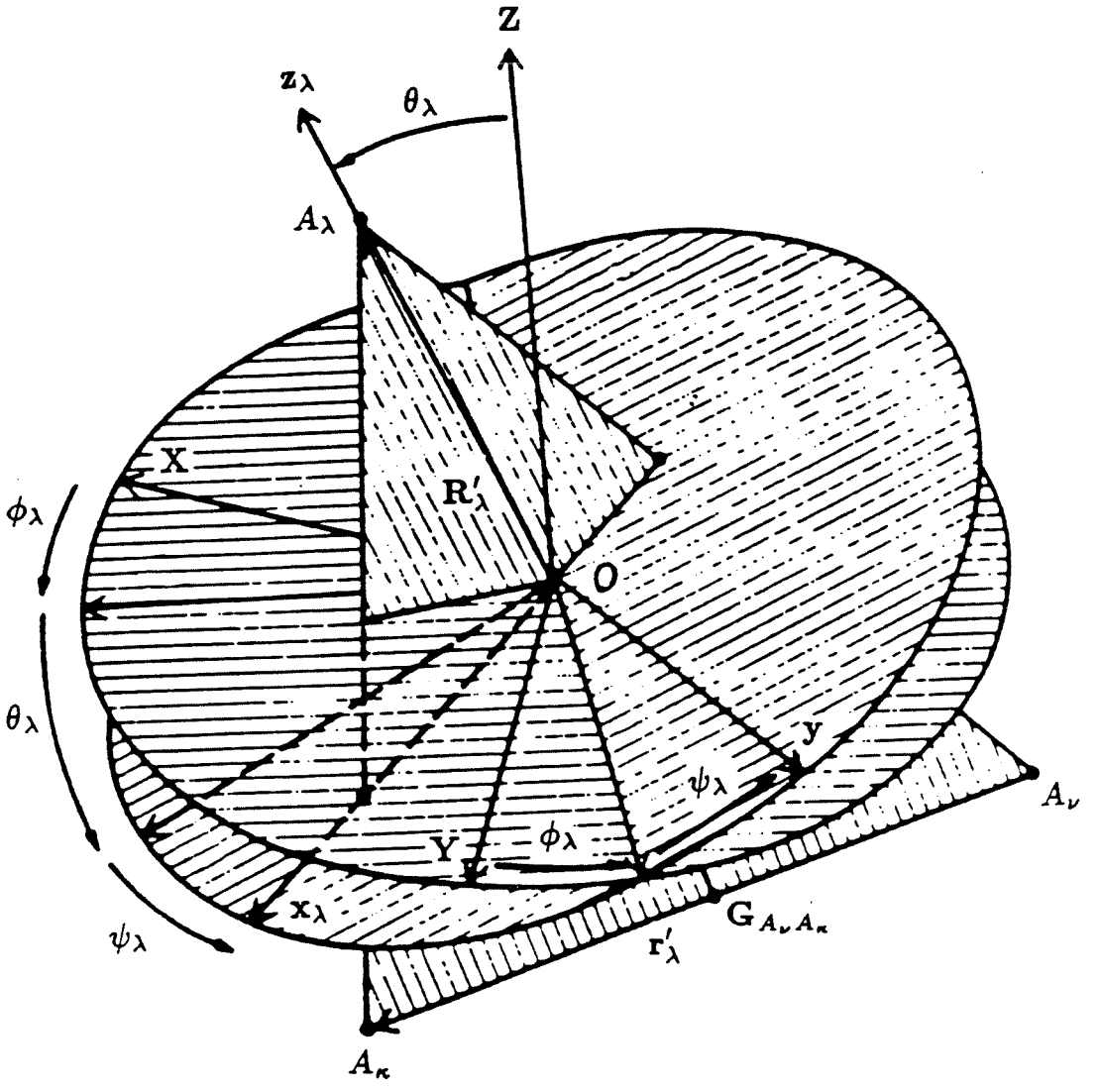
Z
z_λ
θ_λ
A_λ
X
R'_λ
O
ϕ_λ
θ_λ
ψ_λ
y
A_ν
Y
ϕ_λ
x_λ
$G_{A_\nu A_\kappa}$
r'_λ
A_κ

Fig. 2.1

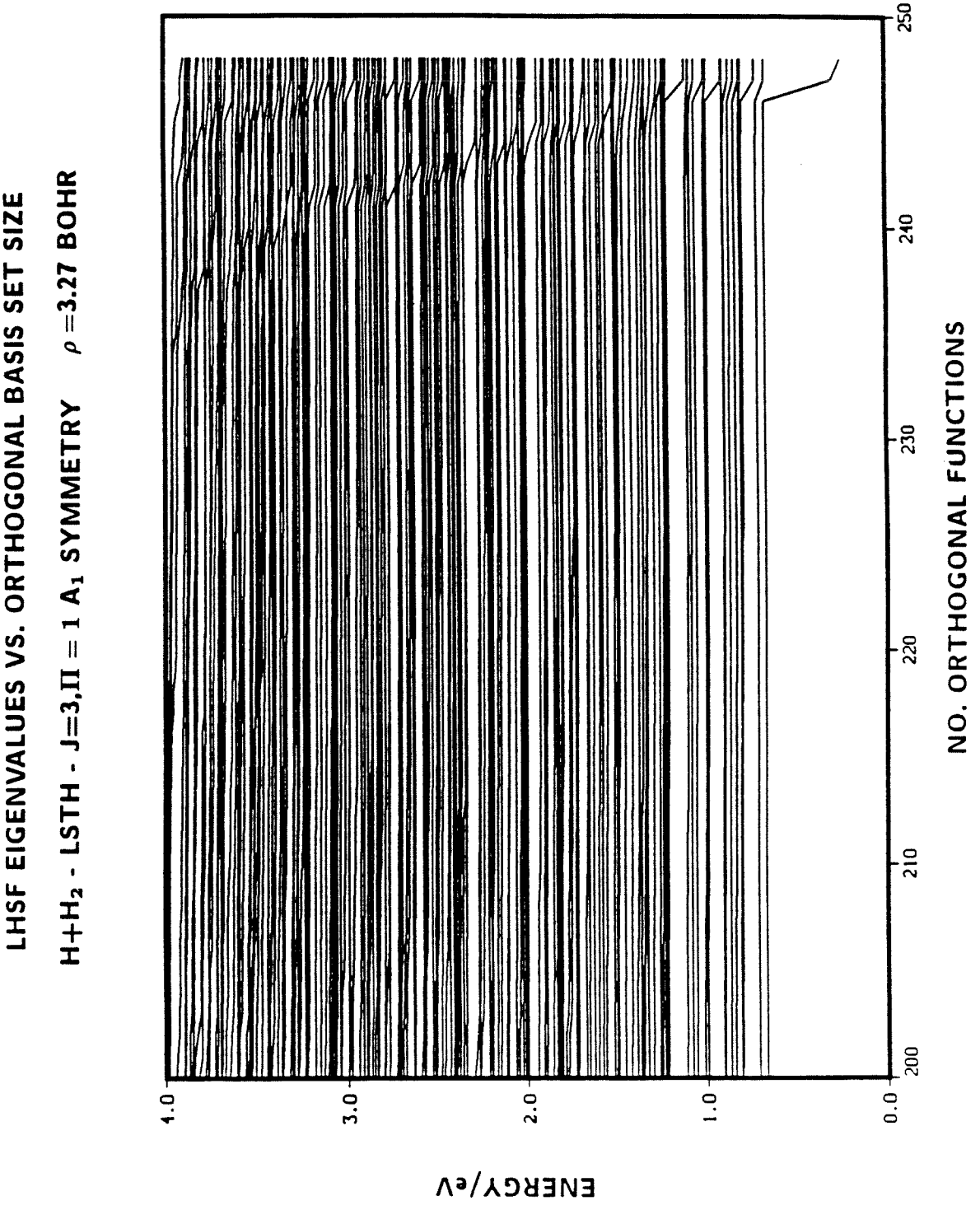
LHSF EIGENVALUES VS. ORTHOGONAL BASIS SET SIZE
H+H2 - LSTH - J=3,Π = 1 A1 SYMMETRY ρ =3.27 BOHR
ENERGY/eV
4.0
3.0
2.0
1.0
0.0
200
210
220
230
240
250
NO. ORTHOGONAL FUNCTIONS

Fig. 2.2

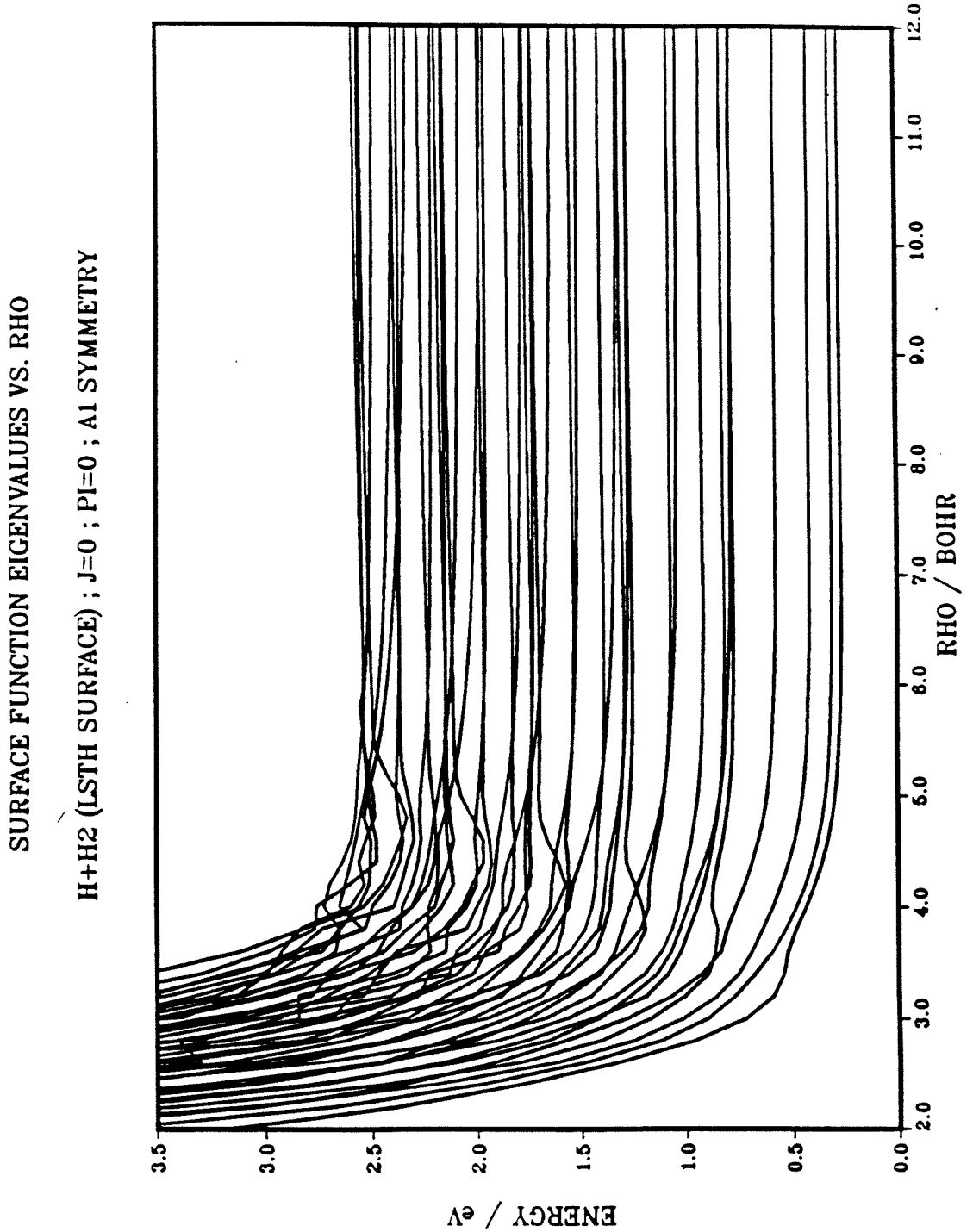
SURFACE FUNCTION EIGENVALUES VS. RHO
H+H2 (LSTH SURFACE) ; J=0 ; PI=0 ; A1 SYMMETRY
ENERGY / eV
RHO / BOHR
3.5
3.0
2.5
2.0
1.5
1.0
0.5
0.0
2.0
3.0
4.0
5.0
6.0
7.0
8.0
9.0
10.0
11.0
12.0

Fig. 4.1a

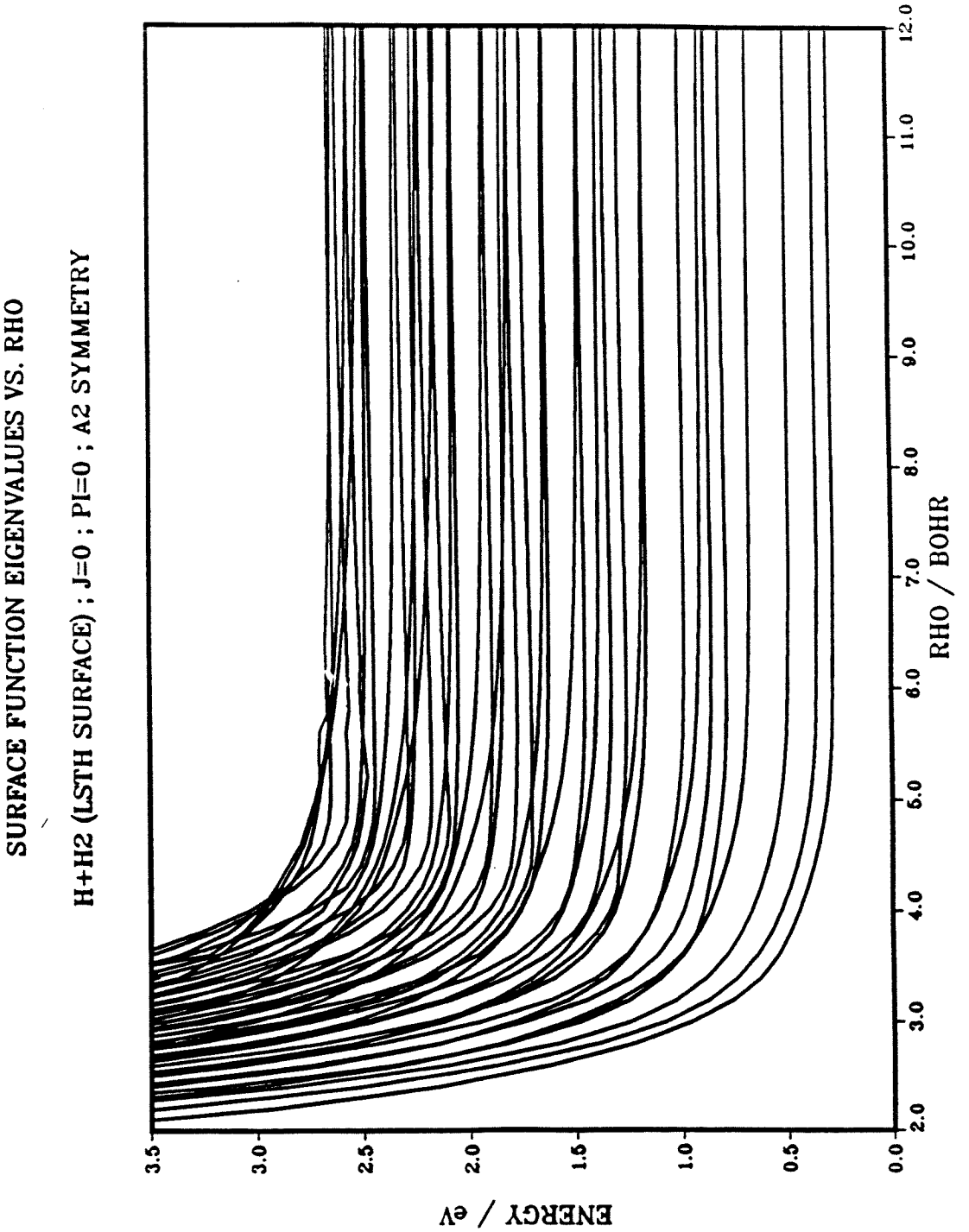
SURFACE FUNCTION EIGENVALUES VS. RHO
H+H2 (LSTH SURFACE) ; J=0 ; PI=0 ; A2 SYMMETRY
ENERGY / eV
RHO / BOHR
0.0
0.5
1.0
1.5
2.0
2.5
3.0
3.5
2.0
3.0
4.0
5.0
6.0
7.0
8.0
9.0
10.0
11.0
12.0

Fig. 4.1b

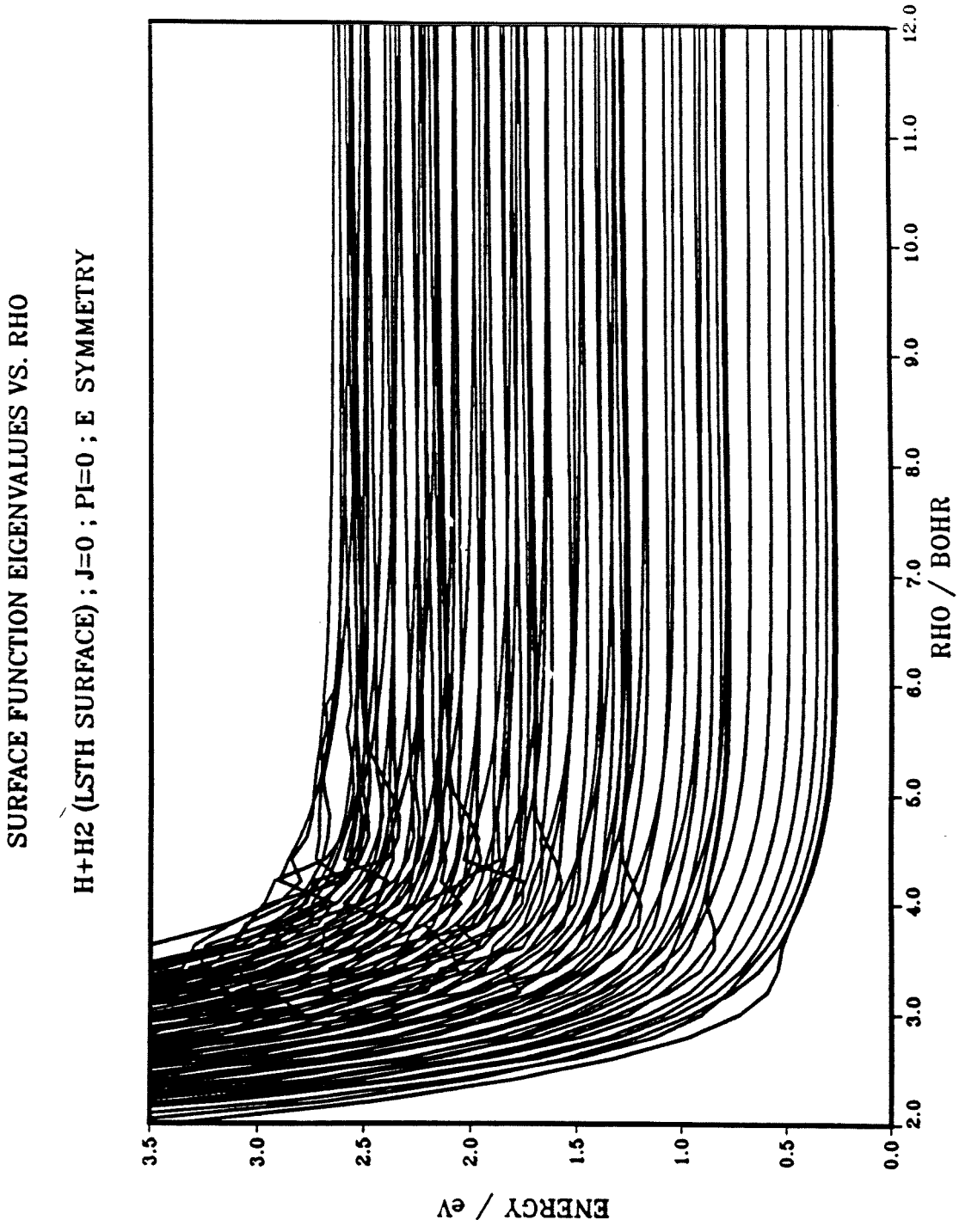
SURFACE FUNCTION EIGENVALUES VS. RHO
H+H2 (LSTH SURFACE) ; J=0 ; PI=0 ; E SYMMETRY
ENERGY / eV
RHO / BOHR
3.5
3.0
2.5
2.0
1.5
1.0
0.5
0.0
2.0
3.0
4.0
5.0
6.0
7.0
8.0
9.0
10.0
11.0
12.0

Fig. 4.1c

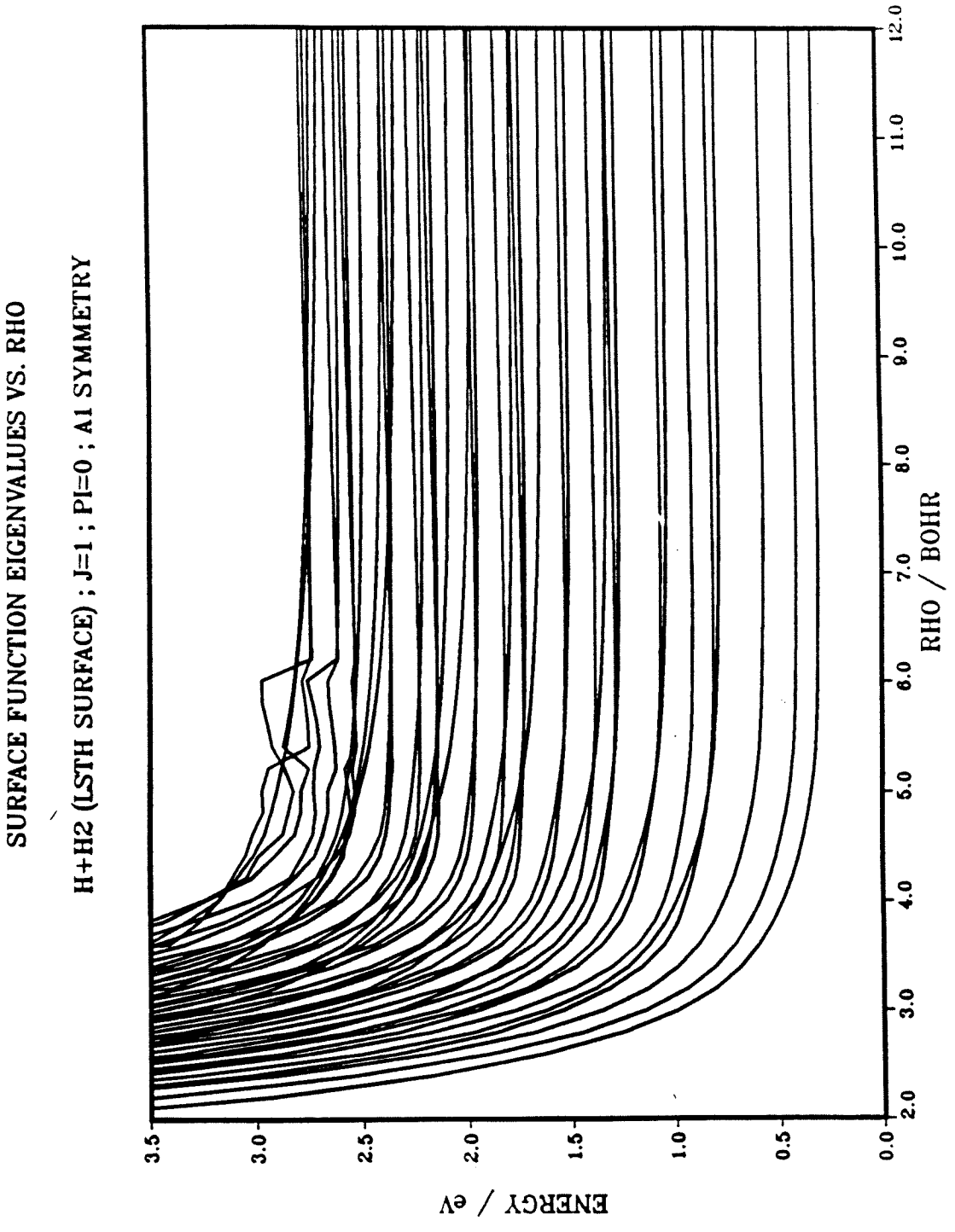
SURFACE FUNCTION EIGENVALUES VS. RHO
H+H2 (LSTH SURFACE) ; J=1 ; PI=0 ; A1 SYMMETRY
ENERGY / eV
RHO / BOHR
0.0
0.5
1.0
1.5
2.0
2.5
3.0
3.5
2.0
3.0
4.0
5.0
6.0
7.0
8.0
9.0
10.0
11.0
12.0

Fig. 4.2a

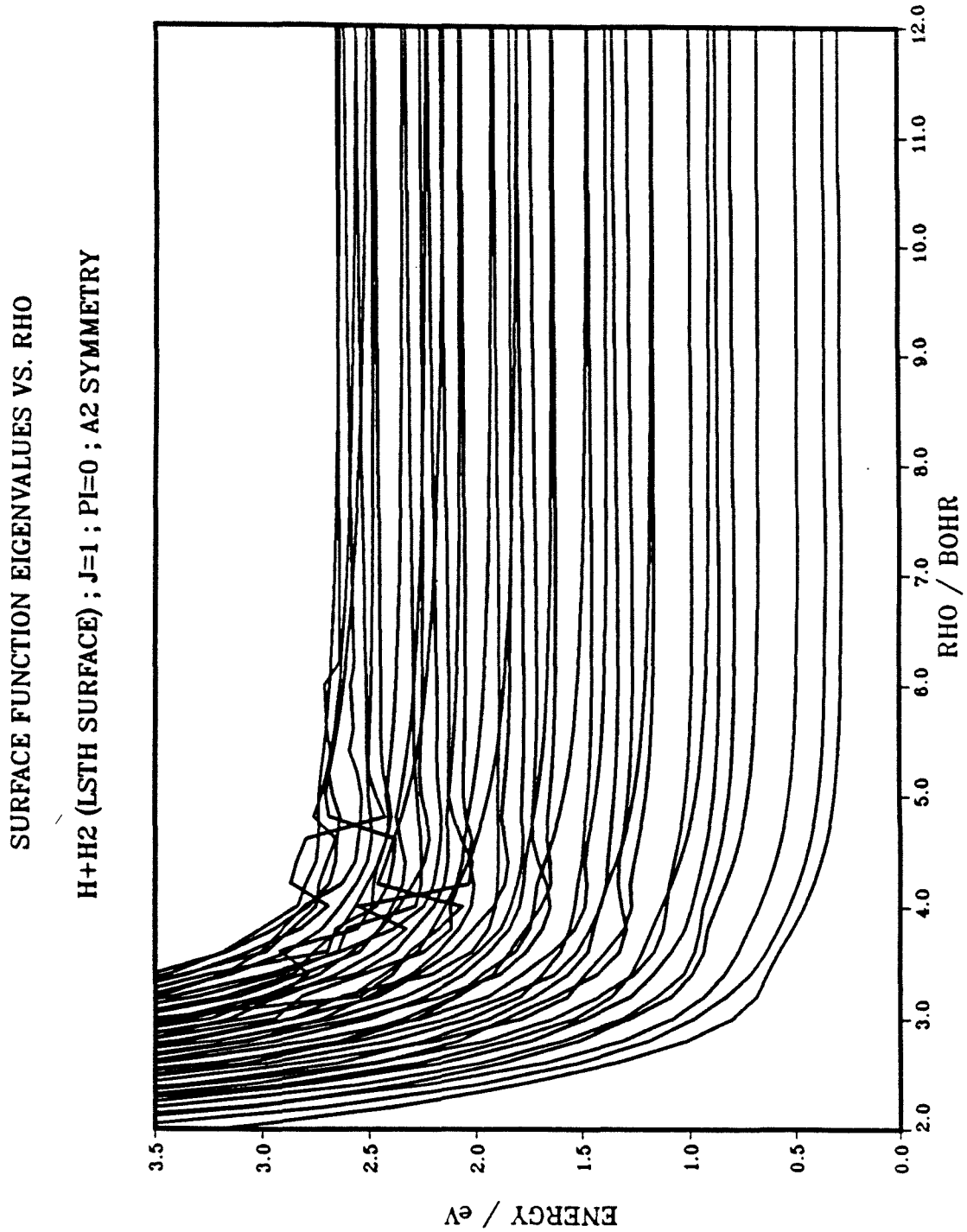
SURFACE FUNCTION EIGENVALUES VS. RHO
H+H2 (LSTH SURFACE) ; J=1 ; PI=0 ; A2 SYMMETRY
ENERGY / eV
RHO / BOHR
3.5
3.0
2.5
2.0
1.5
1.0
0.5
0.0
2.0
3.0
4.0
5.0
6.0
7.0
8.0
9.0
10.0
11.0
12.0

Fig. 4.2b

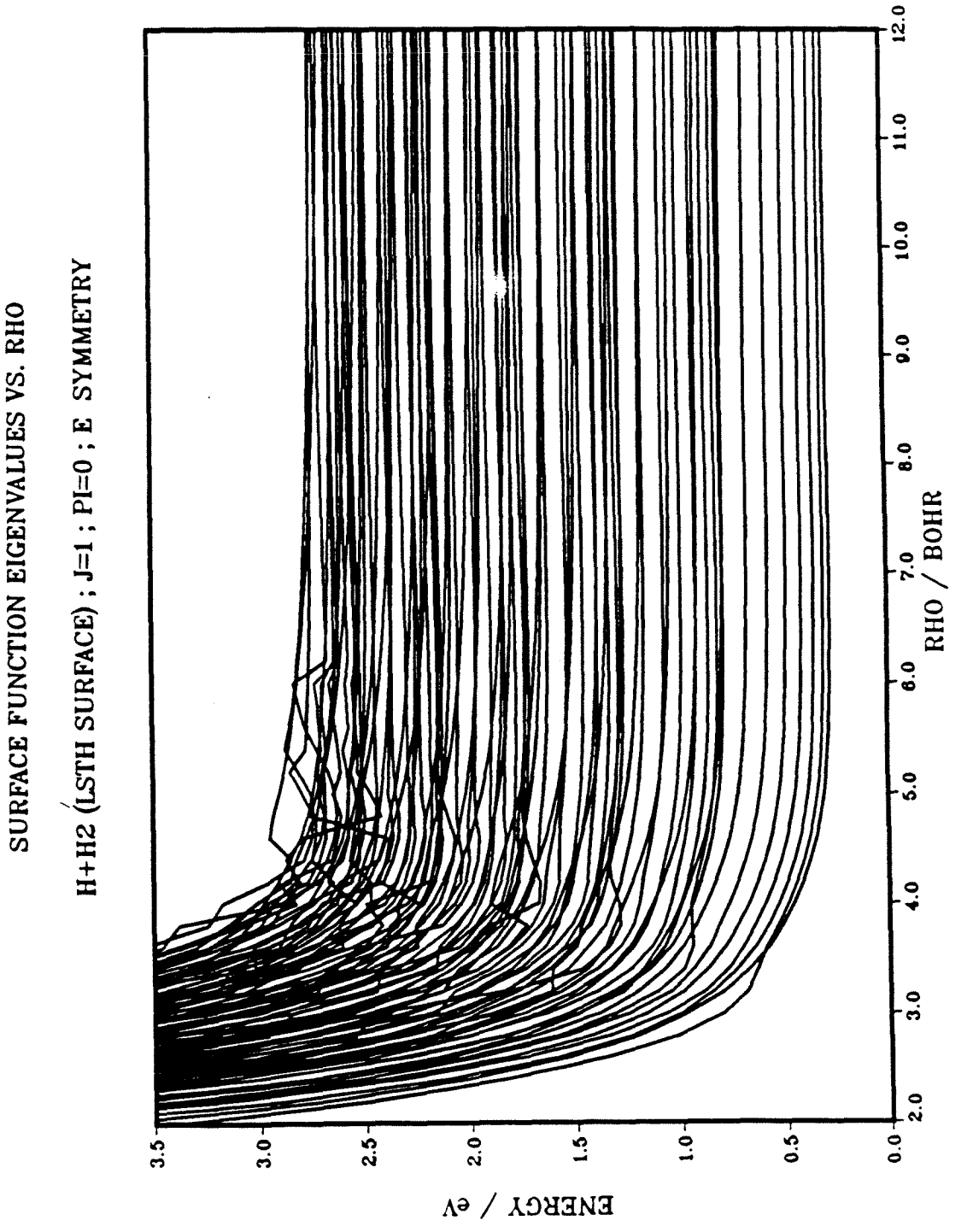
SURFACE FUNCTION EIGENVALUES VS. RHO
H+H2 (LSTH SURFACE) ; J=1 ; PI=0 ; E SYMMETRY
ENERGY / eV
RHO / BOHR
0.0
0.5
1.0
1.5
2.0
2.5
3.0
3.5
2.0
3.0
4.0
5.0
6.0
7.0
8.0
9.0
10.0
11.0
12.0

Fig. 4.2c

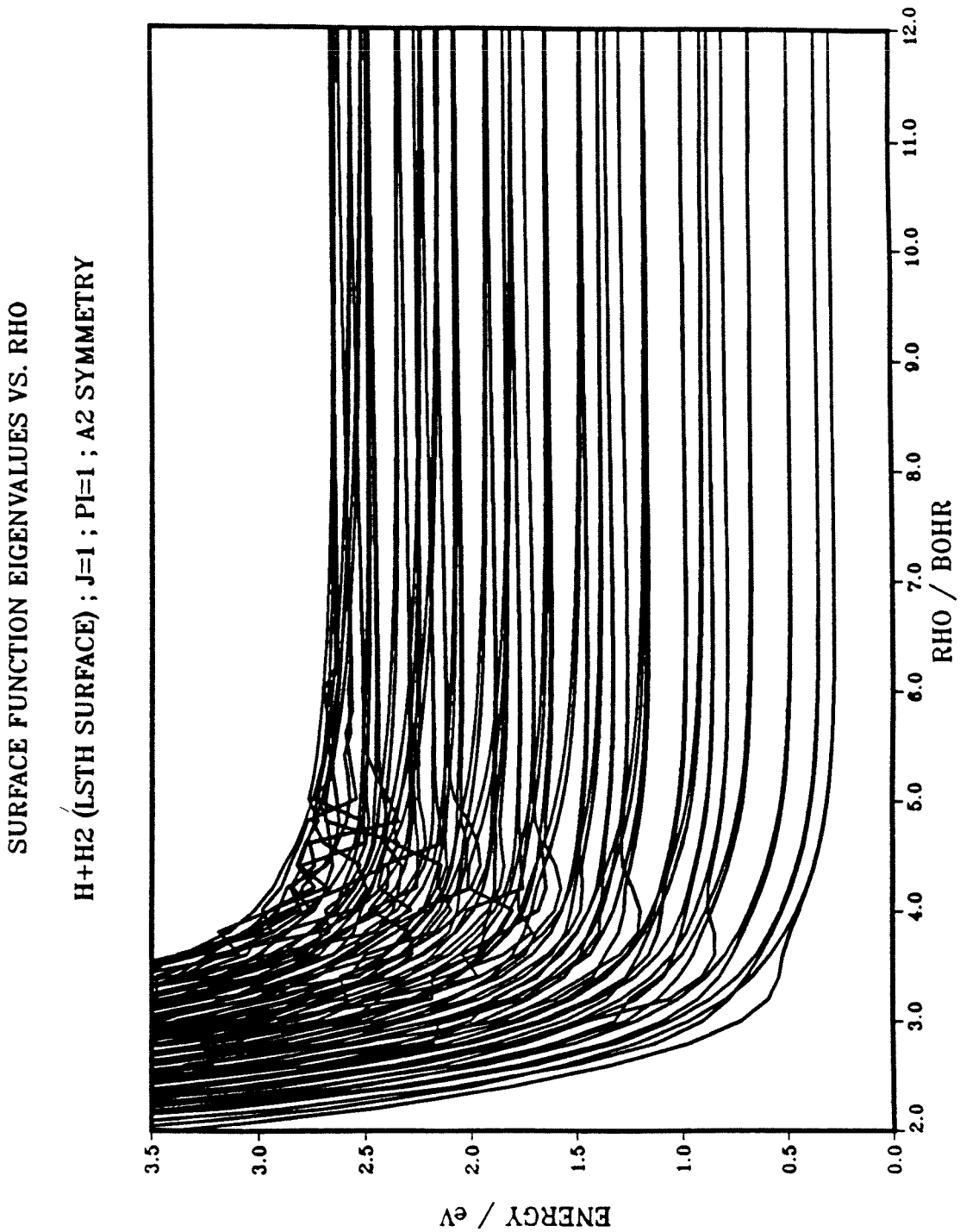
SURFACE FUNCTION EIGENVALUES VS. RHO
H+H2 (LSTH SURFACE) ; J=1 ; PI=1 ; A2 SYMMETRY
ENERGY / eV
RHO / BOHR
0.0
0.5
1.0
1.5
2.0
2.5
3.0
3.5
2.0
3.0
4.0
5.0
6.0
7.0
8.0
9.0
10.0
11.0
12.0

Fig. 4.3

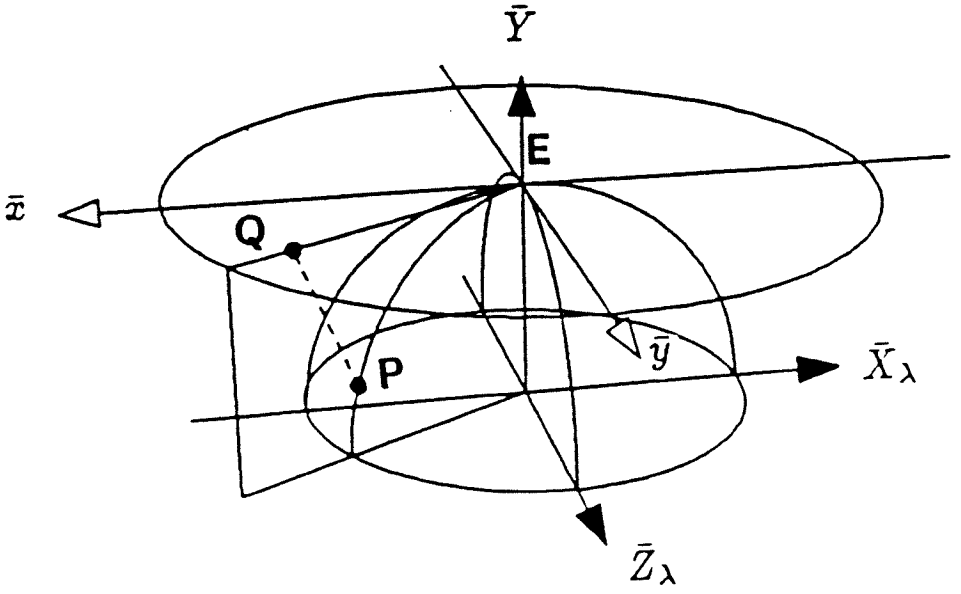

Fig. 4.4

ρ = 2 bohr

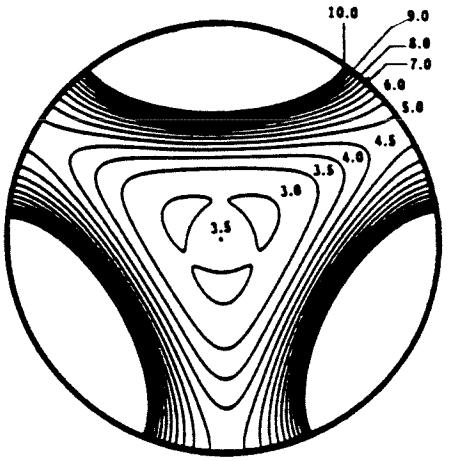

ρ = 3.27 bohr

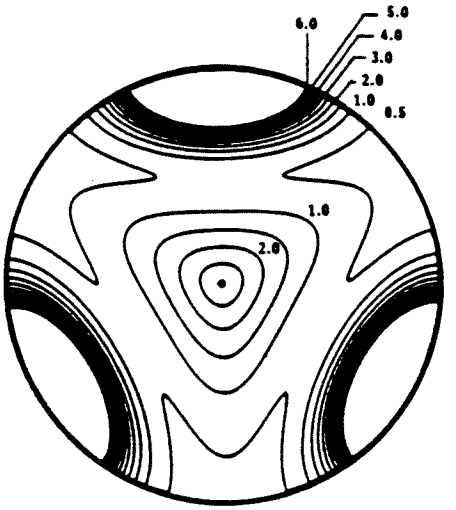

ρ = 6 bohr

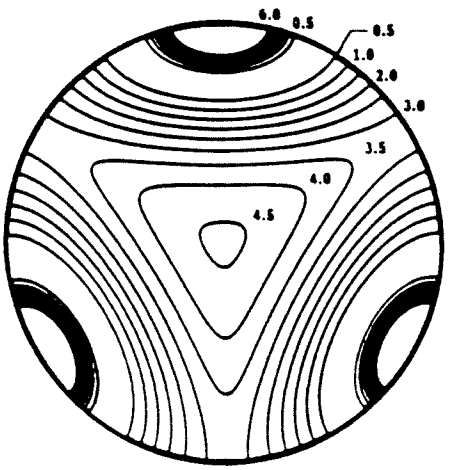

Fig. 4.5

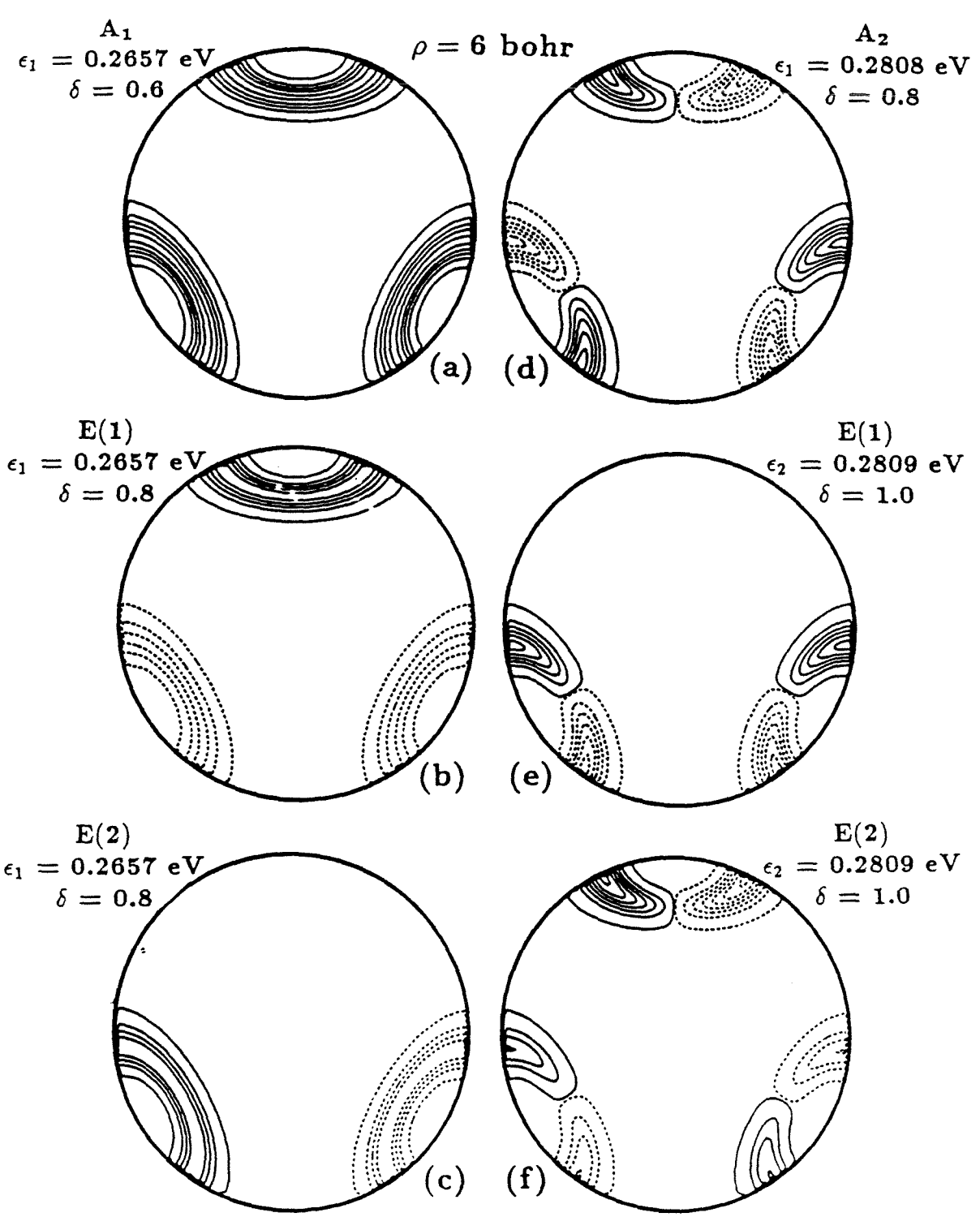
J = 0
ρ = 6 bohr
A1
ϵ1 = 0.2657 eV
δ = 0.6
A2
ϵ1 = 0.2808 eV
δ = 0.8
(a)
(d)
E(1)
ϵ1 = 0.2657 eV
δ = 0.8
E(1)
ϵ2 = 0.2809 eV
δ = 1.0
(b)
(e)
E(2)
ϵ1 = 0.2657 eV
δ = 0.8
E(2)
ϵ2 = 0.2809 eV
δ = 1.0
(c)
(f)

Fig. 4.6

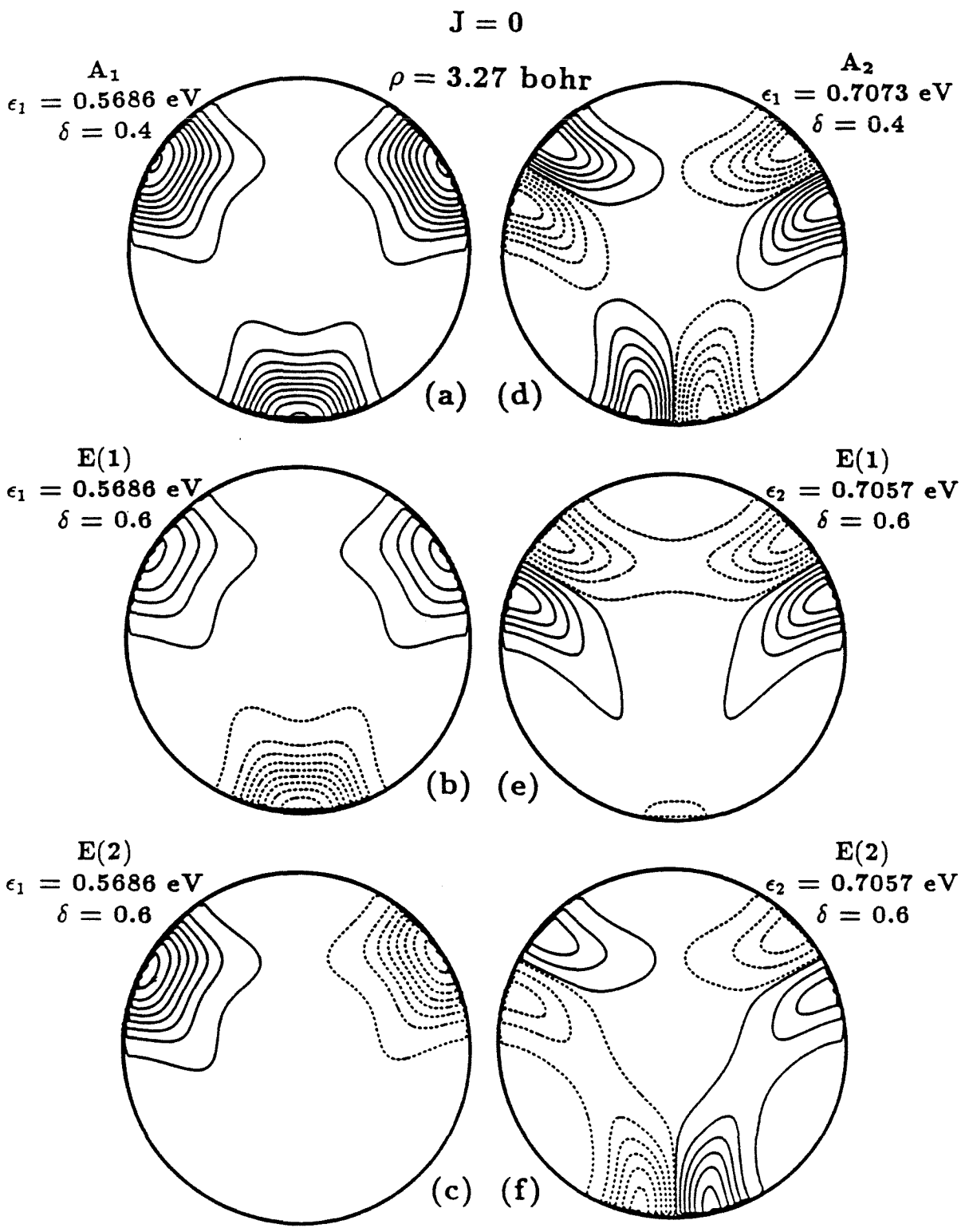
J = 0
ρ = 3.27 bohr
A1
ϵ1 = 0.5686 eV
δ = 0.4
A2
ϵ1 = 0.7073 eV
δ = 0.4
(a)
(d)
E(1)
ϵ1 = 0.5686 eV
δ = 0.6
E(1)
ϵ2 = 0.7057 eV
δ = 0.6
(b)
(e)
E(2)
ϵ1 = 0.5686 eV
δ = 0.6
E(2)
ϵ2 = 0.7057 eV
δ = 0.6
(c)
(f)

Fig. 4.7

$J = 0$

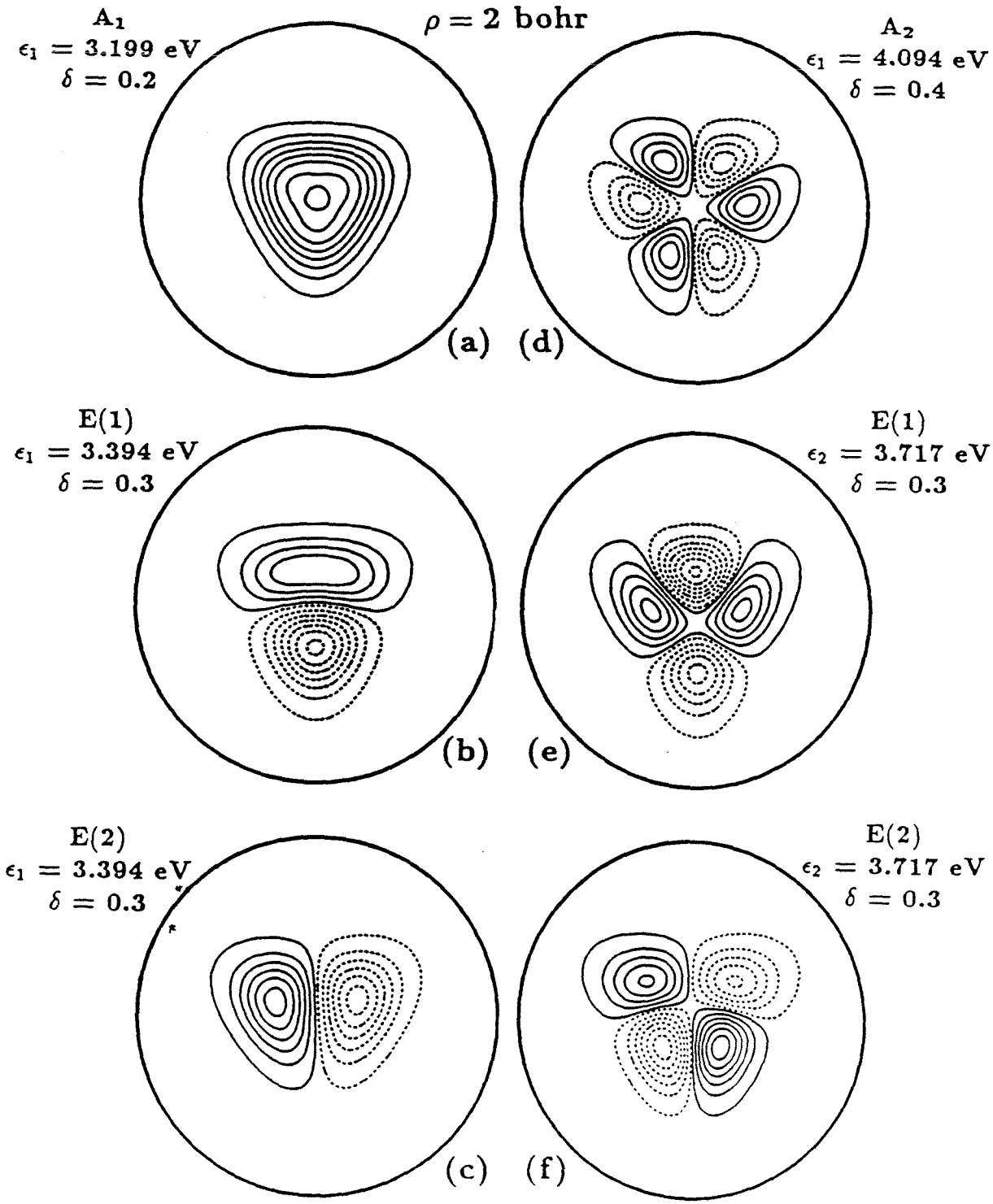
$\rho = 2$ bohr
A_1
$\epsilon_1 = 3.199$ eV
$\delta = 0.2$
(a)
A_2
$\epsilon_1 = 4.094$ eV
$\delta = 0.4$
(d)
E(1)
$\epsilon_1 = 3.394$ eV
$\delta = 0.3$
(b)
E(1)
$\epsilon_2 = 3.717$ eV
$\delta = 0.3$
(e)
E(2)
$\epsilon_1 = 3.394$ eV
$\delta = 0.3$
(c)
E(2)
$\epsilon_2 = 3.717$ eV
$\delta = 0.3$
(f)

Fig. 4.8

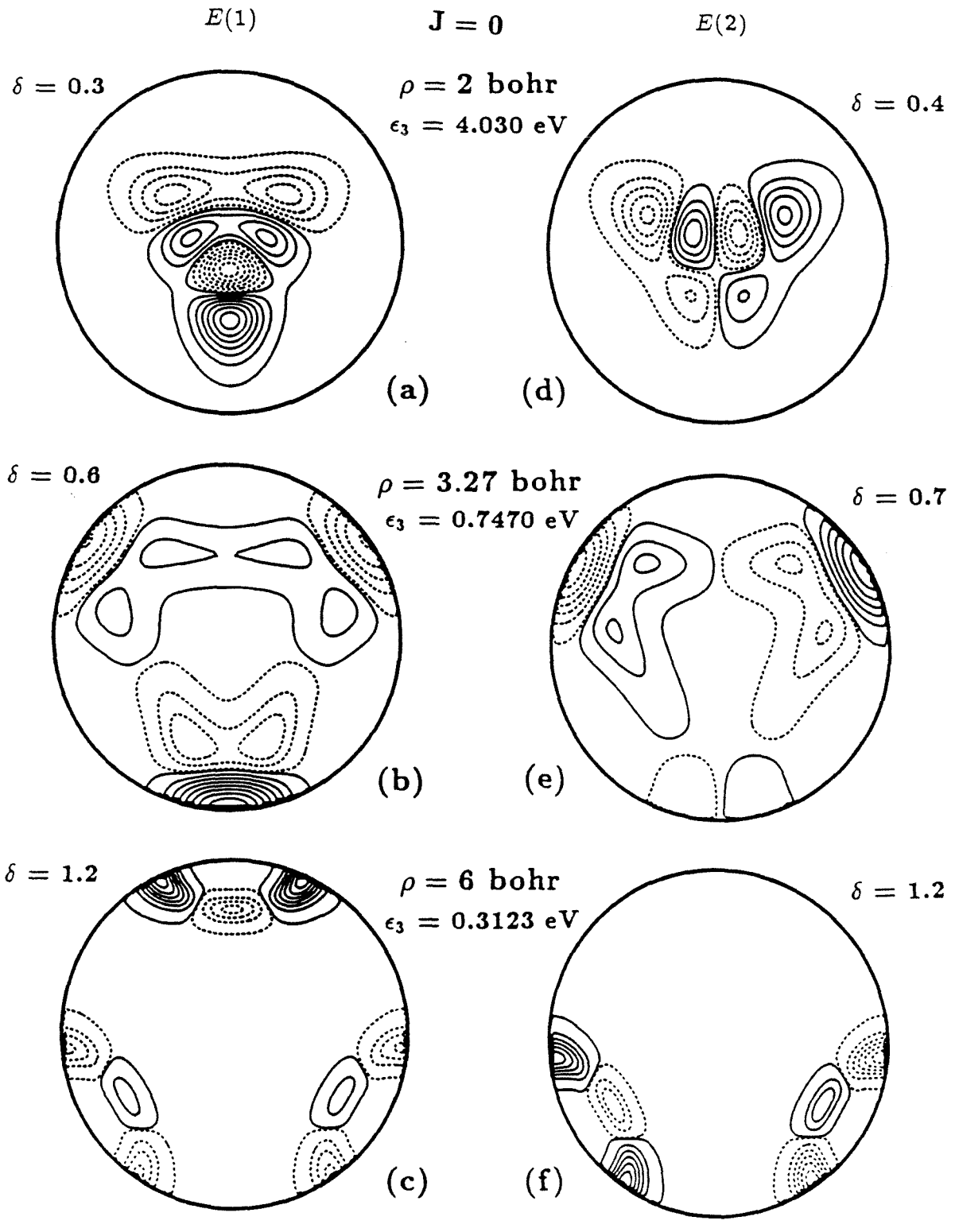
E(1)
J = 0
E(2)
δ = 0.3
ρ = 2 bohr
ε3 = 4.030 eV
δ = 0.4
(a)
(d)
δ = 0.6
ρ = 3.27 bohr
ε3 = 0.7470 eV
δ = 0.7
(b)
(e)
δ = 1.2
ρ = 6 bohr
ε3 = 0.3123 eV
δ = 1.2
(c)
(f)

Fig. 4.9

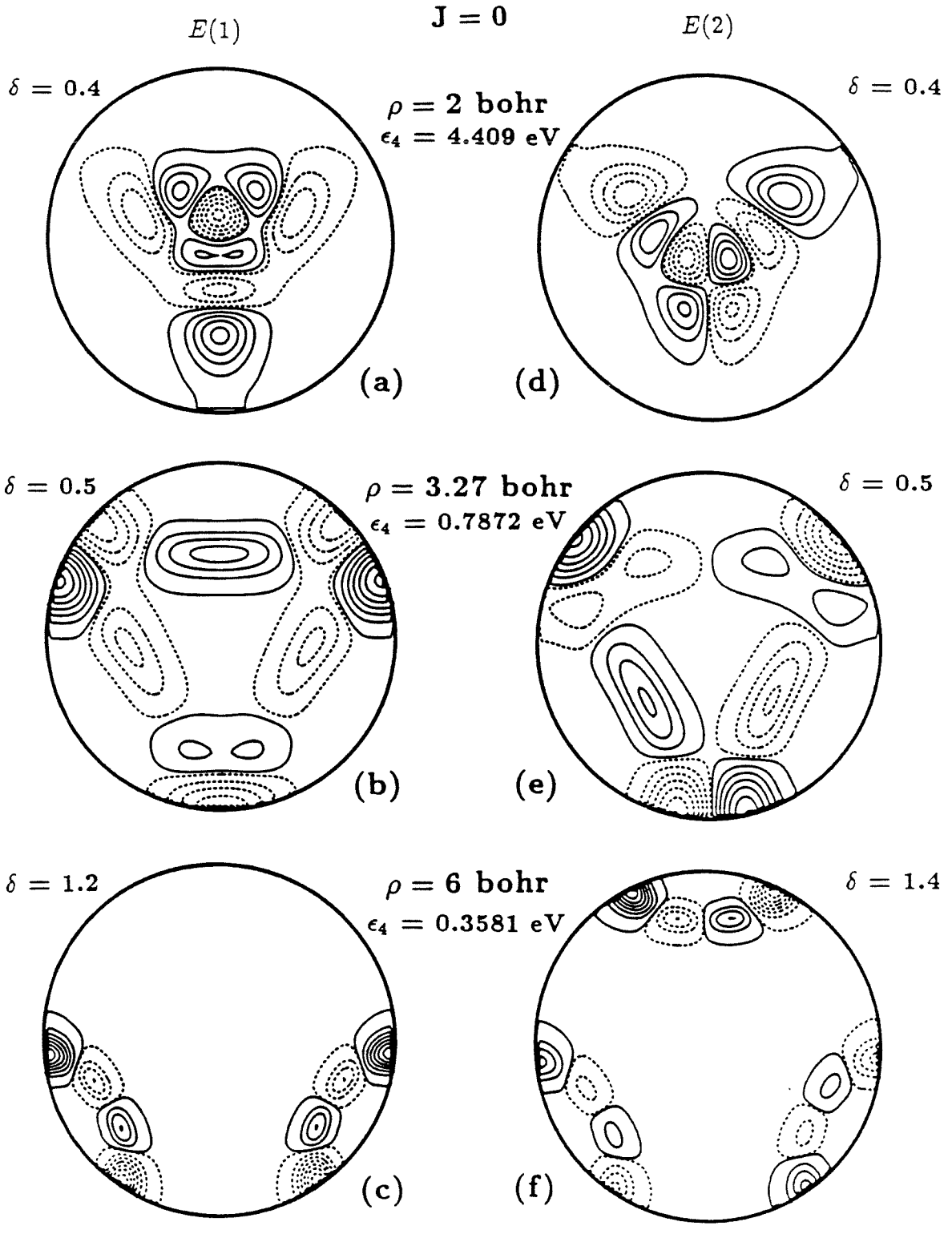
J = 0
E(1)
E(2)
δ = 0.4
ρ = 2 bohr
ϵ4 = 4.409 eV
δ = 0.4
(a)
(d)
δ = 0.5
ρ = 3.27 bohr
ϵ4 = 0.7872 eV
δ = 0.5
(b)
(e)
δ = 1.2
ρ = 6 bohr
ϵ4 = 0.3581 eV
δ = 1.4
(c)
(f)

Fig. 4.10

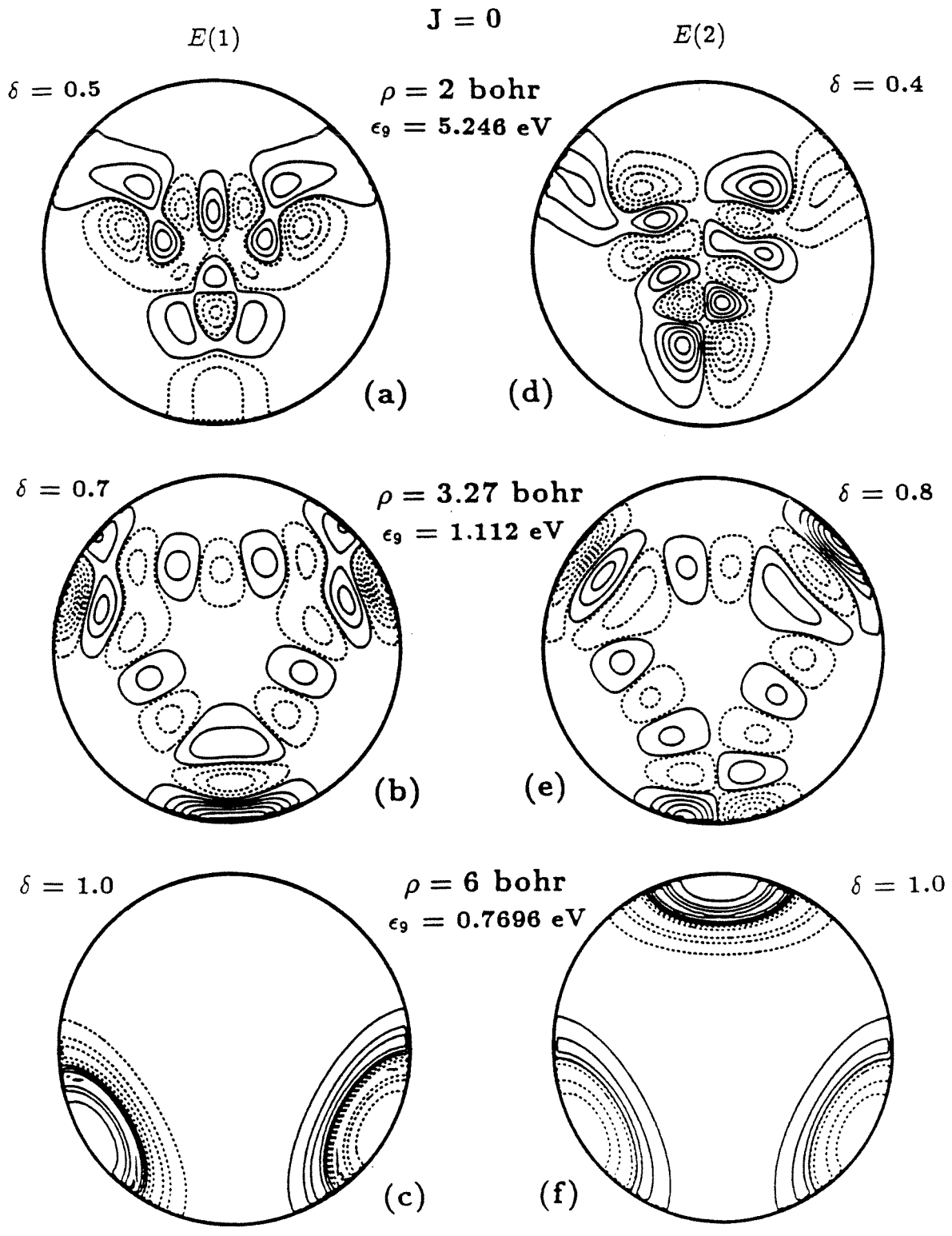
J = 0
E(1)
E(2)
δ = 0.5
ρ = 2 bohr
ε9 = 5.246 eV
δ = 0.4
(a)
(d)
δ = 0.7
ρ = 3.27 bohr
ε9 = 1.112 eV
δ = 0.8
(b)
(e)
δ = 1.0
ρ = 6 bohr
ε9 = 0.7696 eV
δ = 1.0
(c)
(f)

Fig. 4.11

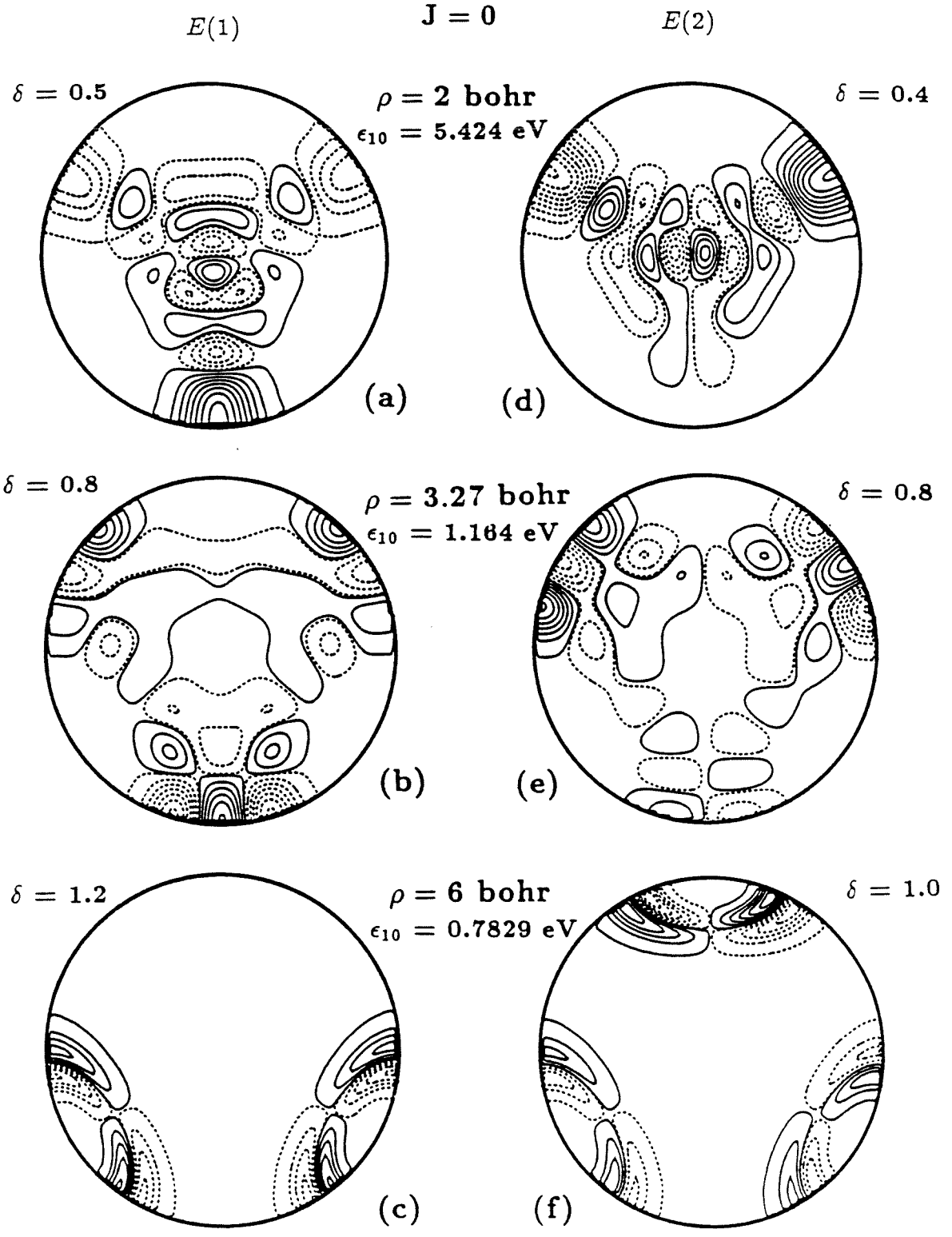
J = 0
E(1)
E(2)
δ = 0.5
ρ = 2 bohr
ε10 = 5.424 eV
δ = 0.4
(a)
(d)
δ = 0.8
ρ = 3.27 bohr
ε10 = 1.164 eV
δ = 0.8
(b)
(e)
δ = 1.2
ρ = 6 bohr
ε10 = 0.7829 eV
δ = 1.0
(c)
(f)

Fig. 4.12

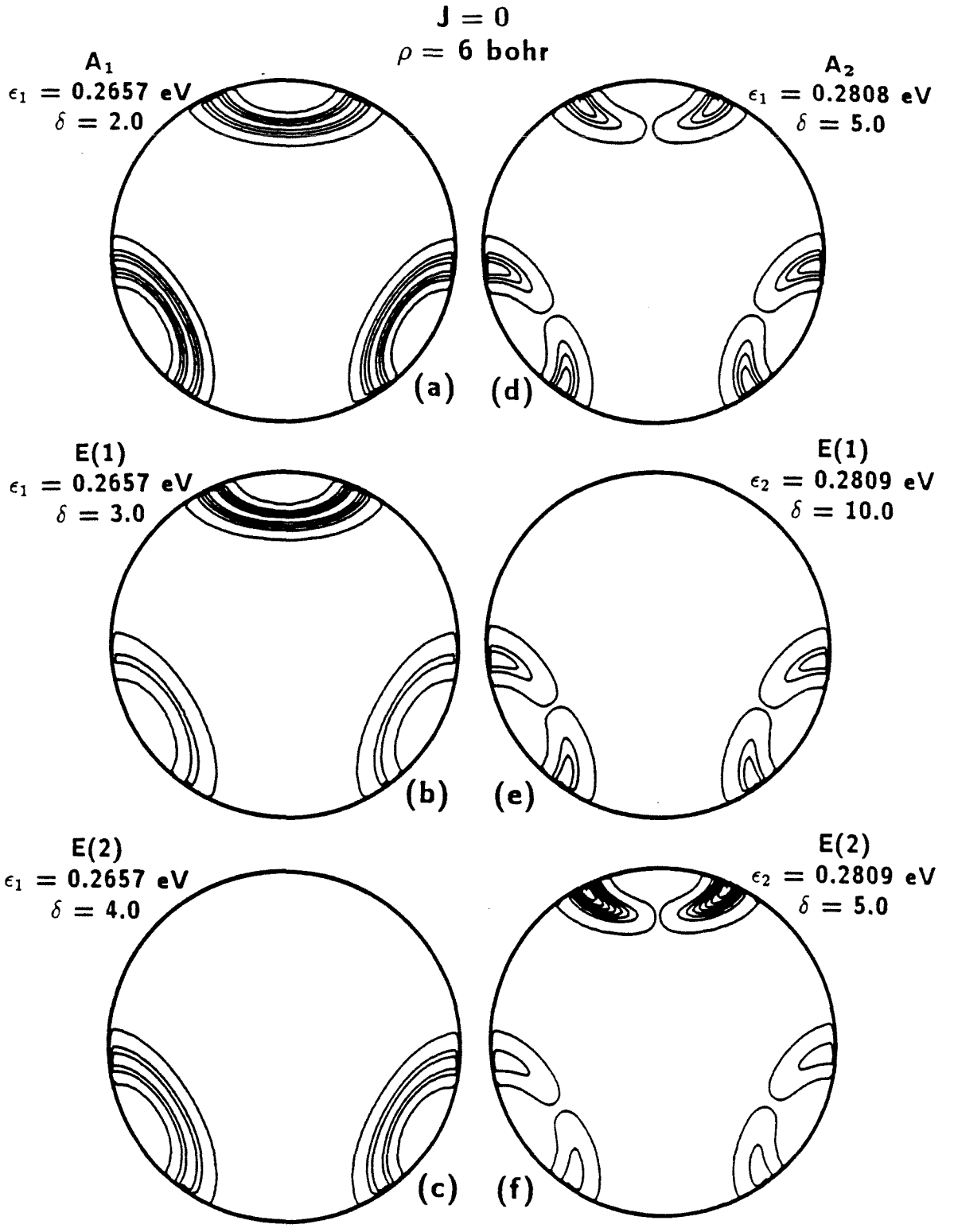
J = 0
ρ = 6 bohr
A1
ϵ1 = 0.2657 eV
δ = 2.0
(a)
A2
ϵ1 = 0.2808 eV
δ = 5.0
(d)
E(1)
ϵ1 = 0.2657 eV
δ = 3.0
(b)
E(1)
ϵ2 = 0.2809 eV
δ = 10.0
(e)
E(2)
ϵ1 = 0.2657 eV
δ = 4.0
(c)
E(2)
ϵ2 = 0.2809 eV
δ = 5.0
(f)

Fig. 4.13

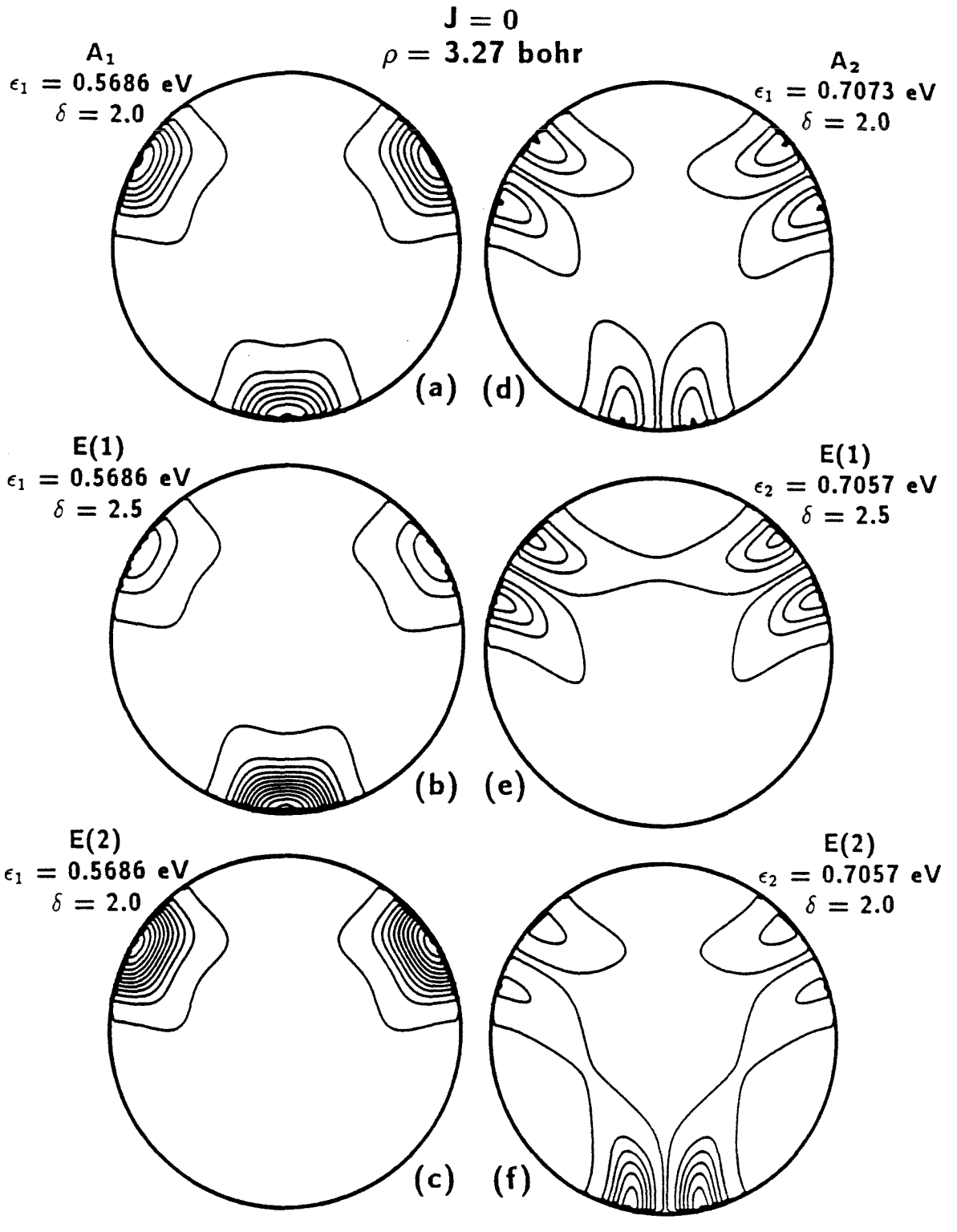
J = 0
ρ = 3.27 bohr
A1
ϵ1 = 0.5686 eV
δ = 2.0
A2
ϵ1 = 0.7073 eV
δ = 2.0
(a)
(d)
E(1)
ϵ1 = 0.5686 eV
δ = 2.5
E(1)
ϵ2 = 0.7057 eV
δ = 2.5
(b)
(e)
E(2)
ϵ1 = 0.5686 eV
δ = 2.0
E(2)
ϵ2 = 0.7057 eV
δ = 2.0
(c)
(f)

Fig. 4.14

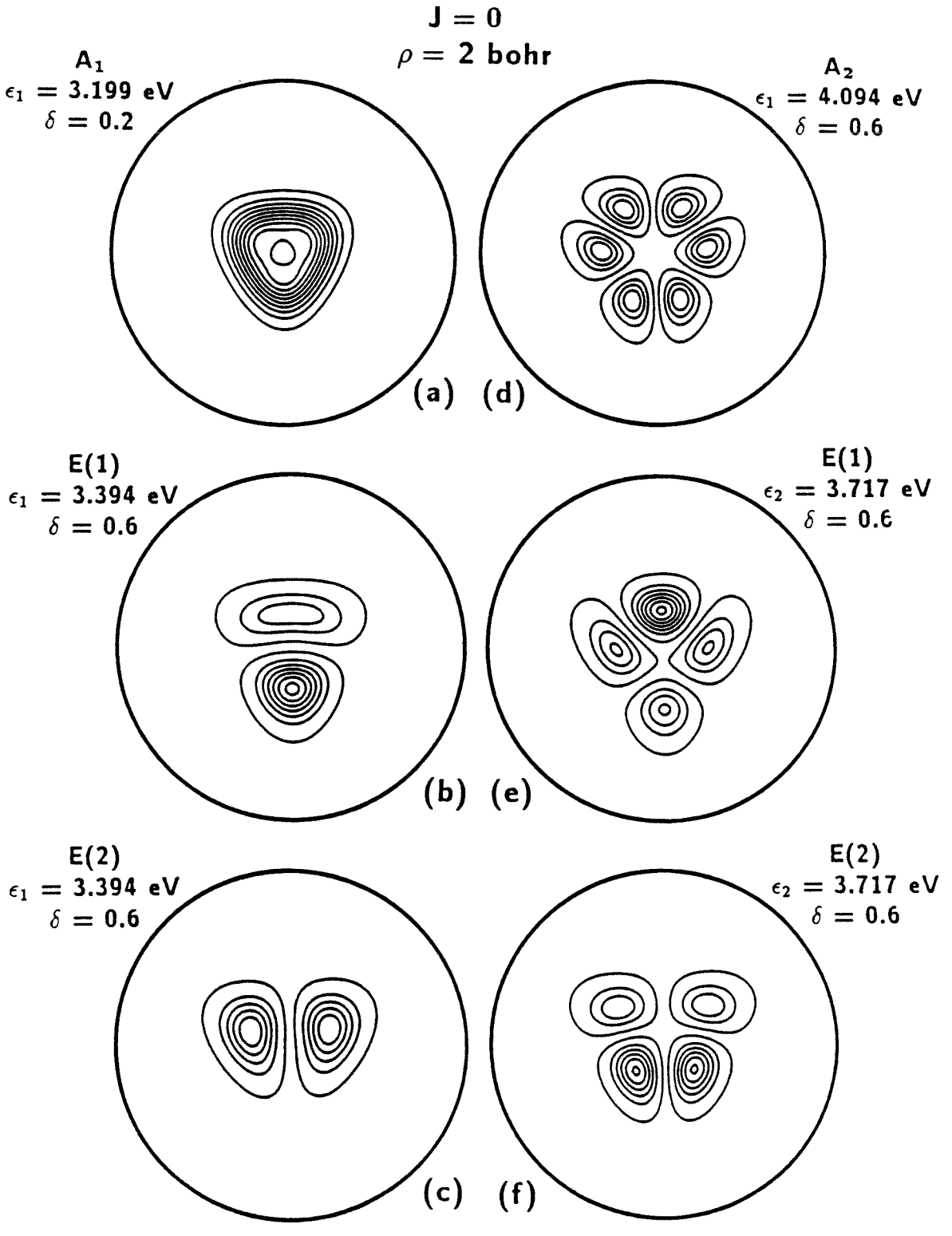
J = 0
ρ = 2 bohr
A1
ϵ1 = 3.199 eV
δ = 0.2
A2
ϵ1 = 4.094 eV
δ = 0.6
(a)
(d)
E(1)
ϵ1 = 3.394 eV
δ = 0.6
E(1)
ϵ2 = 3.717 eV
δ = 0.6
(b)
(e)
E(2)
ϵ1 = 3.394 eV
δ = 0.6
E(2)
ϵ2 = 3.717 eV
δ = 0.6
(c)
(f)

Fig. 4.15

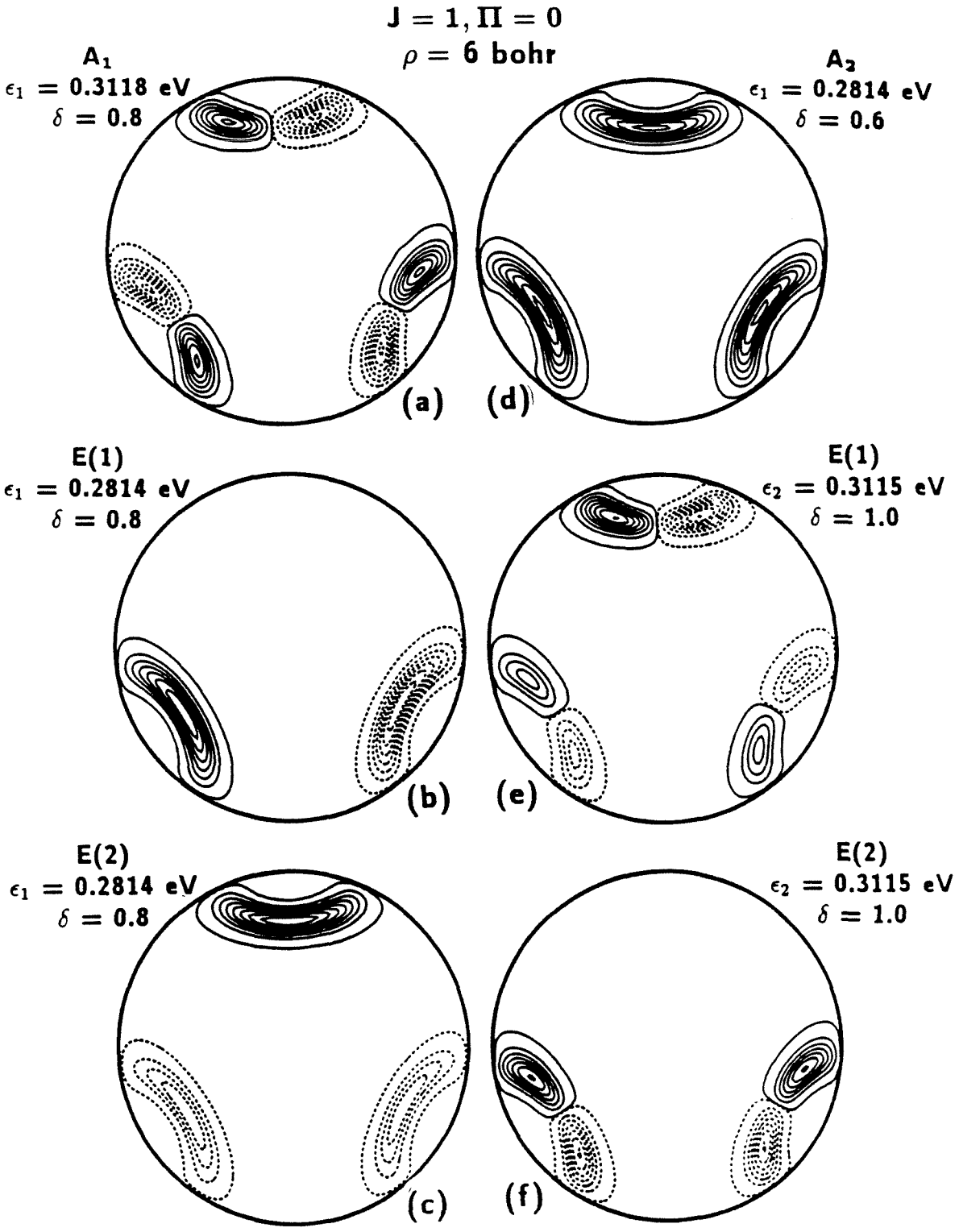
J = 1, Π = 0
ρ = 6 bohr
A1
ϵ1 = 0.3118 eV
δ = 0.8
A2
ϵ1 = 0.2814 eV
δ = 0.6
(a)
(d)
E(1)
ϵ1 = 0.2814 eV
δ = 0.8
E(1)
ϵ2 = 0.3115 eV
δ = 1.0
(b)
(e)
E(2)
ϵ1 = 0.2814 eV
δ = 0.8
E(2)
ϵ2 = 0.3115 eV
δ = 1.0
(c)
(f)

Fig. 4.16

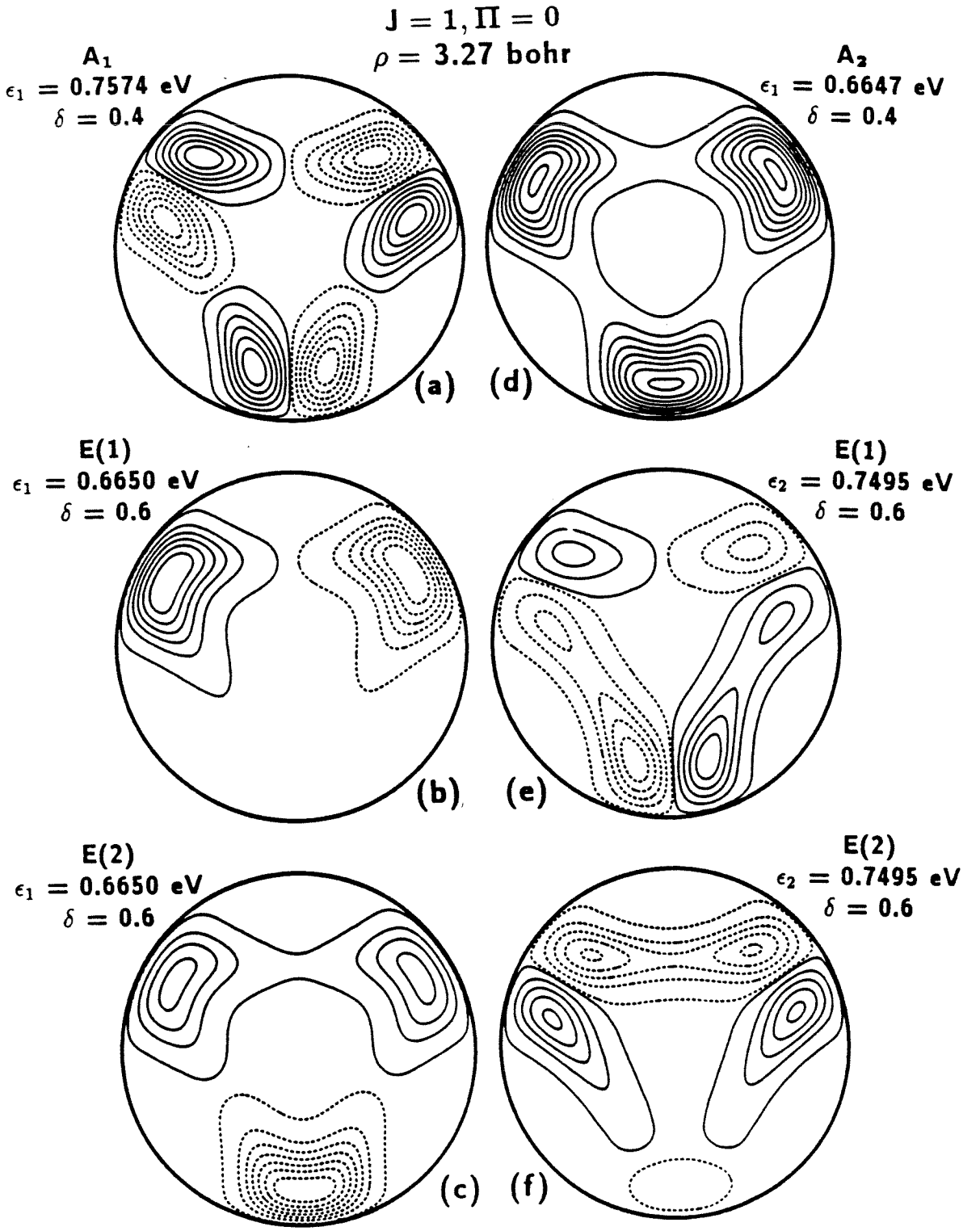
J = 1, Π = 0
ρ = 3.27 bohr
A1
ϵ1 = 0.7574 eV
δ = 0.4
A2
ϵ1 = 0.6647 eV
δ = 0.4
(a)
(d)
E(1)
ϵ1 = 0.6650 eV
δ = 0.6
E(1)
ϵ2 = 0.7495 eV
δ = 0.6
(b)
(e)
E(2)
ϵ1 = 0.6650 eV
δ = 0.6
E(2)
ϵ2 = 0.7495 eV
δ = 0.6
(c)
(f)

Fig. 4.17

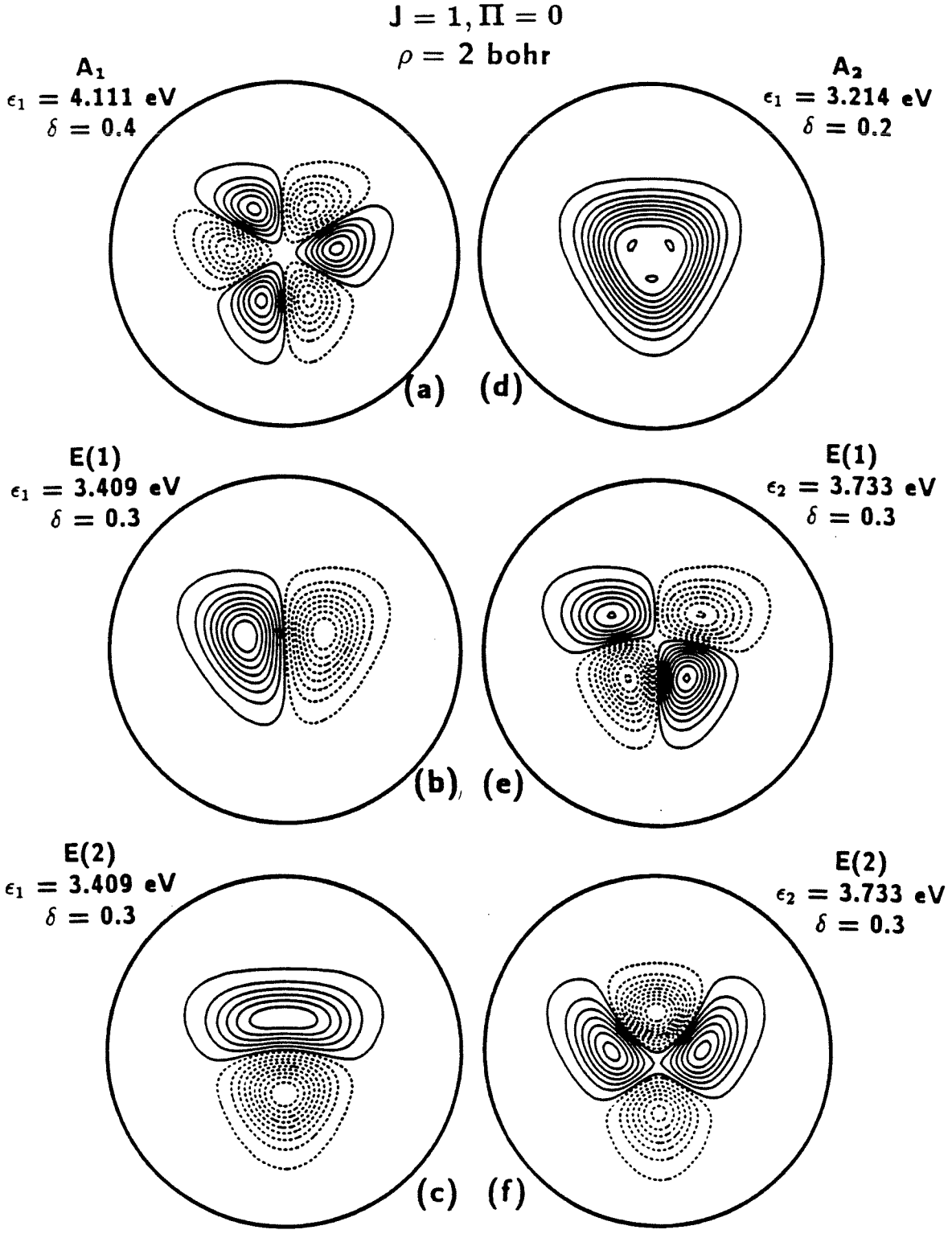
J = 1, Π = 0
ρ = 2 bohr
A1
ϵ1 = 4.111 eV
δ = 0.4
A2
ϵ1 = 3.214 eV
δ = 0.2
(a)
(d)
E(1)
ϵ1 = 3.409 eV
δ = 0.3
E(1)
ϵ2 = 3.733 eV
δ = 0.3
(b)
(e)
E(2)
ϵ1 = 3.409 eV
δ = 0.3
E(2)
ϵ2 = 3.733 eV
δ = 0.3
(c)
(f)

Fig. 4.18

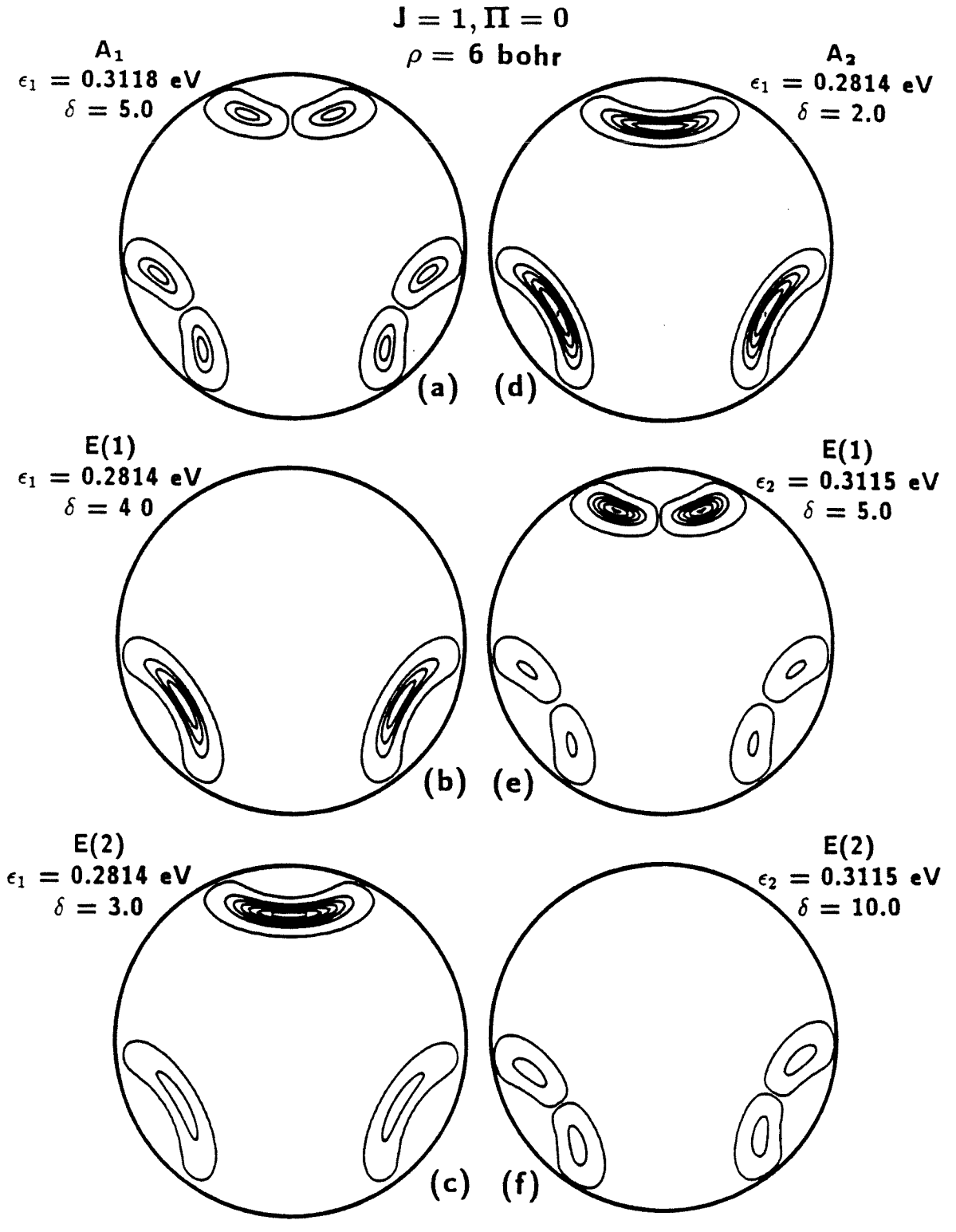
J = 1, Π = 0
ρ = 6 bohr
A1
ϵ1 = 0.3118 eV
δ = 5.0
A2
ϵ1 = 0.2814 eV
δ = 2.0
(a)
(d)
E(1)
ϵ1 = 0.2814 eV
δ = 4 0
E(1)
ϵ2 = 0.3115 eV
δ = 5.0
(b)
(e)
E(2)
ϵ1 = 0.2814 eV
δ = 3.0
E(2)
ϵ2 = 0.3115 eV
δ = 10.0
(c)
(f)

Fig. 4.19

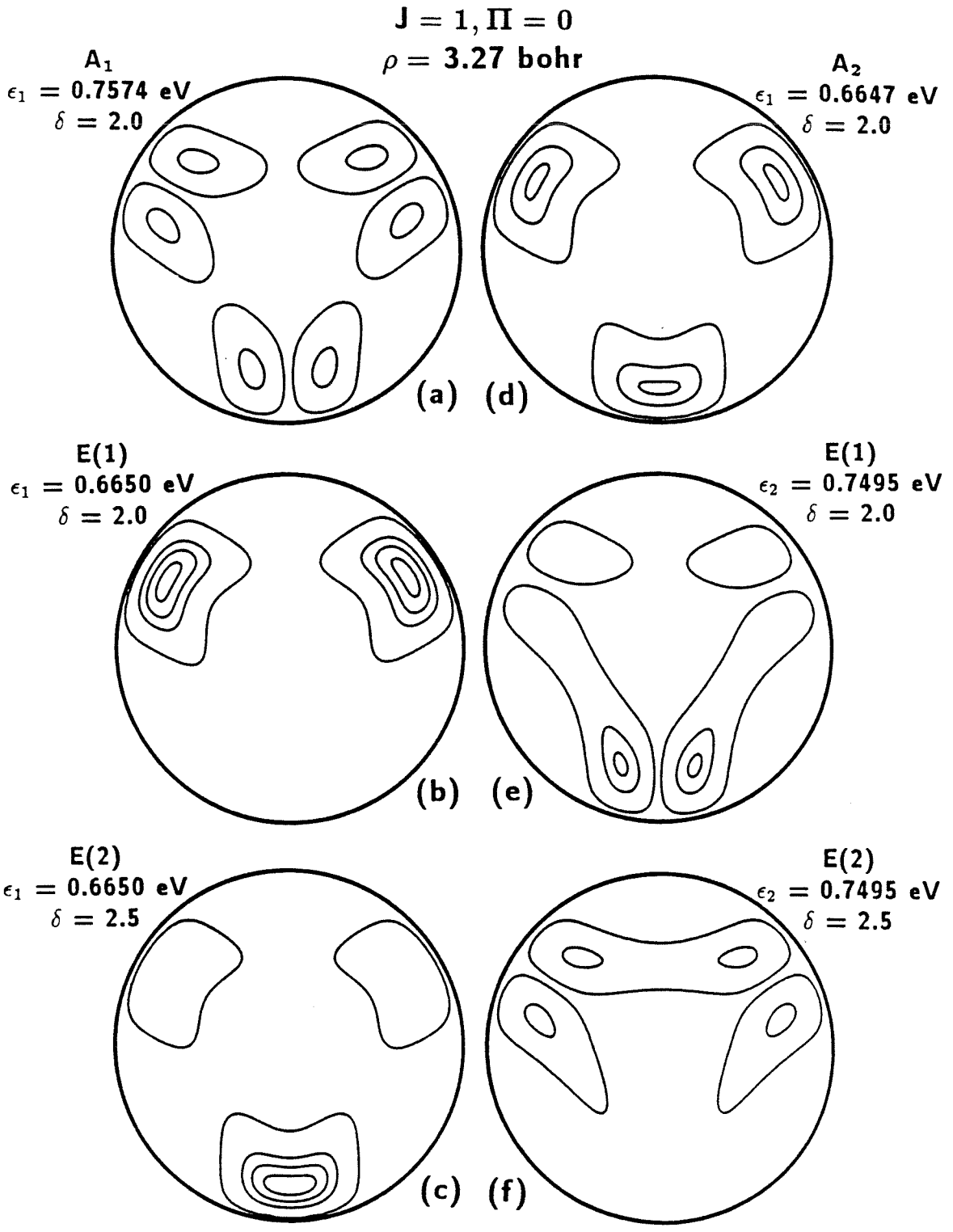
J = 1, Π = 0
ρ = 3.27 bohr
A1
ϵ1 = 0.7574 eV
δ = 2.0
A2
ϵ1 = 0.6647 eV
δ = 2.0
(a)
(d)
E(1)
ϵ1 = 0.6650 eV
δ = 2.0
E(1)
ϵ2 = 0.7495 eV
δ = 2.0
(b)
(e)
E(2)
ϵ1 = 0.6650 eV
δ = 2.5
E(2)
ϵ2 = 0.7495 eV
δ = 2.5
(c)
(f)

Fig. 4.20

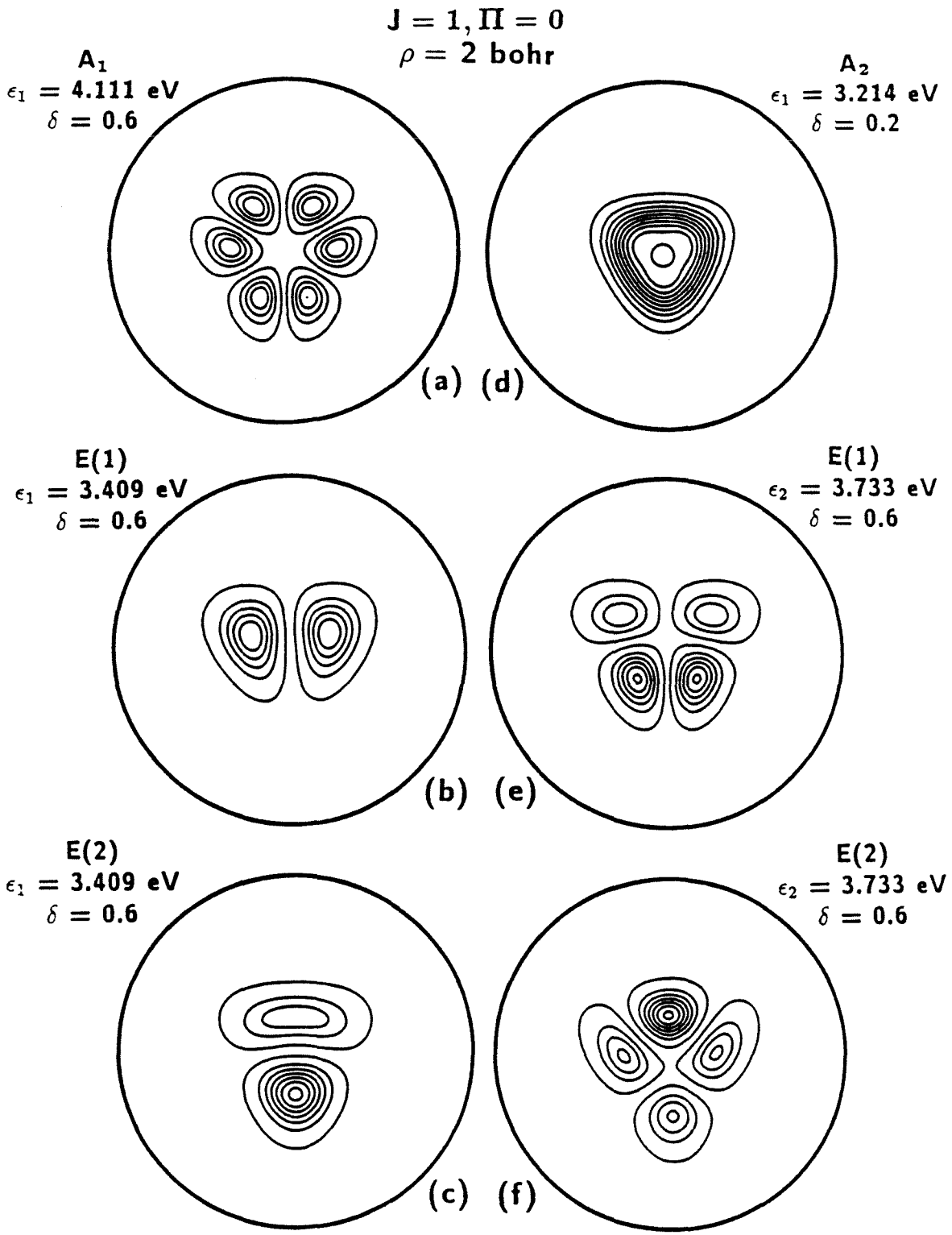
J = 1, Π = 0
ρ = 2 bohr
A1
ε1 = 4.111 eV
δ = 0.6
A2
ε1 = 3.214 eV
δ = 0.2
(a)
(d)
E(1)
ε1 = 3.409 eV
δ = 0.6
E(1)
ε2 = 3.733 eV
δ = 0.6
(b)
(e)
E(2)
ε1 = 3.409 eV
δ = 0.6
E(2)
ε2 = 3.733 eV
δ = 0.6
(c)
(f)

Fig. 4.21

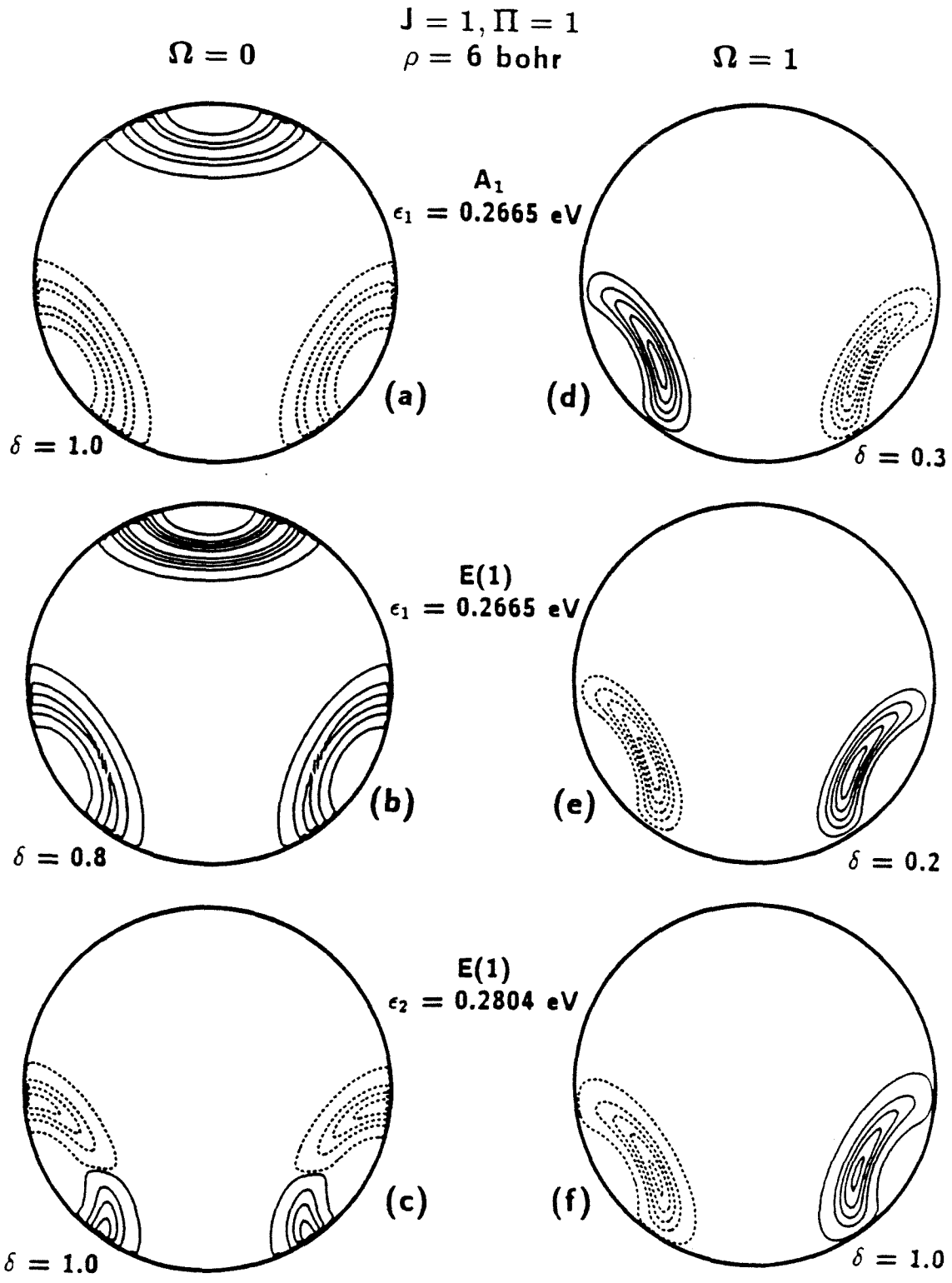
J = 1, Π = 1
Ω = 0
ρ = 6 bohr
Ω = 1
A1
ϵ1 = 0.2665 eV
(a)
(d)
δ = 1.0
δ = 0.3
E(1)
ϵ1 = 0.2665 eV
(b)
(e)
δ = 0.8
δ = 0.2
E(1)
ϵ2 = 0.2804 eV
(c)
(f)
δ = 1.0
δ = 1.0

Fig. 4.22

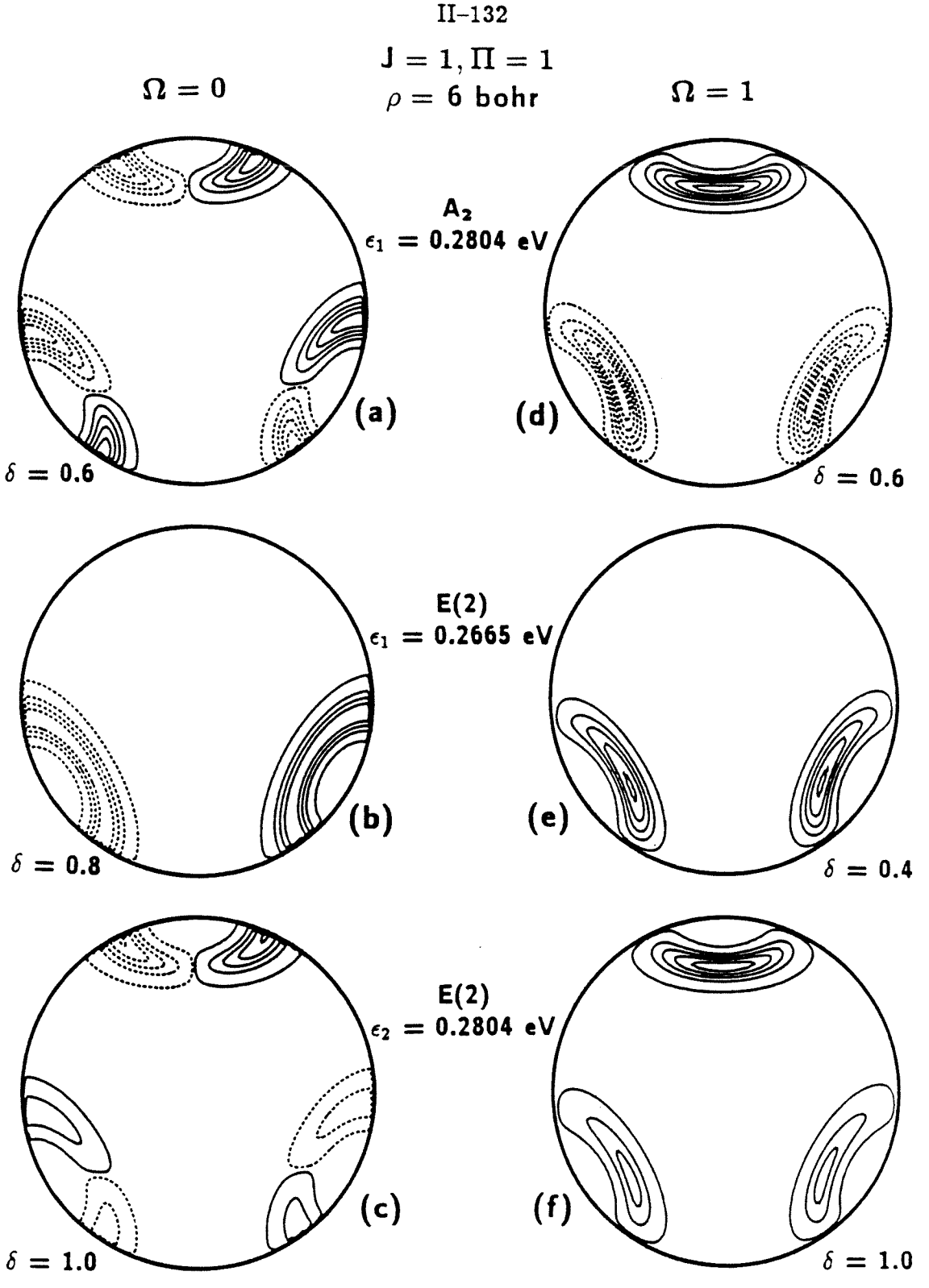
J = 1, Π = 1
ρ = 6 bohr
Ω = 0
Ω = 1
A2
ε1 = 0.2804 eV
(a)
(d)
δ = 0.6
δ = 0.6
E(2)
ε1 = 0.2665 eV
(b)
(e)
δ = 0.8
δ = 0.4
E(2)
ε2 = 0.2804 eV
(c)
(f)
δ = 1.0
δ = 1.0

Fig. 4.23

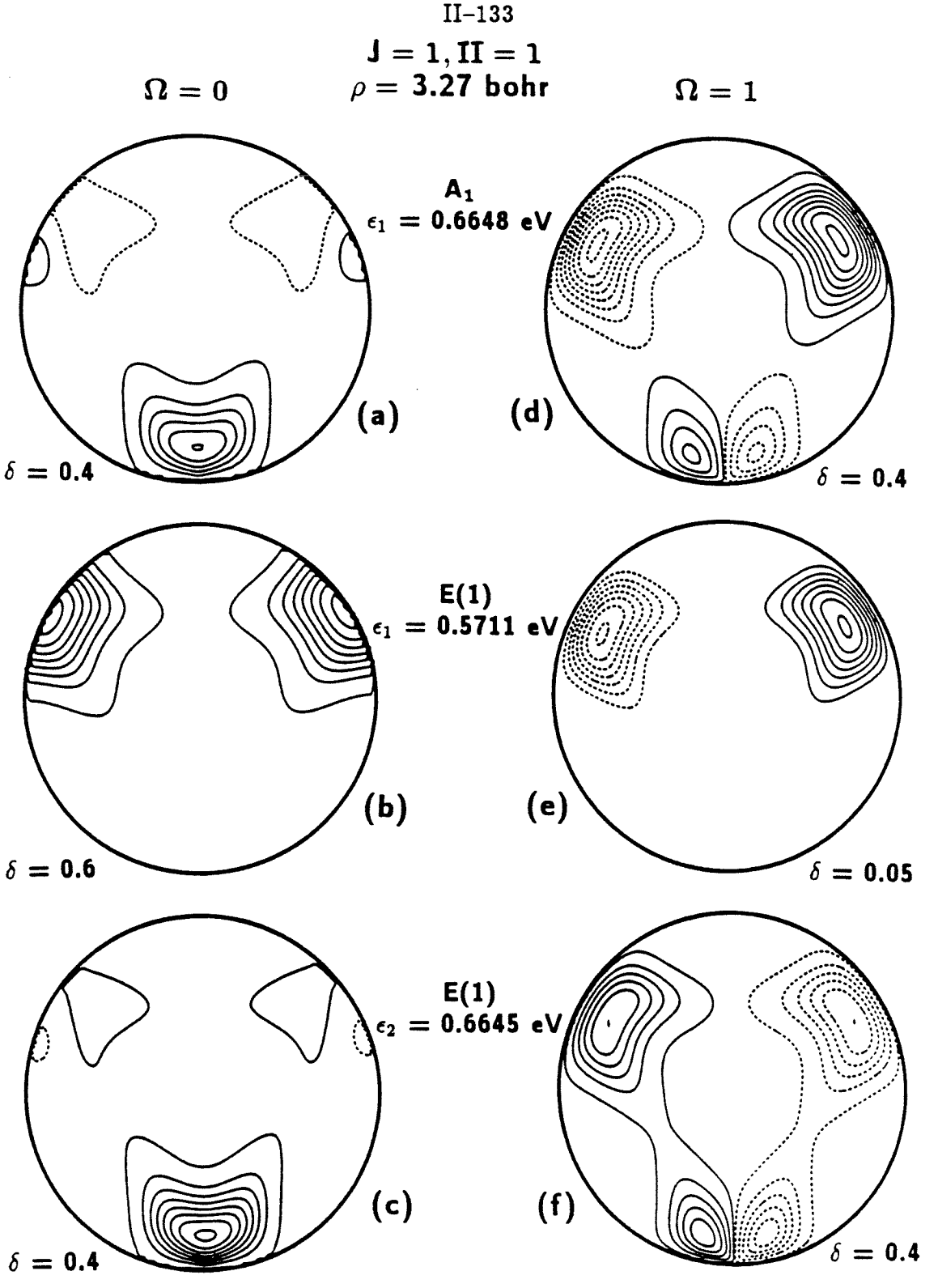
J = 1, II = 1
Ω = 0
ρ = 3.27 bohr
Ω = 1
A1
ε1 = 0.6648 eV
(a)
(d)
δ = 0.4
δ = 0.4
E(1)
ε1 = 0.5711 eV
(b)
(e)
δ = 0.6
δ = 0.05
E(1)
ε2 = 0.6645 eV
(c)
(f)
δ = 0.4
δ = 0.4

Fig. 4.24

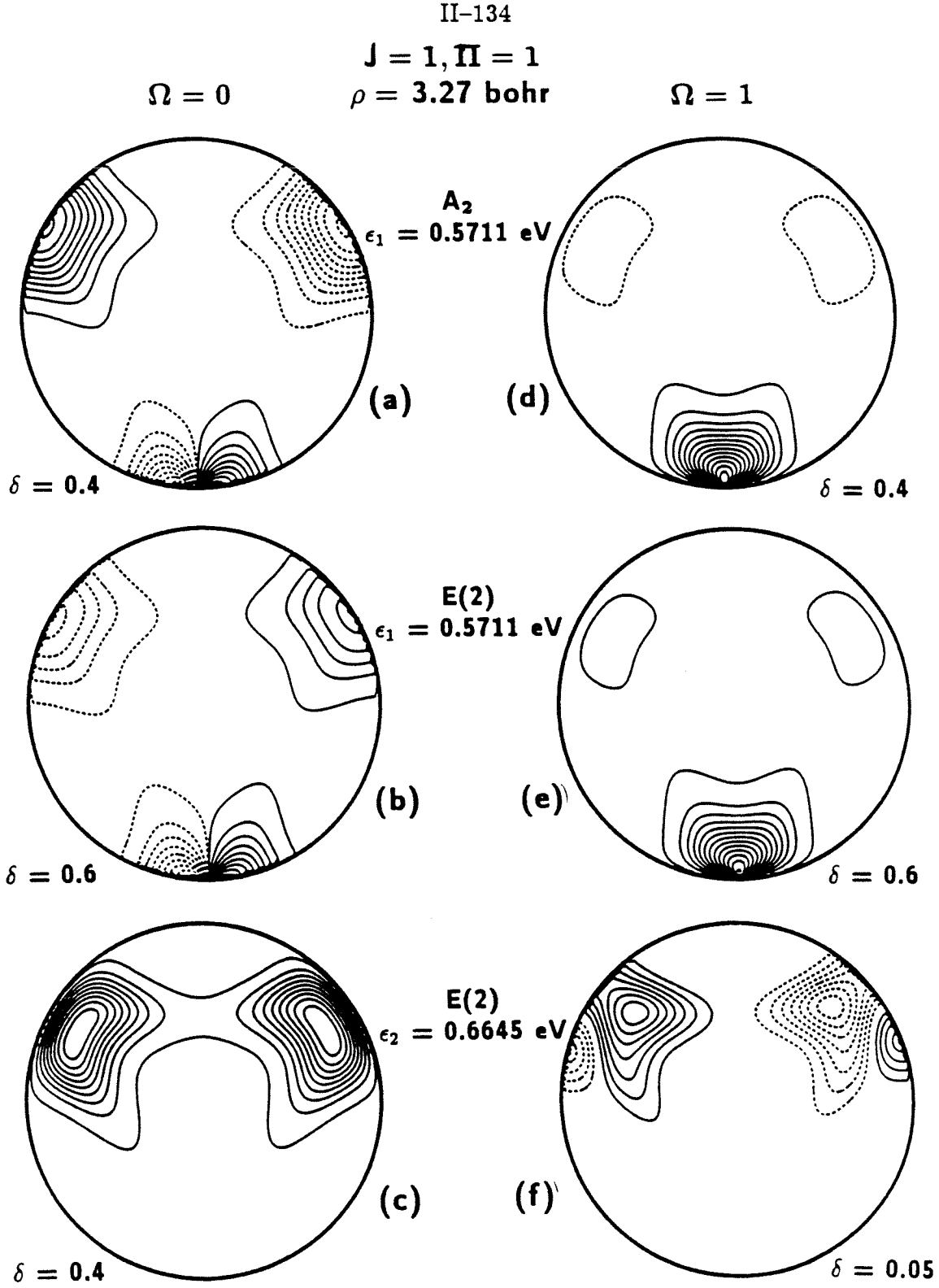
J = 1, Π = 1
Ω = 0
ρ = 3.27 bohr
Ω = 1
A2
ε1 = 0.5711 eV
(a)
(d)
δ = 0.4
δ = 0.4
E(2)
ε1 = 0.5711 eV
(b)
(e)
δ = 0.6
δ = 0.6
E(2)
ε2 = 0.6645 eV
(c)
(f)
δ = 0.4
δ = 0.05

Fig. 4.25

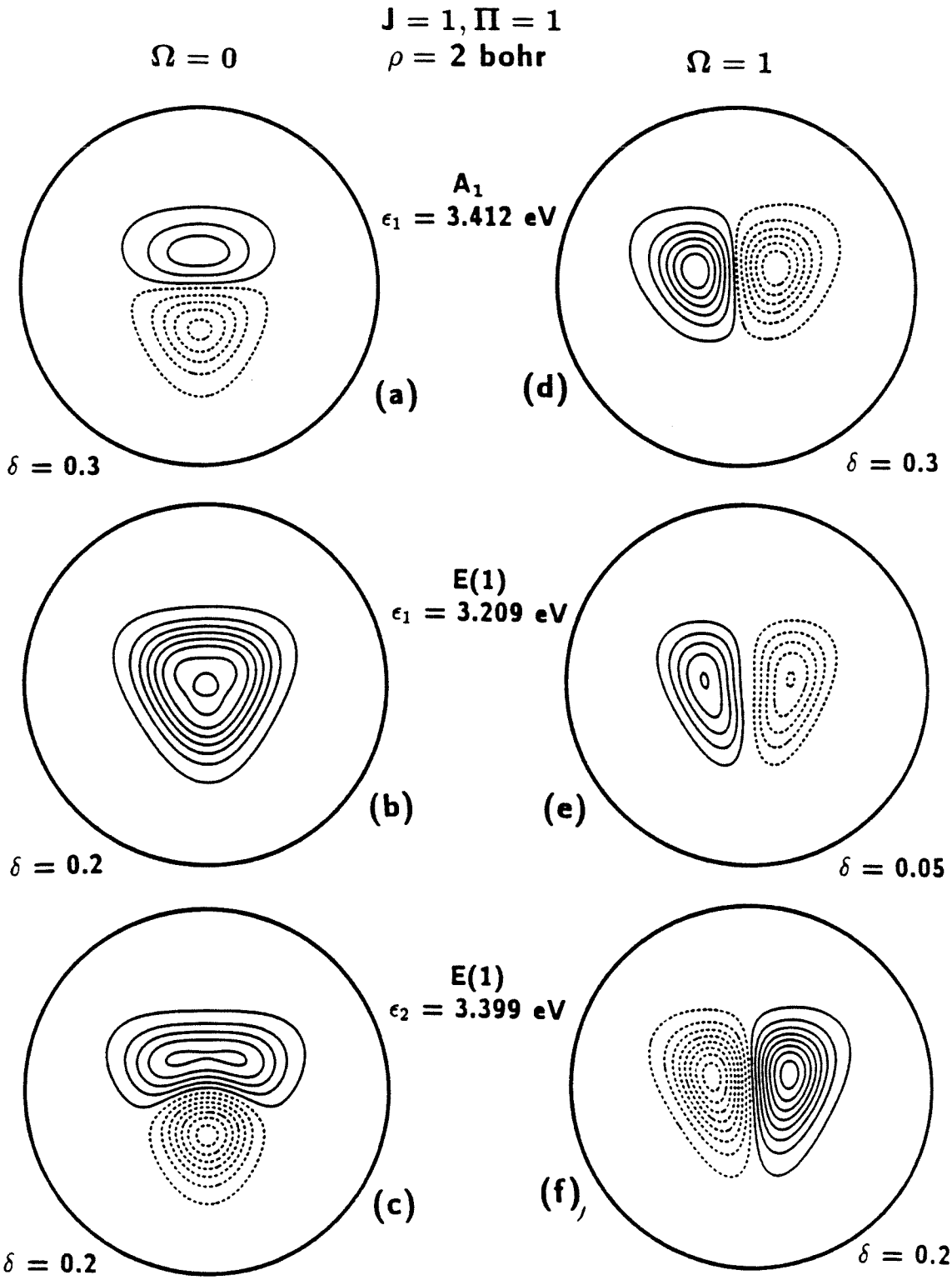
J = 1, Π = 1
ρ = 2 bohr
Ω = 0
Ω = 1
A1
ϵ1 = 3.412 eV
(a)
(d)
δ = 0.3
δ = 0.3
E(1)
ϵ1 = 3.209 eV
(b)
(e)
δ = 0.2
δ = 0.05
E(1)
ϵ2 = 3.399 eV
(c)
(f)
δ = 0.2
δ = 0.2

Fig. 4.26

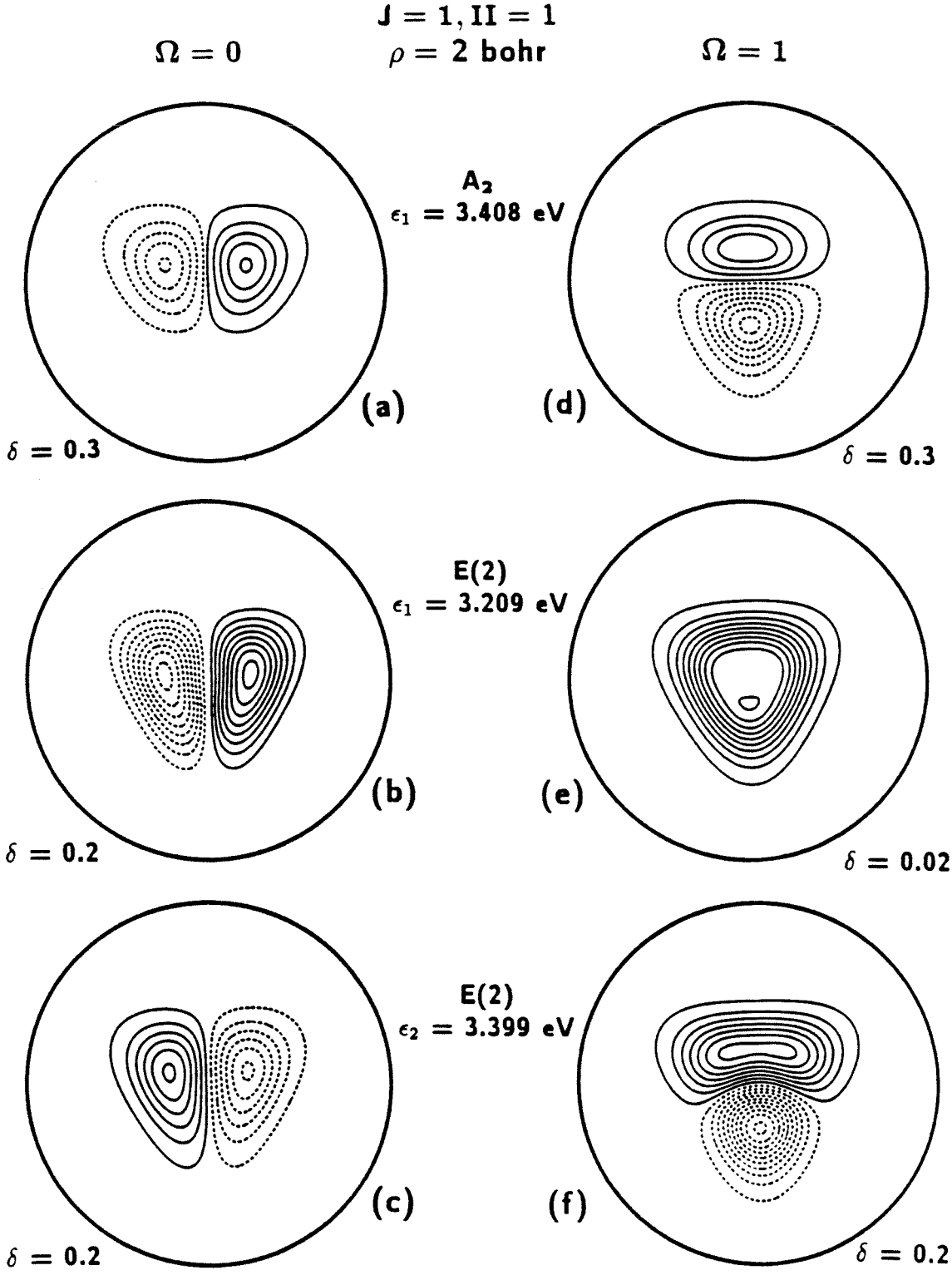
J = 1, II = 1
Ω = 0
ρ = 2 bohr
Ω = 1
A2
ε1 = 3.408 eV
(a)
(d)
δ = 0.3
δ = 0.3
E(2)
ε1 = 3.209 eV
(b)
(e)
δ = 0.2
δ = 0.02
E(2)
ε2 = 3.399 eV
(c)
(f)
δ = 0.2
δ = 0.2

Fig. 4.27

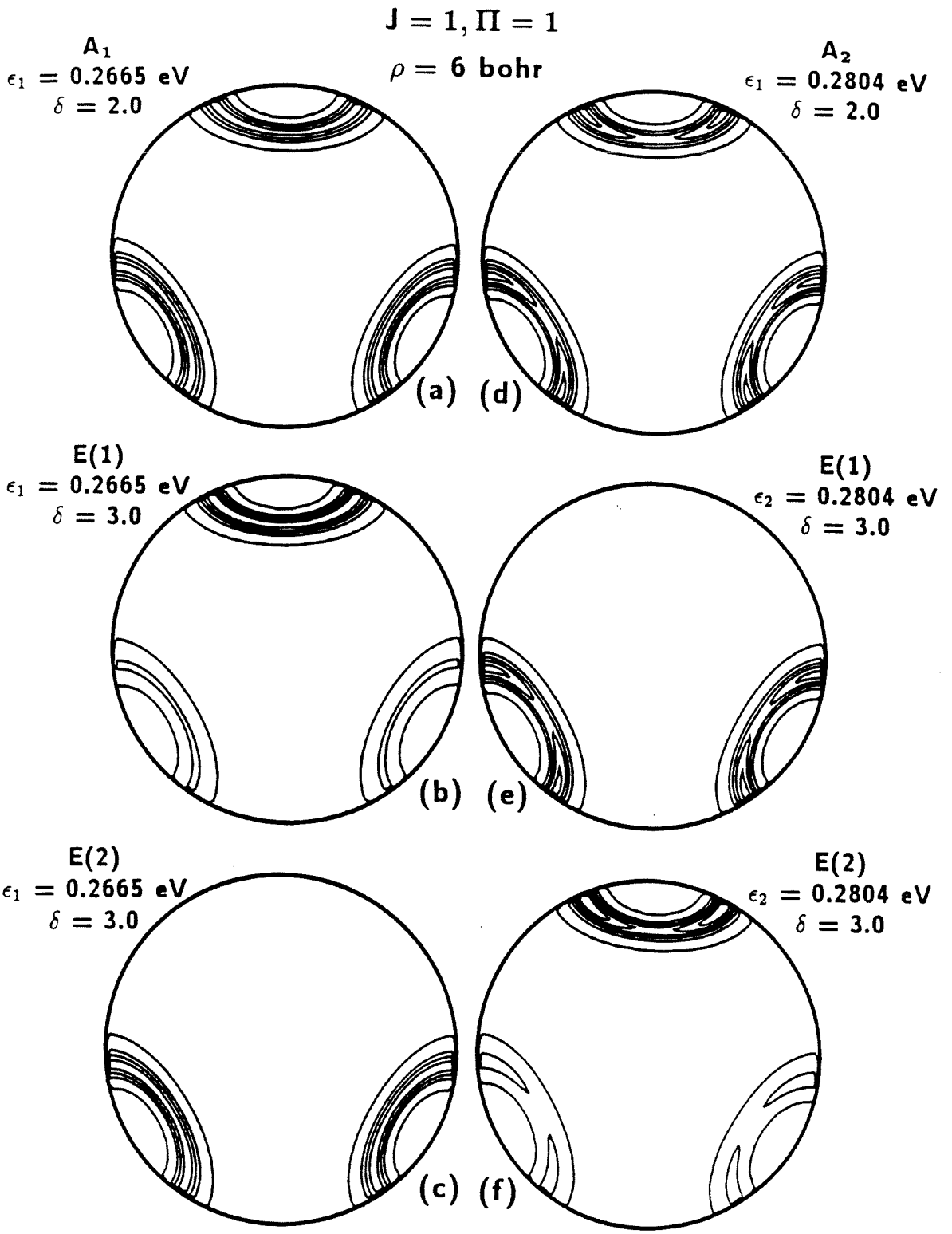
J = 1, Π = 1
ρ = 6 bohr
A1
ϵ1 = 0.2665 eV
δ = 2.0
A2
ϵ1 = 0.2804 eV
δ = 2.0
(a)
(d)
E(1)
ϵ1 = 0.2665 eV
δ = 3.0
E(1)
ϵ2 = 0.2804 eV
δ = 3.0
(b)
(e)
E(2)
ϵ1 = 0.2665 eV
δ = 3.0
E(2)
ϵ2 = 0.2804 eV
δ = 3.0
(c)
(f)

Fig. 4.28

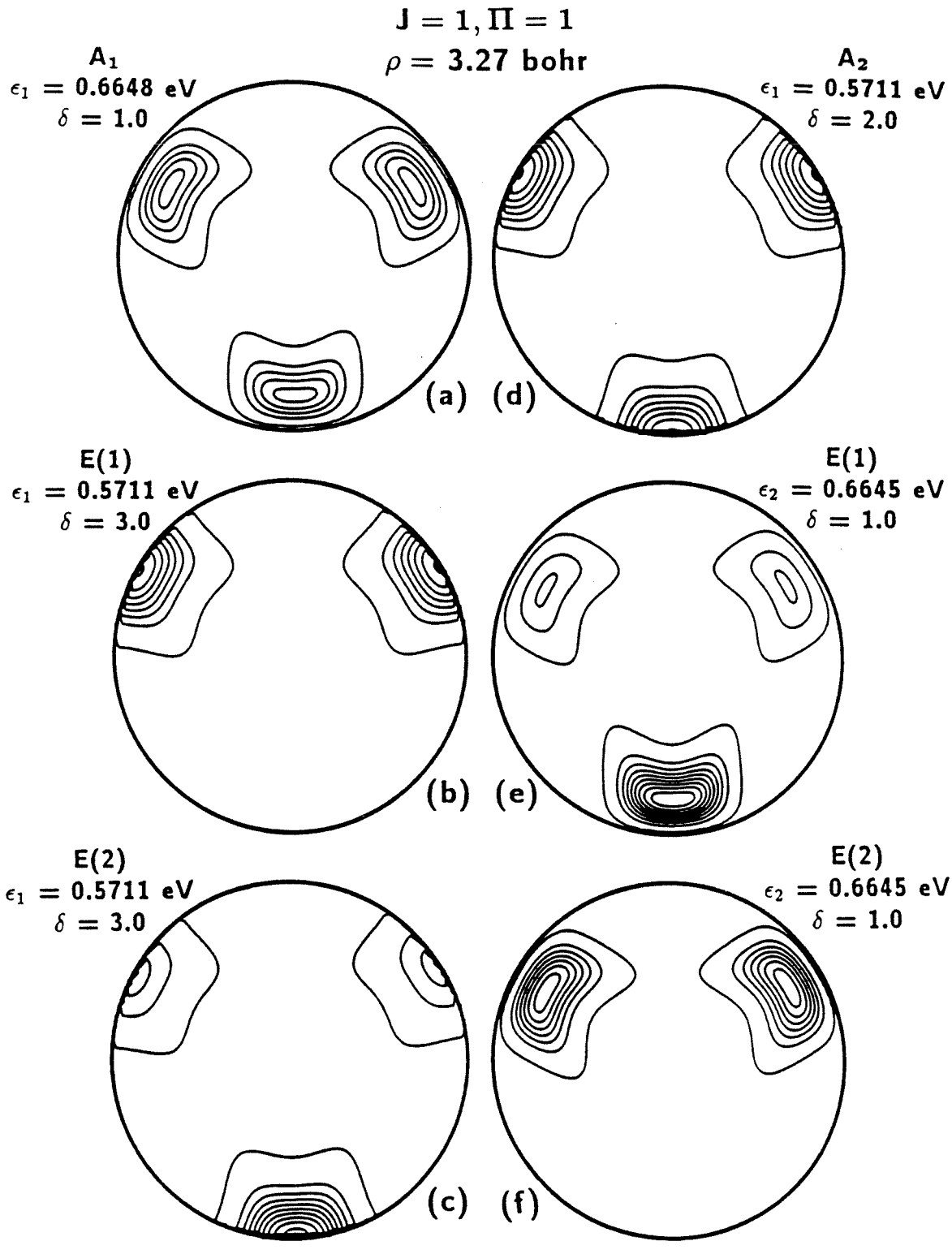
J = 1, Π = 1
ρ = 3.27 bohr
A1
ϵ1 = 0.6648 eV
δ = 1.0
A2
ϵ1 = 0.5711 eV
δ = 2.0
(a)
(d)
E(1)
ϵ1 = 0.5711 eV
δ = 3.0
E(1)
ϵ2 = 0.6645 eV
δ = 1.0
(b)
(e)
E(2)
ϵ1 = 0.5711 eV
δ = 3.0
E(2)
ϵ2 = 0.6645 eV
δ = 1.0
(c)
(f)

Fig. 4.29

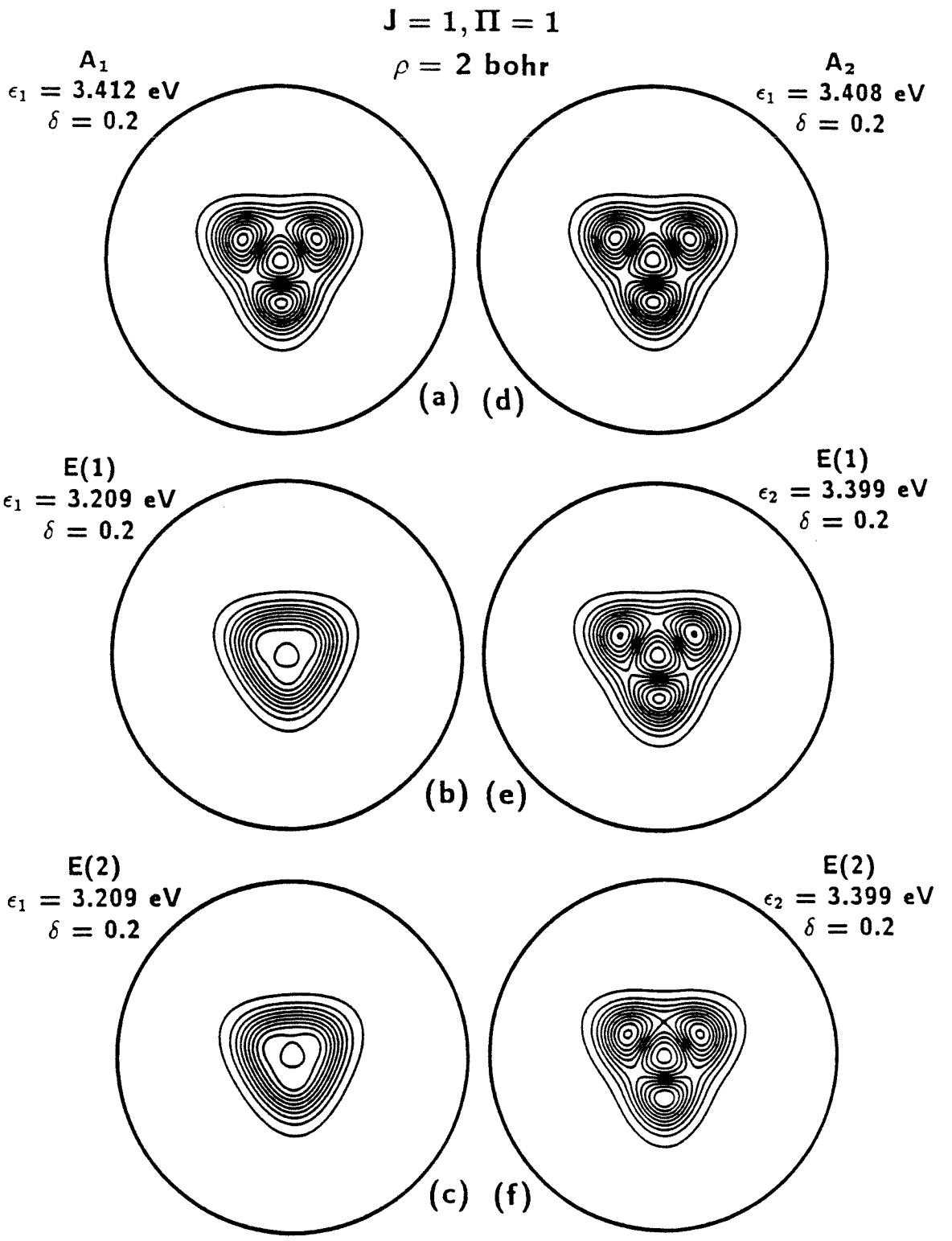
J = 1, Π = 1
ρ = 2 bohr
A1
ϵ1 = 3.412 eV
δ = 0.2
A2
ϵ1 = 3.408 eV
δ = 0.2
(a)
(d)
E(1)
ϵ1 = 3.209 eV
δ = 0.2
E(1)
ϵ2 = 3.399 eV
δ = 0.2
(b)
(e)
E(2)
ϵ1 = 3.209 eV
δ = 0.2
E(2)
ϵ2 = 3.399 eV
δ = 0.2
(c)
(f)

Fig. 4.30

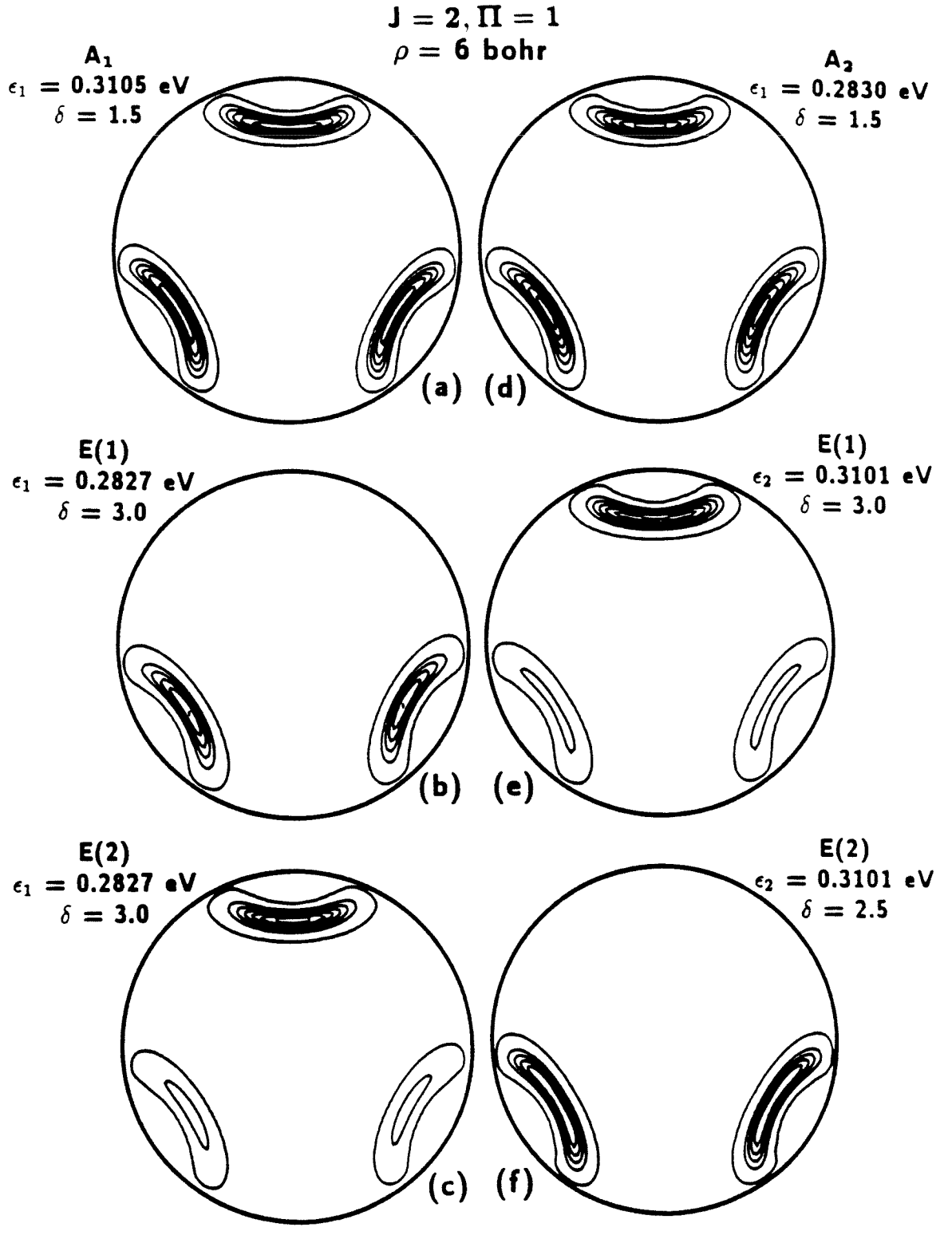
J = 2, Π = 1
ρ = 6 bohr
A1
ϵ1 = 0.3105 eV
δ = 1.5
A2
ϵ1 = 0.2830 eV
δ = 1.5
(a)
(d)
E(1)
ϵ1 = 0.2827 eV
δ = 3.0
E(1)
ϵ2 = 0.3101 eV
δ = 3.0
(b)
(e)
E(2)
ϵ1 = 0.2827 eV
δ = 3.0
E(2)
ϵ2 = 0.3101 eV
δ = 2.5
(c)
(f)

Fig. 4.31

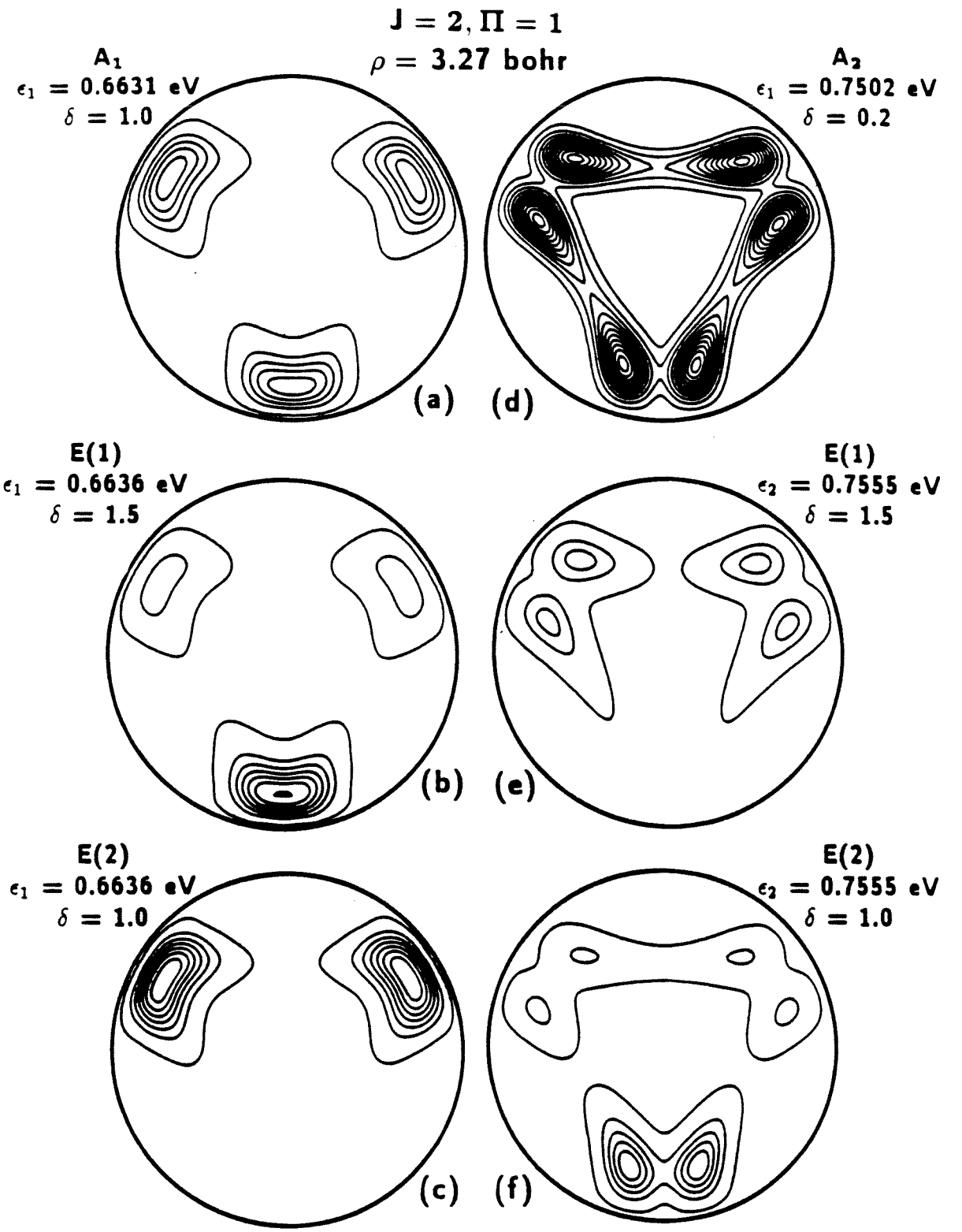
J = 2, Π = 1
ρ = 3.27 bohr
A1
ε1 = 0.6631 eV
δ = 1.0
A2
ε1 = 0.7502 eV
δ = 0.2
(a)
(d)
E(1)
ε1 = 0.6636 eV
δ = 1.5
E(1)
ε2 = 0.7555 eV
δ = 1.5
(b)
(e)
E(2)
ε1 = 0.6636 eV
δ = 1.0
E(2)
ε2 = 0.7555 eV
δ = 1.0
(c)
(f)

Fig. 4.32

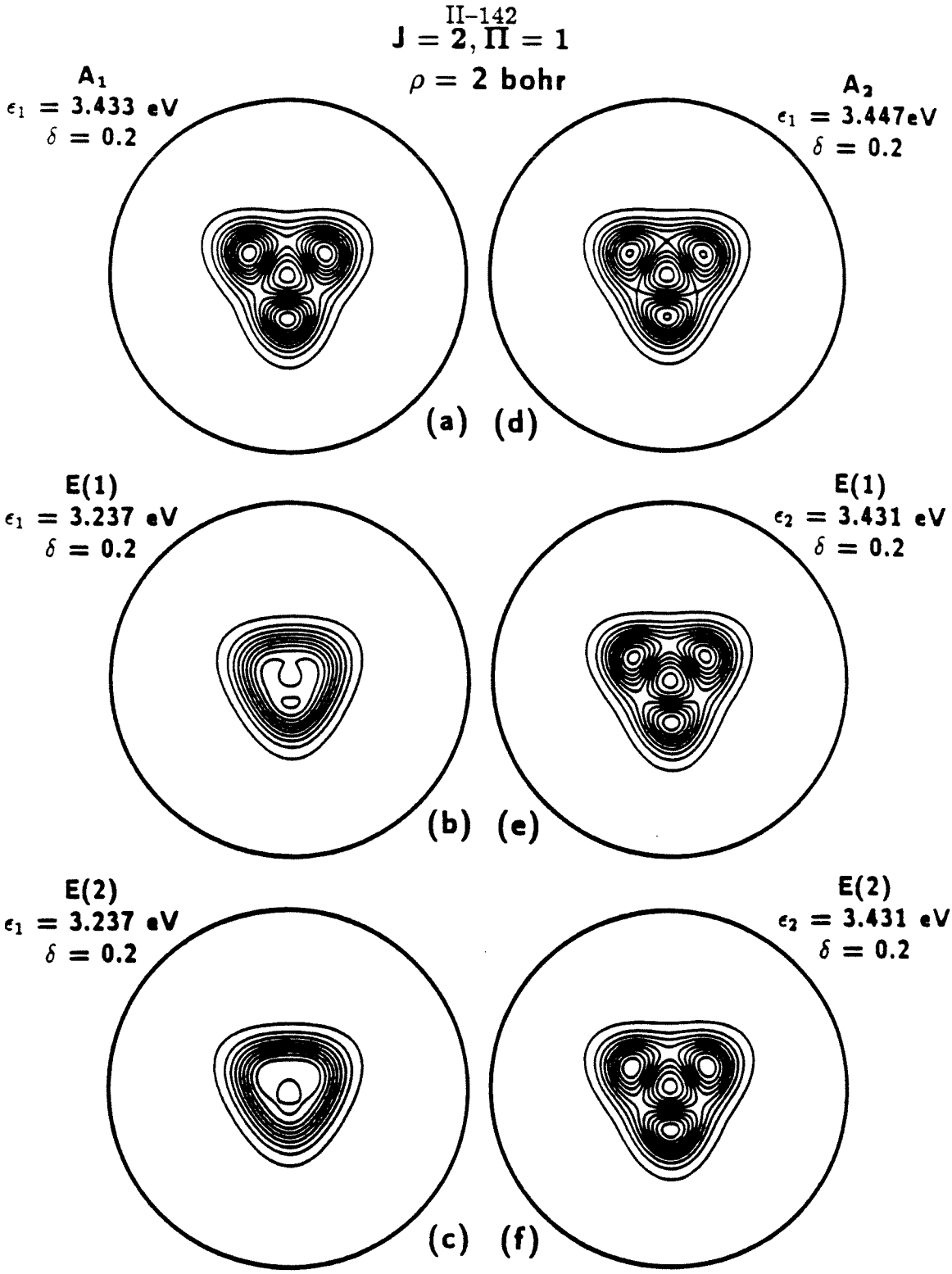
J = 2, Π = 1
ρ = 2 bohr
A1
ϵ1 = 3.433 eV
δ = 0.2
A2
ϵ1 = 3.447eV
δ = 0.2
(a)
(d)
E(1)
ϵ1 = 3.237 eV
δ = 0.2
E(1)
ϵ2 = 3.431 eV
δ = 0.2
(b)
(e)
E(2)
ϵ1 = 3.237 eV
δ = 0.2
E(2)
ϵ2 = 3.431 eV
δ = 0.2
(c)
(f)

Fig. 4.33

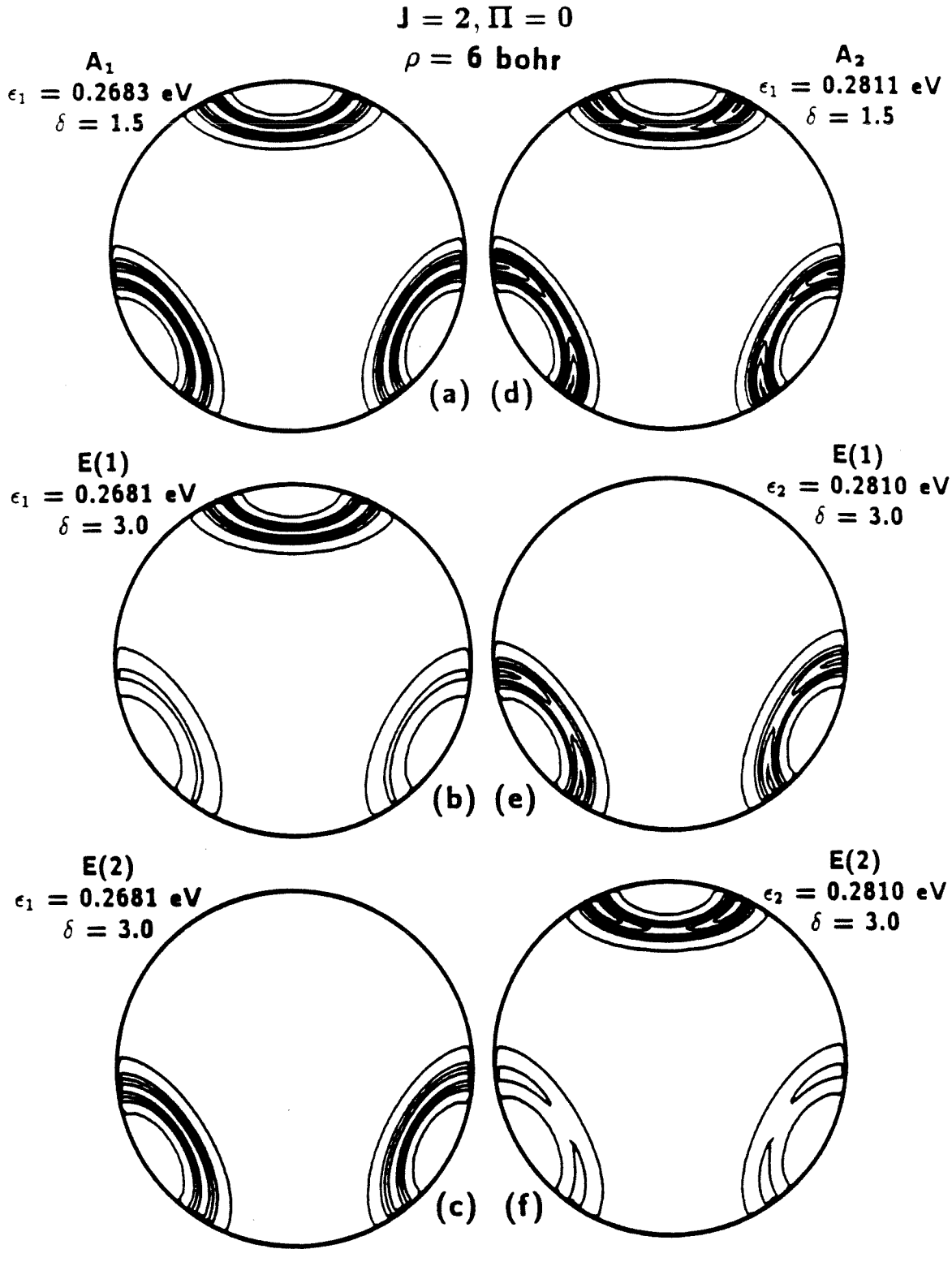
J = 2, Π = 0
ρ = 6 bohr
A1
ϵ1 = 0.2683 eV
δ = 1.5
A2
ϵ1 = 0.2811 eV
δ = 1.5
(a)
(d)
E(1)
ϵ1 = 0.2681 eV
δ = 3.0
E(1)
ϵ2 = 0.2810 eV
δ = 3.0
(b)
(e)
E(2)
ϵ1 = 0.2681 eV
δ = 3.0
E(2)
ϵ2 = 0.2810 eV
δ = 3.0
(c)
(f)

Fig. 4.34

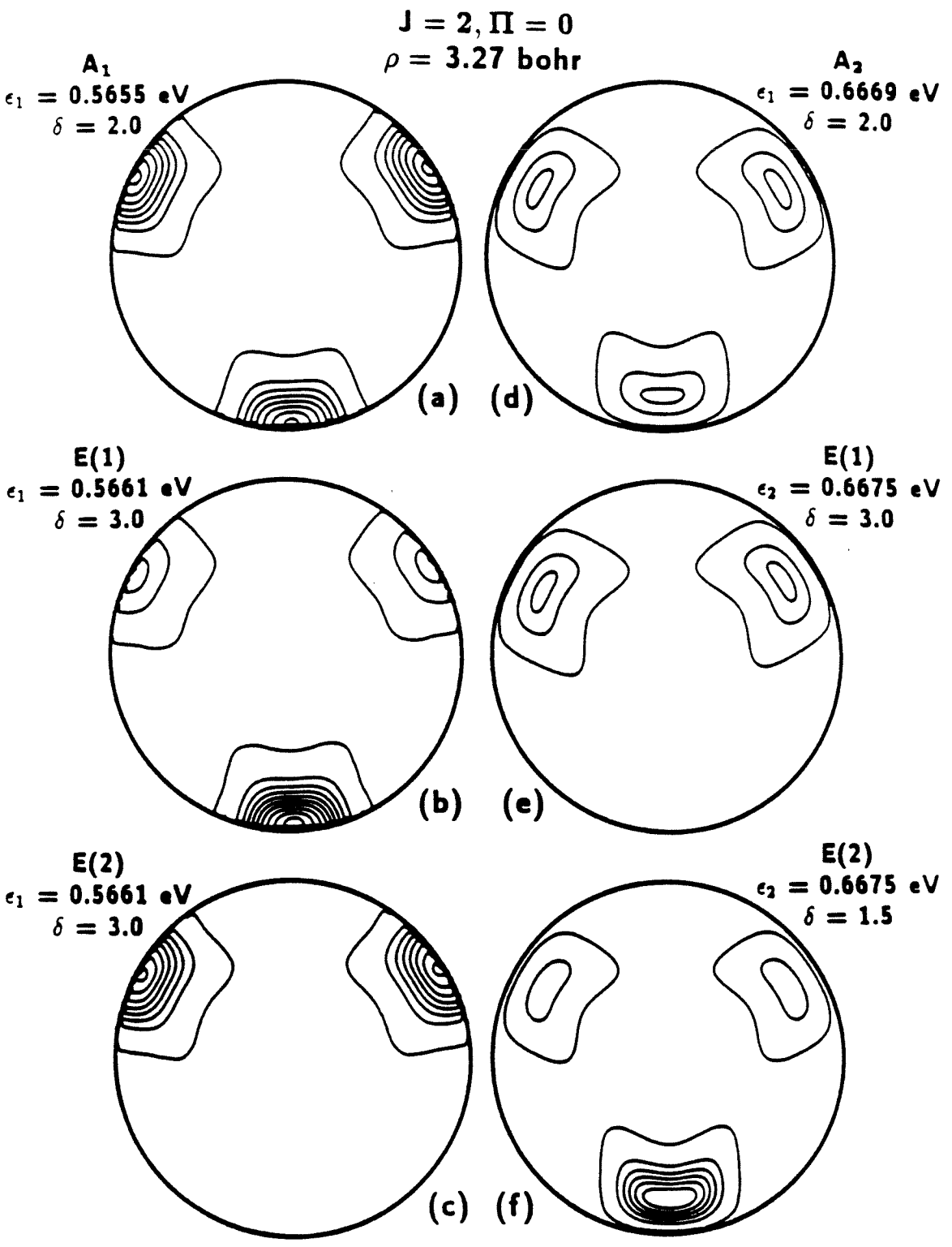
J = 2, Π = 0
ρ = 3.27 bohr
A1
ε1 = 0.5655 eV
δ = 2.0
A2
ε1 = 0.6669 eV
δ = 2.0
(a)
(d)
E(1)
ε1 = 0.5661 eV
δ = 3.0
E(1)
ε2 = 0.6675 eV
δ = 3.0
(b)
(e)
E(2)
ε1 = 0.5661 eV
δ = 3.0
E(2)
ε2 = 0.6675 eV
δ = 1.5
(c)
(f)

Fig. 4.35

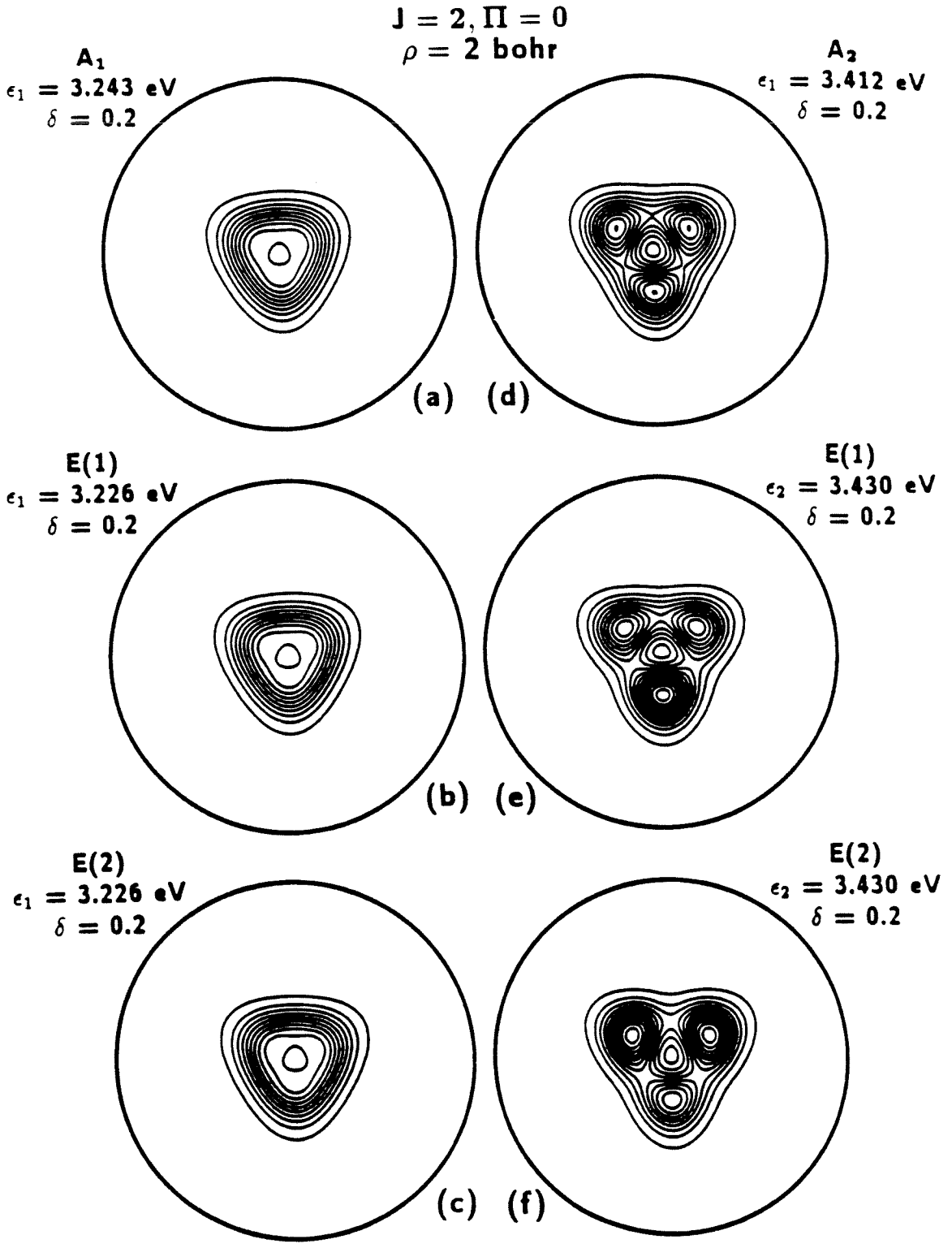
J = 2, Π = 0
ρ = 2 bohr
A1
ε1 = 3.243 eV
δ = 0.2
A2
ε1 = 3.412 eV
δ = 0.2
(a)
(d)
E(1)
ε1 = 3.226 eV
δ = 0.2
E(1)
ε2 = 3.430 eV
δ = 0.2
(b)
(e)
E(2)
ε1 = 3.226 eV
δ = 0.2
E(2)
ε2 = 3.430 eV
δ = 0.2
(c)
(f)

Fig. 4.36

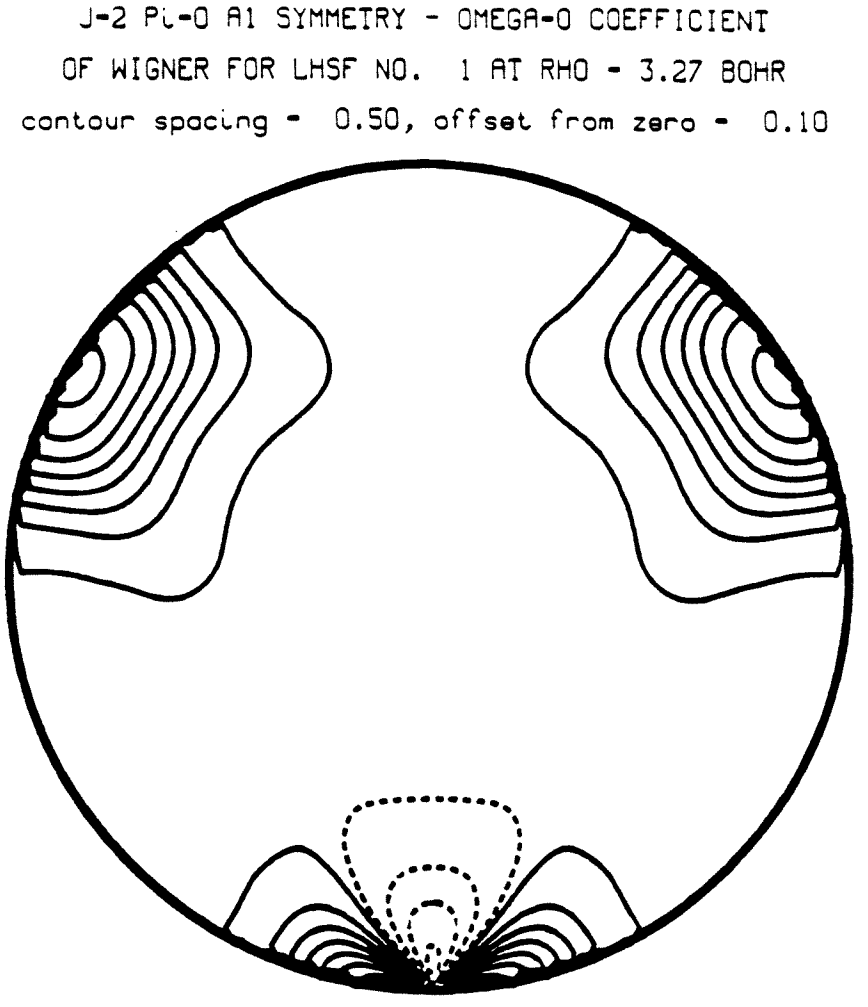
J-2 PL-O A1 SYMMETRY - OMEGA-O COEFFICIENT
OF WIGNER FOR LHSF NO. 1 AT RHO - 3.27 BOHR
contour spacing - 0.50, offset from zero - 0.10

Fig. 4.37a

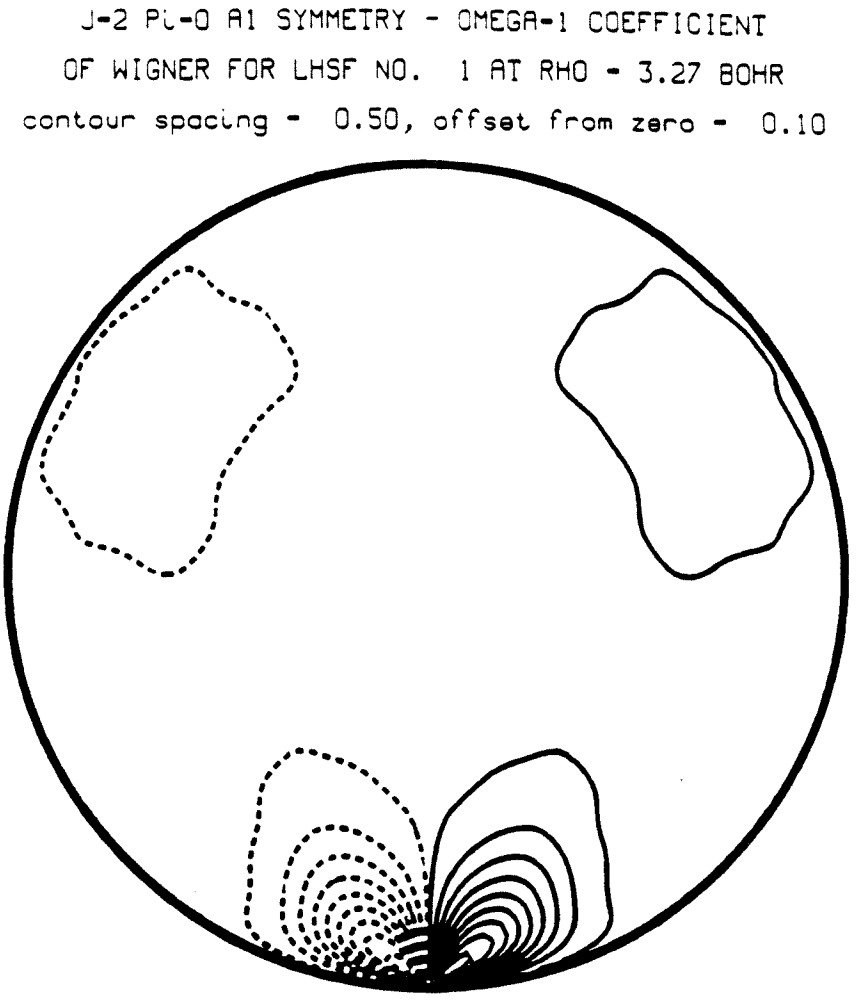
J-2 PL-O A1 SYMMETRY - OMEGA-1 COEFFICIENT
OF WIGNER FOR LHSF NO. 1 AT RHO = 3.27 BOHR
contour spacing = 0.50, offset from zero = 0.10

Fig. 4.37b

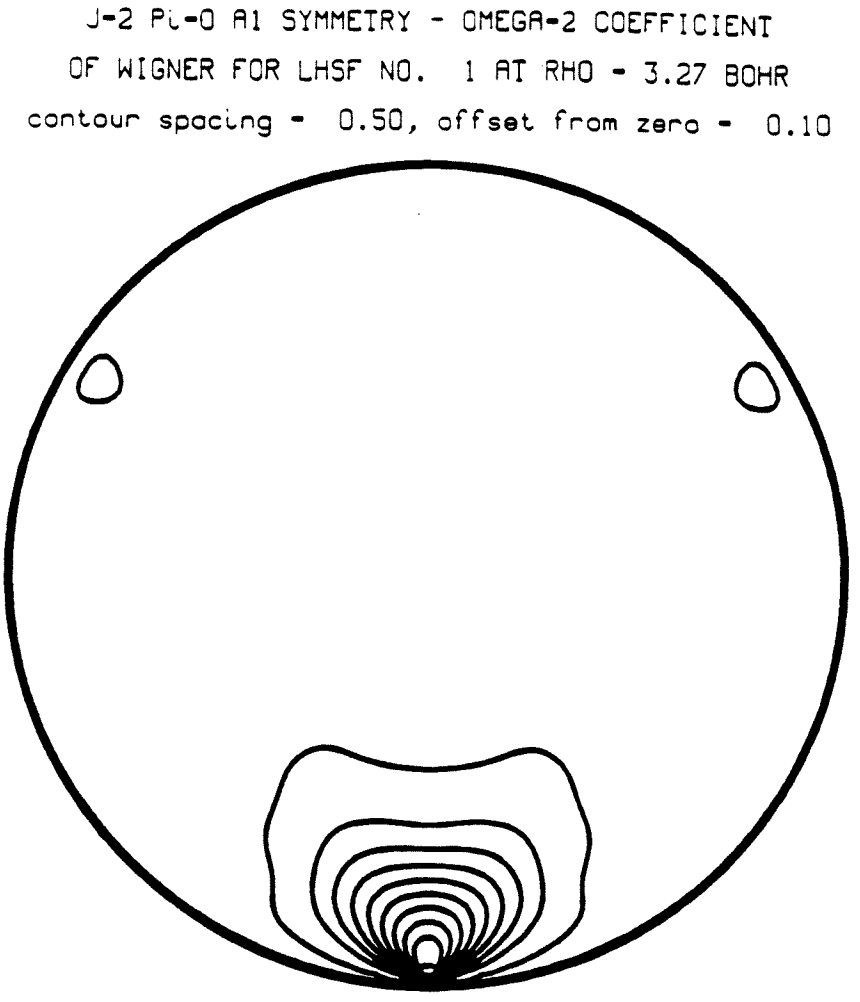
J-2 Pt-O A1 SYMMETRY - OMEGA-2 COEFFICIENT
OF WIGNER FOR LHSF NO. 1 AT RHO = 3.27 BOHR
contour spacing = 0.50, offset from zero = 0.10

Fig. 4.37c

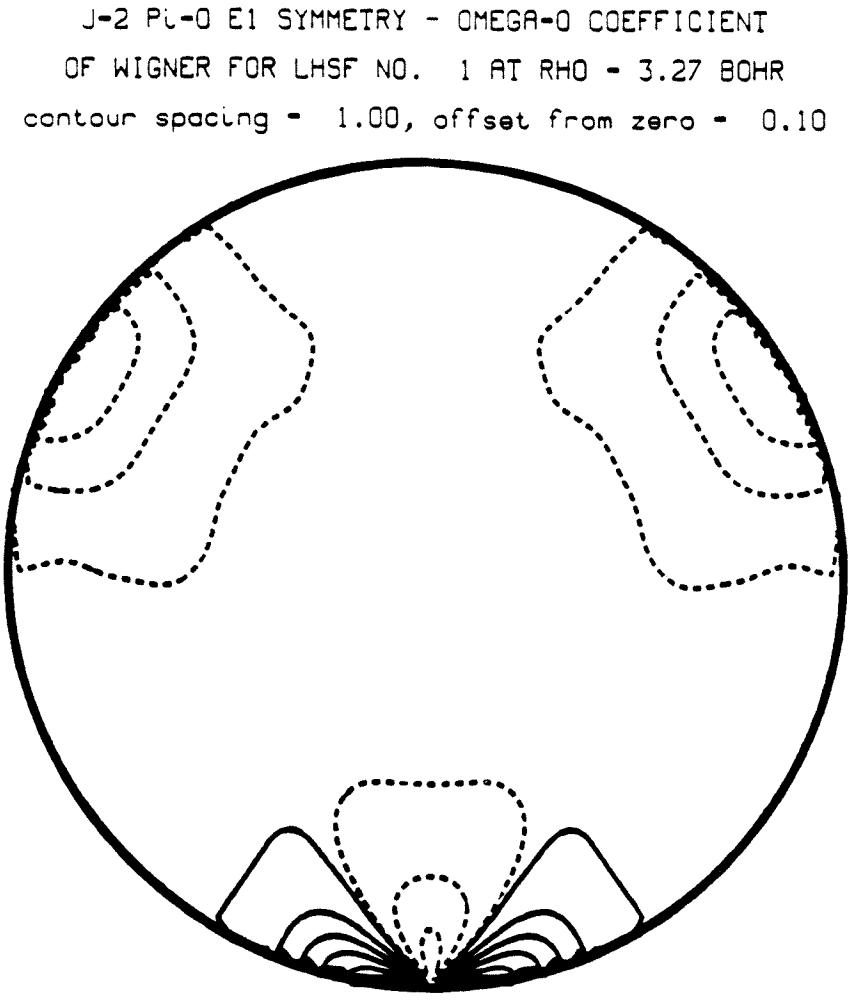
J-2 Pt-O E1 SYMMETRY - OMEGA-0 COEFFICIENT
OF WIGNER FOR LHSF NO. 1 AT RHO - 3.27 BOHR
contour spacing - 1.00, offset from zero - 0.10

Fig. 4.37d

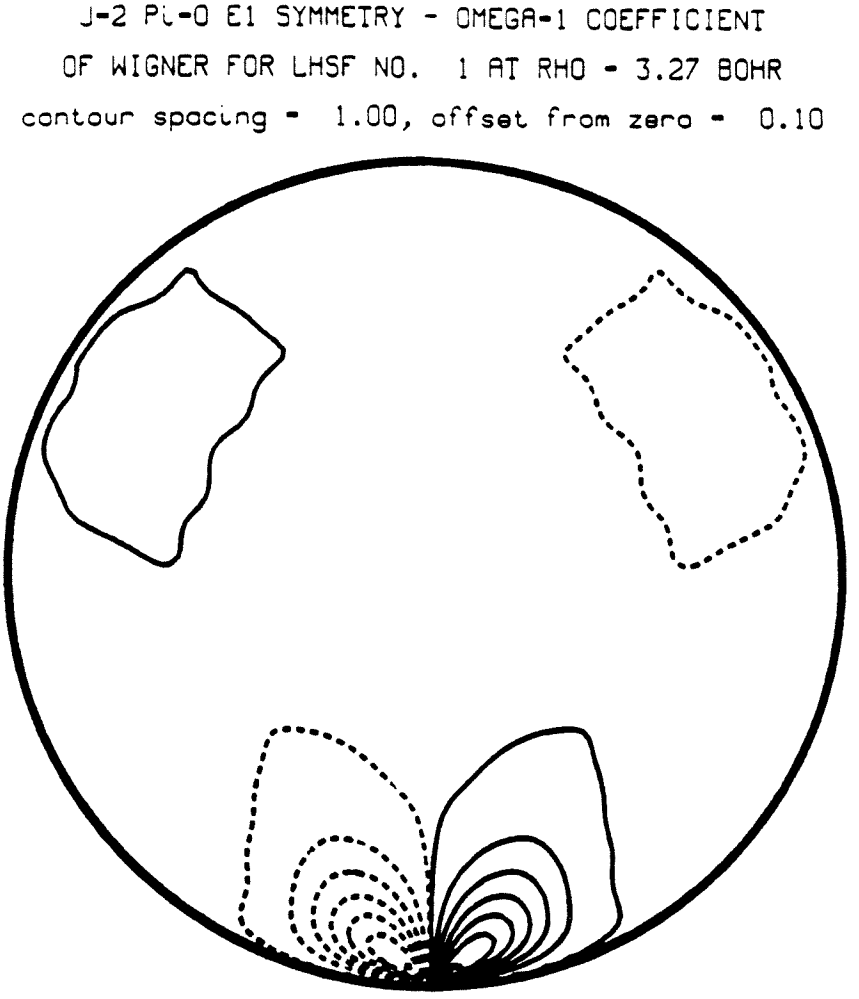
J-2 Pi-O E1 SYMMETRY - OMEGA-1 COEFFICIENT
OF WIGNER FOR LHSF NO. 1 AT RHO - 3.27 BOHR
contour spacing - 1.00, offset from zero - 0.10

Fig. 4.37e

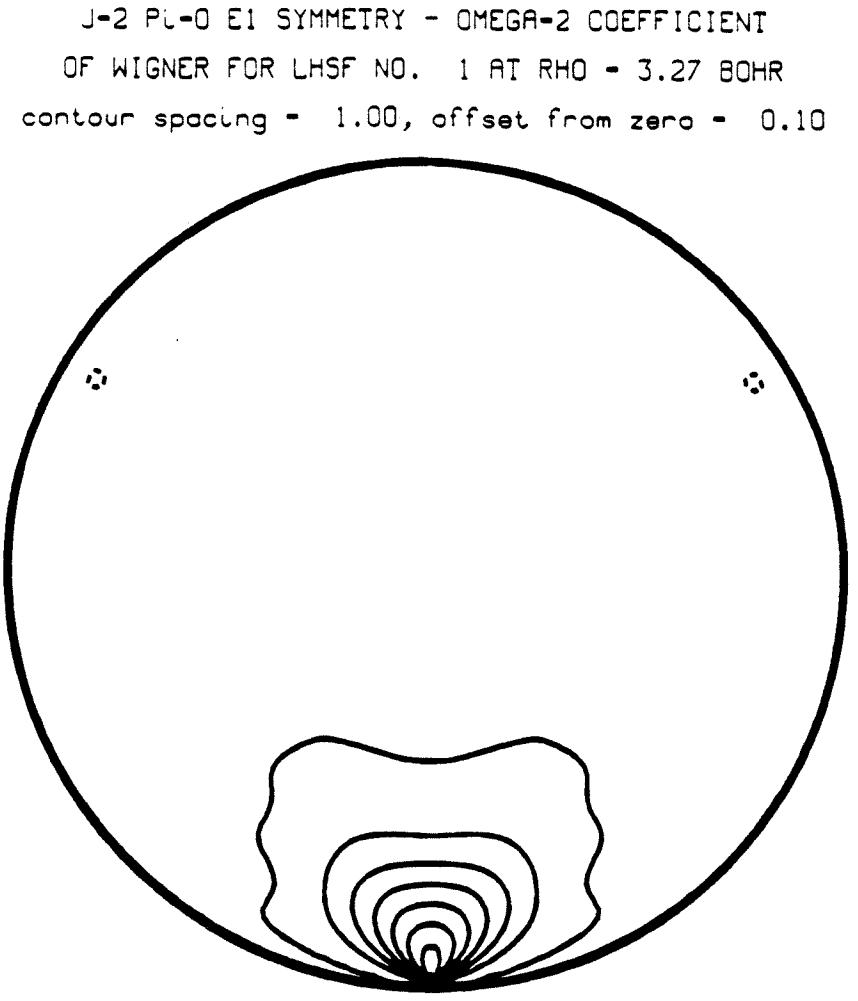
J-2 PL-O E1 SYMMETRY - OMEGA-2 COEFFICIENT
OF WIGNER FOR LHSF NO. 1 AT RHO = 3.27 BOHR
contour spacing = 1.00, offset from zero = 0.10

Fig. 4.37f

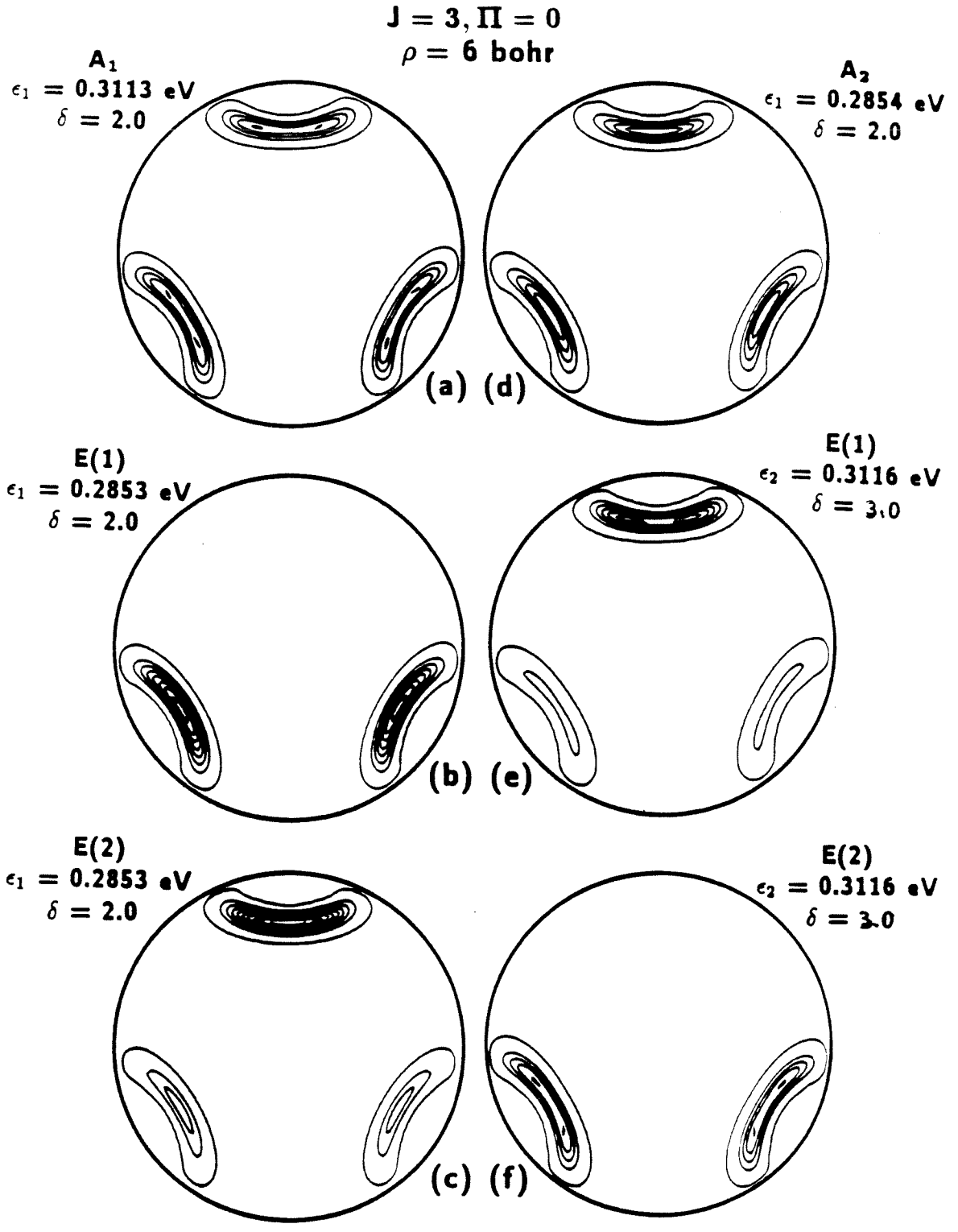
J = 3, Π = 0
ρ = 6 bohr
A1
ε1 = 0.3113 eV
δ = 2.0
A2
ε1 = 0.2854 eV
δ = 2.0
(a) (d)
E(1)
ε1 = 0.2853 eV
δ = 2.0
E(1)
ε2 = 0.3116 eV
δ = 3.0
(b) (e)
E(2)
ε1 = 0.2853 eV
δ = 2.0
E(2)
ε2 = 0.3116 eV
δ = 3.0
(c) (f)

Fig. 4.38

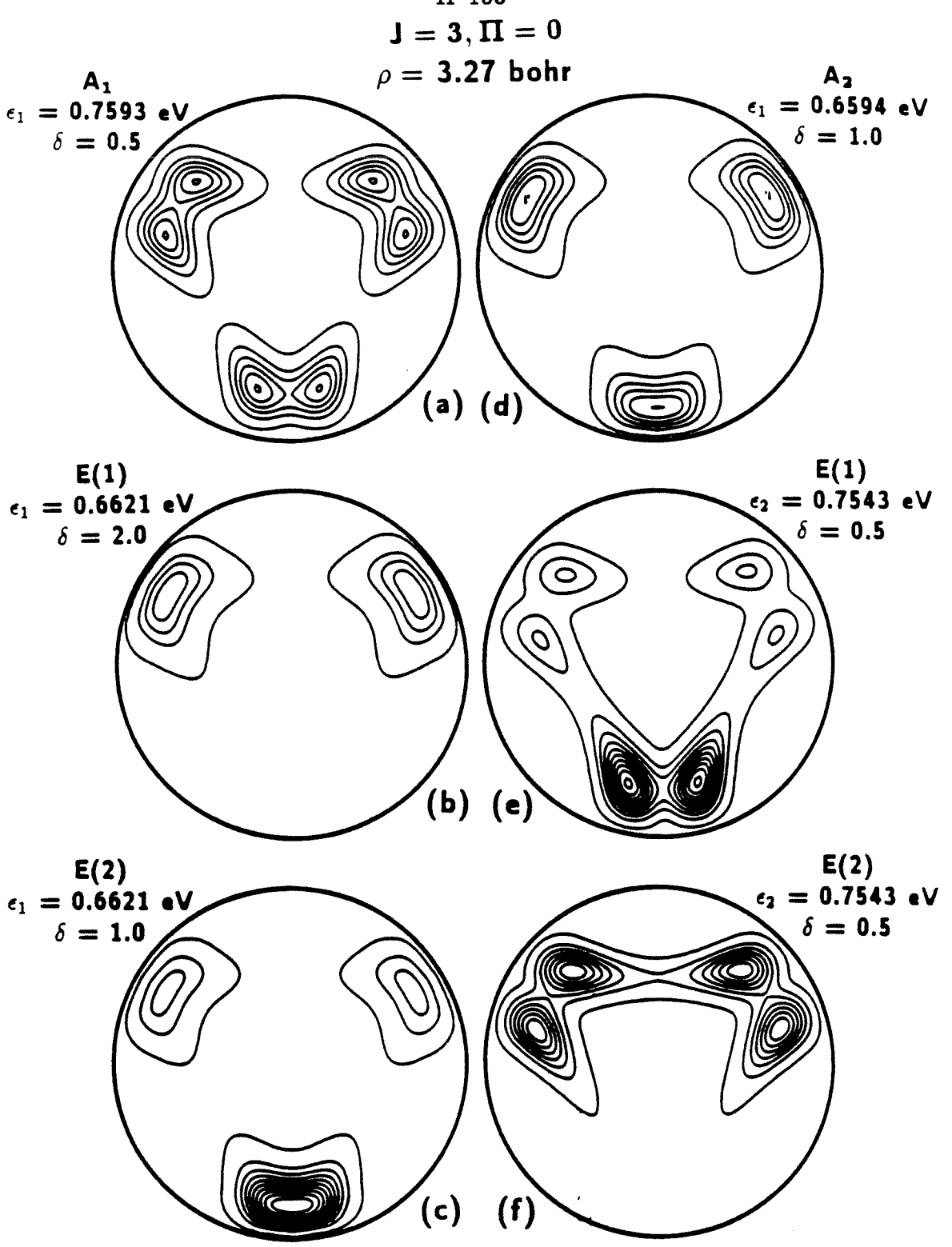
J = 3, Π = 0
ρ = 3.27 bohr
A1
ε1 = 0.7593 eV
δ = 0.5
A2
ε1 = 0.6594 eV
δ = 1.0
(a)
(d)
E(1)
ε1 = 0.6621 eV
δ = 2.0
E(1)
ε2 = 0.7543 eV
δ = 0.5
(b)
(e)
E(2)
ε1 = 0.6621 eV
δ = 1.0
E(2)
ε2 = 0.7543 eV
δ = 0.5
(c)
(f)

Fig. 4.39

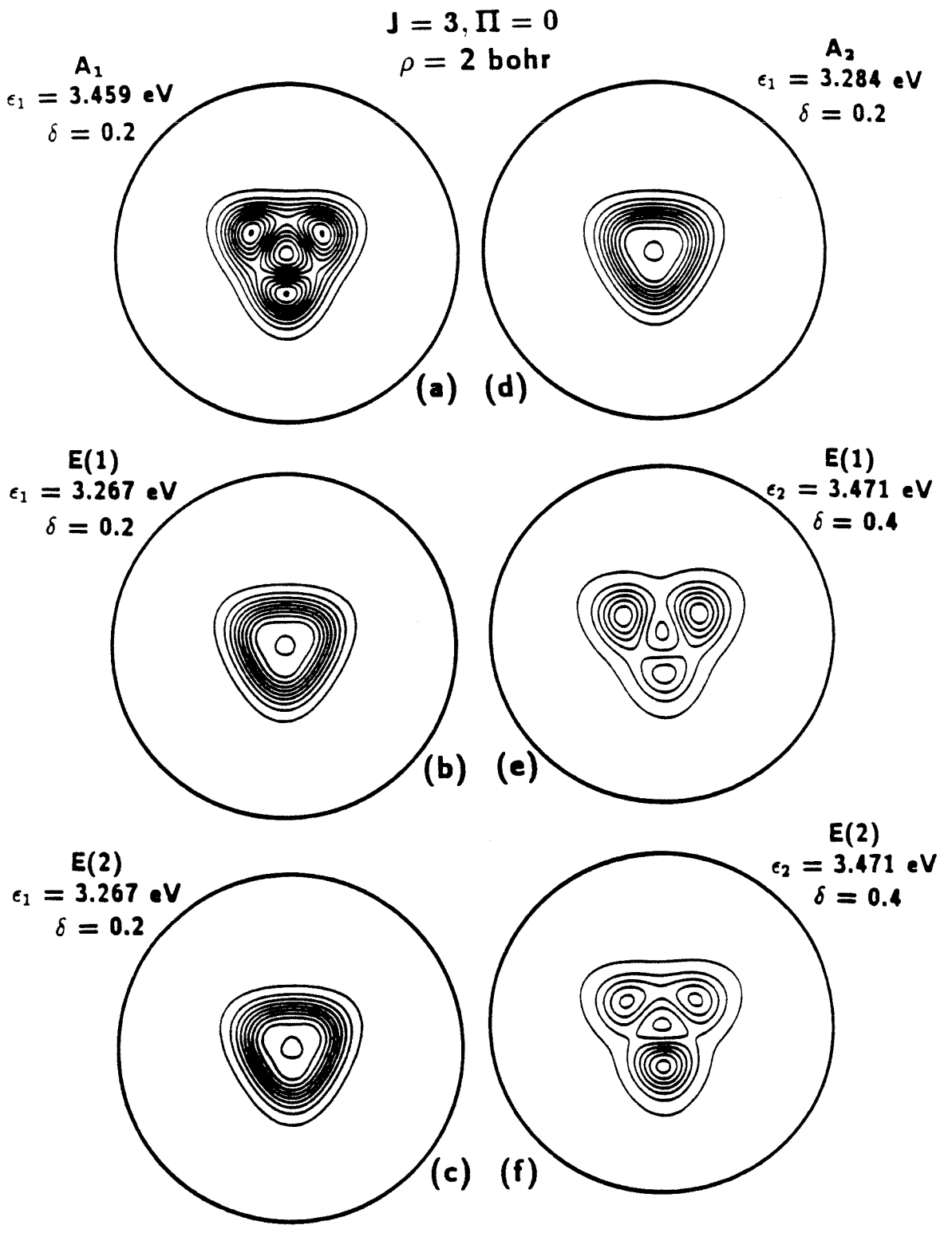
J = 3, Π = 0
ρ = 2 bohr
A1
ϵ1 = 3.459 eV
δ = 0.2
A2
ϵ1 = 3.284 eV
δ = 0.2
(a)
(d)
E(1)
ϵ1 = 3.267 eV
δ = 0.2
E(1)
ϵ2 = 3.471 eV
δ = 0.4
(b)
(e)
E(2)
ϵ1 = 3.267 eV
δ = 0.2
E(2)
ϵ2 = 3.471 eV
δ = 0.4
(c)
(f)

Fig. 4.40

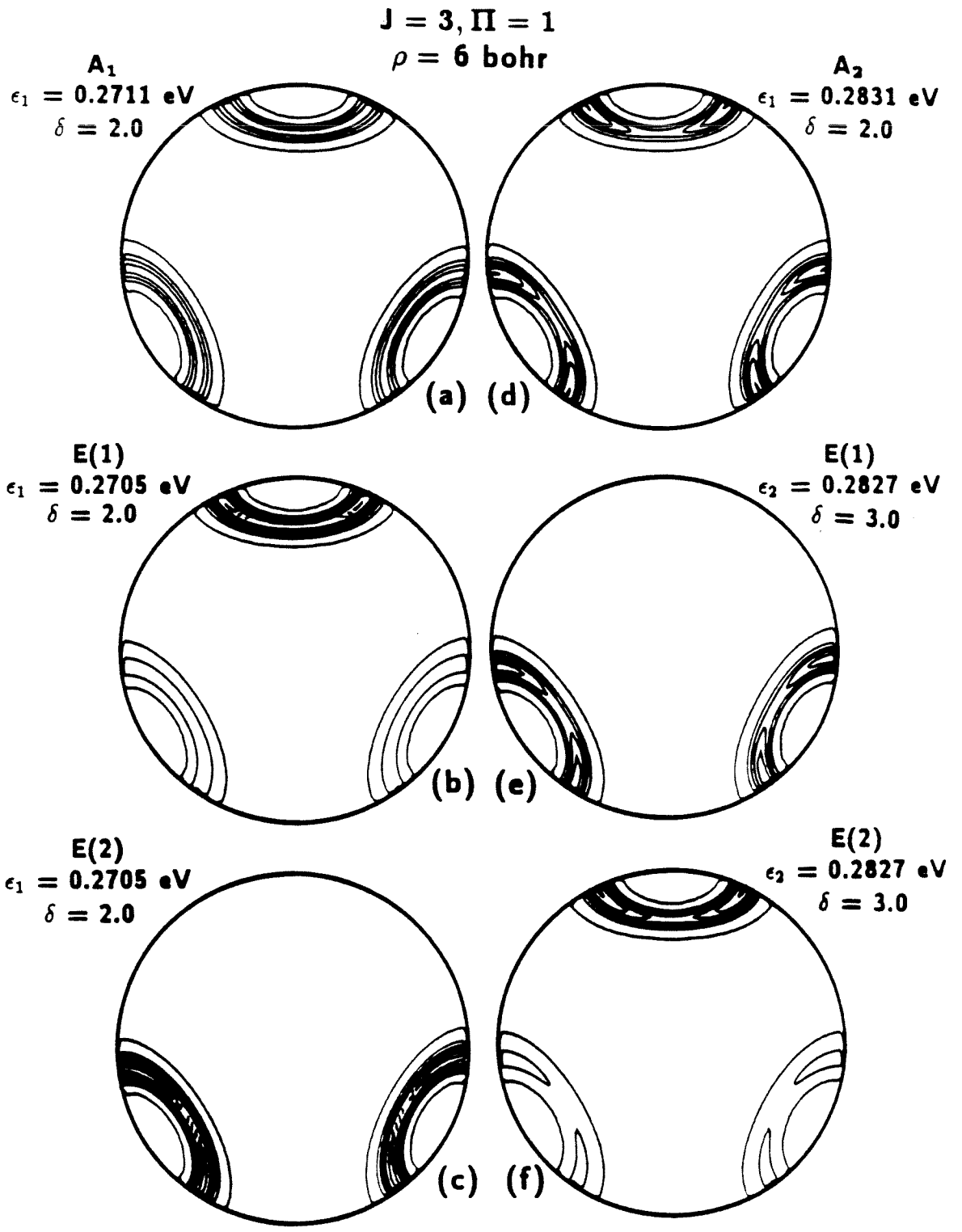
J = 3, Π = 1
ρ = 6 bohr
A1
ϵ1 = 0.2711 eV
δ = 2.0
A2
ϵ1 = 0.2831 eV
δ = 2.0
(a)
(d)
E(1)
ϵ1 = 0.2705 eV
δ = 2.0
E(1)
ϵ2 = 0.2827 eV
δ = 3.0
(b)
(e)
E(2)
ϵ1 = 0.2705 eV
δ = 2.0
E(2)
ϵ2 = 0.2827 eV
δ = 3.0
(c)
(f)

Fig. 4.41

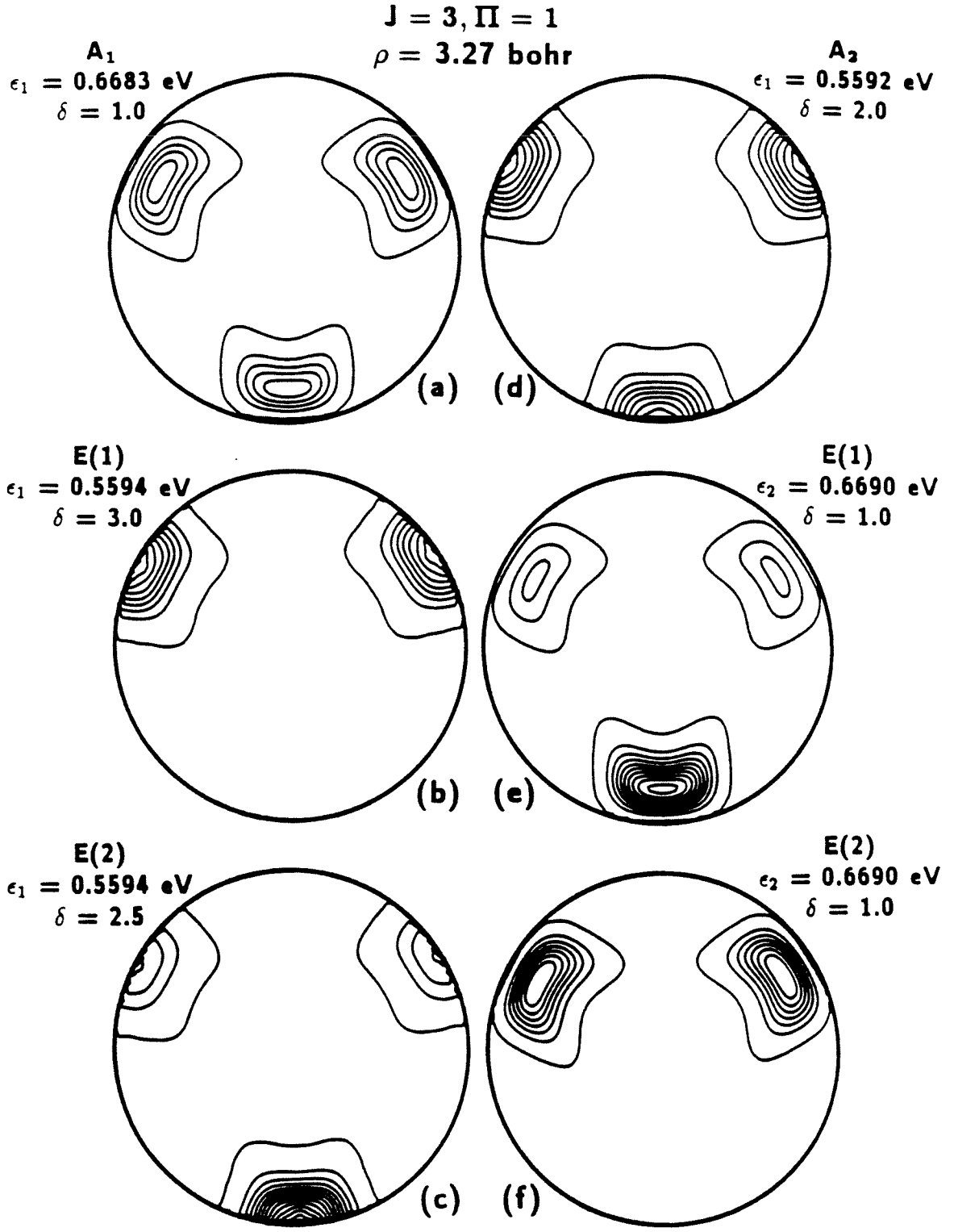
J = 3, Π = 1
ρ = 3.27 bohr
A1
ε1 = 0.6683 eV
δ = 1.0
A2
ε1 = 0.5592 eV
δ = 2.0
(a)
(d)
E(1)
ε1 = 0.5594 eV
δ = 3.0
E(1)
ε2 = 0.6690 eV
δ = 1.0
(b)
(e)
E(2)
ε1 = 0.5594 eV
δ = 2.5
E(2)
ε2 = 0.6690 eV
δ = 1.0
(c)
(f)

Fig. 4.42

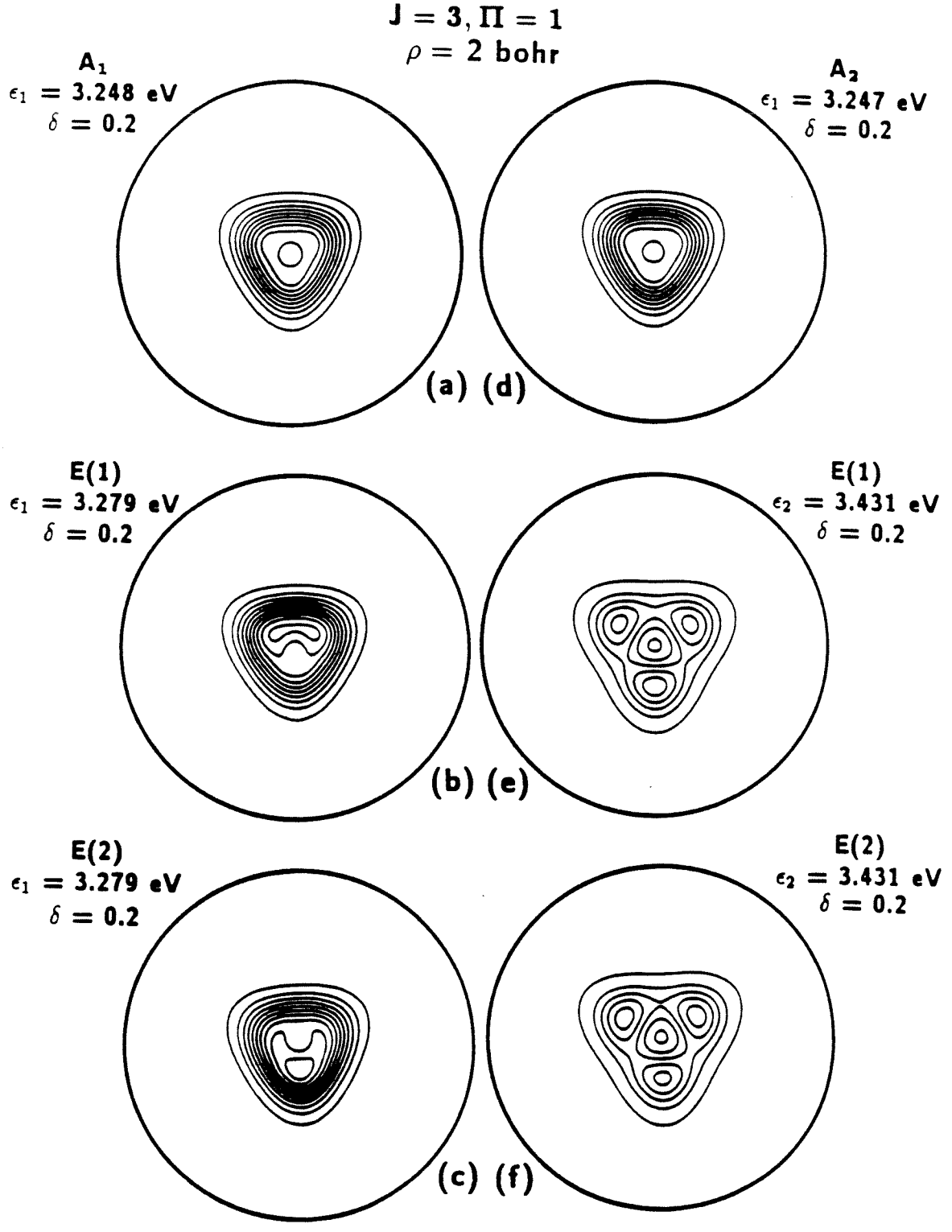
J = 3, Π = 1
ρ = 2 bohr
A1
ε1 = 3.248 eV
δ = 0.2
A2
ε1 = 3.247 eV
δ = 0.2
(a) (d)
E(1)
ε1 = 3.279 eV
δ = 0.2
E(1)
ε2 = 3.431 eV
δ = 0.2
(b) (e)
E(2)
ε1 = 3.279 eV
δ = 0.2
E(2)
ε2 = 3.431 eV
δ = 0.2
(c) (f)

Fig. 4.43

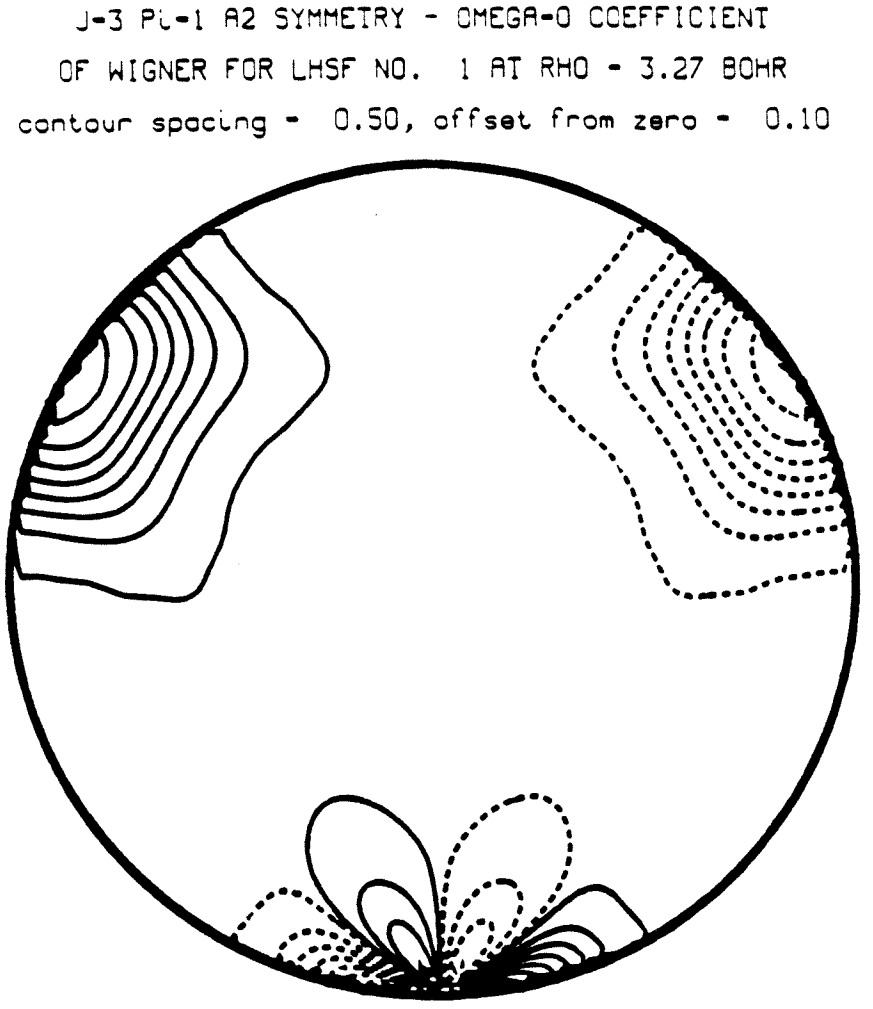
J-3 PL-1 A2 SYMMETRY - OMEGA-0 COEFFICIENT
OF WIGNER FOR LHSF NO. 1 AT RHO - 3.27 BOHR
contour spacing - 0.50, offset from zero - 0.10

Fig. 4.44a

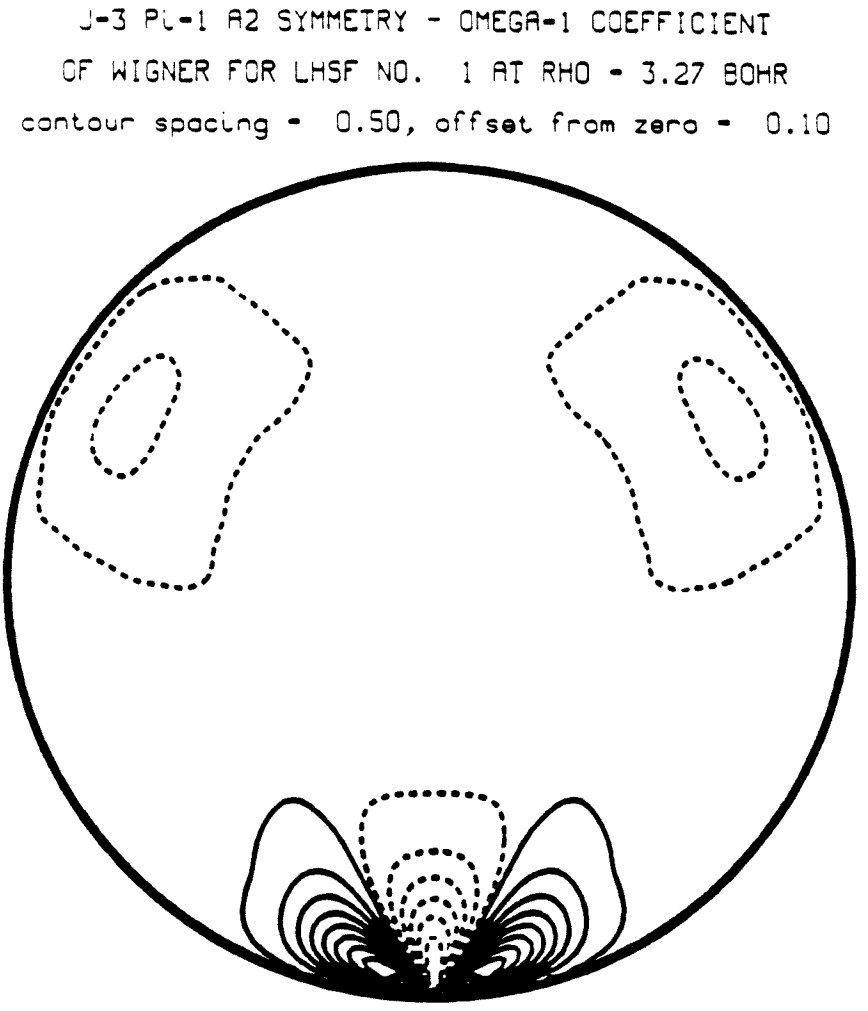
J-3 PL-1 A2 SYMMETRY - OMEGA-1 COEFFICIENT
OF WIGNER FOR LHSF NO. 1 AT RHO = 3.27 BOHR
contour spacing = 0.50, offset from zero = 0.10

Fig. 4.44b

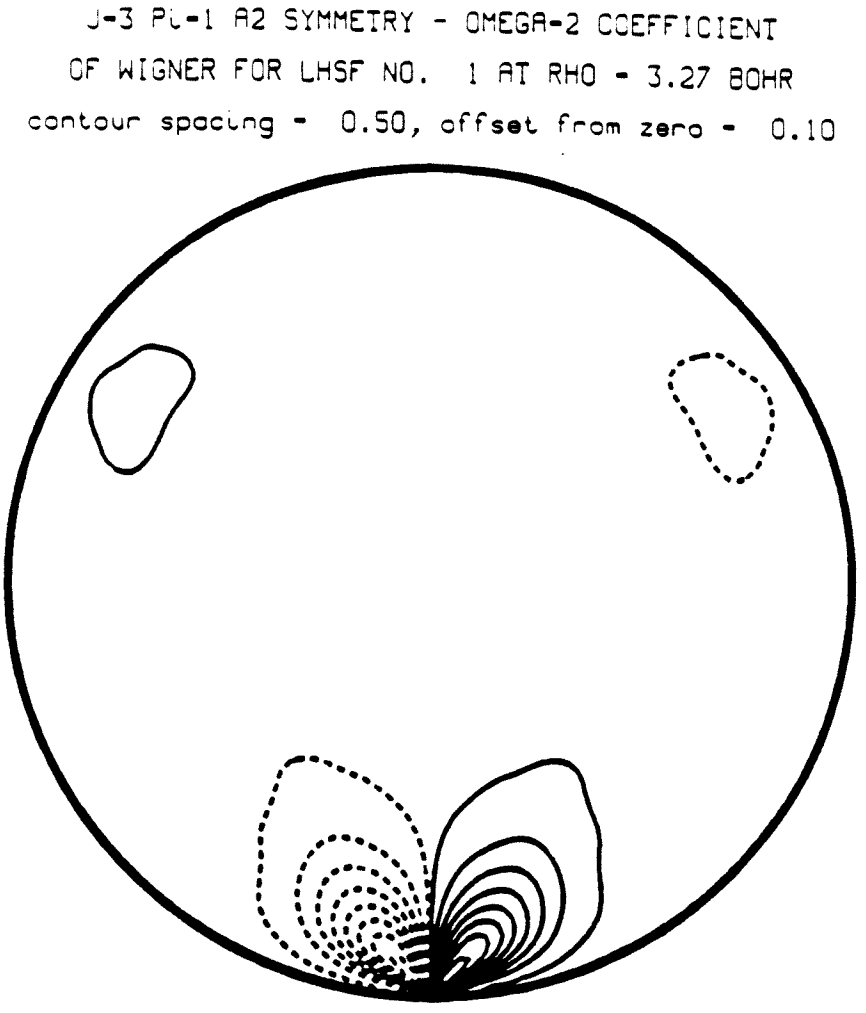
J-3 Pt-1 A2 SYMMETRY - OMEGA-2 COEFFICIENT
OF WIGNER FOR LHSF NO. 1 AT RHO - 3.27 BOHR
contour spacing - 0.50, offset from zero - 0.10

Fig. 4.44c

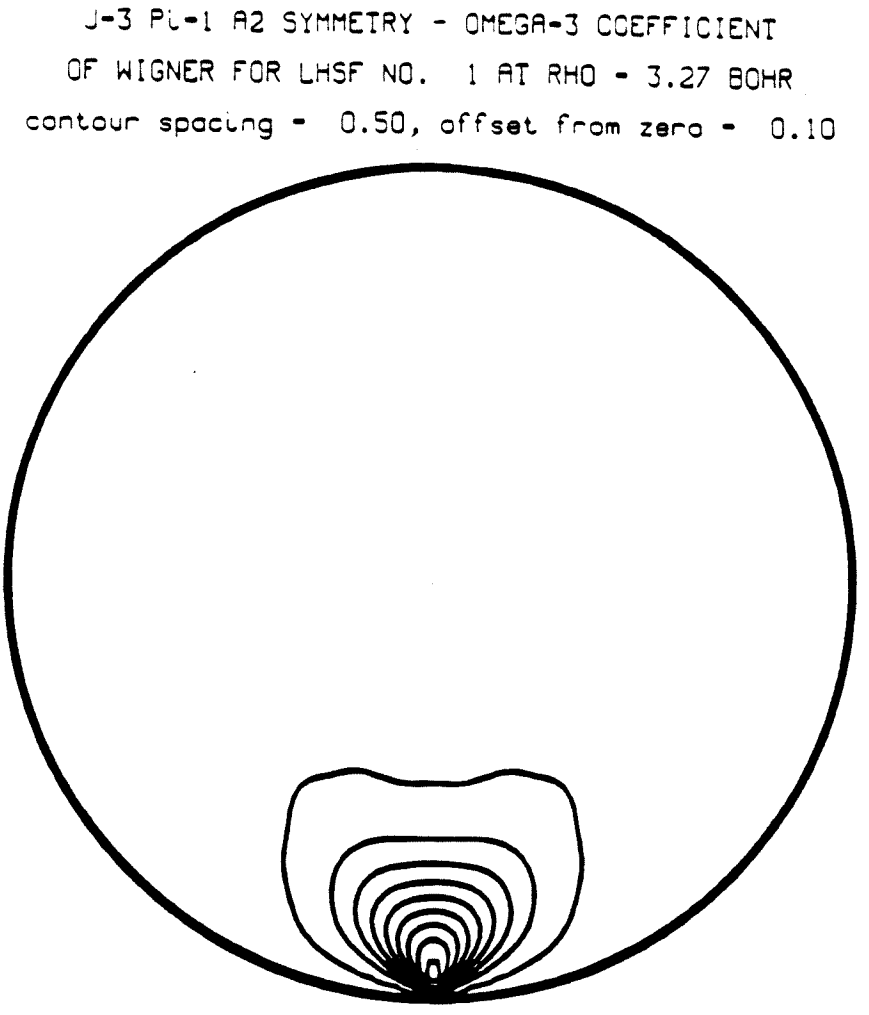
J-3 PL-1 A2 SYMMETRY - OMEGA-3 COEFFICIENT
OF WIGNER FOR LHSF NO. 1 AT RHO - 3.27 BOHR
contour spacing - 0.50, offset from zero - 0.10

Fig. 4.44d

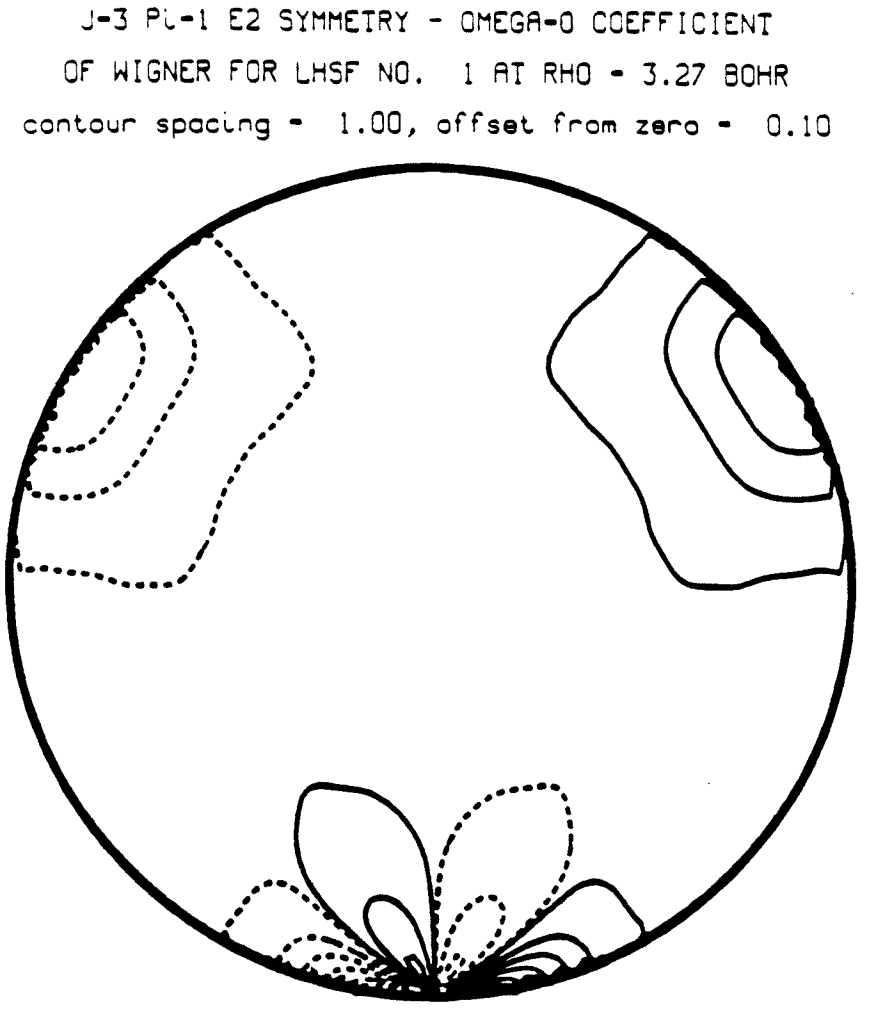
J-3 PL-1 E2 SYMMETRY - OMEGA-0 COEFFICIENT
OF WIGNER FOR LHSF NO. 1 AT RHO = 3.27 BOHR
contour spacing = 1.00, offset from zero = 0.10

Fig. 4.45a

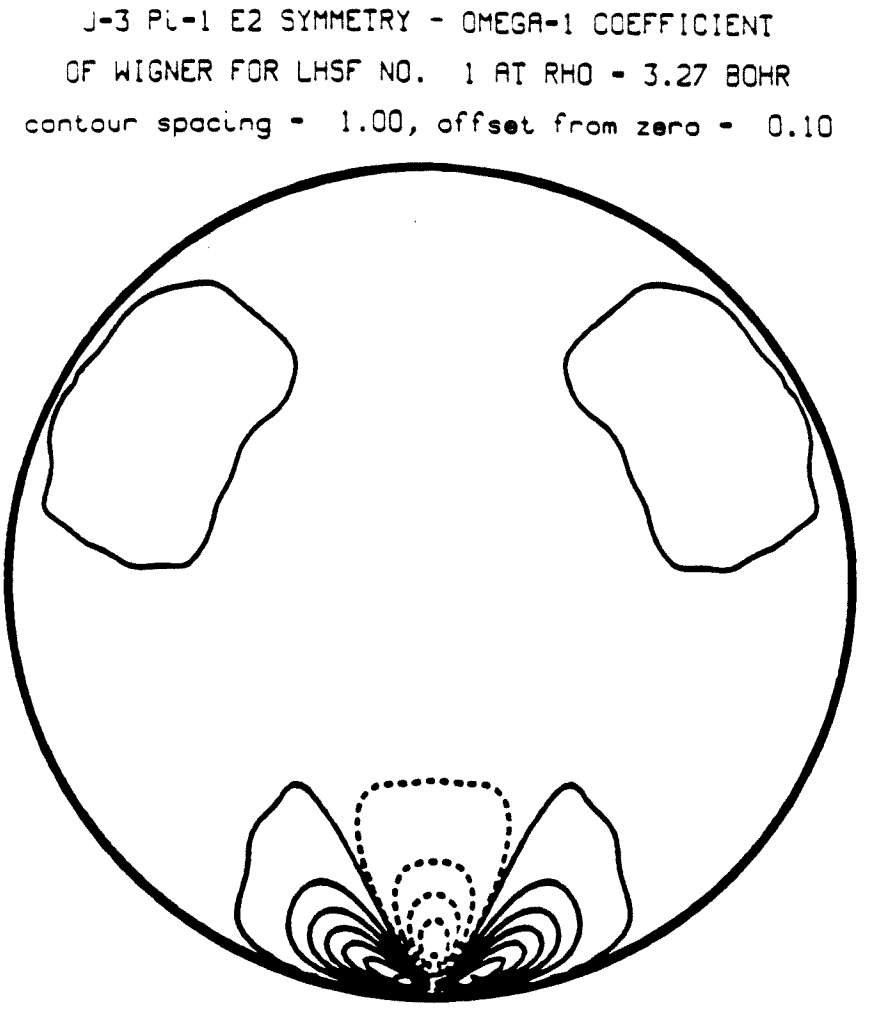
J-3 Pt-1 E2 SYMMETRY - OMEGA-1 COEFFICIENT
OF WIGNER FOR LHSF NO. 1 AT RHO = 3.27 BOHR
contour spacing = 1.00, offset from zero = 0.10

Fig. 4.45b

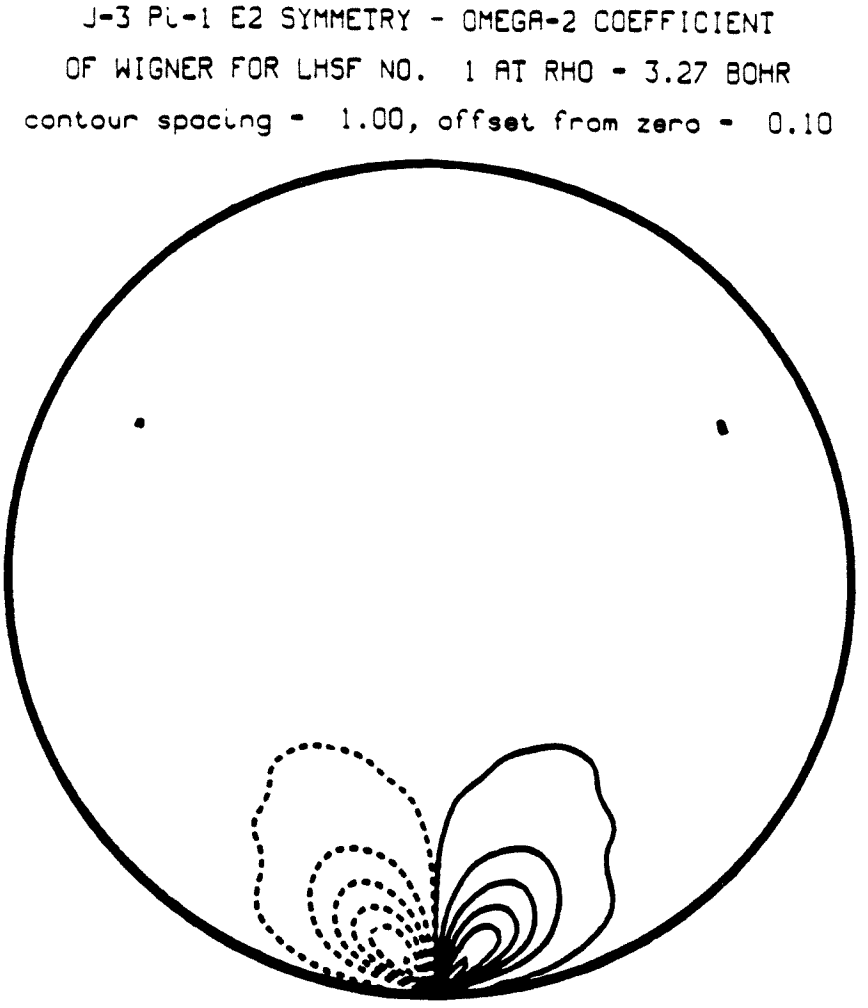
J-3 PL-1 E2 SYMMETRY - OMEGA-2 COEFFICIENT
OF WIGNER FOR LHSF NO. 1 AT RHO = 3.27 BOHR
contour spacing = 1.00, offset from zero = 0.10

Fig. 4.45c

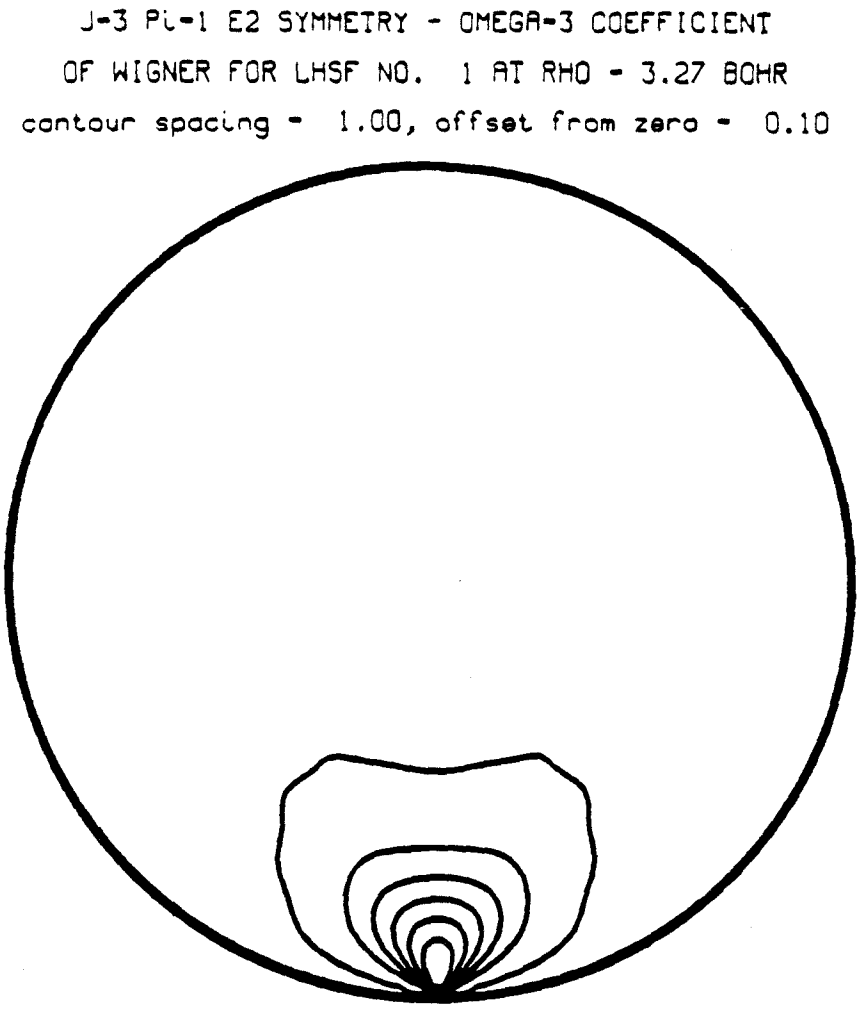
J=3 Pi=1 E2 SYMMETRY - OMEGA=3 COEFFICIENT
OF WIGNER FOR LHSF NO. 1 AT RHO = 3.27 BOHR
contour spacing = 1.00, offset from zero = 0.10

Fig. 4.45d

III. CALCULATION OF ACCURATE PARTIAL WAVE CROSS SECTIONS FOR 3-DIMENSIONAL REACTIVE SCATTERING[†]

Steven A. Cuccaro[¶] and Aron Kuppermann

Arthur Amos Noyes Laboratory of Chemical Physics,
Division of Chemistry and Chemical Engineering,[‡]
California Institute of Technology,
Pasadena, California 91125

(Received)

Abstract

We present a method for calculation of accurate differential and integral cross sections for reactive atom-diatom scattering, based on the calculation of surface functions in symmetrized hyperspherical coordinates. Scattering matrices and cross sections for the $J = 0$ through 3 partial waves for the $H + H_2$ system are presented, both with and without corrections for the presence of the conical intersection of the H_3 potential.

1. INTRODUCTION

In the year 1975, Kuppermann and Schatz[1,2] reported the first converged calculation in three dimensions of integral and differential cross sections for the reactive scattering of an atom by a diatomic molecule; the calculation was performed on the Porter-Karplus potential (PK2)[3] for the reaction $H + H_2 \rightarrow H_2 + H$, and was converged up to an energy of 0.7 eV above the minimum of the potential. In that same year, Elkowitz and Wyatt[4,5] published integral cross sections for that reaction with minor approximations, and in 1978 Walker, Stechel and Light[6] repeated the latter calculations on the more accurated LSTH potential energy surface.[7] No subsequent converged integral cross section results were reported until 1988,[8,9] and not until 1989 were new converged differential cross section results published.[10–13] The methods used in these early calculations were difficult to apply to higher energy calculations and to systems of less symmetry than $H + H_2$, due to the speed and memory limitations imposed by the computational technology at the time; however, the development of new techniques and the advances in computational power over the years have since made these more difficult calculations feasible. Beginning in 1986 with the publication by Kuppermann and Hipes[14,15] of $J = 0$ partial wave results for the $H + H_2$ reaction up to energies of 1.6 eV above threshhold using symmetrized hyperspherical coordinates, a surge of publications has occurred. There are now converged calculations for the systems $H + H_2$ and $D + H_2$,[1,2,4–6,8–36] $F + H_2$, $F + D_2$ and $F + HD$,[37–45] $O + H_2$,[46,47] $H + HBr$,[48] and $Cl + HCl$.[21,49]

These calculations are of three basic types: the propagation methods of Kuppermann *et al.*,[14–17] Pack *et al.*,[18–20,37,38] Schatz,[21,49] Linderberg *et al.*,[22] and Launay and Le Dorneuf,[9] all involving some form of hyperspherical coordinates; the variational methods of the Truhlar and Kouri groups,[13,23–30,39–42,46–48] Zhang and Miller,[11,12,31,32] and Manolopoulos and Wyatt,[10,33,34,43–45] using Jacobi coordinates; and the recent work of Webster and Light[35,36] using a "natural collision coordinate"[50] method related to the methods of the early work[1,2,4–6].

The variational methods may be further divided according to the variational principle used in the method. Miller *et al.* use a Kohn[51] variational expression to directly calculate the scattering matrix[52,53] **S**, while Manolopoulos and Wyatt obtain the logarithmic derivative matrix[54] for the wavefunction using a Kohn principle. Since the variational principle in each of these cases is applied to the matrix of interest rather than to the wavefunction itself, the matrices are obtained to one order more accuracy than the wavefunction;[55] this is computationally advantageous since the wavefunction is not itself needed for the calculation of scattering cross sections once the log derivative or scattering matrix has been obtained. Truhlar, Kouri *et al.* instead use a generalization of a variational principle due to Newton[56] in their $\mathcal{L}^2$-AD GNVP method, with the variation applied to an amplitude density (the wavefunction multiplied by a reference potential which asymptotically approaches zero). In all these methods, the scattering wavefunction is expanded in terms of basis functions for the reactants and products, expressed in terms of the Jacobi coordinates of the arrangement channel. The couplings between these basis sets are evaluated through multi-dimensional exchange integrals,[57] which leads to a matrix system of linear equations that must be solved to obtain the scattering matrix for the three-particle system. The Kohn principle is simpler to apply, since the matrix elements are calculated over the hamiltonian H, while in the Newton principle the calculation is over the Green's function of a reference hamiltonian; however, the Newton principle methods have been found to converge more rapidly.[58] The major difficulties in these variational methods are the expense of the calculation of the large number of exchange integrals, which depend on the total energy of the system and so must be recalculated for each energy, and the memory required for a calculation with a sufficiently large basis set for accurate results.

The propagation method calculations, on the other hand, are based on an expression of the problem in terms of a hyperspherical coordinate system, which describes the degrees of freedom of the system of particles in terms of a single distance

variable (the hyperradius) and five hyperangles. In these methods the Schrödinger equation is solved for fixed hyperradius to obtain "surface functions" in the hyperangles, so called since they are defined on the surface of a hypersphere; the hyperradius is treated as the generalized collision coordinate for the system. The definitions of the surface functions used is different for each hyperspherical coordinate method. When these surface functions are substituted back into the Schrödinger equation, the result is a system of coupled second order linear differential equations in the hyperradius, which as a consequence of the differing surface functions differs from one method to another. The surface functions are independent of the total energy of the system, and thus if scattering calculations at many energies are desired the time spent in evaluating the surface functions becomes unimportant. An important property of these methods is that the hyperspherical coordinates yield an effective description of the wavefunctions even for heavy-light-heavy mass combinations which result in large overlaps between reactant and product channels.[59,60] Finally, for the case of collision-induced dissociation,[61,62] they yield a discretized representation of the dissociation continuum, which the other methods based on Jacobi coordinates do not.

There is more than one possible set of hyperspherical coordinates which may be used for these propagation calculations. The coordinates introduced by Delves[63] (currently used by Schatz[21,49]) and by Whitten and Smith[64] both share the disadvantage that certain configurations of the system may be described by more than one set of internal coordinates (*i.e.*, the coordinates on which the potential depends), so that there is not a 1 to 1 relation between internal configurations of the system and values of the sets of internal coordinates. In addition, the transformation of the three internal coordinates from a set based on one arrangement channel to another is not orthogonal. Kuppermann[65] developed a set of symmetrized hyperspherical coordinates (SHC) which does not have this undesirable characteristic, and suggested that these coordinates would be an appropriate system for the study

of reactive scattering problems;[65,66] they are currently in use by this group.[14–17] Other sets of symmetrized hyperspherical coordinates have been designed so as to treat all three arrangement channels in equivalent ways; these have been proposed by Johnson,[67] Mead[68] (used by Linderberg *et al.*[22]), and Pack and Parker[18–20,37,38] (also used by Launay and Le Dorneuf[9]).

Once the surface functions are calculated, the resulting coupled equations in the hyperradius must be solved. Kuppermann *et al.* recast the problem into an equation for the logarithmic derivative of the wavefunction, which transforms the problem from a second-order spherical Bessel linear differential matrix equation into a Ricatti-Bessel equation, which is first-order but nonlinear; the solution for this equation is then found using a variant[69] of Johnson's logarithmic derivative program.[54] Schatz has preferred to use a sin/cos reference potential method[70] to enable recovery of the scattering wavefunction from the calculation. Launay and Le Dorneuf have used the De Vogelaere algorithm,[71] Pack and Parker use the VIVAS method[72], and Linderberg an implementation of R-matrix theory approach.[52,73]

In a previous paper (I), we described our method of calculation of surface functions using symmetrized hyperspherical coordinates, applied it to the H + H_2 system, and discussed the properties of these functions. The present paper is concerned with the use of such surface functions in determining the scattering matrices and differential and integral cross sections, and the application to H + H_2. Section 2 presents a brief review of the determination of the propagation equation from the expansion of the wavefunction in terms of surface functions, and describes the formalism for the propagation for general triatomic systems. In section 3, the asymptotic boundary conditions are invoked for determination of the **R** and **S** matrices of the system, and in section 4 the formalism for determination of the cross sections from the **S** matrix is developed. Section 5 is a description of the logarithmic derivative algorithm used in the calculation of the scattering matrices. In section 6, the results of testing the convergence of our propagation method are presented,

and the results of our calculations are given in section 7. A summary of the main points of this paper is provided in section 8.

2. FORMALISM FOR PROPAGATION

2.1 Surface Function Expansion and Propagation Equation

In a previous paper (I) we derived the expression for the six-dimensional partial wave wavefunction $\Psi^{JM\Pi\Gamma_k}$ in terms of five-dimensional local hyperspherical surface functions (LHSF) $\Phi_n^{JM\Pi\Gamma_k}$. We provide here a brief outline of this derivation to clarify the discussion to follow.

The Schrödinger equation of the six-dimensional system, expressed in body-fixed symmetrized hyperspherical coordinates (SHC),[14–16,65,66] is

$$\hat{H}_\lambda(\rho,\zeta_\lambda) = \hat{T}(\rho) + \hat{h}_\lambda(\zeta_\lambda;\rho) \tag{2.1.1}$$

with the hyperradial kinetic energy operator defined by

$$\hat{T}(\rho) = -\frac{\hbar^2}{2\mu}\rho^{-\frac{5}{2}}\frac{\partial^2}{\partial\rho^2}\rho^{\frac{5}{2}} + \frac{15\hbar^2}{2\mu\rho^2} \tag{2.1.2}$$

and the surface hamiltonian

$$\hat{h}_\lambda(\zeta_\lambda;\rho) = \frac{\hat{\Lambda}^2(\zeta_\lambda)}{2\mu\rho^2} + V(\rho,\omega_\lambda,\gamma_\lambda) \tag{2.1.3}$$

where $\hat{\Lambda}^2$ is the grand canonical angular momentum operator. The $\Psi^{JM\Pi\Gamma_k}$ are eigenfunctions of this hamiltonian with energy E, as well as eigenfunctions of the square of the total angular momentum operator $\hat{J}^2$, the operator $\hat{J}_Z$ for the projection of that angular momentum on the space-fixed $\mathbf{Z}$ axis, the operator $\hat{\mathcal{I}}$ for inversion through the center of mass of the system and the projection operators[74] $\hat{P}^\Gamma_{kk}$ for the Γ irreducible representation (IR) of the permutation group[75] P_p of the identical atoms of the system (where for three particles p may take on the values 1, 2 or 3):

$$\hat{H}_\lambda\Psi^{JM\Pi\Gamma_k}(\rho,\zeta_\lambda) = E\Psi^{JM\Pi\Gamma_k}(\rho,\zeta_\lambda) \tag{2.1.4}$$

$$\hat{J}^2(\theta_\lambda,\phi_\lambda,\psi_\lambda,\gamma_\lambda)\Psi^{JM\Pi\Gamma_k}(\rho,\zeta_\lambda) = \hbar^2 J(J+1)\Psi^{JM\Pi\Gamma_k}(\rho,\zeta_\lambda) \tag{2.1.5}$$

$$\hat{J}_z(\phi_\lambda)\Psi^{JM\Pi\Gamma_k}(\rho,\zeta_\lambda) = \hbar M \Psi^{JM\Pi\Gamma_k}(\rho,\zeta_\lambda) \tag{2.1.6}$$

$$\hat{\mathcal{I}}(\theta_\lambda,\phi_\lambda,\psi_\lambda)\Psi^{JM\Pi\Gamma_k}(\rho,\zeta_\lambda) = (-1)^{\Pi}\Psi^{JM\Pi\Gamma_k}(\rho,\zeta_\lambda) \tag{2.1.7}$$

$$\hat{P}^{\Gamma'}_{ii}(\zeta_\lambda)\Psi^{JM\Pi\Gamma_k}(\rho,\zeta_\lambda) = \delta^{\Gamma'}_{\Gamma}\delta^{k}_{i}\Psi^{JM\Pi\Gamma_k}(\rho,\zeta_\lambda) \tag{2.1.8}$$

The $\Phi_n^{JM\Pi\Gamma_k}$ are the eigenfunctions of the surface function hamiltonian with eigenvalues $\epsilon_n^{J\Pi\Gamma}(\rho)$, as well as of $\hat{J}^2$, $\hat{J}_z$, $\hat{\mathcal{I}}$ and $\hat{P}^{\Gamma}_{kk}$, with the same eigenvalues as those of the $\Psi^{JM\Pi\Gamma_k}(\rho,\zeta_\lambda)$. The index k scans the number of rows (or columns) of the irreducible representation Γ.

We express the $\Psi^{JM\Pi\Gamma_k}$ as an expansion in terms of these surface functions as

$$\Psi^{JM\Pi\Gamma_k}(\rho,\zeta_\lambda) = \rho^{-\frac{5}{2}}\sum_n b_n^{J\Pi\Gamma}(\rho;\bar{\rho})\Phi_n^{JM\Pi\Gamma_k}(\zeta_\lambda;\bar{\rho}). \tag{2.1.9}$$

The coefficients $b_n^{J\Pi\Gamma}$ turn out to be independent of M and of k. To solve for these coefficients, the $\Phi_n^{JM\Pi\Gamma_k}$ are determined at a set of discrete values of $\bar{\rho}$, labelled $\bar{\rho}_i$ with the index i ranging from zero at the smallest value of $\bar{\rho}$ in the set and increasing with $\bar{\rho}$. The $b_n^{J\Pi\Gamma}$ are found to satisfy

$$\begin{aligned}\left\{-\frac{\hbar^2}{2\mu}\frac{d^2}{d\rho^2}+\frac{15\hbar^2}{8\mu\rho^2}+\left(\frac{\bar{\rho}_i}{\rho}\right)^2\epsilon_n^{J\Pi\Gamma}(\bar{\rho}_i)-E\right\}b_n^{J\Pi\Gamma}(\rho;\bar{\rho}_i)\\ +\sum_{n'}b_{n'}^{J\Pi\Gamma}(\rho;\bar{\rho}_i)[\boldsymbol{\mathcal{I}}^{J\Pi\Gamma}]_n^{n'}(\rho;\bar{\rho}_i)=0\end{aligned} \tag{2.1.10}$$

in which the interaction matrix $\boldsymbol{\mathcal{I}}^{J\Pi\Gamma}$, which is a measure of the coupling of the LHSF functions by the potential (or equivalently of the change in the wavefunction as a function of ρ from the values at $\rho=\bar{\rho}_i$), is defined by

$$[\boldsymbol{\mathcal{I}}^{J\Pi\Gamma}]_n^{n'}(\rho;\bar{\rho}_i) = \left\langle \Phi_n^{JM\Pi\Gamma_k}(\zeta_\lambda);\bar{\rho}_i \,\middle|\, \bar{V}(\rho,\omega_\lambda,\gamma_\lambda;\bar{\rho}_i) \,\middle|\, \Phi_{n'}^{JM\Pi\Gamma_k}(\zeta_\lambda;\bar{\rho}_i)\right\rangle. \tag{2.1.11}$$

(where the bra-ket notation denotes integration over the five hyperangles), with the interaction potential $\bar{V}(\rho,\omega_\lambda,\gamma_\lambda;\bar{\rho}_i)$ defined by

$$\bar{V}(\rho,\omega_\lambda,\gamma_\lambda;\bar{\rho}_i) = V(\rho,\omega_\lambda,\gamma_\lambda) - \left(\frac{\bar{\rho}_i}{\rho}\right)^2 V(\bar{\rho}_i,\omega_\lambda,\gamma_\lambda). \tag{2.1.12}$$

The details of the calculation of these functions and matrices are not necessary for understanding what is to follow; they may be found in (I).

The expansion (2.1.9) is exact in the case of an infinite LHSF basis; since the basis set actually used in the calculation must be finite, the expansion will become inaccurate for sufficiently large values of $|\rho - \bar{\rho}_i|$, as some of the coupling caused by the presence of the interaction potential will involve functions excluded from our finite basis. Accordingly, the coefficients $b(\rho;\bar{\rho}_i)$ are calculated as a function of ρ in a region near $\bar{\rho}_i$ corresponding to a hyperspherical shell. It is therefore necessary for determination of the scattering wavefunction at all ρ to smoothly match the wavefunction calculated for each shell across the boundary $\rho = \rho_{i,i+1}$ of adjacent hyperspherical shells. This is accomplished by imposing the conditions

$$b_n^{J\Pi\Gamma}(\rho_{i,i+1};\bar{\rho}_{i+1}) = \sum_{n'} b_{n'}^{J\Pi\Gamma}(\rho_{i,i+1};\bar{\rho}_i)[\mathcal{O}^{J\Pi\Gamma}]_n^{n'}(\bar{\rho}_{i+1},\bar{\rho}_i); \tag{2.1.13}$$

$$\left(\frac{\partial b_n^{J\Pi\Gamma}(\rho;\bar{\rho}_{i+1})}{\partial\rho}\right)_{\rho\to\rho_{i,i+1}^{(+)}} = \sum_{n'}\left(\frac{\partial b_{n'}^{J\Pi\Gamma}(\rho;\bar{\rho}_i)}{\partial\rho}\right)_{\rho\to\rho_{i,i+1}^{(-)}} [\mathcal{O}^{J\Pi\Gamma}]_n^{n'}(\bar{\rho}_{i+1},\bar{\rho}_i); \tag{2.1.14}$$

in which the overlap matrices $\mathcal{O}^{J\Pi\Gamma}$ are defined by

$$[\mathcal{O}^{J\Pi\Gamma}]_n^{n'}(\bar{\rho}_{i+1},\bar{\rho}_i) = \left\langle \Phi_n^{JM\Pi\Gamma_k}(\zeta_\lambda;\bar{\rho}_{i+1}) \,\middle|\, \Phi_{n'}^{JM\Pi\Gamma_k}(\zeta_\lambda;\bar{\rho}_i)\right\rangle. \tag{2.1.15}$$

2.2 Logarithmic Derivative Format

Equation (2.1.10) for the ρ-dependent part of the wavefunction has as many linearly independent solutions as there are surface functions in the expansion. Labelling the coefficients $b_n^{J\Pi\Gamma}(\rho;\bar{\rho})$ of these linearly independent solutions by the superscript n', we may write (2.1.10) in matrix form as

$$\ddot{\mathbf{b}}^{J\Pi\Gamma}(\rho;\bar{\rho}_i) = \mathbf{K}(\rho,\bar{\rho}_i)\mathbf{b}^{J\Pi\Gamma}(\rho;\bar{\rho}_i) \tag{2.2.1}$$

where

$$[\mathbf{b}^{J\Pi\Gamma}(\rho;\bar{\rho}_i)]_n^{n'} = b_n^{J\Pi\Gamma,n'}(\rho;\bar{\rho}_i) \tag{2.2.2}$$

and

$$\mathbf{K}(\rho,\bar{\rho}_i) = \frac{2\mu}{\hbar^2}\boldsymbol{\mathcal{I}}^{J\Pi\Gamma}(\rho,\bar{\rho}_i) - \mathbf{k}^2(\rho,\bar{\rho}_i) \tag{2.2.3}$$

in which

$$[\mathbf{k}^2(\rho,\bar{\rho}_i)]_n^{n'} = \frac{2\mu}{\hbar^2}\delta_n^{n'}\left(E - \frac{15\hbar^2}{8\mu\rho^2} - \left(\frac{\bar{\rho}_i}{\rho}\right)^2 \epsilon_n^{J\Pi\Gamma}(\bar{\rho}_i)\right). \tag{2.2.4}$$

The differentiation in equation (2.2.1) is with respect to ρ. If we define the logarithmic derivative[54] of the $\mathbf{b}^{J\Pi\Gamma}$ matrix of coefficients to be

$$\boldsymbol{\mathcal{Y}}^{J\Pi\Gamma}(\rho;\bar{\rho}_i) = \dot{\mathbf{b}}^{J\Pi\Gamma}(\rho,\bar{\rho}_i)\left(\mathbf{b}^{J\Pi\Gamma}(\rho,\bar{\rho}_i)\right)^{-1} \tag{2.2.5}$$

we find by differentiation of (2.2.5) and using (2.2.1) that $\boldsymbol{\mathcal{Y}}$ satisfies the matrix Ricatti-Bessel equation

$$\dot{\boldsymbol{\mathcal{Y}}}^{J\Pi\Gamma}(\rho;\bar{\rho}_i) = \mathbf{K}(\rho,\bar{\rho}_i) - \left(\boldsymbol{\mathcal{Y}}^{J\Pi\Gamma}(\rho;\bar{\rho}_i)\right)^2. \tag{2.2.6}$$

Similarly, equations (2.1.13) and (2.1.14), which interrelate the wavefunction and its derivative in the various LHSF basis sets at different $\bar{\rho}$, may be expressed in matrix form as

$$\mathbf{b}^{J\Pi\Gamma}(\rho;\bar{\rho}_{i+1}) = \left[\boldsymbol{\mathcal{O}}^{J\Pi\Gamma}(\bar{\rho}_{i+1},\bar{\rho}_i)\right]^{-1}\mathbf{b}^{J\Pi\Gamma}(\rho,\bar{\rho}_i)\boldsymbol{\mathcal{O}}^{J\Pi\Gamma}(\bar{\rho}_{i+1},\bar{\rho}_i) \tag{2.2.7}$$

$$\dot{\mathbf{b}}^{J\Pi\Gamma}(\rho;\bar{\rho}_{i+1}) = \left[\boldsymbol{\mathcal{O}}^{J\Pi\Gamma}(\bar{\rho}_{i+1},\bar{\rho}_i)\right]^{-1}\dot{\mathbf{b}}^{J\Pi\Gamma}(\rho,\bar{\rho}_i)\boldsymbol{\mathcal{O}}^{J\Pi\Gamma}(\bar{\rho}_{i+1},\bar{\rho}_i) \tag{2.2.8}$$

Therefore, the log derivative matrices in different $\bar{\rho}$ basis sets can be seen to be related in the same way:

$$\boldsymbol{\mathcal{Y}}^{J\Pi\Gamma}(\rho;\bar{\rho}_{i+1}) = \left[\boldsymbol{\mathcal{O}}^{J\Pi\Gamma}(\bar{\rho}_{i+1},\bar{\rho}_i)\right]^{-1}\boldsymbol{\mathcal{Y}}^{J\Pi\Gamma}(\rho;\bar{\rho}_i)\boldsymbol{\mathcal{O}}^{J\Pi\Gamma}(\bar{\rho}_{i+1},\bar{\rho}_i) \tag{2.2.9}$$

For an infinite LHSF expansion the $\boldsymbol{\mathcal{O}}^{J\Pi\Gamma}$ are unitary and (2.2.9) is equivalent to

$$\boldsymbol{\mathcal{Y}}^{J\Pi\Gamma}(\rho;\bar{\rho}_{i+1}) = \tilde{\boldsymbol{\mathcal{O}}}^{J\Pi\Gamma}(\bar{\rho}_{i+1},\bar{\rho}_i)\boldsymbol{\mathcal{Y}}^{J\Pi\Gamma}(\rho;\bar{\rho}_i)\boldsymbol{\mathcal{O}}^{J\Pi\Gamma}(\bar{\rho}_{i+1},\bar{\rho}_i) \tag{2.2.10}$$

For a finite basis set, (2.2.9) and (2.2.10) are not equivalent and either of them can be used as different continuity considerations for the truncated basis set approximation.

3. ASYMPTOTIC ANALYSIS - R AND S MATRICES

3.1 Physical Asymptotic Conditions

To obtain differential and integral cross sections, it is necessary to use an asymptotic form which corresponds to the physical conditions of a scattering process. The wavefunction of physical interest has asymptotically an incident part which is the product of an incoming plane wave (arbitrarily assigned to be moving in the space-fixed **Z** direction) and the wavefunction for the initial state of the diatomic molecule. The outgoing part of the asymptotic physical wavefunction, corresponding to product particles which are well separated, is a sum over all possible states of the product diatom multiplied by outgoing spherical waves. These two conditions can be combined in our time-independent formalism to give the following set of space-fixed boundary conditions, valid when the total energy of the system is below the system's dissociation energy into three atoms:

$$\Psi_{\bar{\lambda}}^{\lambda' v'_{\lambda'} j'_{\lambda'} m'_{\lambda'}} \underset{R_{\bar{\lambda}} \to \infty}{\sim} \sum_{\lambda} \sum_{v_\lambda j_\lambda m_\lambda} \left[e^{i \mathbf{k}_{\lambda v_\lambda j_\lambda} \cdot \mathbf{R}_\lambda} \delta_{\lambda v_\lambda j_\lambda m_\lambda}^{\lambda' v'_{\lambda'} j'_{\lambda'} m'_{\lambda'}} + \hat{f}_{\lambda v_\lambda j_\lambda m_\lambda}^{\lambda' v'_{\lambda'} j'_{\lambda'} m'_{\lambda'}} (\theta_\lambda, \phi_\lambda) \frac{e^{i k_{\lambda v_\lambda j_\lambda} R_\lambda}}{R_\lambda} \right] \varphi_{\lambda v_\lambda j_\lambda m_\lambda}^{\mathrm{sf}} (\mathbf{r}_\lambda) \tag{3.1.1}$$

where $\{\lambda', \nu', \kappa'\}$ is a cyclic permutation of the arrangement channel indices $\{\alpha, \beta, \gamma\}$ and $\bar{\lambda}$ is a fixed but otherwise arbitrary channel index which corresponds to the asymptotic arrangement channel under examination. The coefficients $\hat{f}_{\lambda v_\lambda j_\lambda m_\lambda}^{\lambda' v'_{\lambda'} j'_{\lambda'} m'_{\lambda'}}$ are the space-fixed scattering amplitudes and contain the information needed for the cross section determination. In this equation, the incoming wave is assumed to be in the λ' channel, which is to say that the incident atom is $A_{\lambda'}$ and the initial diatom is $A_{\nu'} A_{\kappa'}$. The diatomic wavefunction $\varphi_{\lambda v_\lambda j_\lambda m_\lambda}^{\mathrm{sf}}$ is given in space-fixed coordinates by

$$\varphi_{\lambda v_\lambda j_\lambda m_\lambda}^{\mathrm{sf}} (\mathbf{r}_\lambda) = Y_{j_\lambda}^{m_\lambda} (\theta_{\mathbf{r}_\lambda}, \phi_{\mathbf{r}_\lambda}) \frac{\phi_{\lambda v_\lambda j_\lambda} (r_\lambda)}{r_\lambda} \tag{3.1.2}$$

where $\theta_{\mathbf{r}_\lambda}$ and $\phi_{\mathbf{r}_\lambda}$ are the polar coordinates of $\mathbf{r}_\lambda$ with respect to the space-fixed **Z** axis. (The finite range in r_λ of the diatomic wavefunction $\varphi_{\lambda v_\lambda j_\lambda m_\lambda}^{\mathrm{sf}}$ ensures that

the terms in the sum over λ for which $\lambda \neq \bar{\lambda}$ go to zero.) The three quantum numbers $v_\lambda j_\lambda m_\lambda$ specify the state of the asymptotic diatom, with v_λ labeling the vibrational levels, j_λ the rotational angular momentum (the square of the diatomic angular momentum is $j_\lambda(j_\lambda+1)\hbar^2$) and m_λ the orientation of the diatom with respect to the space fixed $\mathbf{Z}$ axis (the projection of the diatomic angular momentum on the $\mathbf{Z}$ axis is $m_\lambda\hbar$). The quantum numbers v_λ, j_λ and m_λ are labeled with the subscript λ to differentiate between the states of distinguishable diatomic molecules. For notational convenience, we will drop these labels when all such indices in an expression label functions in the same arrangement channel. The sum over the diatomic quantum numbers is over all open and closed states for the system. (The state $\lambda' v'_{\lambda'} j'_{\lambda'} m'_{\lambda'}$ is an open state, since it is the initial state of the diatom.)

An alternate form of the physical asymptotic conditions in the body-fixed helicity representation is given by:[2]

$$\begin{aligned}\Psi_{\bar{\lambda}}^{\lambda' v'_{\lambda'} j'_{\lambda'} m'_{\lambda'}} &\underset{R_{\bar{\lambda}}\to\infty}{\sim} e^{i\mathbf{k}_{\lambda' v'_{\lambda'} j'_{\lambda'}}\cdot\mathbf{R}_{\lambda'}}\varphi^{\mathrm{sf}}_{\lambda' v'_{\lambda'} j'_{\lambda'} m'_{\lambda'}}(\mathbf{r}_{\lambda'}) \\ &+\sum_{\lambda}\sum_{v_\lambda j_\lambda \Omega_\lambda} f_{\lambda v_\lambda j_\lambda \Omega_\lambda}^{\lambda' v'_{\lambda'} j'_{\lambda'} m'_{\lambda'}}(\theta_\lambda,\phi_\lambda)\frac{e^{ik_{\lambda v_\lambda j_\lambda}R_\lambda}}{R_\lambda}\varphi^{\mathrm{bf}}_{\lambda v_\lambda j_\lambda \Omega_\lambda}(\mathbf{r}_\lambda)\end{aligned} \tag{3.1.3}$$

where the body-fixed expression for the diatomic wavefunction is given by

$$\varphi^{\mathrm{bf}}_{\lambda v_\lambda j_\lambda \Omega_\lambda}(\mathbf{r}_\lambda) = Y_{j_\lambda}^{\Omega_\lambda}(\gamma_\lambda,\psi_\lambda)\frac{\phi_{\lambda v_\lambda j_\lambda}(r_\lambda)}{r_\lambda} \tag{3.1.4}$$

and the quantum number Ω_λ labels the orientation of the diatom with respect to the body-fixed $\mathbf{z}_\lambda$ axis so that the projection of the diatomic angular momentum on the $\mathbf{z}_\lambda$ axis is $\Omega_\lambda\hbar$. (In this representation, the axes of quantization for the initial and final states of the system are taken to be the directions of the incident and outgoing wavevectors, respectively; the space-fixed $\mathbf{Z}$ axis is chosen to be in the direction of the incident wavevector for simplicity.) As in the space-fixed representation, the sums over the v_λ and j_λ quantum numbers include both open and closed channels.

In this paper we will be interested in calculating the helicity representation scattering amplitudes $f_{\lambda v_\lambda j_\lambda \Omega_\lambda}^{\lambda' v'_{\lambda'} j'_{\lambda'} m'_{\lambda'}}(\theta_\lambda,\phi_\lambda)$. They can be related to the space-fixed

ones with the help of the expression relating the spherical harmonics in the two coordinate systems:[76]

$$Y_j^m(\theta_{r_\lambda}, \phi_{r_\lambda}) = \sum_{\Omega=-j}^{j} D^j_{m\Omega}(\phi_\lambda, \theta_\lambda, 0) Y_j^\Omega(\gamma_\lambda, \psi_\lambda) \tag{3.1.5}$$

Substitution of (3.1.5) into (3.1.2), substituting the result into the second term of (3.1.1) and using (3.1.4) to bring it into the same form as (3.1.3) yields the relation

$$\hat{f}^{\lambda' v'_\lambda, j'_\lambda, m'_{\lambda'}}_{\lambda v_\lambda j_\lambda m_\lambda}(\theta_\lambda, \phi_\lambda) = \sum_{\Omega_\lambda} D^j_{m_\lambda \Omega_\lambda}(\phi_\lambda, \theta_\lambda, 0) f^{\lambda' v'_\lambda, j'_\lambda, m'_{\lambda'}}_{\lambda v_\lambda j_\lambda \Omega_\lambda}(\theta_\lambda, \phi_\lambda) \tag{3.1.6}$$

The wavefunction of (3.1.3) may also be expanded in terms of functions which are eigenfunctions of $\hat{J}^2$, $\hat{J}_Z$, and the projection operators for the P_p permutation group:

$$\Psi^{\lambda' v'_\lambda, j'_\lambda, m'_{\lambda'}}_{\bar{\lambda}} = \sum_{J=0}^{\infty} \sum_{M=-J}^{J} \sum_{\Gamma} \sum_{k} C^{JM\Gamma_k \lambda' v'_\lambda, j'_\lambda, m'_{\lambda'}} \Psi^{JM\Gamma_k \lambda' v'_\lambda, j'_\lambda, m'_{\lambda'}}_{\bar{\lambda}} \tag{3.1.7}$$

3.2 Formalism for Asymptotic Functions - Body-fixed R and S Matrices

For purposes of comparison of the asymptotic forms with the calculated LHSF, we need to determine an expression for the asymptotic form in body-fixed coordinates. In the asymptotic region, the form of these functions is known; since the incident or ejected atom is no longer interacting with the diatomic species, the wavefunction consists of a diatomic molecule wavefunction multiplied by the wavefunction of an atom moving freely in space. We define the asymptotic form for a partial wave body-fixed solution to the Schrödinger equation for an atom-diatom collision at energies below dissociation of the diatom to be

$$\Psi^{JM,n'}_{\lambda} \widetilde{\underset{R_\lambda \to \infty}{}} \sum_{\Omega_\lambda=-J}^{J} \sum_{j_\lambda=|\Omega_\lambda|}^{j^{max}_\lambda} \mathcal{D}^{JM}_{j_\lambda \Omega_\lambda}(\theta_\lambda, \phi_\lambda, \gamma_\lambda, \psi_\lambda) \sum_{v_\lambda=0}^{v^{max}_\lambda} \frac{\phi_{\lambda v_\lambda j_\lambda}(r_\lambda)}{r_\lambda R_\lambda} G^{J,n'}_{\lambda v_\lambda j_\lambda \Omega_\lambda}(R_\lambda) \tag{3.2.1}$$

where λ is now fixed but arbitrary. As previously mentioned, the λ label will be dropped from the v_λ and j_λ indices unless more than one arrangement channel is involved; this applies also to the quantum number Ω_λ.

In equation (3.2.1), the function $\mathcal{D}^{JM}_{j\Omega}$ is defined as

$$\mathcal{D}^{JM}_{j\Omega} = \left(\frac{2J+1}{8\pi^2}\right)^{\frac{1}{2}} D^J_{M\Omega}(\phi_\lambda, \theta_\lambda, \psi_\lambda)\mathcal{P}^\Omega_j(\cos\gamma_\lambda). \tag{3.2.2}$$

with Wigner rotation functions[76] $D^J_{M\Omega}$ and normalized[2] associated Legendre functions $\mathcal{P}^\Omega_j$. The sums over j and v in (3.2.1) formally include all bound states of the diatom, but in practice these sums are truncated to exclude the highest energy states, which can be assumed to have zero amplitude. The function $\phi_{\lambda vj}(r_\lambda)$ is the radial part of the bound state diatomic wavefunction (3.1.4), which is the eigenfunction of the diatomic hamiltonian

$$\hat{h}^\lambda_d = -\frac{\hbar^2}{2\mu}\nabla^2_{\mathbf{r}_\lambda} + v^\lambda_d(r_\lambda) \tag{3.2.3}$$

with energy $e_{\lambda vj}$, where $v^\lambda_d(r_\lambda)$ is the interaction potential of the atoms A_ν and A_κ when isolated from A_λ. The group of indices λvj which specify the asymptotic diatom and its state will occur together frequently; to simplify the notation we define $\vec{\lambda} \equiv \{\lambda v_\lambda j_\lambda\}$, and will use this composite index where appropriate. Due to the finite range of the functions $\phi_{\vec{\lambda}}$ in r_λ, there is no overlap between the functions in different arrangement channels as $\rho \to \infty$; the normalization for these functions is

$$\int_0^{r_{max}} \phi_{\lambda v_\lambda j}(r_\lambda)\phi_{\lambda' v'_{\lambda'} j}(r_{\lambda'})dr_\lambda = \delta^{\lambda' v'_{\lambda'}}_{\lambda v_\lambda} \tag{3.2.4}$$

The coefficients $G^{J,n'}_{\vec{\lambda}\Omega}(R_\lambda)$ are given by[2]

$$G^{J,n'}_{\vec{\lambda}\Omega}(R_\lambda) = |v_{\vec{\lambda}}|^{-\frac{1}{2}} \sum_{\Omega''=-J}^{J} \left[S^{J,\Omega''}_{\vec{\lambda}\Omega}(R_\lambda)A^{J,n'}_{\vec{\lambda}\Omega''} + C^{J,\Omega''}_{\vec{\lambda}\Omega}(R_\lambda)B^{J,n'}_{\vec{\lambda}\Omega''}\right] \tag{3.2.5}$$

where the term $v_{\vec{\lambda}}$ is the channel velocity, defined by

$$v_{\vec{\lambda}} = \frac{\hbar}{\mu}k_{\vec{\lambda}}; \quad k^2_{\vec{\lambda}} = \frac{2\mu}{\hbar^2}(E - e_{\vec{\lambda}}); \tag{3.2.6}$$

For open states, *i.e.*, those states with $E > e_{\vec{\lambda}}$, the resulting wavenumber is real and positive; for closed states ($E < e_{\vec{\lambda}}$) the wavenumber is positive imaginary, so that the parts of the wavefunction in equation (3.2.1) which are associated to closed states of the system decay exponentially. The sum over the diatomic quantum numbers in equation (3.2.1) is over all open and closed states for the system.

The R_λ dependent parts of $G^{J,n'}_{\vec{\lambda}\Omega}(R_\lambda)$ have the form (in notation slightly modified from that of Schatz and Kuppermann[2])

$$\mathcal{X}^{J,\Omega''}_{\vec{\lambda}\Omega}(R_\lambda) = (-1)^{\Omega+\Omega''} |k_{\vec{\lambda}}| R_\lambda \sum_\ell C(Jj\ell;\Omega'',-\Omega'',0) C(Jj\ell;\Omega,-\Omega,0) \bar{\mathcal{X}}^{J,\ell}_{\vec{\lambda}}(R_\lambda) \tag{3.2.7}$$

in which the symbol $\mathcal{X}$ may stand for either $\mathcal{S}$ or $\mathcal{C}$. At this point, one can either choose to represent the wavefunction in terms of traveling waves (the scattering matrix formalism) or in terms of standing waves (the reactance matrix formalism).[52,53] In the scattering matrix formalism, the functions $\bar{\mathcal{S}}^{J,\ell}_{\vec{\lambda}}(R_\lambda)$ and $\bar{\mathcal{C}}^{J,\ell}_{\vec{\lambda}}(R_\lambda)$ corresponding to the $\bar{\mathcal{X}}$ in the right hand side of (3.2.7) are given by

$$\begin{aligned}
\bar{\mathcal{S}}^{J,\ell}_{\vec{\lambda}}(R_\lambda)[S] &= \begin{cases} -\imath \exp\left[\imath\tfrac{\pi}{2}(J+j-\ell)\right] h^{(2)}_\ell(k_{\vec{\lambda}}R_\lambda) & \text{open} \\ 2i_\ell(|k_{\vec{\lambda}}|R_\lambda) & \text{closed} \end{cases} \\
\bar{\mathcal{C}}^{J,\ell}_{\vec{\lambda}}(R_\lambda)[S] &= \begin{cases} \imath \exp\left[-\imath\tfrac{\pi}{2}(J+j-\ell)\right] h^{(1)}_\ell(k_{\vec{\lambda}}R_\lambda) & \text{open} \\ \frac{2}{\pi}\kappa_\ell(|k_{\vec{\lambda}}|R_\lambda) & \text{closed} \end{cases}
\end{aligned} \tag{3.2.8}$$

where the functions $h^{(1)}_\ell$ and $h^{(2)}_\ell$ are the spherical Bessel functions of the third kind and i_ℓ and κ_ℓ are modified spherical Bessel functions of the first and third kinds, respectively.[77] At sufficiently large values of R_λ the modified spherical Bessel functions reduce to sums of exponentials, and the sums over ℓ in (3.2.7) and Ω'' in (3.2.5) may be performed to yield

$$G^{J,n'}_{\vec{\lambda}\Omega}(R_\lambda)[S] = |v_{\vec{\lambda}}|^{-\frac{1}{2}} \begin{cases} \left\{ e^{-\imath\left(k_{\vec{\lambda}}R_\lambda - \frac{\pi}{2}(j+J)\right)} A^{J,n'}_{\vec{\lambda}\Omega}[S] \right. & \\ \qquad \left. - e^{\imath\left(k_{\vec{\lambda}}R_\lambda - \frac{\pi}{2}(j+J)\right)} B^{J,n'}_{\vec{\lambda}\Omega}[S] \right\} & \text{open} \\ \left\{ e^{|k_{\vec{\lambda}}|R_\lambda} A^{J,n'}_{\vec{\lambda}\Omega}[S] + e^{-|k_{\vec{\lambda}}|R_\lambda} B^{J,n'}_{\vec{\lambda}\Omega}[S] \right\} & \text{closed} \end{cases} \tag{3.2.9}$$

where $[S]$ denotes that this is the asymptotic form appropriate for generating the scattering matrix $\mathbf{S}^J$. From the matrices of coefficients

$$[\mathbf{A}^J_\lambda]^{n'}_{vj\Omega}[S] = A^{J,n'}_{\vec{\lambda}\Omega}[S]; \quad [\mathbf{B}^J_\lambda]^{n'}_{vj\Omega}[S] = B^{J,n'}_{\vec{\lambda}\Omega}[S] \tag{3.2.10}$$

one constructs the square matrices

$$\mathbf{A}^J[S] = \begin{bmatrix} \mathbf{A}^J_\alpha \\ \mathbf{A}^J_\beta \\ \mathbf{A}^J_\gamma \end{bmatrix} \qquad \mathbf{B}^J[S] = \begin{bmatrix} \mathbf{B}^J_\alpha \\ \mathbf{B}^J_\beta \\ \mathbf{B}^J_\gamma \end{bmatrix} \tag{3.2.11}$$

which have contributions from all of the arrangement channels. $\mathbf{S}^J$ is found through use of the formula

$$\mathbf{S}^J = \mathbf{B}^J[S]\left(\mathbf{A}^J[S]\right)^{-1} \tag{3.2.12}$$

The scattering matrix is unique, *i.e.*, independent of the particular choice of coefficient matrices **A**[S] and **B**[S], and the part relating open states (which will be called the open part $^o\mathbf{S}$ of the scattering matrix) is unitary and symmetric.[52] We will mainly be interested in the open part of the scattering matrix, since asymptotically only the open states may be populated.

In the reactance matrix formalism, the functions $\bar{S}^{J,\ell}_{\vec{\lambda}}(R_\lambda)$ and $\bar{C}^{J,\ell}_{\vec{\lambda}}(R_\lambda)$ corresponding to the $\bar{\mathcal{X}}$ in the right hand side of (3.2.7) are given by

$$\bar{S}^{J,\ell}_{\vec{\lambda}}(R_\lambda)[R] = \begin{cases} j_\ell(k_{\vec{\lambda}}R_\lambda)\cos\left[\frac{\pi}{2}(J+j-\ell)\right] + \eta_\ell(k_{\vec{\lambda}}R_\lambda)\sin\left[\frac{\pi}{2}(J+j-\ell)\right] & \text{open} \\ 2i_\ell(|k_{\vec{\lambda}}|R_\lambda) & \text{closed} \end{cases}$$

$$\bar{C}^{J,\ell}_{\vec{\lambda}}(R_\lambda)[R] = \begin{cases} j_\ell(k_{\vec{\lambda}}R_\lambda)\sin\left[\frac{\pi}{2}(J+j-\ell)\right] - \eta_\ell(k_{\vec{\lambda}}R_\lambda)\cos\left[\frac{\pi}{2}(J+j-\ell)\right] & \text{open} \\ \frac{2}{\pi}\kappa_\ell(|k_{\vec{\lambda}}|R_\lambda) & \text{closed} \end{cases} \tag{3.2.13}$$

in which j_ℓ and η_ℓ are spherical Bessel functions of the first and second kind, respectively.[77] At sufficiently large R_λ the spherical Bessel functions reduce to trigonometric functions, and we can write, after performing the sum over ℓ in (3.2.7)

and Ω'' in (3.2.5),

$$G^{J,n'}_{\vec{\lambda}\Omega}(R_\lambda)[R] = |v_{\vec{\lambda}}|^{-\frac{1}{2}} \begin{cases} \left\{ \sin\left(k_{\vec{\lambda}}R_\lambda - \frac{\pi}{2}(J+j)\right) A^{J,n'}_{\vec{\lambda}\Omega}[R] \right. & \text{open} \\ \left. \quad + \cos\left(k_{\vec{\lambda}}R_\lambda - \frac{\pi}{2}(J+j)\right) B^{J,n'}_{\vec{\lambda}\Omega}[R] \right\} & \\ \left\{ e^{|k_{\vec{\lambda}}|R_\lambda} A^{J,n'}_{\vec{\lambda}\Omega}[R] + e^{-|k_{\vec{\lambda}}|R_\lambda} B^{J,n'}_{\vec{\lambda}\Omega}[R] \right\} & \text{closed} \end{cases} \tag{3.2.14}$$

where $[R]$ denotes that this is the asymptotic form appropriate for generating the reactance matrix $\mathbf{R}^J$. From the matrices of coefficients $\mathbf{A}^J[R]$ and $\mathbf{B}^J[R]$ (constructed in the same way as in equation (3.2.11) for the matrices for the scattering formalism), we obtain $\mathbf{R}^J$ by using the expression

$$\mathbf{R}^J = \mathbf{B}^J[R]\left(\mathbf{A}^J[R]\right)^{-1} \tag{3.2.15}$$

The reactance matrix is unique, real, and the open part $^{o}\mathbf{R}$ is symmetric.[52]

We will use the reactance matrix formalism due to the numerical convenience of performing real arithmetic. Physical quantities are more closely related to the scattering matrix; however, the $^{o}\mathbf{S}$ matrix, which is all that is needed for determination of the physical properties of the system, is easily obtained from the $^{o}\mathbf{R}$ matrix using the expression[52]

$$^{o}\mathbf{S}^J = \left(\mathbf{I} + \imath\,^{o}\mathbf{R}^J\right)\left(\mathbf{I} - \imath\,^{o}\mathbf{R}^J\right)^{-1} \tag{3.2.16}$$

3.3 Introduction of Permutation and Inversion Symmetries to the Formalism

Since the problem of generating LHSF and propagating the solutions of the Schrödinger equation in the ρ variable has been expressed in terms of eigenfunctions having inversion parity and belonging to irreducible representations (IR) of the permutation group of the system, it will be convenient to express the asymptotic wavefunction in these terms as well. This has the further advantage that since the inversion and projection operators, like the angular momentum operators, are simultaneously knowable with the hamiltonian, the hamiltonian will not couple functions with different parity or symmetry, and scattering matrix elements between these functions will be equal to zero. Therefore, if the index n' includes labels specifying inversion parity and IR, the matrix of coefficients $\mathbf{G}$ can be seen to be block diagonal in Π and Γ, and we will be able to solve for each symmetry-parity combination individually. In addition, functions which have symmetry Γ_i are orthogonal to functions with symmetry Γ_k for $k \neq i$; thus the coefficient submatrix for the doubly-degenerate E IR in the P_3 symmetry is itself block diagonal in the index i. For this particular case, we have shown in (I) that the $\mathbf{S}$ matrix generated by the E functions even with respect to $\gamma_\alpha = \frac{\pi}{2}$ is the same as that generated by the E functions odd with respect to that angle, and therefore it is only necessary to propagate one of the two functions determined by the E symmetry projection operators $\hat{P}^{\Gamma}_{kk}$ (*i.e.*, either $k = 1$ or $k = 2$ but not both) to obtain all the scattering information for this IR.

There are three possible permutation groups for three particles, depending on the number of these particles which are indistinguishable, and the number of operators needed in each case differs. These three permutation groups are: P_1, which corresponds to a system in which all three particles A, B and C are distinguishable, and the only permutation operation under which the hamiltonian is invariant is the identity; P_2, for a system that has two indistinguishable particles (the AB_2

system), and for which the hamiltonian is invariant under the identity and one two-particle permutation; and P_3, for a system with three indistinguishable particles (the A_3 system), with six permutations under which the hamiltonian is invariant: the identity, two three-particle permutations and three two-particle permutations. To distinguish between the different arrangement channels, we have introduced the index τ, which takes on the "value" A in the α channel (*i.e.*, the A + BC channel), B in the β channel (*i.e.*, the B + AC channel) and C in the γ channel (*i.e.*, the C + AB channel) for an ABC system (P_1). In the systems AB_2 or ABB′ with B and B′ indistinguishable (P_2) it is limited to the values A ($\alpha \equiv$ A + BC channel) and B (both $\beta \equiv$ B + AB′ and $\gamma \equiv$ B′ + AB channel), and for an A_3 or AA′A″ system with all three atoms indistinguishable (P_3), it is limited to just the value A. Thus τ will label a set of indistinguishable channels, and specific linear combinations of functions in each member of these sets of channels will be eigenfunctions of the projection operators $\hat{P}^{\Gamma}_{kk}$ and will consequently belong to the Γ_k IR. The symmetry between the channels allows us to use the permutation operators for P_p (where p can be 1, 2 or 3) to find the form of the wavefunction in all channels of type τ in terms of any one of these channels, using the methods discussed in (I). For the cases $p = 2, 3$, it also imposes certain conditions on the coefficients of the distinguishable particle wavefunction to ensure symmetry, and it will be seen that it is only necessary to explicitly consider a single channel out of each set of channels of type τ. We have

$$\Psi_{\lambda}^{JM,n'} = \sum_{\Gamma}\sum_{k} \Psi_{\tau}^{JM\Gamma_k,n'}; \quad \Psi_{\tau}^{JM\Gamma_k,n'} = \hat{P}^{\Gamma}_{kk}\Psi_{\lambda}^{JM,n'} \tag{3.3.1}$$

where the value of τ will depend on the asymptotic atom A_λ. For the P_1 group, the $\Psi_{\tau}^{JM\Gamma_k,n'}$ are:

$$\left.\begin{aligned} \Psi_{\tau=\mathrm{A}}^{JM\{\Gamma_k=A\},n'} &= \Psi_{\alpha}^{JM,n'} \\ \Psi_{\tau=\mathrm{B}}^{JM\{\Gamma_k=A\},n'} &= \Psi_{\beta}^{JM,n'} \\ \Psi_{\tau=\mathrm{C}}^{JM\{\Gamma_k=A\},n'} &= \Psi_{\gamma}^{JM,n'} \end{aligned}\right\} P_1 \tag{3.3.2}$$

The "symmetrized" functions $\Psi_{\tau}^{JM\Gamma_k,n'}$ in this case are exactly the same as the functions defined in each arrangement channel; the notation is given here as it will

be used in the general formalism. In the case of the P_2 group, there are two distinct sets of arrangement channels, and the symmetrized asymptotic wavefunctions may be classified in terms of each of these two sets by the τ label. Therefore we have for equation (3.3.1):

$$\left.\begin{aligned}
\Psi_{\tau=\mathrm{A}}^{JM\{\Gamma_k=A'\},n'} &= \hat{P}^{A'}\Psi_{\alpha}^{JM,n'} \\
\Psi_{\tau=\mathrm{A}}^{JM\{\Gamma_k=A''\},n'} &= \hat{P}^{A''}\Psi_{\alpha}^{JM,n'} \\
\Psi_{\tau=\mathrm{B}}^{JM\{\Gamma_k=A'\},n'} &= \hat{P}^{A'}\Psi_{\beta}^{JM,n'} \\
\Psi_{\tau=\mathrm{B}}^{JM\{\Gamma_k=A''\},n'} &= \hat{P}^{A''}\Psi_{\beta}^{JM,n'}
\end{aligned}\right\} P_2 \tag{3.3.3}$$

and the inverse expressions are

$$\begin{aligned}
\Psi_{\alpha}^{JM,n'} &= \Psi_{\mathrm{A}}^{JMA',n'} + \Psi_{\mathrm{A}}^{JMA'',n'} \\
\Psi_{\beta}^{JM,n'} &= \Psi_{\mathrm{B}}^{JMA',n'} + \Psi_{\mathrm{B}}^{JMA'',n'} \\
\Psi_{\gamma}^{JM,n'} &= \Psi_{\mathrm{B}}^{JMA',n'} - \Psi_{\mathrm{B}}^{JMA'',n'}
\end{aligned} \tag{3.3.4}$$

Finally, for the P_3 group all arrangement channels are indistinguishable, giving

$$\left.\begin{aligned}
\Psi_{\tau=\mathrm{A}}^{JM\{\Gamma_k=A_1\},n'} &= \hat{P}^{A_1}\Psi_{\beta}^{JM,n'} \\
\Psi_{\tau=\mathrm{A}}^{JM\{\Gamma_k=A_2\},n'} &= \hat{P}^{A_2}\Psi_{\beta}^{JM,n'} \\
\Psi_{\tau=\mathrm{A}}^{JM\{\Gamma_k=E_k\},n'} &= \hat{P}^{E}_{kk}\Psi_{\beta}^{JM,n'}
\end{aligned}\right\} P_3 \tag{3.3.5}$$

We have operated here on the β channel function (rather than on the α channel one) for the reasons discussed in (I). The inverse relation is then

$$\Psi_{\beta}^{JM,n'} = \Psi_{\mathrm{A}}^{JMA_1,n'} + \Psi_{\mathrm{A}}^{JMA_2,n'} + \sum_{k}\Psi_{\mathrm{A}}^{JME_k,n'} \tag{3.3.6}$$

The expressions for $\Psi_{\alpha}^{JM,n'}(\rho,\zeta_\alpha)$ and $\Psi_{\gamma}^{JM,n'}(\rho,\zeta_\gamma)$ can be obtained by using the three-particle (cyclic) permutation operators of the P_3 group on the $\Psi_{\beta}^{JM,n'}(\rho,\zeta_\beta)$, the effect of which is to replace the index β by α or γ.

In order to determine the symmetry properties of the distinguishable atom reactance and scattering matrices, we begin by substitution of equation (3.2.5) into equation (3.2.1). We replace the index n' by the set of indices $\lambda' v'_{\lambda'} j'_{\lambda'} \Omega'_{\lambda'}$, and choose the coefficients

$$A^{J,\lambda' v'_{\lambda'} j'_{\lambda'} \Omega'_{\lambda'}}_{\lambda v_\lambda j_\lambda \Omega''_\lambda} = \delta^{\lambda' v'_{\lambda'} j'_{\lambda'} \Omega'_{\lambda'}}_{\lambda v_\lambda j_\lambda \Omega''_\lambda} \qquad B^{J,\lambda' v'_{\lambda'} j'_{\lambda'} \Omega'_{\lambda'}}_{\lambda v_\lambda j_\lambda \Omega''_\lambda} = W^{J\lambda' v'_{\lambda'} j'_{\lambda'} -\Omega'_{\lambda'}}_{\lambda v_\lambda j_\lambda \Omega''_\lambda} \tag{3.3.7}$$

where W may stand for either R or S. The choice of index $-\Omega'_{\lambda'}$ in the W function will be seen to make the scattering matrices become the identity matrix and the differential cross sections of section 4 go to zero in the absence of a potential; it stems from the fact that for the incident wave of the system, $\mathbf{Z}$, which is the projection axis associated with the quantum number $m'_{\lambda'}$, and $\mathbf{z}_{\lambda'}$, which is the projection axis associated with the quantum number $\Omega'_{\lambda'}$, are antiparallel. The corresponding $\mathbf{R}$ or $\mathbf{S}$ matrices are called body-fixed helicity representation matrices. The resulting equation is

$$\Psi_{\lambda}^{JM,\lambda' v'_{\lambda'} j'_{\lambda'} \Omega'_{\lambda'}} \widetilde{\underset{R_{\lambda}\to\infty}{}} \sum_{\Omega_{\lambda}=-J}^{J} \sum_{j_{\lambda}=|\Omega_{\lambda}|}^{j_{\lambda}^{max}} \mathcal{D}^{JM}_{j_{\lambda}\Omega_{\lambda}}(\theta_{\lambda},\phi_{\lambda},\gamma_{\lambda},\psi_{\lambda}) \sum_{v_{\lambda}=0}^{v_{\lambda}^{max}} \frac{\phi_{\vec{\lambda}}(r_{\lambda})}{r_{\lambda}R_{\lambda}} \times$$

$$|v_{\vec{\lambda}}|^{-\frac{1}{2}} \sum_{\Omega''_{\lambda}=-J}^{J} \left(\mathcal{S}^{J,\Omega''_{\lambda}}_{\vec{\lambda}\Omega_{\lambda}}(R_{\lambda}) \delta^{\lambda' v'_{\lambda'} j'_{\lambda'} \Omega'_{\lambda'}}_{\lambda v_{\lambda} j_{\lambda} \Omega''_{\lambda}} + \mathcal{C}^{J,\Omega''_{\lambda}}_{\vec{\lambda}\Omega_{\lambda}}(R_{\lambda}) W^{J\lambda' v'_{\lambda'} j'_{\lambda'} -\Omega'_{\lambda'}}_{\lambda v_{\lambda} j_{\lambda} \Omega''_{\lambda}} \right) \tag{3.3.8}$$

The functions $\mathcal{S}$ and $\mathcal{C}$ depend on the choice of $\mathbf{W}$, and are given in equation (3.2.8) for the $\mathbf{S}$ matrix and in (3.2.13) for the $\mathbf{R}$ matrix. The relationship between (3.2.1) and (3.3.8) is

$$\Psi_{\lambda}^{JM,n'} = \sum_{\lambda' v' j' \Omega'} \Psi_{\lambda}^{JM,\lambda' v' j' \Omega'} A^{J,n'}_{\lambda' v' j' \Omega'} \tag{3.3.9}$$

where $A^{J,n'}_{\lambda' v' j' \Omega'}$ is the general one of (3.2.1) rather than the particular one of (3.3.7).

The action of the various permutation operators which appear as part of the projection operator $\hat{P}^{\Gamma}_{kk}$ on a general function was given in (I), as was the result of applying them to the $\mathcal{D}^{JM}_{j\Omega}$. With this information, we can write the corresponding symmetrized asymptotic wavefunction as

$$\Psi_{\vec{\lambda}}^{JM\Gamma_k,\tau' v'_{\tau'} j'_{\tau'} \Omega'_{\tau'}} \widetilde{\underset{R_{\vec{\lambda}}\to\infty}{}} \sum_{\tau} \sum_{\lambda} \sum_{\Omega_{\tau}=-J}^{J} \sum_{j_{\tau}=|\Omega_{\tau}|}^{j_{\tau}^{max}} c^{\Gamma_k}_{\tau\lambda j_{\tau}} \mathcal{D}^{JM}_{j_{\tau}\Omega_{\tau}}(\theta_{\lambda},\phi_{\lambda},\gamma_{\lambda},\psi_{\lambda}) \sum_{v_{\tau}=0}^{v_{\tau}^{max}} \times$$

$$|v_{\vec{\tau}}|^{-\frac{1}{2}} \frac{\phi_{\vec{\tau}}(r_{\lambda})}{r_{\lambda}R_{\lambda}} \sum_{\Omega''_{\tau}=-J}^{J} \left(\mathcal{S}^{J,\Omega''_{\tau}}_{\vec{\tau}\Omega_{\tau}}(R_{\lambda}) \delta^{\tau' v'_{\tau'} j'_{\tau'} \Omega'_{\tau'}}_{\tau v_{\tau} j_{\tau} \Omega''_{\tau}} + \mathcal{C}^{J,\Omega''_{\tau}}_{\vec{\tau}\Omega_{\tau}}(R_{\lambda}) W^{J\Gamma\tau' v'_{\tau'} j'_{\tau'} -\Omega'_{\tau'}}_{\tau v_{\tau} j_{\tau} \Omega''_{\tau}} \right) \tag{3.3.10}$$

in which we have used the fact that, since the arrangement channels of type τ are all identical, the form of the functions in these arrangement channels must all be the same, and therefore we may replace the label λ in these functions with the label τ. The composite index $\vec{\tau}$ is defined similarly to $\vec{\lambda}$, *i.e.*, $\vec{\tau} \equiv \{\tau v_\tau j_\tau\}$. The coefficients $c^{\Gamma_k}_{\tau\lambda j_\tau}$ are as given in (I); they are defined so that a summation over λ will result in non-zero contributions from all channels of type τ and zero contributions from channels of types $\tau' \neq \tau$, and a summation over both λ and τ will result in a single term from each arrangement channel. (A fuller justification of the summation over τ is given for the asymptotic form of (3.1.1) in appendix A; the arguments used for the latter case are completely applicable to (3.3.10) as well.) The λ channel coordinates are considered to be functions of one of the sets of $\bar{\lambda}$ coordinates, where λ is now a summation index and takes on the values $\{\alpha,\beta,\gamma\}$ and $\bar{\lambda}$ is an arbitrary but otherwise fixed value corresponding to the asymptotic arrangement channel, *i.e.*, $\bar{\lambda}$ is either α, β or γ. For example, if we choose $\bar{\lambda} = \beta$, then the α and γ coordinates are considered to be functions of the β coordinates, for a given configuration of the system. At infinite hyperradius the functions in different arrangement channels do not overlap, and thus wherever any of the λ channel functions is non-zero the ν and κ functions will be exactly zero if $\lambda\nu\kappa$ is a cyclic permutation of $\alpha\beta\gamma$.

Applying the permutation operators to the function (3.3.8) for each value of λ results in a new function localized in an arrangement channel λ'', where the λ and λ'' channels are of the same type τ and λ may or may not equal λ''; comparing this result with the original functional form (3.3.8) after replacement of λ'' by λ yields the symmetry properties of the reactance and scattering matrices. In the case of the P_2 group, we get from the operator which permutes β and γ the following distinguishable atom symmetry properties:

$$\left.\begin{aligned}
W^{\alpha v'_A j'_A \Omega'_A}_{\alpha v_A j_A \Omega_A} &= (-1)^{j_A + j'_A} W^{\alpha v'_A j'_A \Omega'_A}_{\alpha v_A j_A \Omega_A} \\
W^{\beta v'_B j'_B \Omega'_B}_{\beta v j \Omega} &= (-1)^{j_B + j'_B} W^{\gamma v'_B j'_B \Omega'_B}_{\gamma v_B j_B \Omega_B} \\
W^{\beta v'_B j'_B \Omega'_B}_{\gamma v_B j_B \Omega_B} &= (-1)^{j_B + j'_B} W^{\gamma v'_B j'_B \Omega'_B}_{\beta v_B j_B \Omega_B} \\
W^{\beta v'_B j'_B \Omega'_B}_{\alpha v_A j_A \Omega_A} &= (-1)^{j_A + j'_B} W^{\gamma v'_B j'_B \Omega'_B}_{\alpha v_A j_A \Omega_A} \\
W^{\alpha v'_A j'_A \Omega'_A}_{\beta v_B j_B \Omega_B} &= (-1)^{j_B + j'_A} W^{\alpha v'_A j'_A \Omega'_A}_{\gamma v_B j_B \Omega_B}
\end{aligned}\right\} P_2 \qquad (3.3.11)$$

By comparison of equations (3.3.8) and (3.3.10) and using the relations of equation (3.3.11), we may derive the following relations between the irreducible representation **R** and **S** matrices and the corresponding distinguishable particle matrices:

$$\begin{aligned}
W^{A' A v'_A j'_A \Omega'_A}_{A v_A j_A \Omega_A} &= \begin{cases} W^{\alpha v'_A j'_A \Omega'_A}_{\alpha v_A j_A \Omega_A} & j_A \text{ and } j'_A \text{ even} \\ 0 & j_A \text{ or } j'_A \text{ odd} \end{cases} \\
W^{A'' A v'_A j'_A \Omega'_A}_{A v_A j_A \Omega_A} &= \begin{cases} W^{\alpha v'_A j'_A \Omega'_A}_{\alpha v_A j_A \Omega_A} & j_A \text{ and } j'_A \text{ odd} \\ 0 & j_A \text{ or } j'_A \text{ even} \end{cases}
\end{aligned} \qquad (3.3.12)$$

$$\begin{aligned}
W^{A' A v'_A j'_A \Omega'_A}_{B v_B j_B \Omega_B} &= \begin{cases} \sqrt{2} W^{\alpha v'_A j'_A \Omega'_A}_{\beta v_B j_B \Omega_B} & j'_A \text{ even} \\ 0 & j'_A \text{ odd} \end{cases} \\
W^{A'' A v'_A j'_A \Omega'_A}_{B v_B j_B \Omega_B} &= \begin{cases} \sqrt{2} W^{\alpha v'_A j'_A \Omega'_A}_{\beta v_B j_B \Omega_B} & j'_A \text{ odd} \\ 0 & j'_A \text{ even} \end{cases} \\
W^{A' B v'_B j'_B \Omega'_B}_{A v_A j_A \Omega_A} &= \begin{cases} \sqrt{2} W^{\beta v'_B j'_B \Omega'_B}_{\alpha v_A j_A \Omega_A} & j_A \text{ even} \\ 0 & j_A \text{ odd} \end{cases} \\
W^{A'' B v'_B j'_B \Omega'_B}_{A v_A j_A \Omega_A} &= \begin{cases} \sqrt{2} W^{\beta v'_B j'_B \Omega'_B}_{\alpha v_A j_A \Omega_A} & j_A \text{ odd} \\ 0 & j_A \text{ even} \end{cases}
\end{aligned} \qquad (3.3.13)$$

$$\begin{aligned}
W^{A' B v'_B j'_B \Omega'_B}_{B v_B j_B \Omega_B} &= W^{\beta v'_B j'_B \Omega'_B}_{\beta v_B j_B \Omega_B} + (-1)^{j'} W^{\gamma v'_B j'_B \Omega'_B}_{\beta v_B j_B \Omega_B} \\
W^{A'' B v'_B j'_B \Omega'_B}_{B v_B j_B \Omega_B} &= W^{\beta v'_B j'_B \Omega'_B}_{\beta v_B j_B \Omega_B} - (-1)^{j'} W^{\gamma v'_B j'_B \Omega'_B}_{\beta v_B j_B \Omega_B}
\end{aligned} \qquad (3.3.14)$$

The inverse of these relations is

$$
\begin{aligned}
W^{\alpha v'_A j'_A \Omega'_A}_{\alpha v_A j_A \Omega_A} &= W^{A' A v'_A j'_A \Omega'_A}_{A v_A j_A \Omega_A} + W^{A'' A v'_A j'_A \Omega'_A}_{A v_A j_A \Omega} \\
W^{\beta v'_B j'_B \Omega'_B}_{\beta v_B j_B \Omega_B} &= \frac{1}{2}\left(W^{A' B v'_B j'_B \Omega'_B}_{B v_B j_B \Omega_B} + W^{A'' B v'_B j'_B \Omega'_B}_{B v_B j_B \Omega_B}\right) \\
W^{\alpha v' j' \Omega'}_{\beta v_B j_B \Omega_B} &= \frac{1}{\sqrt{2}}\left(W^{A' A v'_A j'_A \Omega'}_{B v_B j_B \Omega_B} + W^{A'' A v'_A j'_A \Omega'}_{B v_B j_B \Omega_B}\right) \\
W^{\beta v'_B j'_B \Omega'_B}_{\alpha v_A j_A \Omega_A} &= \frac{1}{\sqrt{2}}\left(W^{A' B v'_B j'_B \Omega'}_{A v_A j_A \Omega_A} + W^{A'' B v'_B j'_B \Omega'_B}_{A v_A j_A \Omega_A}\right) \\
W^{\beta v'_B j'_B \Omega'_B}_{\gamma v_B j_B \Omega_B} &= \frac{(-1)^{j_B}}{2}\left(W^{A' B v'_B j'_B \Omega'_B}_{B v_B j_B \Omega_B} - W^{A'' B v'_B j'_B \Omega'_B}_{B v_B j_B \Omega_B}\right)
\end{aligned}
\tag{3.3.15}
$$

Since all three arrangement channels are indistinguishable for the P_3 permutation group, τ may take on only one value, and so it is not necessary to label the P_3 IR **W** matrices of (3.3.10) with τ and τ'. We can therefore drop the τ labels for all indices. To obtain the P_3 group relations, we take the results of the P_2 symmetry given in equation (3.3.11) and use the symmetry with respect to cyclic permutation of the three atoms to write[2]

$$
\left.
\begin{aligned}
W^{\lambda v' j' \Omega'}_{\lambda v j \Omega} &= W^{\nu v' j' \Omega'}_{\nu v j \Omega} = W^{\kappa v' j' \Omega'}_{\kappa v j \Omega} \\
W^{\lambda v' j' \Omega'}_{\nu v j \Omega} &= W^{\nu v' j' \Omega'}_{\kappa v j \Omega} = W^{\kappa v' j' \Omega'}_{\lambda v j \Omega} \\
W^{\nu v' j' \Omega'}_{\lambda v j \Omega} &= W^{\kappa v' j' \Omega'}_{\nu v j \Omega} = W^{\lambda v' j' \Omega'}_{\kappa v j \Omega} \\
W^{\lambda v' j' \Omega'}_{\lambda v j \Omega} &= (-1)^{j+j'} W^{\lambda v' j' \Omega'}_{\lambda v j \Omega} \\
W^{\lambda v' j' \Omega'}_{\nu v j \Omega} &= (-1)^{j+j'} W^{\nu v' j' \Omega'}_{\lambda v j \Omega}
\end{aligned}
\right\} \quad P_3 \tag{3.3.16}
$$

By comparison of equations (3.3.8) and (3.3.10), and using the relations of equation (3.3.16), we may derive the set of relations between the **R** and **S** matrices for the irreducible representations and those for distinguishable particles:

$$
\begin{aligned}
W^{A_1 v' j' \Omega'}_{v j \Omega} &= \begin{cases} W^{\lambda v' j' \Omega'}_{\lambda v j \Omega} + 2W^{\nu v' j' \Omega'}_{\lambda v j \Omega} & j \text{ and } j' \text{ even} \\ 0 & j \text{ or } j' \text{ odd} \end{cases} \\
W^{A_2 v' j' \Omega'}_{v j \Omega} &= \begin{cases} W^{\lambda v' j' \Omega'}_{\lambda v j \Omega} + 2W^{\nu v' j' \Omega'}_{\lambda v j \Omega} & j \text{ and } j' \text{ odd} \\ 0 & j \text{ or } j' \text{ even} \end{cases} \\
W^{E v' j' \Omega'}_{v j \Omega} &= \begin{cases} W^{\lambda v' j' \Omega'}_{\lambda v j \Omega} - W^{\nu v' j' \Omega'}_{\lambda v j \Omega} & j + j' \text{ even} \\ \sqrt{3} W^{\nu v' j' \Omega'}_{\lambda v j \Omega} & j \text{ even}, j' \text{ odd} \\ -\sqrt{3} W^{\nu v' j' \Omega'}_{\lambda v j \Omega} & j \text{ odd}, j' \text{ even} \end{cases}
\end{aligned}
\tag{3.3.17}
$$

The inverses of these relations are:

$$W^{\lambda v' j' \Omega'}_{\lambda v j \Omega} = \begin{cases} \frac{1}{3} W^{A_1 v' j' \Omega'}_{v j \Omega} + \frac{2}{3} W^{E v' j' \Omega'}_{v j \Omega} & j \text{ and } j' \text{ even} \\ \frac{1}{3} W^{A_2 v' j' \Omega'}_{v j \Omega} + \frac{2}{3} W^{E v' j' \Omega'}_{v j \Omega} & j \text{ and } j' \text{ odd} \\ 0 & j + j' \text{ odd} \end{cases}$$

$$W^{\nu v' j' \Omega'}_{\lambda v j \Omega} = \begin{cases} \frac{1}{3} W^{A_1 v' j' \Omega'}_{v j \Omega} - \frac{1}{3} W^{E v' j' \Omega'}_{v j \Omega} & j \text{ and } j' \text{ even} \\ \frac{1}{3} W^{A_2 v' j' \Omega'}_{v j \Omega} - \frac{1}{3} W^{E v' j' \Omega'}_{v j \Omega} & j \text{ and } j' \text{ odd} \\ \frac{1}{\sqrt{3}} W^{E v' j' \Omega'}_{v j \Omega} & j \text{ even, } j' \text{ odd} \\ -\frac{1}{\sqrt{3}} W^{E v' j' \Omega'}_{v j \Omega} & j \text{ odd, } j' \text{ even} \end{cases} \tag{3.3.18}$$

We can define the parity wavefunctions $\Psi^{JM\Pi\Gamma_k,n'}_{\bar{\lambda}}$ by[74]

$$\Psi^{JM\Gamma_k,n'}_{\bar{\lambda}} = \sum_{\Pi=0}^{1} \Psi^{JM\Pi\Gamma_k,n'}_{\bar{\lambda}} \; ; \qquad \Psi^{JM\Pi\Gamma_k,n'}_{\bar{\lambda}} = \frac{1}{2}(1 + (-1)^{\Pi} \hat{\mathcal{I}}) \Psi^{JM\Gamma_k,n'}_{\bar{\lambda}} \tag{3.3.19}$$

Since the inversion parity operator acts only on the generalized Wigner rotation function as $\hat{\mathcal{I}} \mathcal{D}^{JM}_{j\Omega} = (-1)^J \mathcal{D}^{JM}_{j,-\Omega}$, we get from (3.3.10) that

$$\Psi^{JM\Pi\Gamma_k,\tau' v'_\tau, j'_\tau, \Omega'_\tau}_{\tau} \underset{R_{\bar{\lambda}} \to \infty}{\sim} \sum_{\tau} \sum_{\lambda} \sum_{\Omega_\tau = -J}^{J} \sum_{j_\tau = |\Omega_\tau|}^{j^{max}_\tau} c^{\Gamma_k}_{\tau \lambda j_\tau} \mathcal{D}^{JM\Pi}_{j_\tau \Omega_\tau}(\theta_\lambda, \phi_\lambda, \gamma_\lambda, \psi_\lambda) \sum_{v_\tau=0}^{v^{max}_\tau} \times$$

$$\frac{\phi_{\vec{\tau}}(r_\lambda)}{r_\lambda R_\lambda} |v_{\vec{\tau}}|^{-\frac{1}{2}} \sum_{\Omega''_\tau = -J}^{J} \left(S^{J,\Omega''_\tau}_{\vec{\tau}\Omega_\tau}(R_\lambda) \delta^{\tau' v'_\tau, j'_\tau, \Omega'_\tau}_{\tau v_\tau j_\tau \Omega''_\tau} + C^{J,\Omega''_\tau}_{\vec{\tau}\Omega_\tau}(R_\lambda) W^{J\Gamma \tau' v'_\tau, j'_\tau, -\Omega'_\tau}_{\tau v_\tau j_\tau \Omega''_\tau} \right) \tag{3.3.20}$$

where the function $\mathcal{D}^{JM\Pi}_{j\Omega}$ is defined by

$$\mathcal{D}^{JM\Pi}_{j\Omega}(\theta_\lambda, \phi_\lambda, \gamma_\lambda, \psi_\lambda) = D^{J\Pi}_{M\Omega}(\phi_\lambda, \theta_\lambda, \psi_\lambda) \mathcal{P}^{\Omega}_{j}(\cos \gamma_\lambda) \tag{3.3.21}$$

and the $D^{J\Pi}_{M\Omega}$ are as defined in equation (2.5.2) of (I). The orthonormality properties of this function are given by

$$\mathcal{D}^{*\,J'M'\Pi'}_{j'\Omega'}(\theta_\lambda, \phi_\lambda, \gamma_\lambda, \psi_\lambda) \mathcal{D}^{JM\Pi}_{j\Omega}(\theta_\lambda, \phi_\lambda, \gamma_\lambda, \psi_\lambda) \sin\theta_\lambda d\theta_\lambda d\phi_\lambda \sin\gamma_\lambda d\gamma_\lambda d\psi_\lambda$$
$$= \frac{1 + (-1)^{J+\Pi} \delta^0_\Omega}{2} \delta^{J'}_{J} \delta^{M'}_{M} \delta^{\Pi'}_{\Pi} \delta^{j'}_{j} \delta^{\Omega'}_{\Omega} \tag{3.3.22}$$

Since

$$\mathcal{D}^{JM\Pi}_{j\Omega} = (-1)^{J+\Pi} \mathcal{D}^{JM\Pi}_{j,-\Omega} \tag{3.3.23}$$

we can rewrite (3.3.20) with the range of the summation index Ω_τ limited to non-negative values as:

$$\Psi_{\bar{\lambda}}^{JM\Pi\Gamma_k,\tau' v'_\tau j'_\tau \Omega'_\tau} \widetilde{R_{\bar{\lambda}}\to\infty} \sum_\tau \sum_\lambda \sum_{\Omega_\tau=0}^{J} \sum_{j_\tau=|\Omega_\tau|}^{j_\tau^{max}} c_{\tau\lambda j_\tau}^{\Gamma_k} \mathcal{D}_{j_\tau\Omega_\tau}^{JM\Pi}(\theta_\lambda,\phi_\lambda,\gamma_\lambda,\psi_\lambda)\times$$
$$\sum_{v_\tau=0}^{v_\tau^{max}} \frac{\phi_{\vec{\tau}}(r_\lambda)}{r_\lambda R_\lambda}|v_{\vec{\tau}}|^{-\frac{1}{2}} \frac{1}{1+\delta^0_{\Omega_\tau}} \sum_{\Omega''_\tau=-J}^{J}$$
$$\Big\{ \left(S^{J,\Omega''_\tau}_{\vec{\tau}\Omega_\tau}(R_\lambda)\delta^{\tau' v'_\tau j'_\tau \Omega'_\tau}_{\tau v_\tau j_\tau \Omega''_\tau} + C^{J,\Omega''_\tau}_{\vec{\tau}\Omega_\tau}(R_\lambda) W^{J\Gamma\tau' v'_\tau j'_\tau -\Omega'_\tau}_{\tau v_\tau j_\tau \Omega''_\tau} \right)$$
$$+(-1)^{J+\Pi}\left(S^{J,\Omega''_\tau}_{\vec{\tau},-\Omega_\tau}(R_\lambda)\delta^{\tau' v'_\tau j'_\tau \Omega'_\tau}_{\tau v_\tau j_\tau \Omega''_\tau} + C^{J,\Omega''_\tau}_{\vec{\tau},-\Omega_\tau}(R_\lambda) W^{J\Gamma\tau' v'_\tau j'_\tau -\Omega'_\tau}_{\tau v_\tau j_\tau \Omega''_\tau} \right) \Big\} \tag{3.3.24}$$

With some straightforward manipulation this can be reorganized into the form

$$\Psi_{\bar{\lambda}}^{JM\Pi\Gamma_k,\tau' v'_\tau j'_\tau \Omega'_\tau} \widetilde{R_{\bar{\lambda}}\to\infty} \sum_\tau \sum_\lambda \sum_{\Omega_\tau=0}^{J} \sum_{j_\tau=|\Omega_\tau|}^{j_\tau^{max}} c_{\tau\lambda j_\tau}^{\Gamma_k} \mathcal{D}_{j_\tau\Omega_\tau}^{JM\Pi}(\theta_\lambda,\phi_\lambda,\gamma_\lambda,\psi_\lambda)\times$$
$$\sum_{v_\tau=0}^{v_\tau^{max}} \frac{\phi_{\vec{\tau}}(r_\lambda)}{r_\lambda R_\lambda}|v_{\vec{\tau}}|^{-\frac{1}{2}} \left(\frac{1+\delta^0_{\Omega'_{\tau'}}}{1+\delta^0_{\Omega_\tau}} \right)^{\frac{1}{2}} \sum_{\Omega''_\tau=0}^{J}$$
$$\left(S^{J\Pi,\Omega''_\tau}_{\vec{\tau}\Omega_\tau}(R_\lambda) E^{J\Pi\tau' v'_\tau j'_\tau \Omega'_\tau}_{\tau v_\tau j_\tau \Omega''_\tau} + C^{J\Pi,\Omega''_\tau}_{\vec{\tau}\Omega_\tau}(R_\lambda) W^{J\Pi\Gamma\tau' v'_\tau j'_\tau -\Omega'_\tau}_{\tau v_\tau j_\tau \Omega''_\tau} \right) \tag{3.3.25}$$

in which both indices Ω_τ and Ω''_τ are greater than or equal to zero, and

$$\mathcal{X}^{J\Pi,\Omega''_\tau}_{\vec{\tau}\Omega_\tau}(R_\lambda) = (-1)^{\Omega_\tau+\Omega''_\tau}|k_{\vec{\tau}}|R_\lambda \sum_\ell \left[\frac{1+(-1)^{\Pi+j-\ell}}{(1+\delta^0_{\Omega_\tau})^{\frac{1}{2}}(1+\delta^0_{\Omega''_\tau})^{\frac{1}{2}}} \right]$$
$$\times C(Jj\ell;\Omega''_\tau,-\Omega''_\tau,0) C(Jj\ell;\Omega_\tau,-\Omega_\tau,0) \bar{\mathcal{X}}^{J,\ell}_{\vec{\tau}}(R_\lambda) \tag{3.3.26}$$

where as in section 3.2 $\mathcal{X}$ stands for either $\mathcal{S}$ or $\mathcal{C}$, and similarly $\bar{X}$ stands for either $\bar{S}$ or $\bar{C}$. In addition,

$$E^{J\Pi\tau' v'_\tau j'_\tau \Omega'_\tau}_{\tau v_\tau j_\tau \Omega_\tau} = \delta^{\tau' v'_\tau j'_\tau}_{\tau v_\tau j_\tau} \frac{\left(\delta^{\Omega'_{\tau'}}_{\Omega_\tau} + (-1)^{J+\Pi}\delta^{\Omega'_{\tau'}}_{-\Omega_\tau} \right)}{(1+\delta^0_{\Omega'_{\tau'}})^{\frac{1}{2}}(1+\delta^0_{\Omega_\tau})^{\frac{1}{2}}} \tag{3.3.27}$$

and

$$W^{J\Pi\Gamma\tau' v'_{\tau'} j'_{\tau'} \Omega'_{\tau'}}_{\tau v_\tau j_\tau \Omega_\tau} = \frac{\left(W^{J\Gamma\tau' v'_{\tau'} j'_{\tau'} \Omega'_{\tau'}}_{\tau v_\tau j_\tau \Omega_\tau} + (-1)^{J+\Pi} W^{J\Gamma\tau' v'_{\tau'} j'_{\tau'} \Omega'_{\tau'}}_{\tau v_\tau j_\tau -\Omega_\tau}\right)}{(1+\delta^0_{\Omega'_{\tau'}})^{\frac{1}{2}}(1+\delta^0_{\Omega_\tau})^{\frac{1}{2}}} \tag{3.3.28}$$

where $\Omega' \geq 0$ and $\Omega \geq 0$. (The terms $(1+\delta^0_\Omega)$ are needed for the ${}^{\circ}\mathbf{S}^{J\Pi\Gamma}$ matrix to be unitary.) Furthermore,

$$\left(E^{J\Pi}\right)^{\tau' v'_{\tau'} j'_{\tau'} \Omega'_{\tau'}}_{\tau v_\tau j_\tau, \Omega_\tau = 0} = \left(E^{J\Pi}\right)^{\tau' v'_{\tau'} j'_{\tau'} \Omega'_{\tau'} = 0}_{\tau v_\tau j_\tau \Omega_\tau} = \frac{1}{2}\left[1+(-1)^{J+\Pi}\right] \delta^{\tau' v'_{\tau'} j'_{\tau'} \Omega'_{\tau'}}_{\tau v_\tau j_\tau \Omega'_\tau} \tag{3.3.29}$$

$$\begin{aligned}
\left(W^{J\Pi\Gamma}\right)^{\tau' v'_{\tau'} j'_{\tau'} \Omega'_{\tau'}}_{\tau v_\tau j_\tau, \Omega_\tau = 0} &= \frac{1}{2}\left[1+(-1)^{J+\Pi}\right] \left(W^{J\Pi\Gamma}\right)^{\tau' v'_{\tau'} j'_{\tau'} \Omega'_{\tau'}}_{\tau v_\tau j_\tau \Omega_\tau = 0} \\
\left(W^{J\Pi\Gamma}\right)^{\tau' v'_{\tau'} j'_{\tau'} \Omega'_{\tau'} = 0}_{\tau v_\tau j_\tau \Omega_\tau} &= \frac{1}{2}\left[1+(-1)^{J+\Pi}\right] \left(W^{J\Pi\Gamma}\right)^{\tau' v'_{\tau'} j'_{\tau'} \Omega'_{\tau'} = 0}_{\tau v_\tau j_\tau \Omega_\tau}
\end{aligned} \tag{3.3.30}$$

As a result, the $\Omega = 0$ rows and $\Omega' = 0$ columns of $\mathbf{E}^{J\Pi}$ and $\mathbf{W}^{J\Pi\Gamma}$ can be omitted for $J+\Pi$ odd, which decreases the dimension of these matrices compared with the $J+\Pi$ even case. The $\mathbf{W}^{J\Gamma}$ matrices have Ω and Ω' ranging from $-J$ to J, while for the $\mathbf{W}^{J\Pi\Gamma}$ matrices these indices range from 0 to J for $J+\Pi$ even and from 1 to J for $J+\Pi$ odd. The $\mathbf{W}^{J\Gamma}$ can be expressed in terms of the $\mathbf{W}^{J\Pi\Gamma}$ as follows, with Π' and Π'' defined so that $(-1)^J = (-1)^{\Pi'} = -(-1)^{\Pi''}$:

$$\left(W^{J\Gamma}\right)^{\tau' v'_{\tau'} j'_{\tau'} \Omega'_{\tau'}}_{\tau v_\tau j_\tau \Omega_\tau} = \begin{cases}
\left(W^{J\Pi'\Gamma}\right)^{\tau' v'_{\tau'} j'_{\tau'} |\Omega'_{\tau'}|}_{\tau v_\tau j_\tau |\Omega_\tau|} & \Omega_\tau = \Omega'_{\tau'} = 0 \\
\frac{1}{\sqrt{2}}\left(W^{J\Pi'\Gamma}\right)^{\tau' v'_{\tau'} j'_{\tau'} |\Omega'_{\tau'}|}_{\tau v_\tau j_\tau |\Omega_\tau|} & \Omega_\tau \Omega'_{\tau'} = 0, \Omega_\tau \neq \Omega'_{\tau'} \\
\left(W^{J\Pi'\Gamma}\right)^{\tau' v'_{\tau'} j'_{\tau'} |\Omega'_{\tau'}|}_{\tau v_\tau j_\tau |\Omega_\tau|} + \left(W^{J\Pi''\Gamma}\right)^{\tau' v'_{\tau'} j'_{\tau'} |\Omega'_{\tau'}|}_{\tau v_\tau j_\tau |\Omega_\tau|} & \Omega_\tau \Omega'_{\tau'} > 0 \\
\left(W^{J\Pi'\Gamma}\right)^{\tau' v'_{\tau'} j'_{\tau'} |\Omega'_{\tau'}|}_{\tau v_\tau j_\tau |\Omega_\tau|} - \left(W^{J\Pi''\Gamma}\right)^{\tau' v'_{\tau'} j'_{\tau'} |\Omega'_{\tau'}|}_{\tau v_\tau j_\tau |\Omega_\tau|} & \Omega_\tau \Omega'_{\tau'} < 0
\end{cases} \tag{3.3.31}$$

The general form of the parity wavefunction (3.3.19) is obtained from equation (3.3.25) through right-multiplication by a coefficient matrix:

$$\Psi_{\bar{\lambda}}^{JM\Pi\Gamma_k,n'} = \sum_{\tau'v'j'\Omega'} \Psi_{\bar{\lambda}}^{JM\Pi\Gamma_k,\tau'v'j'\Omega'} A_{\tau'v'j'\Omega'}^{J\Pi\Gamma,n'} (1+\delta_{\Omega'}^0)^{-\frac{1}{2}}$$

$$\widetilde{R_{\bar{\lambda}}\to\infty} \sum_{\tau} \sum_{\lambda} \sum_{\Omega=0}^{J} \sum_{j=\Omega}^{\infty} c_{\tau\lambda j}^{\Gamma_k} \mathcal{D}_{j\Omega}^{JM\Pi}(\theta_\lambda,\phi_\lambda,\gamma_\lambda,\psi_\lambda) \sum_{v=0}^{\infty} \frac{\phi_{\bar{\tau}}(r_\lambda)}{r_\lambda R_\lambda} G_{\bar{\tau}\Omega}^{J\Pi\Gamma,n'}(R_\lambda) \tag{3.3.32}$$

in which, using equations (3.3.25) and (3.2.5), we have defined

$$G_{\bar{\tau}\Omega}^{J\Pi\Gamma,n'}(R_\lambda) = |v_{\bar{\tau}}|^{-\frac{1}{2}} \sum_{\Omega''=0}^{J} \left[S_{\bar{\tau}\Omega}^{J\Pi,\Omega''}(R_\lambda) A_{\bar{\tau}\Omega''}^{J\Pi\Gamma,n'} + C_{\bar{\tau}\Omega}^{J\Pi,\Omega''}(R_\lambda) B_{\bar{\tau}\Omega''}^{J\Pi\Gamma,n'} \right] \tag{3.3.33}$$

3.4 Asymptotic Transformation from Hyperspherical to Jacobi Coordinates and Determination of the R Matrix

The wavefunction of equation (3.3.32) may be expressed in terms of hyperspherical coordinate surface functions. The overlap between arrangement channels in the asymptotic region goes to zero, and the LHSF are simply related to the wavefunction for an isolated diatom and a free particle. In this region, only the effect of the symmetry operations links the different channels together, since the magnitude of the LHSF in the regions between the arrangement channels (corresponding to three seperated particles) goes to zero. For example, in an AB_2 system, the LHSF in this region may be divided into those of type A (A + B_2) and those of type B (linear combinations of the two B + AB channels). Due to the isolation of the arrangement channels, the primitives of type $\tau' \neq \tau$ will not contribute to LHSF of type τ; for our AB_2 example, the LHSF of type A will have zero contributions from primitives of type B, and the LHSF of type B will have zero contributions from primitives of type A. We can therefore define a new numbering index n_τ to enumerate the asymptotic LHSF of type τ in each symmetry Γ, such that this index has the same value as the index n determined by energy ordering of all LHSF with symmetry Γ; accordingly, there is no $n_{\tau'}$ index with the same value as an index n_τ when $\tau' \neq \tau$. We then have

$$\Phi_n^{JM\Pi\Gamma_k} \underset{\rho\to\infty}{\sim} \Phi_{\tau,n_\tau}^{JM\Pi\Gamma_k} \tag{3.4.1}$$

where the τ-dependent set of surface functions is defined by

$$\Phi_{\tau,n_\tau}^{JM\Pi\Gamma_k}(\zeta_{\bar{\lambda}};\bar{\rho}) = \sum_{vj\Omega} a_{\tau vj\Omega n_\tau}^{J\Pi\Gamma}(\bar{\rho}) F_{\tau vj\Omega}^{J\Pi\Gamma_k}(\zeta_{\bar{\lambda}};\bar{\rho}) \tag{3.4.2}$$

and

$$F_{\tau vj\Omega}^{J\Pi\Gamma_k}(\zeta_{\bar{\lambda}};\bar{\rho}) = \sum_{\lambda} c_{\tau\lambda j}^{\Gamma_k} \mathcal{D}_{j\Omega}^{JM\Pi}(\theta_\lambda,\phi_\lambda,\gamma_\lambda,\psi_\lambda) \frac{t_{\tau vj\Omega}^J(\omega_\lambda;\bar{\rho})}{\sin\omega_\lambda} \tag{3.4.3}$$

with numerically determined $t_{\tau vj\Omega}^J$. The $a_{\tau vj\Omega n_\tau}^{J\Pi\Gamma}(\bar{\rho})$ are determined in the process of calculating the LHSF (see paper I). (This representation of the surface functions in

terms of τ is only valid asymptotically; it is possible in the regions where the $F^{J\Pi\Gamma_k}_{\tau v j\Omega}$ of one channel overlap with those of another arrangement channel of type τ' for the LHSF to contain contributions from both τ and τ' basis sets.) The expansion of the wavefunction in the LHSF which corresponds to equation (3.3.32) is obtained from equation (2.1.9) by modifying the labeling of the coefficients $b^{J\Pi\Gamma}$ from n to τ, n_τ according to equation (3.4.1):

$$\Psi^{JM\Pi\Gamma_k,n'}_{\bar\lambda}(\rho,\zeta_{\bar\lambda}) \underset{R_{\bar\lambda}\to\infty}{\sim} \rho^{-\frac{5}{2}} \sum_\tau \sum_{n_\tau} b^{J\Pi\Gamma,n'}_{\tau,n_\tau}(\rho;\bar\rho)\Phi^{JM\Pi\Gamma_k}_{\tau,n_\tau}(\zeta_{\bar\lambda};\bar\rho) \tag{3.4.4}$$

We may now solve for the $\mathbf{R}^{J\Pi\Gamma}$ matrix for each parity and IR. Multiplication of both sides of (3.4.4) by the function $\Phi^{JM\Pi\Gamma_k *}_{\bar\tau,n_\tau}(\zeta_{\bar\lambda};\bar\rho)$, (where $\bar\tau$ is defined to be the type of arrangement channel $\bar\lambda$), choosing $\bar\rho = \bar\rho_{i_{max}} = \bar\rho_{max}$ and $\rho = \rho_{i_{max},i_{max}+1} = \rho_{max}$, and using the orthonormality of the LHSF, we find that

$$b^{J\Pi\Gamma,n'}_{\bar\tau,n_\tau}(\rho_{max};\bar\rho_{max}) = \rho^{\frac{5}{2}}_{max}\left\langle \Phi^{JM\Pi\Gamma_k}_{\bar\tau,n_\tau}(\zeta_{\bar\lambda};\bar\rho_{max}) \middle| \Psi^{JM\Pi\Gamma_k,n'}_{\bar\lambda}(\rho_{max},\zeta_{\bar\lambda})\right\rangle \tag{3.4.5}$$

Substitution of equations (3.3.32), (3.4.2) and (3.4.3) into the right hand side of equation (3.4.5), and noting that the integral of two asymptotic functions in different arrangement channels is zero, yields

$$\begin{aligned} b^{J\Pi\Gamma,n'}_{\bar\tau,n_\tau}(\rho_{max};\bar\rho_{max}) = \rho^{\frac{5}{2}}_{max} \sum_{\lambda v j\Omega}\sum_{v' j'\Omega'} & a^{J\Pi\Gamma}_{\bar\tau v' j'\Omega' n_\tau}(\bar\rho_{max})\left|v_{\bar\tau v j}\right|^{-\frac{1}{2}} c^{\Gamma_k}_{\bar\tau\lambda j'} c^{\Gamma_k}_{\bar\tau\lambda j} \times \\ & \left\langle \mathcal{D}^{JM\Pi}_{j'\Omega'}(\theta_\lambda,\phi_\lambda,\gamma_\lambda,\psi_\lambda) \middle| \mathcal{D}^{JM\Pi}_{j\Omega}(\theta_\lambda,\phi_\lambda,\gamma_\lambda,\psi_\lambda)\right\rangle \times \\ & \int t^J_{\bar\tau v' j'\Omega'}(\omega_\lambda;\bar\rho_{max}) \frac{\phi_{\bar\tau v j}(r_\lambda)}{r_\lambda R_\lambda} G^{J\Pi\Gamma,n'}_{\bar\tau v j\Omega}(R_\lambda)\sin\omega_\lambda d\omega_\lambda \end{aligned} \tag{3.4.6}$$

where R_λ and r_λ are considered to be functions of ω_λ:

$$R_\lambda = \rho_{max}\cos\frac{\omega_\lambda}{2} \qquad\qquad r_\lambda = \rho_{max}\sin\frac{\omega_\lambda}{2} \tag{3.4.7}$$

The integral over the $\mathcal{D}^{JM\Pi}_{j\Omega}$ functions is analytic, yielding $\delta^{j'\Omega'}_{j\Omega}\frac{(1+(-1)^{J+\Pi}\delta^0_\Omega)}{2}$; this

reduces (3.4.6) to

$$b^{J\Pi\Gamma,n'}_{\tau,n_\tau}(\rho_{max};\bar{\rho}_{max}) = \rho_{max}^{\frac{5}{2}} \sum_{\lambda v' v j \Omega} a^{J\Pi\Gamma}_{\tau v' j \Omega n_\tau}(\bar{\rho}_{max}) \frac{(1+(-1)^{J+\Pi}\delta^0_\Omega)}{2} (c^{\Gamma_k}_{\tau\lambda j})^2 \times \int t^J_{\tau v' j\Omega}(\omega_\lambda;\bar{\rho}_{max}) \frac{\phi_{\bar{\tau}}(r_\lambda)}{r_\lambda R_\lambda} G^{J\Pi\Gamma,n'}_{\bar{\tau}\Omega}(R_\lambda) \sin\omega_\lambda d\omega_\lambda \tag{3.4.8}$$

in which we have without loss of generality simplified the notation by replacement of $\bar{\tau}$ with τ. At this point we substitute the explicit form of $G^{J\Pi\Gamma,n'}_{\bar{\tau}\Omega}(R_\lambda)$ from equation (3.3.33) into equation (3.4.8) to obtain

$$b^{J\Pi\Gamma,n'}_{\tau,n_\tau}(\rho_{max};\bar{\rho}_{max}) = \rho_{max}^{\frac{5}{2}} \sum_{\lambda v' v j \Omega \Omega'} a^{J\Pi\Gamma}_{\tau v' j \Omega n_\tau}(\bar{\rho}_{max}) |v_{\bar{\tau}}|^{-\frac{1}{2}} \frac{(1+(-1)^{J+\Pi}\delta^0_\Omega)}{2} \times (c^{\Gamma_k}_{\tau\lambda j})^2 \left[A^{J\Pi\Gamma,n'}_{\bar{\tau}\Omega'} \int t^J_{\tau v' j\Omega}(\omega_\lambda;\bar{\rho}_{max}) \frac{\phi_{\bar{\tau}}(r_\lambda)}{r_\lambda R_\lambda} S^{J\Pi,\Omega'}_{\bar{\tau}\Omega}(R_\lambda) \sin\omega_\lambda d\omega_\lambda + B^{J\Pi,n'}_{\bar{\tau}\Omega'} \int t^J_{\tau v' j\Omega}(\omega_\lambda;\bar{\rho}_{max}) \frac{\phi_{\bar{\tau}}(r_\lambda)}{r_\lambda R_\lambda} C^{J\Pi,\Omega'}_{\bar{\tau}\Omega}(R_\lambda) \sin\omega_\lambda d\omega_\lambda \right] \tag{3.4.9}$$

We can simplify this equation further by recognizing that the channel label λ only labels the coordinates ω_λ, R_λ and r_λ, and the functions all have the same form in each channel of type τ. The sum over λ therefore includes only the term $(c^{\Gamma_k}_{\tau\lambda j})^2$, and this sum equals 1. (This also eliminates the label k from the equation.) We now have

$$b^{J\Pi\Gamma,n'}_{\tau,n_\tau}(\rho_{max};\bar{\rho}_{max}) = \rho_{max}^{\frac{5}{2}} \sum_{v' v j \Omega \Omega'} a^{J\Pi\Gamma}_{\tau v' j \Omega n_\tau}(\bar{\rho}_{max}) |v_{\bar{\tau}}|^{-\frac{1}{2}} \frac{(1+(-1)^{J+\Pi}\delta^0_\Omega)}{2} \times \left[A^{J\Pi\Gamma,n'}_{\bar{\tau}\Omega'} \int t^J_{\tau v' j\Omega}(\omega;\bar{\rho}_{max}) \frac{\phi_{\bar{\tau}}(r)}{rR} S^{J\Pi,\Omega'}_{\bar{\tau}\Omega}(R) \sin\omega d\omega + B^{J\Pi\Gamma,n'}_{\bar{\tau}\Omega'} \int t^J_{\tau v' j\Omega}(\omega;\bar{\rho}_{max}) \frac{\phi_{\bar{\tau}}(r)}{rR} C^{J\Pi,\Omega'}_{\bar{\tau}\Omega}(R) \sin\omega d\omega \right] \tag{3.4.10}$$

with

$$R = \rho_{max} \cos\frac{\omega}{2} \qquad\qquad r = \rho_{max} \sin\frac{\omega}{2} \tag{3.4.11}$$

where we have removed the channel index from the variables, since the integration may be performed in any arrangement channel coordinate system of type τ. Finally,

we substitute equation (3.3.26) into equation (3.4.10) to get

$$b^{J\Pi\Gamma,n'}_{\tau,n_\tau}(\rho_{max};\bar{\rho}_{max}) = \rho_{max}^{\frac{3}{2}} \sum_{v'j\Omega} a^{J\Pi\Gamma}_{\tau v' j\Omega n_\tau}(\bar{\rho}_{max}) \left(\frac{1+(-1)^{J+\Pi}\delta^0_\Omega}{1+\delta^0_\Omega}\right)$$
$$\times \sum_{\ell v\Omega'} (-1)^{\Omega+\Omega'} \left|\frac{\mu}{\hbar} k_{\bar{r}}\right|^{\frac{1}{2}} \left[\frac{1+(-1)^{\Pi+j-\ell}}{1+\delta^0_{\Omega'}}\right]$$
$$\times C(Jj\ell;\Omega,-\Omega,0) C(Jj\ell;\Omega',-\Omega',0) \int t^J_{\tau v' j\Omega}(\omega;\bar{\rho}_{max}) \phi_{\bar{r}}(r)$$
$$\times \left[\bar{S}^{J,\ell}_{\bar{r}}(R) A^{J\Pi\Gamma,n'}_{\bar{r}\Omega'} + \bar{C}^{J,\ell}_{\bar{r}}(R) B^{J\Pi\Gamma,n'}_{\bar{r}\Omega'}\right] \cos\frac{\omega}{2} d\omega \tag{3.4.12}$$

with R and r given by (3.4.11).

The matrix version of equation (3.4.12) has the form

$$\mathbf{b}^{J\Pi\Gamma}_\tau(\rho_{max};\bar{\rho}_{max}) = \mathbf{a}^{J\Pi\Gamma}_\tau(\bar{\rho}_{max}) \left[\boldsymbol{\mathcal{S}}^{J\Pi}_\tau(\rho_{max};\bar{\rho}_{max}) \mathbf{A}^{J\Pi\Gamma}_\tau + \boldsymbol{\mathcal{C}}^{J\Pi}_\tau(\rho_{max};\bar{\rho}_{max}) \mathbf{B}^{J\Pi\Gamma}_\tau\right] \tag{3.4.13}$$

in which

$$\left[\mathbf{b}^{J\Pi\Gamma}_\tau\right]^{n'}_{n_\tau}(\rho_{max};\bar{\rho}_{max}) = b^{J\Pi\Gamma,n'}_{\tau n_\tau}(\rho_{max};\bar{\rho}_{max}) \tag{3.4.14}$$

$$\left[\mathbf{a}^{J\Pi\Gamma}_\tau\right]^{vj\Omega}_{n_\tau}(\bar{\rho}_{max}) = a^{J\Pi\Gamma}_{\tau vj\Omega n_\tau}(\bar{\rho}_{max}) \tag{3.4.15}$$

$$\left[\boldsymbol{\mathcal{X}}^{J\Pi}_\tau\right]^{v'j'\Omega'}_{vj\Omega}(\rho_{max};\bar{\rho}_{max}) = \delta^{j'}_j \rho_{max}^{\frac{3}{2}} (-1)^{\Omega+\Omega'} \left|\frac{\mu}{\hbar} k_{\tau v' j}\right|^{\frac{1}{2}} \left(\frac{1+(-1)^{J+\Pi}\delta^0_\Omega}{(1+\delta^0_\Omega)(1+\delta^0_{\Omega'})}\right)$$
$$\times \sum_\ell \left(1+(-1)^{\Pi+j-\ell}\right) C(Jj\ell;\Omega,-\Omega,0) C(Jj\ell;\Omega',-\Omega',0)$$
$$\times \int t^J_{\tau vj\Omega}(\omega;\bar{\rho}_{max}) \phi_{\tau v' j}(r) \bar{\mathcal{X}}^{J,\ell}_{\tau v' j}(R) \cos\frac{\omega}{2} d\omega \tag{3.4.16}$$

$$\left[\mathbf{A}^{J\Pi\Gamma}_\tau\right]^{n'}_{v'j'\Omega'} = A^{J\Pi\Gamma,n'}_{\tau v' j'\Omega'} \; ; \quad \left[\mathbf{B}^{J\Pi\Gamma}_\tau\right]^{n'}_{v'j'\Omega'} = B^{J\Pi\Gamma,n'}_{\tau v' j'\Omega'} \tag{3.4.17}$$

where (3.4.11) must be used to perform the integration over ω. For a system with P_3 symmetry, τ takes on only one value, and equation (3.4.13) is the complete description of the Γ IR. As such, we can drop the index τ and simply write

$$P_3: \quad \mathbf{b}^{J\Pi\Gamma}(\rho_{max};\bar{\rho}_{max}) = \mathbf{a}^{J\Pi\Gamma}(\bar{\rho}_{max}) \Big[\boldsymbol{\mathcal{S}}^{J\Pi}(\rho_{max};\bar{\rho}_{max}) \mathbf{A}^{J\Pi\Gamma}$$
$$+ \boldsymbol{\mathcal{C}}^{J\Pi}(\rho_{max};\bar{\rho}_{max}) \mathbf{B}^{J\Pi\Gamma}\Big] \tag{3.4.18}$$

When a lower degree of symmetry exists, it is necessary to consider the set of $\mathbf{b}_\tau^{J\Pi\Gamma}$ matrices for the two or three different distinguishable arrangement channels. In these cases, the index n' spans all the values of τ for this system, and the $\mathbf{b}_\tau^{J\Pi\Gamma}$, $\mathbf{A}_\tau^{J\Pi\Gamma}$ and $\mathbf{B}_\tau^{J\Pi\Gamma}$ matrices are rectangular. The square matrix $\mathbf{b}^{J\Pi\Gamma}$ for the Γ IR coefficients equivalent to equation (3.4.18) is constructed from the various pieces as follows:

$$P_2: \quad \mathbf{b}^{J\Pi\Gamma} = \begin{bmatrix} \mathbf{b}^{J\Pi\Gamma}_{\tau=\mathrm{A}} \\ \mathbf{b}^{J\Pi\Gamma}_{\tau=\mathrm{B}} \end{bmatrix} = \begin{bmatrix} \mathbf{a}^{J\Pi\Gamma}_{\tau=\mathrm{A}} & \mathbf{0} \\ \mathbf{0} & \mathbf{a}^{J\Pi\Gamma}_{\tau=\mathrm{B}} \end{bmatrix} \left(\begin{bmatrix} \boldsymbol{\mathcal{S}}^{J\Pi}_{\tau=\mathrm{A}} & \mathbf{0} \\ \mathbf{0} & \boldsymbol{\mathcal{S}}^{J\Pi}_{\tau=\mathrm{B}} \end{bmatrix} \begin{bmatrix} \mathbf{A}^{J\Pi\Gamma}_{\tau=\mathrm{A}} \\ \mathbf{A}^{J\Pi\Gamma}_{\tau=\mathrm{B}} \end{bmatrix} + \begin{bmatrix} \boldsymbol{\mathcal{C}}^{J\Pi}_{\tau=\mathrm{A}} & \mathbf{0} \\ \mathbf{0} & \boldsymbol{\mathcal{C}}^{J\Pi}_{\tau=\mathrm{B}} \end{bmatrix} \begin{bmatrix} \mathbf{B}^{J\Pi\Gamma}_{\tau=\mathrm{A}} \\ \mathbf{B}^{J\Pi\Gamma}_{\tau=\mathrm{B}} \end{bmatrix} \right) \tag{3.4.19}$$

$$P_1: \quad \mathbf{b}^{J\Pi\Gamma} = \begin{bmatrix} \mathbf{b}^{J\Pi}_{\tau=\mathrm{A}} \\ \mathbf{b}^{J\Pi}_{\tau=\mathrm{B}} \\ \mathbf{b}^{J\Pi}_{\tau=\mathrm{C}} \end{bmatrix} = \begin{bmatrix} \mathbf{a}^{J\Pi}_{\tau=\mathrm{A}} & \mathbf{0} & \mathbf{0} \\ \mathbf{0} & \mathbf{a}^{J\Pi}_{\tau=\mathrm{B}} & \mathbf{0} \\ \mathbf{0} & \mathbf{0} & \mathbf{a}^{J\Pi}_{\tau=\mathrm{C}} \end{bmatrix} \times \left(\begin{bmatrix} \boldsymbol{\mathcal{S}}^{J\Pi}_{\tau=\mathrm{A}} & \mathbf{0} & \mathbf{0} \\ \mathbf{0} & \boldsymbol{\mathcal{S}}^{J\Pi}_{\tau=\mathrm{B}} & \mathbf{0} \\ \mathbf{0} & \mathbf{0} & \boldsymbol{\mathcal{S}}^{J\Pi}_{\tau=\mathrm{C}} \end{bmatrix} \begin{bmatrix} \mathbf{A}^{J\Pi}_{\tau=\mathrm{A}} \\ \mathbf{A}^{J\Pi}_{\tau=\mathrm{B}} \\ \mathbf{A}^{J\Pi}_{\tau=\mathrm{C}} \end{bmatrix} + \begin{bmatrix} \boldsymbol{\mathcal{C}}^{J\Pi}_{\tau=\mathrm{A}} & \mathbf{0} & \mathbf{0} \\ \mathbf{0} & \boldsymbol{\mathcal{C}}^{J\Pi}_{\tau=\mathrm{B}} & \mathbf{0} \\ \mathbf{0} & \mathbf{0} & \boldsymbol{\mathcal{C}}^{J\Pi}_{\tau=\mathrm{C}} \end{bmatrix} \begin{bmatrix} \mathbf{B}^{J\Pi}_{\tau=\mathrm{A}} \\ \mathbf{B}^{J\Pi}_{\tau=\mathrm{B}} \\ \mathbf{B}^{J\Pi}_{\tau=\mathrm{C}} \end{bmatrix} \right) \tag{3.4.20}$$

In equation (3.4.20), we have dropped the superscript Γ since there is only one irreducible representation. For this equation, replacement of the τ labels with the appropriate channel labels α, β or γ yields the distinguishable particle representation of the system, as is proper for a system with no permutation symmetry.

Equations (3.4.18) through (3.4.20) all have the same format, namely that of (3.4.18):

$$\mathbf{b}^{J\Pi\Gamma} = \mathbf{a}^{J\Pi\Gamma} \left[\boldsymbol{\mathcal{S}}^{J\Pi} \mathbf{A}^{J\Pi\Gamma} + \boldsymbol{\mathcal{C}}^{J\Pi} \mathbf{B}^{J\Pi\Gamma} \right] \tag{3.4.21}$$

with the definition of the matrices in the right hand side given implicitly in those three equations.

Substituting (3.4.20a) into equation (2.2.5) with $\rho = \rho_{max}$ and $\bar{\rho}_i = \bar{\rho}_{max}$, and using equation (3.2.15), we derive the following expression for the reactance matrix in terms of the logarithmic derivative at these values of ρ and $\bar{\rho}_i$:

$$\mathbf{R}^{J\Pi\Gamma} = \left(\boldsymbol{\mathcal{Y}}^{J\Pi\Gamma} \mathbf{a}^{J\Pi\Gamma} \boldsymbol{\mathcal{C}}^{J\Pi} - \mathbf{a}^{J\Pi\Gamma} \dot{\boldsymbol{\mathcal{C}}}^{J\Pi} \right)^{-1} \left(\mathbf{a}^{J\Pi\Gamma} \dot{\boldsymbol{\mathcal{S}}}^{J\Pi} - \boldsymbol{\mathcal{Y}}^{J\Pi\Gamma} \mathbf{a}^{J\Pi\Gamma} \boldsymbol{\mathcal{S}}^{J\Pi} \right) \tag{3.4.22}$$

From our choice of formalism, the matrix $\mathbf{R}^{J\Pi\Gamma}$ determined from this equation has elements denoted by $\left[R^{J\Pi\Gamma}\right]_{\tau v j \Omega}^{\tau' v' j' -\Omega'}$; it is important to note that the ordering of the row and column indices for this matrix are not the same.

4. ASYMPTOTIC ANALYSIS - DIFFERENTIAL AND INTEGRAL CROSS SECTIONS

4.1 Scattering Amplitude Properties

The superscripts of the scattering amplitudes $f_{\lambda v_\lambda j_\lambda \Omega_\lambda}^{\lambda' v'_{\lambda'} j'_{\lambda'} m'_{\lambda'}}$ denote the initial arrangement channel and state for the system, while the subscripts denote the product and its state. In the general case where all three atoms are distinguishable, there are nine different sets of scattering amplitudes corresponding to different selections of initial and final arrangement channels for the system. In the case of a system in which two or all three of the atoms are identical, irreducible representation scattering amplitudes may be used instead; however, these IR scattering amplitudes are related to the distinguishable particle scattering amplitudes by the symmetry operations of the permutation group, and therefore distinguishable particle amplitudes may be obtained from the IR amplitudes. Differential and integral cross sections are obtained from scattering wavefunctions which differ from (3.1.1) and (3.1.3) (if the three atoms are not distinguishable) in that they must satisfy the Pauli principle, as discussed later in this paper.

Application of the projection operators for P_p to the general space-fixed scattering form (3.1.1) and the helicity form (3.1.3) generates the irreducible representation forms

$$\Psi_{\bar{\lambda}}^{\Gamma_k \tau' v'_{\tau'} j'_{\tau'} m'_{\tau'}} \underset{R_{\bar{\lambda}} \to \infty}{\sim} \sum_{\tau} \sum_{\lambda} \sum_{v_\tau j_\tau m_\tau} c_{\tau \lambda j_\tau}^{\Gamma_k} \varphi_{\bar{\tau} m_\tau}^{\mathrm{sf}}(\mathbf{r}_\lambda) \times \left[e^{i \mathbf{k}_\tau \cdot \mathbf{R}_\lambda} \delta_{\tau v_\tau j_\tau m_\tau}^{\tau' v'_{\tau'} j'_{\tau'} m'_{\tau'}} + f_{\tau v j m}^{\Gamma \tau' v' j' m'}(\theta_\lambda, \phi_\lambda) \frac{e^{i k_\tau R_\lambda}}{R_\lambda} \right] \tag{4.1.1}$$

in the space-fixed representation and

$$\Psi_{\bar{\lambda}}^{\Gamma_k \tau' v'_{\tau'} j'_{\tau'} m'_{\tau'}} \underset{R_{\bar{\lambda}} \to \infty}{\sim} \sum_{\tau} \sum_{\lambda} \sum_{v_\tau j_\tau \Omega_\tau} c_{\tau \lambda j_\tau}^{\Gamma_k} \times \left[e^{i \mathbf{k}_{\tau v_\tau j_\tau} \cdot \mathbf{R}_\lambda} \varphi_{\bar{\tau} \Omega_\tau}^{\mathrm{sf}}(\mathbf{r}_\lambda) \delta_{\tau v_\tau j_\tau \Omega_\tau}^{\tau' v'_{\tau'} j'_{\tau'} m'_{\tau'}} + f_{\tau v_\tau j_\tau \Omega_\tau}^{\Gamma \tau' v'_{\tau'} j'_{\tau'} m'_{\tau'}}(\theta_\lambda, \phi_\lambda) \frac{e^{i k_\tau R_\lambda}}{R_\lambda} \varphi_{\bar{\tau} \Omega_\tau}^{\mathrm{bf}}(\mathbf{r}_\lambda) \right] \tag{4.1.2}$$

in the helicity representation, where we have again replaced the indices λ and λ' with τ and τ' where possible. (The derivation of these equations is done in appendix A.) As was mentioned in section 3.3, the coefficients $c^{\Gamma_k}_{\tau\lambda j_\tau}$ cause the summations over τ and λ to access each arrangement channel once and once only. In the case of the P_1 group, for which the atoms are distinguishable, these equations reduce to equations (3.1.1) and (3.1.3) with replacement of the channel labels α, β, and γ with the τ labels A, B, and C, respectively.

Applying the permutation operators to the functions (3.1.1) and (3.1.3) for each value of λ' results in a new function localized in an arrangement channel λ'' of the same type τ, where λ' may or may not equal λ''; comparing this result with the original functional form (3.1.1) or (3.1.3) for the λ'' channel yields the symmetry properties of the distinguishable particle scattering amplitudes. This has already been done for the body-fixed helicity reactance and scattering matrices using equation (3.3.8); proceeding in a similar manner we get the same symmetry properties for the space-fixed and helicity scattering amplitudes as were found for the scattering matrices. These properties may be found by replacing in equations (3.3.11) through (3.3.18) the term W with f and the terms Ω and Ω' with m and m'; the results will be presented explicitly below for future reference.

For the P_2 case, we get from applying the operator which permutes β and γ

$$\left.\begin{aligned}
f^{\alpha v' j' m'}_{\alpha v j \Omega} &= (-1)^{j+j'} f^{\alpha v' j' m'}_{\alpha v j \Omega} \\
f^{\beta v' j' m'}_{\beta v j \Omega} &= (-1)^{j+j'} f^{\gamma v' j' m'}_{\gamma v j \Omega} \\
f^{\beta v' j' m'}_{\gamma v j \Omega} &= (-1)^{j+j'} f^{\gamma v' j' m'}_{\beta v j \Omega} \\
f^{\beta v' j' m'}_{\alpha v j \Omega} &= (-1)^{j+j'} f^{\gamma v' j' m'}_{\alpha v j \Omega} \\
f^{\alpha v' j' m'}_{\beta v j \Omega} &= (-1)^{j+j'} f^{\alpha v' j' m'}_{\gamma v j \Omega}
\end{aligned}\right\} P_2 \qquad (4.1.3)$$

with analogous expressions being valid for the space-fixed scattering amplitudes. (For simplicity of the notation, the channel labels of the v, j, m and Ω quantum numbers have been dropped; they are the same as the channel index of the superscript or subscript in which they appear.) The factors $(-1)^{j+j'}$ are determined by comparison of the result of the operation on equation (3.1.3) with the original equa-

tion; the $(-1)^j$ terms are the result of replacing $\mathbf{r}_\lambda$ with $-\mathbf{r}_\lambda$ in the wavefunction of the diatomic molecule $A_\beta A_\gamma$. Due to these relations, there are only 5 independent scattering amplitude matrices, $\mathbf{f}_\alpha^\alpha$, $\mathbf{f}_\beta^\beta$, $\mathbf{f}_\alpha^\beta$, $\mathbf{f}_\beta^\alpha$, and $\mathbf{f}_\gamma^\beta$; the other 4 are related to these by similarity transformations.

By comparison of the equations (3.1.3) and (4.1.2), and using the relations of (4.1.3), we may derive the following relations between the helicity scattering amplitudes for the irreducible representations and those for distinguishable particles:

$$\begin{aligned} f^{A'\mathrm{A}v'j'm'}_{\mathrm{A}vj\Omega} &= \begin{cases} f^{\alpha v'j'm'}_{\alpha vj\Omega} & j \text{ and } j' \text{ even} \\ 0 & j \text{ or } j' \text{ odd} \end{cases} \\ f^{A''\mathrm{A}v'j'm'}_{\mathrm{A}vj\Omega} &= \begin{cases} f^{\alpha v'j'm'}_{\alpha vj\Omega} & j \text{ and } j' \text{ odd} \\ 0 & j \text{ or } j' \text{ even} \end{cases} \end{aligned} \tag{4.1.4}$$

$$\begin{aligned} f^{A'\mathrm{A}v'j'm'}_{\mathrm{B}vj\Omega} &= \begin{cases} \sqrt{2} f^{\alpha v'j'm'}_{\beta vj\Omega} & j' \text{ even} \\ 0 & j' \text{ odd} \end{cases} \\ f^{A''\mathrm{A}v'j'm'}_{\mathrm{B}vj\Omega} &= \begin{cases} \sqrt{2} f^{\alpha v'j'm'}_{\beta vj\Omega} & j' \text{ odd} \\ 0 & j' \text{ even} \end{cases} \\ f^{A'\mathrm{B}v'j'm'}_{\mathrm{A}vj\Omega} &= \begin{cases} \sqrt{2} f^{\beta v'j'm'}_{\alpha vj\Omega} & j \text{ even} \\ 0 & j \text{ odd} \end{cases} \\ f^{A''\mathrm{B}v'j'm'}_{\mathrm{A}vj\Omega} &= \begin{cases} \sqrt{2} f^{\beta v'j'm'}_{\alpha vj\Omega} & j \text{ odd} \\ 0 & j \text{ even} \end{cases} \end{aligned} \tag{4.1.5}$$

$$\begin{aligned} f^{A'\mathrm{B}v'j'm'}_{\mathrm{B}vj\Omega} &= f^{\beta v'j'm'}_{\beta vj\Omega} + (-1)^{j'} f^{\gamma v'j'm'}_{\beta vj\Omega} \\ f^{A''\mathrm{B}v'j'm'}_{\mathrm{B}vj\Omega} &= f^{\beta v'j'm'}_{\beta vj\Omega} - (-1)^{j'} f^{\gamma v'j'm'}_{\beta vj\Omega} \end{aligned} \tag{4.1.6}$$

Analogous expressions are valid for the space-fixed scattering amplitudes. The inverse of these relations is

$$\begin{aligned} f^{\alpha v'j'm'}_{\alpha vj\Omega} &= f^{A'\mathrm{A}v'j'm'}_{\mathrm{A}vj\Omega} + f^{A''\mathrm{A}v'j'm'}_{\mathrm{A}vj\Omega} \\ f^{\beta v'j'm'}_{\beta vj\Omega} &= \frac{1}{2}\left(f^{A'\mathrm{B}v'j'm'}_{\mathrm{B}vj\Omega} + f^{A''\mathrm{B}v'j'm'}_{\mathrm{B}vj\Omega} \right) \\ f^{\alpha v'j'm'}_{\beta vj\Omega} &= \frac{1}{\sqrt{2}}\left(f^{A'\mathrm{A}v'j'm'}_{\mathrm{B}vj\Omega} + f^{A''\mathrm{A}v'j'm'}_{\mathrm{B}vj\Omega} \right) \\ f^{\beta v'j'm'}_{\alpha vj\Omega} &= \frac{1}{\sqrt{2}}\left(f^{A'\mathrm{B}v'j'm'}_{\mathrm{A}vj\Omega} + f^{A''\mathrm{B}v'j'm'}_{\mathrm{A}vj\Omega} \right) \\ f^{\beta v'j'm'}_{\gamma vj\Omega} &= \frac{(-1)^j}{2}\left(f^{A'\mathrm{B}v'j'm'}_{\mathrm{B}vj\Omega} - f^{A''\mathrm{B}v'j'm'}_{\mathrm{B}vj\Omega} \right) \end{aligned} \tag{4.1.7}$$

with analogous results for the space-fixed quantities.

For the P_3 group, we can take the results of the P_2 symmetry given in equation (4.1.3) and use the symmetry with respect to cyclic permutation of the three atoms to write[2]

$$\left.\begin{array}{l} f^{\lambda v' j' m'}_{\lambda v j \Omega} = f^{\nu v' j' m'}_{\nu v j \Omega} = f^{\kappa v' j' m'}_{\kappa v j \Omega} \\ f^{\lambda v' j' m'}_{\nu v j \Omega} = f^{\nu v' j' m'}_{\kappa v j \Omega} = f^{\kappa v' j' m'}_{\lambda v j \Omega} \\ f^{\nu v' j' m'}_{\lambda v j \Omega} = f^{\kappa v' j' m'}_{\nu v j \Omega} = f^{\lambda v' j' m'}_{\kappa v j \Omega} \\ f^{\lambda v' j' m'}_{\lambda v j \Omega} = (-1)^{j+j'} f^{\lambda v' j' m'}_{\lambda v j \Omega} \\ f^{\lambda v' j' m'}_{\nu v j \Omega} = (-1)^{j+j'} f^{\nu v' j' m'}_{\lambda v j \Omega} \end{array}\right\} P_3 \qquad (4.1.8)$$

Therefore in the P_3 permutation group, there are only two independent scattering amplitude matrices, which may be represented as $\mathbf{f}^{\lambda}_{\lambda}$ and $\mathbf{f}^{\nu}_{\lambda}$.

By comparison of equations (4.1.1) and (4.1.2), and using the relations of equation (4.1.8), we may derive the set of relations between the helicity scattering amplitudes for the irreducible representations and those for distinguishable particles, with analogous expressions being valid for the space-fixed ones:

$$\begin{aligned} f^{A_1 v' j' m'}_{v j \Omega} &= \begin{cases} f^{\lambda v' j' m'}_{\lambda v j \Omega} + 2 f^{\nu v' j' m'}_{\lambda v j \Omega} & j \text{ and } j' \text{ even} \\ 0 & j \text{ or } j' \text{ odd} \end{cases} \\ f^{A_2 v' j' m'}_{v j \Omega} &= \begin{cases} f^{\lambda v' j' m'}_{\lambda v j \Omega} + 2 f^{\nu v' j' m'}_{\lambda v j \Omega} & j \text{ and } j' \text{ odd} \\ 0 & j \text{ or } j' \text{ even} \end{cases} \\ f^{E v' j' m'}_{v j \Omega} &= \begin{cases} f^{\lambda v' j' m'}_{\lambda v j \Omega} - f^{\nu v' j' m'}_{\lambda v j \Omega} & j + j' \text{ even} \\ \sqrt{3} f^{\nu v' j' m'}_{\lambda v j \Omega} & j \text{ even}, j' \text{ odd} \\ -\sqrt{3} f^{\nu v' j' m'}_{\lambda v j \Omega} & j \text{ odd}, j' \text{ even} \end{cases} \end{aligned} \qquad (4.1.9)$$

$$f^{\lambda v' j' m'}_{\lambda v j \Omega} = \begin{cases} \frac{1}{3} f^{A_1 v' j' m'}_{v j \Omega} + \frac{2}{3} f^{E v' j' m'}_{v j \Omega} & j \text{ and } j' \text{ even} \\ \frac{1}{3} f^{A_2 v' j' m'}_{v j \Omega} + \frac{2}{3} f^{E v' j' m'}_{v j \Omega} & j \text{ and } j' \text{ odd} \\ 0 & j + j' \text{ odd} \end{cases}$$

$$f^{\nu v' j' m'}_{\lambda v j \Omega} = \begin{cases} \frac{1}{3} f^{A_1 v' j' m'}_{v j \Omega} - \frac{1}{3} f^{E v' j' m'}_{v j \Omega} & j \text{ and } j' \text{ even} \\ \frac{1}{3} f^{A_2 v' j' m'}_{v j \Omega} - \frac{1}{3} f^{E v' j' m'}_{v j \Omega} & j \text{ and } j' \text{ odd} \\ \frac{1}{\sqrt{3}} f^{E v' j' m'}_{v j \Omega} & j \text{ even}, j' \text{ odd} \\ -\frac{1}{\sqrt{3}} f^{E v' j' m'}_{v j \Omega} & j \text{ odd}, j' \text{ even} \end{cases} \qquad (4.1.10)$$

Since all three arrangement channels are indistinguishable, τ may take on only one value, and so it is not necessary to label the P_3 scattering amplitudes by τ and τ'.

4.2 Relation Between S-matrix and Scattering Amplitudes

We have determined the helicity scattering matrices **S** not only for the specific irreducible representation Γ but also for a specific total angular momentum J and parity Π. Accordingly, it is necessary to obtain the partial wave expansion of equation (3.1.3) in order to express the scattering amplitudes in terms of the $\mathbf{S}^{J\Pi\Gamma}$. The expansion for the plane wave term in terms of total angular momentum quantum quantum number J is known to be[2,79]

$$e^{i\mathbf{k}_\tau\cdot\mathbf{R}_\lambda}Y_j^m(\theta_{r_\lambda},\phi_{r_\lambda})\widetilde{_{R_\lambda\to\infty}}\left(\frac{1}{2k_\tau R_\lambda}\right)\sum_{JMi}\delta_m^M\mathcal{D}_{ji}^{JM}(\theta_\lambda,\phi_\lambda,\gamma_\lambda,\psi_\lambda)\times$$
$$2\pi^{\frac{1}{2}}i^{J+j+1}\sqrt{2J+1}\left(\delta_{-i}^M e^{-i[k_\tau R_\lambda-\frac{\pi}{2}(J+j)]}-\delta_i^M e^{i[k_\tau R_\lambda-\frac{\pi}{2}(J+j)]}\right) \tag{4.2.1}$$

Substitution of (4.2.1) and (3.1.4) into (4.1.2) yields, for the incoming plane wave part of the expression,

$$\Psi_{\bar\lambda}^{\Gamma_k\tau'v'_{\tau'}j'_{\tau'}m'_{\tau'}}(I)\widetilde{_{R_{\bar\lambda}\to\infty}}\sum_{J\lambda}c_{\tau'\lambda j'_{\tau'}}^{\Gamma_k}\left(\frac{\pi^{\frac{1}{2}}i^{J+j'_{\tau'}+1}\sqrt{2J+1}}{k_{\tau'v'_{\tau'}j'_{\tau'}}R_\lambda}\right)\frac{\phi_{\tau'v'_{\tau'}j'_{\tau'}}(r_\lambda)}{r_\lambda}\times$$
$$\mathcal{D}_{j'_{\tau'},-m'_{\tau'}}^{Jm'_{\tau'}}(\theta_\lambda,\phi_\lambda,\gamma_\lambda,\psi_\lambda)e^{-i[k_{\tau'v'_{\tau'}j'_{\tau'}}R_\lambda-\frac{\pi}{2}(J+j'_{\tau'})]} \tag{4.2.2}$$

(where we have used the definition (3.3.21) for the $\mathcal{D}$ functions) and for the outgoing plane and spherical waves we find that

$$\Psi_{\bar\lambda}^{\Gamma_k\tau'v'_{\tau'}j'_{\tau'}m'_{\tau'}}(O)\widetilde{_{R_{\bar\lambda}\to\infty}}\sum_{J\tau\lambda v_\tau j_\tau}c_{\tau\lambda j_\tau}^{\Gamma_k}\frac{\phi_\tau(r_\lambda)}{r_\lambda}\times$$
$$\left[\sum_J\left(\frac{\pi^{\frac{1}{2}}i^{J+j_\tau+1}\sqrt{2J+1}}{k_\tau R_\lambda}\right)\mathcal{D}_{j_\tau m'_{\tau'}}^{Jm'_{\tau'}}(\theta_\lambda,\phi_\lambda,\gamma_\lambda,\psi_\lambda)e^{i[k_\tau R_\lambda-\frac{\pi}{2}(J+j_\tau)]}\delta_{\tau v_\tau j_\tau}^{\tau'v'_{\tau'}j'_{\tau'}}\right.$$
$$\left.+\frac{e^{ik_\tau R_\lambda}}{R_\lambda}\sum_{\Omega_\tau}f_{\tau v_\tau j_\tau\Omega_\tau}^{J\Gamma\tau'v'_{\tau'}j'_{\tau'}m'_{\tau'}}(\theta_\lambda,\phi_\lambda)Y_{j_\tau}^{\Omega_\tau}(\gamma_\lambda,\psi_\lambda)\right] \tag{4.2.3}$$

The m' and $-m'$ in the superscript and subscript of $\mathcal{D}$ in (4.2.2) and the m' in the corresponding term of (4.2.3) resulted from the δ_m^M and δ_{-i}^M of (4.2.1).

Let us in (3.1.3) replace λ' by τ' since the latter scans the independent arrangement channels as explained in the paragraph preceding (3.3.1). The partial wave

expansion of the resulting $\Psi_{\bar{\lambda}}^{\tau' v'_{\tau'} j'_{\tau'} m'_{\tau'}}$ corresponding to (3.1.7) can be written as

$$\Psi_{\bar{\lambda}}^{\tau' v'_{\tau'} j'_{\tau'} m'_{\tau'}} = \sum_{J=0}^{\infty} \sum_{M=-J}^{J} \sum_{\Gamma} \sum_{k} C^{JM\Gamma_k \tau' v'_{\tau'} j'_{\tau'} m'_{\tau'}} \Psi_{\bar{\lambda}}^{JM\Gamma_k \tau' v'_{\tau'} j'_{\tau'} m'_{\tau'}} \tag{4.2.4}$$

The expression in the scattering matrix formalism is obtained by replacing the index $m'_{\tau'}$ with Ω':

$$\Psi_{\bar{\lambda}}^{\Gamma_k \tau' v'_{\tau'} j'_{\tau'} \Omega'_{\tau'}} = \sum_{JM} C^{JM\Gamma_k \tau' v'_{\tau'} j'_{\tau'} \Omega'_{\tau'}} \Psi_{\bar{\lambda}}^{JM\Gamma_k \tau' v'_{\tau'} j'_{\tau'} \Omega'_{\tau'}} \tag{4.2.5}$$

where $\Psi_{\bar{\lambda}}^{JM\Gamma_k \tau' v'_{\tau'} j'_{\tau'} \Omega'_{\tau'}}$ has the asymptotic form given by equation (3.3.10). Substitution of the asymptotic forms for the open parts of the $\mathcal{S}_{\bar{\tau}\Omega}^{J,\Omega''}$ and $\mathcal{C}_{\bar{\tau}\Omega}^{J,\Omega''}$ from equation (3.2.8) with

$$A_{\tau v_\tau j_\tau \Omega_\tau}^{J\Gamma \tau' v'_{\tau'} j'_{\tau'} \Omega'_{\tau'}}[S] = \delta_{\tau v_\tau j_\tau \Omega_\tau}^{\tau' v'_{\tau'} j'_{\tau'} \Omega'_{\tau'}} \tag{4.2.6}$$

$$B_{\tau v_\tau j_\tau \Omega_\tau}^{J\Gamma \tau' v'_{\tau'} j'_{\tau'} \Omega'_{\tau'}}[S] = S_{\tau v_\tau j_\tau \Omega_\tau}^{\tau' v'_{\tau'} j'_{\tau'} -\Omega'_{\tau'}} \tag{4.2.7}$$

yields

$$\Psi_{\bar{\lambda}}^{\Gamma_k \tau' v'_{\tau'} j'_{\tau'} \Omega'_{\tau'}}(I) \widetilde{_{R_{\bar{\lambda}} \to \infty}} \sum_{JM\Gamma k} C^{JM\Gamma_k \tau' v'_{\tau'} j'_{\tau'} \Omega'_{\tau'}} \sum_{\lambda} c_{\tau' \lambda j'_{\tau'}}^{\Gamma_k} \mathcal{D}_{j'_{\tau'} \Omega'_{\tau'}}^{JM}(\theta_\lambda, \phi_\lambda, \gamma_\lambda, \psi_\lambda) \times \frac{\phi_{\tau' v'_{\tau'} j'_{\tau'}}(r_\lambda)}{r_\lambda R_\lambda} \left| v_{\tau' v'_{\tau'} j'_{\tau'}} \right|^{-\frac{1}{2}} e^{-i[k_{\tau' v'_{\tau'} j'_{\tau'}} R_\lambda - \frac{\pi}{2}(J + j'_{\tau'})]} \tag{4.2.8}$$

$$\Psi_{\bar{\lambda}}^{\Gamma_k \tau' v'_{\tau'} j'_{\tau'} \Omega'_{\tau'}}(O) \widetilde{_{R_{\bar{\lambda}} \to \infty}} - \sum_{JM} C^{JM\Gamma_k \tau' v'_{\tau'} j'_{\tau'} \Omega'_{\tau'}} \sum_{\tau} \sum_{\lambda \Omega_\tau j_\tau} c_{\tau \lambda j_\tau}^{\Gamma_k} \times \tag{4.2.9}$$

$$\mathcal{D}_{j_\tau \Omega_\tau}^{JM}(\theta_\lambda, \phi_\lambda, \gamma_\lambda, \psi_\lambda) \frac{\phi_{\bar{\tau}}(r_\lambda)}{r_\lambda R_\lambda} \left| v_{\bar{\tau}} \right|^{-\frac{1}{2}} e^{i[k_{\bar{\tau}} R_\lambda - \frac{\pi}{2}(J + j_\tau)]} \left[S^{J\Gamma} \right]_{\tau v_\tau j_\tau \Omega_\tau}^{\tau' v'_{\tau'} j'_{\tau'} -\Omega'_{\tau'}}$$

(The $\mathbf{S}^{J\Gamma}$ non-parity scattering matrices are related to the parity ones of section 3 by equation (3.3.31).)

Since the asymptotic expressions (4.1.2) involving the scattering amplitudes and (4.2.5) involving the scattering matrix have the same initial conditions apart from the axis on which the the projection of the rotational angular momentum is specified, they can be simply related by

$$\Psi^{\Gamma_k \tau' v'_{\tau'} j'_{\tau'} m'_{\tau'}} = \sum_{\Omega'_{\tau'}} K_{\Omega'_{\tau'}}^{m'_{\tau'}} \Psi^{\Gamma_k \tau' v'_{\tau'} j'_{\tau'} \Omega'_{\tau'}} \tag{4.2.10}$$

Comparison of the equations for the initial wavevector (4.2.2) and (4.2.8) allows us to determine the constant factors in (4.2.10) and also the coefficients $C^{JM\Gamma_k\tau' v'_{\tau'} j'_{\tau'} \Omega'_{\tau'}}$ in (4.2.5); due to the orthogonality of the $\mathcal{D}$ functions, we must have

$$K^{m'_{\tau'}}_{\Omega'_{\tau'}} = \delta^{m'_{\tau'}}_{-\Omega'_{\tau'}} \tag{4.2.11}$$

$$C^{JM\Gamma_k,\tau' v'_{\tau'} j'_{\tau'} \Omega'_{\tau'}} = \delta^{M}_{-\Omega'_{\tau'}} \left(\frac{\pi\hbar(2J+1)}{\mu k_{\tau' v'_{\tau'} j'_{\tau'}}} \right)^{\frac{1}{2}} i^{J+j'_{\tau'}+1} \tag{4.2.12}$$

We may now equate the outgoing waves of equations (4.2.3) and (4.2.9) using equation (4.2.10) by substituting the values of the coefficients from equations (4.2.11) and (4.2.12):

$$\begin{aligned}
&\sum_{\tau\lambda v_\tau j_\tau \Omega_\tau} c^{\Gamma_k}_{\tau\lambda j_\tau} \frac{\phi_{\tau v_\tau j_\tau}(r_\lambda)}{r_\lambda} f^{\Gamma\tau' v'_{\tau'} j'_{\tau'} m'_{\tau'}}_{\tau v_\tau j_\tau \Omega_\tau}(\theta_\lambda, \phi_\lambda) Y^{\Omega_\tau}_{j_\tau}(\gamma_\lambda, \psi_\lambda) \frac{e^{ik_{\bar{\tau}} R_\lambda}}{R_\lambda} \\
&= \sum_{J\tau\lambda v_\tau j_\tau \Omega_\tau} c^{\Gamma_k}_{\tau\lambda j_\tau} \left| \frac{v_{\tau' v'_{\tau'} j'_{\tau'}}}{v_{\bar{\tau}}} \right|^{\frac{1}{2}} \left(\frac{\pi^{\frac{1}{2}} i^{J+j'_{\tau'}+1} \sqrt{2J+1}}{k_{\tau' v'_{\tau'} j'_{\tau'}} R_\lambda} \right) \frac{\phi_{\bar{\tau}}(r_\lambda)}{r_\lambda} \times \\
&\mathcal{D}^{Jm'}_{j_\tau \Omega_\tau}(\theta_\lambda, \phi_\lambda, \gamma_\lambda, \psi_\lambda) e^{i[k_{\bar{\tau}} R_\lambda - \frac{\pi}{2}(J+j_\tau)]} \left(\delta^{\tau' v'_{\tau'} j'_{\tau'} m'_{\tau'}}_{\tau v_\tau j_\tau \Omega_\tau} - \left[S^{J\Gamma} \right]^{\tau' v'_{\tau'} j'_{\tau'} m'_{\tau'}}_{\tau v_\tau j_\tau \Omega_\tau} \right)
\end{aligned} \tag{4.2.13}$$

Multiplication of both sides of (4.2.13) by $Y^{*\Omega''_{\tau''}}_{j''_{\tau''}}(\gamma_{\lambda''}, \psi_{\lambda''}) \phi_{\tau'' v''_{\tau''} j''_{\tau''}}(r_{\lambda''})$ integrating over $\gamma_{\lambda''}, \psi_{\lambda''}$ and $r_{\lambda''}$ and replacing double-primed terms by unprimed terms yields

$$\begin{aligned}
&f^{\Gamma\tau' v'_{\tau'} j'_{\tau'} m'_{\tau'}}_{\tau v_\tau j_\tau \Omega_\tau}(\theta_\lambda, \phi_\lambda) = \\
&\left| \frac{v_{\tau' v'_{\tau'} j'_{\tau'}}}{v_{\tau v_\tau j_\tau}} \right|^{\frac{1}{2}} \frac{i^{j'_{\tau'} - j_\tau + 1}}{2k_{\tau' v'_{\tau'} j'_{\tau'}}} \sum_{J=0}^{\infty} (2J+1) D^{J}_{m'_{\tau'}, \Omega_\tau}(\phi_\lambda, \theta_\lambda, 0) \left[T^{J\Gamma} \right]^{\tau' v'_{\tau'} j'_{\tau'} m'_{\tau'}}_{\tau v_\tau j_\tau \Omega_\tau}
\end{aligned} \tag{4.2.14}$$

where the transition matrix $\mathbf{T}^{J\Gamma}$ is defined as

$$\mathbf{T}^{J\Gamma} = \mathbf{I} - \mathbf{S}^{J\Gamma} \tag{4.2.15}$$

and the $\mathbf{S}^{J\Gamma}$ are given in terms of the calculated parity matrices $\mathbf{S}^{J\Pi\Gamma}$ in equation (3.3.31). From this point forward, the quantum numbers v, j and Ω will be assumed to bear the subscript τ and the quantum numbers v', j' and m' the subscript τ'.

4.3 Determination of Helicity Cross Sections

The differential cross section for scattering is defined as the ratio of the outgoing flux into a particular direction per unit solid scattering angle for a particular final state of the diatom to the total incident flux. These numbers can be obtained in irreducible representation format from the scattering amplitudes (4.2.14); however, the calculation of these functions has been done in mass-scaled coordinates, which affects the normalization of the wavefunctions. Accordingly, it is necessary to undo the mass scaling before determining the cross sections. The unscaled formula for the helicity wavefunction is obtained from (4.1.2) by replacing the scaled coordinates by unscaled, and noting that the normalization of their associated functions may change as well. Using primes to denote unscaled quantities, we have:

$$\Psi^{\prime\Gamma_k\tau'v'j'm'}_{\lambda} \underset{R_\lambda\to\infty}{\sim} \sum_{\tau}\sum_{\lambda}\sum_{vj} c^{\Gamma_k}_{\tau\lambda j}\frac{\phi'_\tau(r'_\lambda)}{r'_\lambda}\left[Y_j^{m'}(\theta_{\mathbf{r}_\lambda},\phi_{\mathbf{r}_\lambda})e^{i\mathbf{k}'_\tau\cdot\mathbf{R}'_\lambda}\delta^{\tau'v'j'}_{\tau vj}\right.$$
$$\left. + \sum_{\Omega} f^{\Gamma\tau'v'j'm'}_{\tau vj\Omega}(\theta_\lambda,\phi_\lambda)Y_j^{\Omega}(\gamma_\lambda,\psi_\lambda)\frac{e^{ik'_\tau R'_\lambda}}{R'_\lambda}\right] \tag{4.3.1}$$

In terms of these unscaled functions, the helicity irreducible representation differential cross section is defined by

$$\sigma^{\Gamma\tau'v'j'm'}_{\tau vj\Omega}(\theta_\lambda,\phi_\lambda) = \frac{v'_{\tau vj}}{v'_{\tau'v'j'}}\left|f^{\prime\Gamma\tau'v'j'm'}_{\tau vj\Omega}(\theta_\lambda,\phi_\lambda)\right|^2 \tag{4.3.2}$$

The relation between mass-scaled and unscaled coordinates is[2]

$$\mathbf{R}_\lambda = \left(\frac{\mu_{\lambda,\nu\kappa}}{\mu}\right)^{\frac{1}{2}}\mathbf{R}'_\lambda; \quad \mathbf{r}_\lambda = \left(\frac{\mu_{\nu\kappa}}{\mu}\right)^{\frac{1}{2}}\mathbf{r}'_\lambda \tag{4.3.3}$$

where

$$\mu_{\nu\kappa} = \frac{m_\nu m_\kappa}{m_\nu + m_\kappa} \quad \mu_{\lambda,\nu\kappa} = \frac{m_\lambda(m_\nu+m_\kappa)}{m_\lambda+m_\nu+m_\kappa}$$
$$\mu = \left(\frac{m_\lambda m_\nu m_\kappa}{m_\lambda+m_\nu+m_\kappa}\right)^{\frac{1}{2}} = (\mu_{\lambda,\nu\kappa}\mu_{\nu\kappa})^{-\frac{1}{2}} \tag{4.3.4}$$

We note that, from the forms of equation (4.3.4), equation (4.3.3) may be rewritten as

$$\mathbf{R}_\lambda = a_\lambda\mathbf{R}'_\lambda; \quad \mathbf{r}_\lambda = a_\lambda^{-1}\mathbf{r}'_\lambda \tag{4.3.5}$$

where we have defined

$$a_\lambda = \left(\frac{\mu_{\lambda,\nu\kappa}}{\mu}\right)^{\frac{1}{2}} = \left(\frac{\mu}{\mu_{\nu\kappa}}\right)^{\frac{1}{2}} = \left(\frac{\mu_{\lambda,\nu\kappa}}{\mu_{\nu\kappa}}\right)^{\frac{1}{4}} \tag{4.3.6}$$

When two or more atoms are identical, the terms a_λ and $a_{\lambda'}$ are equal if the λ and λ' arrangement channels are both of type τ; we will therefore use the symbol a_τ in the following discussion when appropriate.

The wave vector $\mathbf{k}_{\lambda vj}$ in equation (3.2.6) has a magnitude proportional to the square root of the reduced mass μ. The function corresponding to unscaled coordinates depends on the reduced mass $\mu_{\lambda,\nu\kappa}$, and accordingly

$$\mathbf{k'}_{\tau vj} = a_\tau \mathbf{k}_{\tau vj} \tag{4.3.7}$$

Therefore we have

$$\begin{aligned} \mathbf{k}'_{\tau vj} \cdot \mathbf{R}'_\lambda &= \mathbf{k}_{\tau vj} \cdot \mathbf{R}_\lambda \\ k'_{\lambda vj} R'_\lambda &= k_{\lambda vj} R_\lambda \end{aligned} \tag{4.3.8}$$

Similarly, the channel velocities are proportional to $\mu^{-\frac{1}{2}}$ and the unscaled velocities will be given by

$$v'_{\tau vj} = a_\tau^{-1} v_{\tau vj} \tag{4.3.9}$$

The normalization of the function $\phi'_{\bar{\tau}}(r'_\lambda)$ is determined from the equations

$$\int_0^{r_\lambda^{max}} |\phi_{\bar{\tau}}(r_\lambda)|^2 \, dr_\lambda = 1 = a_\tau^{-1} \int_0^{r_\lambda'^{max}} |\phi_{\bar{\tau}}(r'_\lambda)|^2 \, dr'_\lambda \tag{4.3.10}$$

and

$$\int_0^{r_\lambda'^{max}} |\phi'_{\bar{\tau}}(r'_\lambda)|^2 \, dr'_\lambda = 1 \tag{4.3.11}$$

Comparison of these equations leads to the relation

$$\phi_{\bar{\tau}}(r'_\lambda) = a_\tau^{1/2} \phi'_{\bar{\tau}}(r'_\lambda) \tag{4.3.12}$$

Examination of the incoming plane wave parts of equations (4.2.2) and (4.3.1) after taking into account the above information shows that

$$\Psi'^{\Gamma_k \tau' v' j' m'} = a_{\tau'}^{-\frac{5}{2}} \Psi^{\Gamma_k \tau' v' j' m'} \tag{4.3.13}$$

Comparison of the outgoing wave parts then yields

$$f'^{\Gamma\tau'v'j'm'}_{\tau vj\Omega}(\theta_\lambda,\phi_\lambda) = \left(\frac{a_\tau}{a_{\tau'}^3}\right)^{\frac{1}{2}} f^{\Gamma\tau'v'j'm'}_{\tau vj\Omega}(\theta_\lambda,\phi_\lambda) \tag{4.3.14}$$

and we can therefore express the differential cross section in terms of mass-scaled quantities as

$$\sigma^{\Gamma\tau'v'j'm'}_{\tau vj\Omega}(\theta_\lambda,\phi_\lambda) = a_{\tau'}^{-2}\frac{v_{\tau vj}}{v_{\tau'v'j'}}\left|f^{\Gamma\tau'v'j'm'}_{\tau vj\Omega}(\theta_\lambda,\phi_\lambda)\right|^2 \tag{4.3.15}$$

Substitution of equation (4.2.14) into equation (4.3.15) finally yields

$$\sigma^{\Gamma\tau'v'j'm'}_{\tau vj\Omega}(\theta_\lambda) = \frac{1}{4k'^2_{\tau'v'j'}}\left|\sum_{J=0}^{\infty}(2J+1)d^J_{m'\Omega}(\theta_\lambda)\left[T^{J\Gamma}\right]^{\tau'v'j'm'}_{\tau vj\Omega}\right|^2 \tag{4.3.16}$$

These differential cross sections are seen to be independent of ϕ_λ.[2]

The integral cross section $Q^{\Gamma\tau'v'j'm'}_{\tau vjm}$ is obtained by integration of (4.3.16) over θ_λ and ϕ_λ. The integral over ϕ_λ yields a factor of 2π, and the orthonormality of the d^J functions[76] can be used to get

$$Q^{\Gamma\tau'v'j'm'}_{\tau vj\Omega} = \frac{\pi}{k'^2_{\tau'v'j'}}\sum_{J=0}^{\infty}(2J+1)\left|\left[T^{J\Gamma}\right]^{\tau'v'j'm'}_{\tau vj\Omega}\right|^2 \tag{4.3.17}$$

4.4 Inclusion of Nuclear Spin - Observable Cross Sections

When the three-particle system under consideration has P_2 or P_3 permutation symmetry, the nuclear spin of the identical particles must be taken into account. The hamiltonian which was used in the previous sections does not have spin-dependent terms, and as a result the total nuclear motion wavefunction can be written as a direct product of the spatial wavefunction which satisfies the spin-independent (nuclear motion) Schrödinger equation and a nuclear spin wavefunction. This total wavefunction is required to be either symmetric (for bosons) or antisymmetric (for fermions) with respect to interchange of the identical nuclei; accordingly, the calculated IR cross sections must be appropriately combined to yield the observable cross sections.[80]

The total nuclear spin wavefunction can be written as a product of three individual nuclei wavefunctions, each of which is a simultaneous eigenfunction of the square of the corresponding spin angular momentum $\hat{s}_i^2$ (with eigenvalue $\hbar^2 s_i(s_i+1)$) and of its projection on the space-fixed $\mathbf{Z}$ axis $\hat{s}_{Zi}$ (with eigenvalue $\hbar m_{s_i}$). Alternately, we may couple the spin angular momenta of the individual nuclei together; the result is a simultaneous eigenfunction of the square of the total spin angular momentum $\hat{S}^2$ (with eigenvalue $\hbar^2 S(S+1)$), of its projection on the space-fixed $\mathbf{Z}$ axis $\hat{S}_Z$ (with eigenvalue $\hbar M_S$), as well as of the $\hat{s}_i^2$ and $\hat{s}_{iZ}$ (with eigenvalues as above). In addition, the permutation and projection operators of P_p act on the spin wavefunction as well as the spatial wavefunction, and the spin functions can be chosen as eigenfunctions of the projection operators $\hat{P}^{\Gamma}_{kk}$.

For the case of the P_2 group, there are two identical nuclei with spin s and another different nucleus; this latter particle is not affected by the permutation operators and therefore its spin will not enter into the discussion to follow. The quantum number S associated with the square of the sum of the angular momenta of the two identical particles is an integer in the range $[0, 2s]$, and there are $2S+1$ M_S states for each value of S for a total of $(2s+1)^2$ states. The irreducible

representation associated with each of the corresponding nuclear spin functions can be found by examination of the angular momentum coupling by Clebsch-Gordon coefficients:[81] since the spin functions contain a term $C(ssS;m_1m_2M_s)$, functions with $S+2s$ even will have A' spin symmetry, while those with $S+2s$ odd will have A'' symmetry. (A more complete analysis appears in appendix B.) The irreducible representation of the spin function is independent of the projection of S on the **Z** axis.[80]

The direct product rules for the P_2 representations are as follows:

$$A' \otimes A' = A'' \otimes A'' = A' \qquad A' \otimes A'' = A'' \otimes A' = A'' \tag{4.4.1}$$

For fermions, $2s$ is odd, and we require that the overall space-spin nuclear wavefunction have symmetry A''; accordingly, an A' spatial function is paired with a spin function of even S (symmetry A'') and an A'' spatial function with a spin function of odd S (symmetry A'). Since for bosons the quantity $2s$ is even and the overall wavefunction must have A' symmetry, the same S-rule (but opposite nuclear spin symmetry rule) applies in this case as did for fermions: an A' spatial function is paired with a spin function of even S (symmetry A') and an A'' spatial function with a spin function of odd S (symmetry A'').

The physically observable cross sections, which must obey the proper spin statistics, can be derived by weighting the irreducible representation cross sections by the relative number of states with even S and odd S. The number of states with even values of S, including the degeneracy of the M_S quantum number, is

$$N_S^e = \frac{1}{2}(2s+1)(2s+1+(-1)^{2s}) \tag{4.4.2}$$

while the number with odd S is

$$N_S^o = \frac{1}{2}(2s+1)(2s+1-(-1)^{2s}) \tag{4.4.3}$$

the sum of these two quantities being $(2s+1)^2$. Thus in the observable cross sections the A' state will have a weight of $\frac{N_S^e}{(2s+1)^2}$, while the A'' state will be weighted by

$\frac{N_S^o}{(2s+1)^3}$. If we denote the spin-weighted (observed) cross sections by $\sigma_{rvj\Omega}^{r'v'j'm'}$, we find that the appropriate values for these quantities for an AB_2 system are:

$$\sigma_{Avj\Omega}^{Av'j'm'} = \begin{cases} \frac{2s+1+(-1)^{2s}}{2(2s+1)}\sigma_{Avj\Omega}^{A'Av'j'm'} & j \text{ and } j' \text{ even} \\ 0 & j+j' \text{ odd} \\ \frac{2s+1-(-1)^{2s}}{2(2s+1)}\sigma_{Avj\Omega}^{A''Av'j'm'} & j \text{ and } j' \text{ odd} \end{cases}$$

$$\sigma_{Avj\Omega}^{Bv'j'm'} = \begin{cases} \frac{2s+1+(-1)^{2s}}{2(2s+1)}\sigma_{Avj\Omega}^{A'Bv'j'm'} & j \text{ even} \\ \frac{2s+1-(-1)^{2s}}{2(2s+1)}\sigma_{Avj\Omega}^{A''Bv'j'm'} & j \text{ odd} \end{cases} \qquad (4.4.4)$$

$$\sigma_{Bvj\Omega}^{Av'j'm'} = \begin{cases} \frac{2s+1+(-1)^{2s}}{2(2s+1)}\sigma_{Bvj\Omega}^{A'Av'j'm'} & j' \text{ even} \\ \frac{2s+1-(-1)^{2s}}{2(2s+1)}\sigma_{Bvj\Omega}^{A''Av'j'm'} & j' \text{ odd} \end{cases}$$

$$\sigma_{Bvj\Omega}^{Bv'j'm'} = \frac{2s+1+(-1)^{2s}}{2(2s+1)}\sigma_{Bvj\Omega}^{A'Bv'j'm'} + \frac{2s+1-(-1)^{2s}}{2(2s+1)}\sigma_{Bvj\Omega}^{A''Bv'j'm'} \qquad (4.4.5)$$

In the (nonreactive) σ_A^A cross section, it can be seen that the diatomic rotation parity is preserved. As an example, for the case $s = 1/2$ (*e.g.*, F + H_2), the observable cross sections are

$$\sigma_{Avj\Omega}^{Av'j'm'} = \begin{cases} \frac{1}{4}\sigma_{Avj\Omega}^{A'Av'j'm'} & j \text{ and } j' \text{ even} \\ 0 & j+j' \text{ odd} \\ \frac{3}{4}\sigma_{Avj\Omega}^{A''Av'j'm'} & j \text{ and } j' \text{ odd} \end{cases}$$

$$\sigma_{Avj\Omega}^{Bv'j'm'} = \begin{cases} \frac{1}{4}\sigma_{Avj\Omega}^{A'Bv'j'm'} & j \text{ even} \\ \frac{3}{4}\sigma_{Avj\Omega}^{A''Bv'j'm'} & j \text{ odd} \end{cases} \qquad (4.4.6)$$

$$\sigma_{Bvj\Omega}^{Av'j'm'} = \begin{cases} \frac{1}{4}\sigma_{Bvj\Omega}^{A'Av'j'm'} & j' \text{ even} \\ \frac{3}{4}\sigma_{Bvj\Omega}^{A''Av'j'm'} & j' \text{ odd} \end{cases}$$

$$\sigma_{Bvj\Omega}^{Bv'j'm'} = \frac{1}{4}\sigma_{Bvj\Omega}^{A'Bv'j'm'} + \frac{3}{4}\sigma_{Bvj\Omega}^{A''Bv'j'm'}$$

The symmetry properties for the P_3 group are not as easy to determine. In this case, there are three identical nuclei of spin s, and the sum of their spin angular momenta S can have integer values in the range $[0, 3s]$ for integer s, while for half-odd integer s it can have half-odd integer values in the range $[\frac{1}{2}, 3s]$; the total number of states is $(2s+1)^3$. The direct product rules for the P_3 representations

are:

$$A_1 \otimes A_1 = A_2 \otimes A_2 = A_1$$
$$A_2 \otimes A_1 = A_1 \otimes A_2 = A_2$$
$$E \otimes A_1 = A_1 \otimes E = E \qquad (4.4.7)$$
$$E \otimes A_2 = A_2 \otimes E = E$$
$$E \otimes E = A_1 \oplus A_2 \oplus E$$

The number of symmetrized spin states can be determined in the following way. We start with the set of states $|s(1)m_s(1)\rangle|s(2)m_s(2)\rangle|s(3)m_s(3)\rangle$, where since the three particles are identical $s(1) = s(2) = s(3) = s$. These functions are eigenfunctions of $\hat{S}_Z$ (with eigenvalue $M_s = m_s(1) + m_s(2) + m_s(3)$) but are not necessarily eigenvectors of $\hat{S}^2$ or of a projection operator. There are $2s + 1$ unsymmetrized states with $m_s(1) = m_s(2) = m_s(3)$, and application of the projection operators shows that these each transform as A_1; there are $2s(2s + 1)$ unsymmetrized states with $m_s(1) = m_s(2) \neq m_s(3)$, which the projection operators couple with the $2s(2s + 1)$ $m_s(1) \neq m_s(2) = m_s(3)$ and $2s(2s + 1)$ $m_s(1) = m_s(3) \neq m_s(2)$ states to yield a total of $2s(2s + 1)$ A_1 and $2s(2s + 1)$ (doubly degenerate) E states; and finally there are $2s(2s - 1)(2s + 1)$ states with all three m_s values unequal which are coupled by the projection operators into $2s(2s - 1)(2s + 1)/6$ A_1 and A_2 functions and $2s(2s-1)(2s+1)/3$ E functions. The total number of spin states of each symmetry is therefore given by

$$N_{A_1} = (2s+1)(2s+2)(2s+3)/6; \quad N_{A_2} = 2s(4s^2-1)/6; \quad N_E = 2s(2s+1)(2s+2)/3 \qquad (4.4.8)$$

with $N_{A_1} + N_{A_2} + 2N_E = (2s + 1)^3$ as they should. We note here that the IR decomposition of a member of the original set of states is determined solely by the number of equal values of m_s, and as a consequence there is no correlation between Γ and M_s (*i.e.*, the irreducible representation is independent of M_s); however, it will be seen that there is a correlation between Γ and S.

From examination of the multiplication table (4.4.7), we see that for bosons

A_1 spin symmetry functions must be paired with A_1 spatial symmetry functions to generate a total wavefunction with A_1 permutation symmetry. Similarly, the A_2 spin functions must be paired with A_2 spatial functions and E spin functions with E spatial functions to generate the physically acceptable total wavefunctions with A_1 symmetry. For fermions, where we require the total wavefunction to have A_2 symmetry, we see that A_1 spin functions pair with the A_2 spatial functions, A_2 spin functions with the A_1 spatial functions, and E spin functions with the E spatial functions. The spatial part of the wavefunction for any initial state may be decomposed into a sum of A_1, A_2 and E irreducible representation spatial wavefunctions as per equation (3.3.1); however, knowing the initial rotational quantum number j', we may say with complete generality that the wavefunction will decompose into an A_1 and an E part for even j', or into an A_2 and an E part for odd j', since there are no A_1 states with odd j' or A_2 states with even j'. Therefore, we would like a more compact quantity representing the total number of A_1 or A_2 spatial states available, depending on whether the particles are fermions or bosons and on the value of j'. Examination of (4.4.8) shows that the individual terms in the products giving N_{A_1} and N_{A_2} have a one-to-one correspondence if the number 2 is subtracted from each term in N_{A_1}; as a consequence, bosons will always have more A_1 spin-weighted spatial states than A_2 spin-weighted spatial states, while the opposite is true for fermions. With this information, we find that the quantity N_A, which is the number of spin states for either the A_1 or A_2 spatial wavefunction, depending on the value of j' and on the spin statistics of the particles, may be written as

$$N_A = \left[2s + (-1)^{j'+2s}\right]\left[2s + 1 + (-1)^{j'+2s}\right]\left[2s + 2 + (-1)^{j'+2s}\right]/6 \qquad (4.4.9)$$

and that therefore the total number of spin states corresponding to any initial condition of the spatial wavefunction of the system is the sum of this number and N_E, which is found after some algebraic manipulation to be

$$N_s = N_A + N_E = \frac{1}{2}(2s+1)^2\left[2s + 1 + (-1)^{j'+2s}\right] \qquad (4.4.10)$$

The final result[80] is then obtained by weighting the Γ irreducible representation cross sections by $\frac{N_\Gamma}{N_s}$ and summing over Γ, which yields

$$\sigma_{vj\Omega}^{v'j'm'} = \begin{cases} \frac{1}{3}\frac{2s+1+2(-1)^{2s}}{(2s+1)}\sigma_{vj\Omega}^{A_1v'j'm'} + \frac{2}{3}\frac{2s+1-(-1)^{2s}}{(2s+1)}\sigma_{vj\Omega}^{Ev'j'm'} & j \text{ and } j' \text{ even} \\ \frac{1}{3}\frac{2s+1-2(-1)^{2s}}{(2s+1)}\sigma_{vj\Omega}^{A_2v'j'm'} + \frac{2}{3}\frac{2s+1+(-1)^{2s}}{(2s+1)}\sigma_{vj\Omega}^{Ev'j'm'} & j \text{ and } j' \text{ odd} \\ \frac{2}{3}\frac{2s+1-(-1)^{2s+j'}}{(2s+1)}\sigma_{vj\Omega}^{Ev'j'm'} & \text{otherwise} \end{cases} \tag{4.4.11}$$

(The details of the analysis which results in the above equations appears in appendix B.) The tau labels are the same for each arrangement channel and are therefore dropped from the notation.

For $s = 0$ (*e.g.* ^{16}O) there can be only one nuclear spin state, with $S = 0$; this state has A_1 symmetry. Since the overall wavefunction must also have A_1 symmetry in this case, the only allowed spatial symmetry is A_1, with weight 1. (Note that in this case only even values of j are allowed for the diatoms, as is observed in nature.) For $s = 1/2$ (*e.g.* H) there is a quartet spin state for $S = 3/2$; since the $M_S = 3/2$ term transforms as A_1 by the arguments presented after (4.4.7) and the IR is independent of M_S, each member of the quartet will transform independently as A_1. This leaves two $S = 1/2$ doublet states, and each pair of these states with the same M_S value transforms as E. There are no A_2 spin states for $s = 1/2$, so the A_1 spatial symmetry does not contribute to the cross sections. The explicit form for the observable cross sections in this case is

$$P_3, s = 1/2 : \sigma_{vj\Omega}^{v'j'm'} = \begin{cases} \sigma_{vj\Omega}^{Ev'j'm'} & j \text{ and } j' \text{ even} \\ \frac{2}{3}\sigma_{vj\Omega}^{A_2v'j'm'} + \frac{1}{3}\sigma_{vj\Omega}^{Ev'j'm'} & j \text{ and } j' \text{ odd} \\ \frac{1}{3}\sigma_{vj\Omega}^{Ev'j'm'} & j \text{ even}, j' \text{ odd} \\ \sigma_{vj\Omega}^{Ev'j'm'} & j \text{ odd}, j' \text{ even} \end{cases} \tag{4.4.12}$$

In the case $s = 1$ (*e.g.* D), the following spin states exist: for $S = 3$ there is a single septuplet state, each member of which transforms as A_1; for $S = 2$ there are two pentuplet states, and each pair of these functions with the same M_S value transforms as E; for $S = 1$ there are three triplet states, and each set which has

the same M_S transform as $A_1 \oplus E$; and for $S = 0$ there is a singlet A_2 state.

$$P_3, s = 1 : \sigma_{vj\Omega}^{v'j'm'} = \begin{cases} \frac{5}{9}\sigma_{vj\Omega}^{A_1 v'j'm'} + \frac{4}{9}\sigma_{vj\Omega}^{Ev'j'm'} & j \text{ and } j' \text{ even} \\ \frac{1}{9}\sigma_{vj\Omega}^{A_2 v'j'm'} + \frac{8}{9}\sigma_{vj\Omega}^{Ev'j'm'} & j \text{ and } j' \text{ odd} \\ \frac{8}{9}\sigma_{vj\Omega}^{Ev'j'm'} & j \text{ even}, j' \text{ odd} \\ \frac{4}{9}\sigma_{vj\Omega}^{Ev'j'm'} & j \text{ odd}, j' \text{ even} \end{cases} \tag{4.4.13}$$

The discussion above has assumed that the initial nuclei are not spin-selected. To model the case where the initial total spin of the nuclei is known, it would be necessary to take into account the available symmetries for that spin and the number of spin states, and weight the contributions to the cross section accordingly.

4.5 The H_3 Conical Intersection

The above formalism for reactive scattering implicitly assumes that the Born-Oppenheimer approximation is valid and that the reaction occurs on the ground state electronic potential energy surface which the approximation provides. Since the minimum of the first excited electronic state surface is 2.7 eV above the minimum of the ground state surface (which is the bottom of the potential well for the H_2 diatom and is our choice for the zero of energy), it would seem to be a very good approximation for the energy range of our calculation (0–1.6 eV). However, there is a complication for the H_3 case, which is the existence of a conical intersection of the ground and first excited electronic states for equilateral triangular configurations of the nuclei ($\omega_\lambda = \gamma_\lambda = \frac{\pi}{2}$).[82–85] If one traces a path in nuclear configuration space which encloses the line of the conical intersection and returns to the original configuration, the electronic wavefunction if forced to be real changes sign. Since the total wavefunction including electronic and nuclear parts must be single-valued and continuous, there must be a compensating sign change in the nuclear wavefunction. This is known as the molecular Aharonov-Bohm effect[83–86] and is an example of Berry's geometric phase.[87]

The surface functions which were used in the calculation of the scattering matrices do not have the geometric phase effect built in, and modification of the basis set

to satisfy the requirements of this effect would be non-trivial. However, such a modification is not necessary. It has been shown formally in a semiclassical discussion[85] that, under the condition that the wavefunction be negligible in regions of configuration space near the half-plane described in our coordinate system by $\gamma_\lambda = \frac{\pi}{2}$ and $\omega_\lambda > \frac{\pi}{2}$, the only effect of the geometric phase is to reverse the sign of the exchange scattering amplitudes. This corresponds to a change of the distinguishable particle matrix from $\mathbf{S}$ to $\bar{\mathbf{S}}$ as follows:

$$\left[\bar{\mathbf{S}}^{J\Pi}\right]_{\lambda v j\Omega}^{\lambda' v' j' \Omega'} = \begin{cases} \left[\mathbf{S}^{J\Pi}\right]_{\lambda v j\Omega}^{\lambda' v' j' \Omega'} & \lambda = \lambda' \\ -\left[\mathbf{S}^{J\Pi}\right]_{\lambda v j\Omega}^{\lambda' v' j' \Omega'} & \lambda \neq \lambda' \end{cases} \tag{4.5.1}$$

The correct IR $\mathbf{S}$ matrices may be found by using this expression in equation (3.3.17); in terms of the calculated IR matrices, they are given by

$$\left[\bar{\mathbf{S}}^{J\Pi A_1}\right]_{\lambda v j\Omega}^{\lambda' v' j' \Omega'} = \begin{cases} -\frac{1}{3}\left[\mathbf{S}^{J\Pi A_1}\right]_{\lambda v j\Omega}^{\lambda' v' j' \Omega'} + \frac{4}{3}\left[\mathbf{S}^{J\Pi E}\right]_{\lambda v j\Omega}^{\lambda' v' j' \Omega'} & j \text{ and } j' \text{ even} \\ 0 & \text{otherwise} \end{cases}$$

$$\left[\bar{\mathbf{S}}^{J\Pi A_2}\right]_{\lambda v j\Omega}^{\lambda' v' j' \Omega'} = \begin{cases} -\frac{1}{3}\left[\mathbf{S}^{J\Pi A_2}\right]_{\lambda v j\Omega}^{\lambda' v' j' \Omega'} + \frac{4}{3}\left[\mathbf{S}^{J\Pi E}\right]_{\lambda v j\Omega}^{\lambda' v' j' \Omega'} & j \text{ and } j' \text{ odd} \\ 0 & \text{otherwise} \end{cases}$$

$$\left[\bar{\mathbf{S}}^{J\Pi E}\right]_{\lambda v j\Omega}^{\lambda' v' j' \Omega'} = \begin{cases} \frac{1}{3}\left[\mathbf{S}^{J\Pi A_1}\right]_{\lambda v j\Omega}^{\lambda' v' j' \Omega'} + \frac{2}{3}\left[\mathbf{S}^{J\Pi E}\right]_{\lambda v j\Omega}^{\lambda' v' j' \Omega'} & j \text{ and } j' \text{ even} \\ \frac{1}{3}\left[\mathbf{S}^{J\Pi A_2}\right]_{\lambda v j\Omega}^{\lambda' v' j' \Omega'} + \frac{2}{3}\left[\mathbf{S}^{J\Pi E}\right]_{\lambda v j\Omega}^{\lambda' v' j' \Omega'} & j \text{ and } j' \text{ odd} \\ -\left[\mathbf{S}^{J\Pi E}\right]_{\lambda v j\Omega}^{\lambda' v' j' \Omega'} & \text{otherwise} \end{cases} \tag{4.5.2}$$

Accordingly, the results of the present calculations are valid with trivial modification if the conditions above hold. A calculation for the $J = 0$ partial wave of H + H_2 with the geometric phase effect included has been performed in order to test the validity of the condition at energies approaching 2.0 eV;[88] the results show that for the energy range of the present calculation it will suffice to use equation (4.5.2) to determine the cross sections under the influence of the conical intersection.

5. LOGARITHMIC DERIVATIVE ALGORITHM

5.1 Solution of the log derivative equation

As has been mentioned previously in (I), the bulk of the computational effort will be in the propagation of the coupled equations (2.2.6), and as a consequence we need an efficient method for the propagation. We use a modified version of the log derivative propagator of Johnson[54] In this method, the initial log derivative matrix is set to correspond to a wavefunction with very small amplitude, and the matrix is propagated according to the rules

$$\begin{aligned} \mathbf{Z}_0 &= \mathbf{P}+\Delta\rho\boldsymbol{\mathcal{Y}}(\rho_0)+\mathbf{V}_0 \\ \mathbf{Z}_i &= 2\mathbf{P}+\mathbf{V}_i+\mathbf{Q}[\mathbf{Z}_{i-1}]^{-1}\mathbf{Q}; \quad i=1,N_I-1 \\ \boldsymbol{\mathcal{Y}}(\rho_{N_I}) &= (\mathbf{P}+\mathbf{V}_{N_I}+\mathbf{Q}[\mathbf{Z}_{N_I-1}]^{-1}\mathbf{Q})/\Delta\rho \end{aligned} \tag{5.1.1}$$

where there are N_I steps of size $\Delta\rho = (\rho_{N_I}-\rho_0)/N_I$ between calculations of the log derivative $\boldsymbol{\mathcal{Y}}$, and the potential terms $\mathbf{V}_i$ are given by

$$\mathbf{V}_i = \begin{cases} \frac{\Delta\rho}{3}\mathbf{U}_i & i=0,N_I \\ \frac{2\Delta\rho}{3}\mathbf{U}_i & i=2,4,6,\ldots N_I-2 \\ 8\mathbf{I}-8\left[\mathbf{I}-\frac{\Delta\rho^2}{6}\mathbf{U}_i\right]^{-1} & i=1,3,5,\ldots N_I-1 \end{cases} \tag{5.1.2}$$

with the matrix $\mathbf{U}$ defined as

$$\mathbf{U} = \mathbf{K}-\mathbf{K}_{\mathrm{ref}} \tag{5.1.3}$$

In the original Johnson propagator, which was used for propagation of the $J=0$ and 1 results, the matrices $\mathbf{P}$ and $\mathbf{Q}$ are both equal to the identity matrix $\mathbf{I}$, which corresponds to $\mathbf{K}_{\mathrm{ref}} = \mathbf{0}$; also, for this version the initial log derivative matrix was set to $(10^{30})\mathbf{I}$. For the higher J partial waves, the propagator was modified according to the method of Manolopoulos[69] to have a constant (non-zero) reference potential, which was defined to be

$$\begin{aligned} [\mathbf{K}_{\mathrm{ref}}]_n^{n'} &= \delta_n^{n'}[\mathbf{K}_{\frac{N}{2}}]_n^n \\ &= \delta_n^{n'}p_n^2 \end{aligned} \tag{5.1.4}$$

with $\mathbf{K}_{\frac{N}{2}}$ being the value of $\mathbf{K}$ at the center of the interval between calculations of $\mathcal{Y}$. In view of (2.2.3) and (2.2.4), $\mathbf{U}$ is independent of E in the Manolopoulos modification (but not in the Johnson one). Along with producing a better representation for the wavefunction due to the potential following characteristic, this modification has the advantage of making the inversion in equation (5.1.2) energy-independent, and as the matrix inversion is the most time-consuming part of the calculation, effectively eliminates $\frac{1}{3}$ of the operations and CPU time necessary for the second and subsequent energies. In this version,

$$[\mathbf{P}]_n^{n'} = \delta_n^{n'} \begin{cases} \Delta\rho p_n \coth(\Delta\rho p_n) & p_n^2 \geq 0 \\ \Delta\rho |p_n| \cot(\Delta\rho |p_n|) & p_n^2 < 0 \end{cases} \tag{5.1.5}$$

$$[\mathbf{Q}]_n^{n'} = \delta_n^{n'} \begin{cases} \Delta\rho p_n / \sinh(\Delta\rho p_n) & p_n^2 \geq 0 \\ \Delta\rho |p_n| / \sin(\Delta\rho |p_n|) & p_n^2 < 0 \end{cases} \tag{5.1.6}$$

A small amount of additional work is necessary to calculate these matrices and to perform matrix multiplication with $\mathbf{Q}$; however, this extra effort is small compared to the savings from making the $\mathbf{V}$ matrix energy-independent. In addition, the initial log derivative matrix is more accurately estimated by setting it to the diagonal part of the WKB approximation for the log derivative, *i.e.*, $[\mathcal{Y}(\rho_{\min})]_n^{n'} = \delta_n^{n'} [\mathbf{K}^{\frac{1}{2}}(\rho_{\min})]_n^n$. This change in initial condition does not change the final log derivative significantly if a sufficiently small value of $\bar{\rho}$ is chosen for the starting point, but allows one to start the propagation at a larger value of $\bar{\rho}$ than the previous version would permit.

The input data to the propagation consists of sets of N by N interaction matrices for each value of $\bar{\rho}$ and an N by N overlap matrix between each adjacent pair of $\bar{\rho}$ values, along with an array containing the LHSF energies and the values of ρ at which the interaction matrices were calculated. The total number of available functions N is determined by the smallest number of linearly independent surface functions for all values of $\bar{\rho}$. The actual number of functions propagated may be any positive number less than N, and will be denoted by N_p; the amount of time necessary for the propagation is proportional to that for matrix inversion and therefore

is of order N_p^3.

The formalism for the calculation of the log derivative is invariant when the transpose of the matrix is substituted in its place, and therefore the log derivative is strictly symmetric. However, we do not assume symmetry of the log derivative matrix; the calculated overlap matrices $\mathcal{O}$ are not precisely orthogonal, since the basis sets at each $\bar{\rho}$ are not complete for finite N, and the fact that $\mathcal{O}^{-1} \neq \mathcal{O}^{\mathrm{T}}$ causes the calculated log derivative to deviate from symmetry. This deviation is used as one indicator of the accuracy of the calculation.

The majority of the computational effort for the propagation is in matrix inversion. As a consequence, the time needed for propagation is approximately linear in the number of energies and propagation steps and cubic in the matrix size. The algorithm for the log derivative calculation is well suited for the CRAY architecture; using the LAPACK[89] linear equation solver routines SGETRF and SGETRS on a CRAY Y-MP/864, we achieve speeds ranging from 150 Mflops for small matrix sizes up to 225 Mflops for the largest matrix size used ($N_p = 284$). In this latter case, a 102 step calculation required 51 seconds for each energy. For comparison, a calculation with $N_p = 39$ but the other propagation parameters equal required 0.20 seconds per energy.

5.2 Pre-processing of input data — overlap maximization

The efficiency of calculation of the log derivative may be improved by pre-processing the input data (interaction and overlap matrices) to optimize the propagation. The individual sector basis sets, as generated by the surface function code, are each ordered according to increasing LHSF energy for the value of $\bar{\rho}$ in that sector. This leads to overlap matrices which often have large off-diagonal elements due to avoided crossings in the surface functions as ρ increases, detectable by examination of the adiabatic LHSF eigenvalue-*vs.*-rho curves. When this happens, a poor choice of N_p will result in the inversion of a nearly singular overlap matrix in equation (2.2.9), in which case either the calculation will stop due to a fatal numerical error or the log derivative which results from "successful" propagation will have large errors. This situation can be avoided by careful choice of N_p; however, in practice this solution is unsatisfactory since the result is that a large percentage of possible values of N_p are eliminated from consideration, and convergence tests become both difficult and more expensive (since a large value of N_p must be used to test the accuracy of a smaller value, and the CPU time necessary for propagation goes as N_p^3).

The formalism for the logarithmic derivative does not specify an ordering scheme for the LHSF in the basis set; therefore, we may overcome this problem by reordering the individual $\bar{\rho}$ basis sets to satisfy the criterion that the upper left M by M (where M takes on values from 1 to N) submatrices of the overlap matrix between every value of $\bar{\rho}$ be as close to orthogonal as possible, *i.e.*,

$$\left(\sum_{j=1}^{M} \mathcal{O}_{ji}^2 \geq \sum_{j=1}^{M} \mathcal{O}_{jk}^2, \quad i\in\{1,\ldots M\}, k\in\{M+1,\ldots N\} \right), \quad M\in\{1,\ldots N-1\} \tag{5.2.1}$$

A LHSF basis set is chosen at certain value of $\bar{\rho}$, which we will call $\bar{\rho}_S$, to be the standard basis set against which the bases at the remaining values of $\bar{\rho}$ are compared, and the energy ordering of the LHSF in that basis set is preserved. This fixes the row ordering of the overlap matrix between $\bar{\rho}_S$ and the next smaller $\bar{\rho}$, and the column ordering of the overlap matrix between $\bar{\rho}_S$ and the next larger $\bar{\rho}$.

The order of the columns or rows corresponding to the basis at $\bar{\rho} \neq \bar{\rho}_S$ is then permuted to satisfy (5.3.1), and the same permutation matrix is applied to both right and left sides of the interaction matrices associated with this $\bar{\rho}$ to convert their representation to the new ordering of the basis set. This procedure is iterated for each pair of values of $\bar{\rho}$ adjacent to the standardized values until all have been given the standard ordering. We thus effectively ensure the maximum overlap between adjacent $\bar{\rho}$ basis sets, no matter what number of functions are propagated, and will therefore refer to this procedure as overlap maximization (OM).

The OM procedure is dependent on fixing the order of the basis set at one value of $\bar{\rho}$, after which the others may be reordered with respect to this standard basis set. We have determined that the best basis set to use for this purpose is the (energy ordered) basis set at the largest value of $\bar{\rho}$; the reason is that this set must include all open states of the diatomic molecule if more than the number of open states is propagated, and due to crossing effects this is not necessarily true for any other value of $\bar{\rho}$.

The advantages of using OM are twofold: first, a large reduction in the number of N_p values which yield incorrect log derivatives, which makes convergence testing much easier and can often result in the saving of computation time through the use of a smaller value of N_p; and second, an improvement in the symmetry (and therefore the quality) of the log derivative matrices obtained from propagation, due to the better orthogonality of the overlap matrices used to transform between basis sets at different $\bar{\rho}$.

6. CONVERGENCE TESTS

6.1 General Considerations

Extensive convergence testing has been performed on the log derivative propagator to ensure accuracy of the partial wave cross sections obtained. Since the propagator has no knowledge of the partial wave (J) or symmetry (Π, Γ) of the interaction and overlap matrices which form its input, the convergence tests could be performed on a single partial wave and symmetry and the results applied to a general case. For convenience, the tests were performed using the $J = 0$ (and therefore $\Pi = 0$) partial wave A_1 symmetry results at a total energy of 1.6eV on the LSTH potential energy surface, and the final **S** matrices obtained from the RS analysis were examined to determine convergence. As usual, the overlap maximization procedure was performed on the raw data obtained from running the LHSF code to make the convergence tests easier.

The parameters which are used in the propagation depend on the parameters used in a given LHSF calculation, during which the $\boldsymbol{\mathcal{I}}$ and $\boldsymbol{\mathcal{O}}$ matrices that are the coefficients for the coupled equations (2.1.10) were determined. The quality of the propagation results is of course dependent on the quality of the LHSF basis set used in the wavefunction expansion. The convergence of the LHSF was discussed previously in (I), and for these tests we will assume a good LHSF basis set and correspondingly good $\boldsymbol{\mathcal{I}}$ and $\boldsymbol{\mathcal{O}}$ matrices.

The distance $\Delta\bar{\rho}$ between successive values of $\bar{\rho}$ is fixed in the LHSF calculation, since the $\boldsymbol{\mathcal{I}}$ are determined with a reference potential which depends on the value of $\bar{\rho}$. In addition, the minimum distance $\Delta\rho_I$ between successive interaction matrices is limited by the number of $\boldsymbol{\mathcal{I}}$ matrices actually calculated; however, integer multiples of this quantity may be used in the propagation if not all of the available data is required. Similarly, there is a limitation on the minimum and maximum values of $\bar{\rho}$ in the propagation depending on the respective values in the LHSF calculation, and on the maximum value of N_p, the number of LHSF used as the basis for

the expansion (2.1.10) (or equivalently, the number of rows and columns in the submatrices of $\mathcal{I}$ and $\mathcal{O}$ used in the propagation). The propagation step size $\Delta\rho$ is restricted in our algorithm to be an even number of steps between different $\bar{\rho}$, but is otherwise arbitrary.

The values of ρ at which the $\mathcal{I}$ matrices are calculated are inputs in the LHSF calculation, since the $\mathcal{I}$ are determined using much the same methodology as the LHSF; in addition, the value of $\bar{\rho}$ for the basis set in which a particular $\mathcal{I}(\rho;\bar{\rho})$ is determined is fixed at this time. Two different schemes for the location of the $\mathcal{I}$ were used at different times; the interaction matrices have been calculated in regions centered about a value of $\bar{\rho}$ ($\rho_{i,i+1} = \frac{\bar{\rho}_i+\bar{\rho}_{i+1}}{2}$) and in regions extending from one value of $\bar{\rho}$ to another ($\rho_{i,i+1} = \bar{\rho}_{i+1}$); from the discussion in section 2.1, we expect the former method to be more accurate due to the smaller range of the quantity $|\rho - \bar{\rho}_i|$ which results from a centered region. A change in these parameters would require a new LHSF calculation.

There is one parameter in the LHSF calcuation which will affect the results in a non-obvious fashion. At a particular sufficiently large value of $\bar{\rho}$, the basis set for expansion of the LHSF is assumed separable, so that the computationally expensive two-dimensional integrals needed for the calculation of the LHSF and the $\mathcal{I}$ and $\mathcal{O}$ matrices can be taken to be zero. The value of this parameter is determined by the highest energy surface function needed for the propagation; all LHSF used must have negligible density between channels for this to be a good approximation. Assuming that the wavefunction in the λ arrangement channel would be zero beyond a value for r_λ^{max} of 3.0 bohr, we use the symmetry of the channels to determine that the point with $\omega_\lambda = \pi/3$ and $\gamma_\lambda = 0$ is equidistant between two arrangement channels at fixed ρ, and the relation from (3.4.7) then yields the value 6.0 bohr for this parameter. The adequacy of this choice was tested through propagation of the matrices calculated by a $J = 0$ A_1 LHSF program run with this parameter set to 7.0 bohr and all other parameters equal; when propagated with the same parmeters

as the 6.0 bohr case, the resulting scattering matrix elements differ by no more than 0.009 for all moduli and no more than 4° in the phases for transitions between the 11 states lowest in energy ($v = 0, j = 0 - 10; v = 1, j = 0 - 8$).

We use the unitarity of the °**S** matrix as the first criterion for determination of the acceptability of the results of a propagation. As a unitary matrix, the °S matrix has the property

$$\sum_i |{}^oS_{ij}|^2 = 1 \tag{6.1.1}$$

for all columns j; if a calculated scattering matrix has any column sum which deviates from 1.0 by more than 5%, that scattering matrix is automatically rejected. In the scattering matrices which fulfill this criterion, the convergence of the matrix will be determined in terms of all the elements of the matrix and seperately in terms of the elements with large modulus, as the smaller elements will contribute little to the desired differential cross sections.

6.2 Basic Limitations on Accuracy - fixed grid, N_p variable

The results of the propagation depend strongly on the size of the matrices propagated, which correlates to the number of basis functions N_p used to expand the six-dimensional Schrödinger equation. For small N_p the calculation is unconverged, but even after convergence is acheived there will be small fluctuations in the calculated log derivative matrix elements and the resulting scattering matrix as N_p increases, due to the addition of terms to the propagation matrices with errors of varying magnitude and sign; in addition, there must be a balance between the errors caused by incompleteness of the basis set and the increase in numerical error with the increasing basis set size of the log derivative calculation.

To determine the limits on the accuracy of the calculation due to the numerical methods, a set of calculations with large N_p and small $\Delta\rho$, $\Delta\bar{\rho}$ and $\Delta\rho_I$ was performed. The values of these parameters were chosen to ensure that the errors in the resulting °**S** matrices would not be due to insufficient number of steps in

the propagation or to an insufficient basis set for the propagation. These accurate calculations were performed with a $\Delta\bar{\rho} = 0.025a_0$ grid and a propagation step size $\Delta\rho = 0.003125a_0$, using the logarithmic derivative propagator due to Manolopoulos.[69] The beginning and ending values of $\bar{\rho}$ were 2.0 and 12.0 bohr, respectively. Two interaction matrices were calculated at $\rho = \bar{\rho} \pm \frac{\Delta\bar{\rho}}{4}$, and another two at $\rho = \bar{\rho} \pm \frac{\Delta\bar{\rho}}{2}$; the $\bar{\rho}$ basis set was changed at the latter values of ρ. Various numbers of LHSF were used in the propagation, ranging from 40 to 59. Examination of the unitarity of the open part of the **S** matrices obtained eliminated the values $N_p = 42$ and 53 from consideration as having unacceptable errors, on the basis of the 5% deviation from unity criterion of section 6.1 and further on comparison of the differences of the moduli resulting from these two calculations with those of the others. Inspection of the remaining 18 °**S** matrices reveals no noticable trend in the magnitude of their elements, and so we expect that any systematic error is small. Therefore, we determined the sample mean and standard deviation of the moduli and phases of the open part of the **S** matrix for N_p in the range $N_p \in \{40, 59\}, N_p \neq \{42, 53\}$ to give an estimate of the random error of the calculation. The results, in terms of the maximum standard deviations from the mean value, are given for the moduli in table 6.1 and for the phases in table 6.2.

Using this sample of 18 °**S** matrices, the maximum absolute standard deviation from the mean for the moduli of the °**S** matrix elements ($\sigma_m^{\max}$) was found to be 7.48×10^{-4}, occuring for the transition from $(v' = 0, j' = 10)$ to $(v = 0, j = 8)$ which has a mean value 0.2822. Therefore, assuming a random error distribution and using Student's t-distribution, the calculated mean values are all within 1.58×10^{-3} of the "true" values to a 95% confidence level; most are at least a factor of 2 better. The maximum percent sample standard deviation from the mean ($\%\sigma_m^{\max}$) is 20.6%, occuring for the transition from $(v' = 1, j' = 10)$ to $(v = 0, j = 2)$ which has a mean of order 10^{-3}. In general, the absolute deviations tend to be worse for the states with high rotational quantum numbers. If we limit the comparison to

elements of the **S** matrix with modulus greater than 0.01 (and thus to probabilities greater than 10^{-4}), or further to elements with modulus greater than 0.1 (and probabilities greater than 10^{-2}), we see in table 6.1 that $\%\sigma_m^{\max}$ is reduced to 0.96% and 0.34%, respectively. Therefore, the mean values calculated are accurate within a 95% confidence level to about $\pm 2\%$ for moduli greater than 0.01 and to $\pm 0.7\%$ for moduli greater than 0.1. These mean values of the moduli are assumed to be the converged results.

For the phases of the **S** matrix elements, $\sigma_p^{\max}$ was found to be 8.1° if all elements of the open part of the matrix were considered. Limiting the comparison to elements with modulus greater than 0.01 reduces this figure to 1.2°, while a further limitation to elements with modulus greater than 0.1 yields $\sigma_p^{\max} = 0.23°$. Thus the mean values calculated for the phase are accurate within a 95% confidence level to $\pm 2.4°$ for elements with modulus greater than 0.01 and to $\pm 0.5°$ for elements with modulus greater than 0.1. We assume these mean phases to be the converged results.

We can use these results as a standard to determine the accuracy of the results of calculations with smaller N_p or larger $\Delta\rho$, $\Delta\bar{\rho}$ and $\Delta\bar{\rho}_I$ values. For example, a $J = 0$ A_1 symmetry calculation was performed with the parameters $\Delta\bar{\rho} = 0.2a_0$, $\Delta\rho = 0.1a_0$, and $N_p = 35$. The parameter $\Delta\bar{\rho}_I$ was set equal to $0.1a_0$, with the interaction matrices evaluated at $\bar{\rho}_i$, $\bar{\rho}_i + 0.1a_0$, and $\bar{\rho}_{i+1}$; the $\bar{\rho}$ basis set is changed at $\rho_{i,i+1} = \bar{\rho}_{i+1}$. The beginning and ending values of $\bar{\rho}$ were 2.0 and 12.0 bohr, respectively. Comparison of this run and the converged values reveals that the largest difference for moduli greater than 0.01 is 0.0082; this occurs in an element corresponding to the transition $(v' = 2, j' = 0)$ to $(v = 2, j = 2)$ which has the converged value 0.1685. If we also limit our examination to the first column of the **S** matrix, the largest difference is for the transition $(v' = 0, j' = 0)$ to $(v = 1, j = 8)$; for this transition, the converged value is 0.2396 and the difference is 0.0019. The maximum difference between the phases for moduli greater than 0.01 is 3.9° for the

$(v' = 2, j' = 6)$ to $(v = 2, j = 6)$ transition; for the first column and moduli greater than 0.01, the maximum difference is 2.4° and occurs in the $(v' = 0, j' = 0)$ to $(v = 1, j = 2)$ transition. We can therefore conclude with some confidence that the results of this run are sufficiently accurate for our purposes, and that these values of the parameters will yield converged results.

6.3 Convergence tests - N_p

A set of calculations with different N_p were performed with the fixed parameters $\Delta\bar{\rho} = 0.2a_0$, $\Delta\rho = 0.1a_0$, and $\Delta\bar{\rho}_I = 0.1a_0$, with the interaction matrices evaluated at $\bar{\rho}$, $\bar{\rho}_i + 0.1a_0$, and $\bar{\rho}_{i+1}$; the $\bar{\rho}$ basis set is changed at $\rho_{i,i+1} = \bar{\rho}_{i+1}$. The beginning and ending values of $\bar{\rho}$ were 2.0 and 12.0 bohr, respectively. We used values of N_p in the range from 17 (the number of open states of the system at 1.6 eV) to 40. All scattering matrices with N_p less than 31 were rejected by the poor unitarity criterion, as was the matrix for $N_p = 36$. The results of comparison with the mean values are presented in table 6.1. Comparison of the elements of the remaining matrices with modulus greater than 0.1 reveals that the largest difference in the modulus is less than 0.016 and the largest difference in phase is less than 15° in all cases. There is a clear difference between the values of N_p less than 35 and those equal or above this number; in the case of N_p = 35, 38, 39, and 40, the largest modulus difference is less than 0.009 and the largest phase difference is less than 4°. The calculations with these values of N_p have the characteristic that there are more than 35 functions in the basis set and the worst deviation from unitarity is less than 1% (which excludes $N_p = 37$). It is therefore seen that the condition of good unitarity is necessary but not sufficient to insure convergence, as it does not guarantee that the basis set used is sufficiently complete.

If we compare only the first columns of the scattering matrices, the moduli differ from those of the mean values discussed above by less than 0.004, and the phases differ by less than 5.5° (with one exception - the $N_p = 34$ calculation had one phase difference of 8.2°). If we exclude those elements with mean value of the

modulus less than 0.1, the moduli differ by less than 0.003 and the phases by less than 1.6°.

6.4 Minimum and Maximum $\bar{\rho}$

The minimum value of $\bar{\rho}$, at which the propagation is initiated, is chosen so that the wavefunction can be assumed to be nearly zero at this hyperradius. This choice will of course depend on the total energy of the system; however, the lowest LHSF energy at $\bar{\rho} = 2$ bohr is over 3 eV, and we expect that the wavefunction will be zero for the entire energy range of our calculation. Our use of $\bar{\rho} = 2.0$ bohr has been confirmed by the replacement of the initial condition matrix $10^{30}\mathbf{I}$ with the values determined by the WKB approximation. In either case, the resulting **S** matrices are identical to four digits if all other parameters are held fixed.

The maximum value of $\bar{\rho}$ should be chosen in a region where the potential coupling has essentially gone to zero; this is characterized by independence of the potential of the coordinates R_λ and γ_λ, and results in sparse $\boldsymbol{\mathcal{I}}$ matrices. The rows and columns of these matrices are labeled by the index n of the LHSF basis set; if these labels are replaced by the quantum numbers of the primitive which has the largest overlap with that LHSF (*i.e.*, the major contributor to the LHSF from the primitive basis set), the $\boldsymbol{\mathcal{I}}$ matrix will be seen to be block diagonal in j. (The surface hamiltonian will continue to couple the functions in the Ω quantum number over a longer range, and the dependence of the LHSF on R_λ via the parameter ρ causes potential coupling of the hyperspherical functions in v even at large ρ.) The convergence of the scattering matrices with respect to this parameter was tested in a series of propagation runs with $N_p = 39$, $\Delta\bar{\rho} = 0.2a_0$, $\Delta\rho = \Delta\rho_I = 0.1a_0$ with $\boldsymbol{\mathcal{I}}$ evaluated at $\rho = \bar{\rho} + \Delta\rho_I$ and $\rho = \bar{\rho} + 2\Delta\rho_I$, and the minimum value of $\bar{\rho}$ at 2.0 a_0. A range of values of $\bar{\rho}_{max}$ from 10.0 to 13.0 bohr was used for these calculations, and a summary of the results is presented in table 6.2. We have used the $\bar{\rho}_{max} = 13.0$ bohr calculation as the basis for comparison of the other values of $\bar{\rho}_{max}$. This value for $\bar{\rho}_{max}$ can be justified from the small residual interaction potential between the atom

and diatom at this value of ρ; the difference in potential between a linear ($\gamma_\lambda = 0$) and a T-shaped configuration ($\gamma_\lambda = \frac{\pi}{2}$) for the three values $r_\lambda = 0.08377 a_0$ (r_λ^{min} in the LHSF calculation in this region), 1.304 a_0 (r_λ^{eq}, corresponding to the minimum value of $V(\rho, \omega_\lambda, \gamma_\lambda)$ as a function of ω_λ for $\rho = 13.0 a_0$ and $\gamma_\lambda = 0$), and 3.0 a_0 (r_λ^{max} in the LHSF calculation) is no greater than 7×10^{-5} eV. However, it should be noted that the numerical errors in the calculation increase as $\bar{\rho}_{max}$ increases, and so a larger value of $\bar{\rho}_{max}$ does not necessarily mean a more accurate calculation.

It can be seen that the moduli are essentially converged at 10.0 bohr, as the differences from one calculation to the next are not decreasing in magnitude; however, the phases show a consistent pattern of convergence as $\bar{\rho}_{max}$ increases. The maximum difference in phase for transitions with $|^o S_{ij}|$ greater than 0.1 between $\bar{\rho}_{max} = 12.0$ bohr and $\bar{\rho}_{max} = 13.0$ bohr is 2.4°, and if we examine only the first column of the scattering matrix this difference decreases to 1.3°. Accordingly, we have chosen to use the value $\bar{\rho}_{max} = 12.0$ bohr in our calculations.

7. RESULTS OF SCATTERING CALCULATIONS

7.1 J = 0 Transition Probabilities and Partial Wave Cross Sections

For the case $J = 0$, we will present results of our scattering matrix calculations in several formats. The first set of results will be for the S matrix as originally obtained in the irreducible representation formalism of the first part of this paper; we will analyze the transition probabilities (*i.e.*, the square of the modulus of the S matrix element) with reference to structure in the different partial waves. Next, the effect of the geometric phase due to the H_3 conical intersection on these results will be examined. Finally, partial wave integral cross sections in the irreducible representation and spin-weighted formats will be given, both with and without the geometric phase corrections. In these results, we will describe the initial and final state diatomic quantum numbers in the format (v,j,Ω) (or (v,j,m) for the cross sections) when we include the orientation of the molecule in the description, and in the format (v,j) when the average over the orientation is taken. The transition will be denoted by $(v',j',\Omega') \rightarrow (v,j,\Omega)$. In order to provide some comparison with experiment and with other work in the field, we will concentrate on the transitions from the $v' = 0$, $j' = 0,1,2$ states.

A. J=0 Γ transition probabilities - no conical intersection

The A_1 IR is not important in the calculation of the cross sections for the H + H_2 reaction, since (as was shown in section 4.4) it is forbidden by the spin statistics for fermions of spin 1/2. However, this will not be true for other systems, so a brief description of some features of the $J = 0$ partial wave A_1 IR scattering results will be included for completeness. In figure 7.1 we show the $J = 0$ A_1 probabilities for (0,0,0) $\rightarrow$ (0,j,0), with $j = 0,2,4,6$. (As was shown previously, the A_1 IR contains no states with odd j or j'; in addition, the orientation quantum number must be zero for $J = 0$.) The energy range of the figures is from 0.3 eV to 1.6 eV, and scattering matrices were calculated at 131 energies in this range in evenly

spaced increments of 0.01 eV. The curves are not plotted to the same scale; the multiplication factor for each curve is given on the figure.

Examination of figures 7.1 reveals that the probability of rotational excitation of the product molecule is small for energies near the opening of the $j = 2$ state at 0.3142 eV total energy (0.0439 eV translational energy of the initial (0,0) diatom), but rapidly increases until the bulk of the products may be found in the (0,2) state (figure 7.1b) at a total energy of about 0.65 eV (0.38 eV translational). The probability for this transition then decreases as the particle flus becomes distributed among other states. As the other states become energetically available, there is a similar pattern: a threshhold barrier must be passed before the transition probability rises to a peak value.

Figures 7.2 present the $J = 0$ A_1 probabilities for vibrational and rotational excitation of the (0,0,0) state to the state (1,j,0), with $j = 0, 2, 4, 6$. The curves with final states (1,0,0) and (1,2,0) (figures 7.2a and 7.2b, respectively) show a sharp increase in probability at the energy 0.98 eV, which corresponds to a scattering resonance for the H_3 system. (The energies and characterization of the resonances found in the H_3 system will be discussed in more detail in section 7.3.) The oscillatory behavior of these curves can also be attributed to the resonances of the system; since the amplitude of the transitions is smaller than those for the purely rotational excitation presented in figures 7.1, due to the large energy difference between the initial and final states (0.516 eV minimum), the effect of the resonances on the probabilities becomes more apparent.

The A_2 IR scattering results, which contains results for odd j and j', are given in figures 7.3 for the transitions (0,1,0) $\rightarrow$ (0,j,0), $j = 1, 3, 5, 7$ and in figures 7.4 for the transitions (0,1,0) $\rightarrow$ (1,j,0), $j = 1, 3, 5, 7$. The smooth behavior of all of these curves suggests that the scattering resonances do not affect the transition probabilities in A_2, and in fact an analysis of the symmetry effects on the probable resonance metastable state shows[16b] that for $J = 0$ the A_2 symmetry should have

no resonances in this partial wave. The A_2 transition probabilities for rotational excitation are smaller than those for the A_1 symmetry, due possibly to the lack of resonant enhancement. The behavior of these curves is similar to that of the A_1 curves in one respect, which is the low probability of transition near threshhold followed by a maximum.

The E IR scattering results contain transitions between all possible initial and final states of the system. We present results for transitions (0,0,0) to (0,j,0), $j = 0, 2, 4, 6$ in figure 7.5 and for transitions (0,0,0) to (1,j,0), $j = 0, 2, 4, 6$ in figure 7.6. We also include transitions (0,1,0) to (0,j,0), $j = 1, 3, 5, 7$ in figure 7.7 and (0,1,0) to (1,j,0), $j = 1, 3, 5, 7$ in figure 7.8. These are the transitions which may be affected by the conical intersection. We also include here the $j + j'$ odd transitions which are not affected: the transitions (0,0,0) to (0,j,0), $j = 1, 3, 5, 7$ in figure 7.9, (0,0,0) to (1,j,0), $j = 1, 3, 5, 7$ in figure 7.10, (0,1,0) to (0,j,0), $j = 0, 2, 4, 6$ in figure 7.11, and (0,1,0) to (1,j,0), $j = 0, 2, 4, 6$ in figure 7.12.

B. J=0 Γ transition probabilities - conical intersection included

Modification of the **S** matrices to include the effects of the conical intersection (as discussed in section 4.5) produces a dramatic effect on the $J = 0$ probabilities. Plots of these probabilities are also given as figures 7.13 through 7.20; figure 7.13 contains the transitions including the geometric phase corresponding to those plotted in figure 7.1 with the geometric phase absent, figure 7.14 corresponds with figure 7.2 and so on. The most prominent effect is in the A_1 and A_2 symmetries: when the geometric phase is included in the calculation, the A_1 symmetry curves lose the structure due to resonances which previously occurred in these transitions, and the features appear in the A_2 symmetry which formerly was smooth. This can be explained[88] by the inclusion of the antisymmetry of the electronic wavefunction caused by the geometric phase in the symmetry analysis on the resonant metastable state.

For the E symmetry, the transitions with $j + j'$ odd are unaffected by the

geometric phase. These transitions are effectively reactive transitions, since the nuclear spin symmetry of the H_2 diatom restricts the rotational levels to be even for $S = 0$ and odd for $S = 1$, and there are no spin-dependent terms in the hamiltonian; under these conditions, a change in the diatom rotational parity implies reaction. In addition, the A_1 and A_2 symmetry scattering matrices do not include terms with $j + j'$ odd. Accordingly, there are no interference terms with the non-reactive transitions or other irreducible representations, and the change in phase of the S matrix element has no effect on the probability.

C. $J = 0$ partial wave integral cross sections

From the results of the previous section, it is obvious that the partial wave integral cross sections obtained without the geometric phase included will be incorrect, with the exception of those for transitions with $j + j'$ odd. Because of the history of cross section calculations which neglect the presence of the conical intersection, we will present these incorrect cross sections for purposes of comparison. For convenience, the transitions which are plotted from calculations which include the effect of the geometric phase will be referred to as GP transitions.

The $J = 0$ Pauli antisymmetrized integral cross sections for the transitions (0,0,0) to (0,j,0), $j = 0, 2$ and (0,0,0) to (1,j,0), $j = 0, 2$ are presented in figure 7.21 with the GP effect absent. Figure 7.22 contains the same transitions with the GP included. Similarly, the $J = 0$ Pauli antisymmetrized integral cross sections for the transitions (0,1,0) to (0,j,0), $j = 1, 3$ and (0,1,0) to (1,j,0), $j = 1, 3$ are presented in figure 7.23 with the GP effect absent and figure 7.24 with the GP included. We see that the elastic cross section (0,0,0) to (0,0,0) in panel (a) of figures 7.21 and 7.22 are almost identical on the scale of the plot; the nonreactive component for this transition is much larger than the reactive part, and accordingly the oscillation is the same as would be seen in the distinguishable particle representation of the calculation; the effect of the GP in reversing the sign of the reactive-nonreactive interference is small in this case. This is also true of the elastic cross section (0,1,0) to

(0,1,0), as can be seen in panel (a) of figures 7.23 and 7.24. The inelastic transitions are much more interesting. Comparison of 7.21 (b) with 7.22 (b) reveals that the GP cross section for rotational excitation from (0,0,0) to (0,2,0) at the peak value of 0.65 eV is larger than the cross section calculated without GP by about 33%. The effect is even more dramatic for the (0,0,0) to (1,0,0) transitions (panel (c) on each of these figures), where the peak at the resonance energy 0.98 eV is a factor of 6 larger in the GP cross section. Other energies are also affected, although not as dramatically; in particular, the peak near 1.15 eV in figure 7.21 (c) is absent from 7.22 (c), and the trough at 1.41 eV is much deeper in the GP results. The same qualitative effects may be seen in the (0,0,0) to (1,2,0) transitions; again the peak associated with the 0.98 eV resonance is a factor of 6 larger in the GP cross sections. For the transition (0,1,0) to (0,1,3) (panel (b) of figures 7.23 and 7.24), the GP cross section is a factor of 2 larger at the 0.65 eV peak, and the transition (0,1,0) to (1,1,0) (panel (c) of these figures) is a factor of 4 larger for the GP cross section at the 0.98 eV resonance, and the trough associated with the 1.41 eV resonance is significantly deeper in the GP cross sections. In summary, for the $J = 0$ partial wave and the transitions we have examined, the geometric phase enhances the effect of the resonances, and for the stronger resonances the calculation without geometric phase has been seen to be in error by as much as a factor of six.

To finish the $J = 0$ partial wave section, in figure 7.25 we present the $J = 0$ Pauli antisymmetrized integral cross sections for the transitions (0,0,0) to (0,j,0), $j = 1, 3$ and (0,0,0) to (1,j,0), $j = 1, 3$, and in figure 7.26 the $J = 0$ Pauli antisymmetrized integral cross sections for the transitions (0,1,0) to (0,j,0), $j = 0, 2$ and (0,1,0) to (1,j,0), $j = 0, 2$; the transitions on these latter two plots are unaffected by the GP.

7.2 Partial Wave Cross Sections for J > 0

The $J = 1$ Pauli antisymmetrized integral cross sections for the transitions (0,0,0) to { (1,0,0), (1,2,0), (1,2,1) } are given in figure 7.27 for the case with the GP effect absent, and the same transitions after accounting for the GP are given in figure 7.28. In this partial wave, we see that the GP transitions are affected in the opposite direction; *i.e.*, the peak in the GP cross sections at 0.98 eV is about a factor of 2.5 smaller than the peak in the corresponding cross sections without the GP effect. In general, the cross sections are smaller overall after taking account of the GP effect. The exception is for the (0,0,0) to (1,2,1) transition in figures 7.27(c) and 7.28(c), respectively, where the peak at 1.08 eV is of comparable height in both the GP and no GP cases. The transition (0,1,0) to (1,1,0) of figures 7.27(d) and 7.28(d), respectively, shows an even more pronounced effect; the GP cross section away from resonance decreases in magnitude by about a factor of 2.5, while at the resonance energy the decrease is by a factor of 8.5. Figures 7.29 and 7.30 contain the transition (0,1,0) to (1,1,1) as well as the transitions (0,1,1) to (1,1,m) for $m = -1, 0, 1$. We see that the transitions to $m = \pm 1$ are affected only slightly by the GP, while for $m = 0$ the magnitude of the cross sections at the 0.98 eV resonance differs by a factor of 6, with the GP cross sections smaller.

The $J = 2$ Pauli antisymmetrized integral cross sections for the transitions (0,0,0) to { (1,2,0), (1,2,1), (1,2,2) } are given in figure 7.31 for the case with the GP effect absent, and the same transitions after accounting for the GP are given in figure 7.32. In this partial wave, we see that the GP cross sections are again larger than the non-GP cross sections, as was seen for $J = 0$ but not for $J = 1$. This trend also holds for the transition (0,1,0) to (1,1,0) given in figures 7.31(d) and 7.32(d), and for the transitions (0,1,0) to (1,1,1) and (0,1,1) to (1,1,m) for $m = -1, 0, 1$ of figures 7.33 (without GP) and 7.34 (with GP). We see that in this case the lower energy cross section with transitions to $m = \pm 1$ are affected only slightly by the GP, but at higher energies the effect is more pronounced. The same

transitions as for the $J = 2$ case are given in figures 7.35 through 7.38 for the $J = 3$ partial wave, with figure 7.35 corresponding to figure 7.31 for $J = 2$ and so on. The $J = 3$ results resemble those for $J = 1$ in that the non-GP cross sections contain the more prominent resonance effects. For this partial wave, all transitions shown are substantially changed by addition of the GP.

From the results for these four partial waves with J from 0 to 3, we see that in the cross sections with GP added, the resonances tend to interfere constructively with the non-resonant part of the cross sections for even values of J, while for odd J the interference tends to be destructive. This is the opposite of the effect for the transitions with no GP, for which the constructive interference is for odd J. The result of this alternation between constructive and destructive interference is that the sum over these four partial waves with and without the GP included look very similar. In figures 7.39 through 7.42, we present figures giving the partial wave integral cross sections summed from $J = 0$ to 3, for the same transitions as given for the $J = 2$ and $J = 3$ partial waves; we also give the summed and averaged integral cross section summed from $J = 0$ to 3 for the transitions (0,0) to (1,0), (0,0) to (1,2), (0,1) to (1,1) and (0,1) to (1,0) for the calculations without GP in figure 7.43 and with GP in figure 7.44. We see that the larger transitions with and without the GP present in the sum over the partial wave cross sections, and as a consequence all of the summed and averaged cross sections given, have approximately the same behavior as a function of energy, the major difference being the magnitude of the cross section.

Of course, four partial waves is insufficient to converge the integral cross section results, and for these low values of J the partial wave with the largest value of J will dominate due to the $2J + 1$ degeneracy. Accordingly, the summed set of cross sections which has constructive interference between the resonant and non-resonant cross sections for this value of J will be larger than the other set; for $J = 1$ and 3, the non-GP cross sections are smaller than the GP cross section, but for $J = 0$

and 2 and presumably for $J = 4$ as well, the GP cross sections will be larger. It is therefore not possible to predict the final behavior of the integral cross section calculated with inclusion of the conical intersection effect from the current data. However, it can be seen that the difference, if any, will depend on the difference between the largest contributors to the integral cross sections, as the differences between the smaller contributors associated with small J tend to cancel out in the sum over J.

7.3 Resonances in the Partial Wave Results

The effect of scattering resonances in the partial wave results is evident from the oscillatory structures visible in the various probability and cross section plots. The variation in the plots is caused by the interference between a direct process and the resonant process,[90–94] which occurs through the formation of a metastable three particle complex in the strong interaction region of the potential.[2,91] The interference caused by the resonant process is over a small range of energy, corresponding to an energy level of the metastable complex broadened by the short lifetime of the state; outside of this range the amplitude of the resonant process goes to zero.

To better quantify the resonances, we generate collision lifetime matrices using the procedure due to Smith[95] on the scattering matrices which we have generated. The procedure was found to be very sensitive to the symmetry of the input **S** matrices, and accordingly the ${}^{\circ}\mathbf{S}^{J\Pi}$ matrices used in the lifetime analysis were generated from symmetrized ${}^{\circ}\mathbf{R}^{J\Pi}$ matrices to reduce the numerical noise in this calculation. The resulting lifetime matrix, defined as

$$\mathbf{L} = \frac{\partial \mathbf{S}^{\dagger}}{\partial E}\mathbf{S} \tag{7.3.1}$$

is then diagonalized, and the eigenvalues examined as functions of the total energy of the system. The maxima of these functions, which are by definition at energies for which the collision complex has a longer lifetime, correspond to the resonances of the system.

We have labelled the resonances by a set of quantum numbers, first used for this purpose by Colton and Schatz[96] and Bowman,[97] which are those appropriate for a stable linear triatomic molecule; they are $(v_1, v_2^{|K|}, v_3)$, in which v_1 is the symmetric stretch quantum number, v_2 the bend quantum number with vibrational angular momentum quantum number K, and v_3 the antisymmetric stretch quantum number. K is the projection of the total angular momentum of the system along the molecular axis, and is called the vibrational angular momentum since it arises from the linear superposition of the degenerate bending modes of the linear triatomic system. (We have changed the notation for the angular momentum quantum number K from the original notation, which used the index Ω, to avoid confusion with our projection of the total angular momentum on the $\mathbf{z}_\lambda$ axis.) $|K|$ may take on any of the allowed values of the projection quantum number, *i.e.*, for $J + \Pi$ odd it may have values from 1 to J and for $J + \Pi$ even it may take on values from 0 to J. The v_2 quantum number is restricted to values such that $v_2 - |K|$ is even.[98]

To determine the energies of the resonances, the scattering calculation was performed every 0.01 eV; this is sufficient to fully converge the resonance lifetimes for the longer-lived states, as has been shown by comparison[16b] in the $J = 0$ case with results from a similar calculation using a finer energy grid.[15] We have compared the calculated resonance energies with those found in the latter calculation and with the resonance energies predicted by Bowman,[97] Colton and Schatz,[96] Pollak,[99] and Garret and coworkers;[100] we include the table of reference 16b for the $J = 0$ and 1 partial waves as table 7.1.

The eigenvalues of the lifetime matrix for H + H_2 on the LSTH surface for the A_2 irreducible represention and $J = 3$ are plotted *vs.* energy in figures 7.45 for $\Pi = 0$ and 1, without the geometric phase effect; these two plots contain peaks representing all of the resonances for the H_3 system which have been found in our calculations thus far. The results given here are provided as they were calculated, with no smoothing. An individual lifetime matrix eigenvalue begins with a lifetime

of zero, drops down to a relatively low value, and then begins to increase. For clarity, the initial decrease in the curves has been deleted where possible; however, an artifact of the method for calculation of the energy derivative of the **S** matrix is that there is sometimes a peak near threshhold in the calculated curves, which for a finer grid of energies will vanish, and these artifacts are visible at about 1.15 eV and 1.45 eV for the $\Pi = 1$ plot and 1.45 eV for the $\Pi = 0$ plot.

The lifetime analysis gives no information on the correct choice of quantum numbers for the linear triatomic state which is associated to the various resonance energies; this choice is made by comparison with the results of other workers, using methods which provide this information.[99] The resonances in the $\Pi = 0$ graph are all labelled with odd $|K|$ values, and those in the $\Pi = 1$ graph all have even $|K|$; this is in accord with the selection rule for the resonances in the A_1 and A_2 irreducible representations (all resonances affect the E irreducible representation) which was found previously:[16b]

$$(-1)^{\Pi+|K|} = X_\Gamma \qquad \Gamma = \{A_1, A_2\} \qquad X_\Gamma = \{1, -1\} \qquad \text{no GP} \qquad (7.3.2)$$

This selection rule is explained by a simple model, which assumes that no resonances can exist in the case where the scattering wavefunction vanishes identically for all configurations of the system in the vicinity of the saddle point of the potential energy surface (*i.e.*, at $\rho = 3.270145$ bohr and $\omega = \pi$) for which the distances of the two end atoms to the central atom are equal (which corresponds to configurations with $\gamma_\lambda = \frac{\pi}{2}$). The selection rule (7.3.2) follows from the equivalence under these conditions of the permutation of the two end atoms (an operation with eigenvalue $X_\Gamma = 1$ or -1 if Γ is A_1 or A_2, respectively) and the result of consecutive operations by the inversion operator (eigenvalue $(-1)^\Pi$) and an operator which rotates the system by π about the system's principle axis of inertia (eigenvalue $(-1)^K$).

Inclusion of the geometric phase in these calculations is found to reverse this selection rule, with the additional factor of -1 due to the sign change of the electronic

wavefunction;[88] the resulting selection rule in this case is

$$(-1)^{\Pi+|K|} = -X_\Gamma \qquad \Gamma = \{A_1, A_2\} \qquad X_\Gamma = \{1, -1\} \qquad \text{GP} \qquad (7.3.3)$$

8. SUMMARY

In this paper, we have presented a detailed formalism for the calculation of differential and integral cross sections for atom-diatom reactive scattering, using an expansion of the wavefunction in terms of local hyperspherical surface functions in symmetrized hyperspherical coordinates. The formalism includes decomposition into irreducible representations of the permutation symmetry and inversion parity of the system in order to reduce the computational effort necessary. The results of application of these techniques to the H + H_2 system for partial waves $J = 0$ through 3 has also been given, in the form of transition probabilities and partial wave integral cross sections. The geometric phase effect due to the H_3 conical intersection was included *a posteriori* and shown to have a major effect on the behavior of individual J partial wave cross sections, but less of an effect after summing these cross sections over J.

References

† Work supported in part by DOE grant DE-AS03-83ER and AFAL contract F04611-86-K-0067. One of the authors (SAC) also thanks NSF for a Graduate Fellowship. Most of the calculations were performed on the CRAY X-MP/48, SCS-40 and CRAY Y-MP/864 computers at the NSF San Diego Supercomputing Center.

¶ Work performed in partial fulfillment of the requirements for the Ph.D. degree in Chemistry at the California Institute of Technology.

‡ Contribution number

1. A. Kuppermann and G. C. Schatz, *J. Chem. Phys.* **62**, 2502 (1975).

2. G. C. Schatz and A. Kuppermann, *J. Chem. Phys.* **65**, 4642,4668 (1976).

3. R. N. Porter and M. Karplus, *J. Chem. Phys.* **40**, 1105 (1964).

4. A. B. Elkowitz and R. E. Wyatt, *J. Chem. Phys.* **62**, 2504 (1975).

5. A. B. Elkowitz and R. E. Wyatt, *J. Chem. Phys.* **63**, 702 (1975).

6. R. B. Walker, E. B. Stechel and J. C. Light, *J. Chem. Phys.* **69**, 2922 (1978).

7. P. Siegbahn and B. Liu, *J. Chem. Phys.* **68**, 2457 (1978); D. G. Truhlar and C. J. Horowitz, *J. Chem. Phys.* **68**, 2466 (1978); **71**, 1514E (1979).

8. J. Z. H. Zhang and W. H. Miller, *Chem. Phys. Lett.* **153**, 465 (1988).

9. J. M. Launay and M. Le Dorneuf, *Chem. Phys. Lett.* **163**, 178 (1989).

10. D. E. Manolopoulos and R. E. Wyatt, *Chem. Phys. Lett.* **159**, 123 (1989).

11. J. Z. H. Zhang and W. H. Miller, *J. Chem. Phys.* **91**, 1528 (1989); **92**, 1811 (1990).

12. J. Z. H. Zhang and W. H. Miller, *J. Chem. Phys.* **88**, 4549 (1988); **90**, 7610 (1989); *Chem. Phys. Lett.* **159**, 130 (1989).

13. M. Zhao, D. G. Truhlar, D. W. Schwenke and D. J. Kouri, *J. Phys. Chem.*

94, 7074 (1990).

14. A. Kuppermann and P. G. Hipes, *J. Chem. Phys.* **84**, 5962 (1986).

15. P. G. Hipes and A. Kuppermann, *Chem. Phys. Lett.* **133**, 1 (1987).

16. S. A. Cuccaro, P. G. Hipes and A. Kuppermann, a) *Chem. Phys. Lett.* **154**, 155 (1989); b) **157**, 440 (1989).

17. Y. M. Wu, S. A. Cuccaro, P. G. Hipes and A. Kuppermann, *Chem. Phys. Lett.* **168**, 429 (1990).

18. G. A. Parker, R. T. Pack, B. J. Archer and R. B. Walker, *Chem. Phys. Lett.* **137**, 564 (1987).

19. R. T. Pack and G. A. Parker, *J. Chem. Phys.* **87**, 3888 (1987); **90**, 3511 (1989).

20. T. J. Park and J. C. Light, *J. Chem. Phys.* **91**, 974 (1989).

21. G. C. Schatz, *Chem. Phys. Lett.* **150**, 92 (1988).

22. J. Linderberg, *Int. J. Quant. Chem. Symp.* **19**, 467 (1986); J. Linderberg and B. Vessal, *Int. J. Quant. Chem.* **31**, 65 (1987); J. Linderberg, S. B. Padkjaer, Y. Öhrn and B. Vessal, *J. Chem. Phys.* **90**, 6254 (1989).

23. J. Z. H. Zhang, D. J. Kouri, K. Haug, D. W. Schwenke, Y. Shima and D. G. Truhlar, *J. Chem. Phys.* **88**, 2492 (1988).

24. M. Mladenovic, M. Zhao, D. G. Truhlar, D. W. Schwenke, Y. Sun and D. J. Kouri, *Chem. Phys. Lett.* **146**, 358 (1988).

25. M. Zhao, M. Mladenovic, D. G. Truhlar, D. W. Schwenke, Y. Sun, D. J. Kouri and N. C. Blais, *J. Am. Chem. Soc.* **111**, 852 (1989).

26. M. Mladenovic, M. Zhao, D. G. Truhlar, D. W. Schwenke, Y. Sun and D. J. Kouri, *J. Phys. Chem.* **92**, 7035 (1988).

27. M. Zhao, M. Mladenovic, D. G. Truhlar, D. W. Schwenke, O. Sharafeddin, Y. Sun and D. J. Kouri, *J. Chem. Phys.* **91**, 5302 (1989).

28. K. Haug, D. W. Schwenke, Y. Shima, D. G. Truhlar, J. Z. H. Zhang and K. J. Kouri, *J. Phys. Chem.* **90**, 6757 (1986).

29. M. Zhao, D. G. Truhlar, Y. Sun, D. J. Kouri and D. W. Schwenke, *Chem. Phys. Lett.* **156**, 281 (1989).

30. N. C. Blais, M. Zhao, M. Mladenovic, D. G. Truhlar, D. W. Schwenke, Y. Sun and D. J. Kouri, *J. Chem. Phys.* **91**, 1038 (1989).

31. J. Z. H. Zhang and W. H. Miller, *Chem. Phys. Lett.* **140**, 329 (1987); **153**, 465 (1988); **159**, 130 (1989).

32. S. M. Auerbach, J. Z. H. Zhang and W. H. Miller, *J. Chem. S. F.* **86**, 1701 (1990).

33. D. E. Manolopoulos and R. E. Wyatt, *Chem. Phys. Lett.* **152**, 23 (1988).

34. D. E. Manolopoulos and R. E. Wyatt, *J. Chem. Phys.* **92**, 810 (1990).

35. F. Webster and J. C. Light, *J. Chem. Phys.* **90**, 265 (1989).

36. F. Webster and J. C. Light, *J. Chem. Phys.* **90**, 300 (1989).

37. J. D. Kress, Z. Bačić, G. A. Parker and R. T. Pack, *Chem. Phys. Lett.* **157**, 585 (1989); **170**, 306 (1990).

38. Z. Bačić, J. D. Kress, G. A. Parker and R. T. Pack, *J. Chem. Phys.* **92**, 2344 (1990).

39. C. Yu, D. J. Kouri, M. Zhao, D. G. Truhlar and D. W. Schwenke, *Chem. Phys. Lett.* **157**, 491 (1989).

40. C. Yu, Y. Sun, D. J. Kouri, P. Halvick, D. G. Truhlar and D. W. Schwenke, *J. Chem. Phys.* **90**, 7608 (1989).

41. C. Yu, D. J. Kouri, M. Zhao, D. G. Truhlar and D. W. Schwenke, *Int. J. Quant. Chem. Symp.* **23**, 45 (1989).

42. M. Zhao, D. G. Truhlar, D. W. Schwenke, C. H. Yu and D. J. Kouri, *J. Phys. Chem.* **94**, 7062 (1990).

43. D. E. Manolopoulos, M. D'Mello and R. E. Wyatt, *J. Chem. Phys.* **93**, 403 (1990).

44. M. D'Mello, D. E. Manolopoulos and R. E. Wyatt, *Chem. Phys. Lett.* **168**, 113 (1990).

45. D. E. Manolopoulos, M. D'Mello, R. E. Wyatt and R. B. Walker, *Chem. Phys. Lett.* **169**, 482 (1990).

46. K. Haug, D. W. Schwenke, D. G. Truhlar, Y. Zhang, J. Z. H. Zhang and D. J. Kouri, *J. Chem. Phys.* **87**, 1892 (1987).

47. J. Z. H. Zhang, Y. Zhang, D. J. Kouri, B. C. Garrett, K. Haug, D. W. Schwenke and D. G. Truhlar, *Faraday Discuss. Chem. Soc.* **84**, 371 (1987).

48. Y. C. Zhang, J. Z. H. Zhang, D. J. Kouri, K. Haug, D. W. Schwenke and D. G. Truhlar, *Phys. Rev. Lett* **60**, 2367 (1988).

49. G. C. Schatz, *Chem. Phys. Lett.* **151**, 409 (1988); *J. Chem. Phys.* **90**, 3582 (1989).

50. R. A. Marcus, *J. Chem. Phys.* **45**, 4493 (1966).

51. W. Kohn, *Phys. Rev.* **74**, 1763 (1948).

52. A. M. Lane and R. G. Thomas, *Rev. Mod. Phys.* **30**, 257 (1958).

53. M. F. Mott and H. S. W. Massey, **The Theory of Atomic Collisions**, 3rd edition (Oxford Univ. Press, Oxford, 1987), pp. 390, 391.

54. B. R. Johnson, *J. Comp. Phys.* **12**, 445 (1973); *J. Chem. Phys.* **67**, 4086

(1977).

55. R. K. Nesbet, **Variational Methods in Electron-Atom Scattering Theory** (Plenum Press, New York, 1980), ch. 2.

56. R. G. Newton, **Scattering Theory of Particles and Waves** (Springer, New York, 1982), p. 320.

57. W. H. Miller, *J. Chem. Phys.* **50**, 407 (1969).

58. B. Ramachandran, T.-G. Wei and R. E. Wyatt, *J. Chem. Phys.* **89**, 6785 (1988).

59. J. A. Kaye and A. Kuppermann, *Chem. Phys. Lett.* **77**, 573 (1981).

60. J. Manz and J. Römelt, *Chem. Phys. Lett.* **77**, 172 (1981).

61. J. Manz and J. Römelt, *Chem. Phys. Lett.* **81**, 179 (1981).

62. J. A. Kaye and A. Kuppermann, *Chem. Phys. Lett.* **78**, 546 (1981).

63. L. M. Delves, *Nucl. Phys.* **9**, 391 (1958); **20**, 275 (1960).

64. F. T. Smith, *J. Math. Phys.* **3**, 735 (1962); *J. Chem. Phys.* **38**, 1304 (1963); R. C. Whitten and F. T. Smith, *J. Math. Phys.* **9**, 1103 (1968).

65. A. Kuppermann, *Chem. Phys. Lett.* **32**, 374 (1975).

66. R. T. Ling and A. Kuppermann, in: **Electronic and Atomic Collisions, Abstracts of Papers of the 9th International Conference on the Physics of Electronic and Atomic Collisions**, Seattle, Washington, 24–30 July, 1975, Vol. 1, eds. J. Risley and R. Geballe (Univ. Washington Press, Seattle, 1975) pp. 353, 354.

67. B. R. Johnson, *J. Chem. Phys.* **73**, 5051 (1980).

68. C. A. Mead, *Chem. Phys.* **49**, 23 (1980); *J. Chem. Phys.* **72**, 3839 (1980).

69. D. E. Manolopoulos, *J. Chem. Phys.* **85**, 6425 (1986).

70. M. H. Alexander, in: **Algorithms and Computer Codes for Atomic and Molecular Quantum Scattering Theory**, ed. L. Thomas, NRCC proceedings No. 5, page 75.

71. R. De Vogelaere, *J. Res. Nat. Bur. Std.* **54**, 119 (1955).

72. G. A. Parker, T. G. Schmalz and J. C. Light, *J. Chem. Phys.* **73**, 1757 (1980); G. A. Parker, J. C. Light and B. R. Johnson, *Chem. Phys. Lett.* **73**, 572 (1980).

73. E. P. Wigner and L. Eisenbud, *Phys. Rev.* **72**, 29 (1947); J. L. Jackson, *Phys. Rev.* **83**, 301 (1951); J. C. Light and R. B. Walker, *J. Chem. Phys.* **65**, 4272 (1976).

74. M. Hamermesh, **Group Theory** (Addison-Wesley, Reading, Mass., 1962), p. 113.

75. E. Wigner, **Group Theory** (Academic Press, New York, 1959).

76. A. S. Davydov, **Quantum Mechanics**, 2^{nd} edition (Pergamon Press, Oxford, 1976), pp. 167, 178.

77. AMS 55, **Handbook of Mathematical Functions**, eds. M. Abramowitz and I. A. Stegun, (National Bureau of Standards, Washington, D. C., 1972) pp. 437,443.

78. M. Jacob and G. C. Wick, *Ann. Phys.* **7**, 404 (1959).

79. R. T. Pack, *J. Chem. Phys.* **60**, 633 (1974).

80. W. H. Miller, *J. Chem. Phys.* **50**, 407 (1969).

81. reference 76, pp. 171.

82. H. C. Longuet-Higgins, U. Öpik, M. H. L. Pryce and R. A. Sack, *Proc. Roy.*

Soc. A **244**, 1 (1958); G. Herzberg and H. C. Longuet-Higgins, *Discuss. Faraday Soc.* **35**, 77 (1963); H. C. Longuet-Higgins, *Adv. Spec.* **2**, 429 (1961).

83. C. A. Mead and D. G. Truhlar, *J. Chem. Phys.* **70**, 2284 (1979).

84. C. A. Mead, *Chem. Phys.* **49**, 23 (1980).

85. C. A. Mead, *J. Chem. Phys.* **72**, 3839 (1980).

86. Y. Aharonov and D. Bohm, *Phys. Rev.* **115**, 485 (1959).

87. M. V. Berry, *Proc. Roy. Soc. A* **392**, 45 (1984).

88. B. Lepetit and A. Kuppermann, *Chem. Phys. Lett.* **166**, 581 (1990).

89. J. Demmel, *Proceedings of the 1989 IEEE Control Systems Society Workshop on Computer-Aided Control System Design (CACSD), Dec. 16, 1989*; pg. 1.

90. G. C. Schatz and A. Kuppermann, *J. Chem. Phys.* **59**, 964 (1973).

91. A. Kuppermann, in: **Potential Energy Surface and Dynamics Calculations**, ed. D. G. Truhlar (Plenum Press, New York, 1981), pp. 405, 414.

92. E. F. Hayes and R. B. Walker, in: **Resonances**, ACS Symposium Series **263** (Am. Chem. Soc., Washington, 1984), p. 493.

93. D. W. Schwenke and D. G. Truhlar, *J. Chem. Phys.* **87**, 1095 (1987).

94. B. Gazdy and J. M. Bowman, *Phys. Rev. A.* **36**, 3083 (1987).

95. F. T. Smith, *Phys. Rev.* **118**, 349 (1960).

96. M. C. Colton and G. C. Schatz, *Chem. Phys. Lett.* **124**, 256 (1986).

97. J. M. Bowman, *Chem. Phys. Lett.* **124**, 260 (1986).

98. G. Herzberg, **Infrared and Raman Spectra of Polyatomic Molecules**, (Van Nostrand, Princeton, 1945), p. 272.

99. E. Pollak, *Chem. Phys. Lett.* **137**, 171 (1987); *J. Chem. Phys.* **90**, 3619

(1986).

100. B. C. Garrett, D. W. Schwenke, R. T. Skodje, D. Thirumalai, T. C. Thompson and D. G. Truhlar, in: **Resonances**, Am. Chem. Soc. Symp. Ser., **263**, (Am. Chem. Soc., Washington, 1984), p. 375.

Table 6.1: Largest modulus and phase differences of ${}^{o}\mathbf{S}^{J=0,A_1}$ matrix elements from converged values: $E = 1.6$ eV

$|\Delta_{max}|{}^{o}\mathbf{S}_{ij}||^{a}$

N_p	WU[b]	all elements[c]	$\lvert{}^{o}\mathbf{S}_{ij}\rvert \geq 0.1$[d]	$\lvert{}^{o}\mathbf{S}_{i1}\rvert$[e]	$\lvert{}^{o}\mathbf{S}_{i1}\rvert \geq 0.1$[f]
32	0.61%	0.0119	0.0119	0.0021	0.0021
33	0.46%	0.0077	0.0077	0.0023	0.0023
34	0.58%	0.0192	0.0085	0.0026	0.0026
35	0.71%	0.0107	0.0082	0.0027	0.0027
37	2.2%	0.0530	0.0160	0.0025	0.0025
38	0.53%	0.0072	0.0072	0.0025	0.0025
39	0.71%	0.0067	0.0067	0.0021	0.0021
40	0.81%	0.0063	0.0063	0.0020	0.0020

$|\Delta_{max}{}^{o}\phi_{ij}|/\text{degrees}^{g}$

32	0.61%	78.8	15.2	4.35	1.55
33	0.46%	77.8	15.2	5.44	1.20
34	0.58%	115.3	14.5	8.21	1.09
35	0.71%	108.8	3.93	4.13	1.15
37	2.2%	169.4	7.47	3.67	1.20
38	0.53%	52.3	3.53	2.86	1.26
39	0.71%	28.8	3.42	3.21	1.20
40	0.81%	37.7	2.73	2.99	1.20

[a] Maximum absolute deviation of $|{}^{o}\mathbf{S}_{ij}|$ with respect to the converged value; $i, j \in [1, 17]$ are row and column indices, respectively.

[b] Worst Unitarity - deviation of largest or smallest column sum from 1.0.

[c] Largest modulus or phase differences from converged values for all elements of the °S matrix.

[d] Largest modulus or phase differences from converged values for elements of the °S matrix with modulus greater than or equal to 0.1.

[e] Largest modulus or phase differences from converged values for elements in the first column of the °S matrix.

[f] Largest modulus or phase differences from converged values for elements in the first column of the °S matrix with modulus greater than or equal to 0.1.

[g] Maximum absolute deviation of the phase of ${}^{o}\mathbf{S}_{ij}$ with respect to the converged value.

Table 6.2: Convergence of moduli and phases of ${}^{o}\mathbf{S}^{J=0,A_1}$ with increasing $\bar{\rho}^{max}$ comparison with $\bar{\rho}^{max} = 13.0a_0$ (WU[a]=0.65%)

$|\Delta_{max}|{}^{o}\mathbf{S}_{ij}||^{b}$

$\bar{\rho}^{max}/a_0$	WU[a]	*all elements*[c]	$\lvert{}^{o}\mathbf{S}_{ij}\rvert \geq 0.1$[d]	$\lvert{}^{o}\mathbf{S}_{i1}\rvert \geq 0.1$[e]
10.0	0.67%	0.0047	0.0047	0.0026
10.4	0.75%	0.0080	0.0048	0.0012
10.8	0.76%	0.0071	0.0039	0.0009
11.2	0.59%	0.0040	0.0025	0.0025
11.6	0.60%	0.0036	0.0036	0.0031
12.0	0.70%	0.0038	0.0038	0.0028
12.2	0.78%	0.0059	0.0042	0.0019
12.4	0.91%	0.0055	0.0043	0.0017
12.6	0.72%	0.0031	0.0028	0.0012
12.8	0.69%	0.0030	0.0016	0.0009

$|\Delta_{max}{}^{o}\phi_{ij}|/\text{degrees}^{f}$

10.0	0.67%	21.14	10.71	3.27
10.4	0.75%	50.82	8.02	2.86
10.8	0.76%	41.48	5.96	2.35
11.2	0.59%	31.91	5.73	2.18
11.6	0.60%	20.40	4.64	1.83
12.0	0.70%	32.71	2.41	1.20
12.2	0.78%	23.92	2.01	1.26
12.4	0.91%	21.31	2.12	1.32
12.6	0.72%	41.94	1.49	0.92
12.8	0.69%	22.23	0.57	0.57

[a] Worst Unitarity - deviation of largest or smallest column sum from 1.0.

[b] Maximum absolute deviation of $|{}^{o}\mathbf{S}_{ij}|$ with respect to the value at $\bar{\rho}^{max} = 13.0$ bohr; $i, j \in [1, 17]$ are row and column indices, respectively.

[c] Largest modulus or phase differences from $\bar{\rho}^{max} = 13.0$ values for all elements of $|{}^{o}\mathbf{S}|$.

[d] Largest modulus or phase differences from values at $\bar{\rho}^{max} = 13.0$ bohr for elements of $|{}^{o}\mathbf{S}|$ with modulus greater than or equal to 0.1.

[e] Largest modulus or phase differences from values at $\bar{\rho}^{max} = 13.0$ bohr for elements in the first column of $|{}^{o}\mathbf{S}|$ with modulus greater than or equal to 0.1.

[f] Maximum absolute deviation of the phase of $|{}^{o}\mathbf{S}_{ij}|$ with respect to $\bar{\rho}^{max} = 13.0$ bohr values.

Table 7.1: Resonance characteristics for LSTH[a] potential energy surface.

J	Assignment	Current results		FE[b]		RPO[c]	SCSA[d]	CEQB[e]	CS[f]
		E(eV)	Lifetime(fs)	E(eV)	Lifetime(fs)	E(eV)	E(eV)	E(eV)	E(eV)
0,1	$(0,0^0,0)$	0.65	11	0.65	11				
1	$(0,1^1,0)$	0.77	9						
0,1	$(0,2^0,0)$	0.88	10	0.880	10				
0,1	$(1,0^0,0)$	0.98	28	0.981	28	0.981	0.98	0.97	
1	$(0,3^1,0)$	1.00	8						
1	$(1,1^1,0)$	1.09	29			1.085	1.09	1.09	1.10
0,1	$(0,4^0,0)$	1.10	5						
0,1	$(1,2^0,0)$	1.19	8	1.191		1.186		1.20	1.20
1	$(0,5^1,0)$	1.22	6						
0,1	$(2,0^0,0)$	1.36	30	1.364	31	1.374	1.24	1.35	
1	$(2,1^1,0)$	1.45	38			1.461	1.35		
0	?	1.50	4						
0,1	$(2,2^0,0)$	1.54	12	1.55±0.03		1.545	1.46		
1	$(2,3^1,0)$	1.63	8			1.641			
0,1	$(2,4^0,0)$	1.72[g]	5			1.734			

a) Reference 7.
b) P. G. Hipes, Three Dimensional Atom-Diatom Reactive Scattering Calculations Using Symmetrised Hyperspherical Coordinates, Ph. D. Thesis, California Institute of Technology, 1988; unpublished results.
c) Resonant Periodic Orbit results, Ref. 99.
d) Small Curvature Semiclassical Adiabatic results, Ref. 100.
e) Collinear Exact Quantum with Adiabatic Bend results, Ref. 97.
f) Coupled State results, Ref. 96.
g) This resonance energy is less accurate than the rest.

Figure Captions

Figure 7.1 $J = 0$ A_1 transition probabilities as a function of total energy for transitions of the type (0,0,0) $\rightarrow$ (0,j,0), with $j = 0, 2, 4, 6$ for H+H_2 on the LSTH potential energy surface. Scattering matrices were calculated every 0.01 eV in the range $E \in [0.3, 1.6]$. The lower abscissas in each panel indicates the total system energy while the upper abscissas indicates the corresponding initial state translational energy. The arrows pointing to the upper abscissa indicate the threshhold energies for the opening of the (v, j) states of H_2, with the longest arrows pointing to the opening of the asymptotic states with $v = 0$, the medium length to the opening of the states with $v = 1$ and the shortest corresponding to the opening of the $v = 2$ states. The scaling factor for the transition is printed on the plot.

Figure 7.2 $J = 0$ A_1 transition probabilities as a function of total energy for transitions of the type (0,0,0) $\rightarrow$ (1,j,0), with $j = 0, 2, 4, 6$ for H+H_2 on the LSTH potential energy surface. See caption of figure 7.1 for additional information.

Figure 7.3 $J = 0$ A_2 transition probabilities as a function of total energy for transitions of the type (0,1,0) $\rightarrow$ (0,j,0), with $j = 1, 3, 5, 7$ for H+H_2 on the LSTH potential energy surface. See caption of figure 7.1 for additional information.

Figure 7.4 $J = 0$ A_2 transition probabilities as a function of total energy for transitions of the type (0,1,0) $\rightarrow$ (1,j,0), with $j = 1, 3, 5, 7$ for H+H_2 on the LSTH potential energy surface. See caption of figure 7.1 for additional information.

Figure 7.5 $J = 0$ E transition probabilities as a function of total energy for transitions of the type (0,0,0) $\rightarrow$ (0,j,0), with $j = 0, 2, 4, 6$ for H+H_2 on the LSTH potential energy surface. See caption of figure 7.1 for additional information.

Figure 7.6 $J = 0$ E transition probabilities as a function of total energy for transitions of the type (0,0,0) $\rightarrow$ (1,j,0), with $j = 0, 2, 4, 6$ for H+H_2 on the LSTH potential energy surface. See caption of figure 7.1 for additional information.

Figure 7.7 $J = 0$ E transition probabilities as a function of total energy for transitions of the type (0,1,0) $\rightarrow$ (0,j,0), with $j = 1,3,5,7$ for H+H_2 on the LSTH potential energy surface. See caption of figure 7.1 for additional information.

Figure 7.8 $J = 0$ E transition probabilities as a function of total energy for transitions of the type (0,1,0) $\rightarrow$ (1,j,0), with $j = 1,3,5,7$ for H+H_2 on the LSTH potential energy surface. See caption of figure 7.1 for additional information.

Figure 7.9 $J = 0$ E transition probabilities as a function of total energy for transitions of the type (0,0,0) $\rightarrow$ (0,j,0), with $j = 1,3,5,7$ for H+H_2 on the LSTH potential energy surface. See caption of figure 7.1 for additional information.

Figure 7.10 $J = 0$ E transition probabilities as a function of total energy for transitions of the type (0,0,0) $\rightarrow$ (1,j,0), with $j = 1,3,5,7$ for H+H_2 on the LSTH potential energy surface. See caption of figure 7.1 for additional information.

Figure 7.11 $J = 0$ E transition probabilities as a function of total energy for transitions of the type (0,1,0) $\rightarrow$ (0,j,0), with $j = 0,2,4,6$ for H+H_2 on the LSTH potential energy surface. See caption of figure 7.1 for additional information.

Figure 7.12 $J = 0$ E transition probabilities as a function of total energy for transitions of the type (0,1,0) $\rightarrow$ (1,j,0), with $j = 0,2,4,6$ for H+H_2 on the LSTH potential energy surface. See caption of figure 7.1 for additional information.

Figure 7.13 Same as figure 7.1, with conical intersection effect included in the calculation.

Figure 7.14 Same as figure 7.2, with conical intersection effect included in the calculation.

Figure 7.15 Same as figure 7.3, with conical intersection effect included in the calculation.

Figure 7.16 Same as figure 7.4, with conical intersection effect included in the

calculation.

Figure 7.17 Same as figure 7.5, with conical intersection effect included in the calculation.

Figure 7.18 Same as figure 7.6, with conical intersection effect included in the calculation.

Figure 7.19 Same as figure 7.7, with conical intersection effect included in the calculation.

Figure 7.20 Same as figure 7.8, with conical intersection effect included in the calculation.

Figure 7.21 $J = 0$ Pauli antisymmetrized integral cross sections for the transitions (0,0,0) to (0,j,0), $j = 0, 2$ and (0,0,0) to (1,j,0), $j = 0, 2$. Scattering matrices were calculated every 0.01 eV in the range $E \in [0.3, 1.6]$. The lower abscissas in each panel indicates the total system energy while the upper abscissas indicates the corresponding initial state translational energy. The arrows pointing to the upper abscissa indicate the threshhold energies for the opening of the (v, j) states of H_2, with the longest arrows pointing to the opening of the asymptotic states with $v = 0$, the medium length to the opening of the states with $v = 1$ and the shortest corresponding to the opening of the $v = 2$ states. The scaling factor for each transition is printed on the plot.

Figure 7.22 Same as figure 7.21, with conical intersection effect included in the calculation.

Figure 7.23 $J = 0$ Pauli antisymmetrized integral cross sections for the transitions (0,1,0) to (0,j,0), $j = 1, 3$ and (0,1,0) to (1,j,0), $j = 1, 3$. See caption to figure 7.21 for additional information.

Figure 7.24 Same as figure 7.23, with conical intersection effect included in the calculation.

Figure 7.25 $J = 0$ Pauli antisymmetrized integral cross sections for the transitions (0,0,0) to (0,j,0), $j = 1, 3$ and (0,0,0) to (1,j,0), $j = 1, 3$. See caption to figure 7.21 for additional information.

Figure 7.26 $J = 0$ Pauli antisymmetrized integral cross sections for the transitions (0,1,0) to (0,j,0), $j = 0, 2$ and (0,1,0) to (1,j,0), $j = 0, 2$. See caption to figure 7.21 for additional information.

Figure 7.27 $J = 1$ Pauli antisymmetrized integral cross sections for the transitions: (a) (0,0,0) to (1,0,0); (b) (0,0,0) to (1,2,0); (c) (0,0,0) to (1,2,1). (d) (0,1,0) to (1,1,0). See caption to figure 7.21 for additional information.

Figure 7.28 Same as figure 7.27, with conical intersection effect included in the calculation.

Figure 7.29 $J = 1$ Pauli antisymmetrized integral cross sections for the transitions: (a) (0,1,0) to (1,1,1); (b) (0,1,1) to (1,1,-1); (c) (0,1,1) to (1,1,0); (d) (0,1,1) to (1,1,1). See caption to figure 7.21 for additional information.

Figure 7.30 Same as figure 7.29, with conical intersection effect included in the calculation.

Figure 7.31 $J = 2$ Pauli antisymmetrized integral cross sections for the transitions: (a) (0,0,0) to (1,2,0); (b) (0,0,0) to (1,2,1); (c) (0,0,0) to (1,2,2). (d) (0,1,0) to (1,1,0). See caption to figure 7.21 for additional information.

Figure 7.32 Same as figure 7.31, with conical intersection effect included in the calculation.

Figure 7.33 $J = 2$ Pauli antisymmetrized integral cross sections for the transitions: (a) (0,1,0) to (1,1,1); (b) (0,1,1) to (1,1,-1); (c) (0,1,1) to (1,1,0); (d) (0,1,1) to (1,1,1). See caption to figure 7.21 for additional information.

Figure 7.34 Same as figure 7.33, with conical intersection effect included in the

calculation.

Figure 7.35 $J = 3$ Pauli antisymmetrized integral cross sections for the transitions: (a) (0,0,0) to (1,2,0); (b) (0,0,0) to (1,2,1); (c) (0,0,0) to (1,2,2). (d) (0,1,0) to (1,1,0). See caption to figure 7.21 for additional information.

Figure 7.36 Same as figure 7.35, with conical intersection effect included in the calculation.

Figure 7.37 $J = 3$ Pauli antisymmetrized integral cross sections for the transitions: (a) (0,1,0) to (1,1,1); (b) (0,1,1) to (1,1,-1); (c) (0,1,1) to (1,1,0); (d) (0,1,1) to (1,1,1). See caption to figure 7.21 for additional information.

Figure 7.38 Same as figure 7.37, with conical intersection effect included in the calculation.

Figure 7.39 Pauli antisymmetrized integral cross sections summed over partial waves J=0 to 3 for the transitions: (a) (0,0,0) to (1,2,0); (b) (0,0,0) to (1,2,1); (c) (0,0,0) to (1,2,2). (d) (0,1,0) to (1,1,0). See caption to figure 7.21 for additional information.

Figure 7.40 Same as figure 7.39, with conical intersection effect included in the calculation.

Figure 7.41 Pauli antisymmetrized integral cross sections summed over partial waves J=0 to 3 for the transitions: (a) (0,1,0) to (1,1,1); (b) (0,1,1) to (1,1,-1); (c) (0,1,1) to (1,1,0); (d) (0,1,1) to (1,1,1). See caption to figure 7.21 for additional information.

Figure 7.42 Same as figure 7.41, with conical intersection effect included in the calculation.

Figure 7.43 Pauli antisymmetrized integral cross sections summed over partial waves $J = 0$ to 3, also summed over final orientation Ω and averaged over initial

orientation m', for the transitions: (a) (0,0) to (1,0); (b) (0,0) to (1,2); (c) (0,1) to (1,1); (d) (0,1) to (1,0). See caption to figure 7.21 for additional information.

Figure 7.44 Same as figure 7.43, with conical intersection effect included in the calculation.

Figure 7.45 Lifetime matrix eigenvalues (in femtoseconds) for the LSTH potential energy surface of the H_3 system in the $J = 3$ partial wave and A_2 irreducible representation as a function of total energy E (in eV), for the cases (a) $\Pi = 0$ and (b) $\Pi = 1$. The peaks in the set of curves correspond to resonances of the H_3 system, and are labelled according to the convention for linear triatomic molecular states, as discussed in text.

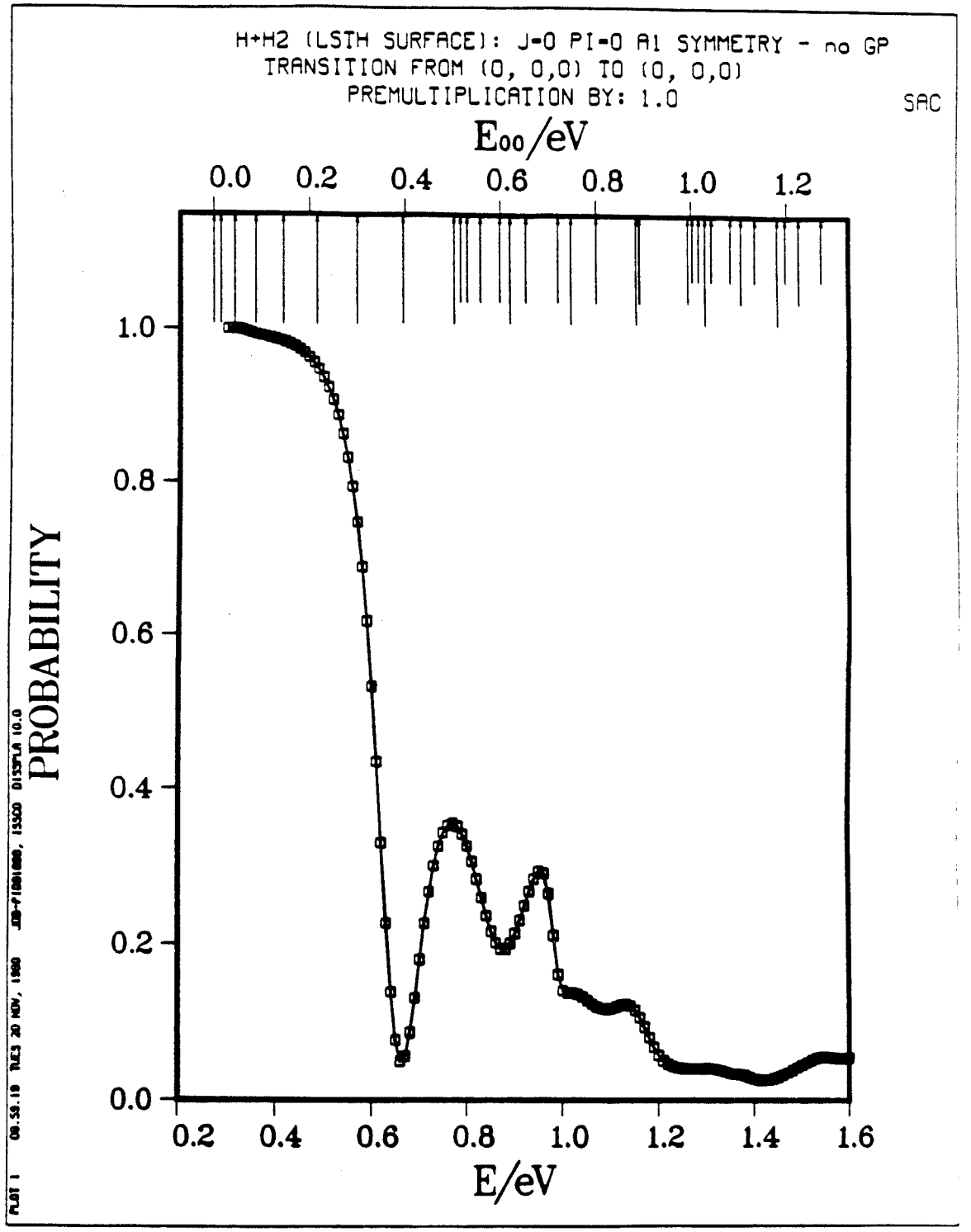
H+H2 (LSTH SURFACE): J=0 PI=0 A1 SYMMETRY - no GP
TRANSITION FROM (0, 0,0) TO (0, 0,0)
PREMULTIPLICATION BY: 1.0
SAC
E00/eV
0.0
0.2
0.4
0.6
0.8
1.0
1.2
PROBABILITY
0.0
0.2
0.4
0.6
0.8
1.0
E/eV
0.2
0.4
0.6
0.8
1.0
1.2
1.4
1.6

Fig. 7.1a

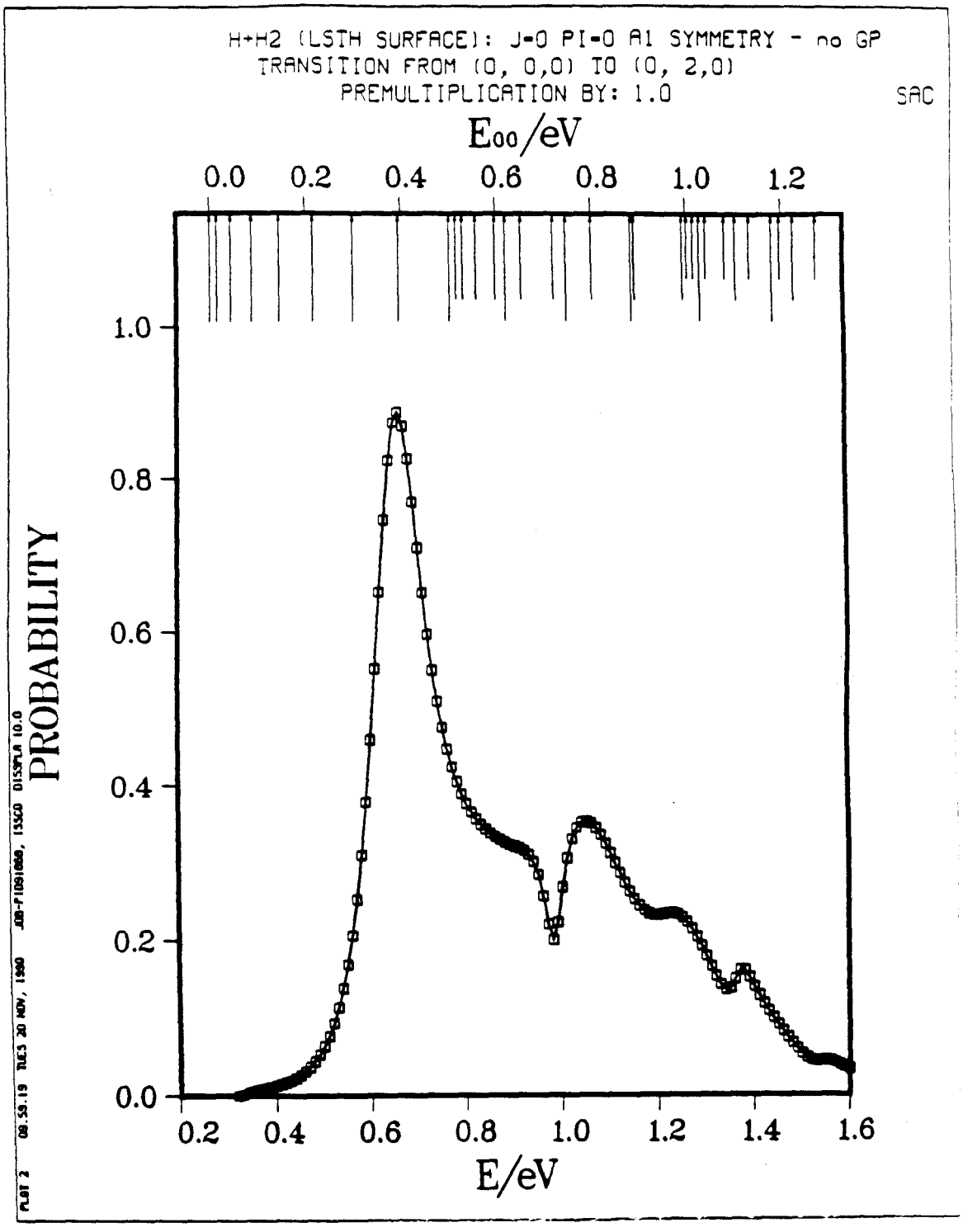
H+H2 (LSTH SURFACE): J=0 PI=0 A1 SYMMETRY - no GP
TRANSITION FROM (0, 0,0) TO (0, 2,0)
PREMULTIPLICATION BY: 1.0
SAC
E00/eV
0.0
0.2
0.4
0.6
0.8
1.0
1.2
PROBABILITY
0.0
0.2
0.4
0.6
0.8
1.0
0.2
0.4
0.6
0.8
1.0
1.2
1.4
1.6
E/eV

Fig. 7.1b

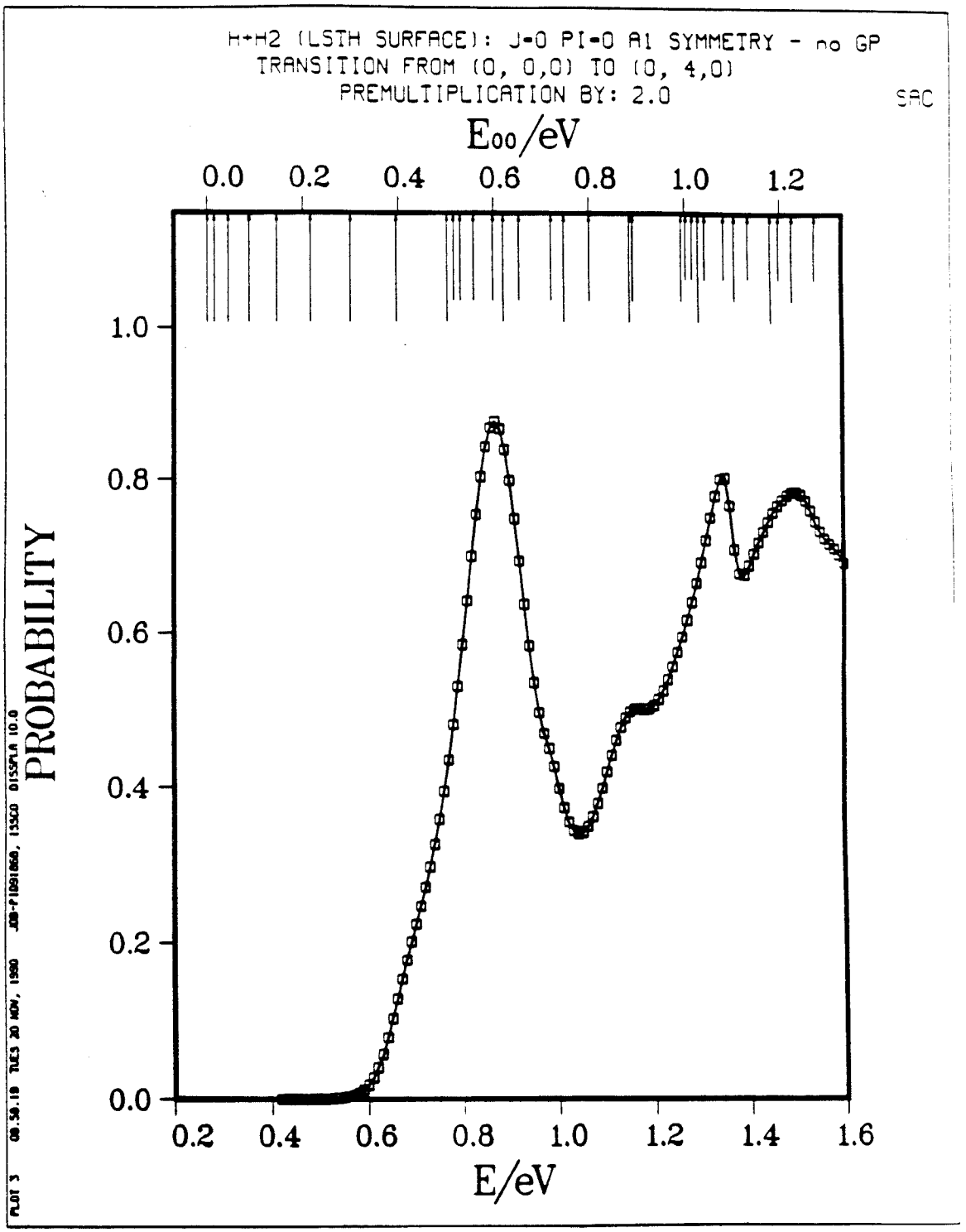
H+H2 (LSTH SURFACE): J=0 PI=0 A1 SYMMETRY - no GP
TRANSITION FROM (0, 0,0) TO (0, 4,0)
PREMULTIPLICATION BY: 2.0
SRC
E00/eV
0.0
0.2
0.4
0.6
0.8
1.0
1.2
PROBABILITY
0.0
0.2
0.4
0.6
0.8
1.0
E/eV
0.2
0.4
0.6
0.8
1.0
1.2
1.4
1.6

Fig. 7.1c

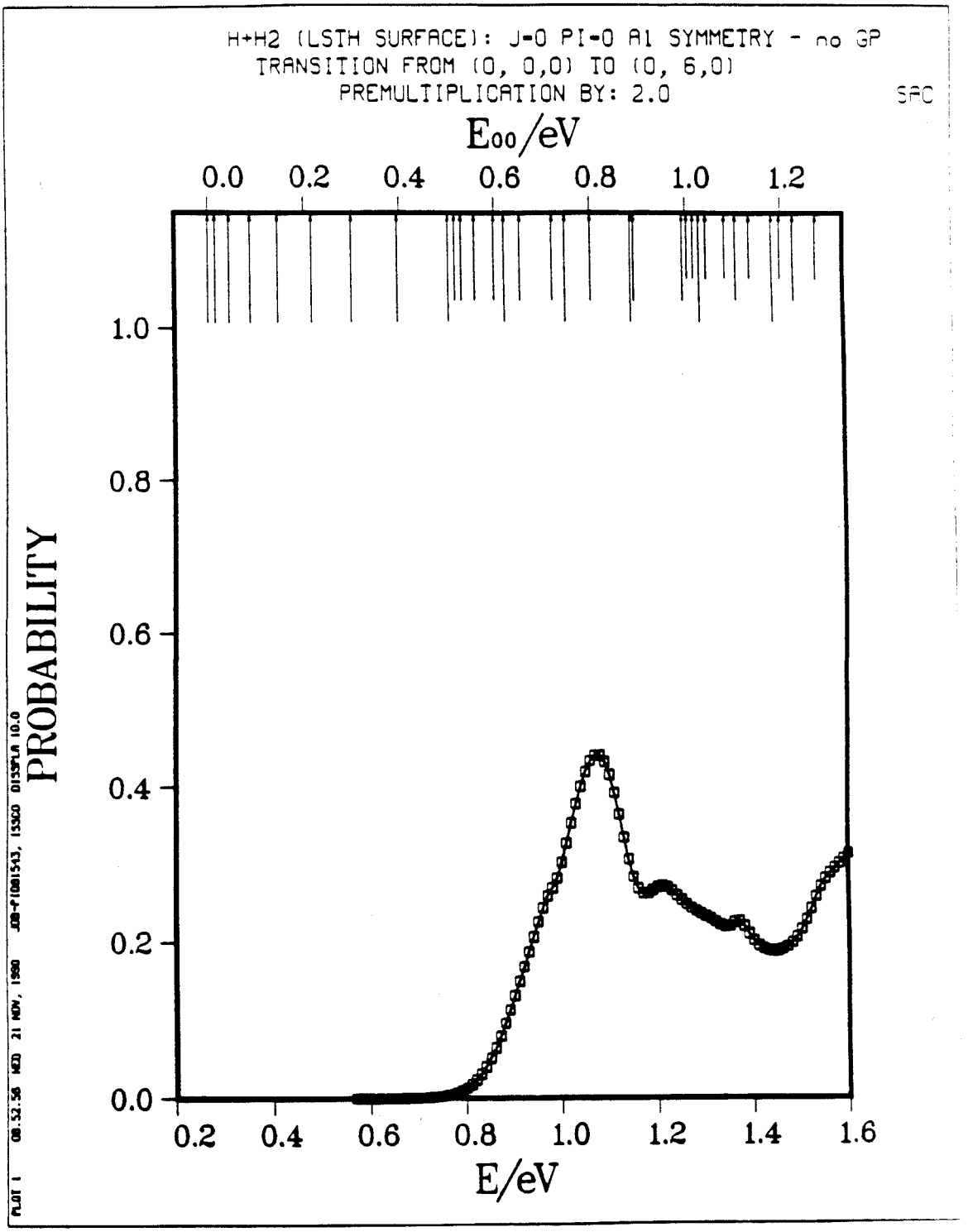
H+H2 (LSTH SURFACE): J=0 PI=0 A1 SYMMETRY - no GP
TRANSITION FROM (0, 0,0) TO (0, 6,0)
PREMULTIPLICATION BY: 2.0
SPC
E00/eV
0.0
0.2
0.4
0.6
0.8
1.0
1.2
PROBABILITY
0.0
0.2
0.4
0.6
0.8
1.0
E/eV
0.2
0.4
0.6
0.8
1.0
1.2
1.4
1.6
PLOT 1 08.52.56 WED 21 NOV, 1990 JOB-P1081543, 15320 DISSPLA 10.0

Fig. 7.1d

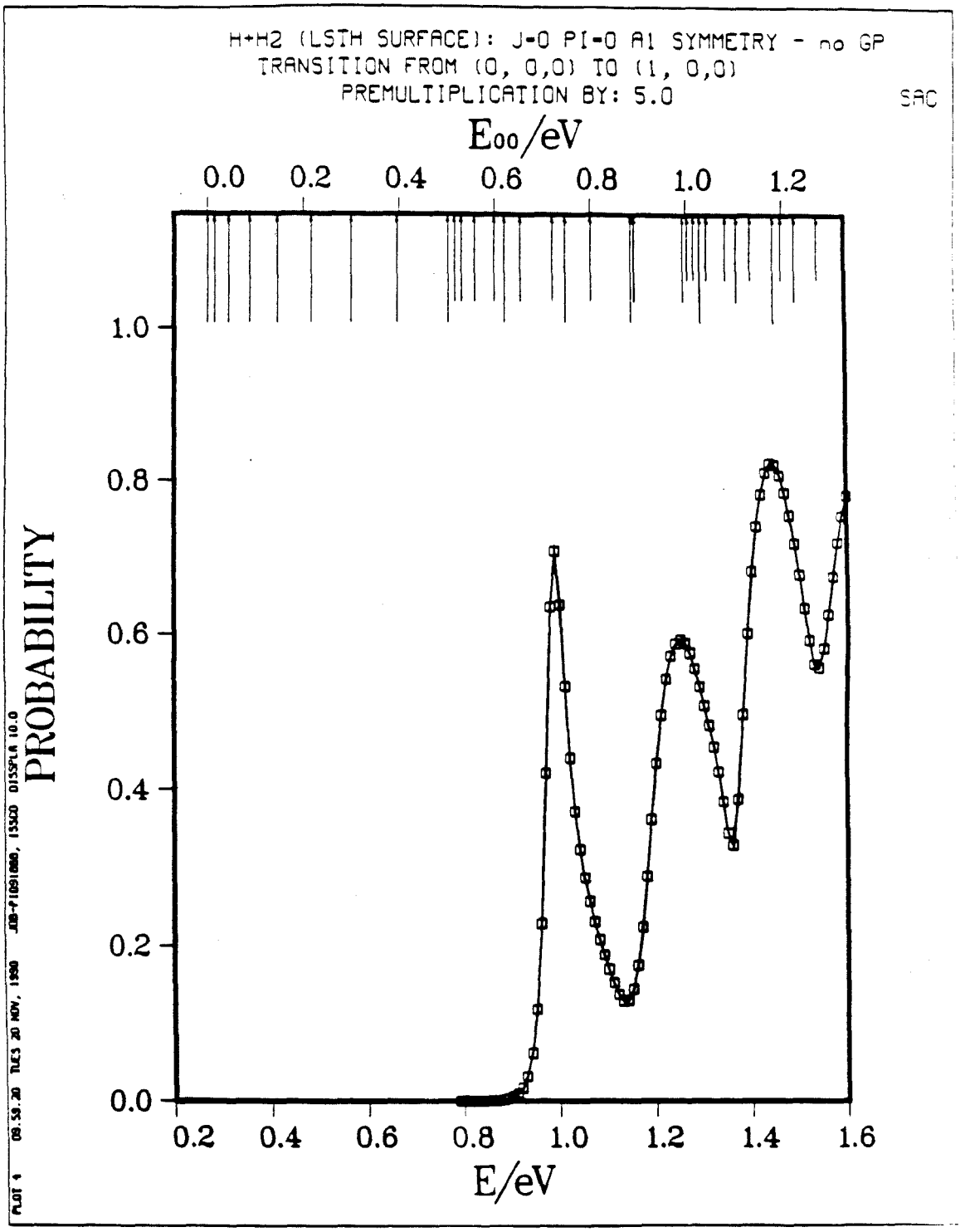
H+H2 (LSTH SURFACE): J=0 PI=0 A1 SYMMETRY - no GP
TRANSITION FROM (0, 0,0) TO (1, 0,0)
PREMULTIPLICATION BY: 5.0
SAC
E00/eV
0.0
0.2
0.4
0.6
0.8
1.0
1.2
PROBABILITY
0.0
0.2
0.4
0.6
0.8
1.0
E/eV
0.2
0.4
0.6
0.8
1.0
1.2
1.4
1.6

Fig. 7.2a

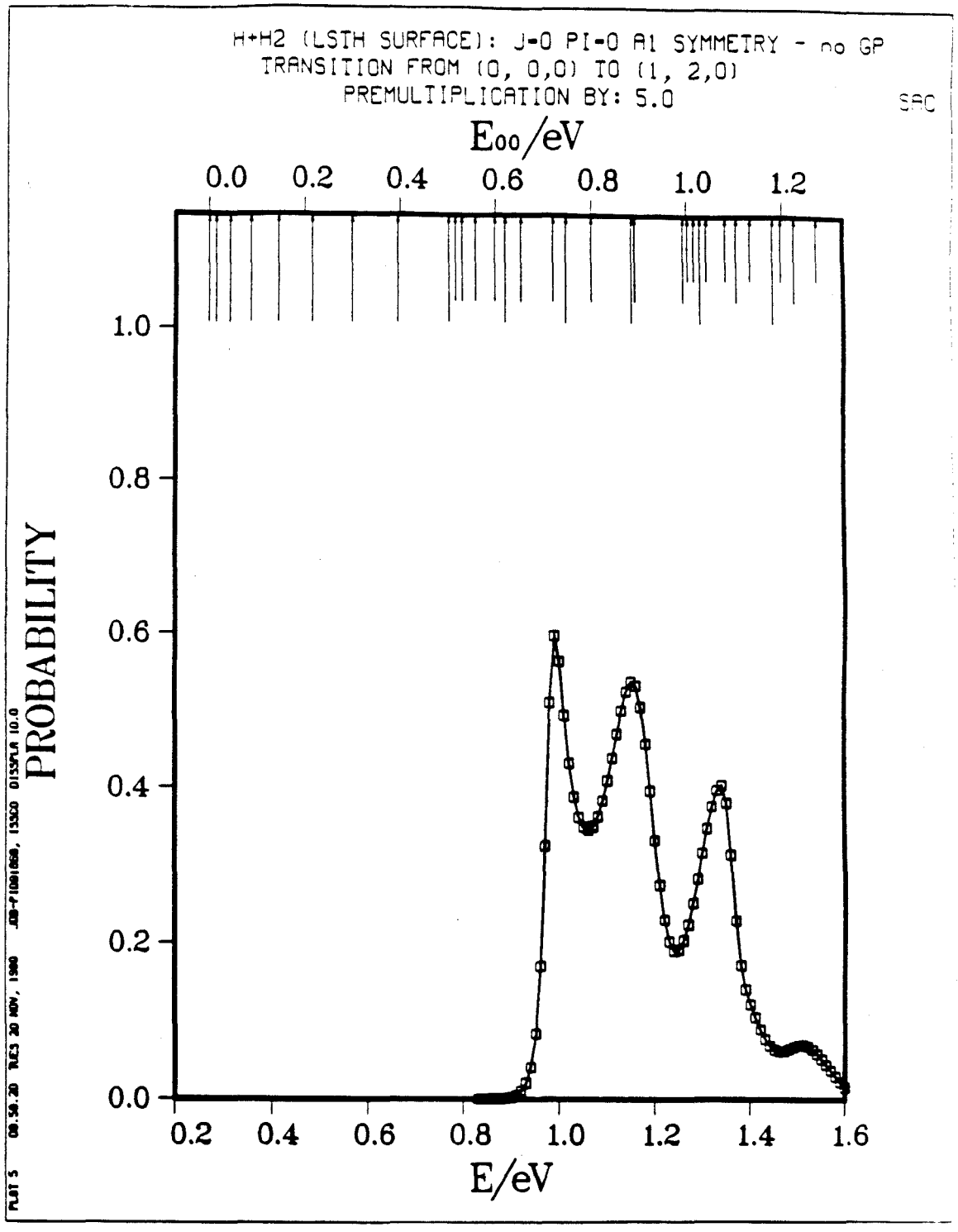
H+H2 (LSTH SURFACE): J=0 PI=0 A1 SYMMETRY - no GP
TRANSITION FROM (0, 0,0) TO (1, 2,0)
PREMULTIPLICATION BY: 5.0
SAC
E00/eV
0.0
0.2
0.4
0.6
0.8
1.0
1.2
PROBABILITY
0.0
0.2
0.4
0.6
0.8
1.0
E/eV
0.2
0.4
0.6
0.8
1.0
1.2
1.4
1.6

Fig. 7.2b

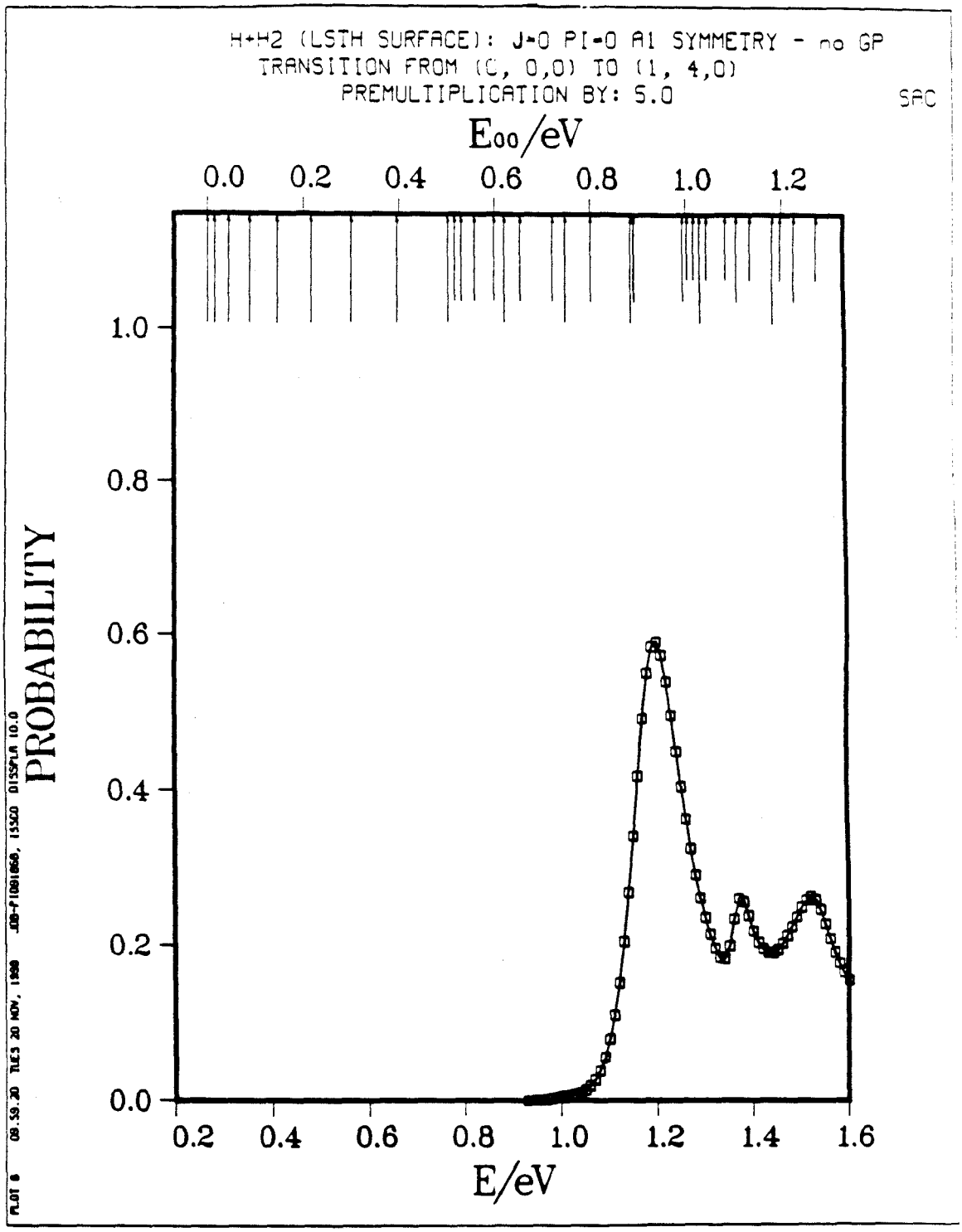
H+H2 (LSTH SURFACE): J=0 PI=0 A1 SYMMETRY - no GP
TRANSITION FROM (0, 0,0) TO (1, 4,0)
PREMULTIPLICATION BY: 5.0
SAC
E00/eV
0.0
0.2
0.4
0.6
0.8
1.0
1.2
PROBABILITY
0.0
0.2
0.4
0.6
0.8
1.0
1.2
1.4
1.6
E/eV

Fig. 7.2c

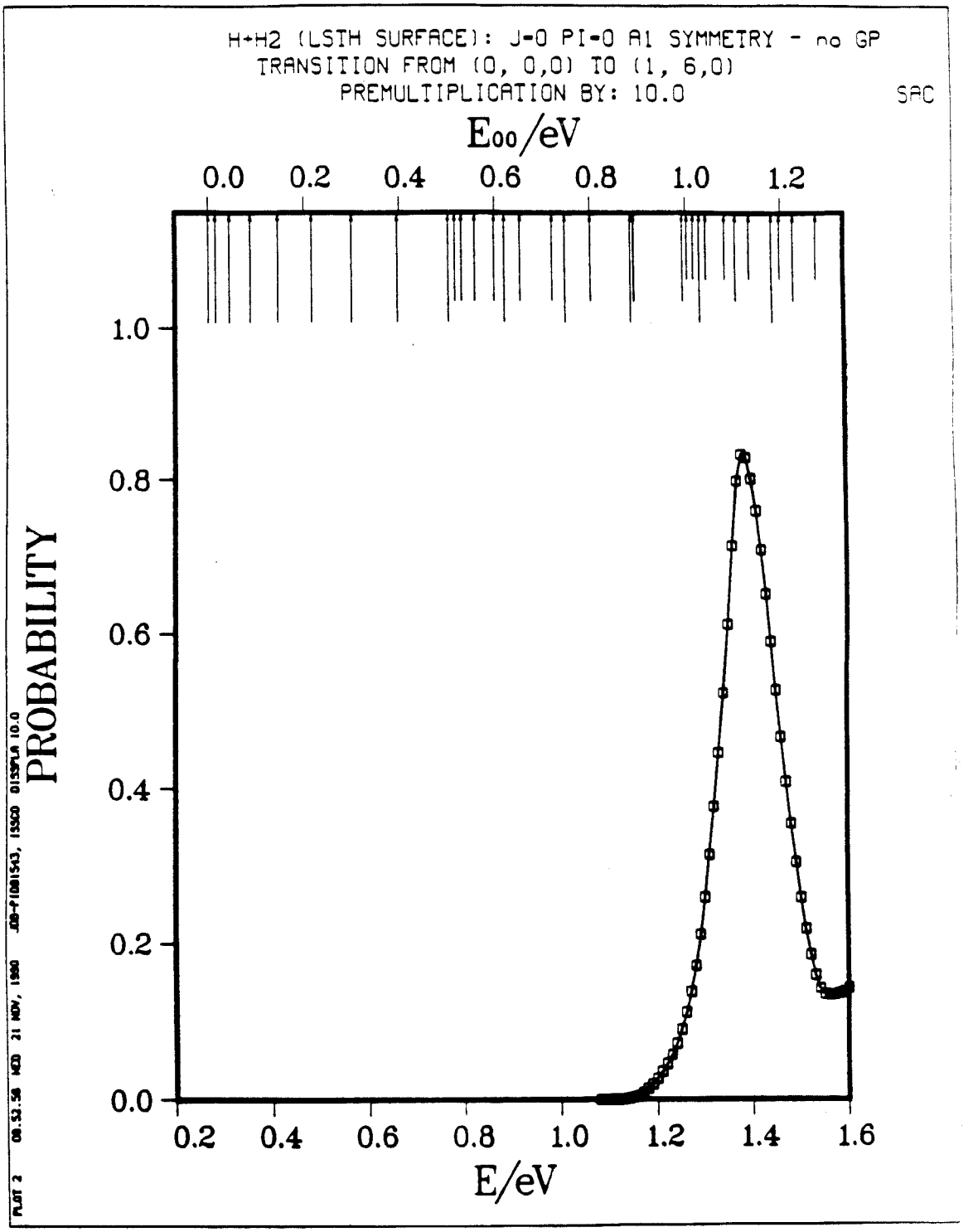
H+H2 (LSTH SURFACE): J=0 PI=0 A1 SYMMETRY - no GP
TRANSITION FROM (0, 0,0) TO (1, 6,0)
PREMULTIPLICATION BY: 10.0
SRC
E00/eV
0.0
0.2
0.4
0.6
0.8
1.0
1.2
PROBABILITY
0.0
0.2
0.4
0.6
0.8
1.0
E/eV
0.2
0.4
0.6
0.8
1.0
1.2
1.4
1.6

Fig. 7.2d

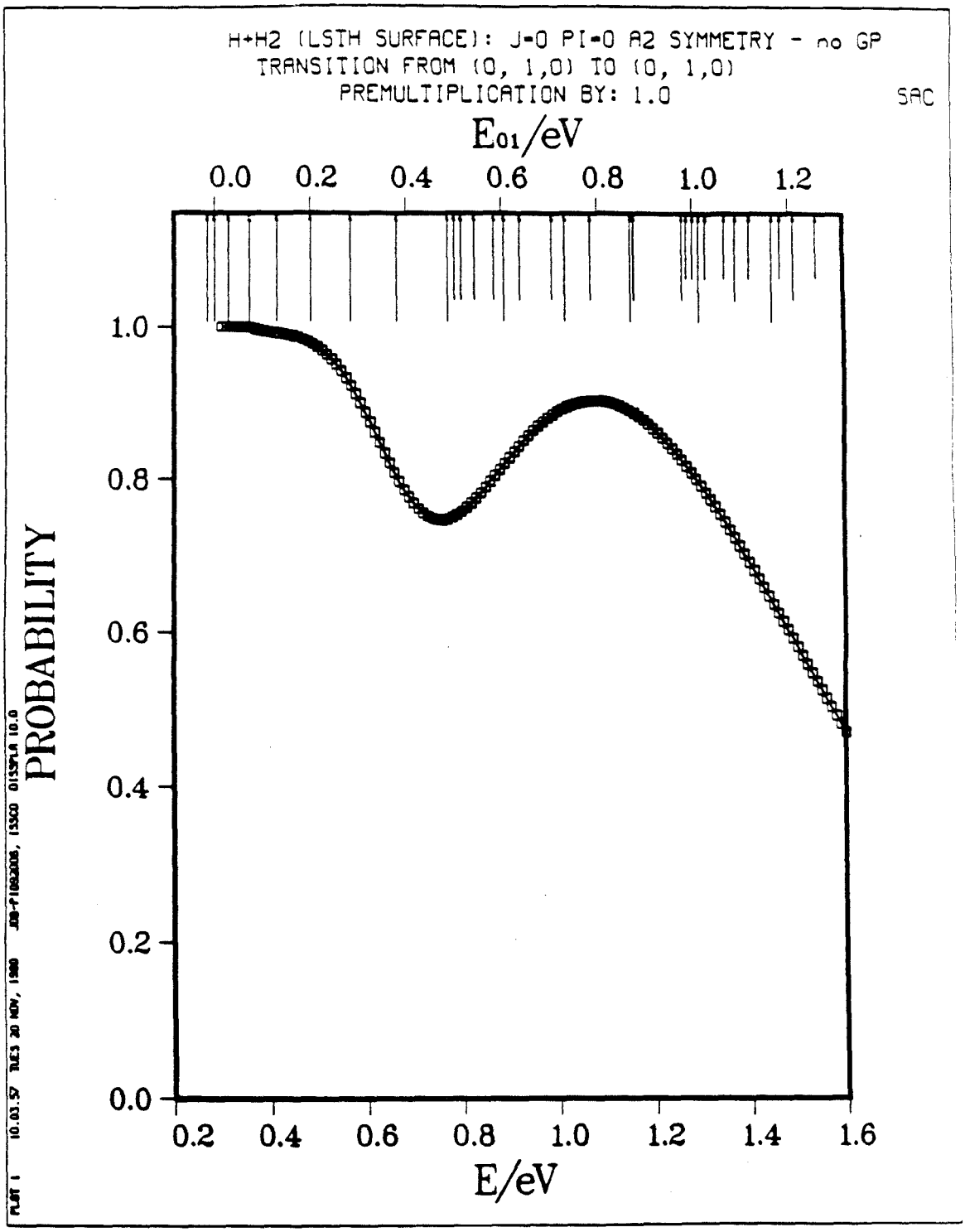
H+H2 (LSTH SURFACE): J=0 PI=0 A2 SYMMETRY - no GP
TRANSITION FROM (0, 1,0) TO (0, 1,0)
PREMULTIPLICATION BY: 1.0
SAC
E01/eV
0.0
0.2
0.4
0.6
0.8
1.0
1.2
PROBABILITY
1.0
0.8
0.6
0.4
0.2
0.0
0.2
0.4
0.6
0.8
1.0
1.2
1.4
1.6
E/eV

Fig. 7.3a

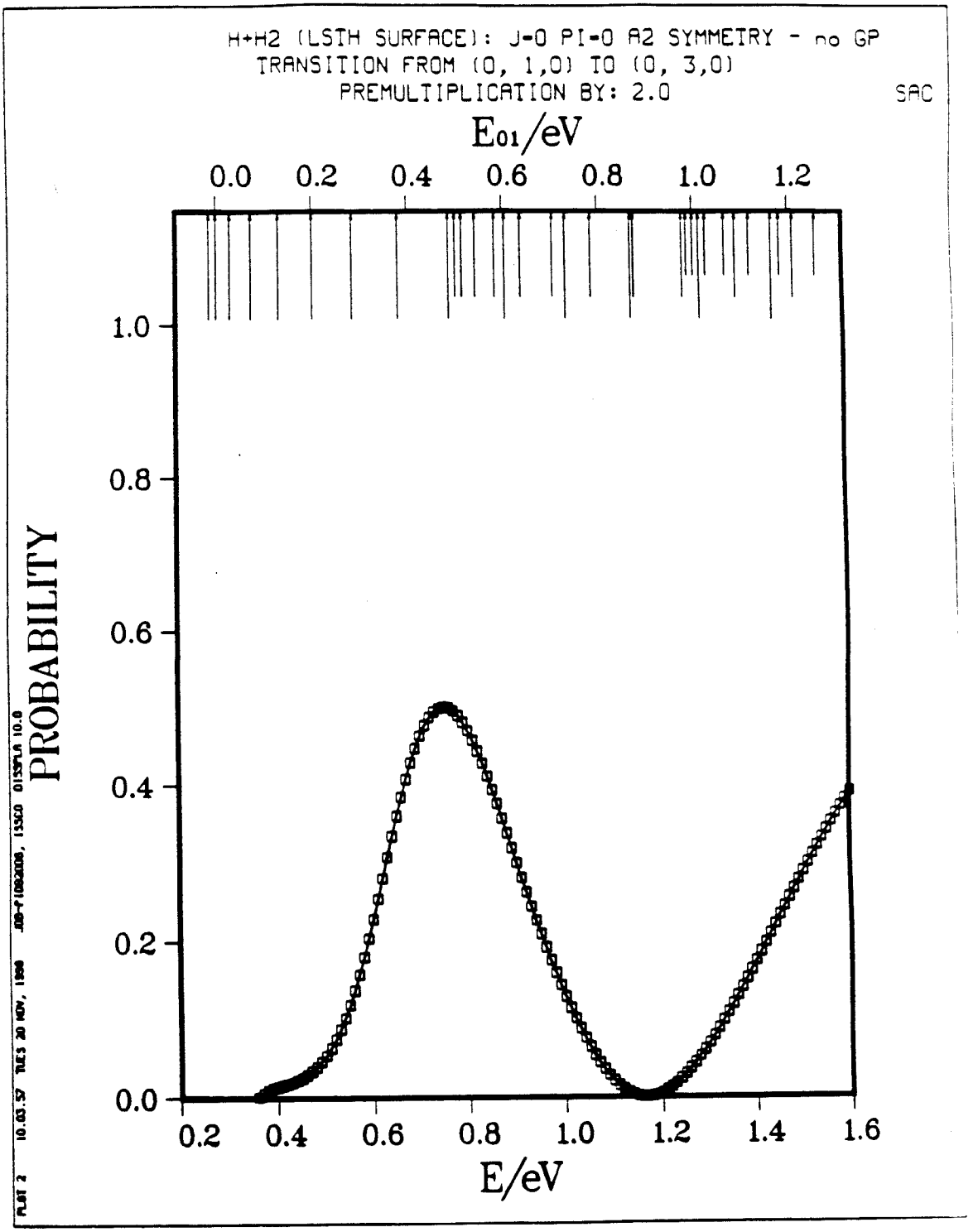
H+H2 (LSTH SURFACE): J=0 PI=0 A2 SYMMETRY - no GP
TRANSITION FROM (0, 1,0) TO (0, 3,0)
PREMULTIPLICATION BY: 2.0
SAC
E01/eV
0.0
0.2
0.4
0.6
0.8
1.0
1.2
PROBABILITY
0.0
0.2
0.4
0.6
0.8
1.0
E/eV
0.2
0.4
0.6
0.8
1.0
1.2
1.4
1.6

Fig. 7.3b

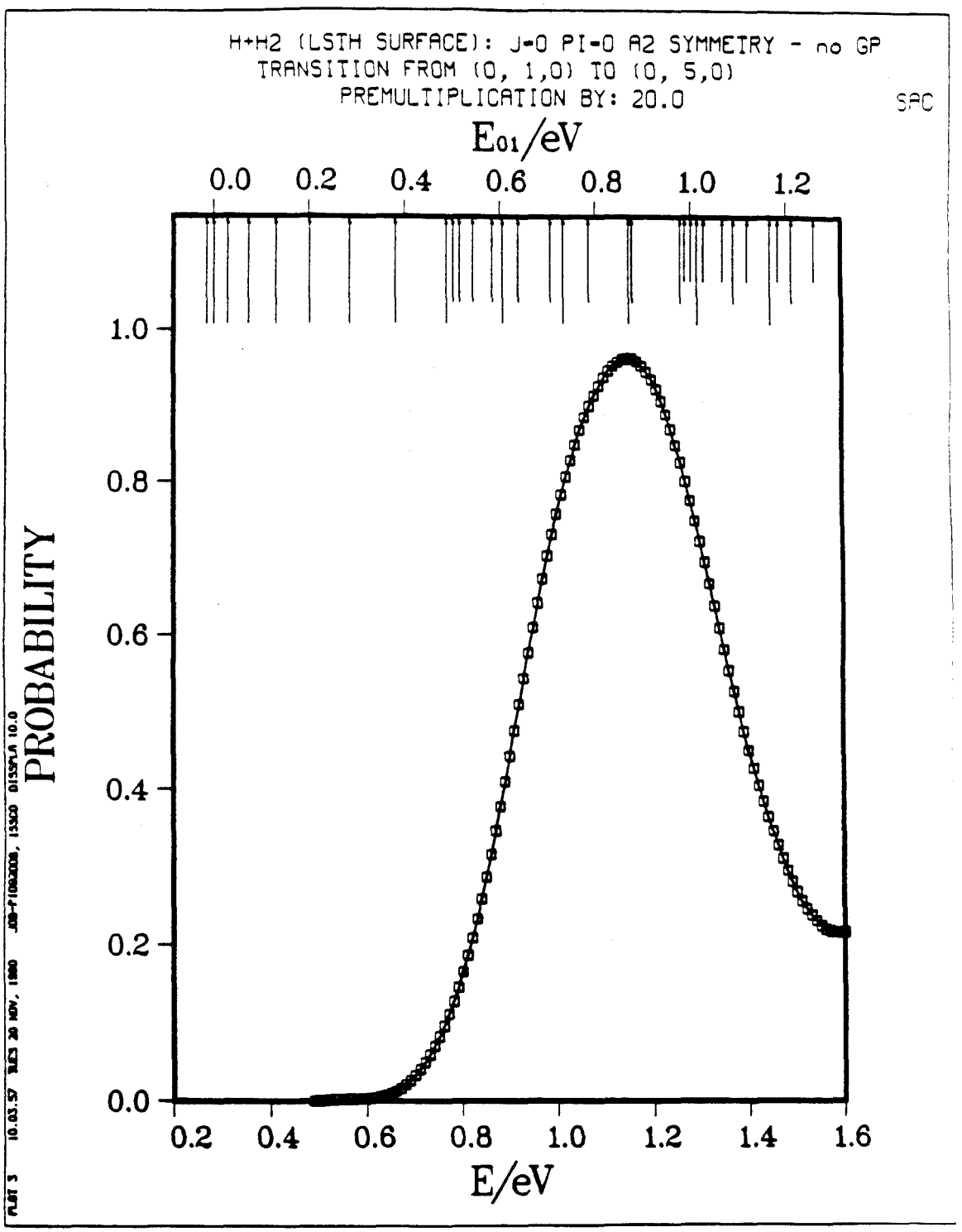
H+H2 (LSTH SURFACE): J=0 PI=0 A2 SYMMETRY - no GP
TRANSITION FROM (0, 1,0) TO (0, 5,0)
PREMULTIPLICATION BY: 20.0
SAC
E01/eV
0.0
0.2
0.4
0.6
0.8
1.0
1.2
PROBABILITY
0.0
0.2
0.4
0.6
0.8
1.0
E/eV
0.2
0.4
0.6
0.8
1.0
1.2
1.4
1.6

Fig. 7.3c

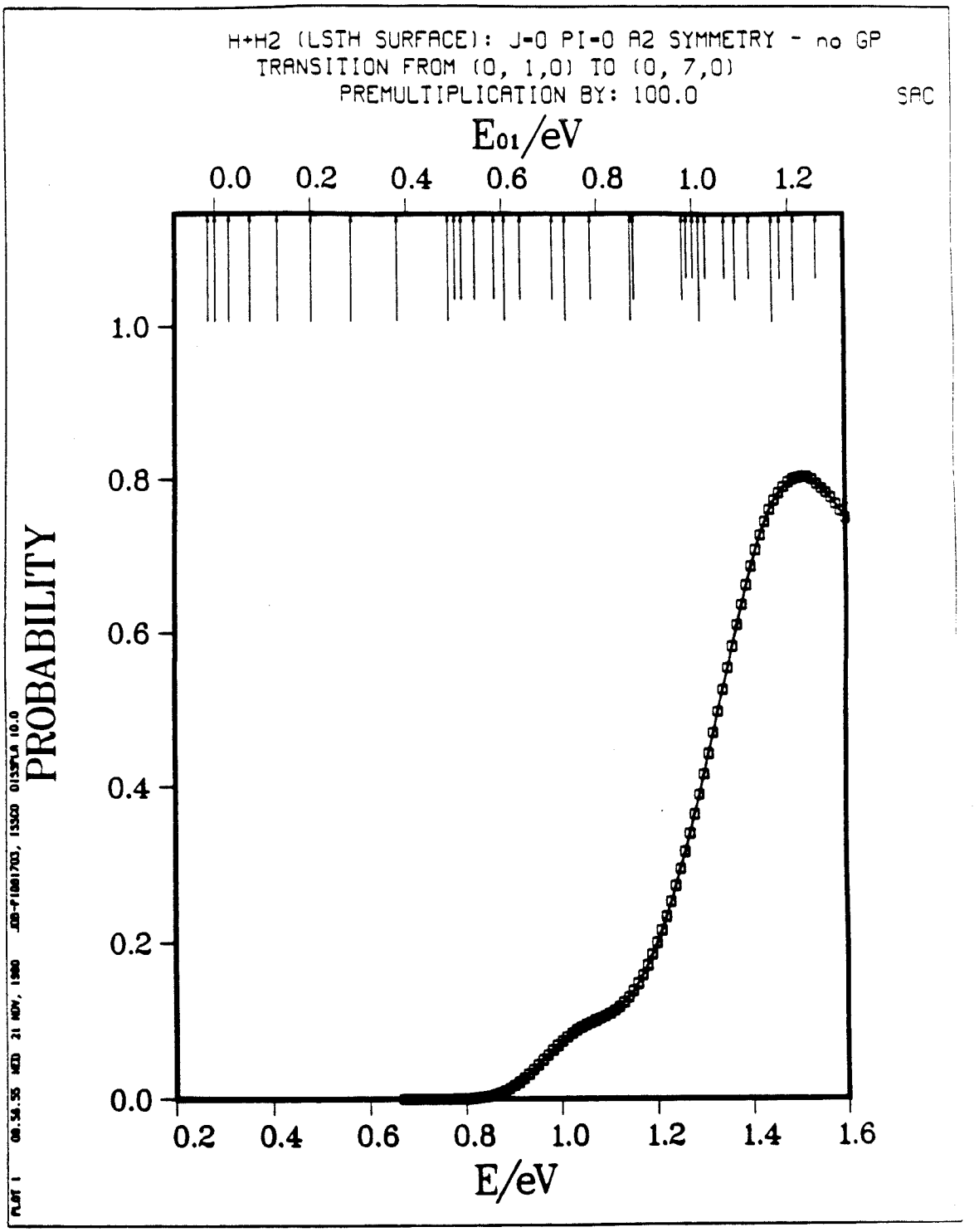
H+H2 (LSTH SURFACE): J=0 PI=0 A2 SYMMETRY - no GP
TRANSITION FROM (0, 1,0) TO (0, 7,0)
PREMULTIPLICATION BY: 100.0
SAC
E01/eV
0.0
0.2
0.4
0.6
0.8
1.0
1.2
PROBABILITY
0.0
0.2
0.4
0.6
0.8
1.0
E/eV
0.2
0.4
0.6
0.8
1.0
1.2
1.4
1.6

Fig. 7.3d

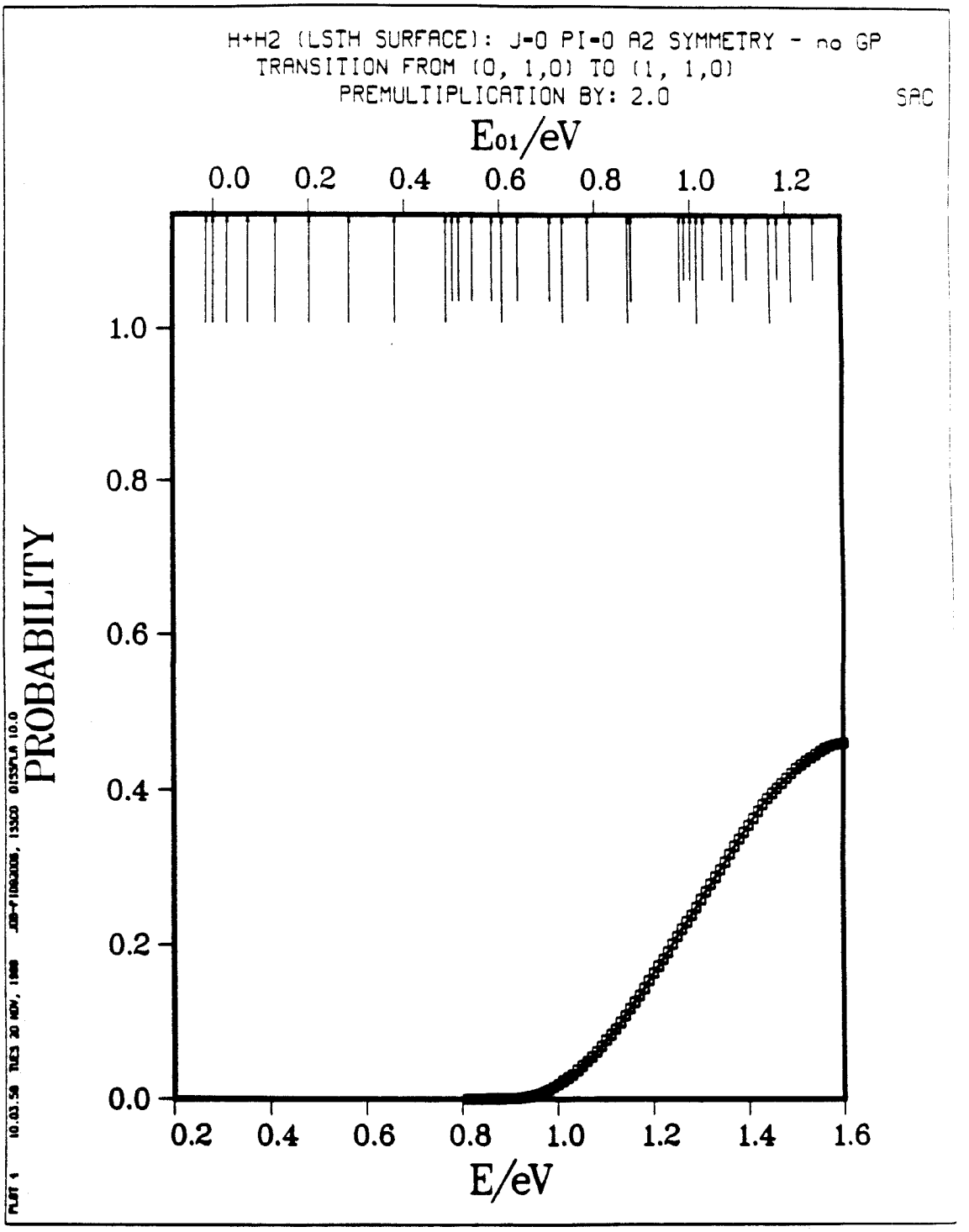
H+H2 (LSTH SURFACE): J=0 PI=0 A2 SYMMETRY - no GP
TRANSITION FROM (0, 1,0) TO (1, 1,0)
PREMULTIPLICATION BY: 2.0
SAC
E01/eV
0.0
0.2
0.4
0.6
0.8
1.0
1.2
PROBABILITY
0.0
0.2
0.4
0.6
0.8
1.0
E/eV
0.2
0.4
0.6
0.8
1.0
1.2
1.4
1.6

Fig. 7.4a

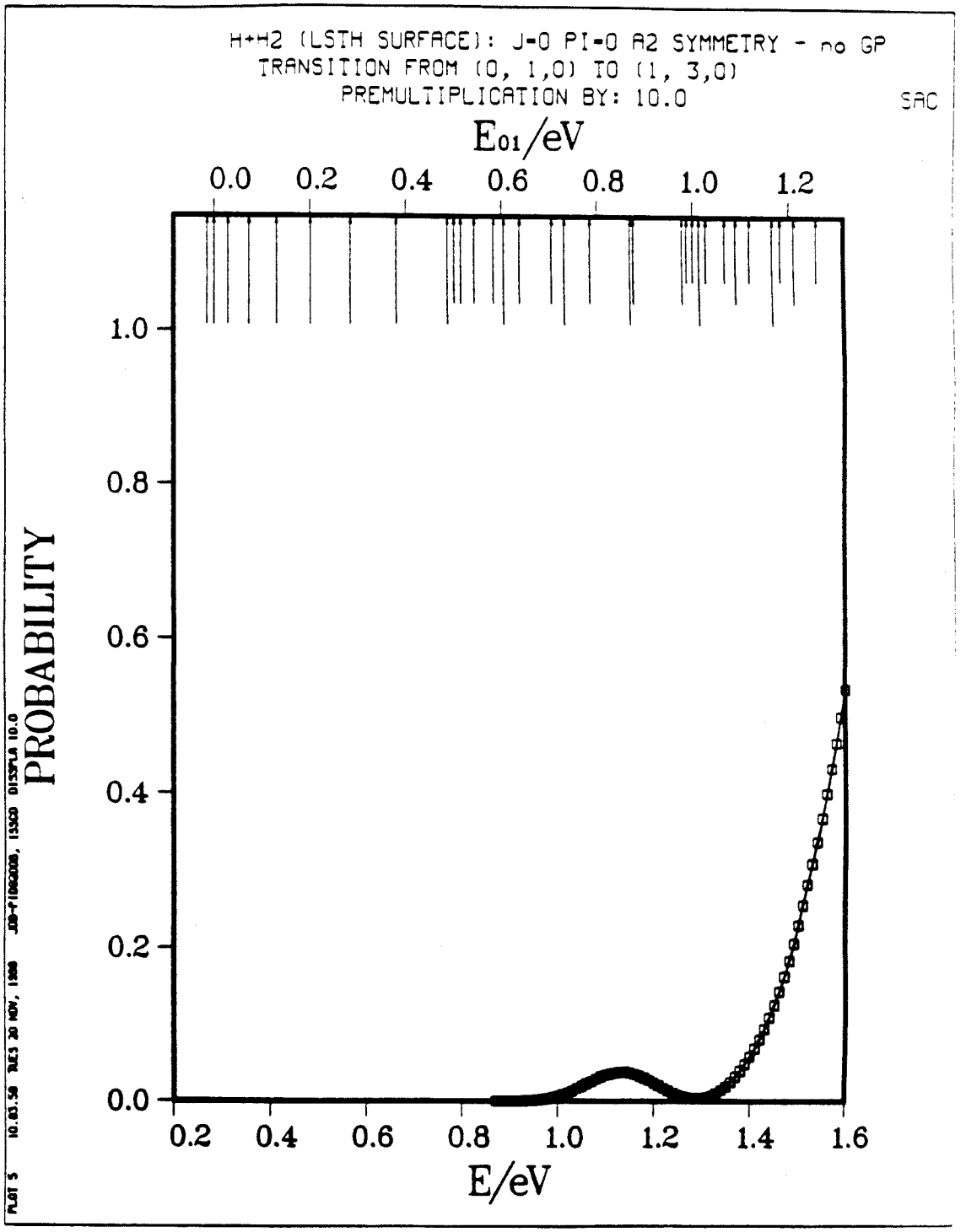
H+H2 (LSTH SURFACE): J=0 PI=0 A2 SYMMETRY - no GP
TRANSITION FROM (0, 1,0) TO (1, 3,0)
PREMULTIPLICATION BY: 10.0
SAC
E01/eV
0.0
0.2
0.4
0.6
0.8
1.0
1.2
PROBABILITY
1.0
0.8
0.6
0.4
0.2
0.0
0.2
0.4
0.6
0.8
1.0
1.2
1.4
1.6
E/eV

Fig. 7.4b

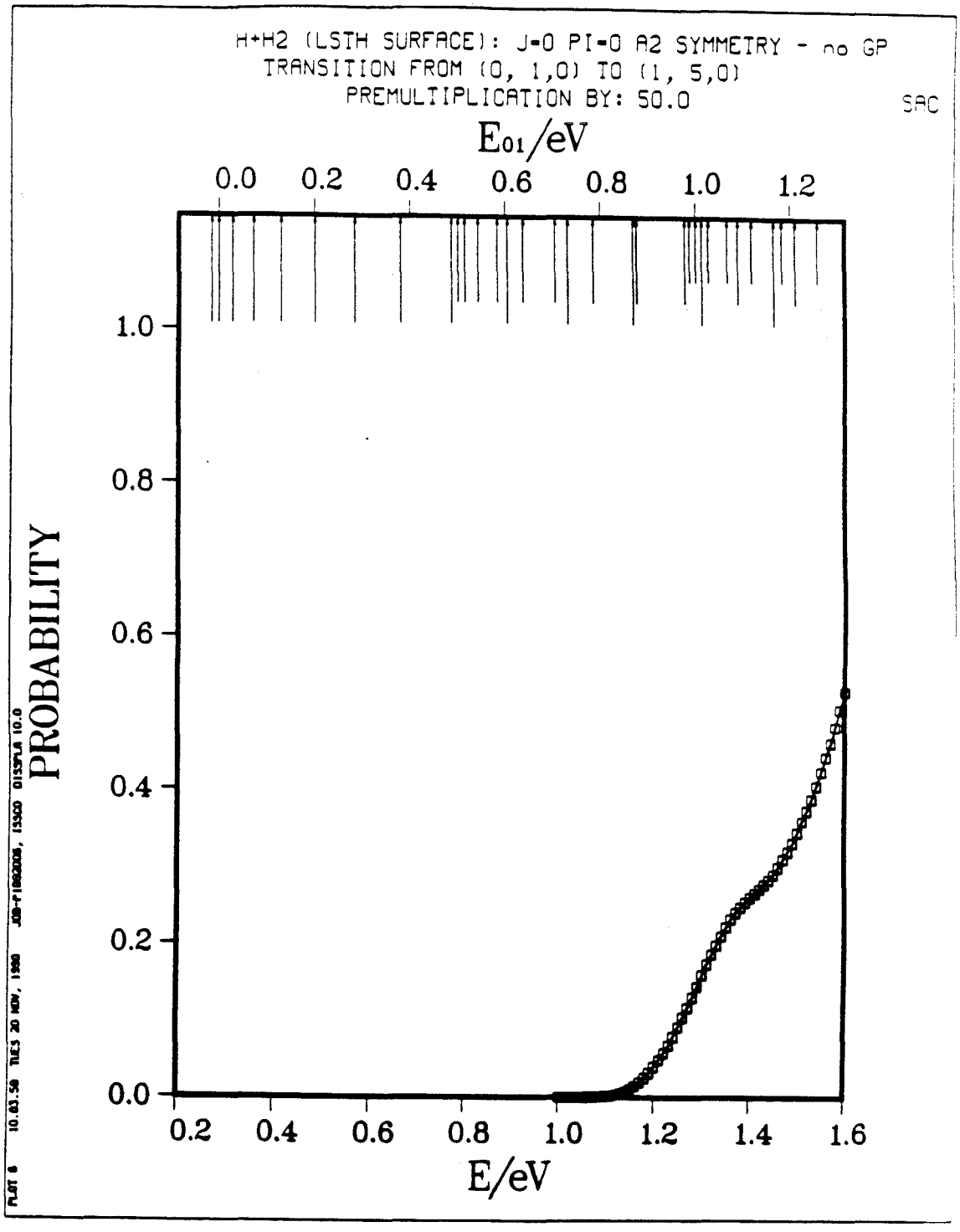
H+H2 (LSTH SURFACE): J=0 PI=0 A2 SYMMETRY - no GP
TRANSITION FROM (0, 1,0) TO (1, 5,0)
PREMULTIPLICATION BY: 50.0
SRC
E01/eV
0.0
0.2
0.4
0.6
0.8
1.0
1.2
PROBABILITY
0.0
0.2
0.4
0.6
0.8
1.0
E/eV
0.2
0.4
0.6
0.8
1.0
1.2
1.4
1.6

Fig. 7.4c

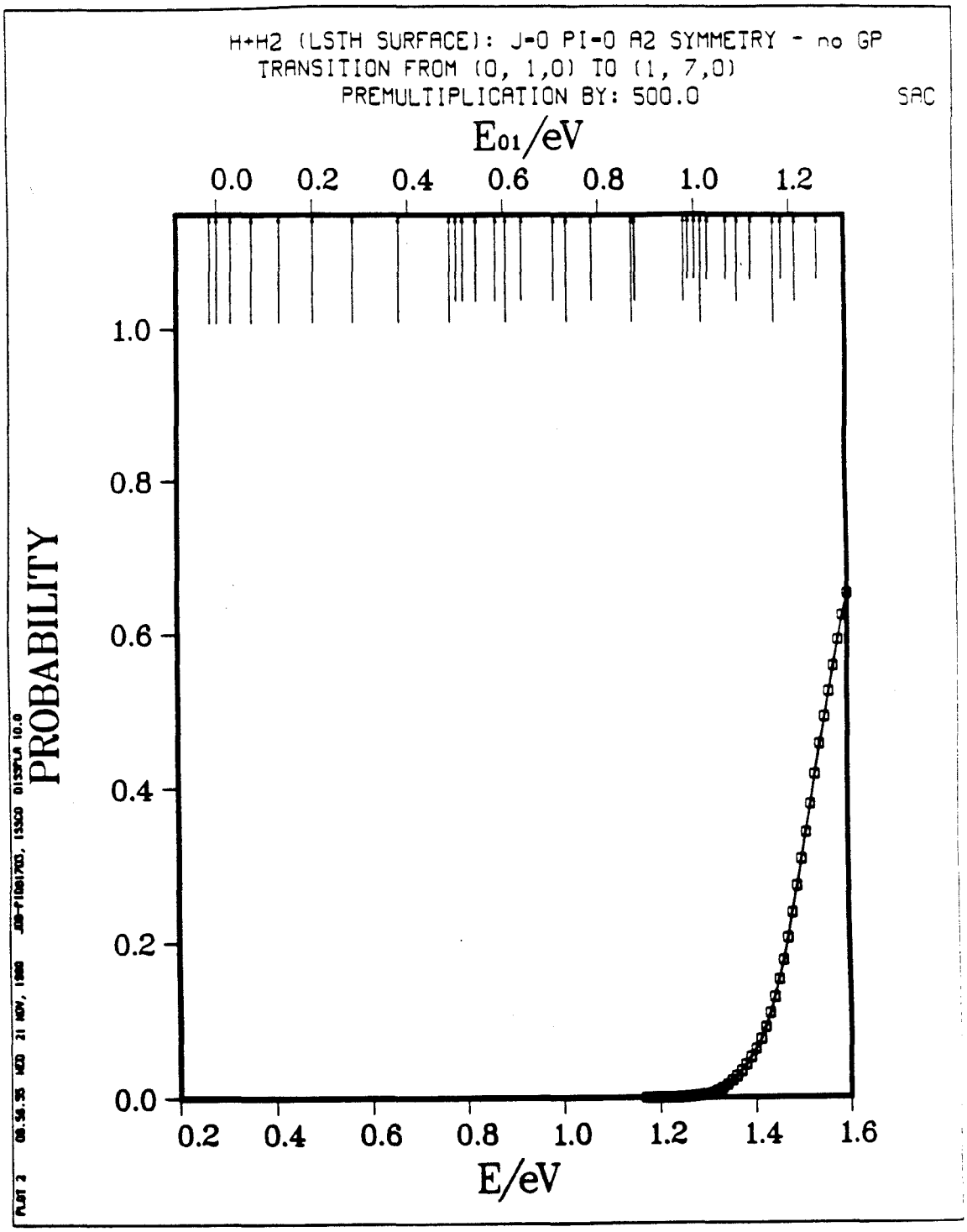
H+H2 (LSTH SURFACE): J=0 PI=0 A2 SYMMETRY - no GP
TRANSITION FROM (0, 1,0) TO (1, 7,0)
PREMULTIPLICATION BY: 500.0
SAC
E01/eV
0.0
0.2
0.4
0.6
0.8
1.0
1.2
PROBABILITY
0.0
0.2
0.4
0.6
0.8
1.0
E/eV
0.2
0.4
0.6
0.8
1.0
1.2
1.4
1.6

Fig. 7.4d

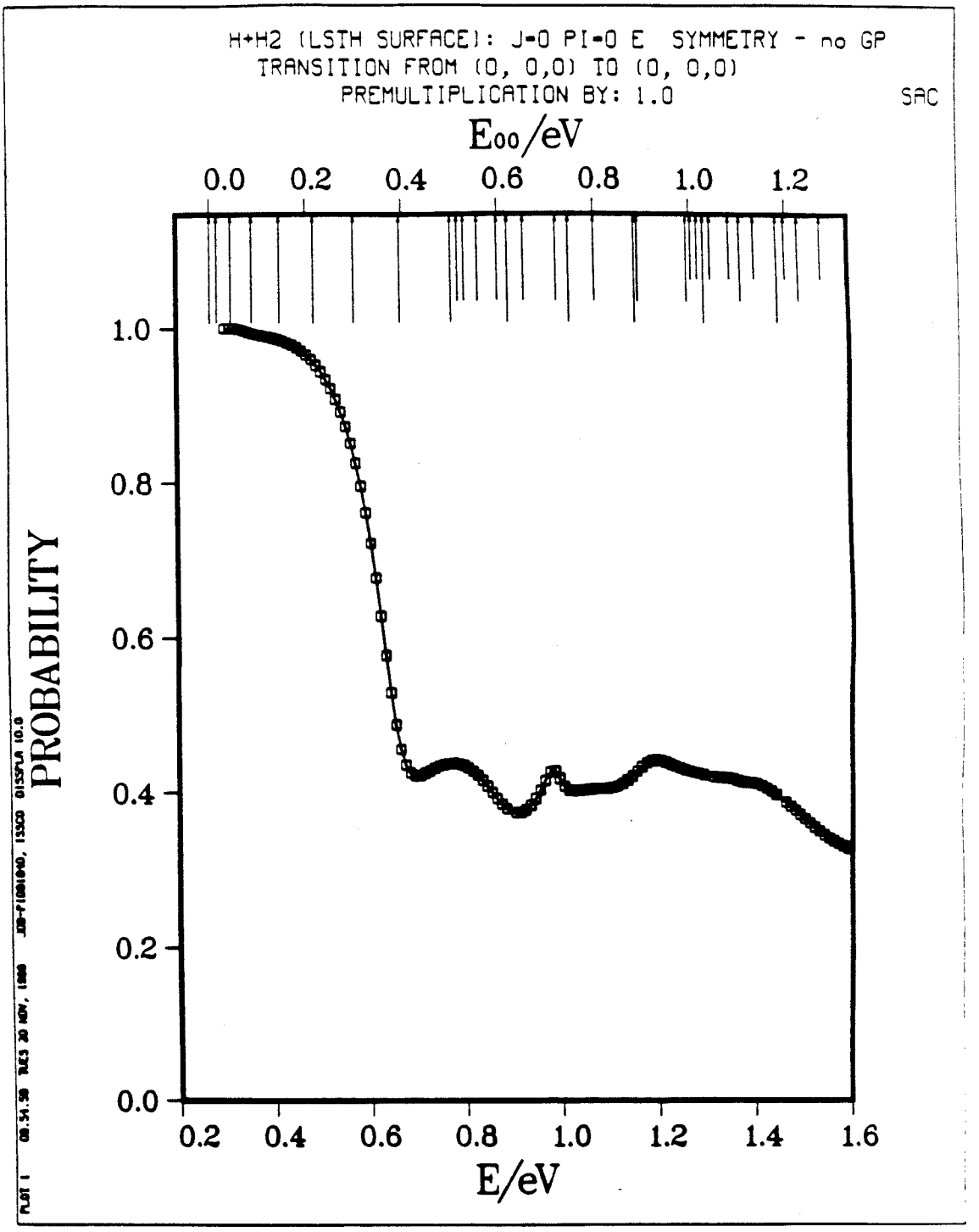
H+H2 (LSTH SURFACE): J=0 PI=0 E SYMMETRY - no GP
TRANSITION FROM (0, 0,0) TO (0, 0,0)
PREMULTIPLICATION BY: 1.0
SAC
E00/eV
0.0
0.2
0.4
0.6
0.8
1.0
1.2
PROBABILITY
0.0
0.2
0.4
0.6
0.8
1.0
E/eV
0.2
0.4
0.6
0.8
1.0
1.2
1.4
1.6

Fig. 7.5a

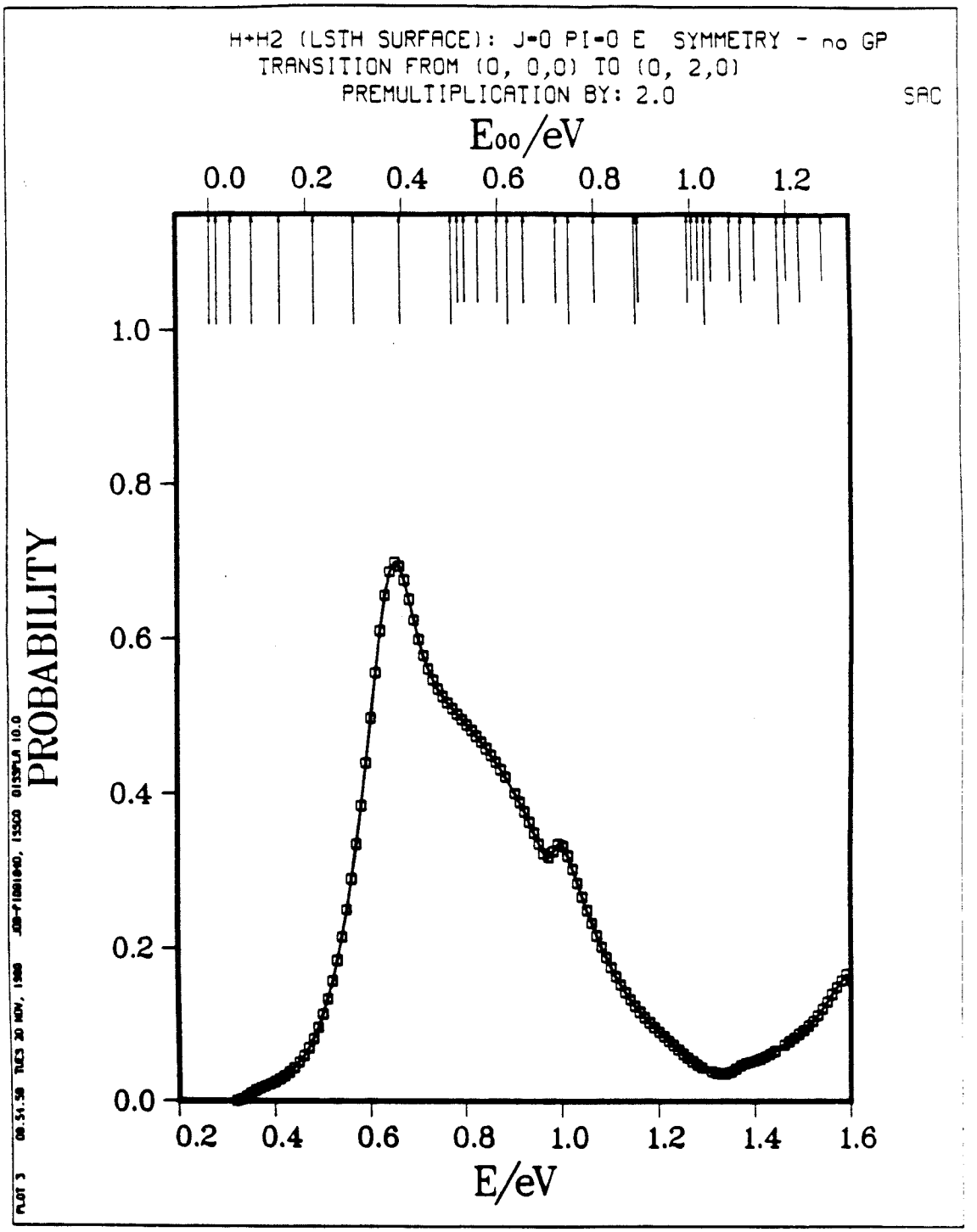
H+H2 (LSTH SURFACE): J=0 PI=0 E SYMMETRY - no GP
TRANSITION FROM (0, 0,0) TO (0, 2,0)
PREMULTIPLICATION BY: 2.0
SAC
E00/eV
0.0
0.2
0.4
0.6
0.8
1.0
1.2
PROBABILITY
0.0
0.2
0.4
0.6
0.8
1.0
E/eV
0.2
0.4
0.6
0.8
1.0
1.2
1.4
1.6

Fig. 7.5b

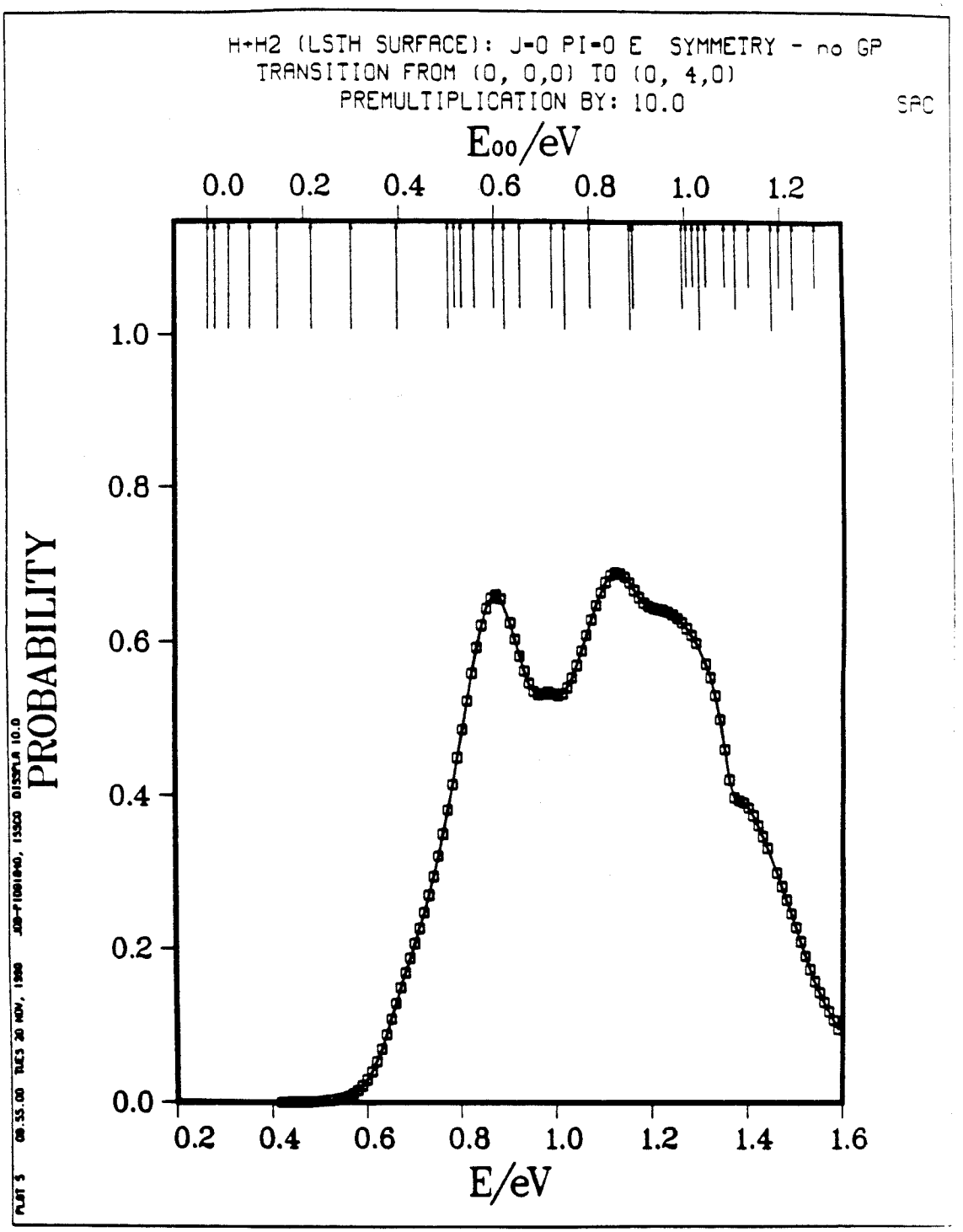
H+H2 (LSTH SURFACE): J=0 PI=0 E SYMMETRY - no GP
TRANSITION FROM (0, 0,0) TO (0, 4,0)
PREMULTIPLICATION BY: 10.0
SAC
E00/eV
0.0
0.2
0.4
0.6
0.8
1.0
1.2
PROBABILITY
0.0
0.2
0.4
0.6
0.8
1.0
E/eV
0.2
0.4
0.6
0.8
1.0
1.2
1.4
1.6

Fig. 7.5c

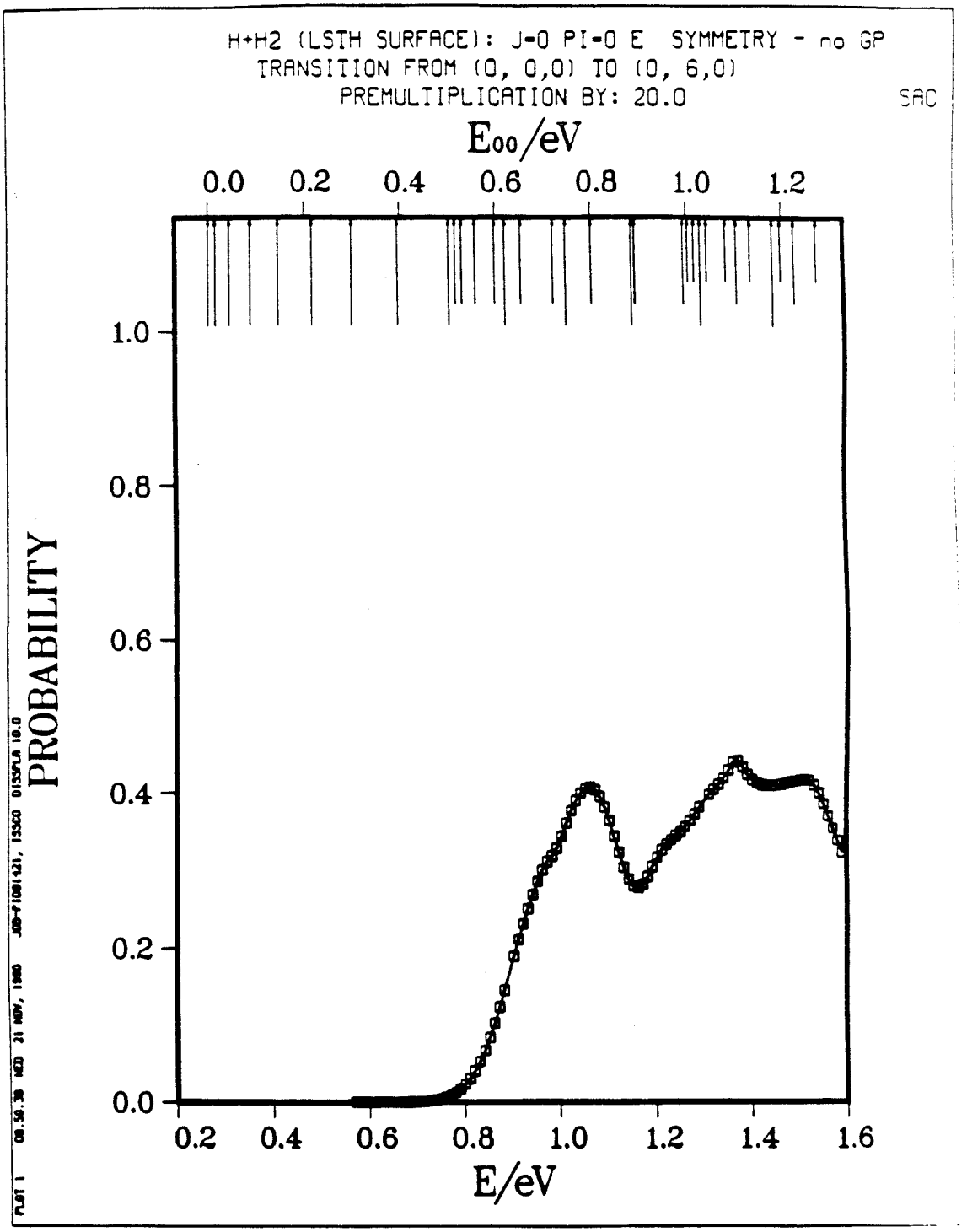
H+H2 (LSTH SURFACE): J=0 PI=0 E SYMMETRY - no GP
TRANSITION FROM (0, 0,0) TO (0, 6,0)
PREMULTIPLICATION BY: 20.0
SAC
E00/eV
0.0
0.2
0.4
0.6
0.8
1.0
1.2
PROBABILITY
0.0
0.2
0.4
0.6
0.8
1.0
0.2
0.4
0.6
0.8
1.0
1.2
1.4
1.6
E/eV

Fig. 7.5d

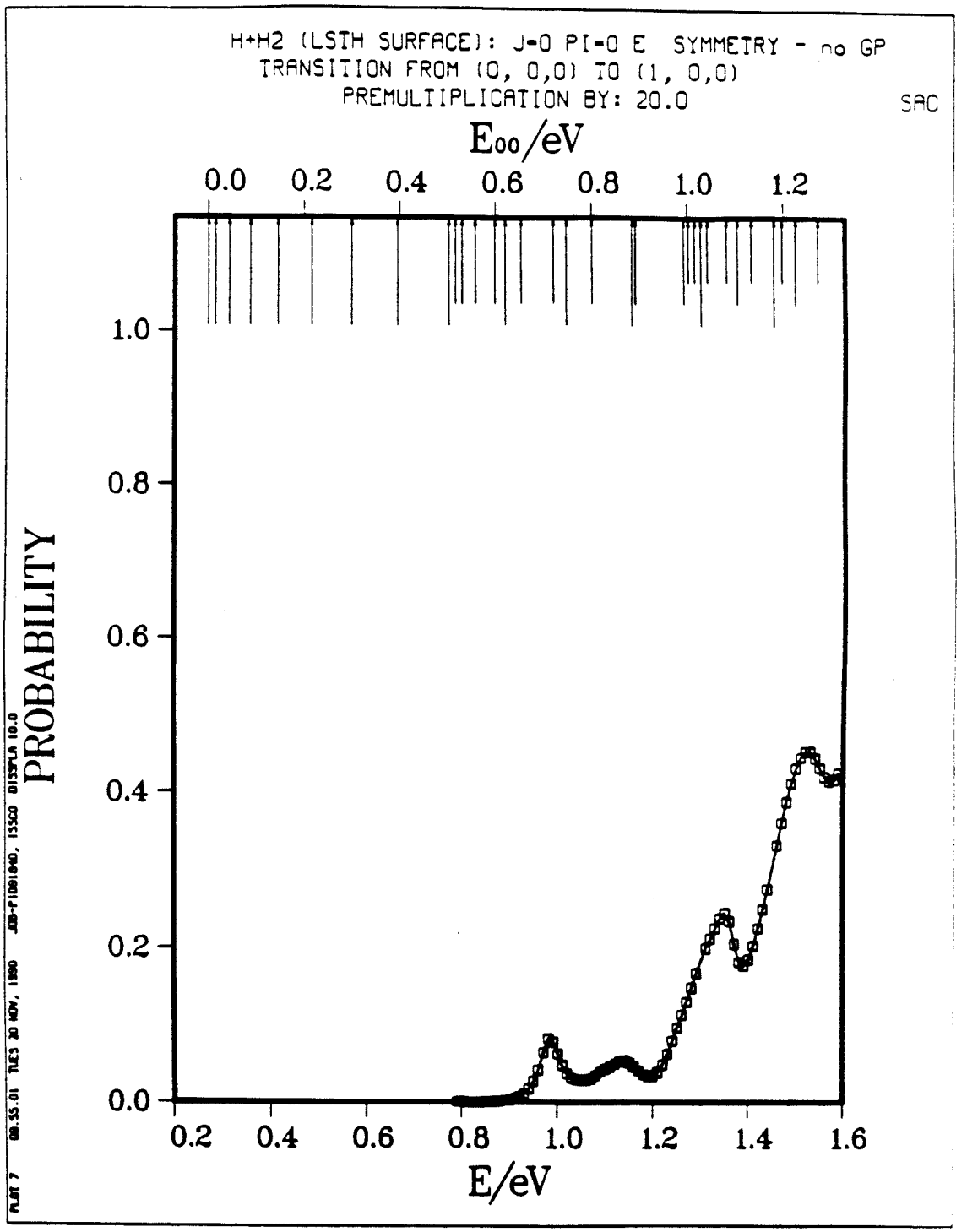
H+H2 (LSTH SURFACE): J=0 PI=0 E SYMMETRY - no GP
TRANSITION FROM (0, 0,0) TO (1, 0,0)
PREMULTIPLICATION BY: 20.0
SAC
E00/eV
0.0
0.2
0.4
0.6
0.8
1.0
1.2
PROBABILITY
1.0
0.8
0.6
0.4
0.2
0.0
0.2
0.4
0.6
0.8
1.0
1.2
1.4
1.6
E/eV

Fig. 7.6a

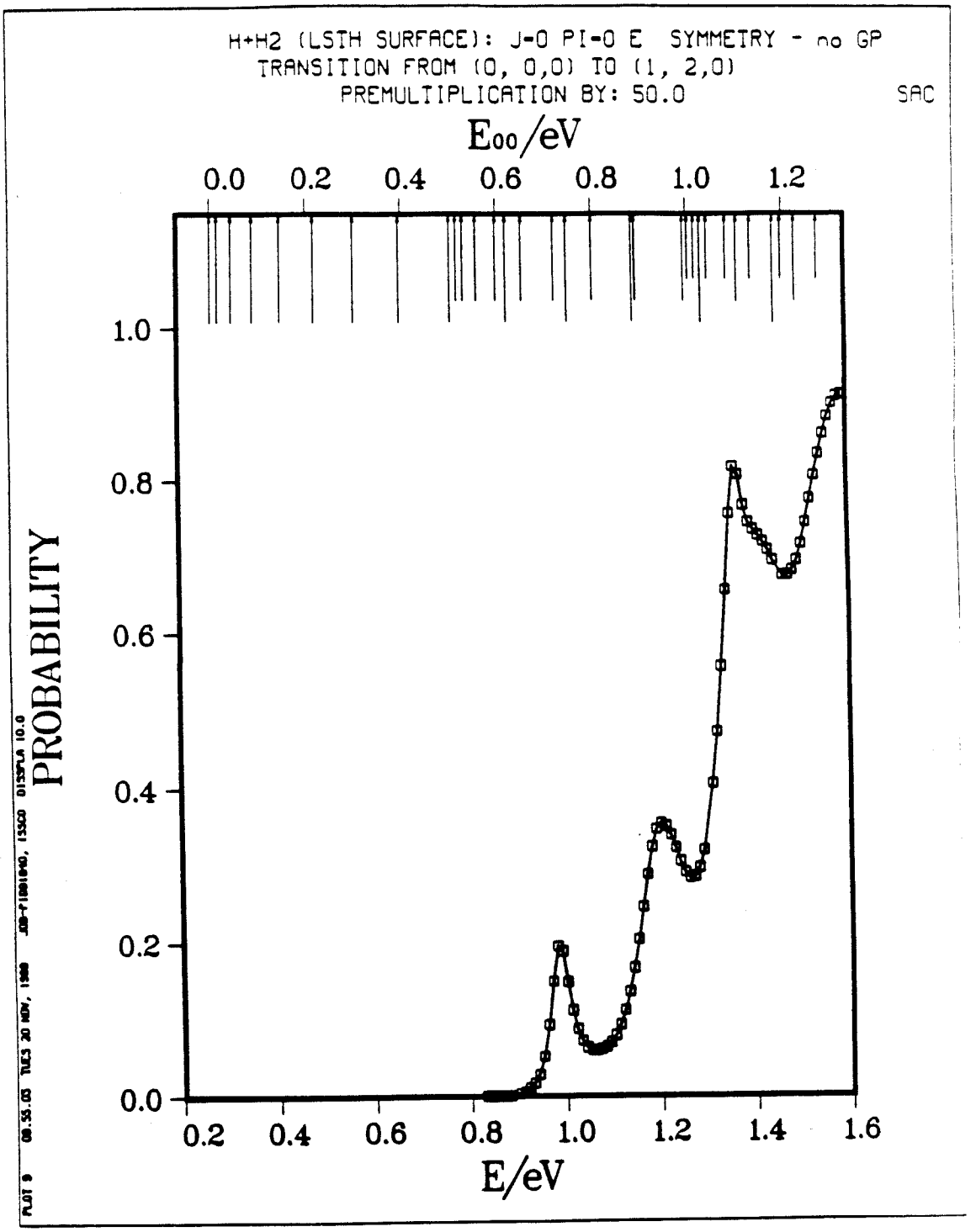
H+H2 (LSTH SURFACE): J=0 PI=0 E SYMMETRY - no GP
TRANSITION FROM (0, 0,0) TO (1, 2,0)
PREMULTIPLICATION BY: 50.0
SAC
E00/eV
0.0
0.2
0.4
0.6
0.8
1.0
1.2
PROBABILITY
0.0
0.2
0.4
0.6
0.8
1.0
E/eV
0.2
0.4
0.6
0.8
1.0
1.2
1.4
1.6

Fig. 7.6b

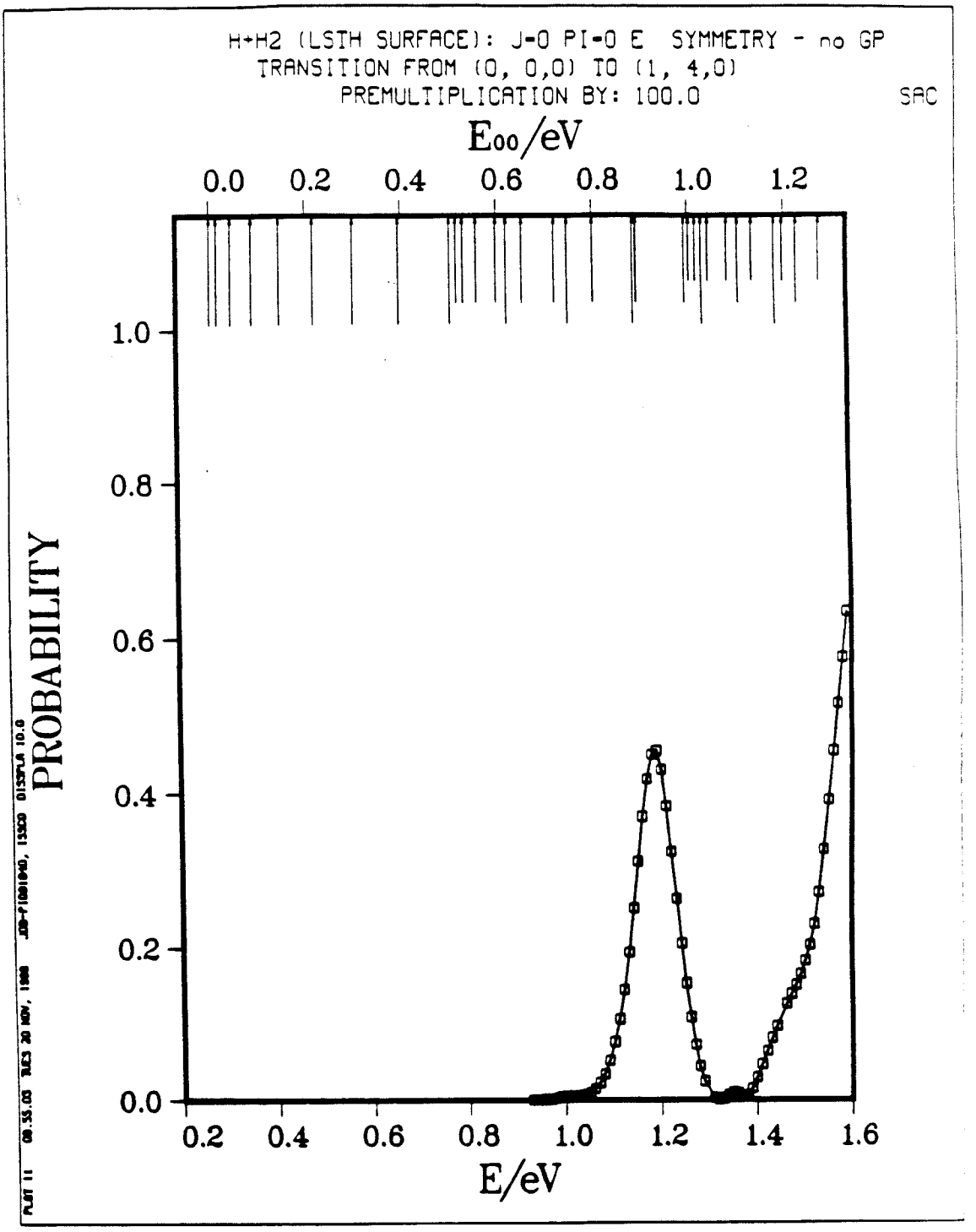
H+H2 (LSTH SURFACE): J=0 PI=0 E SYMMETRY - no GP
TRANSITION FROM (0, 0,0) TO (1, 4,0)
PREMULTIPLICATION BY: 100.0
SAC
E00/eV
0.0
0.2
0.4
0.6
0.8
1.0
1.2
PROBABILITY
0.0
0.2
0.4
0.6
0.8
1.0
E/eV
0.2
0.4
0.6
0.8
1.0
1.2
1.4
1.6

Fig. 7.6c

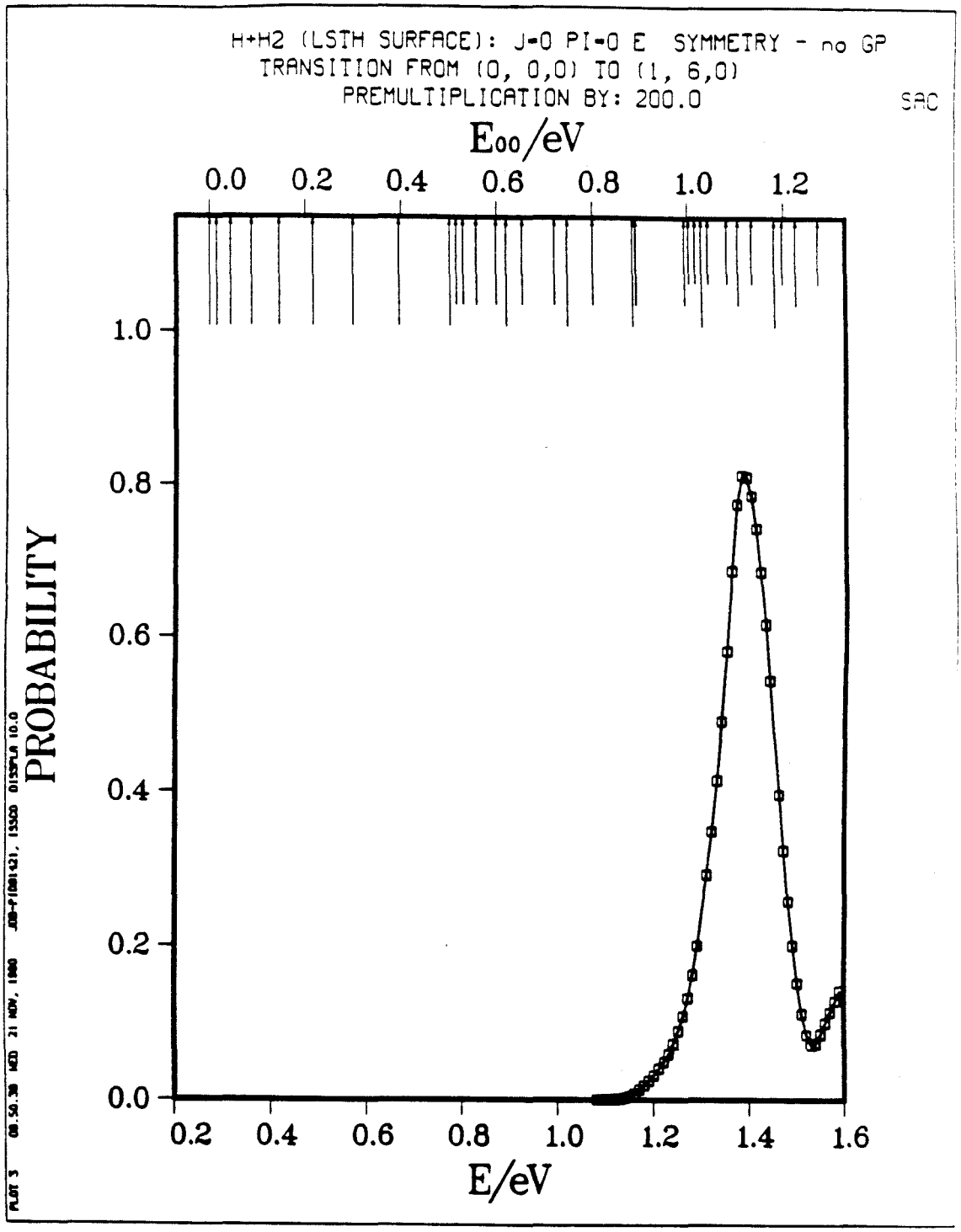
H+H2 (LSTH SURFACE): J=0 PI=0 E SYMMETRY - no GP
TRANSITION FROM (0, 0,0) TO (1, 6,0)
PREMULTIPLICATION BY: 200.0
SAC
E00/eV
0.0
0.2
0.4
0.6
0.8
1.0
1.2
PROBABILITY
0.0
0.2
0.4
0.6
0.8
1.0
0.2
0.4
0.6
0.8
1.0
1.2
1.4
1.6
E/eV

Fig. 7.6d

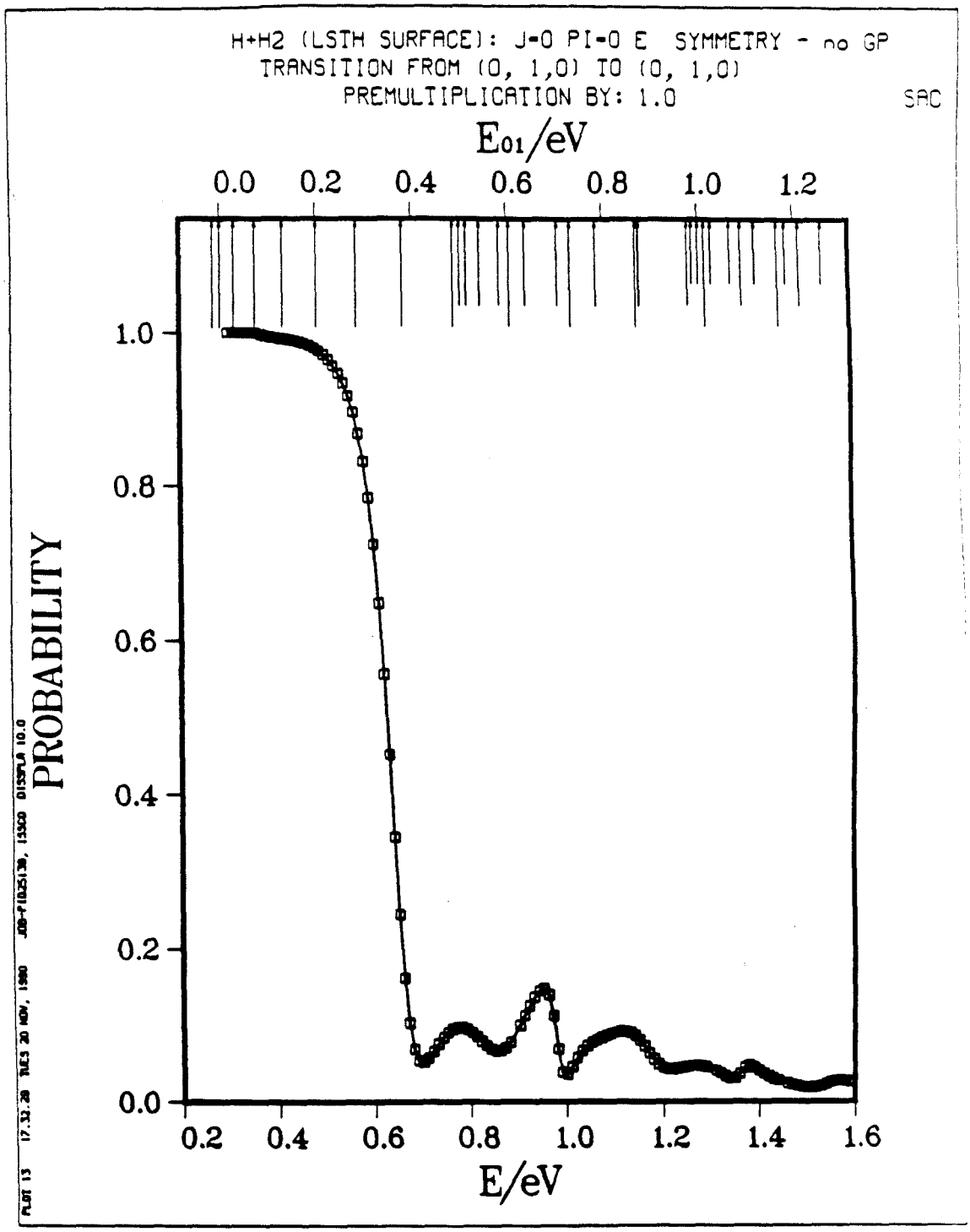
H+H2 (LSTH SURFACE): J=0 PI=0 E SYMMETRY - no GP
TRANSITION FROM (0, 1,0) TO (0, 1,0)
PREMULTIPLICATION BY: 1.0
SAC
E01/eV
0.0
0.2
0.4
0.6
0.8
1.0
1.2
PROBABILITY
0.0
0.2
0.4
0.6
0.8
1.0
E/eV
0.2
0.4
0.6
0.8
1.0
1.2
1.4
1.6

Fig. 7.7a

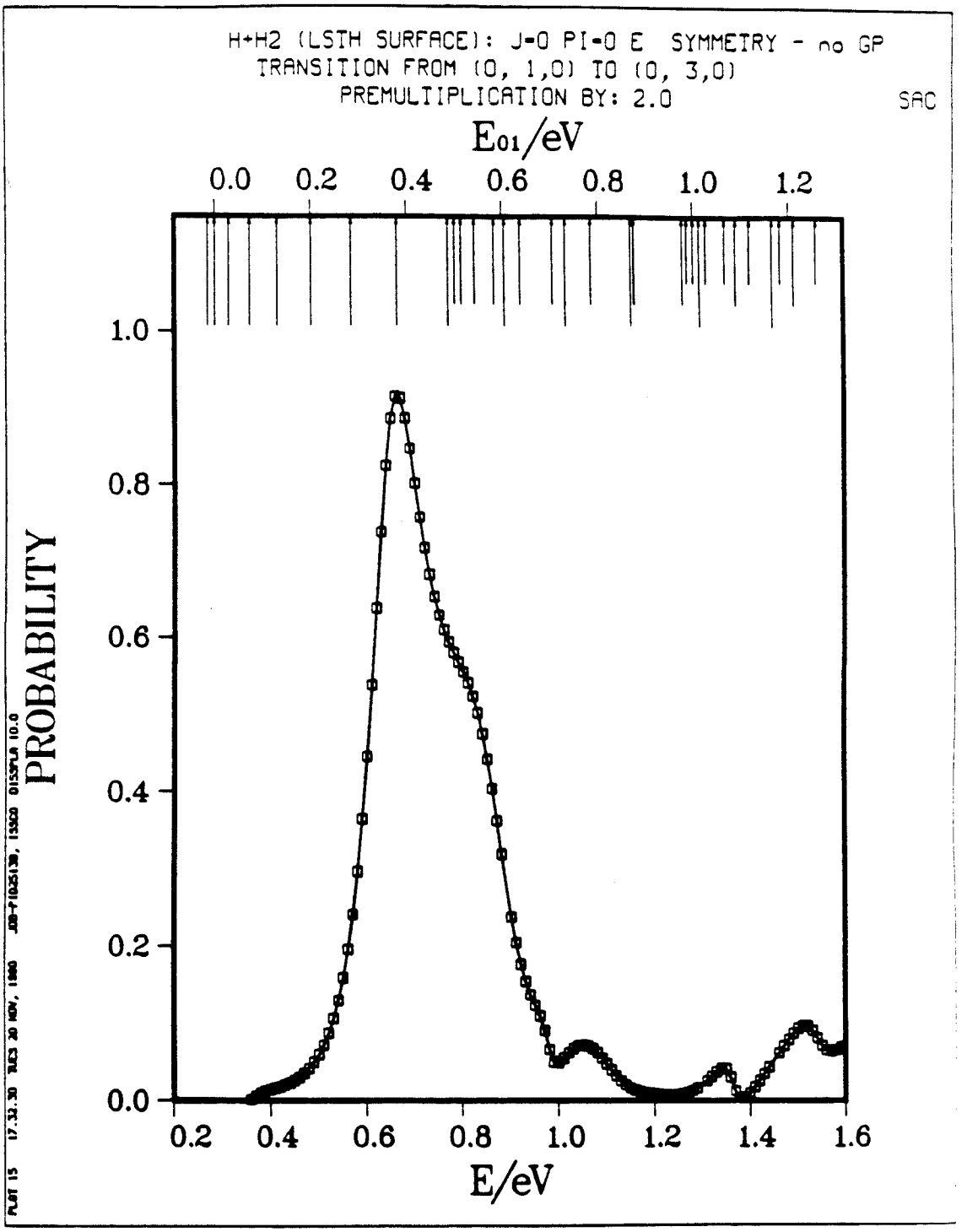
H+H2 (LSTH SURFACE): J=0 PI=0 E SYMMETRY - no GP
TRANSITION FROM (0, 1,0) TO (0, 3,0)
PREMULTIPLICATION BY: 2.0
SAC
E01/eV
0.0
0.2
0.4
0.6
0.8
1.0
1.2
PROBABILITY
0.0
0.2
0.4
0.6
0.8
1.0
0.2
0.4
0.6
0.8
1.0
1.2
1.4
1.6
E/eV

Fig. 7.7b

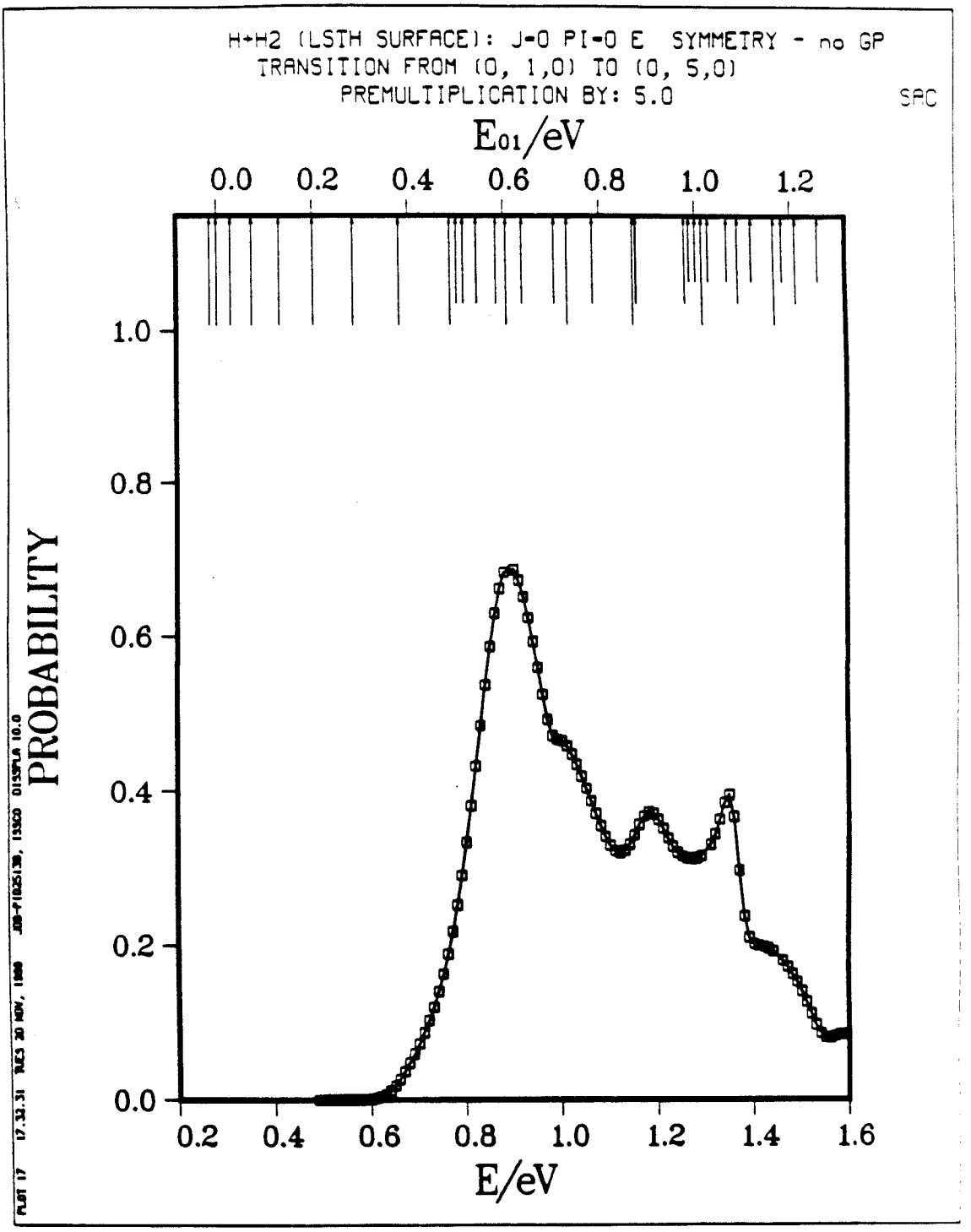
H+H2 (LSTH SURFACE): J=0 PI=0 E SYMMETRY - no GP
TRANSITION FROM (0, 1,0) TO (0, 5,0)
PREMULTIPLICATION BY: 5.0
SPC
E01/eV
0.0
0.2
0.4
0.6
0.8
1.0
1.2
PROBABILITY
0.0
0.2
0.4
0.6
0.8
1.0
E/eV
0.2
0.4
0.6
0.8
1.0
1.2
1.4
1.6

Fig. 7.7c

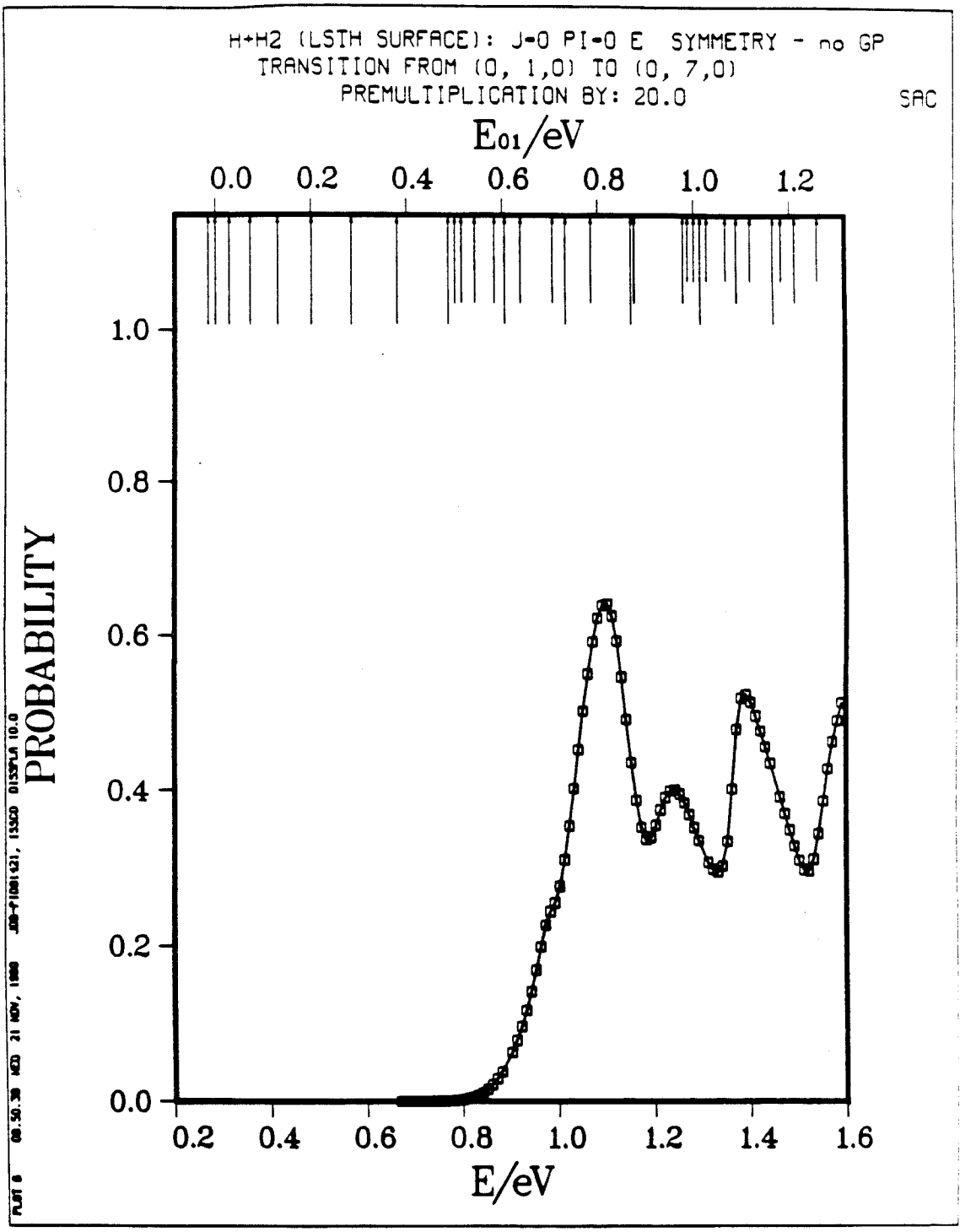
H+H2 (LSTH SURFACE): J=0 PI=0 E SYMMETRY - no GP
TRANSITION FROM (0, 1,0) TO (0, 7,0)
PREMULTIPLICATION BY: 20.0
SAC
E01/eV
0.0
0.2
0.4
0.6
0.8
1.0
1.2
PROBABILITY
0.0
0.2
0.4
0.6
0.8
1.0
E/eV
0.2
0.4
0.6
0.8
1.0
1.2
1.4
1.6

Fig. 7.7d

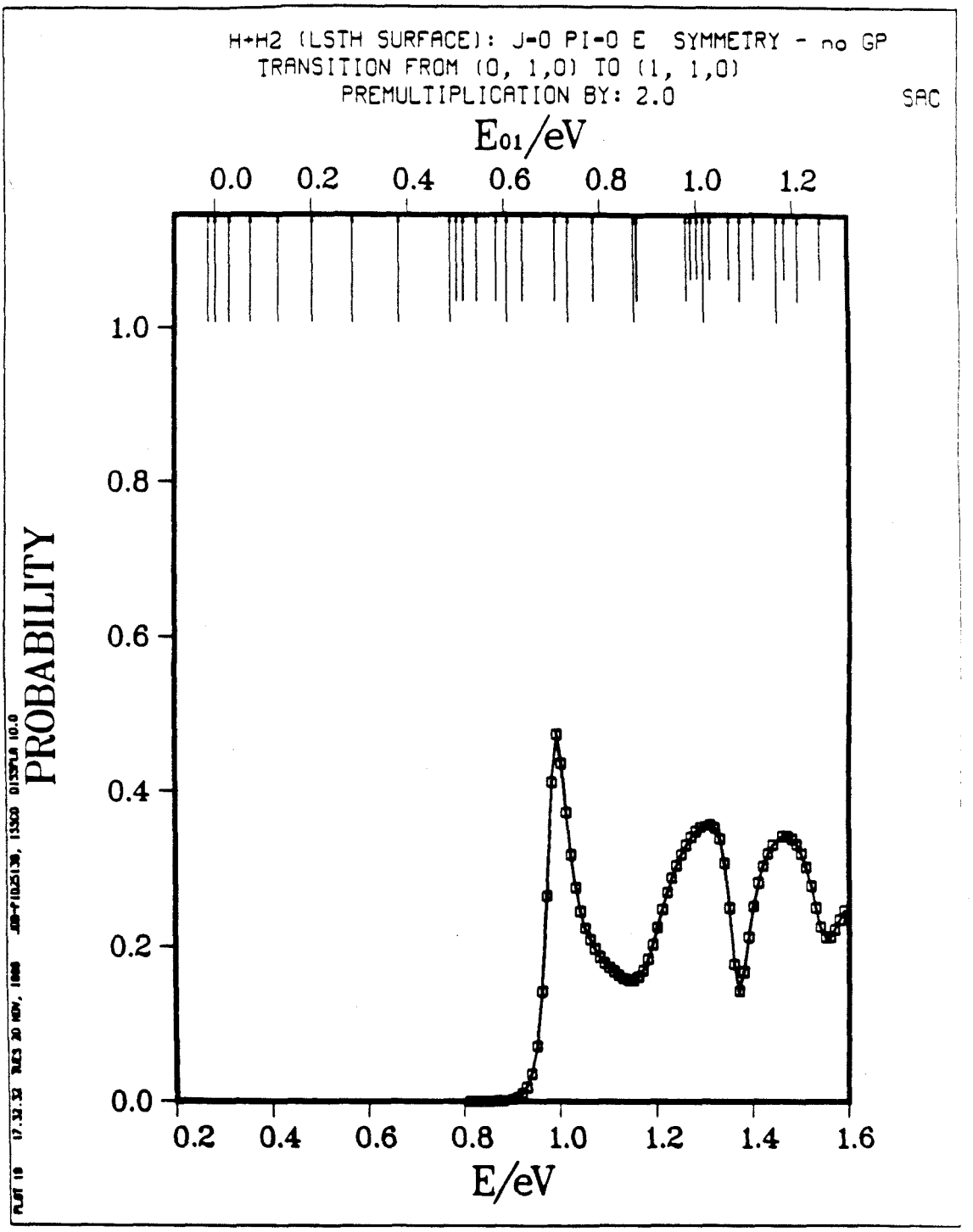
H+H2 (LSTH SURFACE): J=0 PI=0 E SYMMETRY - no GP
TRANSITION FROM (0, 1,0) TO (1, 1,0)
PREMULTIPLICATION BY: 2.0
SAC
E01/eV
0.0
0.2
0.4
0.6
0.8
1.0
1.2
PROBABILITY
0.0
0.2
0.4
0.6
0.8
1.0
E/eV
0.2
0.4
0.6
0.8
1.0
1.2
1.4
1.6

Fig. 7.8a

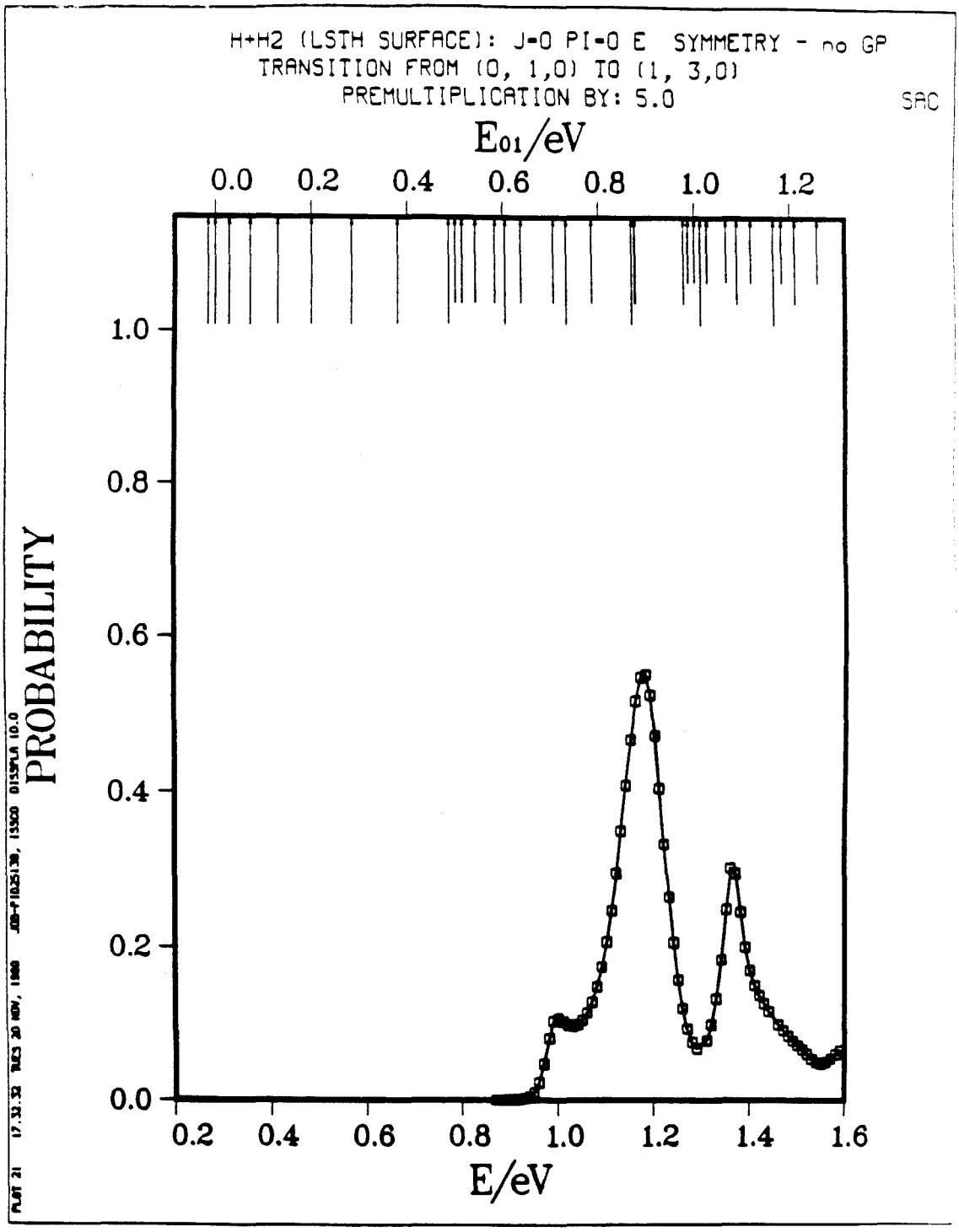
H+H2 (LSTH SURFACE): J=0 PI=0 E SYMMETRY - no GP
TRANSITION FROM (0, 1,0) TO (1, 3,0)
PREMULTIPLICATION BY: 5.0
SRC
E01/eV
0.0
0.2
0.4
0.6
0.8
1.0
1.2
PROBABILITY
0.0
0.2
0.4
0.6
0.8
1.0
E/eV
0.2
0.4
0.6
0.8
1.0
1.2
1.4
1.6

Fig. 7.8b

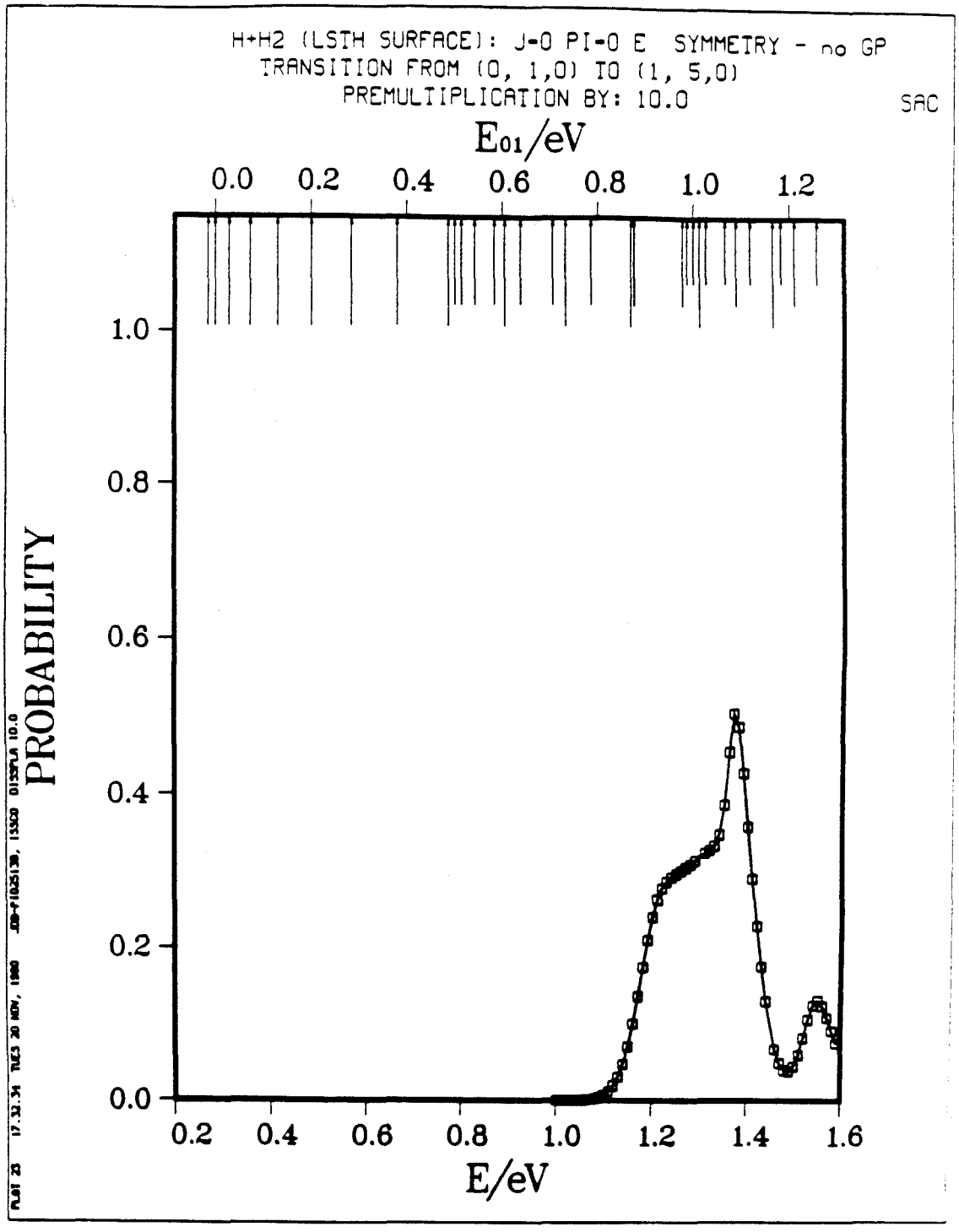
H+H2 (LSTH SURFACE): J=0 PI=0 E SYMMETRY - no GP
TRANSITION FROM (0, 1,0) TO (1, 5,0)
PREMULTIPLICATION BY: 10.0
SAC
E01/eV
0.0
0.2
0.4
0.6
0.8
1.0
1.2
PROBABILITY
0.0
0.2
0.4
0.6
0.8
1.0
E/eV
0.2
0.4
0.6
0.8
1.0
1.2
1.4
1.6

Fig. 7.8c

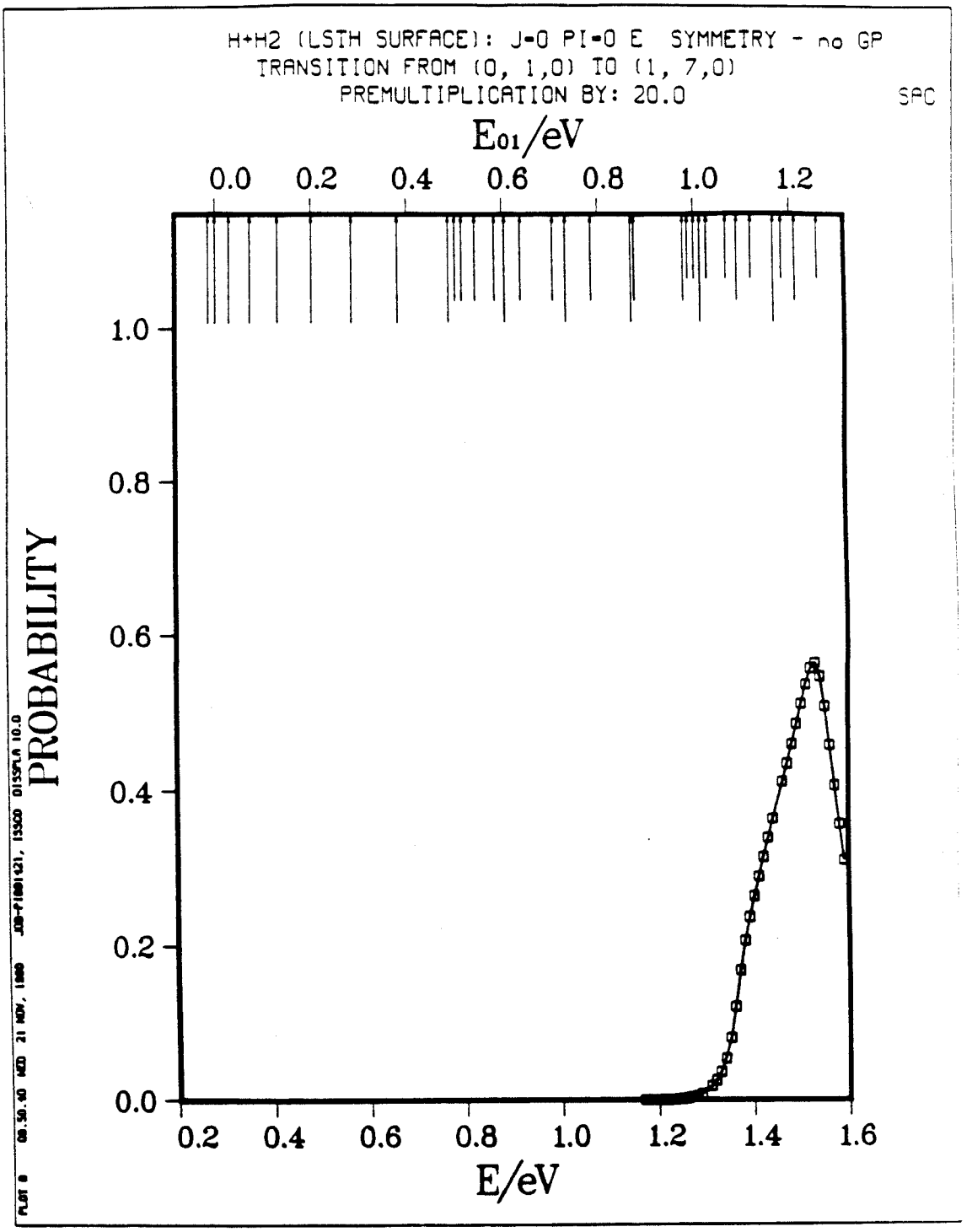
H+H2 (LSTH SURFACE): J=0 PI=0 E SYMMETRY - no GP
TRANSITION FROM (0, 1,0) TO (1, 7,0)
PREMULTIPLICATION BY: 20.0
SPC
E01/eV
0.0
0.2
0.4
0.6
0.8
1.0
1.2
PROBABILITY
1.0
0.8
0.6
0.4
0.2
0.0
0.2
0.4
0.6
0.8
1.0
1.2
1.4
1.6
E/eV

Fig. 7.8d

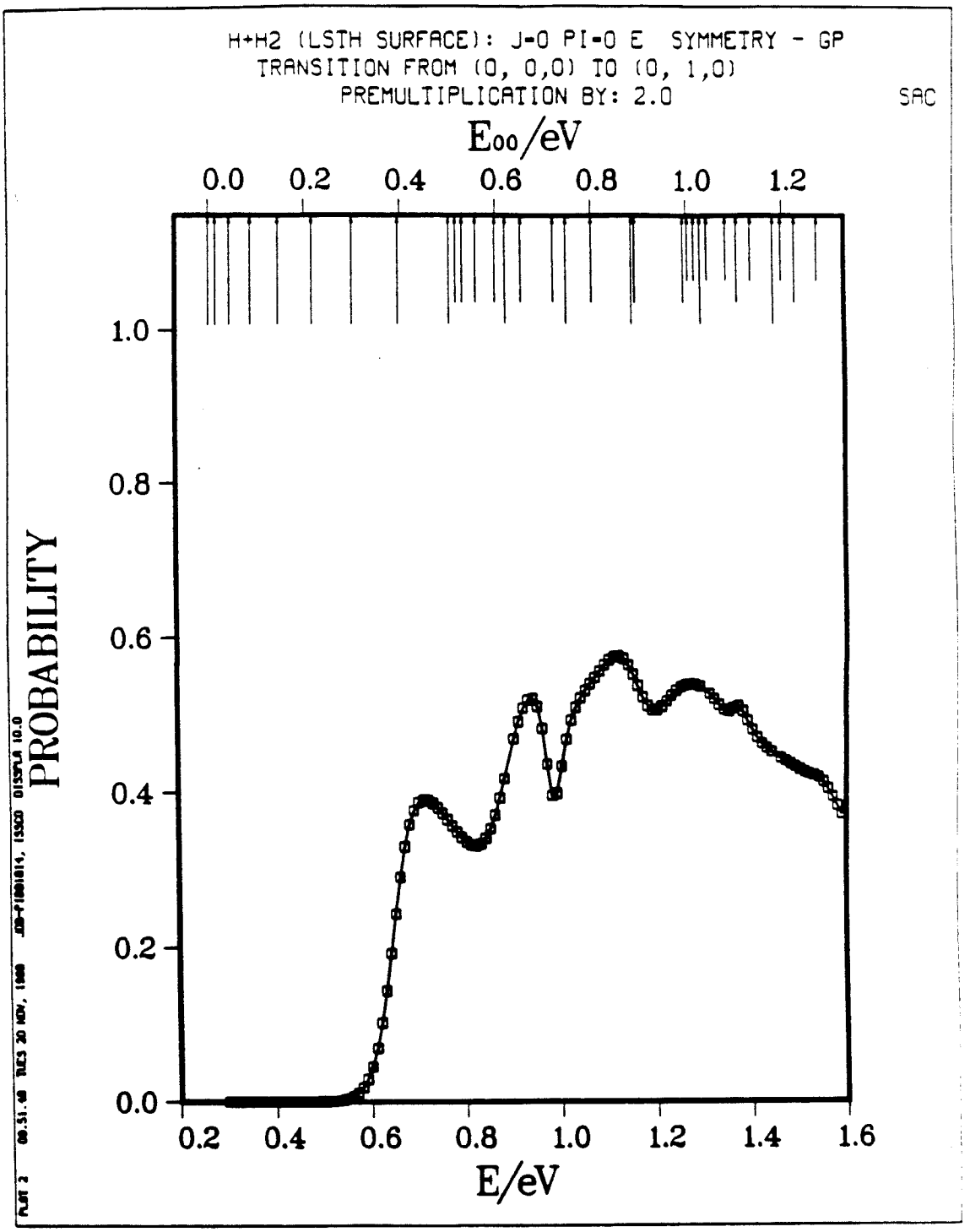
H+H2 (LSTH SURFACE): J=0 PI=0 E SYMMETRY - GP
TRANSITION FROM (0, 0,0) TO (0, 1,0)
PREMULTIPLICATION BY: 2.0
SAC
Eoo/eV
0.0
0.2
0.4
0.6
0.8
1.0
1.2
PROBABILITY
0.0
0.2
0.4
0.6
0.8
1.0
E/eV
0.2
0.4
0.6
0.8
1.0
1.2
1.4
1.6

Fig. 7.9a

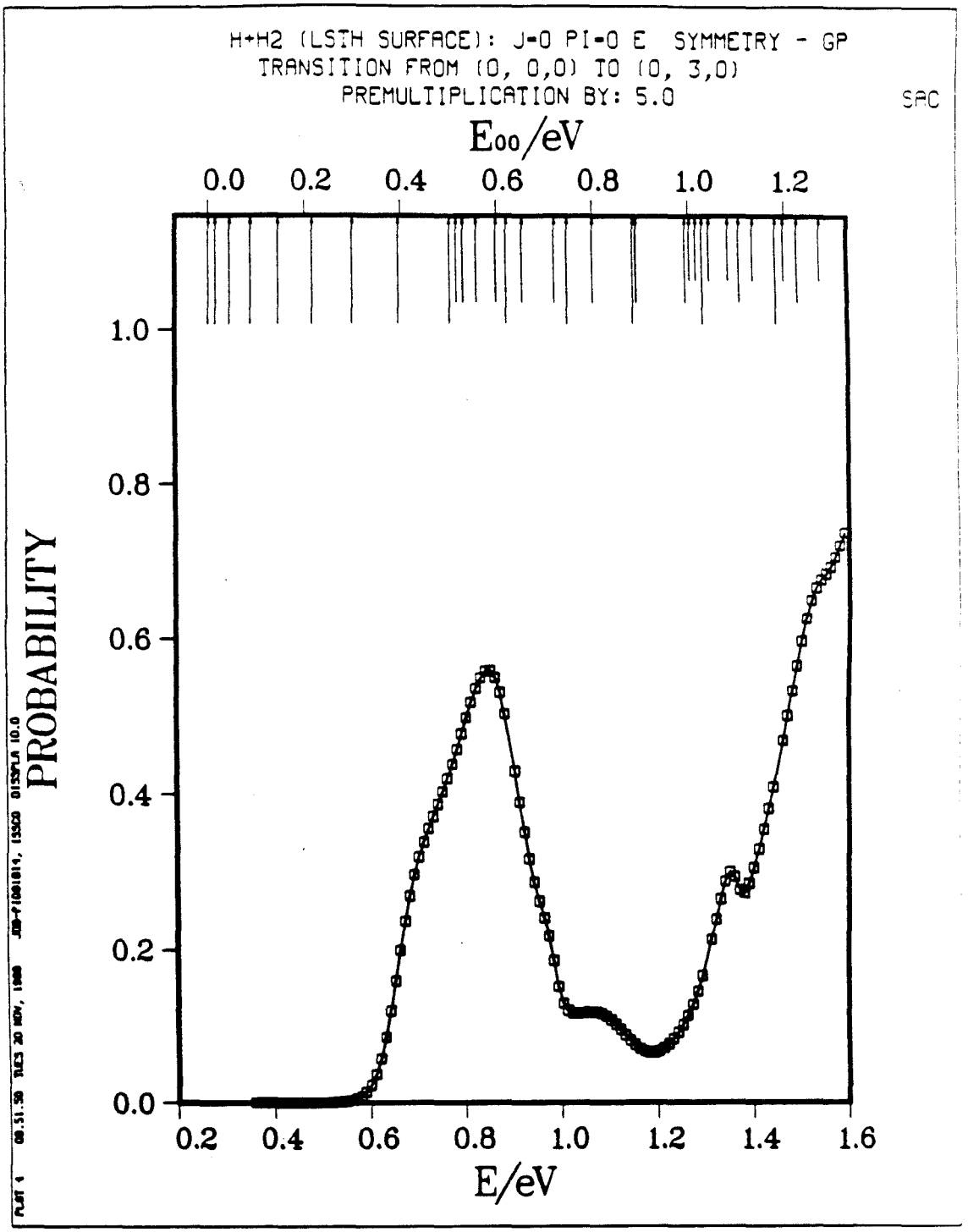
H+H2 (LSTH SURFACE): J=0 PI=0 E SYMMETRY - GP
TRANSITION FROM (0, 0,0) TO (0, 3,0)
PREMULTIPLICATION BY: 5.0
SAC
E00/eV
0.0
0.2
0.4
0.6
0.8
1.0
1.2
PROBABILITY
0.0
0.2
0.4
0.6
0.8
1.0
E/eV
0.2
0.4
0.6
0.8
1.0
1.2
1.4
1.6

Fig. 7.9b

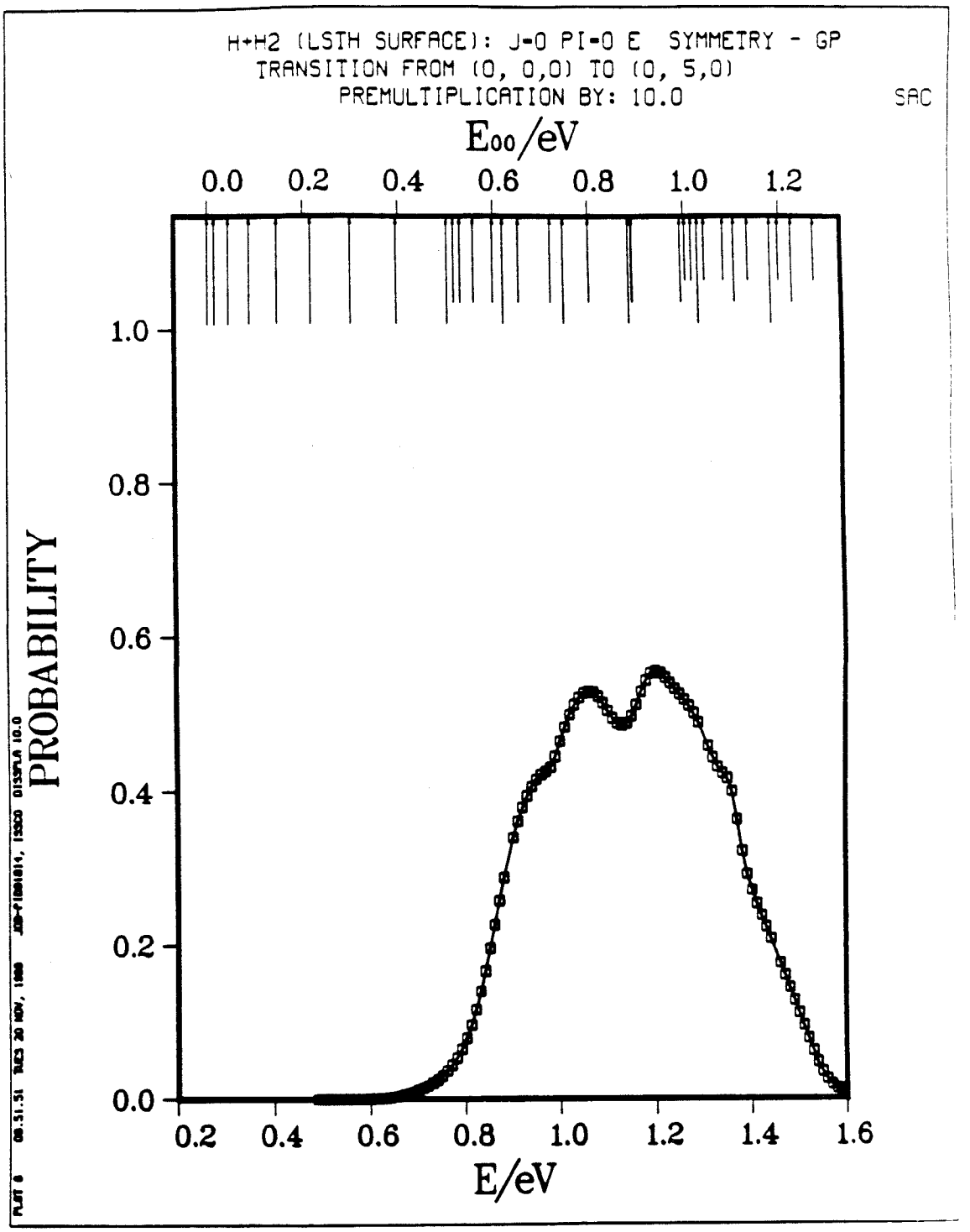
H+H2 (LSTH SURFACE): J=0 PI=0 E SYMMETRY - GP
TRANSITION FROM (0, 0,0) TO (0, 5,0)
PREMULTIPLICATION BY: 10.0
SAC
E00/eV
0.0
0.2
0.4
0.6
0.8
1.0
1.2
PROBABILITY
1.0
0.8
0.6
0.4
0.2
0.0
0.2
0.4
0.6
0.8
1.0
1.2
1.4
1.6
E/eV

Fig. 7.9c

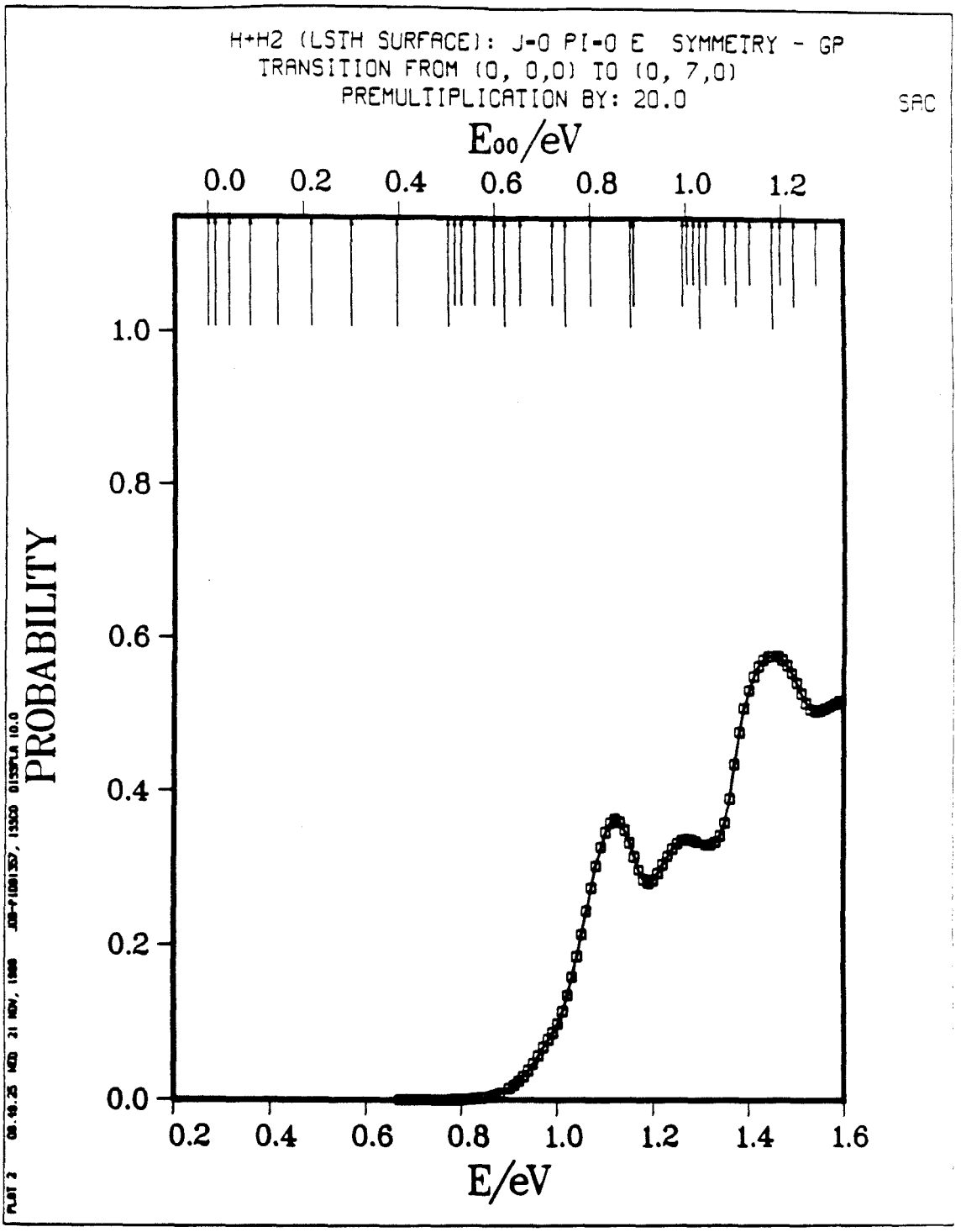
H+H2 (LSTH SURFACE): J=0 PI=0 E SYMMETRY - GP
TRANSITION FROM (0, 0,0) TO (0, 7,0)
PREMULTIPLICATION BY: 20.0
SRC
E00/eV
0.0
0.2
0.4
0.6
0.8
1.0
1.2
PROBABILITY
0.0
0.2
0.4
0.6
0.8
1.0
E/eV
0.2
0.4
0.6
0.8
1.0
1.2
1.4
1.6

Fig. 7.9d

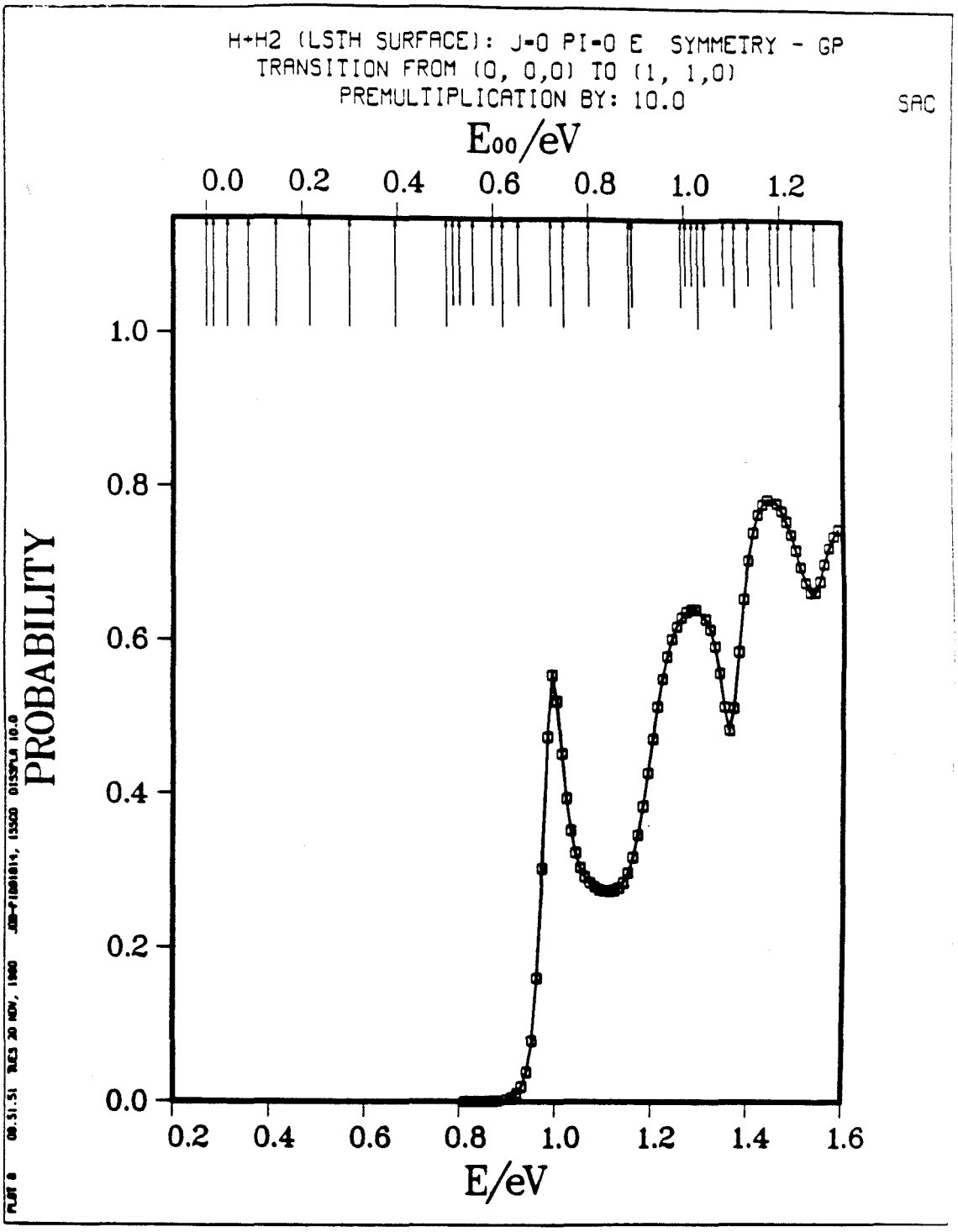
H+H2 (LSTH SURFACE): J=0 PI=0 E SYMMETRY - GP
TRANSITION FROM (0, 0,0) TO (1, 1,0)
PREMULTIPLICATION BY: 10.0
SAC
E00/eV
0.0
0.2
0.4
0.6
0.8
1.0
1.2
PROBABILITY
0.0
0.2
0.4
0.6
0.8
1.0
E/eV
0.2
0.4
0.6
0.8
1.0
1.2
1.4
1.6

Fig. 7.10a

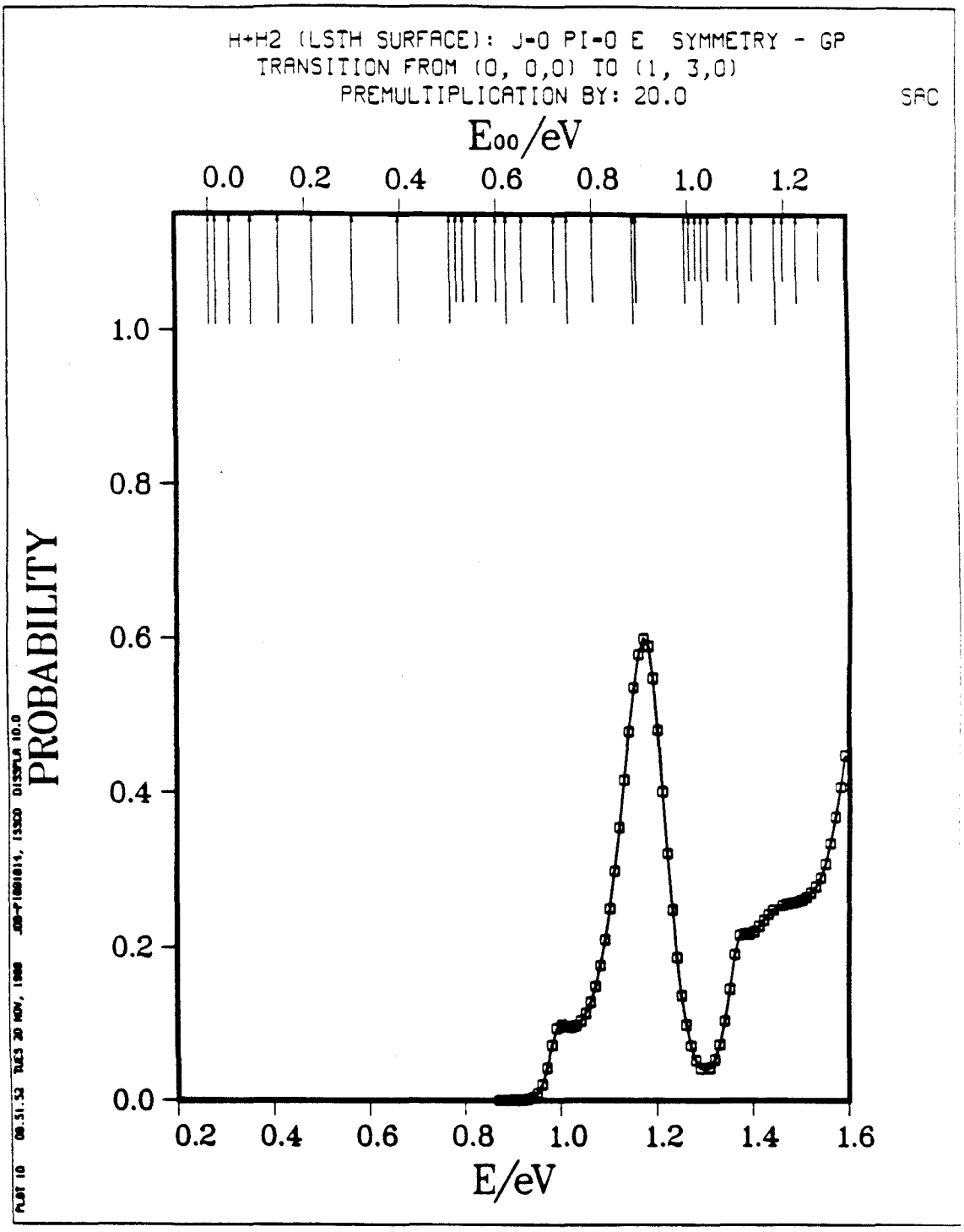
H+H2 (LSTH SURFACE): J=0 PI=0 E SYMMETRY - GP
TRANSITION FROM (0, 0,0) TO (1, 3,0)
PREMULTIPLICATION BY: 20.0
SAC
E00/eV
0.0
0.2
0.4
0.6
0.8
1.0
1.2
PROBABILITY
1.0
0.8
0.6
0.4
0.2
0.0
0.2
0.4
0.6
0.8
1.0
1.2
1.4
1.6
E/eV

Fig. 7.10b

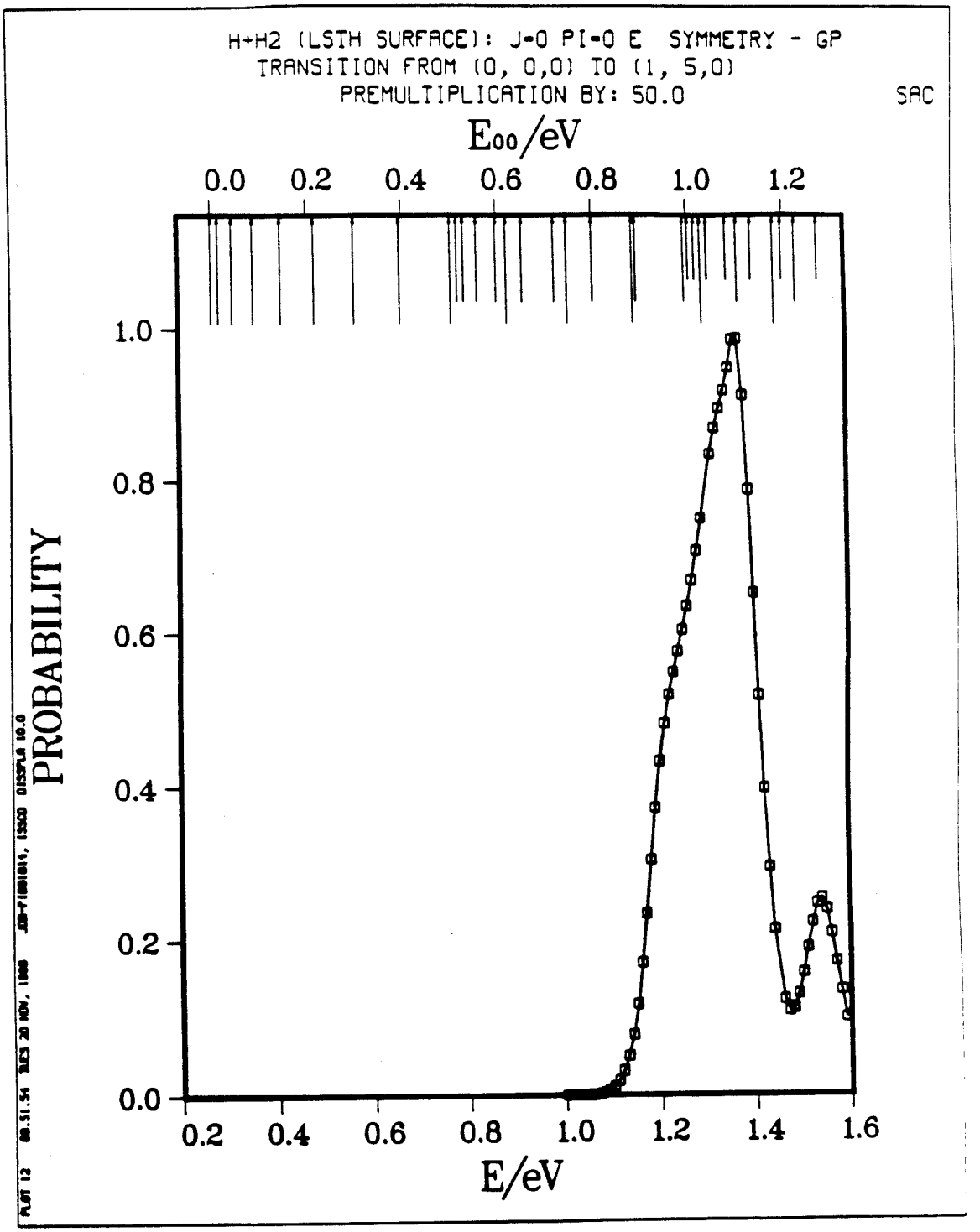
H+H2 (LSTH SURFACE): J=0 PI=0 E SYMMETRY - GP
TRANSITION FROM (0, 0,0) TO (1, 5,0)
PREMULTIPLICATION BY: 50.0
SAC
E00/eV
0.0
0.2
0.4
0.6
0.8
1.0
1.2
PROBABILITY
0.0
0.2
0.4
0.6
0.8
1.0
E/eV
0.2
0.4
0.6
0.8
1.0
1.2
1.4
1.6

Fig. 7.10c

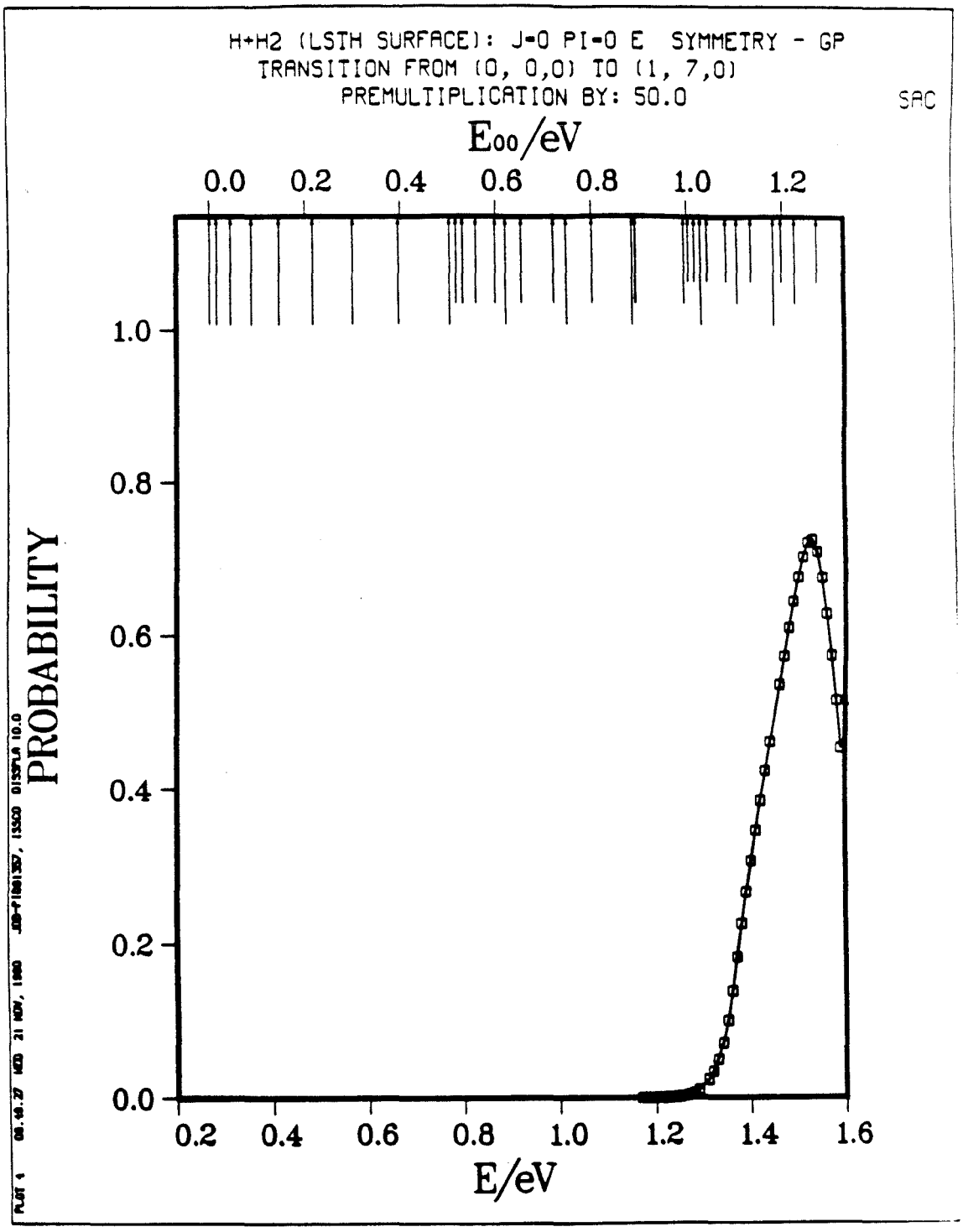
H+H2 (LSTH SURFACE): J=0 PI=0 E SYMMETRY - GP
TRANSITION FROM (0, 0,0) TO (1, 7,0)
PREMULTIPLICATION BY: 50.0
SAC
E00/eV
0.0
0.2
0.4
0.6
0.8
1.0
1.2
PROBABILITY
1.0
0.8
0.6
0.4
0.2
0.0
0.2
0.4
0.6
0.8
1.0
1.2
1.4
1.6
E/eV

Fig. 7.10d

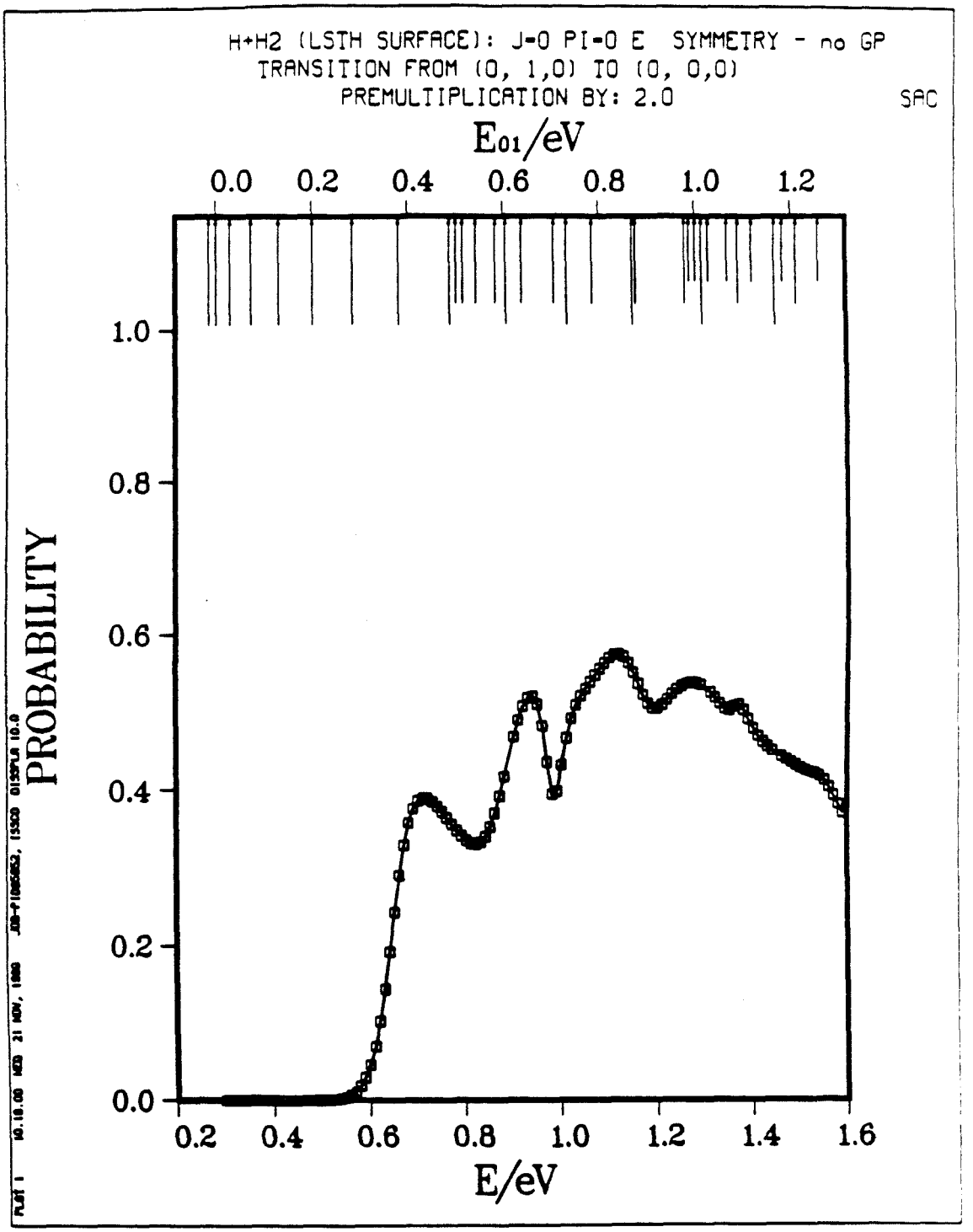
H+H2 (LSTH SURFACE): J=0 PI=0 E SYMMETRY - no GP
TRANSITION FROM (0, 1,0) TO (0, 0,0)
PREMULTIPLICATION BY: 2.0
SAC
E01/eV
0.0
0.2
0.4
0.6
0.8
1.0
1.2
PROBABILITY
0.0
0.2
0.4
0.6
0.8
1.0
E/eV
0.2
0.4
0.6
0.8
1.0
1.2
1.4
1.6

Fig. 7.11a

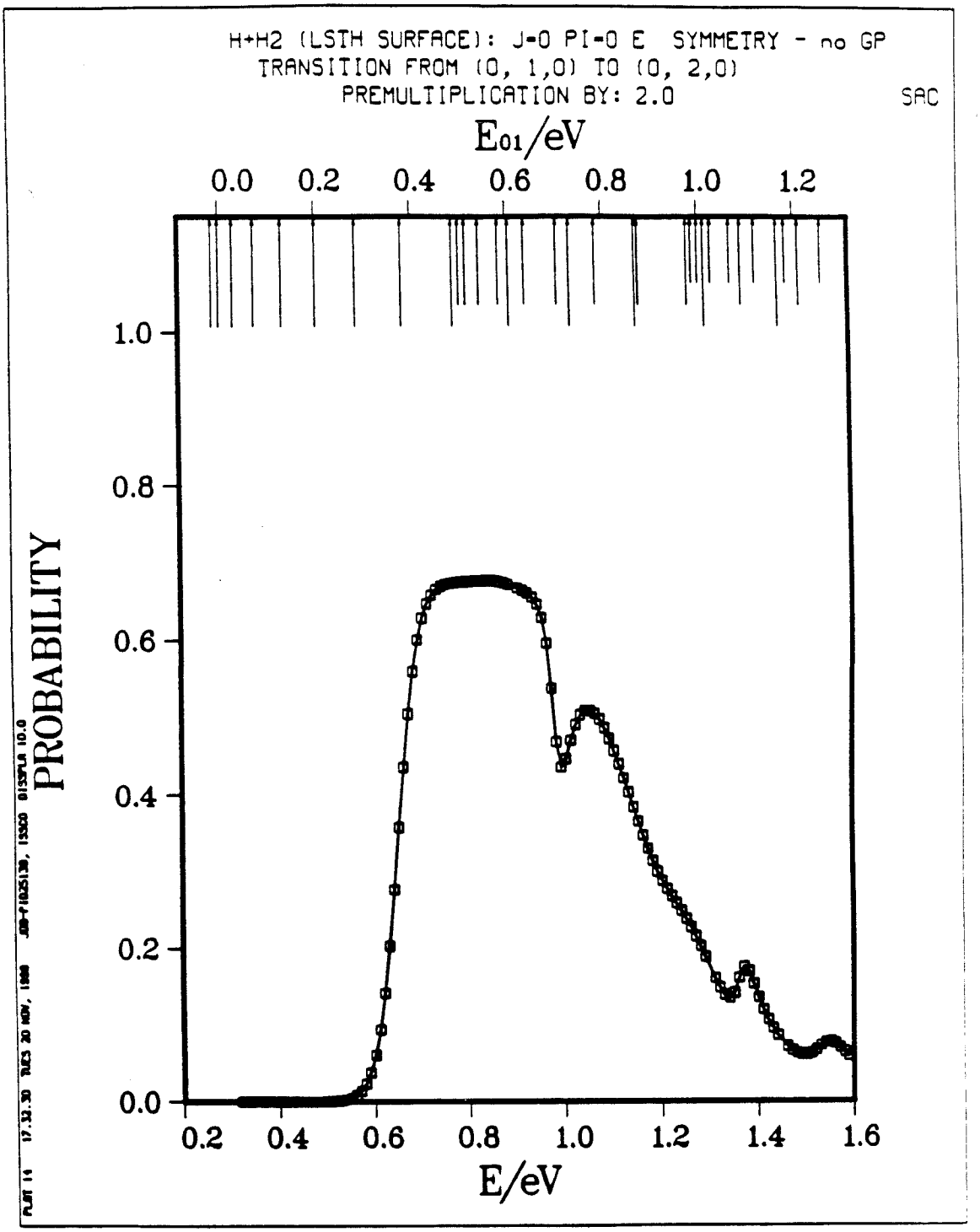
H+H2 (LSTH SURFACE): J=0 PI=0 E SYMMETRY - no GP
TRANSITION FROM (0, 1,0) TO (0, 2,0)
PREMULTIPLICATION BY: 2.0
SAC
E01/eV
0.0
0.2
0.4
0.6
0.8
1.0
1.2
PROBABILITY
0.0
0.2
0.4
0.6
0.8
1.0
E/eV
0.2
0.4
0.6
0.8
1.0
1.2
1.4
1.6

Fig. 7.11b

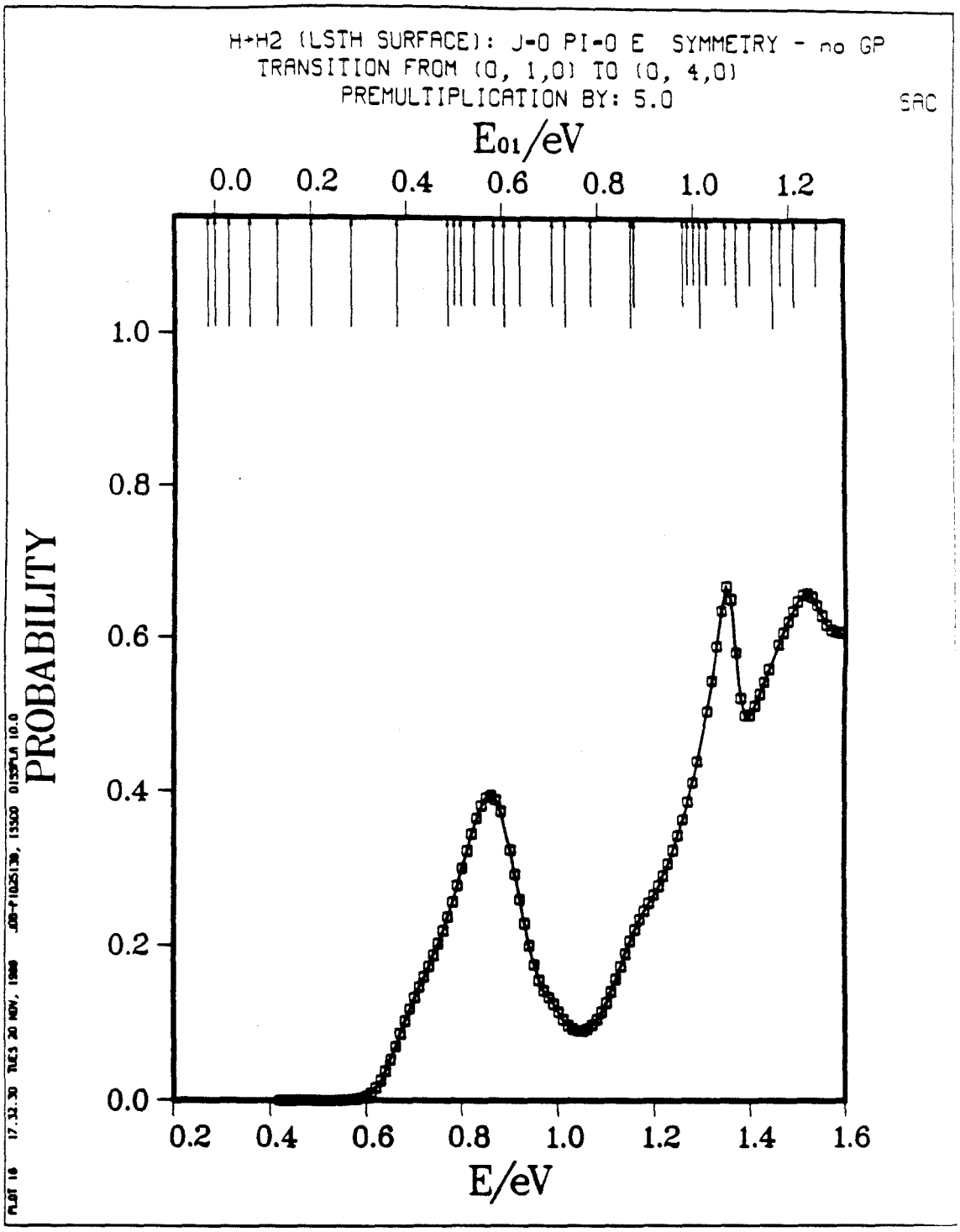
H+H2 (LSTH SURFACE): J=0 PI=0 E SYMMETRY - no GP
TRANSITION FROM (0, 1,0) TO (0, 4,0)
PREMULTIPLICATION BY: 5.0
SAC
E01/eV
0.0
0.2
0.4
0.6
0.8
1.0
1.2
PROBABILITY
0.0
0.2
0.4
0.6
0.8
1.0
0.2
0.4
0.6
0.8
1.0
1.2
1.4
1.6
E/eV

Fig. 7.11c

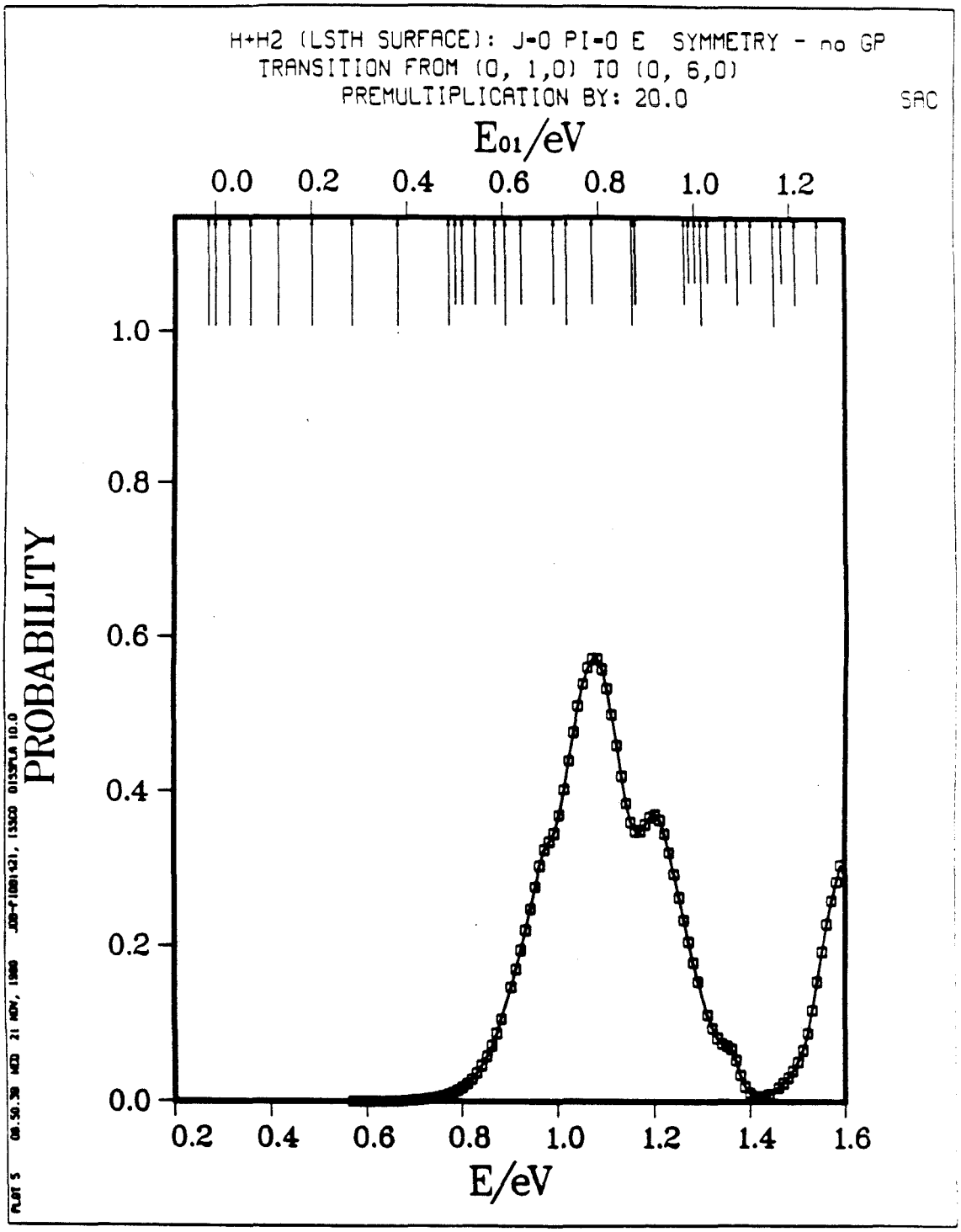
H+H2 (LSTH SURFACE): J=0 PI=0 E SYMMETRY - no GP
TRANSITION FROM (0, 1,0) TO (0, 6,0)
PREMULTIPLICATION BY: 20.0
SAC
E01/eV
0.0
0.2
0.4
0.6
0.8
1.0
1.2
PROBABILITY
0.0
0.2
0.4
0.6
0.8
1.0
E/eV
0.2
0.4
0.6
0.8
1.0
1.2
1.4
1.6

Fig. 7.11d

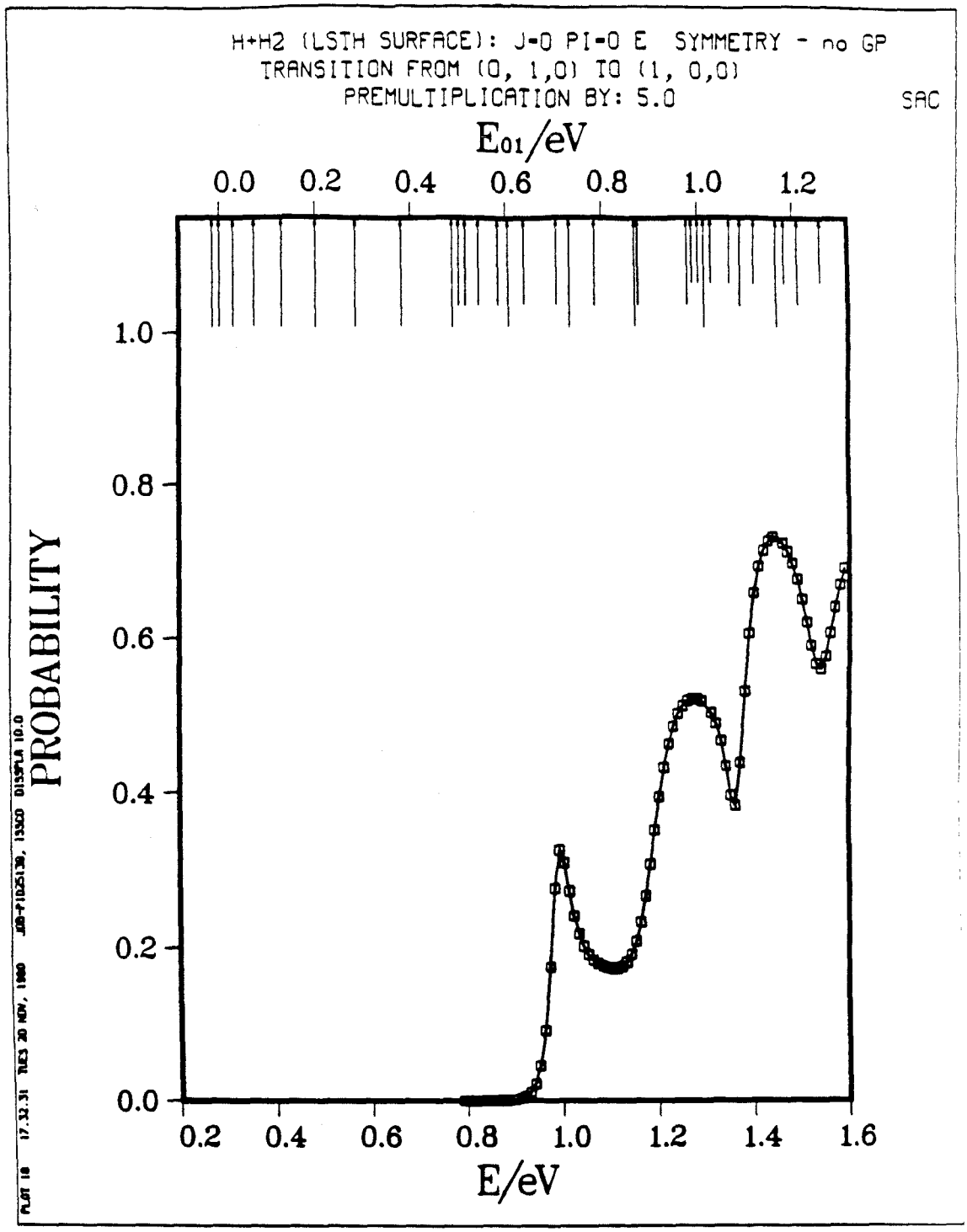
H+H2 (LSTH SURFACE): J=0 PI=0 E SYMMETRY - no GP
TRANSITION FROM (0, 1,0) TO (1, 0,0)
PREMULTIPLICATION BY: 5.0
SAC
E01/eV
0.0
0.2
0.4
0.6
0.8
1.0
1.2
PROBABILITY
0.0
0.2
0.4
0.6
0.8
1.0
E/eV
0.2
0.4
0.6
0.8
1.0
1.2
1.4
1.6

Fig. 7.12a

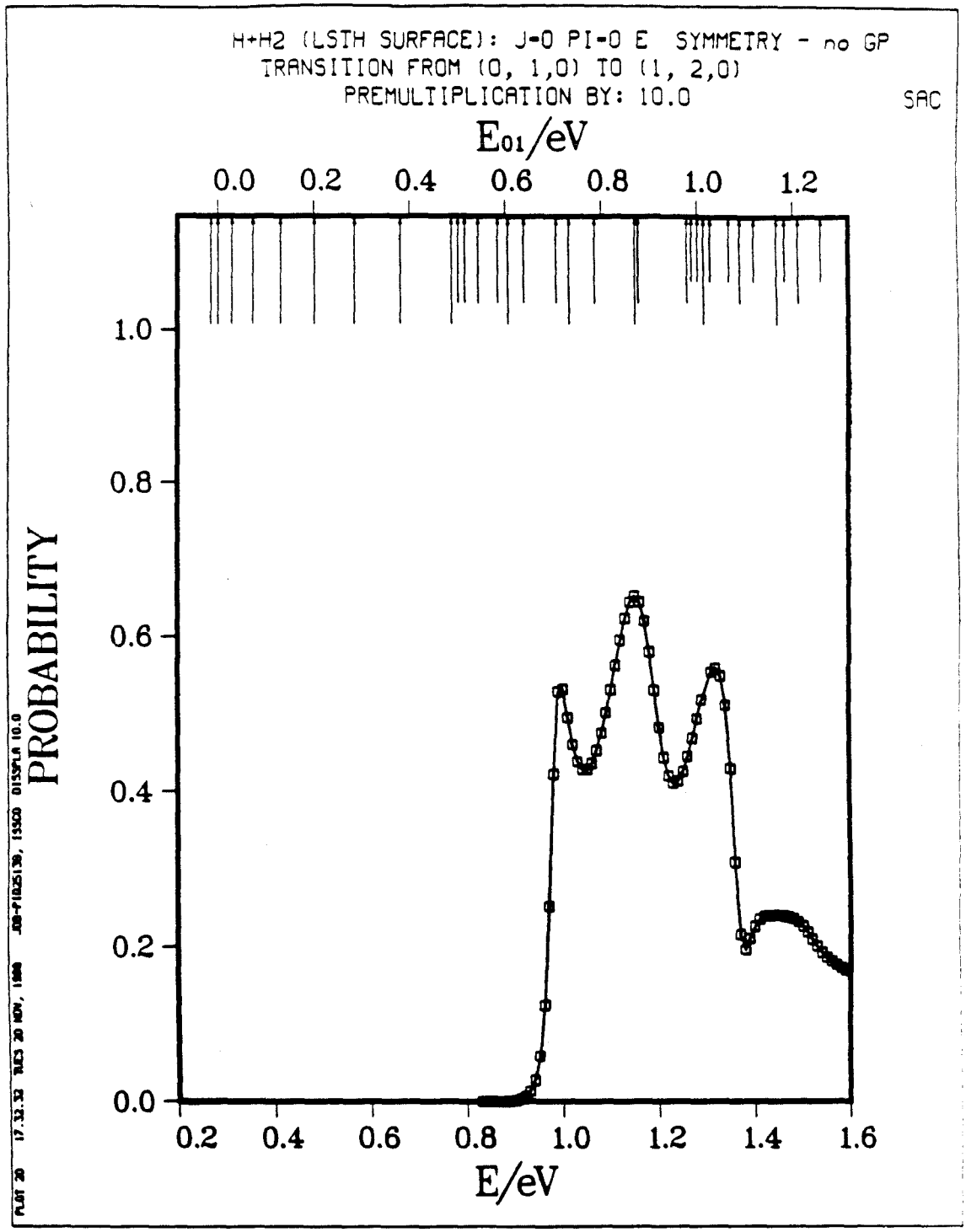
H+H2 (LSTH SURFACE): J=0 PI=0 E SYMMETRY - no GP
TRANSITION FROM (0, 1,0) TO (1, 2,0)
PREMULTIPLICATION BY: 10.0
SAC
E01/eV
0.0
0.2
0.4
0.6
0.8
1.0
1.2
PROBABILITY
0.0
0.2
0.4
0.6
0.8
1.0
E/eV
0.2
0.4
0.6
0.8
1.0
1.2
1.4
1.6

Fig. 7.12b

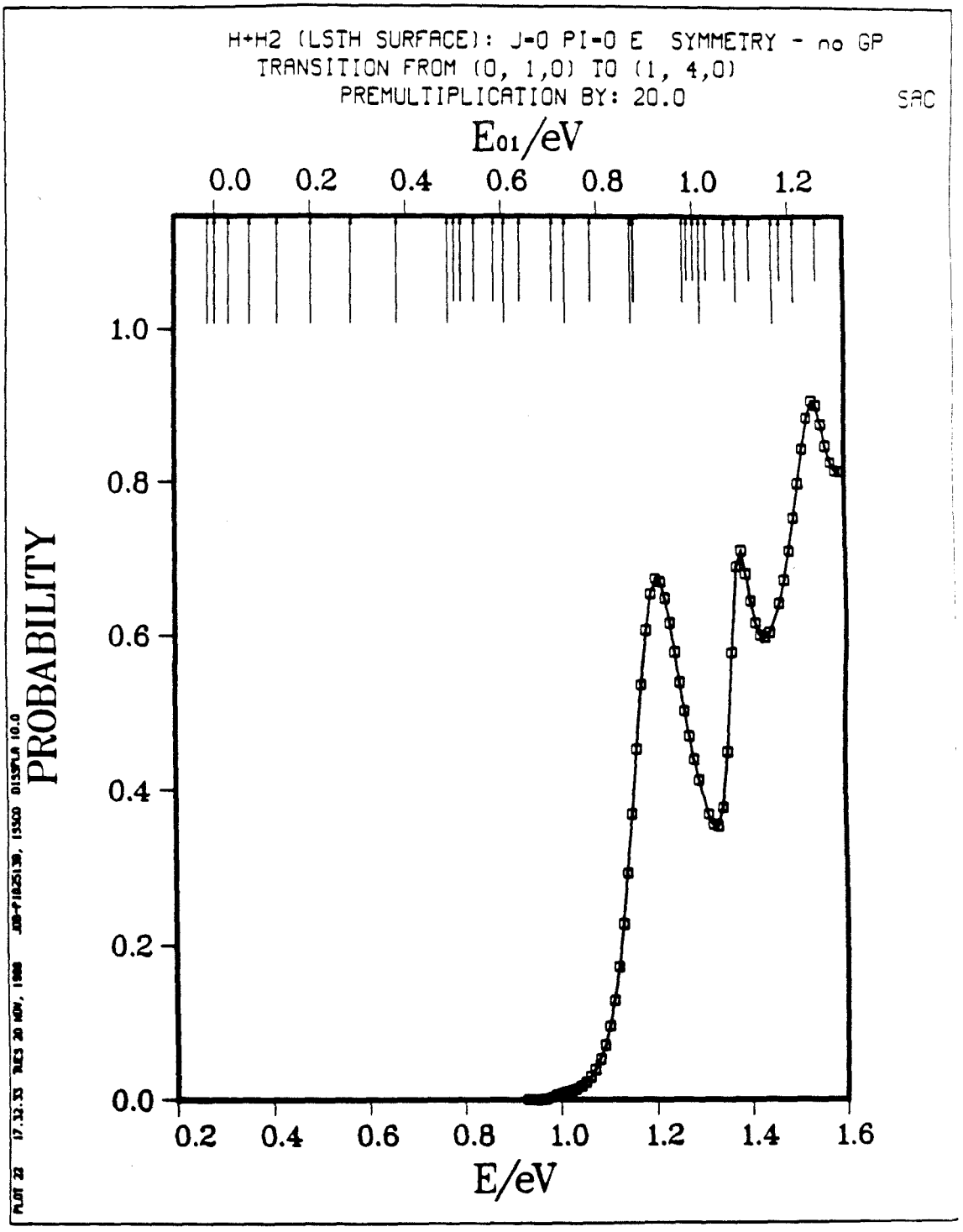
H+H2 (LSTH SURFACE): J=0 PI=0 E SYMMETRY - no GP
TRANSITION FROM (0, 1,0) TO (1, 4,0)
PREMULTIPLICATION BY: 20.0
SAC
E01/eV
0.0
0.2
0.4
0.6
0.8
1.0
1.2
PROBABILITY
0.0
0.2
0.4
0.6
0.8
1.0
E/eV
0.2
0.4
0.6
0.8
1.0
1.2
1.4
1.6

Fig. 7.12c

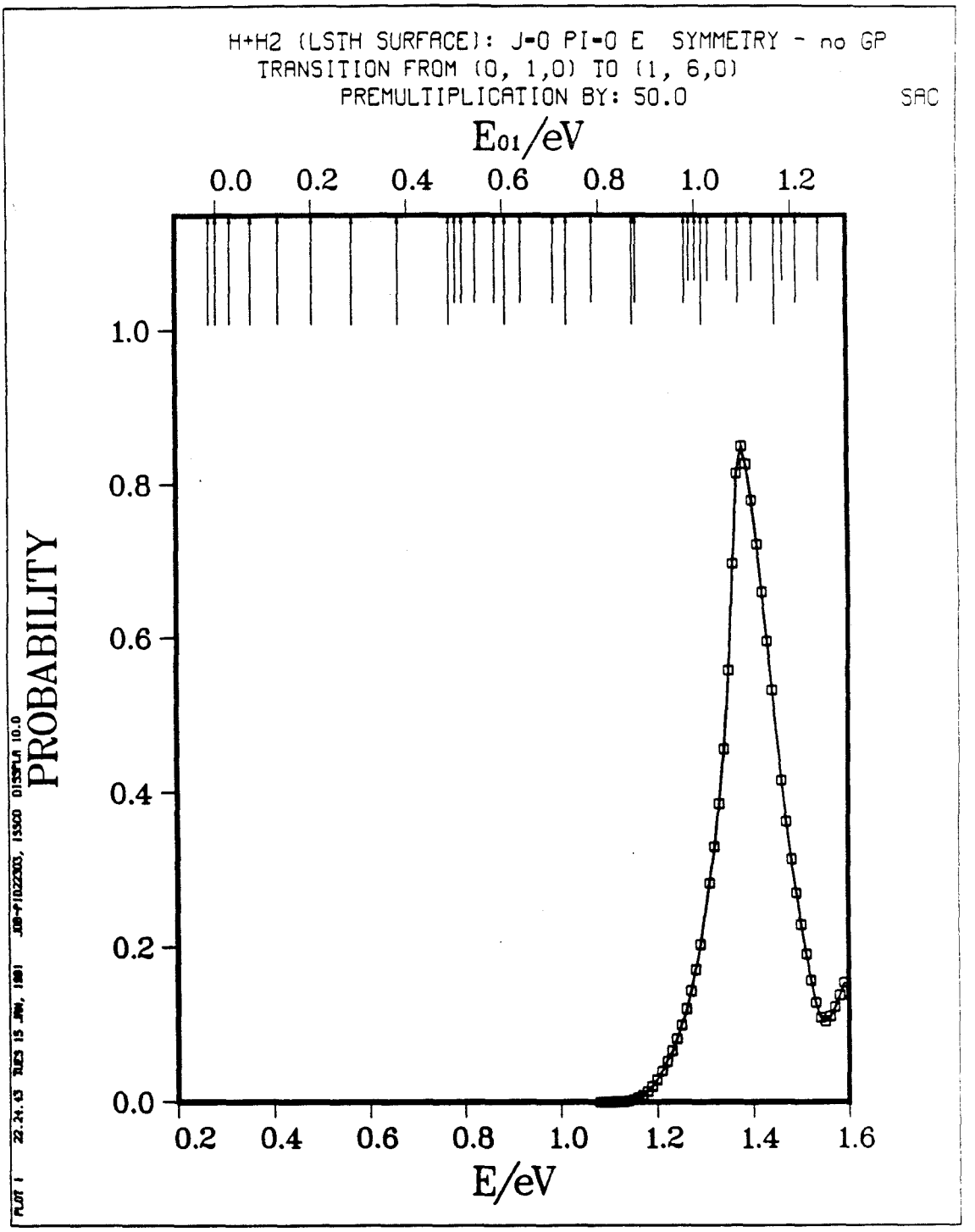
H+H2 (LSTH SURFACE): J=0 PI=0 E SYMMETRY - no GP
TRANSITION FROM (0, 1,0) TO (1, 6,0)
PREMULTIPLICATION BY: 50.0
SAC
E01/eV
0.0
0.2
0.4
0.6
0.8
1.0
1.2
PROBABILITY
0.0
0.2
0.4
0.6
0.8
1.0
E/eV
0.2
0.4
0.6
0.8
1.0
1.2
1.4
1.6

Fig. 7.12d

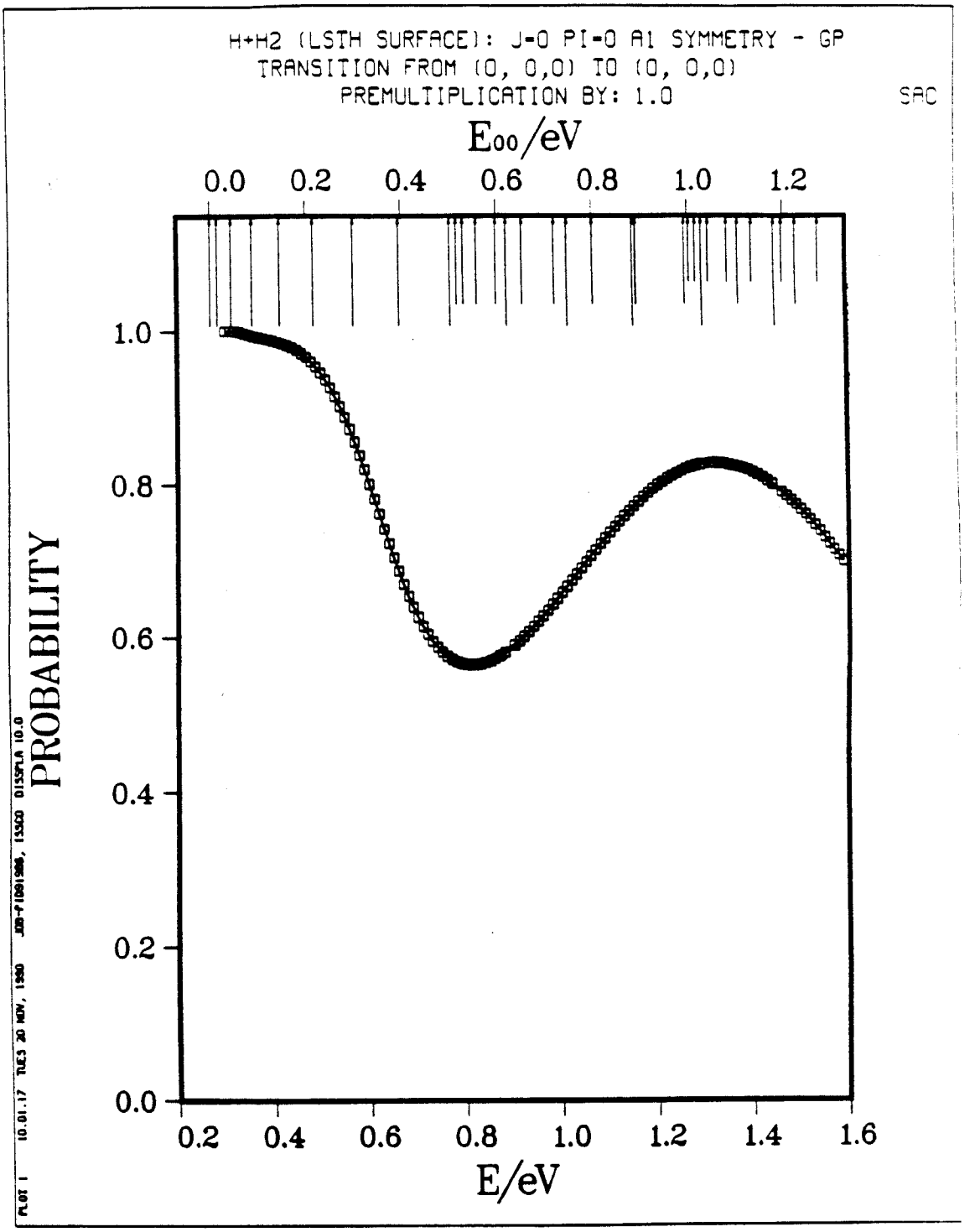
H+H2 (LSTH SURFACE): J=0 PI=0 A1 SYMMETRY - GP
TRANSITION FROM (0, 0,0) TO (0, 0,0)
PREMULTIPLICATION BY: 1.0
SAC
E00/eV
0.0
0.2
0.4
0.6
0.8
1.0
1.2
PROBABILITY
1.0
0.8
0.6
0.4
0.2
0.0
0.2
0.4
0.6
0.8
1.0
1.2
1.4
1.6
E/eV

Fig. 7.13a

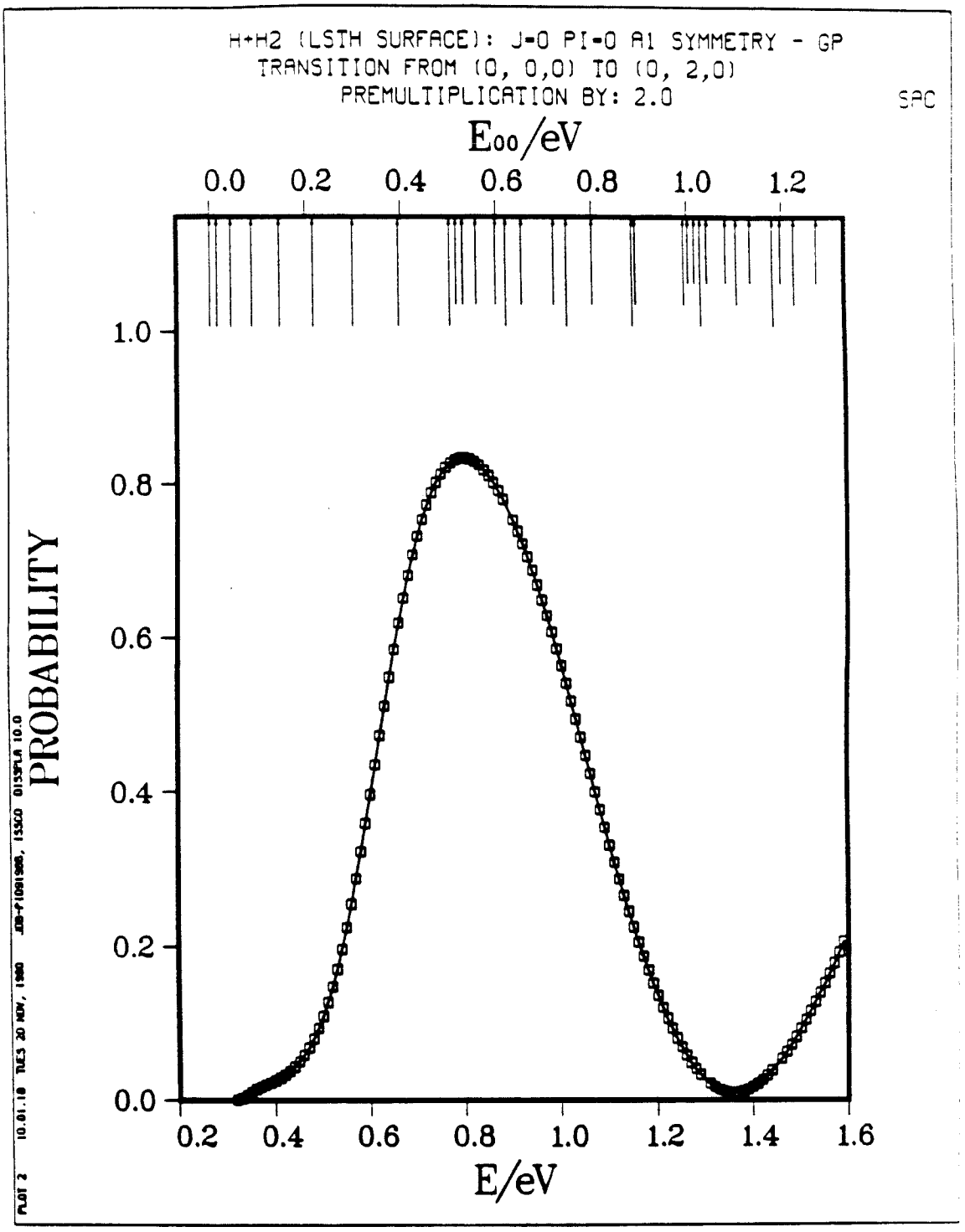
H+H2 (LSTH SURFACE): J=0 PI=0 A1 SYMMETRY - GP
TRANSITION FROM (0, 0,0) TO (0, 2,0)
PREMULTIPLICATION BY: 2.0
SRC
E00/eV
0.0
0.2
0.4
0.6
0.8
1.0
1.2
PROBABILITY
0.0
0.2
0.4
0.6
0.8
1.0
E/eV
0.2
0.4
0.6
0.8
1.0
1.2
1.4
1.6

Fig. 7.13b

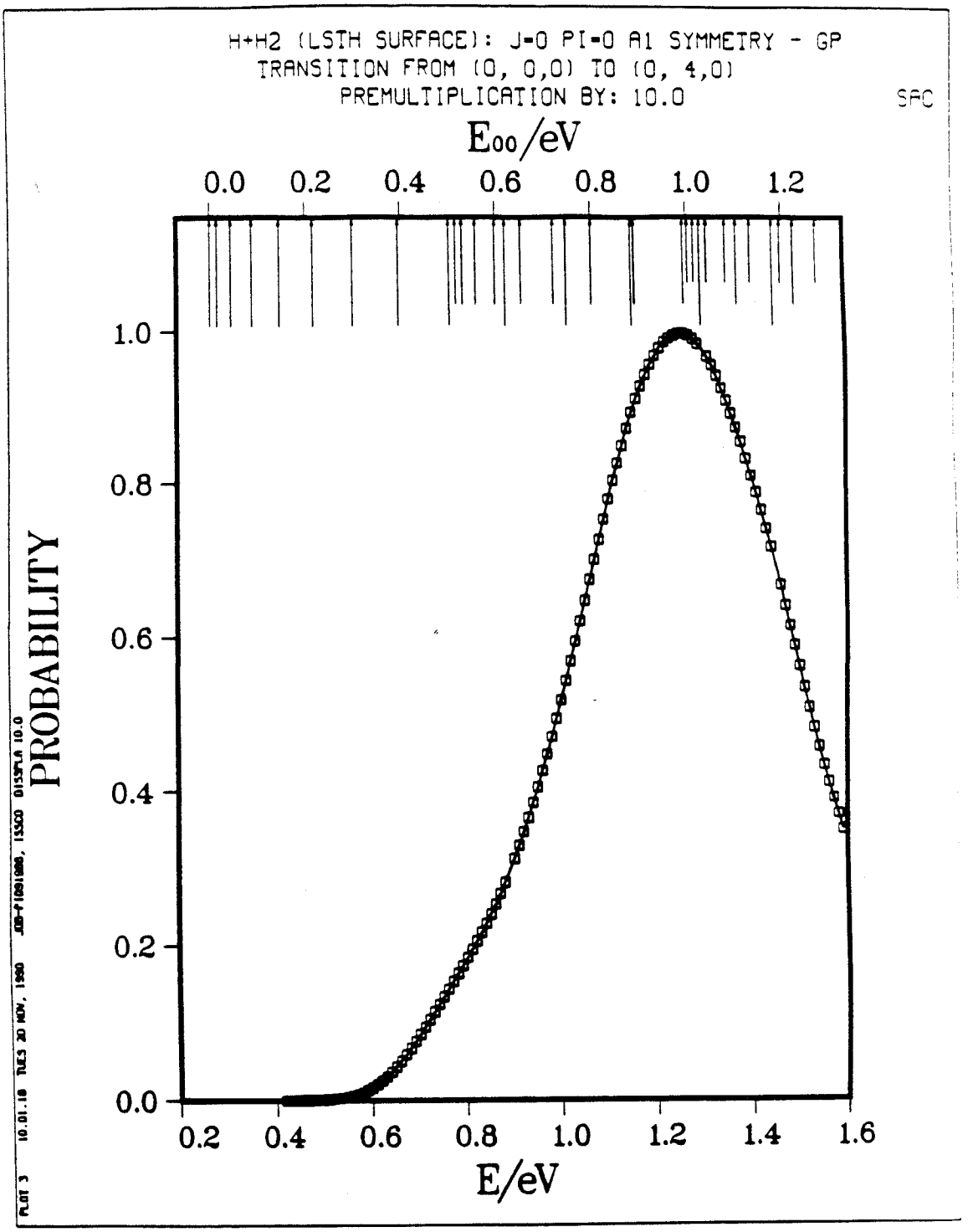
H+H2 (LSTH SURFACE): J=0 PI=0 A1 SYMMETRY - GP
TRANSITION FROM (0, 0,0) TO (0, 4,0)
PREMULTIPLICATION BY: 10.0
SPC
E00/eV
0.0
0.2
0.4
0.6
0.8
1.0
1.2
PROBABILITY
0.0
0.2
0.4
0.6
0.8
1.0
E/eV
0.2
0.4
0.6
0.8
1.0
1.2
1.4
1.6

Fig. 7.13c

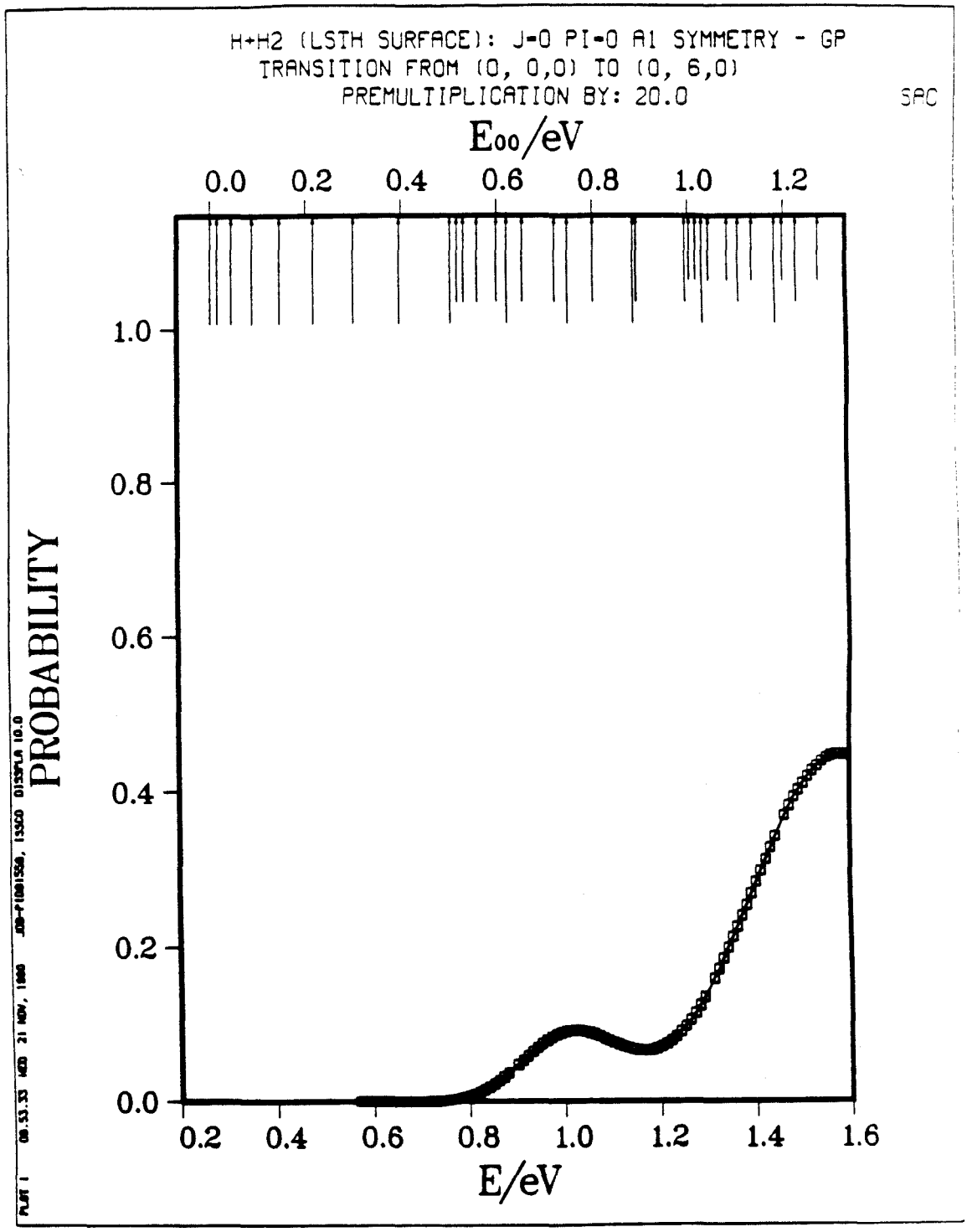
H+H2 (LSTH SURFACE): J=0 PI=0 A1 SYMMETRY - GP
TRANSITION FROM (0, 0,0) TO (0, 6,0)
PREMULTIPLICATION BY: 20.0
SAC
E00/eV
0.0
0.2
0.4
0.6
0.8
1.0
1.2
PROBABILITY
0.0
0.2
0.4
0.6
0.8
1.0
E/eV
0.2
0.4
0.6
0.8
1.0
1.2
1.4
1.6

Fig. 7.13d

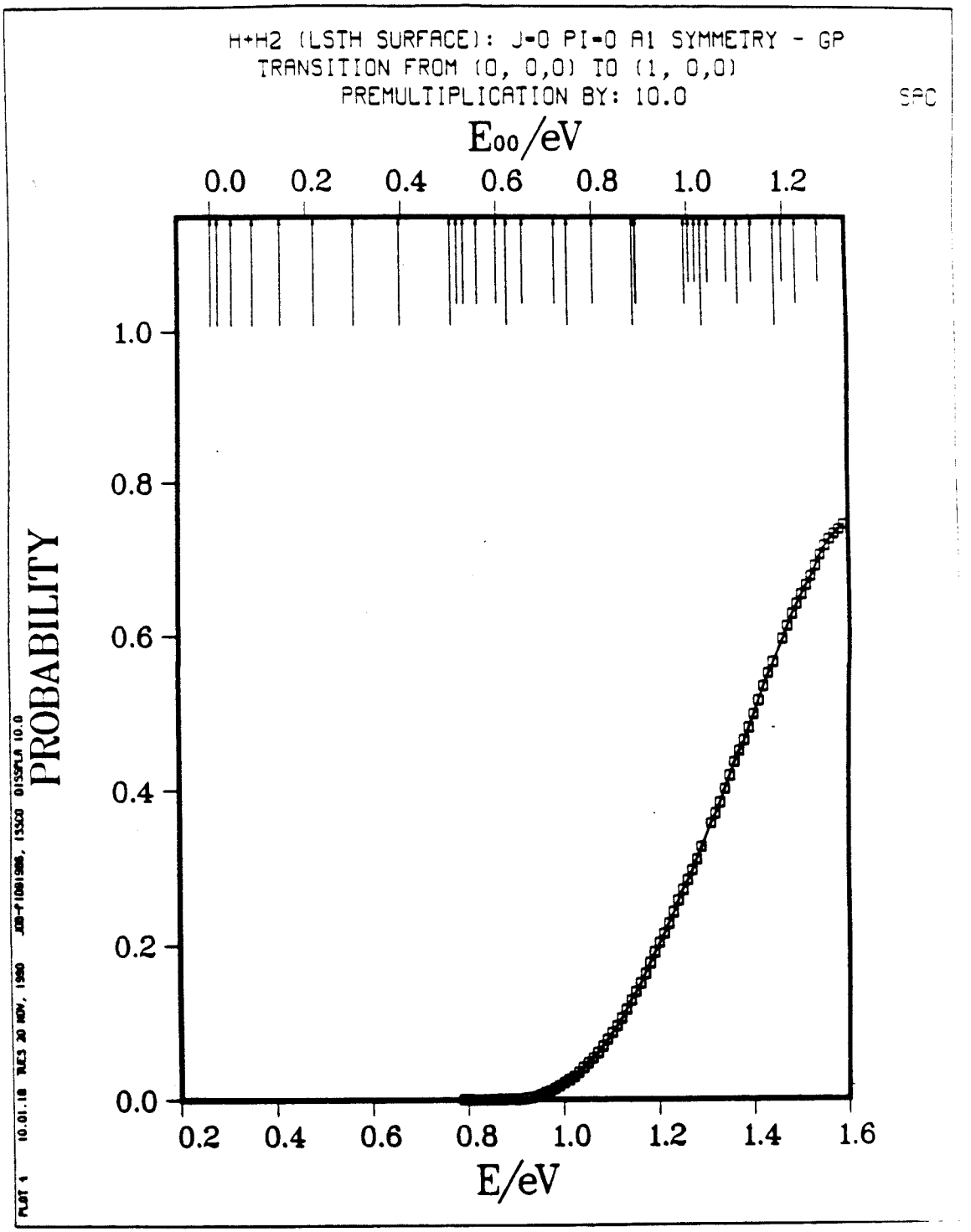
H+H2 (LSTH SURFACE): J=0 PI=0 A1 SYMMETRY - GP
TRANSITION FROM (0, 0,0) TO (1, 0,0)
PREMULTIPLICATION BY: 10.0
SPC
E00/eV
0.0
0.2
0.4
0.6
0.8
1.0
1.2
PROBABILITY
1.0
0.8
0.6
0.4
0.2
0.0
0.2
0.4
0.6
0.8
1.0
1.2
1.4
1.6
E/eV

Fig. 7.14a

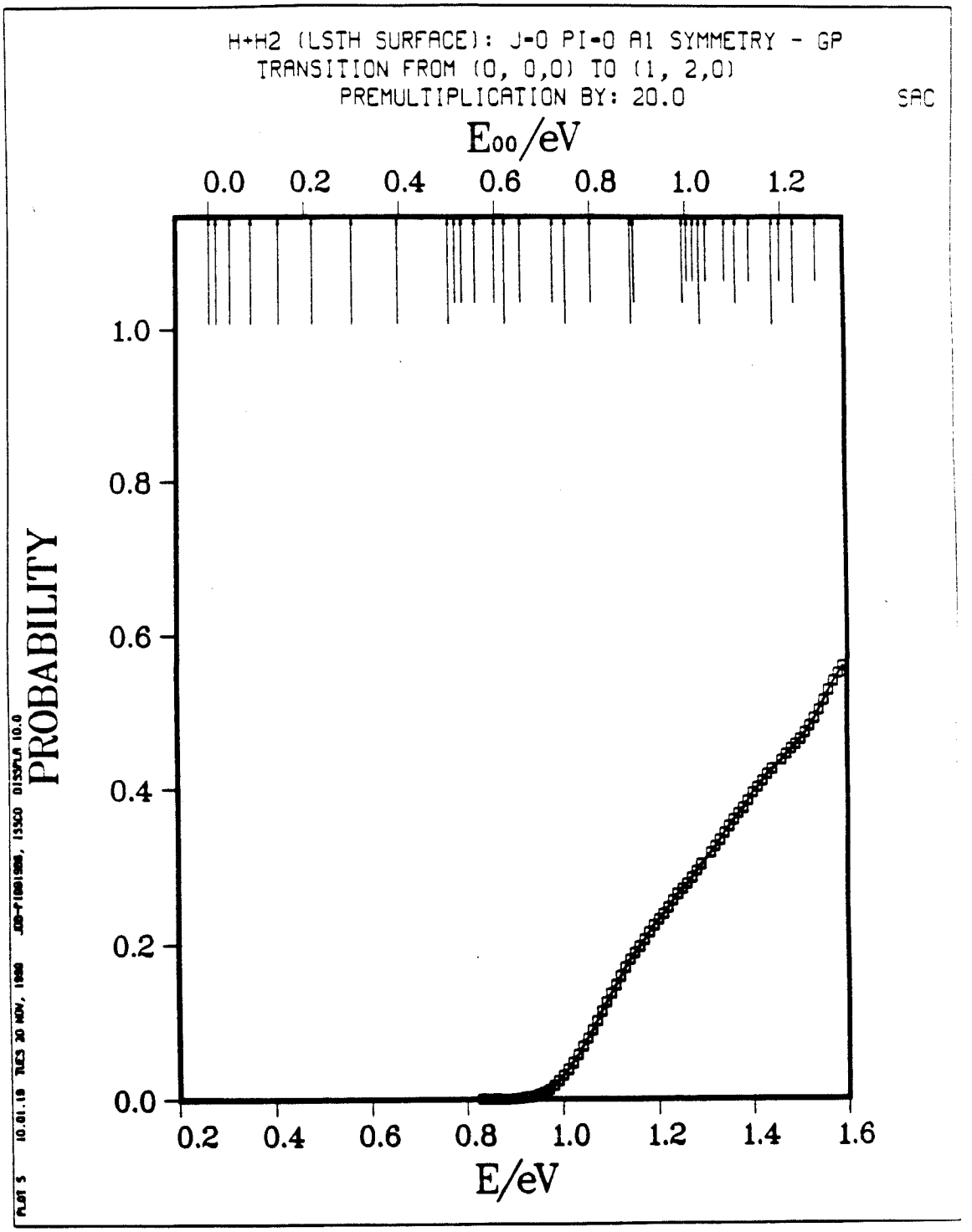
H+H2 (LSTH SURFACE): J=0 PI=0 A1 SYMMETRY - GP
TRANSITION FROM (0, 0,0) TO (1, 2,0)
PREMULTIPLICATION BY: 20.0
SAC
E00/eV
0.0
0.2
0.4
0.6
0.8
1.0
1.2
PROBABILITY
0.0
0.2
0.4
0.6
0.8
1.0
E/eV
0.2
0.4
0.6
0.8
1.0
1.2
1.4
1.6

Fig. 7.14b

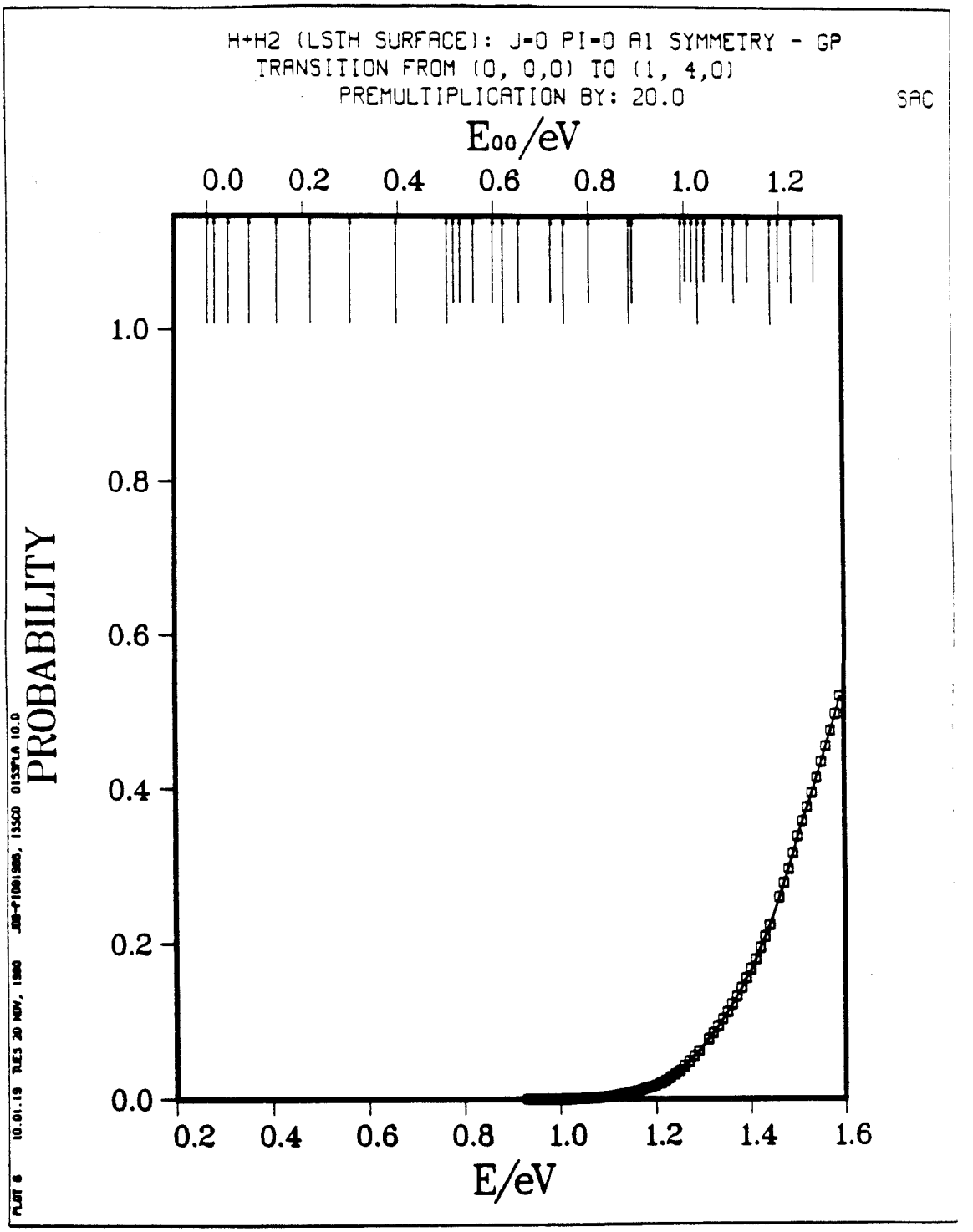
H+H2 (LSTH SURFACE): J=0 PI=0 A1 SYMMETRY - GP
TRANSITION FROM (0, 0,0) TO (1, 4,0)
PREMULTIPLICATION BY: 20.0
SAC
E00/eV
0.0
0.2
0.4
0.6
0.8
1.0
1.2
PROBABILITY
0.0
0.2
0.4
0.6
0.8
1.0
E/eV
0.2
0.4
0.6
0.8
1.0
1.2
1.4
1.6

Fig. 7.14c

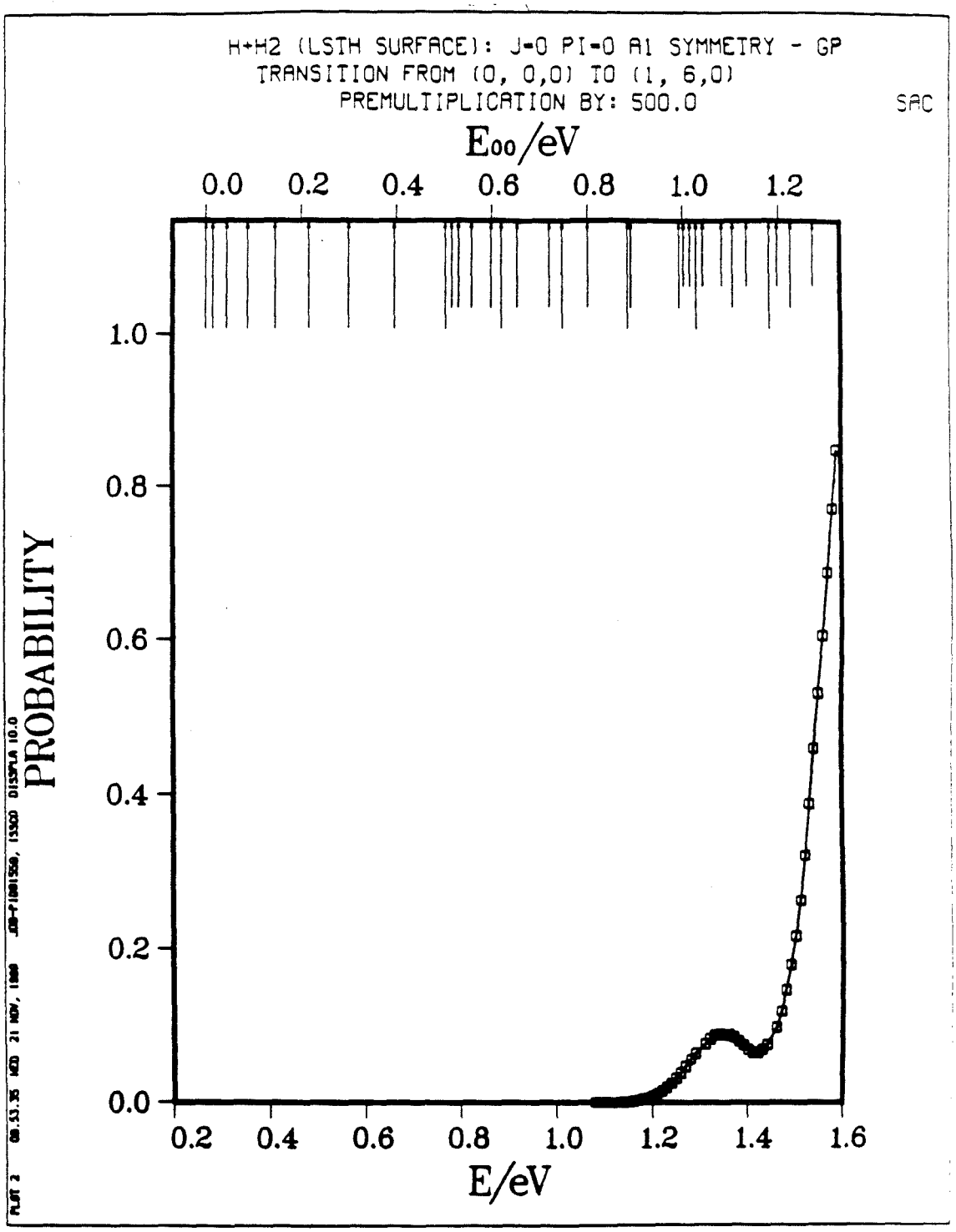
H+H2 (LSTH SURFACE): J=0 PI=0 A1 SYMMETRY - GP
TRANSITION FROM (0, 0,0) TO (1, 6,0)
PREMULTIPLICATION BY: 500.0
SAC
E00/eV
0.0
0.2
0.4
0.6
0.8
1.0
1.2
PROBABILITY
0.0
0.2
0.4
0.6
0.8
1.0
0.2
0.4
0.6
0.8
1.0
1.2
1.4
1.6
E/eV

Fig. 7.14d

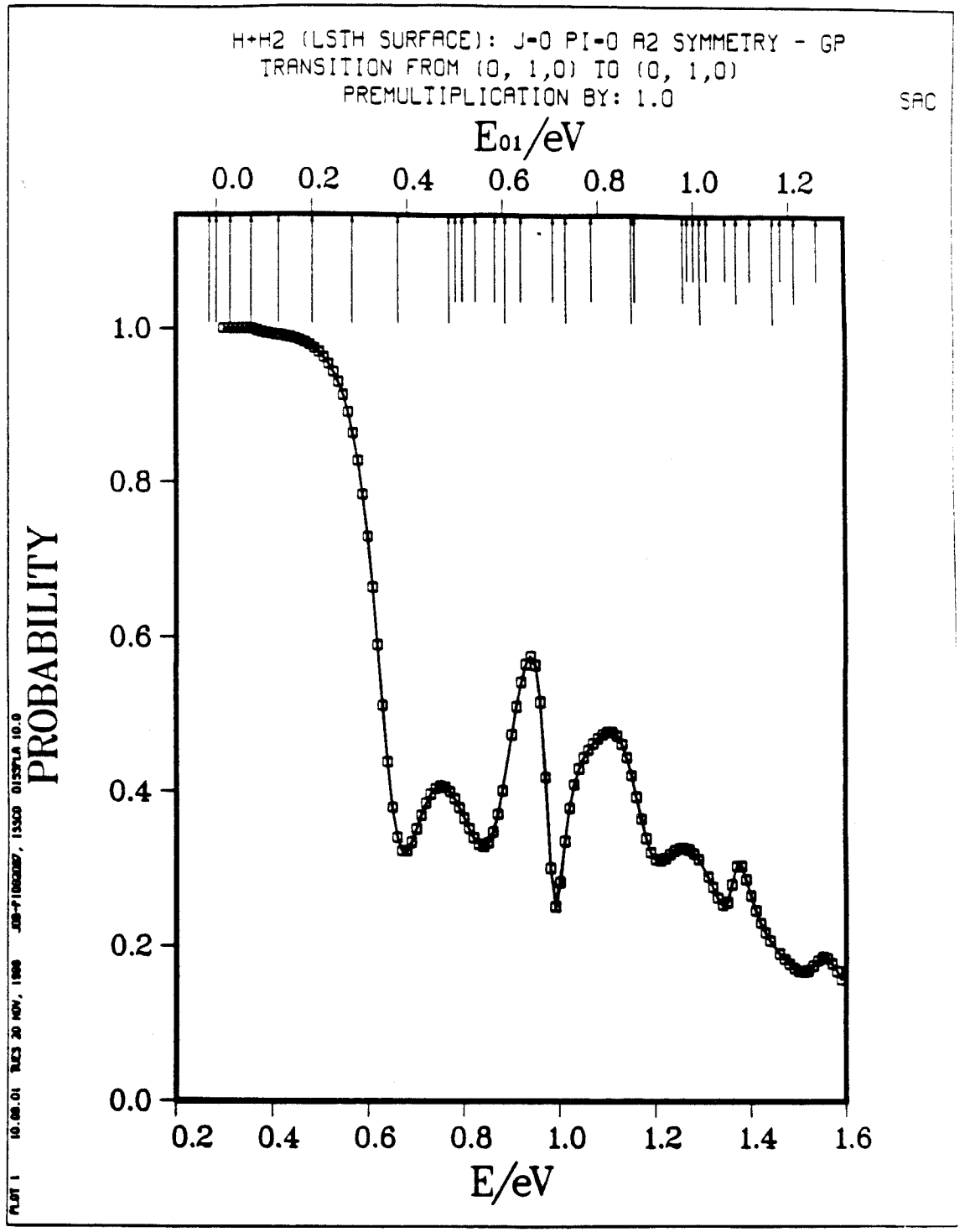
H+H2 (LSTH SURFACE): J=0 PI=0 A2 SYMMETRY - GP
TRANSITION FROM (0, 1,0) TO (0, 1,0)
PREMULTIPLICATION BY: 1.0
SAC
E01/eV
0.0
0.2
0.4
0.6
0.8
1.0
1.2
PROBABILITY
0.0
0.2
0.4
0.6
0.8
1.0
E/eV
0.2
0.4
0.6
0.8
1.0
1.2
1.4
1.6

Fig. 7.15a

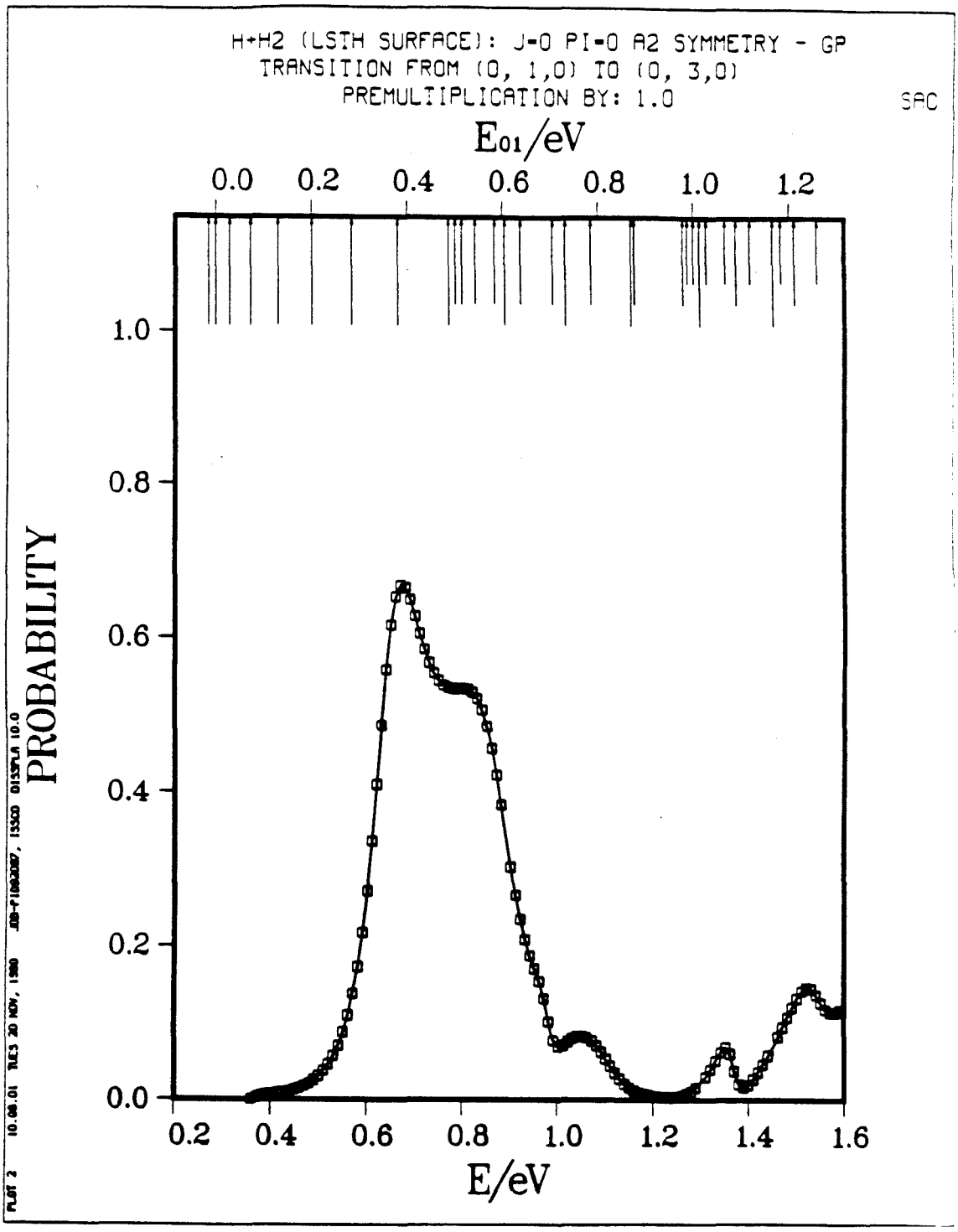
H+H2 (LSTH SURFACE): J=0 PI=0 A2 SYMMETRY - GP
TRANSITION FROM (0, 1,0) TO (0, 3,0)
PREMULTIPLICATION BY: 1.0
SAC
E01/eV
0.0
0.2
0.4
0.6
0.8
1.0
1.2
PROBABILITY
0.0
0.2
0.4
0.6
0.8
1.0
E/eV
0.2
0.4
0.6
0.8
1.0
1.2
1.4
1.6

Fig. 7.15b

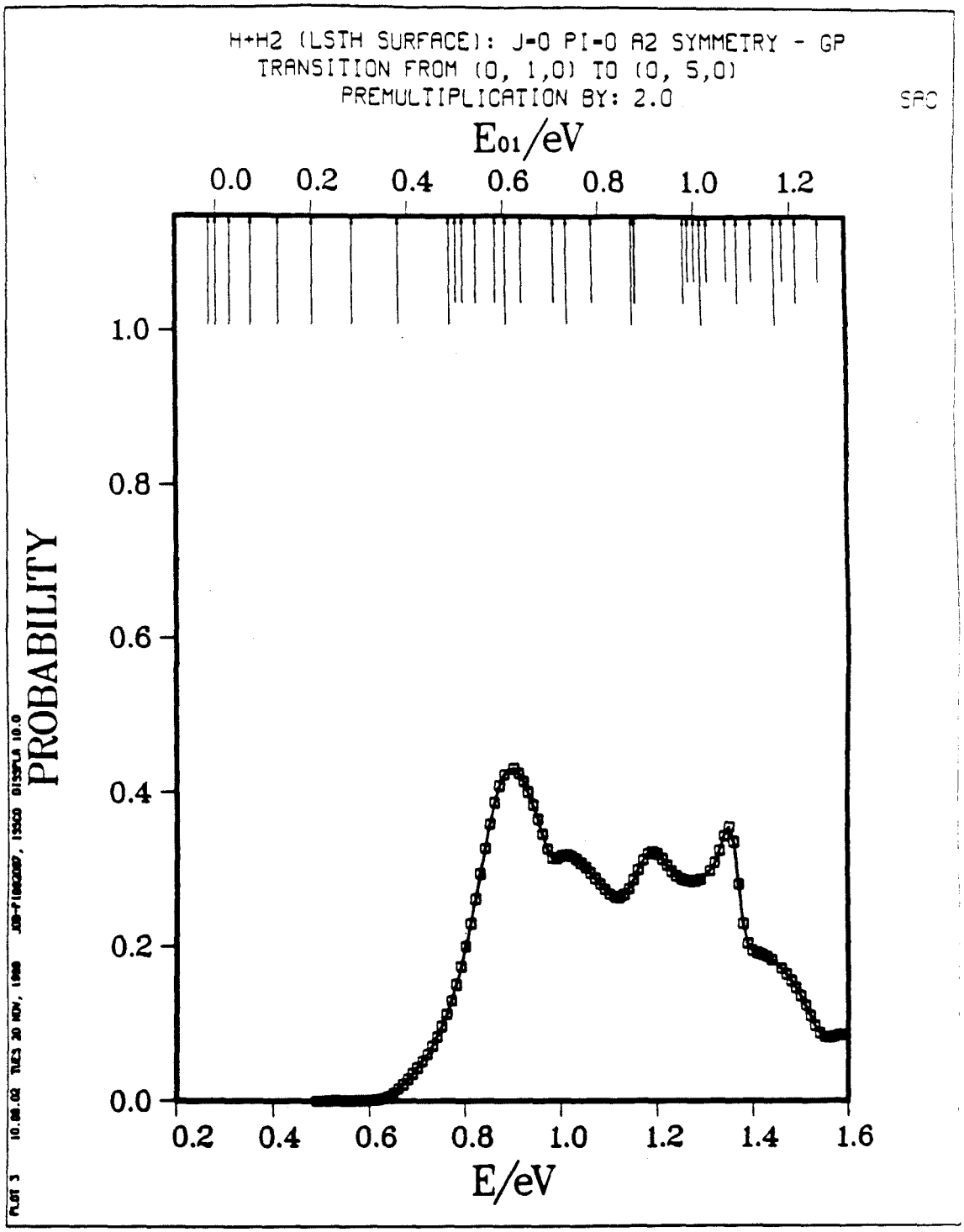
H+H2 (LSTH SURFACE): J=0 PI=0 A2 SYMMETRY - GP
TRANSITION FROM (0, 1,0) TO (0, 5,0)
PREMULTIPLICATION BY: 2.0
SAC
E01/eV
0.0
0.2
0.4
0.6
0.8
1.0
1.2
PROBABILITY
0.0
0.2
0.4
0.6
0.8
1.0
E/eV
0.2
0.4
0.6
0.8
1.0
1.2
1.4
1.6

Fig. 7.15c

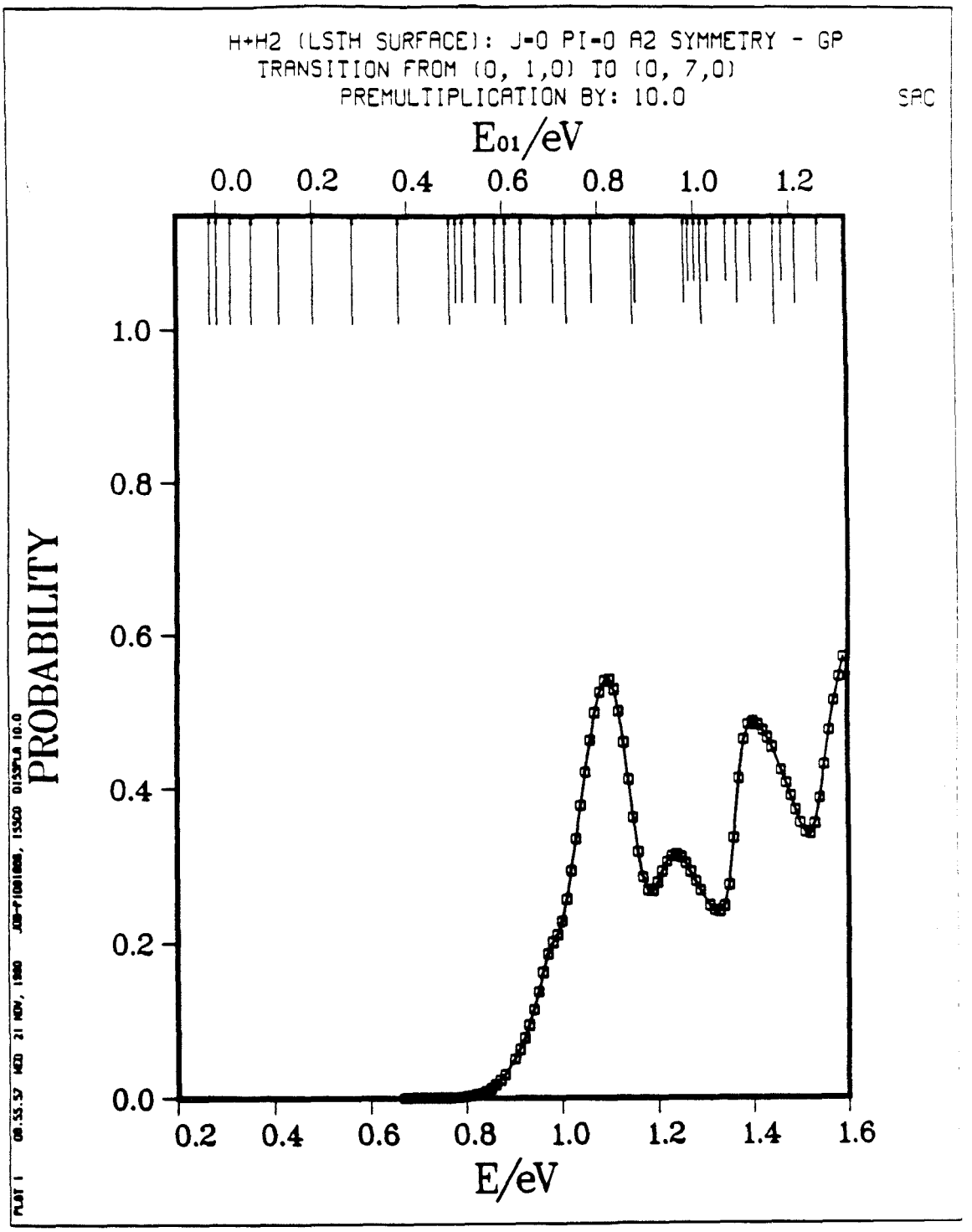
H+H2 (LSTH SURFACE): J=0 PI=0 A2 SYMMETRY - GP
TRANSITION FROM (0, 1,0) TO (0, 7,0)
PREMULTIPLICATION BY: 10.0
SRC
E01/eV
0.0
0.2
0.4
0.6
0.8
1.0
1.2
PROBABILITY
0.0
0.2
0.4
0.6
0.8
1.0
E/eV
0.2
0.4
0.6
0.8
1.0
1.2
1.4
1.6

Fig. 7.15d

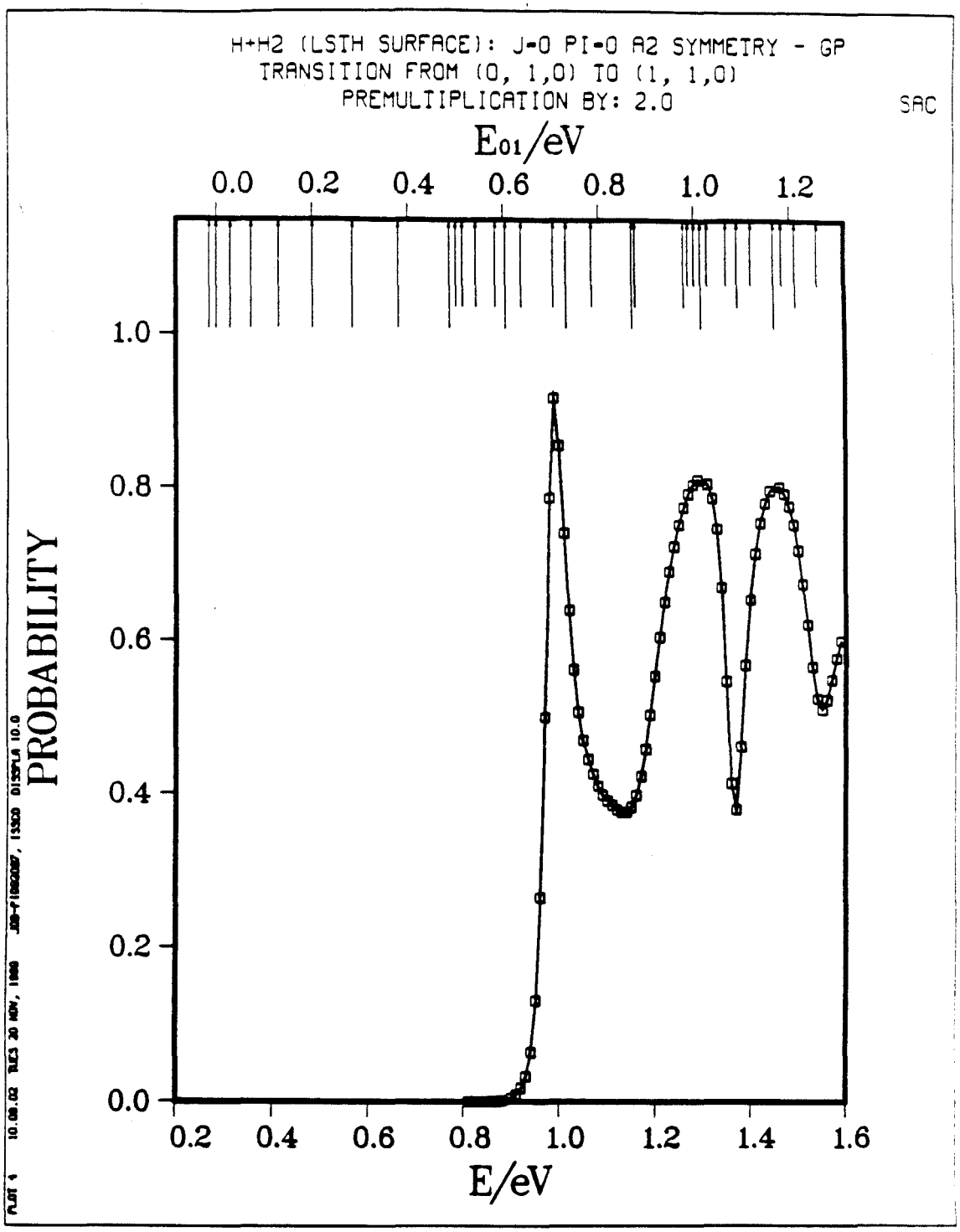
H+H2 (LSTH SURFACE): J=0 PI=0 A2 SYMMETRY - GP
TRANSITION FROM (0, 1,0) TO (1, 1,0)
PREMULTIPLICATION BY: 2.0
SAC
E01/eV
0.0
0.2
0.4
0.6
0.8
1.0
1.2
PROBABILITY
0.0
0.2
0.4
0.6
0.8
1.0
E/eV
0.2
0.4
0.6
0.8
1.0
1.2
1.4
1.6

Fig. 7.16a

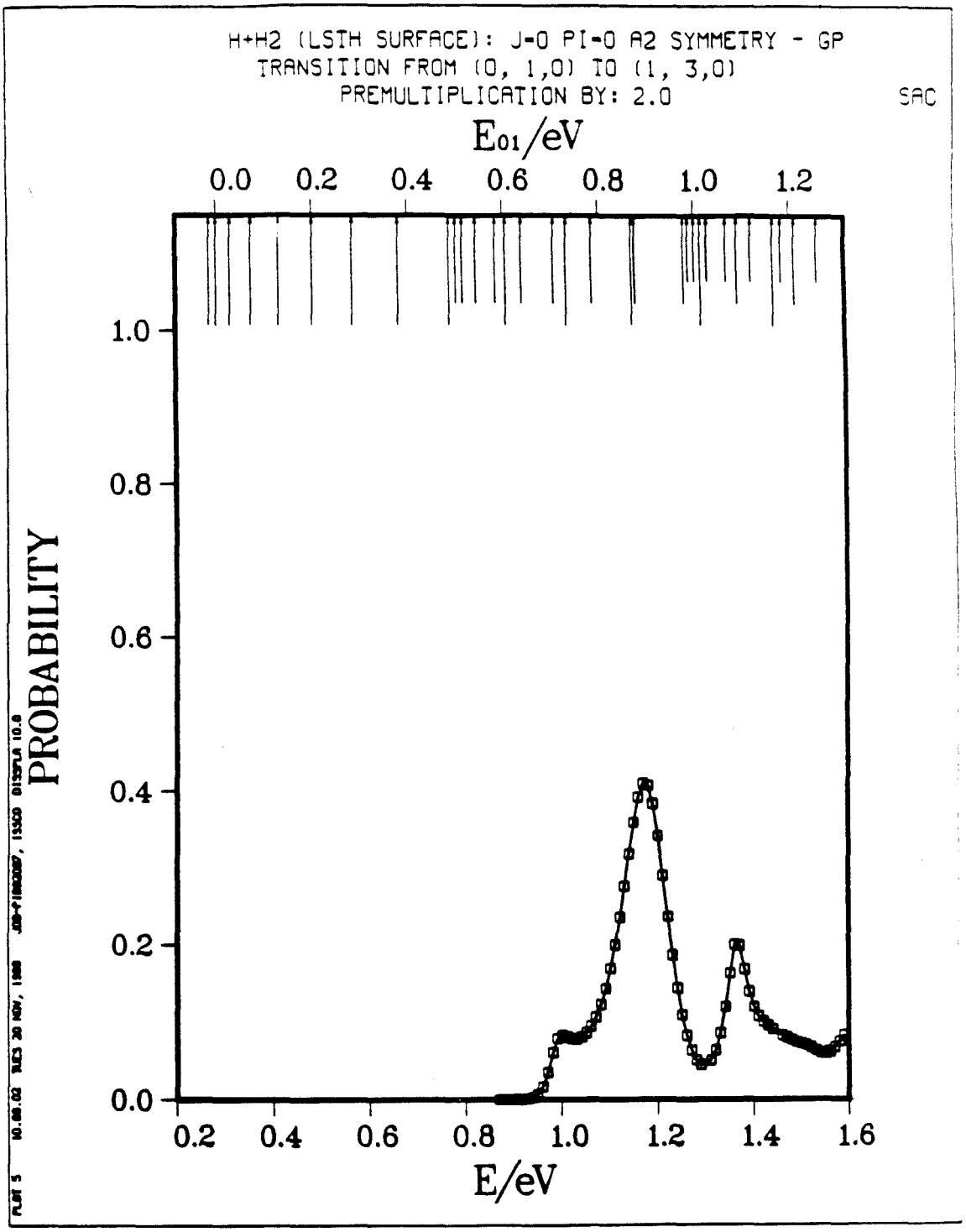
H+H2 (LSTH SURFACE): J=0 PI=0 A2 SYMMETRY - GP
TRANSITION FROM (0, 1,0) TO (1, 3,0)
PREMULTIPLICATION BY: 2.0
SAC
E01/eV
0.0
0.2
0.4
0.6
0.8
1.0
1.2
PROBABILITY
0.0
0.2
0.4
0.6
0.8
1.0
E/eV
0.2
0.4
0.6
0.8
1.0
1.2
1.4
1.6

Fig. 7.16b

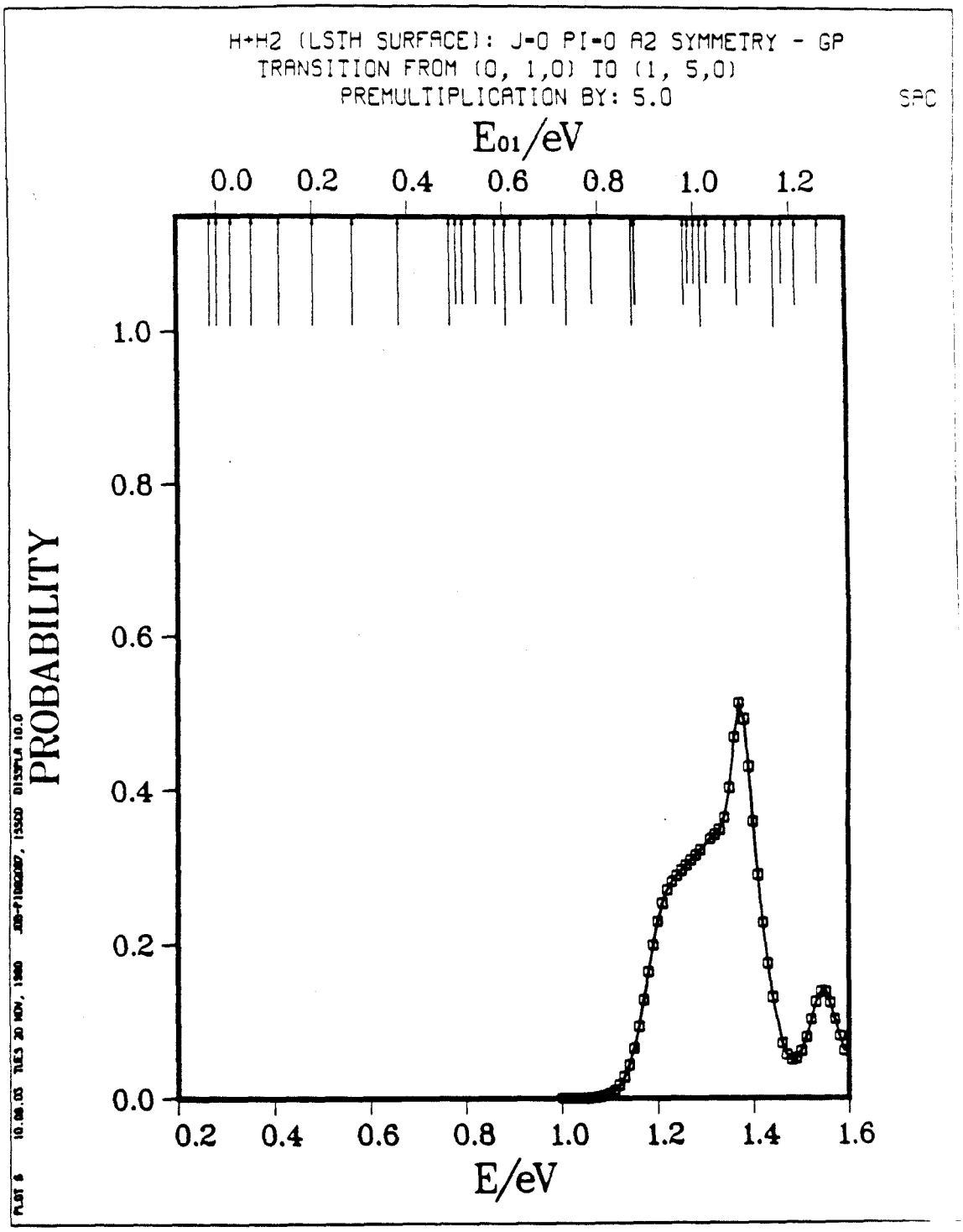
H+H2 (LSTH SURFACE): J=0 PI=0 A2 SYMMETRY - GP
TRANSITION FROM (0, 1,0) TO (1, 5,0)
PREMULTIPLICATION BY: 5.0
SPC
E01/eV
0.0
0.2
0.4
0.6
0.8
1.0
1.2
PROBABILITY
0.0
0.2
0.4
0.6
0.8
1.0
E/eV
0.2
0.4
0.6
0.8
1.0
1.2
1.4
1.6

Fig. 7.16c

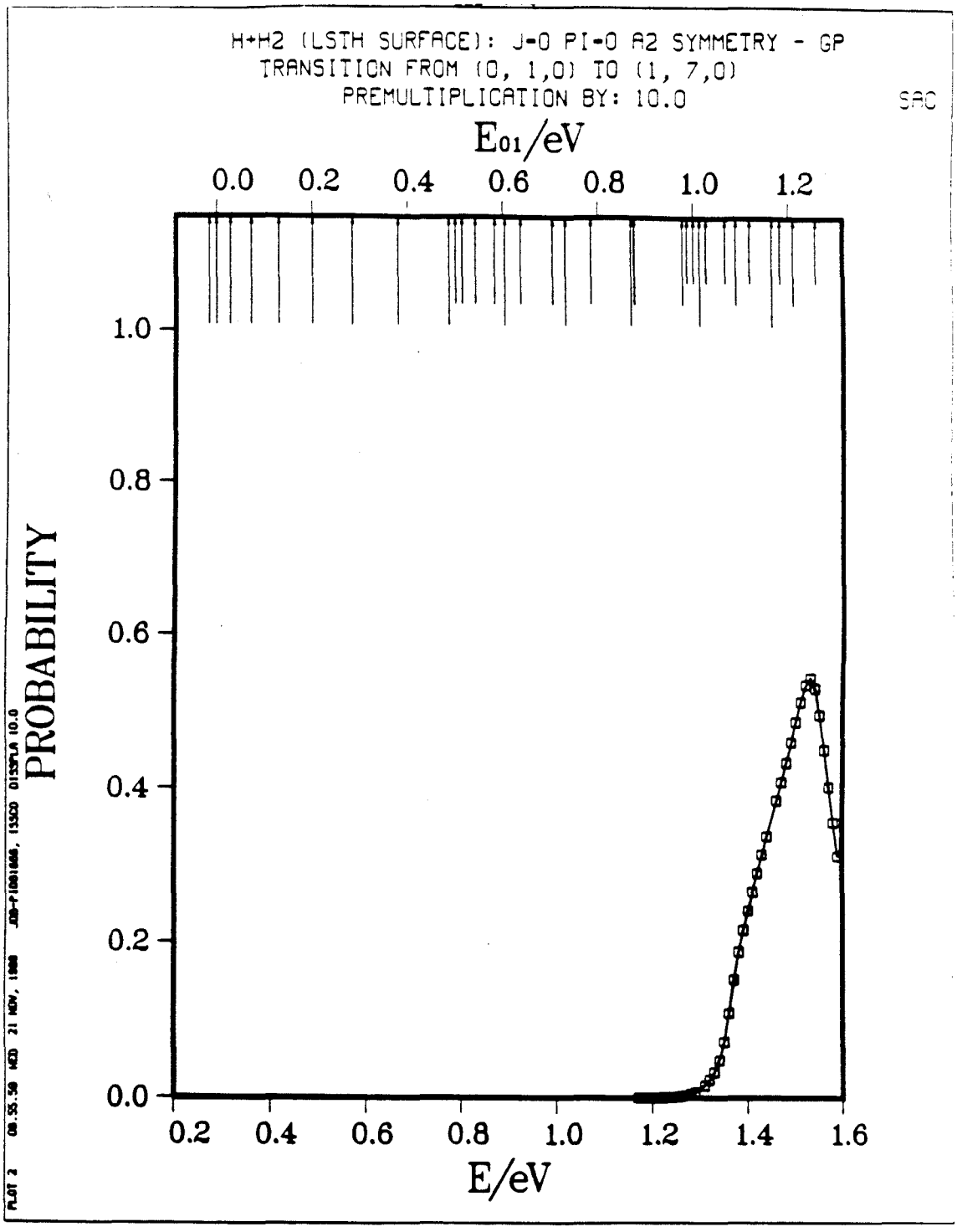
H+H2 (LSTH SURFACE): J=0 PI=0 A2 SYMMETRY - GP
TRANSITION FROM (0, 1,0) TO (1, 7,0)
PREMULTIPLICATION BY: 10.0
SAC
E01/eV
0.0
0.2
0.4
0.6
0.8
1.0
1.2
PROBABILITY
0.0
0.2
0.4
0.6
0.8
1.0
E/eV
0.2
0.4
0.6
0.8
1.0
1.2
1.4
1.6

Fig. 7.16d

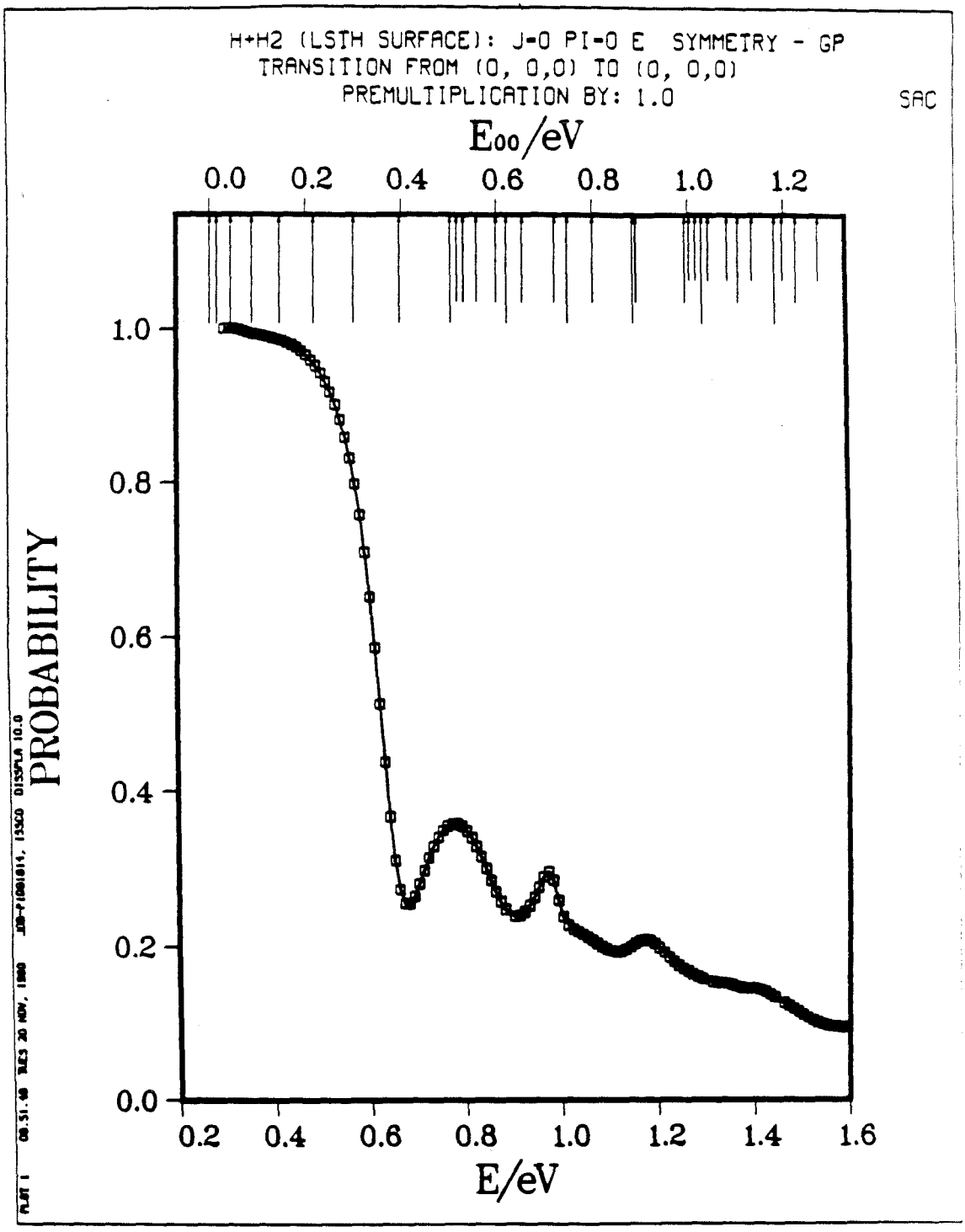
H+H2 (LSTH SURFACE): J=0 PI=0 E SYMMETRY - GP
TRANSITION FROM (0, 0,0) TO (0, 0,0)
PREMULTIPLICATION BY: 1.0
SAC
E00/eV
0.0
0.2
0.4
0.6
0.8
1.0
1.2
PROBABILITY
0.0
0.2
0.4
0.6
0.8
1.0
E/eV
0.2
0.4
0.6
0.8
1.0
1.2
1.4
1.6

Fig. 7.17a

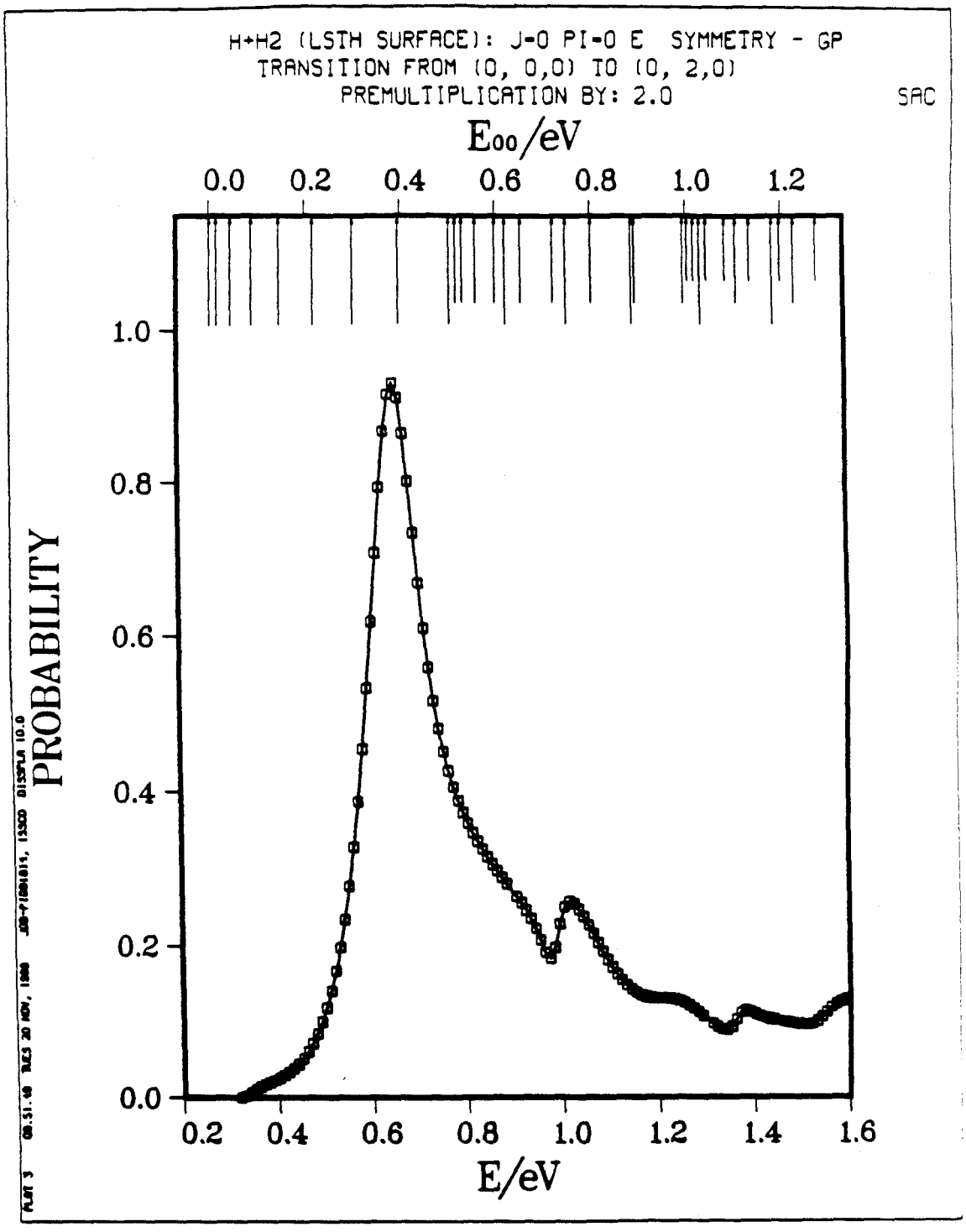
H+H2 (LSTH SURFACE): J=0 PI=0 E SYMMETRY - GP
TRANSITION FROM (0, 0,0) TO (0, 2,0)
PREMULTIPLICATION BY: 2.0
SAC
E00/eV
0.0
0.2
0.4
0.6
0.8
1.0
1.2
PROBABILITY
0.0
0.2
0.4
0.6
0.8
1.0
E/eV
0.2
0.4
0.6
0.8
1.0
1.2
1.4
1.6

Fig. 7.17b

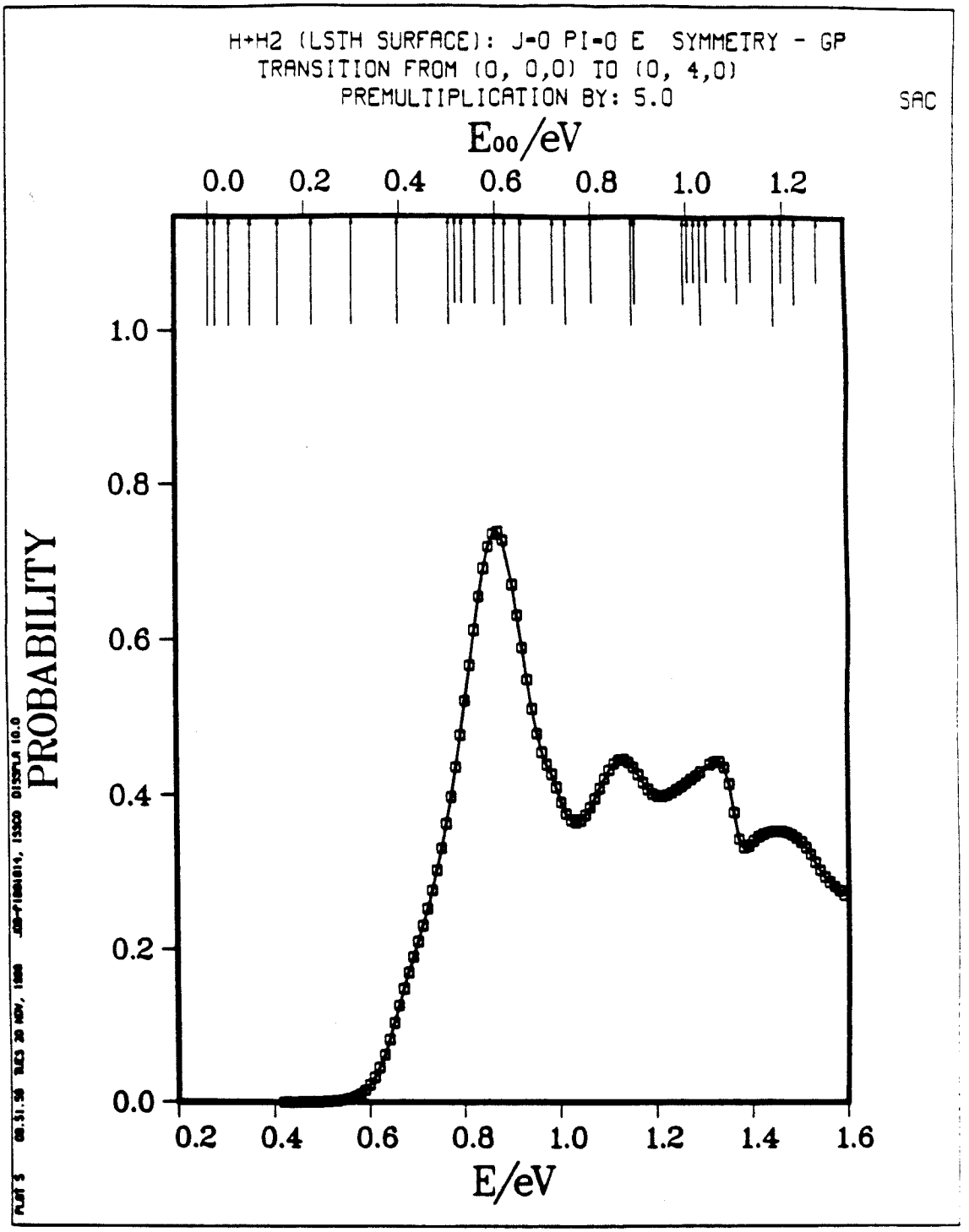
H+H2 (LSTH SURFACE): J=0 PI=0 E SYMMETRY - GP
TRANSITION FROM (0, 0,0) TO (0, 4,0)
PREMULTIPLICATION BY: 5.0
SAC
E00/eV
0.0
0.2
0.4
0.6
0.8
1.0
1.2
PROBABILITY
1.0
0.8
0.6
0.4
0.2
0.0
0.2
0.4
0.6
0.8
1.0
1.2
1.4
1.6
E/eV

Fig. 7.17c

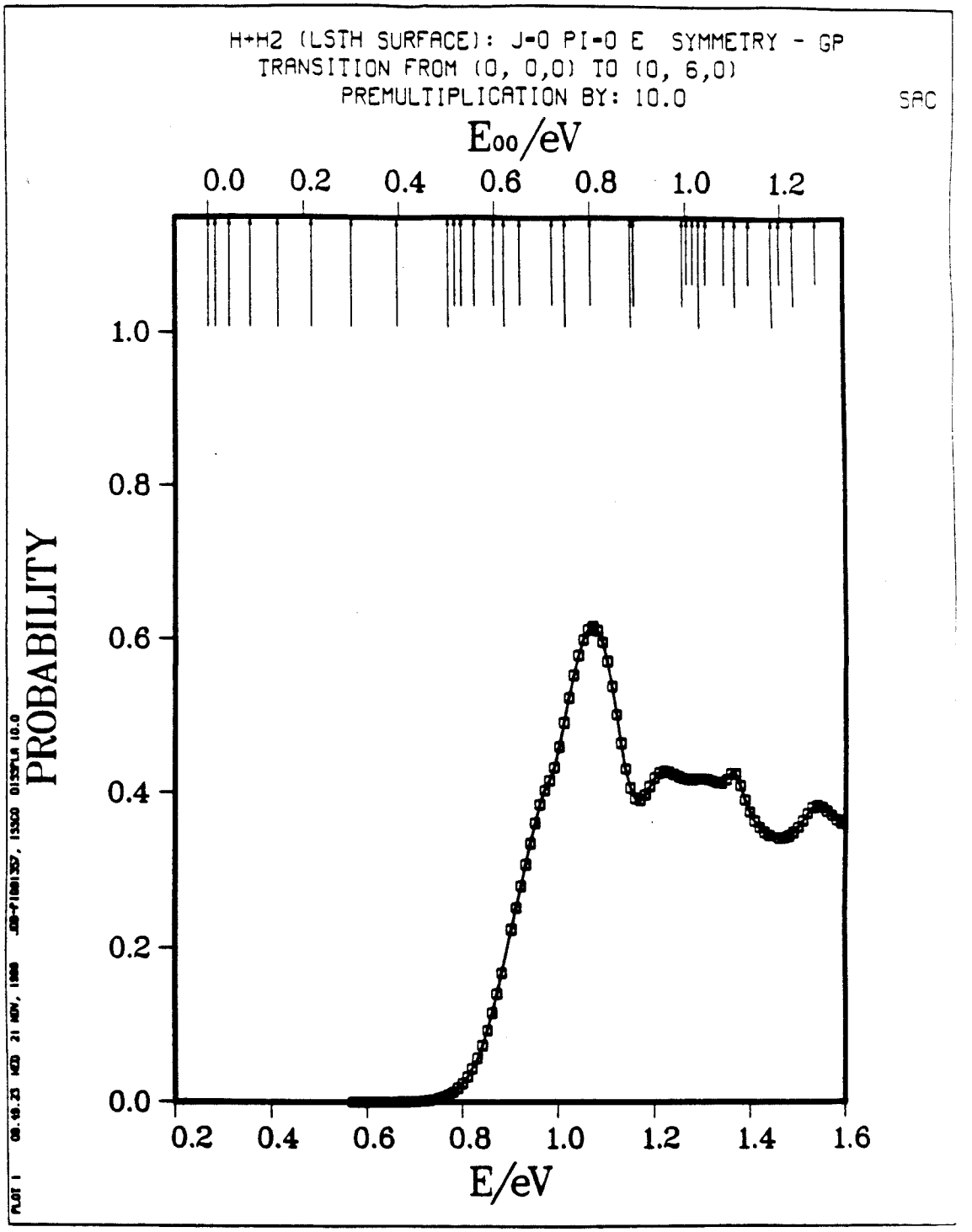
H+H2 (LSTH SURFACE): J=0 PI=0 E SYMMETRY - GP
TRANSITION FROM (0, 0,0) TO (0, 6,0)
PREMULTIPLICATION BY: 10.0
SAC
E00/eV
0.0
0.2
0.4
0.6
0.8
1.0
1.2
PROBABILITY
0.0
0.2
0.4
0.6
0.8
1.0
E/eV
0.2
0.4
0.6
0.8
1.0
1.2
1.4
1.6

Fig. 7.17d

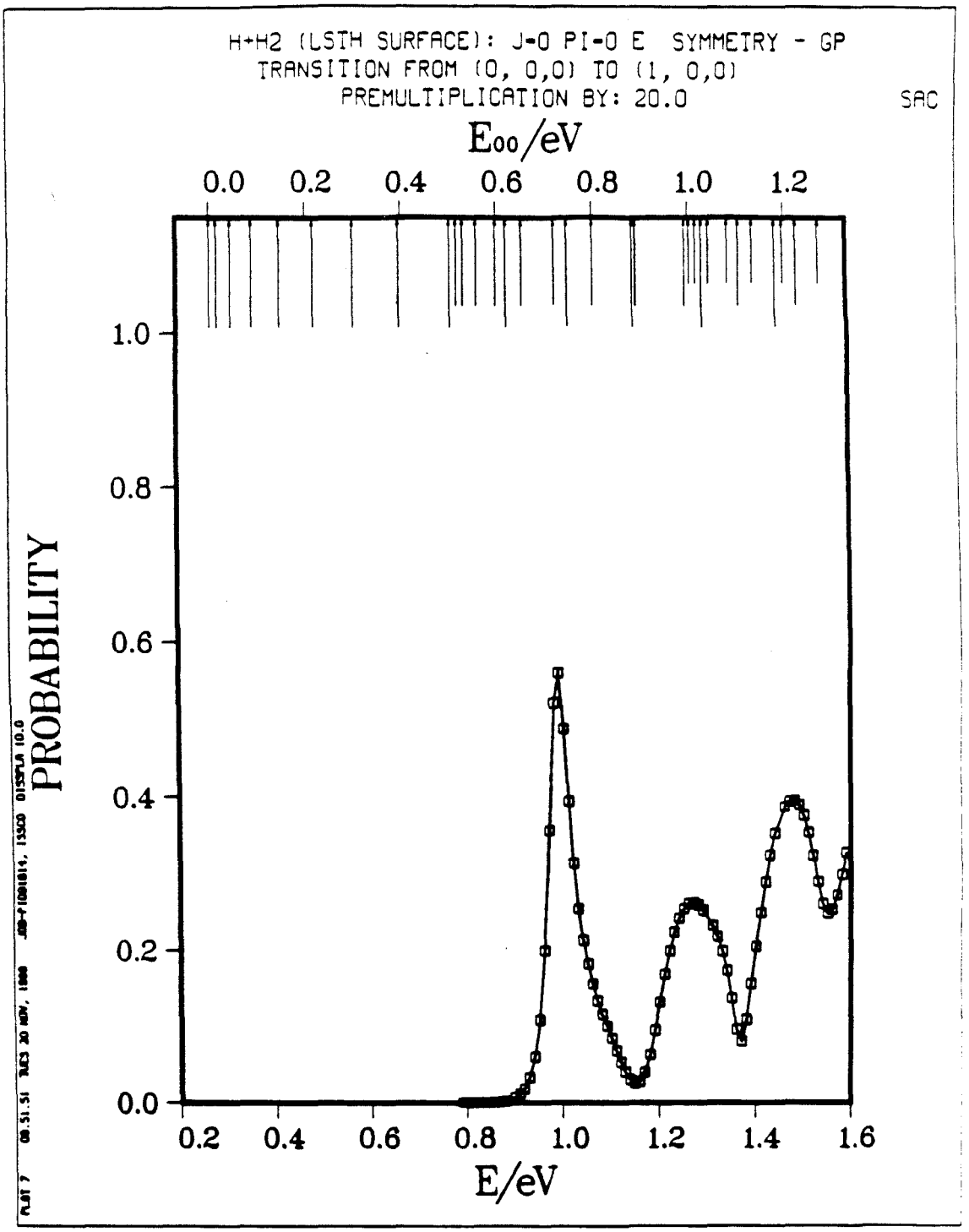
H+H2 (LSTH SURFACE): J=0 PI=0 E SYMMETRY - GP
TRANSITION FROM (0, 0,0) TO (1, 0,0)
PREMULTIPLICATION BY: 20.0
SAC
E00/eV
0.0
0.2
0.4
0.6
0.8
1.0
1.2
PROBABILITY
0.0
0.2
0.4
0.6
0.8
1.0
E/eV
0.2
0.4
0.6
0.8
1.0
1.2
1.4
1.6

Fig. 7.18a

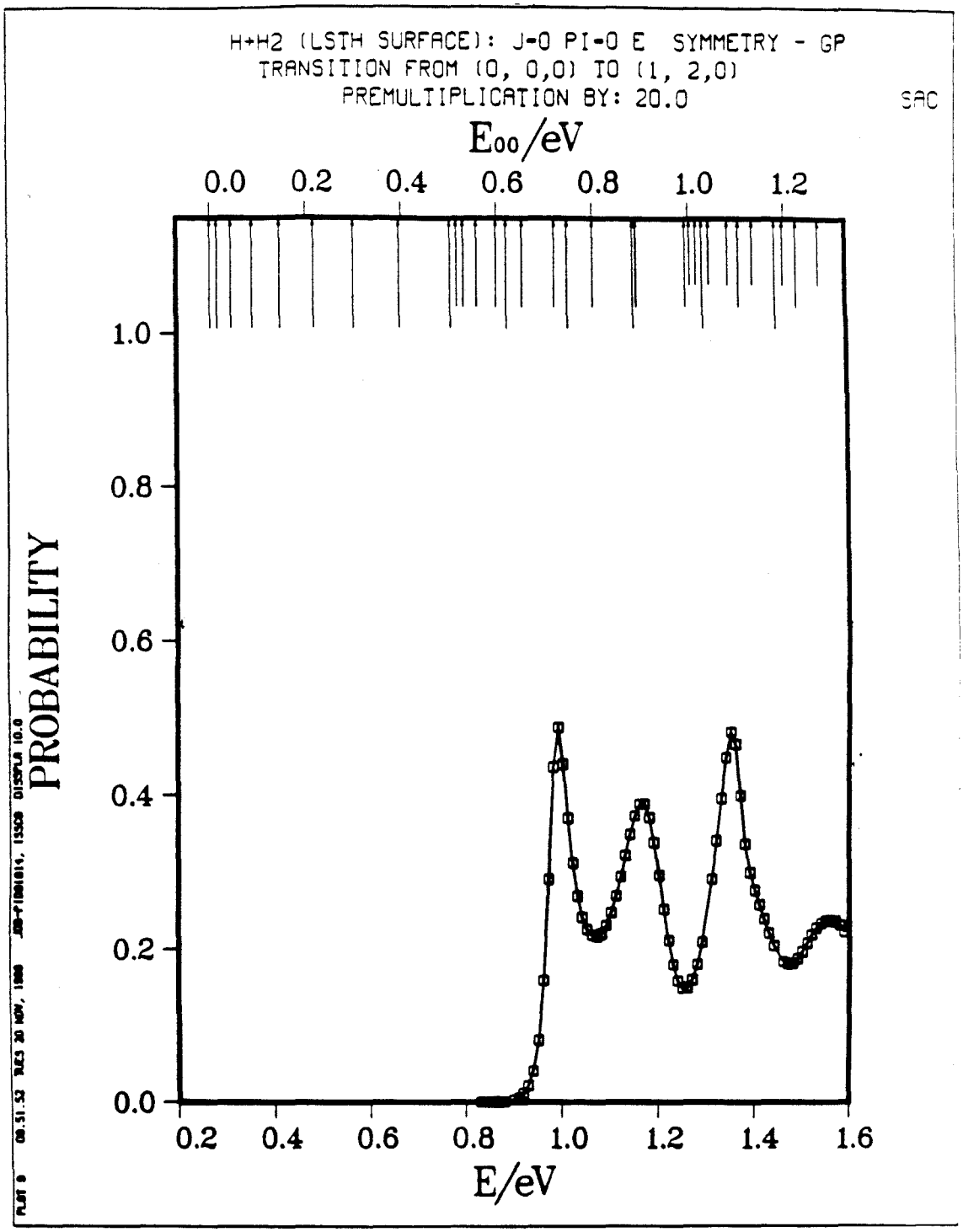
H+H2 (LSTH SURFACE): J=0 PI=0 E SYMMETRY - GP
TRANSITION FROM (0, 0,0) TO (1, 2,0)
PREMULTIPLICATION BY: 20.0
SAC
E00/eV
0.0
0.2
0.4
0.6
0.8
1.0
1.2
PROBABILITY
0.0
0.2
0.4
0.6
0.8
1.0
E/eV
0.2
0.4
0.6
0.8
1.0
1.2
1.4
1.6

Fig. 7.18b

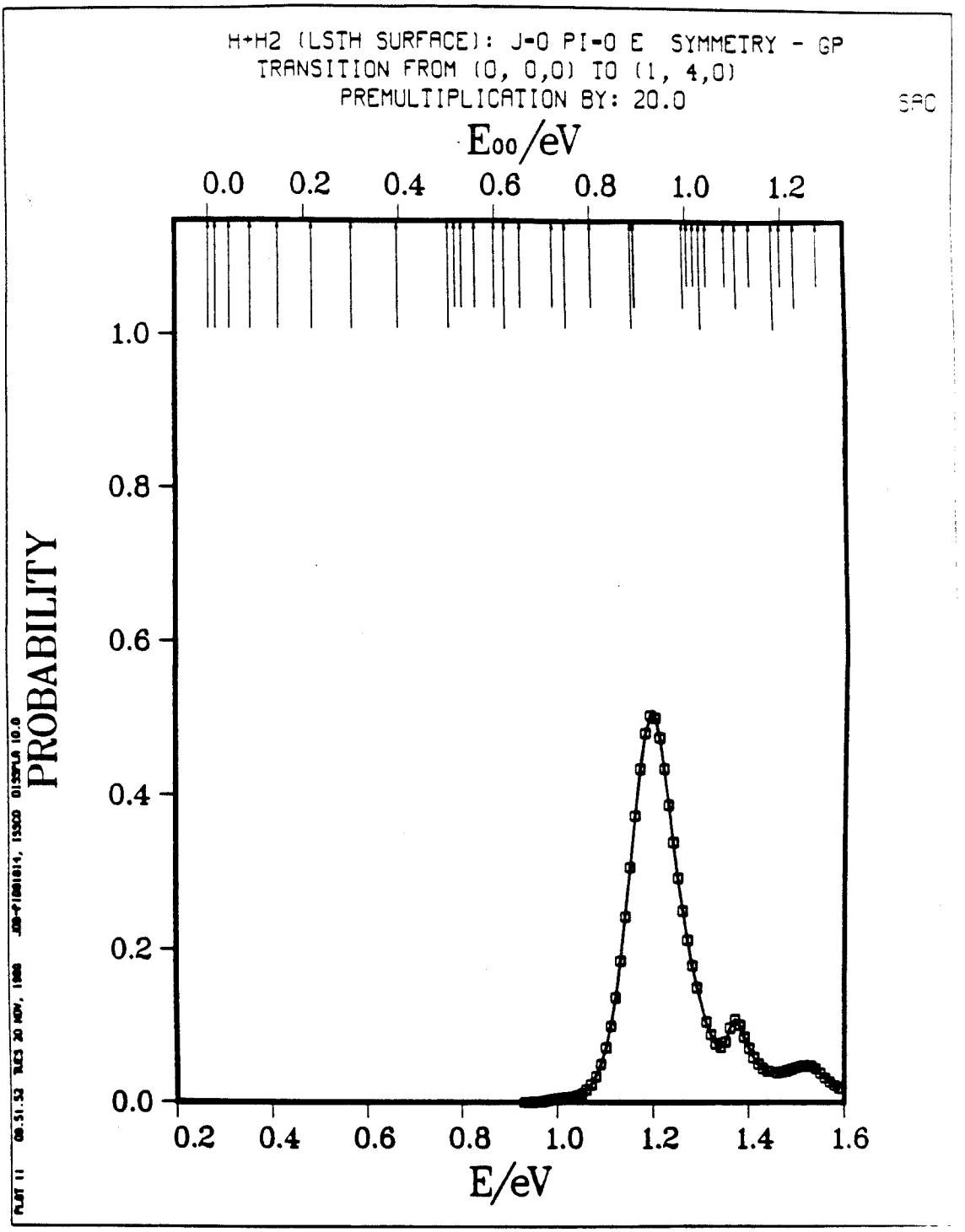
H+H2 (LSTH SURFACE): J=0 PI=0 E SYMMETRY - GP
TRANSITION FROM (0, 0,0) TO (1, 4,0)
PREMULTIPLICATION BY: 20.0
SPC
E00/eV
0.0
0.2
0.4
0.6
0.8
1.0
1.2
PROBABILITY
1.0
0.8
0.6
0.4
0.2
0.0
0.2
0.4
0.6
0.8
1.0
1.2
1.4
1.6
E/eV

Fig. 7.18c

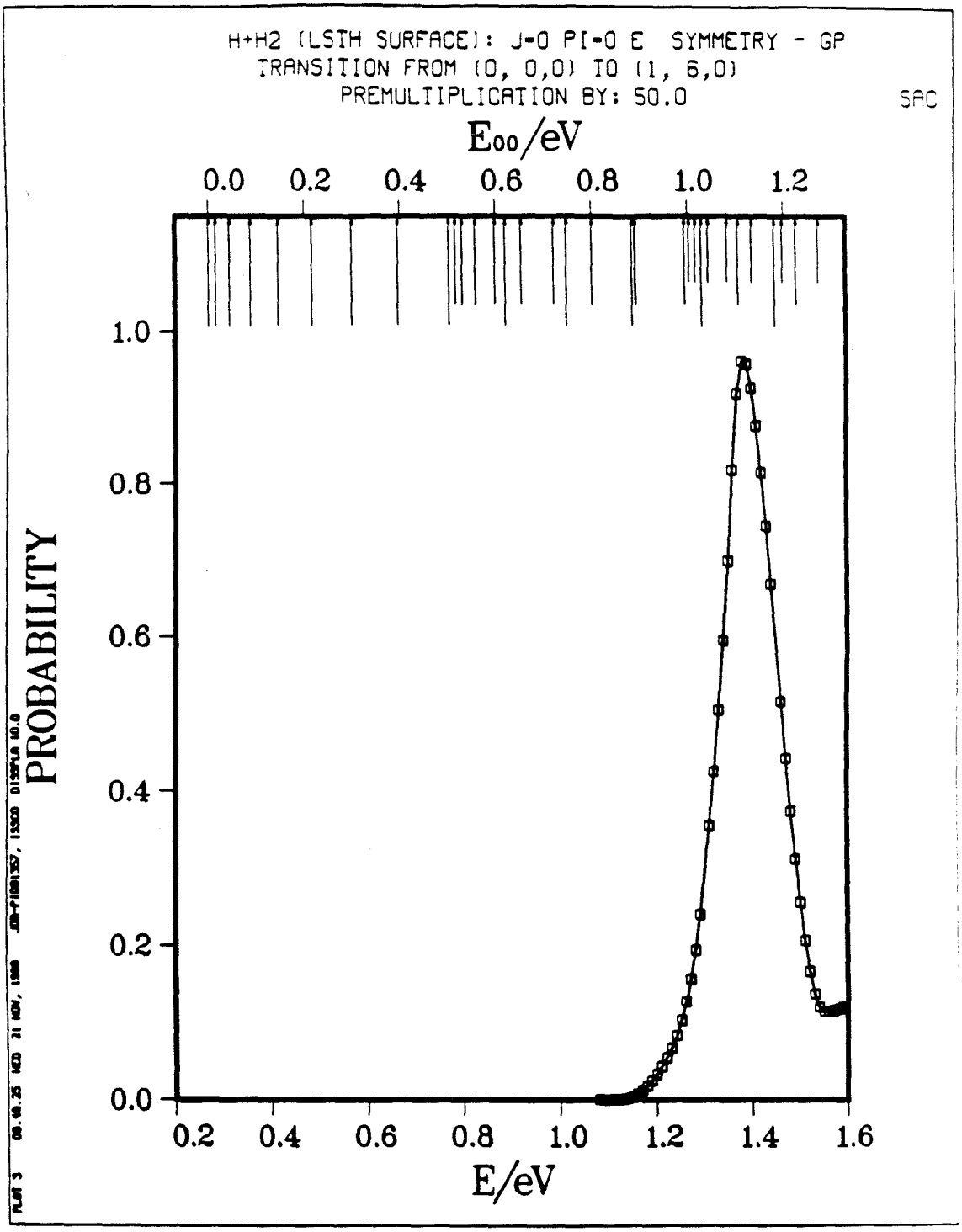
H+H2 (LSTH SURFACE): J=0 PI=0 E SYMMETRY - GP
TRANSITION FROM (0, 0,0) TO (1, 6,0)
PREMULTIPLICATION BY: 50.0
SPC
Eoo/eV
0.0
0.2
0.4
0.6
0.8
1.0
1.2
PROBABILITY
0.0
0.2
0.4
0.6
0.8
1.0
1.2
1.4
1.6
E/eV

Fig. 7.18d

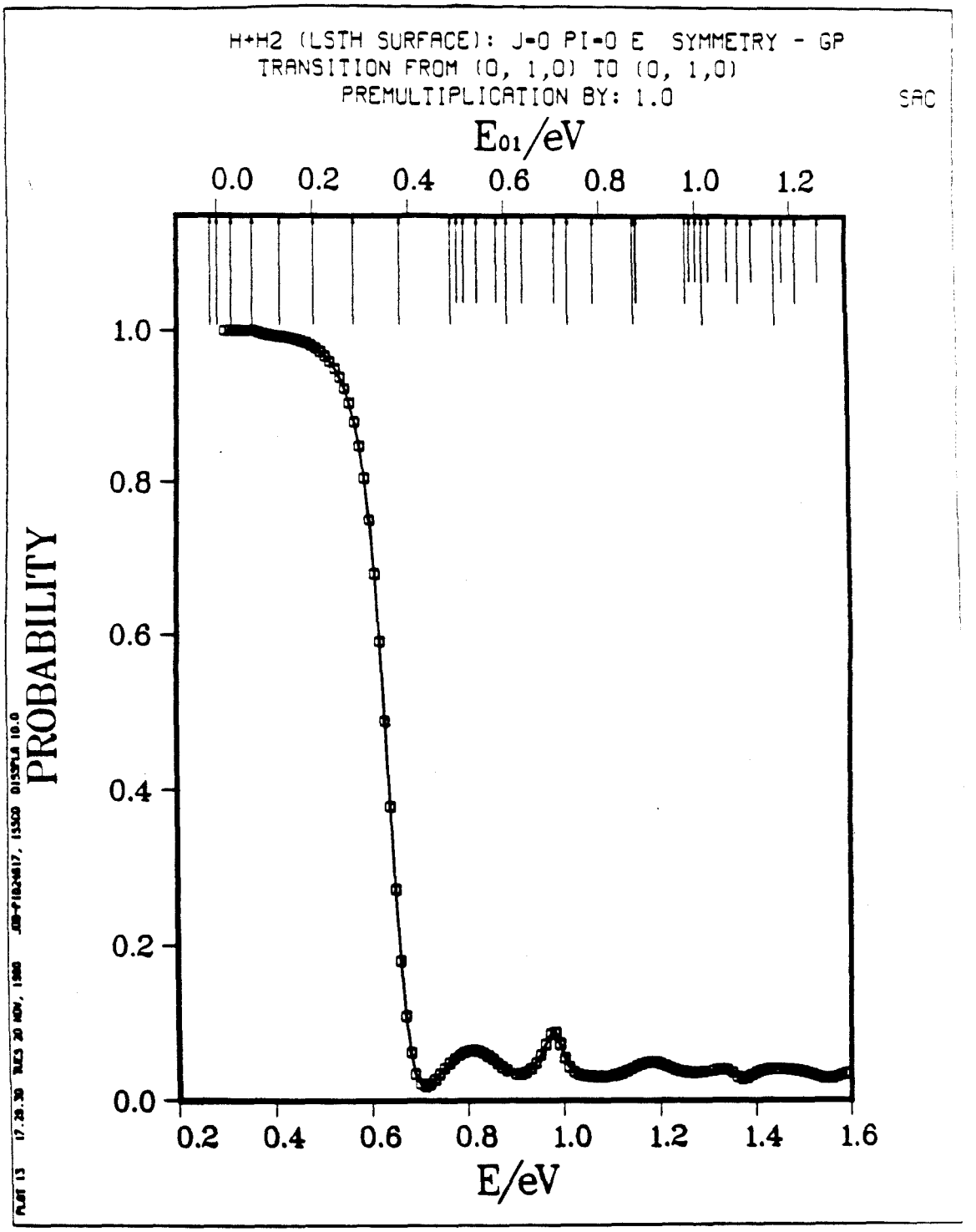
H+H2 (LSTH SURFACE): J=0 PI=0 E SYMMETRY - GP
TRANSITION FROM (0, 1,0) TO (0, 1,0)
PREMULTIPLICATION BY: 1.0
SAC
E01/eV
0.0
0.2
0.4
0.6
0.8
1.0
1.2
PROBABILITY
0.0
0.2
0.4
0.6
0.8
1.0
0.2
0.4
0.6
0.8
1.0
1.2
1.4
1.6
E/eV

Fig. 7.19a

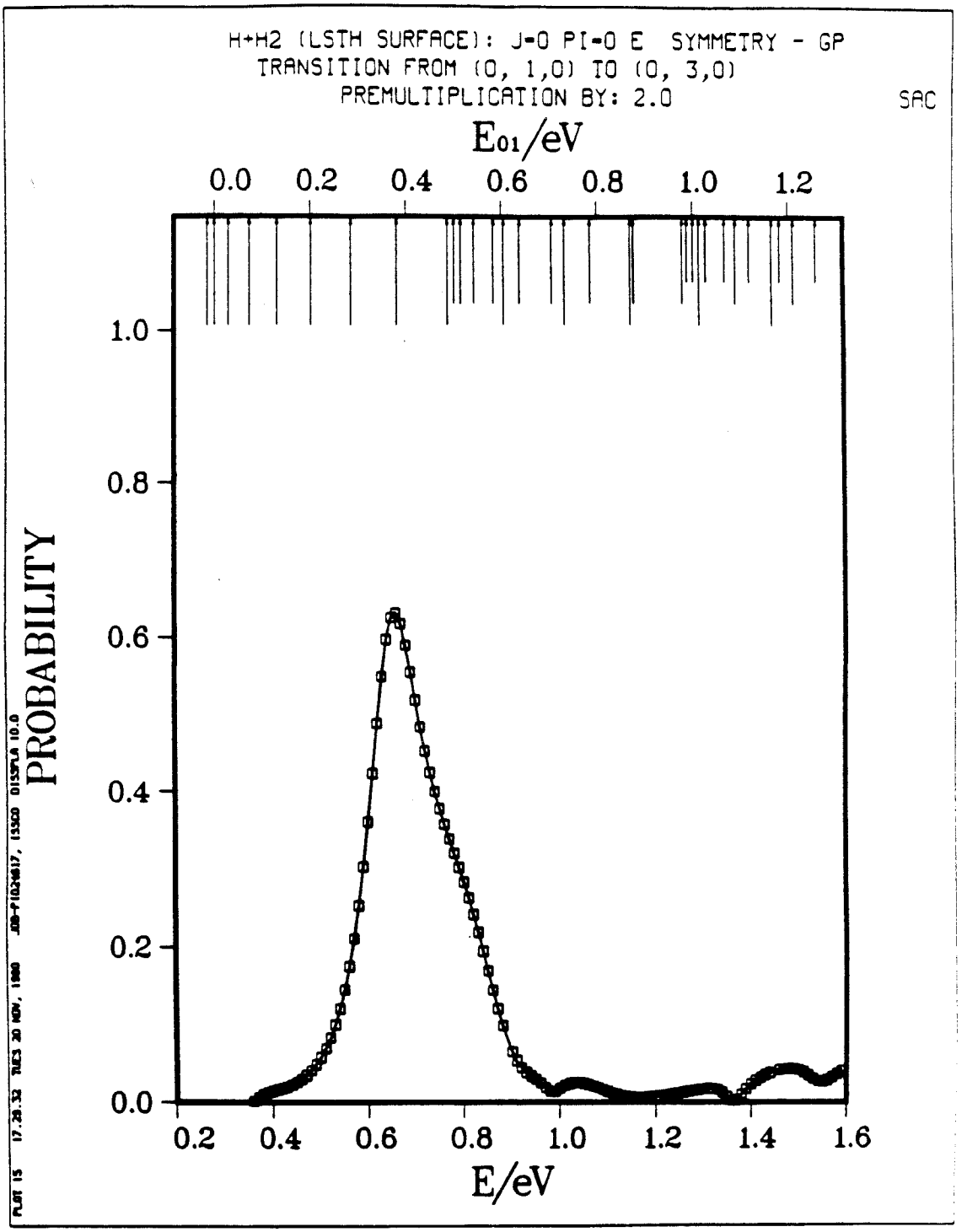
H+H2 (LSTH SURFACE): J=0 PI=0 E SYMMETRY - GP
TRANSITION FROM (0, 1,0) TO (0, 3,0)
PREMULTIPLICATION BY: 2.0
SAC
E01/eV
0.0
0.2
0.4
0.6
0.8
1.0
1.2
PROBABILITY
0.0
0.2
0.4
0.6
0.8
1.0
E/eV
0.2
0.4
0.6
0.8
1.0
1.2
1.4
1.6

Fig. 7.19b

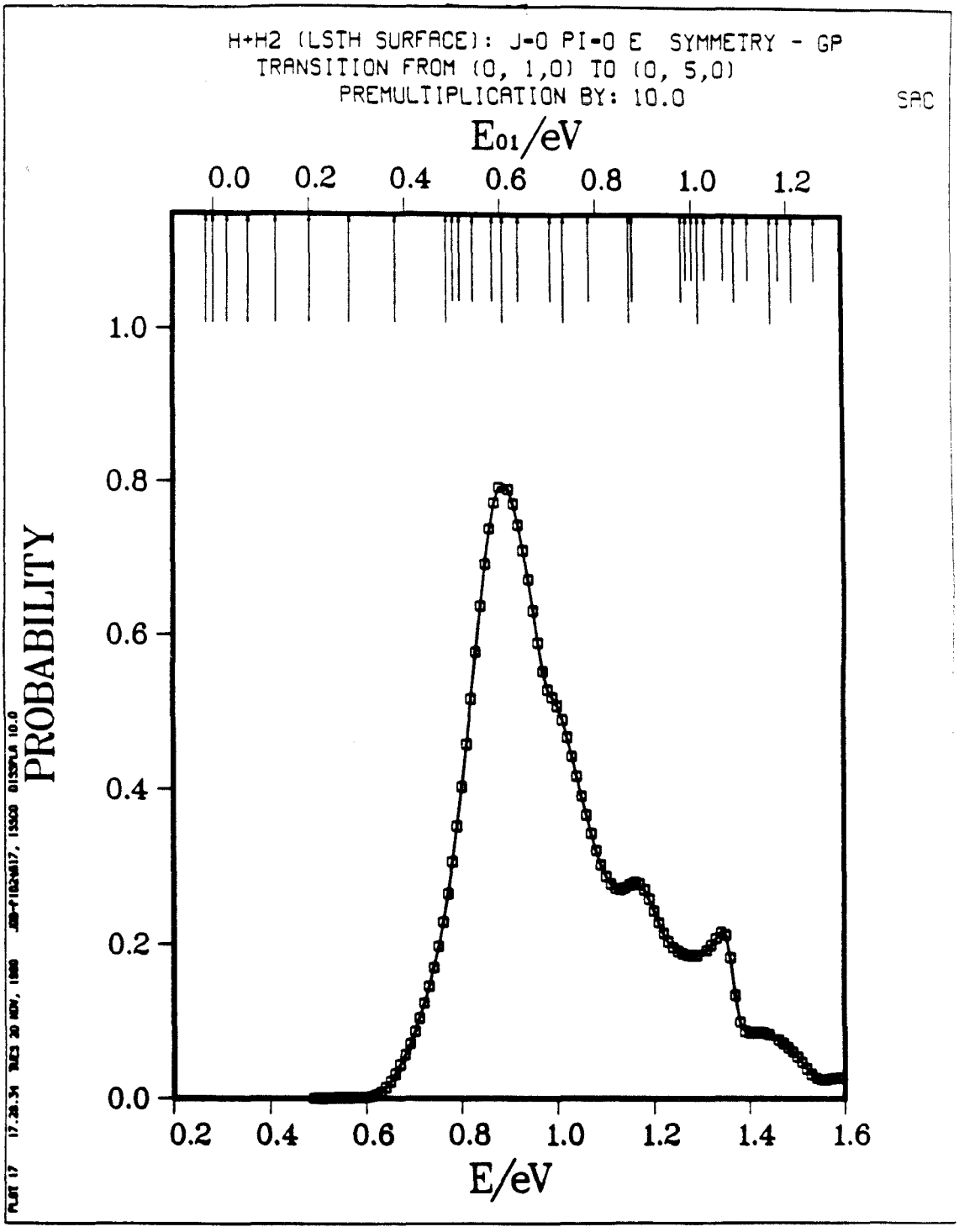
H+H2 (LSTH SURFACE): J=0 PI=0 E SYMMETRY - GP
TRANSITION FROM (0, 1,0) TO (0, 5,0)
PREMULTIPLICATION BY: 10.0
SAC
E01/eV
0.0
0.2
0.4
0.6
0.8
1.0
1.2
PROBABILITY
1.0
0.8
0.6
0.4
0.2
0.0
0.2
0.4
0.6
0.8
1.0
1.2
1.4
1.6
E/eV

Fig. 7.19c

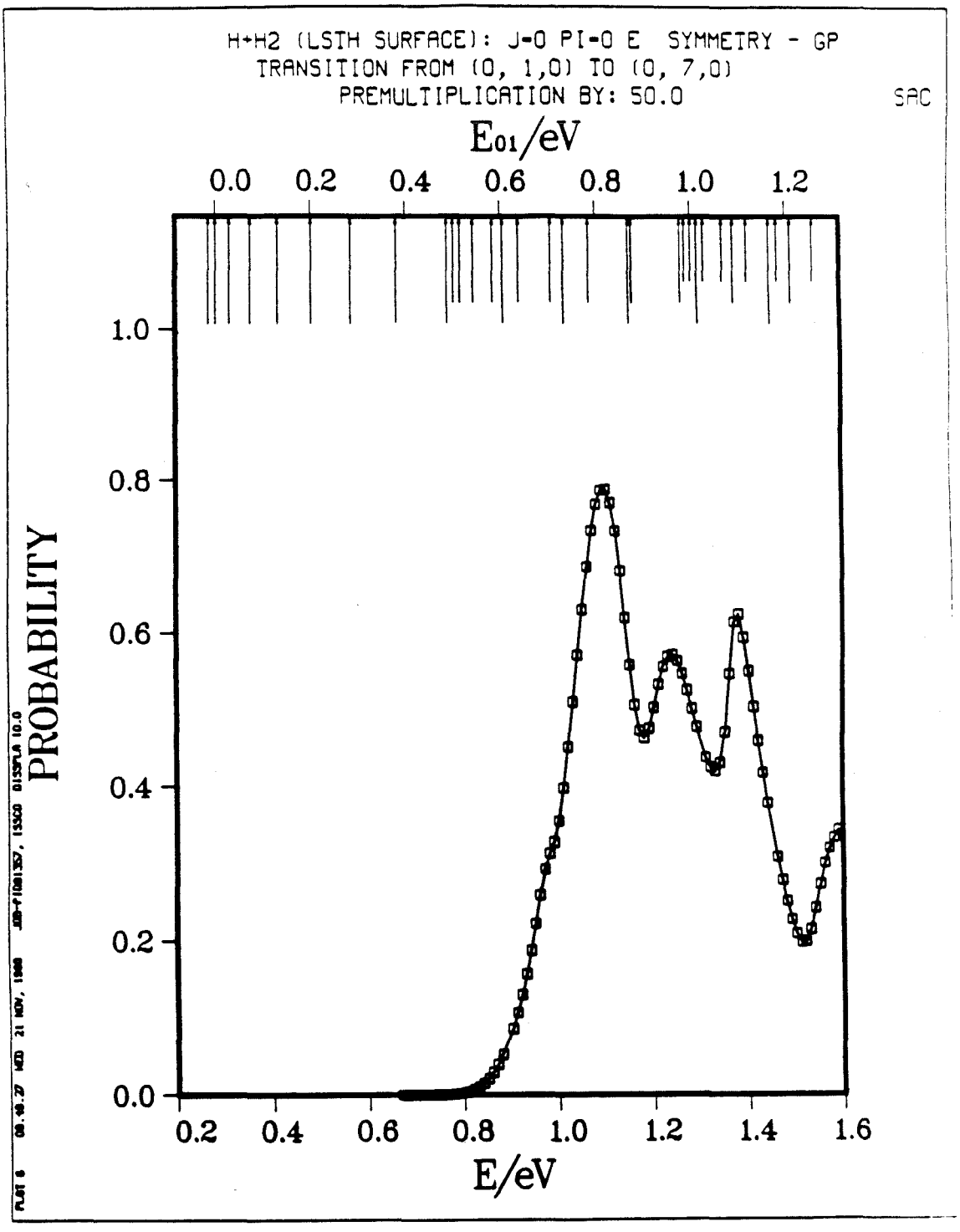
H+H2 (LSTH SURFACE): J=0 PI=0 E SYMMETRY - GP
TRANSITION FROM (0, 1,0) TO (0, 7,0)
PREMULTIPLICATION BY: 50.0
SAC
E01/eV
0.0
0.2
0.4
0.6
0.8
1.0
1.2
PROBABILITY
0.0
0.2
0.4
0.6
0.8
1.0
E/eV
0.2
0.4
0.6
0.8
1.0
1.2
1.4
1.6

Fig. 7.19d

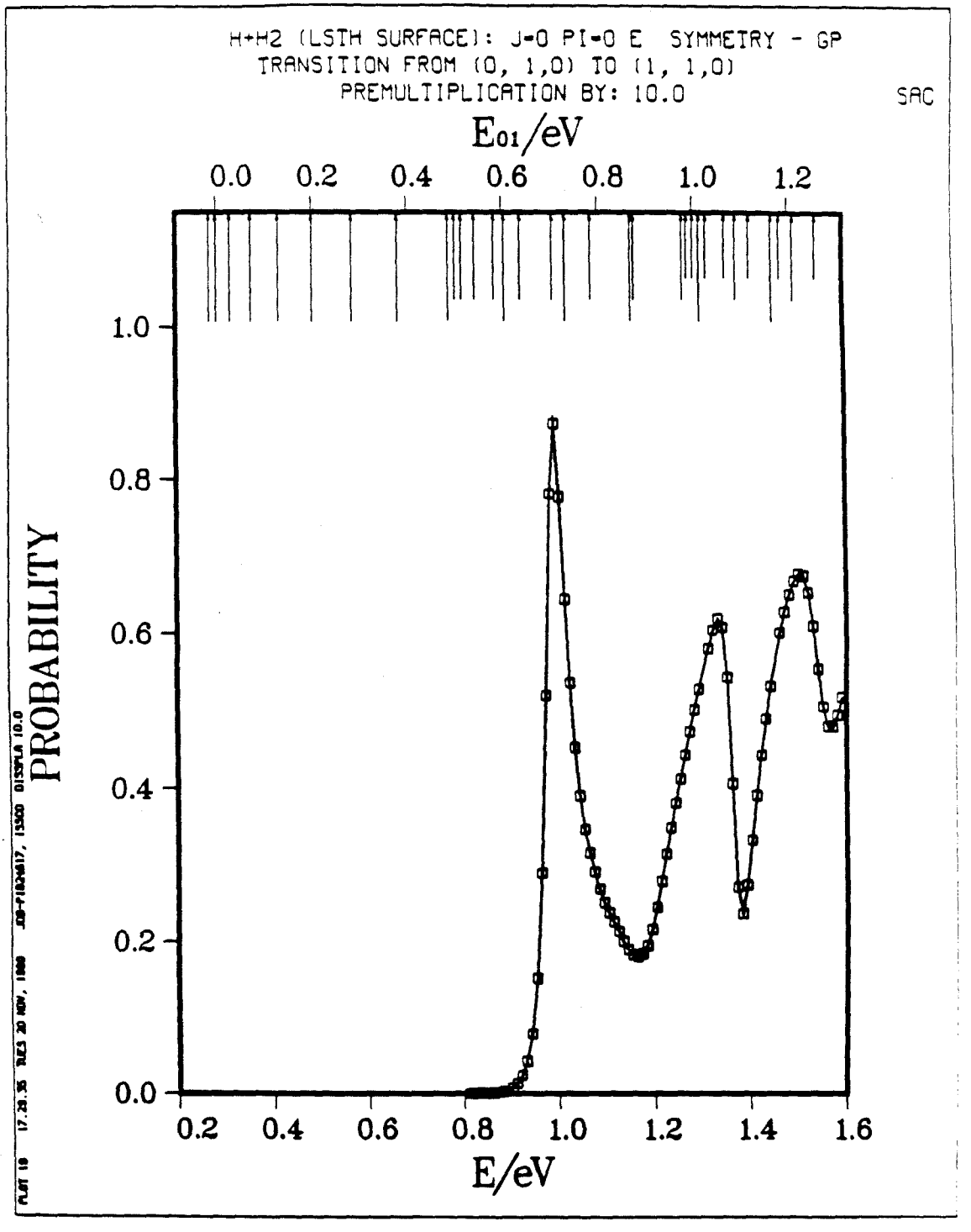
H+H2 (LSTH SURFACE): J=0 PI=0 E SYMMETRY - GP
TRANSITION FROM (0, 1,0) TO (1, 1,0)
PREMULTIPLICATION BY: 10.0
SAC
E01/eV
0.0
0.2
0.4
0.6
0.8
1.0
1.2
PROBABILITY
0.0
0.2
0.4
0.6
0.8
1.0
E/eV
0.2
0.4
0.6
0.8
1.0
1.2
1.4
1.6

Fig. 7.20a

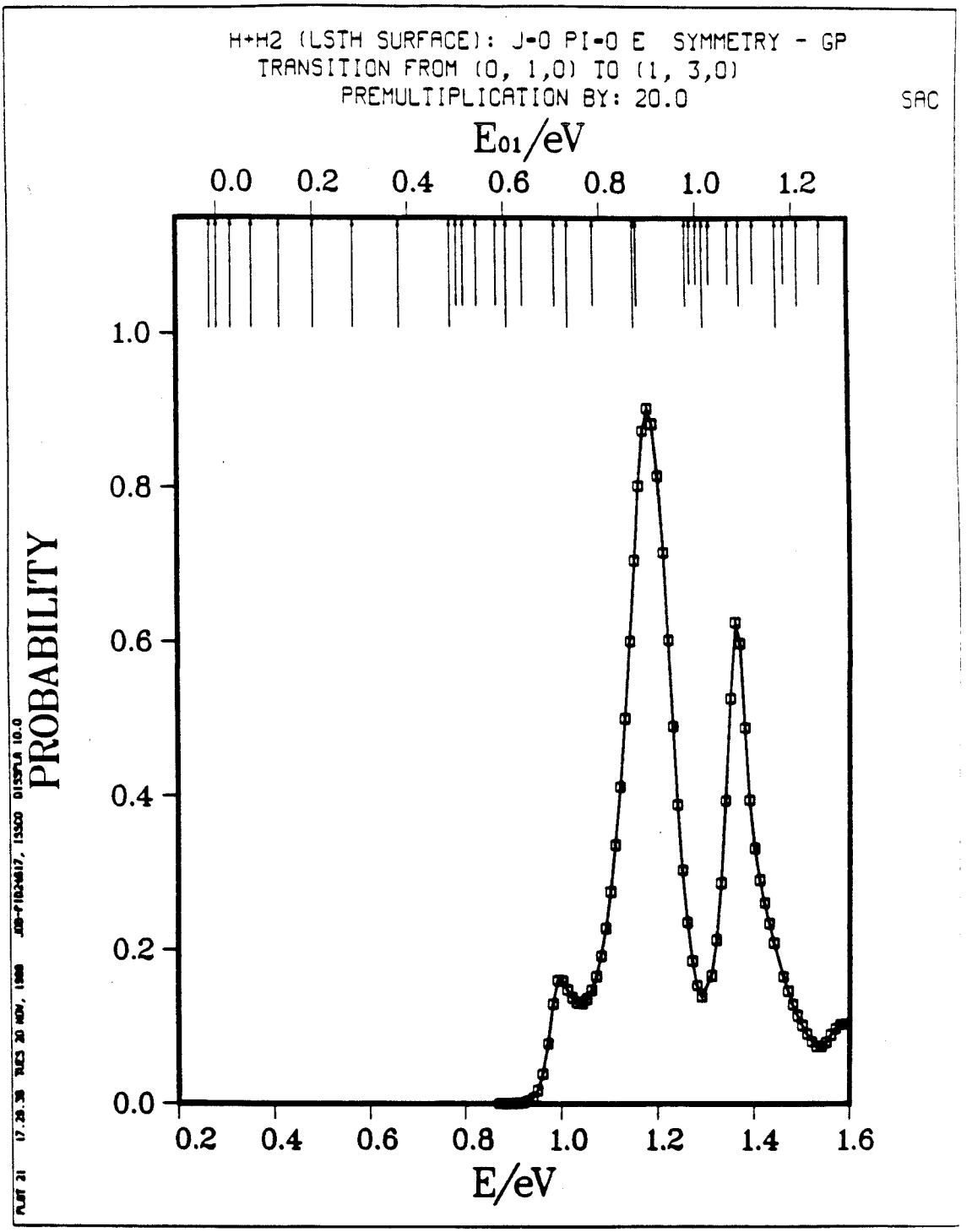
H+H2 (LSTH SURFACE): J=0 PI=0 E SYMMETRY - GP
TRANSITION FROM (0, 1,0) TO (1, 3,0)
PREMULTIPLICATION BY: 20.0
SAC
E01/eV
0.0
0.2
0.4
0.6
0.8
1.0
1.2
PROBABILITY
0.0
0.2
0.4
0.6
0.8
1.0
E/eV
0.2
0.4
0.6
0.8
1.0
1.2
1.4
1.6

Fig. 7.20b

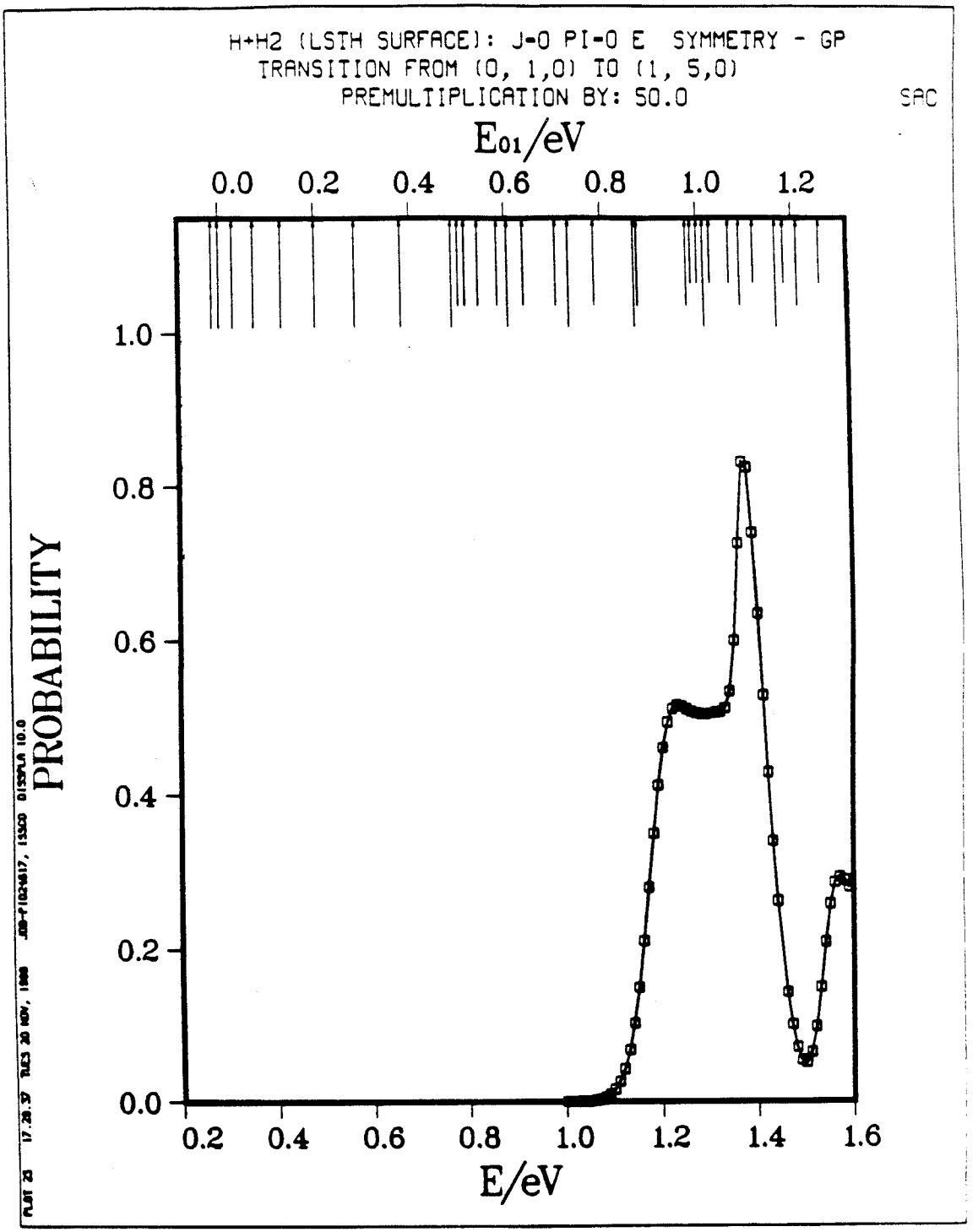
H+H2 (LSTH SURFACE): J=0 PI=0 E SYMMETRY - GP
TRANSITION FROM (0, 1,0) TO (1, 5,0)
PREMULTIPLICATION BY: 50.0
SAC
E01/eV
0.0
0.2
0.4
0.6
0.8
1.0
1.2
PROBABILITY
0.0
0.2
0.4
0.6
0.8
1.0
E/eV
0.2
0.4
0.6
0.8
1.0
1.2
1.4
1.6

Fig. 7.20c

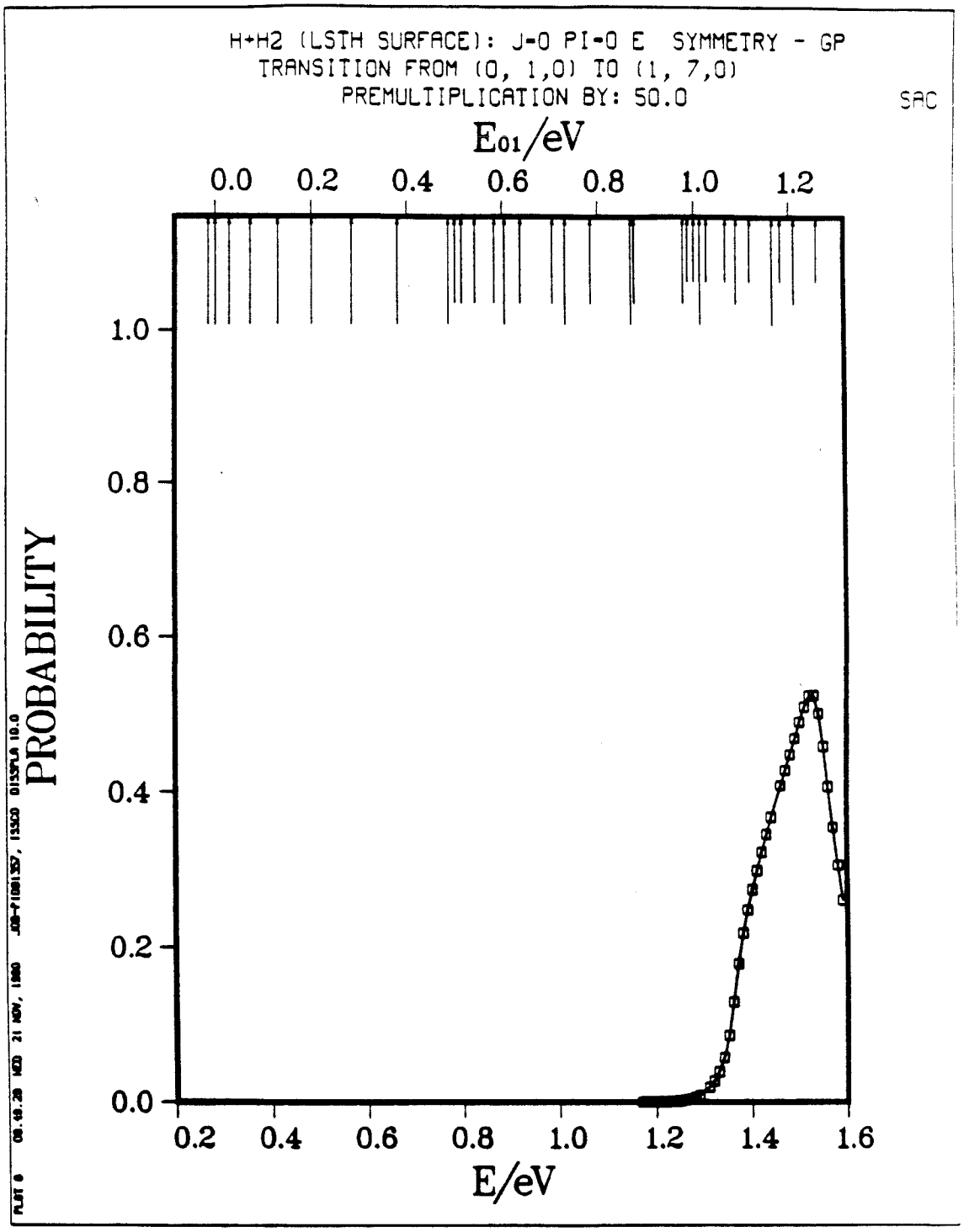
H+H2 (LSTH SURFACE): J=0 PI=0 E SYMMETRY - GP
TRANSITION FROM (0, 1,0) TO (1, 7,0)
PREMULTIPLICATION BY: 50.0
SAC
E01/eV
0.0
0.2
0.4
0.6
0.8
1.0
1.2
PROBABILITY
1.0
0.8
0.6
0.4
0.2
0.0
0.2
0.4
0.6
0.8
1.0
1.2
1.4
1.6
E/eV

Fig. 7.20d

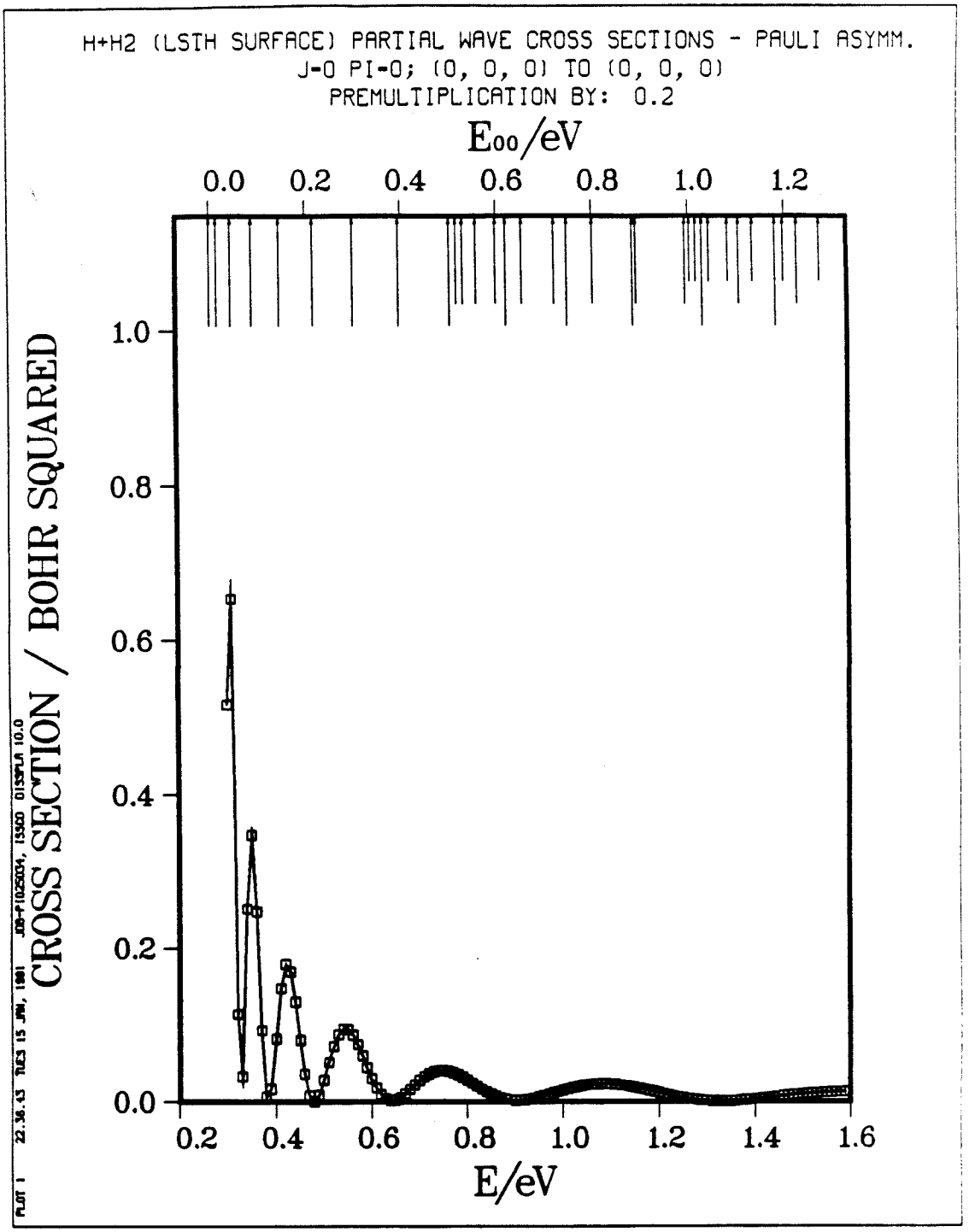
H+H2 (LSTH SURFACE) PARTIAL WAVE CROSS SECTIONS - PAULI ASYMM.
J=0 PI=0; (0, 0, 0) TO (0, 0, 0)
PREMULTIPLICATION BY: 0.2
E00/eV
0.0
0.2
0.4
0.6
0.8
1.0
1.2
CROSS SECTION / BOHR SQUARED
0.0
0.2
0.4
0.6
0.8
1.0
0.2
0.4
0.6
0.8
1.0
1.2
1.4
1.6
E/eV

Fig. 7.21a

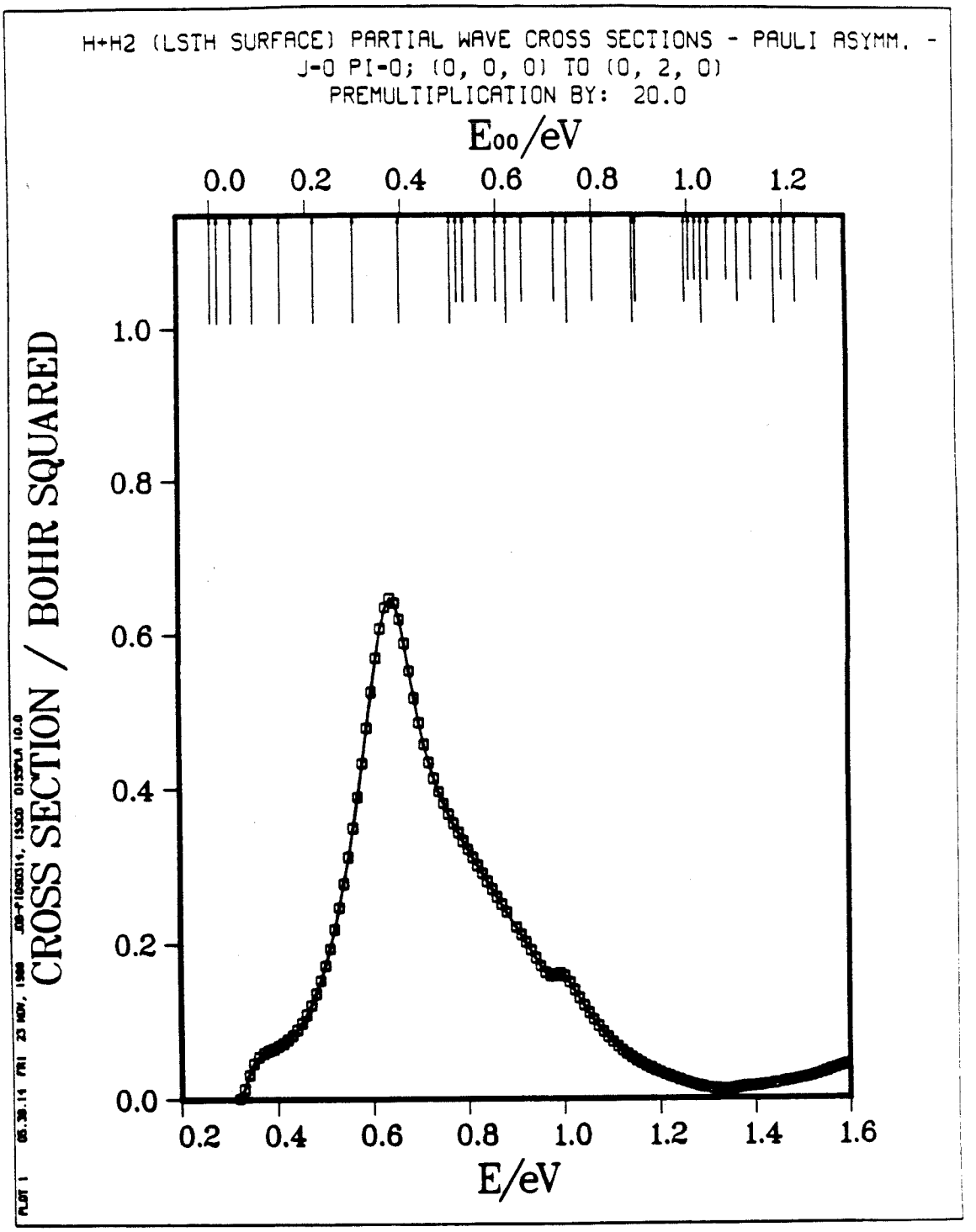
H+H2 (LSTH SURFACE) PARTIAL WAVE CROSS SECTIONS - PAULI ASYMM. -
J-0 PI-0; (0, 0, 0) TO (0, 2, 0)
PREMULTIPLICATION BY: 20.0
E00/eV
0.0
0.2
0.4
0.6
0.8
1.0
1.2
CROSS SECTION / BOHR SQUARED
0.0
0.2
0.4
0.6
0.8
1.0
0.2
0.4
0.6
0.8
1.0
1.2
1.4
1.6
E/eV

Fig. 7.21b

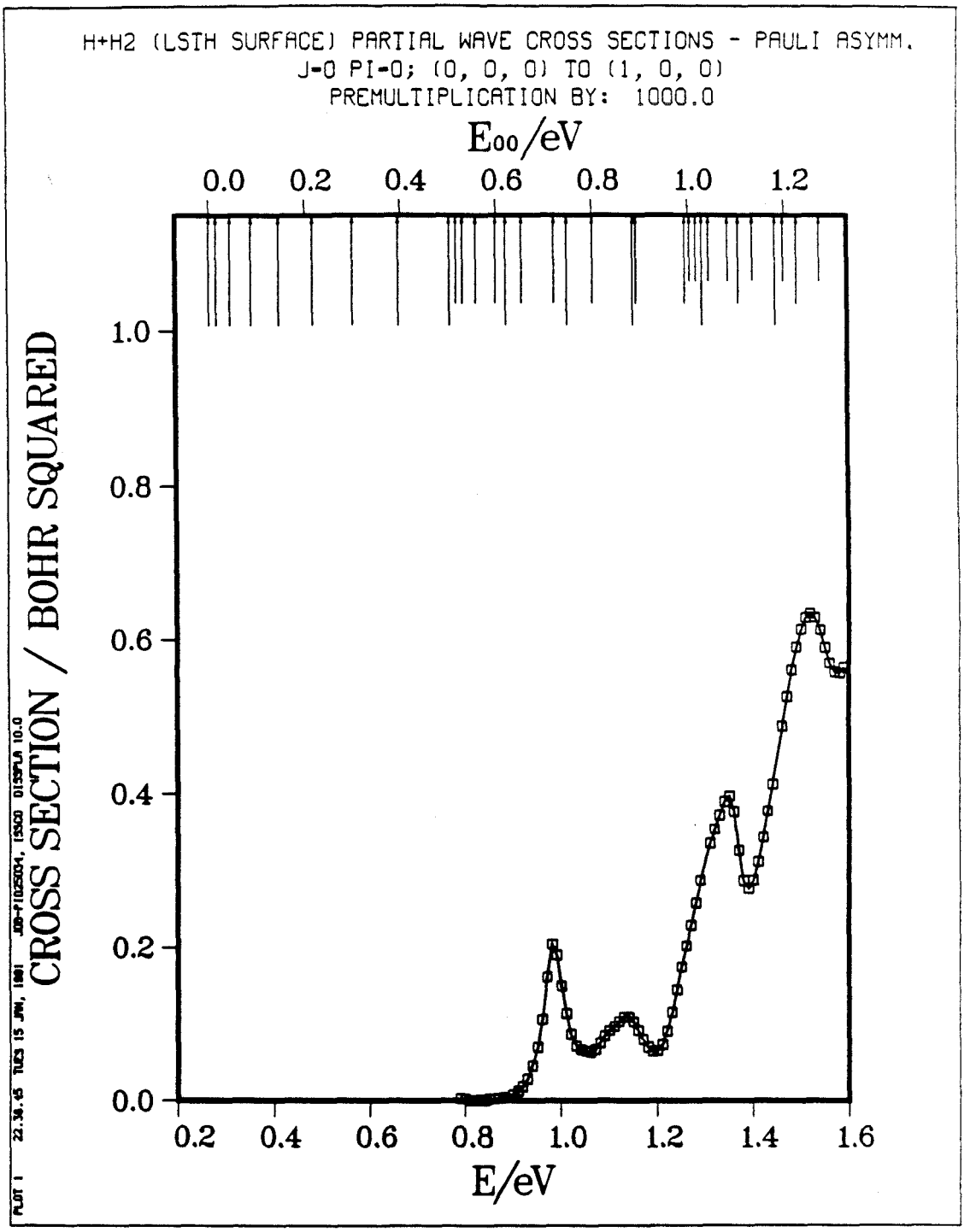
H+H2 (LSTH SURFACE) PARTIAL WAVE CROSS SECTIONS - PAULI ASYMM.
J=0 PI=0; (0, 0, 0) TO (1, 0, 0)
PREMULTIPLICATION BY: 1000.0
E00/eV
0.0
0.2
0.4
0.6
0.8
1.0
1.2
CROSS SECTION / BOHR SQUARED
0.0
0.2
0.4
0.6
0.8
1.0
0.2
0.4
0.6
0.8
1.0
1.2
1.4
1.6
E/eV

Fig. 7.21c

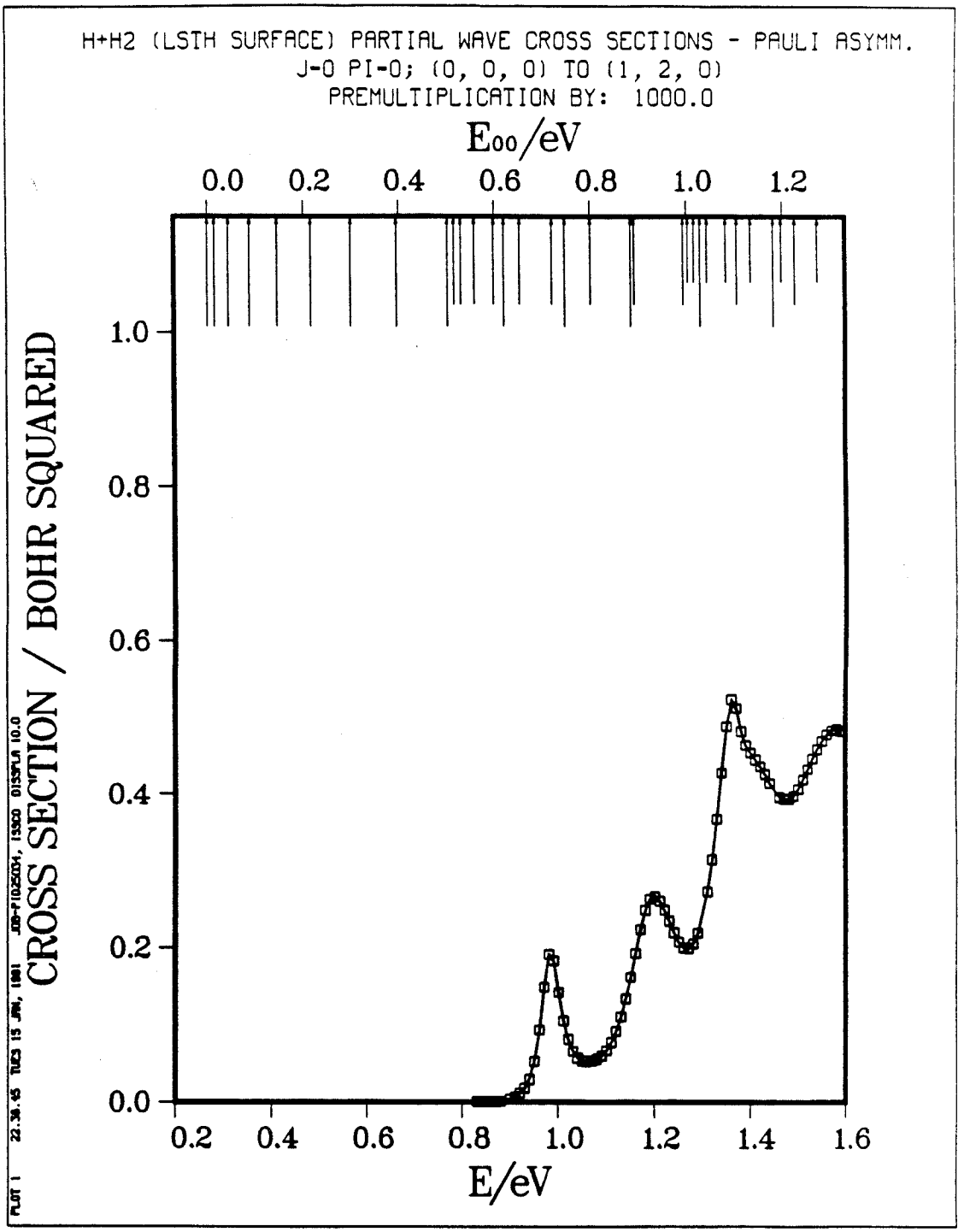
H+H2 (LSTH SURFACE) PARTIAL WAVE CROSS SECTIONS - PAULI ASYMM.
J-0 PI-0; (0, 0, 0) TO (1, 2, 0)
PREMULTIPLICATION BY: 1000.0
E00/eV
0.0
0.2
0.4
0.6
0.8
1.0
1.2
CROSS SECTION / BOHR SQUARED
0.0
0.2
0.4
0.6
0.8
1.0
0.2
0.4
0.6
0.8
1.0
1.2
1.4
1.6
E/eV
PLOT 1 22.38.45 TUES 15 JAN, 1981 JOB-P1025004, 13920 DISSPLA 10.0

Fig. 7.21d

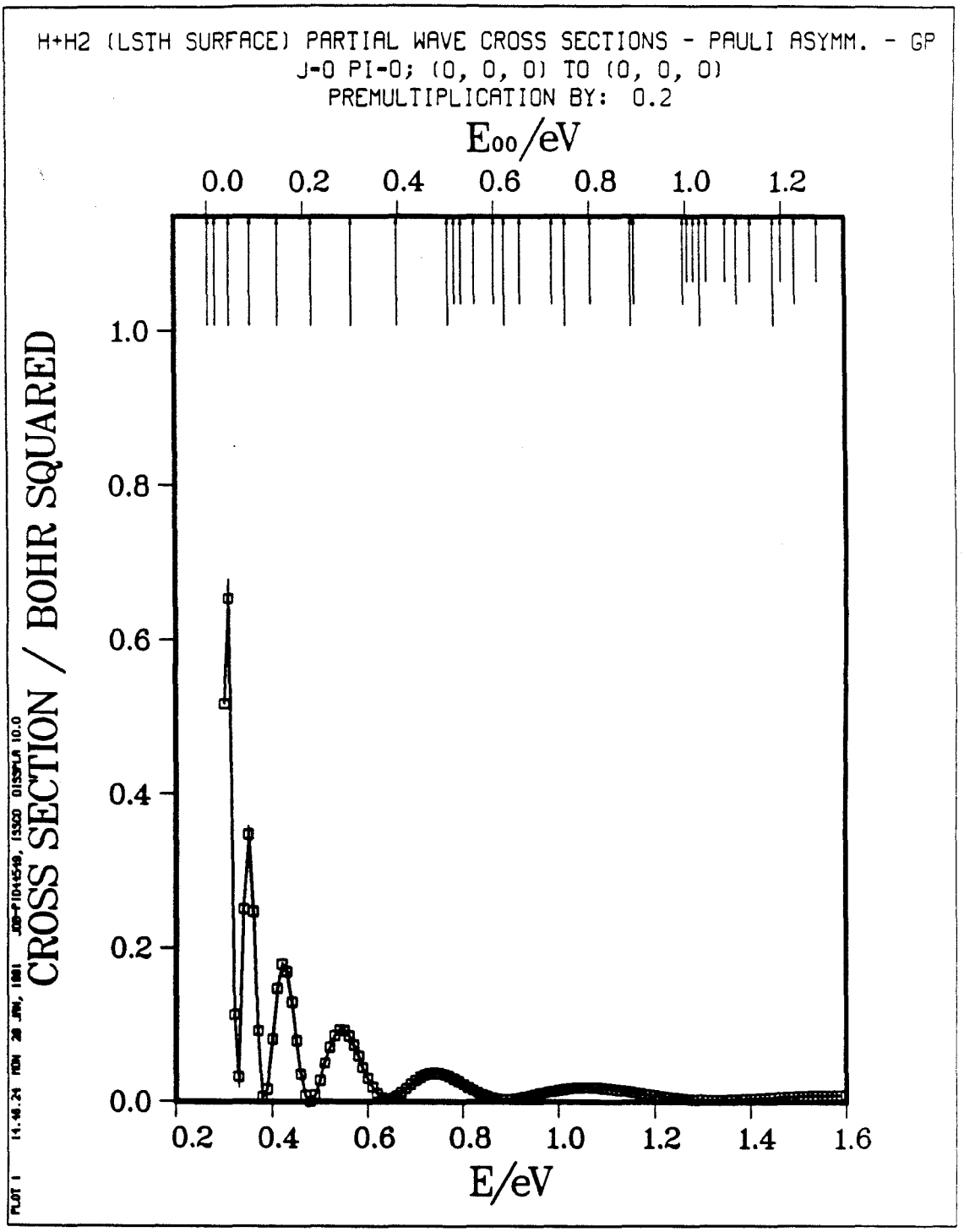
H+H2 (LSTH SURFACE) PARTIAL WAVE CROSS SECTIONS - PAULI ASYMM. - GP
J=0 PI=0; (0, 0, 0) TO (0, 0, 0)
PREMULTIPLICATION BY: 0.2
E00/eV
0.0
0.2
0.4
0.6
0.8
1.0
1.2
CROSS SECTION / BOHR SQUARED
0.0
0.2
0.4
0.6
0.8
1.0
E/eV
0.2
0.4
0.6
0.8
1.0
1.2
1.4
1.6

Fig. 7.22a

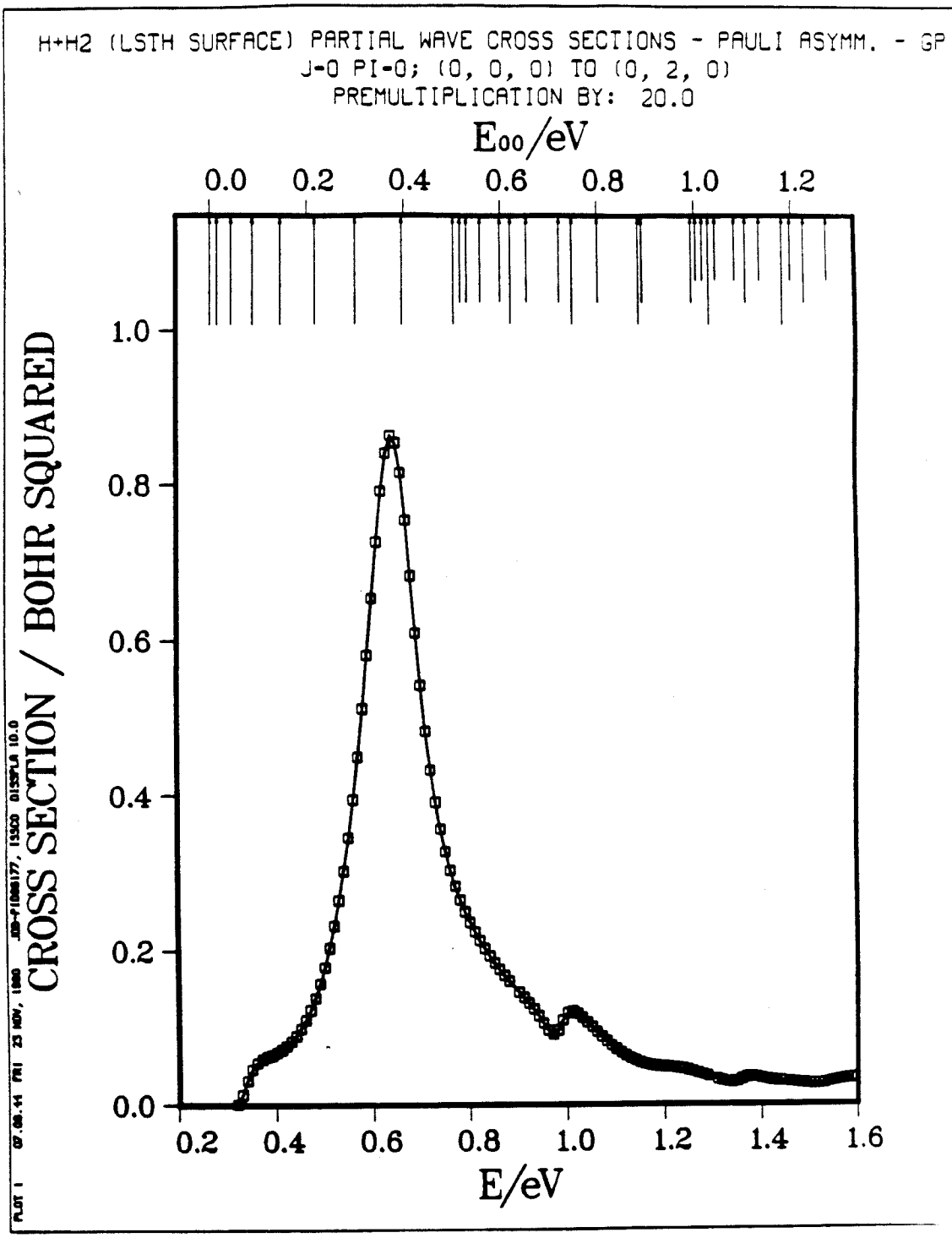
H+H2 (LSTH SURFACE) PARTIAL WAVE CROSS SECTIONS - PAULI ASYMM. - GP
J=0 PI=0; (0, 0, 0) TO (0, 2, 0)
PREMULTIPLICATION BY: 20.0
E00/eV
0.0
0.2
0.4
0.6
0.8
1.0
1.2
CROSS SECTION / BOHR SQUARED
0.0
0.2
0.4
0.6
0.8
1.0
0.2
0.4
0.6
0.8
1.0
1.2
1.4
1.6
E/eV

Fig. 7.22b

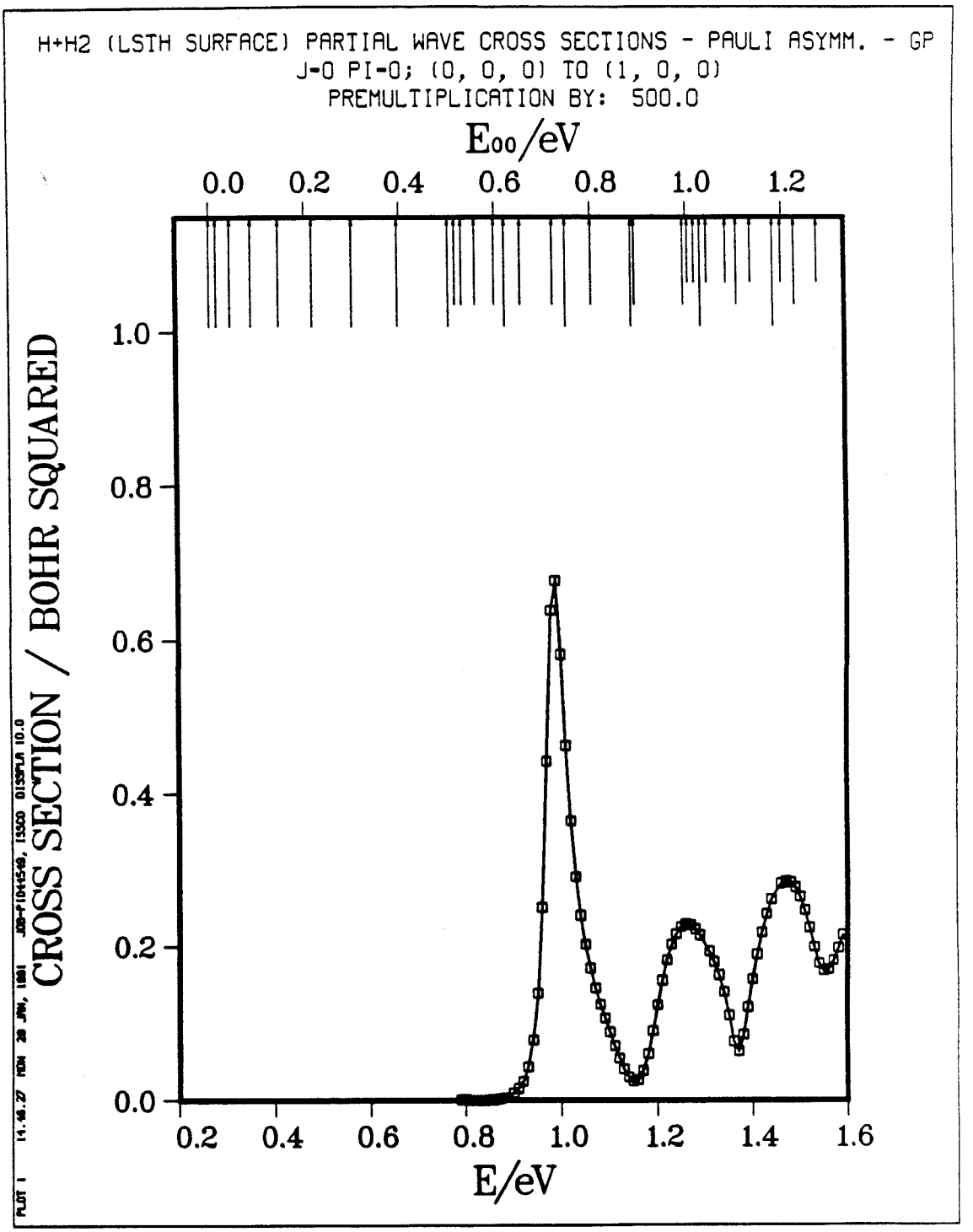
H+H2 (LSTH SURFACE) PARTIAL WAVE CROSS SECTIONS - PAULI ASYMM. - GP
J=0 PI=0; (0, 0, 0) TO (1, 0, 0)
PREMULTIPLICATION BY: 500.0
E00/eV
0.0
0.2
0.4
0.6
0.8
1.0
1.2
CROSS SECTION / BOHR SQUARED
1.0
0.8
0.6
0.4
0.2
0.0
0.2
0.4
0.6
0.8
1.0
1.2
1.4
1.6
E/eV

Fig. 7.22c

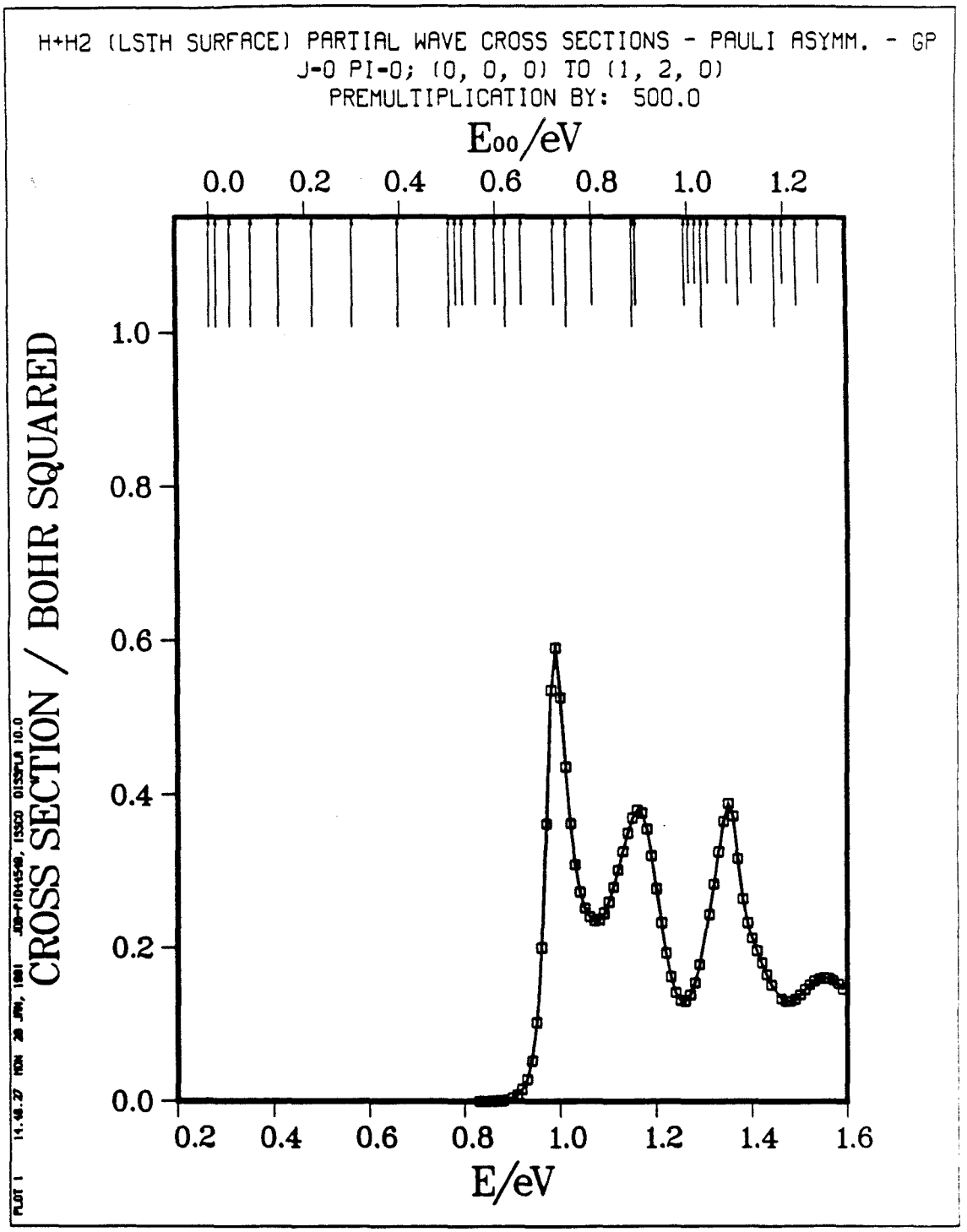
H+H2 (LSTH SURFACE) PARTIAL WAVE CROSS SECTIONS - PAULI ASYMM. - GP
J-0 PI-0; (0, 0, 0) TO (1, 2, 0)
PREMULTIPLICATION BY: 500.0
E00/eV
0.0
0.2
0.4
0.6
0.8
1.0
1.2
CROSS SECTION / BOHR SQUARED
0.0
0.2
0.4
0.6
0.8
1.0
0.2
0.4
0.6
0.8
1.0
1.2
1.4
1.6
E/eV

Fig. 7.22d

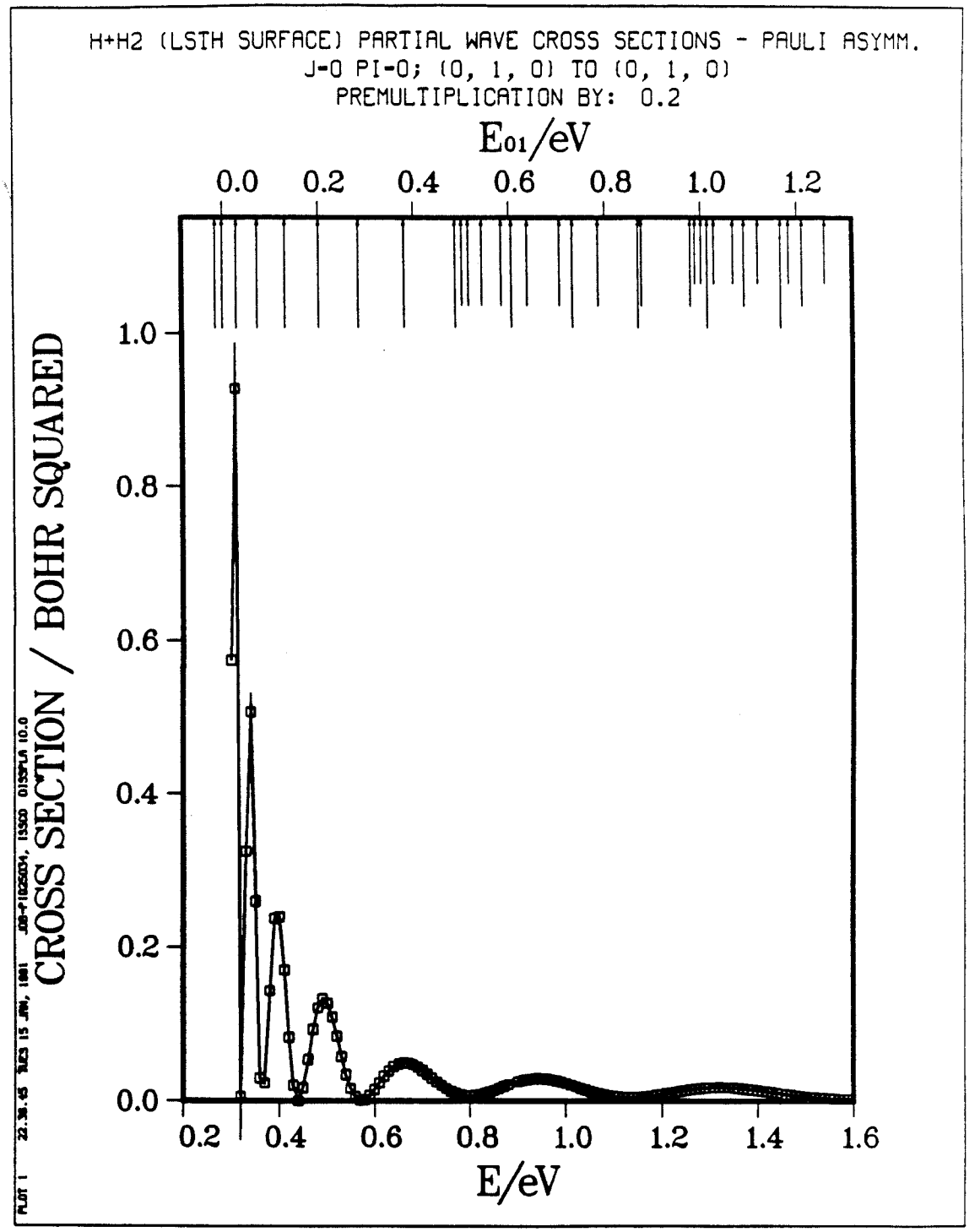
H+H2 (LSTH SURFACE) PARTIAL WAVE CROSS SECTIONS - PAULI ASYMM.
J=0 PI=0; (0, 1, 0) TO (0, 1, 0)
PREMULTIPLICATION BY: 0.2
E01/eV
0.0
0.2
0.4
0.6
0.8
1.0
1.2
CROSS SECTION / BOHR SQUARED
0.0
0.2
0.4
0.6
0.8
1.0
0.2
0.4
0.6
0.8
1.0
1.2
1.4
1.6
E/eV

Fig. 7.23a

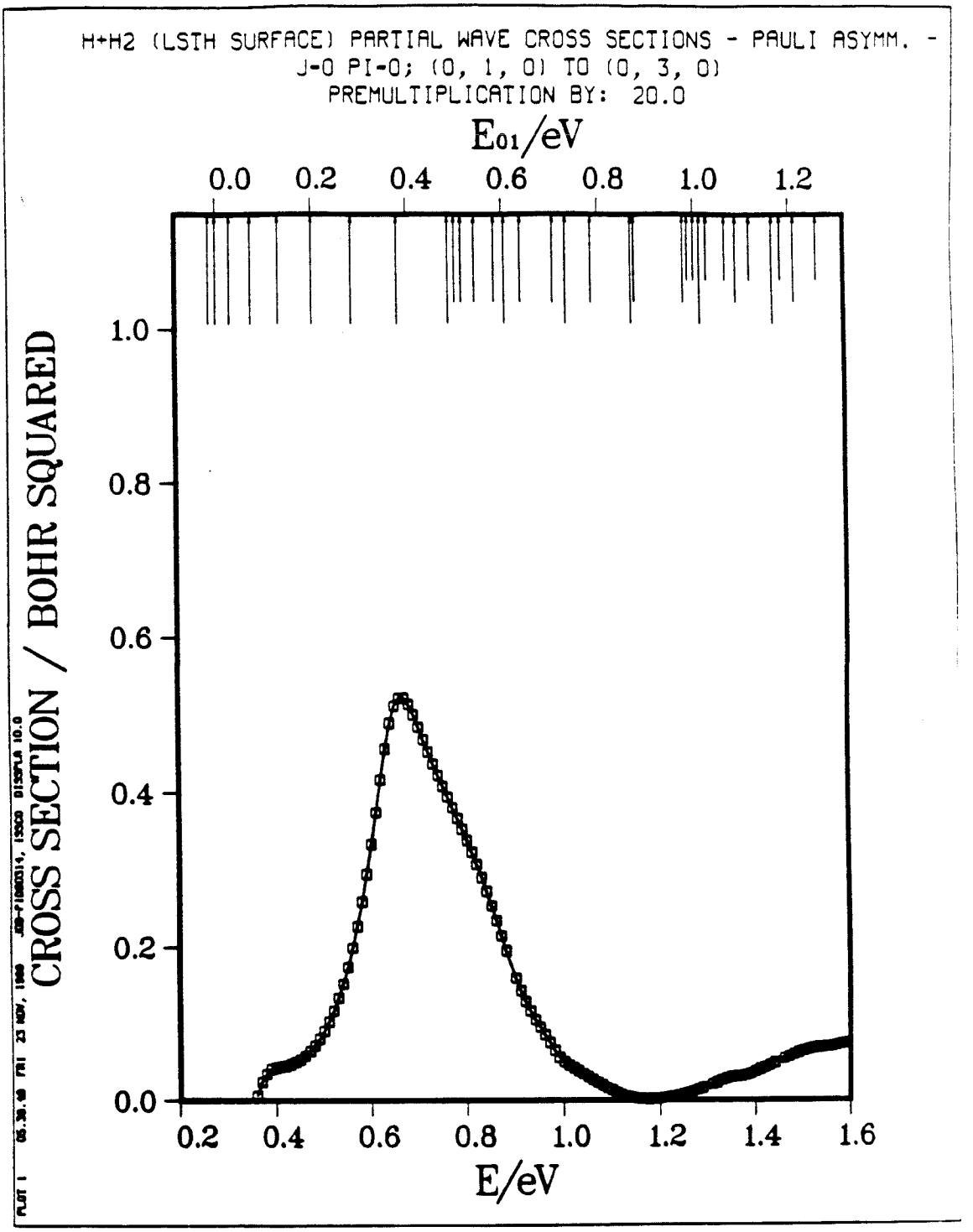
H+H2 (LSTH SURFACE) PARTIAL WAVE CROSS SECTIONS - PAULI ASYMM. -
J-0 PI-0; (0, 1, 0) TO (0, 3, 0)
PREMULTIPLICATION BY: 20.0
E01/eV
0.0
0.2
0.4
0.6
0.8
1.0
1.2
CROSS SECTION / BOHR SQUARED
0.0
0.2
0.4
0.6
0.8
1.0
0.2
0.4
0.6
0.8
1.0
1.2
1.4
1.6
E/eV

Fig. 7.23b

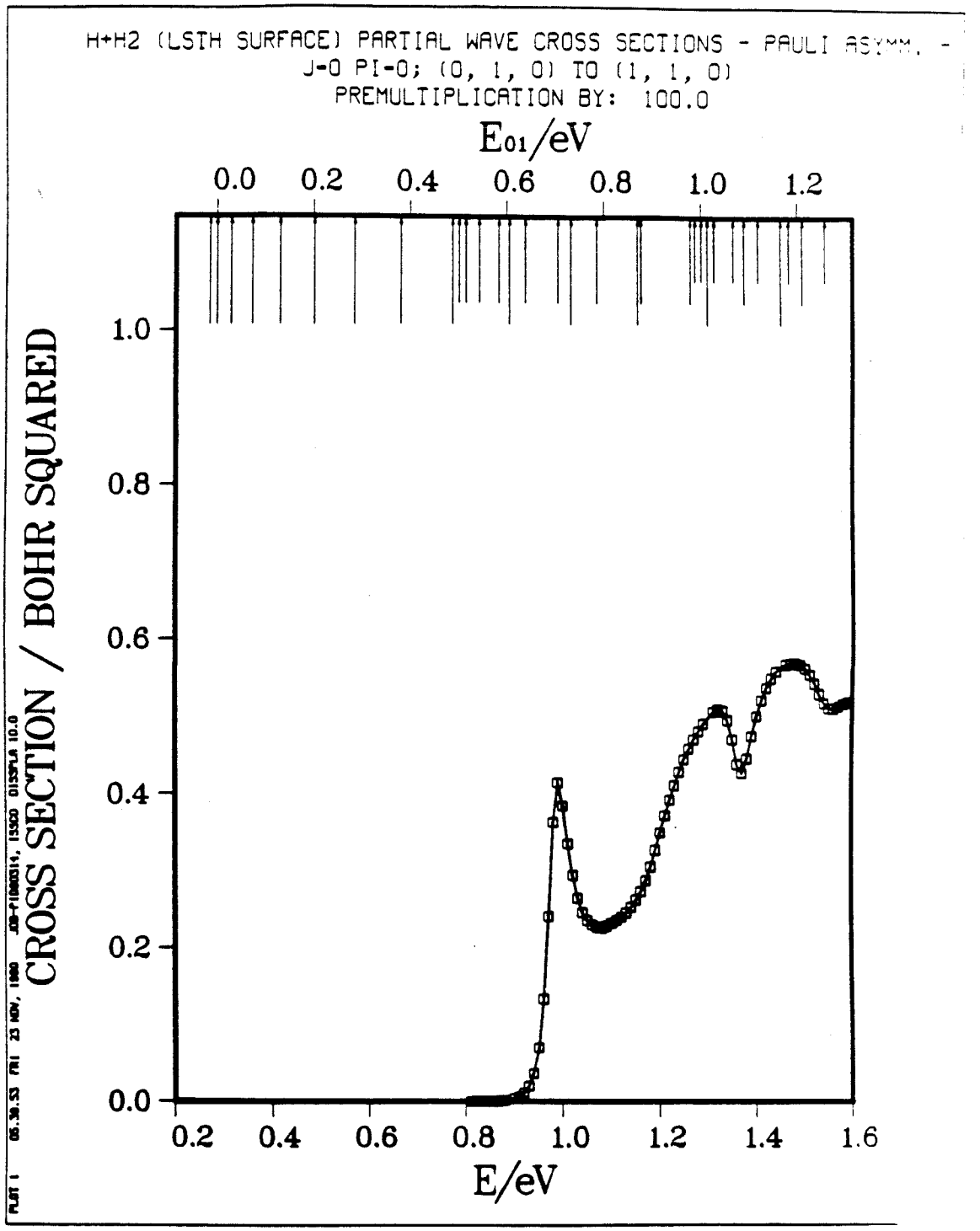
H+H2 (LSTH SURFACE) PARTIAL WAVE CROSS SECTIONS - PAULI ASYMM. -
J=0 PI=0; (0, 1, 0) TO (1, 1, 0)
PREMULTIPLICATION BY: 100.0
E01/eV
0.0
0.2
0.4
0.6
0.8
1.0
1.2
CROSS SECTION / BOHR SQUARED
0.0
0.2
0.4
0.6
0.8
1.0
0.2
0.4
0.6
0.8
1.0
1.2
1.4
1.6
E/eV

Fig. 7.23c

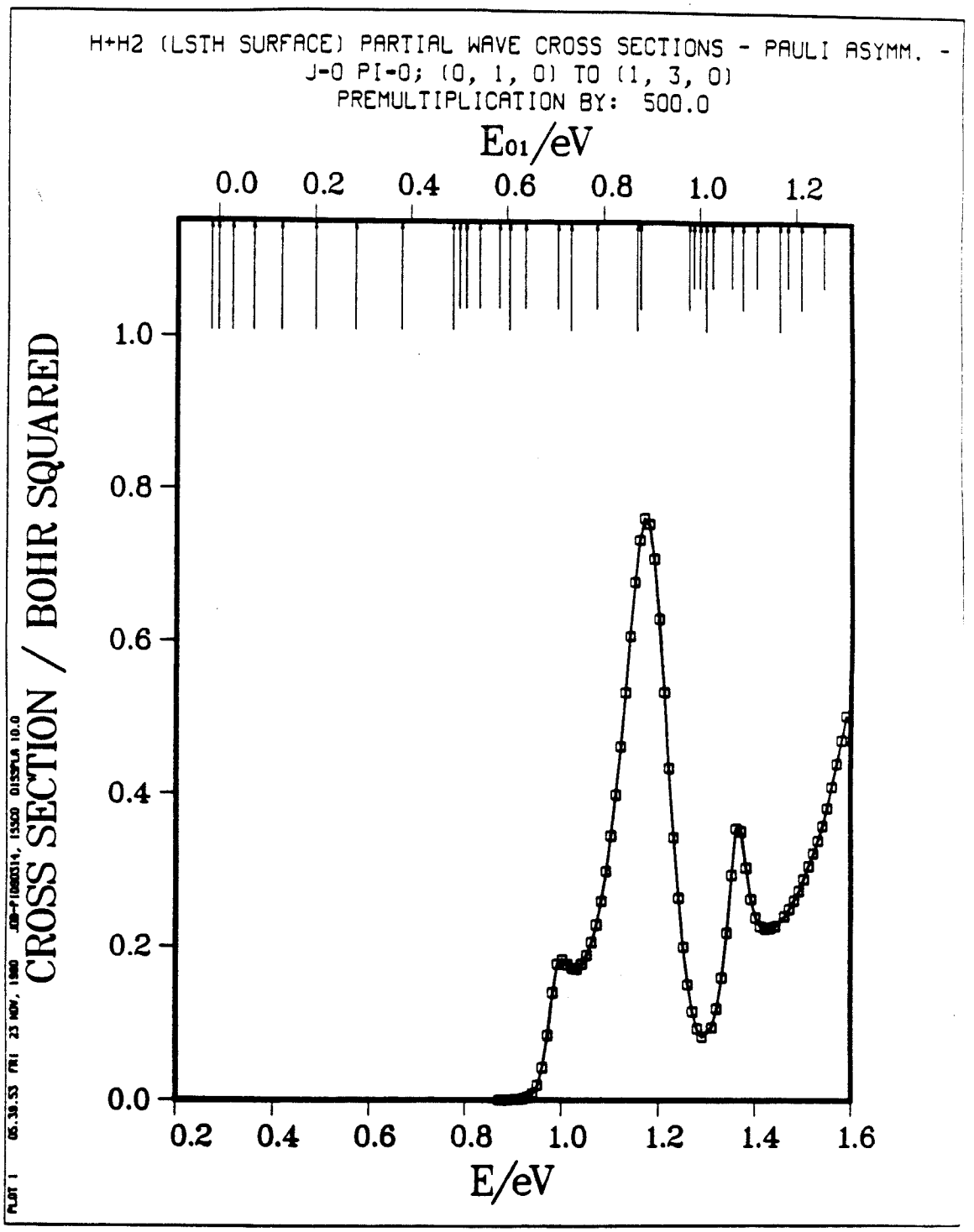
H+H2 (LSTH SURFACE) PARTIAL WAVE CROSS SECTIONS - PAULI ASYMM. -
J=0 PI=0; (0, 1, 0) TO (1, 3, 0)
PREMULTIPLICATION BY: 500.0
E01/eV
0.0
0.2
0.4
0.6
0.8
1.0
1.2
CROSS SECTION / BOHR SQUARED
0.0
0.2
0.4
0.6
0.8
1.0
0.2
0.4
0.6
0.8
1.0
1.2
1.4
1.6
E/eV

Fig. 7.23d

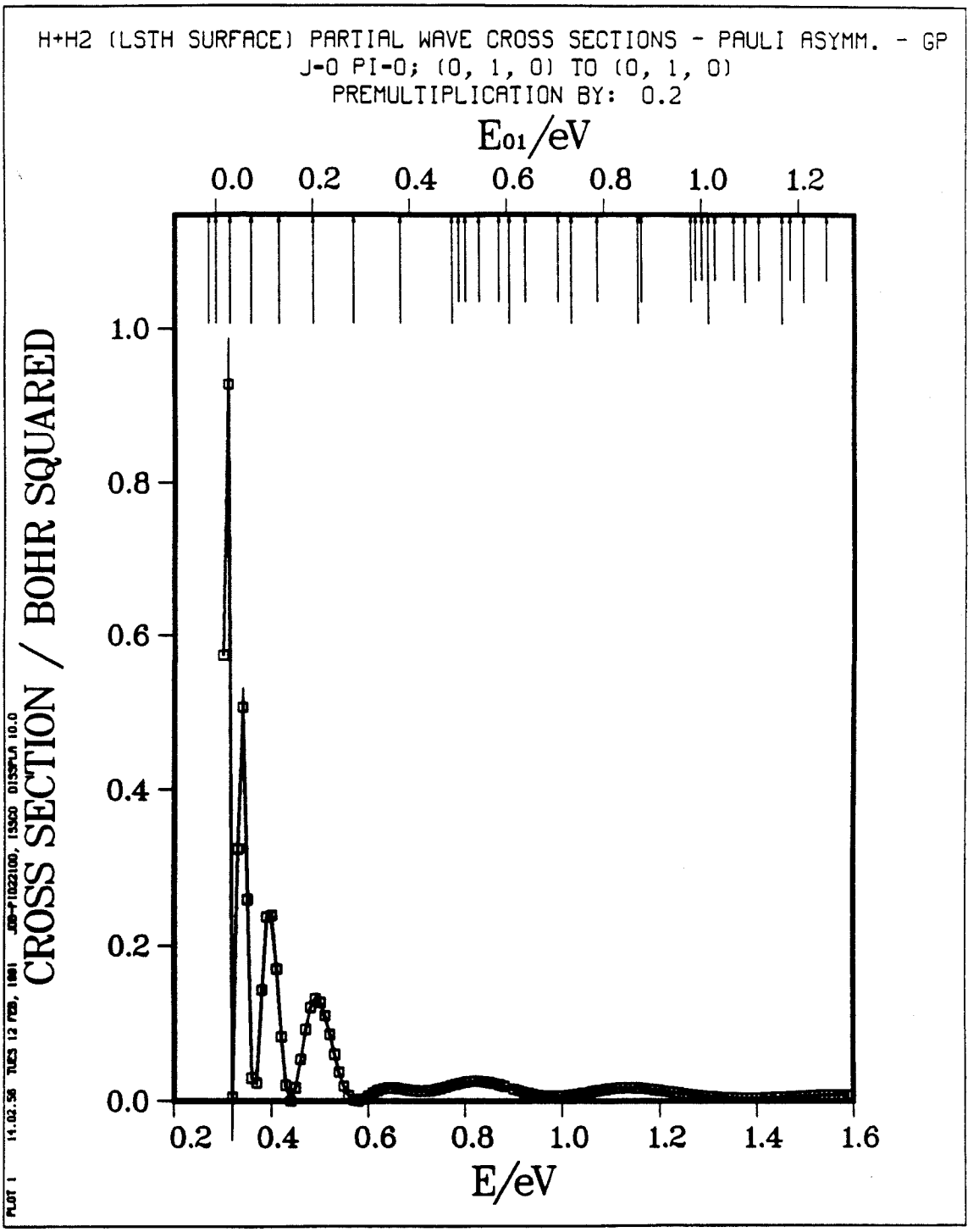
H+H2 (LSTH SURFACE) PARTIAL WAVE CROSS SECTIONS - PAULI ASYMM. - GP
J=0 PI=0; (0, 1, 0) TO (0, 1, 0)
PREMULTIPLICATION BY: 0.2
E01/eV
0.0
0.2
0.4
0.6
0.8
1.0
1.2
CROSS SECTION / BOHR SQUARED
0.0
0.2
0.4
0.6
0.8
1.0
0.2
0.4
0.6
0.8
1.0
1.2
1.4
1.6
E/eV
PLOT 1 14.02.56 TUES 12 FEB, 1991 JOB=T1022100, 13350 DISSPLA 10.0

Fig. 7.24a

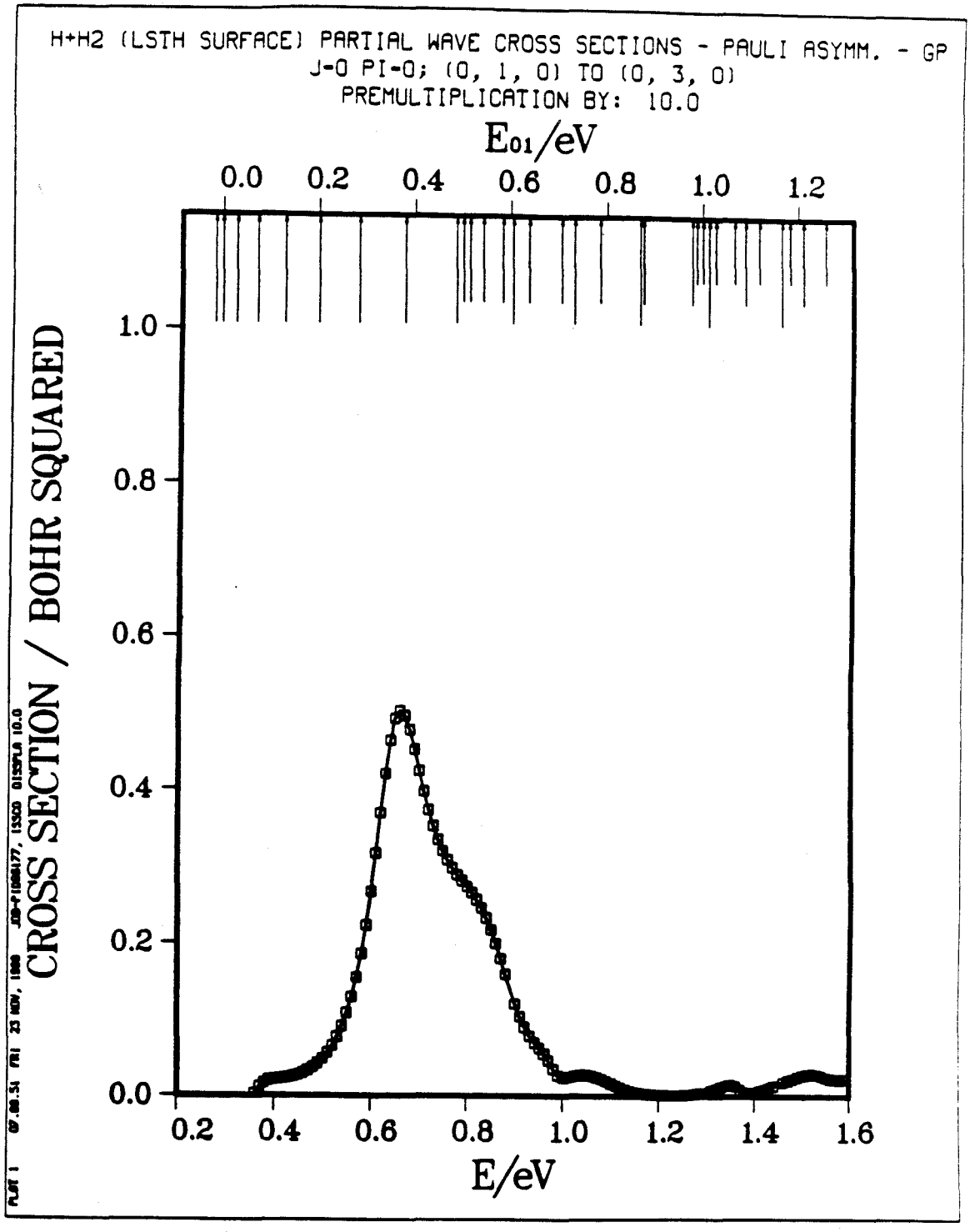
H+H2 (LSTH SURFACE) PARTIAL WAVE CROSS SECTIONS - PAULI ASYMM. - GP
J=0 PI=0; (0, 1, 0) TO (0, 3, 0)
PREMULTIPLICATION BY: 10.0
E01/eV
0.0
0.2
0.4
0.6
0.8
1.0
1.2
CROSS SECTION / BOHR SQUARED
0.0
0.2
0.4
0.6
0.8
1.0
0.2
0.4
0.6
0.8
1.0
1.2
1.4
1.6
E/eV

Fig. 7.24b

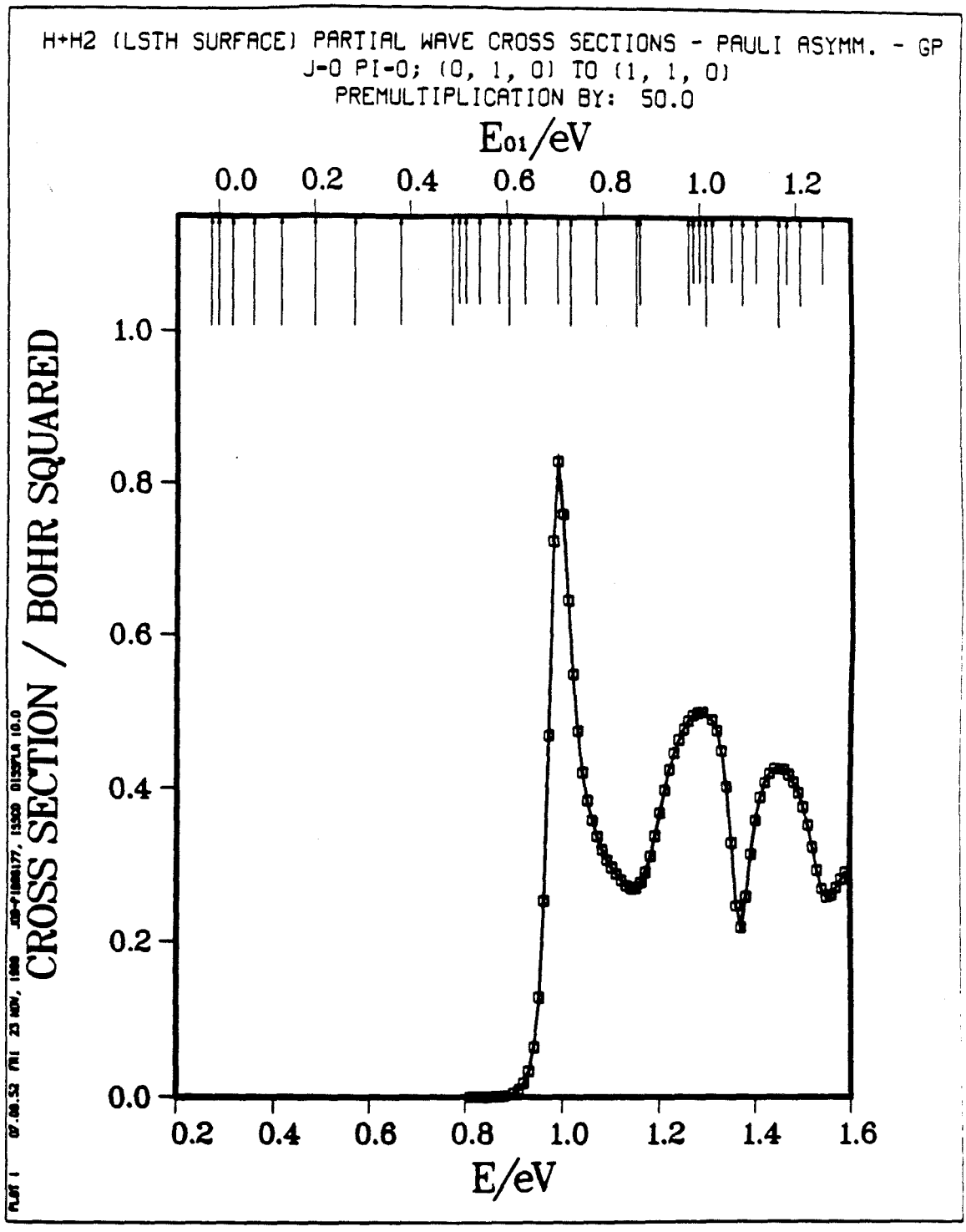
H+H2 (LSTH SURFACE) PARTIAL WAVE CROSS SECTIONS - PAULI ASYMM. - GP
J=0 PI=0; (0, 1, 0) TO (1, 1, 0)
PREMULTIPLICATION BY: 50.0
E01/eV
0.0
0.2
0.4
0.6
0.8
1.0
1.2
CROSS SECTION / BOHR SQUARED
0.0
0.2
0.4
0.6
0.8
1.0
0.2
0.4
0.6
0.8
1.0
1.2
1.4
1.6
E/eV

Fig. 7.24c

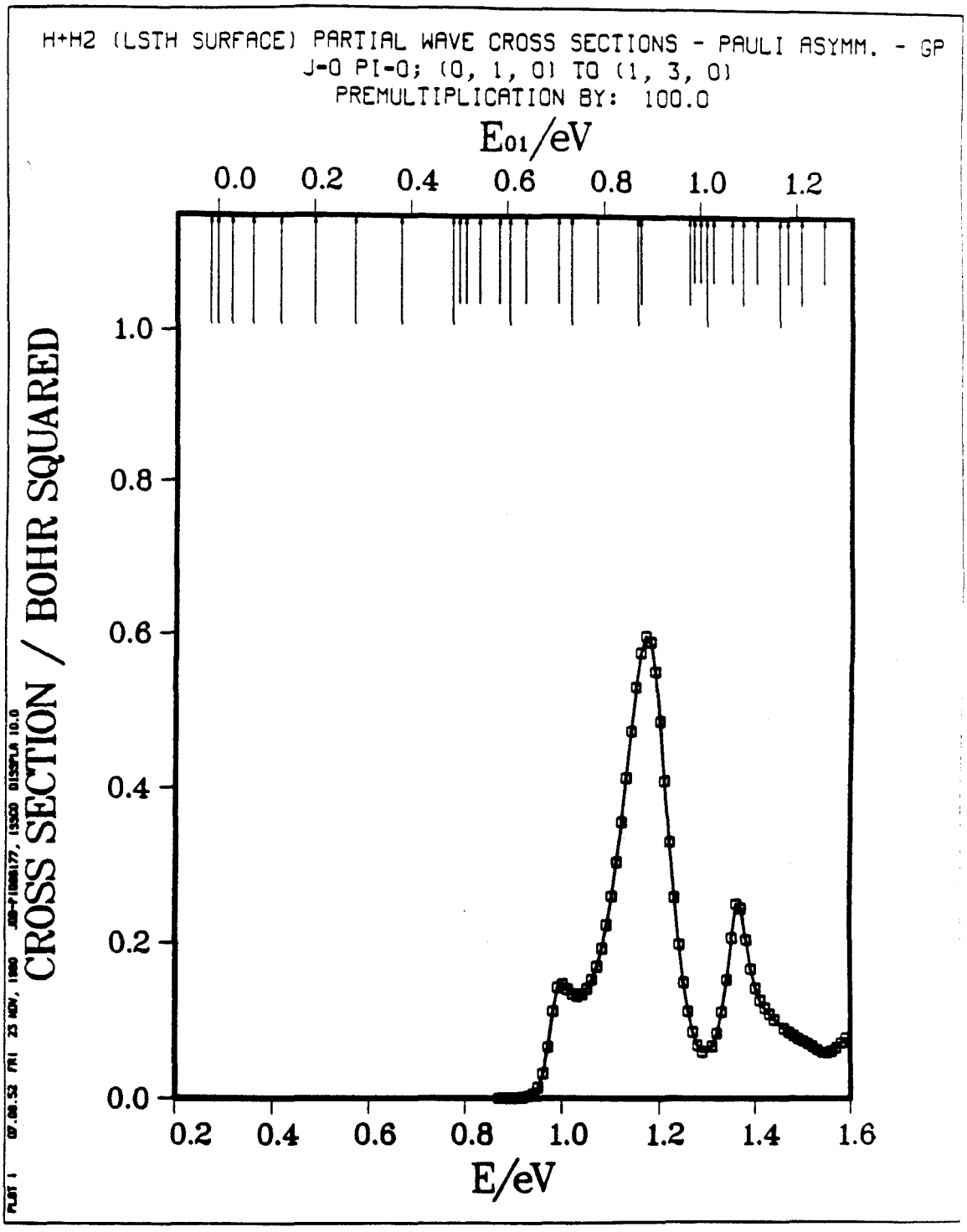
H+H2 (LSTH SURFACE) PARTIAL WAVE CROSS SECTIONS - PAULI ASYMM. - GP
J=0 PI=0; (0, 1, 0) TO (1, 3, 0)
PREMULTIPLICATION BY: 100.0
E01/eV
0.0
0.2
0.4
0.6
0.8
1.0
1.2
CROSS SECTION / BOHR SQUARED
0.0
0.2
0.4
0.6
0.8
1.0
0.2
0.4
0.6
0.8
1.0
1.2
1.4
1.6
E/eV

Fig. 7.24d

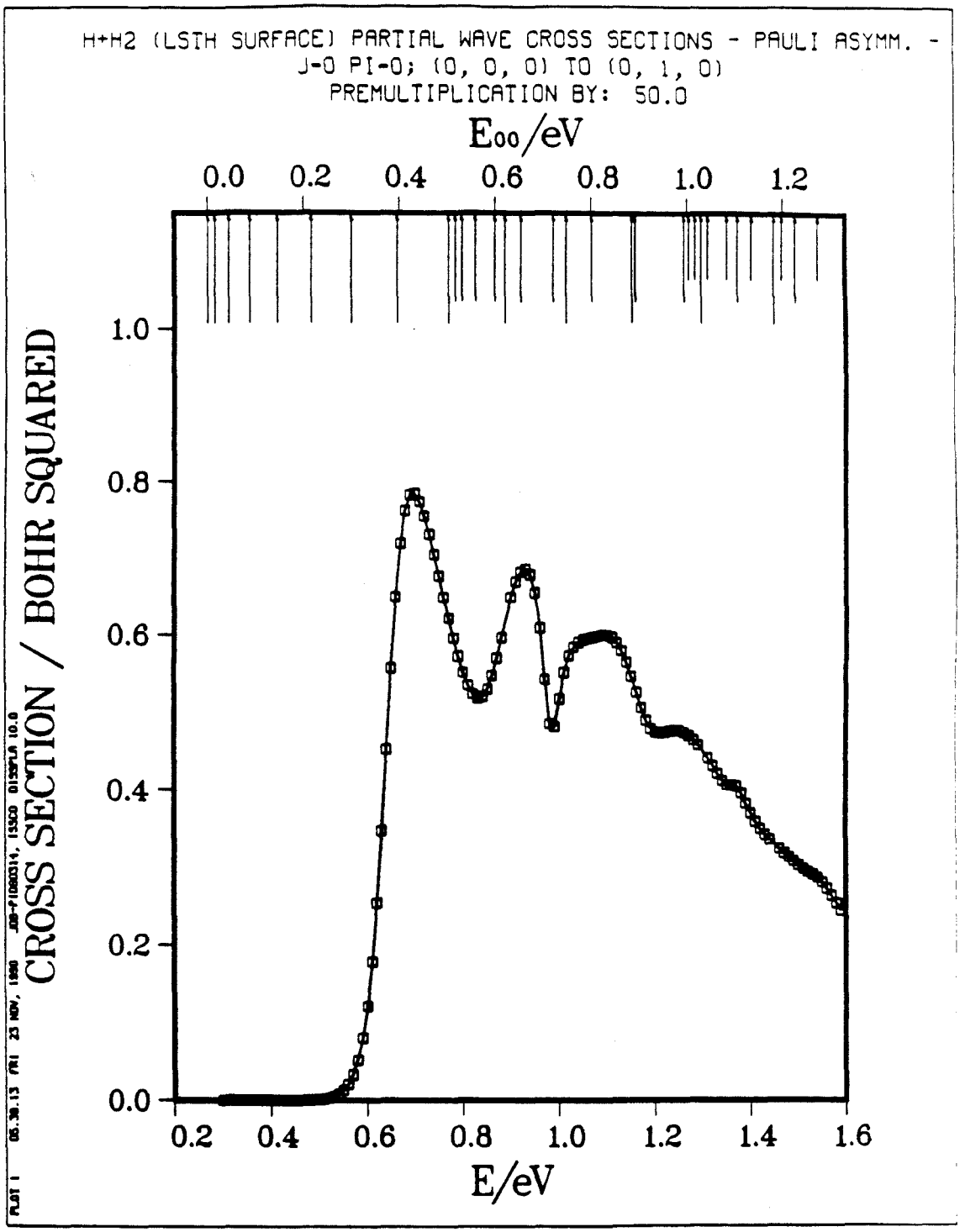
H+H2 (LSTH SURFACE) PARTIAL WAVE CROSS SECTIONS - PAULI ASYMM. -
J-0 PI-0; (0, 0, 0) TO (0, 1, 0)
PREMULTIPLICATION BY: 50.0
E00/eV
0.0
0.2
0.4
0.6
0.8
1.0
1.2
CROSS SECTION / BOHR SQUARED
0.0
0.2
0.4
0.6
0.8
1.0
0.2
0.4
0.6
0.8
1.0
1.2
1.4
1.6
E/eV

Fig. 7.25a

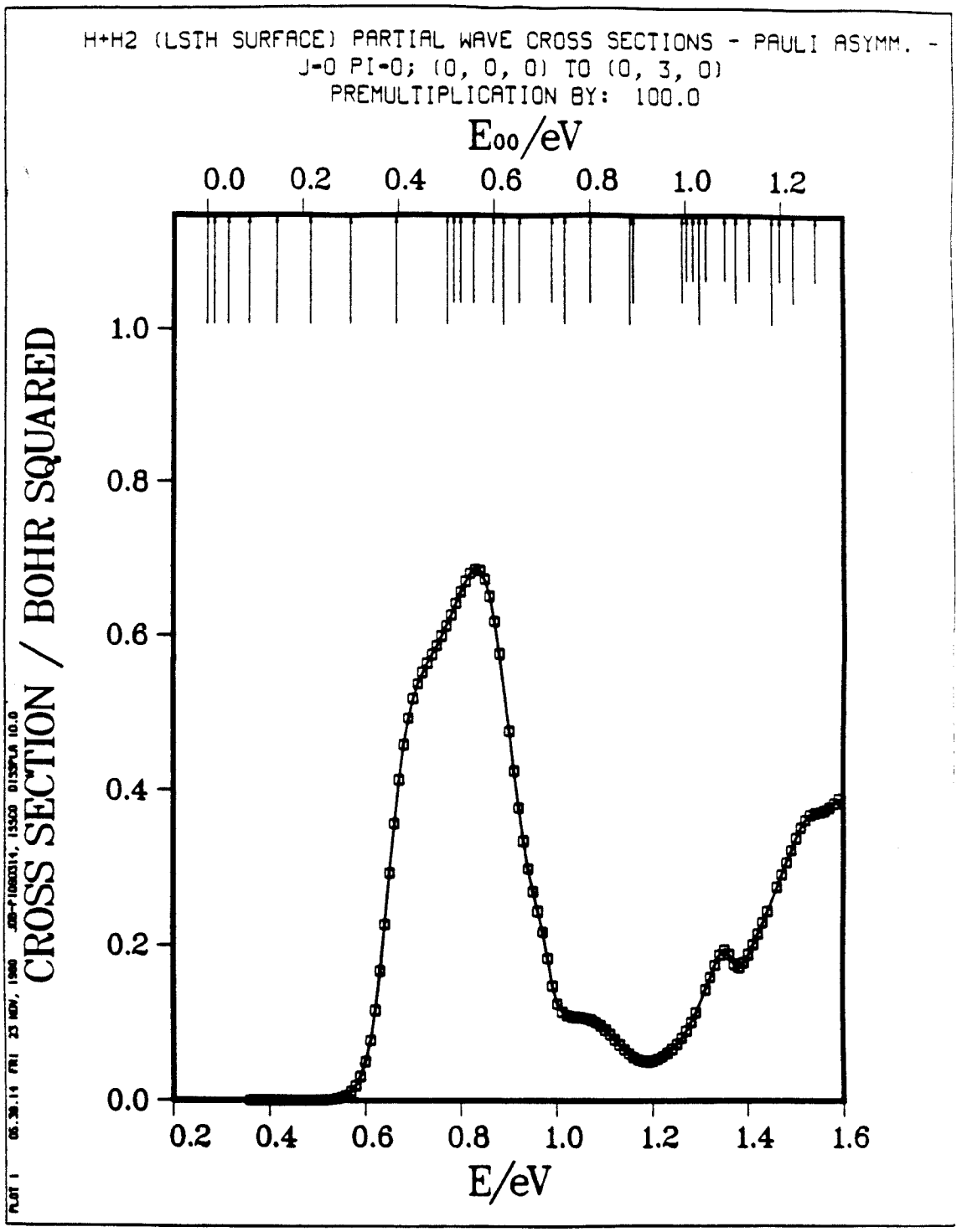
H+H2 (LSTH SURFACE) PARTIAL WAVE CROSS SECTIONS - PAULI ASYMM. -
J=0 PI=0; (0, 0, 0) TO (0, 3, 0)
PREMULTIPLICATION BY: 100.0
E00/eV
0.0
0.2
0.4
0.6
0.8
1.0
1.2
CROSS SECTION / BOHR SQUARED
0.0
0.2
0.4
0.6
0.8
1.0
0.2
0.4
0.6
0.8
1.0
1.2
1.4
1.6
E/eV

Fig. 7.25b

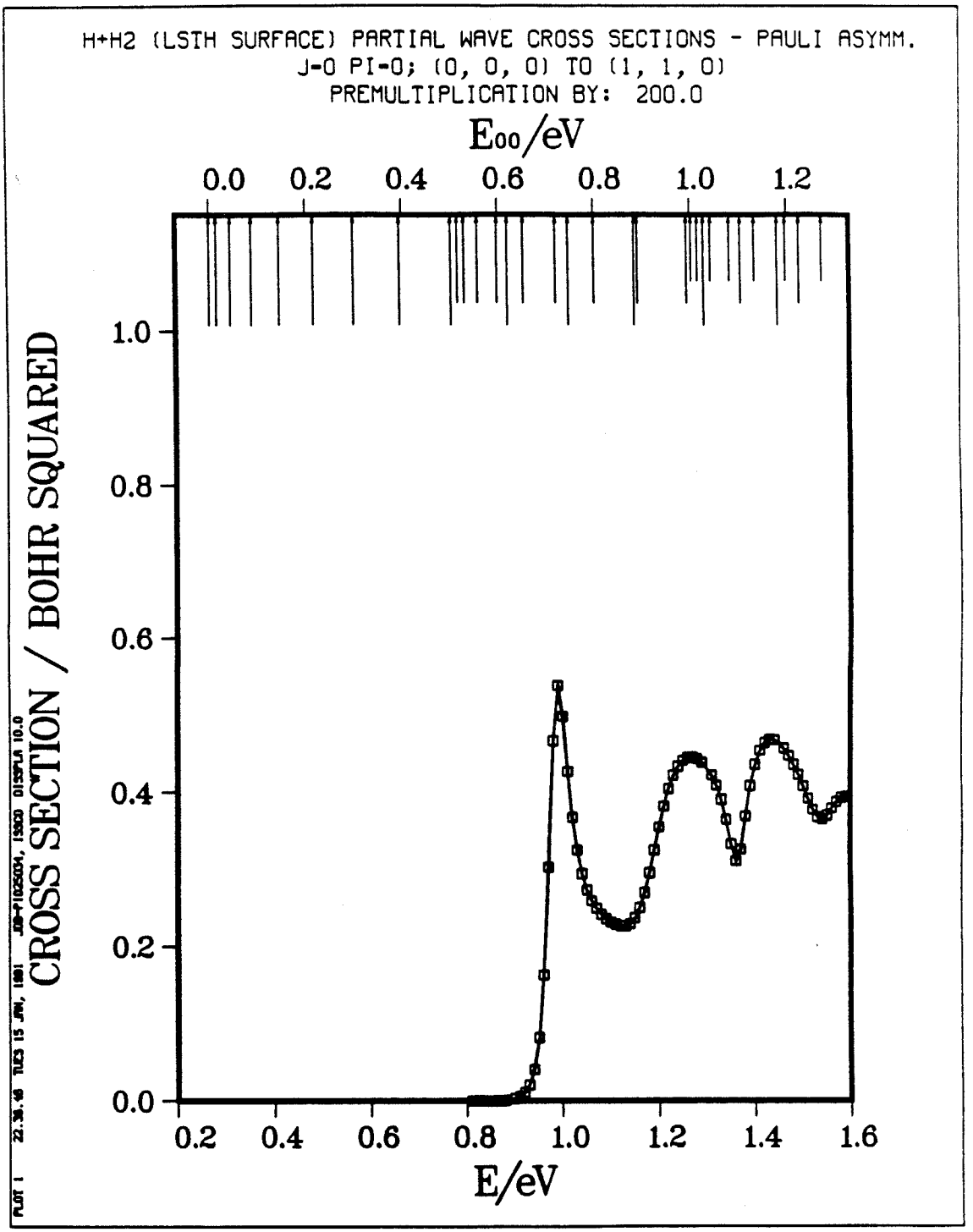
H+H2 (LSTH SURFACE) PARTIAL WAVE CROSS SECTIONS - PAULI ASYMM.
J=0 PI=0; (0, 0, 0) TO (1, 1, 0)
PREMULTIPLICATION BY: 200.0
E00/eV
0.0
0.2
0.4
0.6
0.8
1.0
1.2
CROSS SECTION / BOHR SQUARED
0.0
0.2
0.4
0.6
0.8
1.0
E/eV
0.2
0.4
0.6
0.8
1.0
1.2
1.4
1.6

Fig. 7.25c

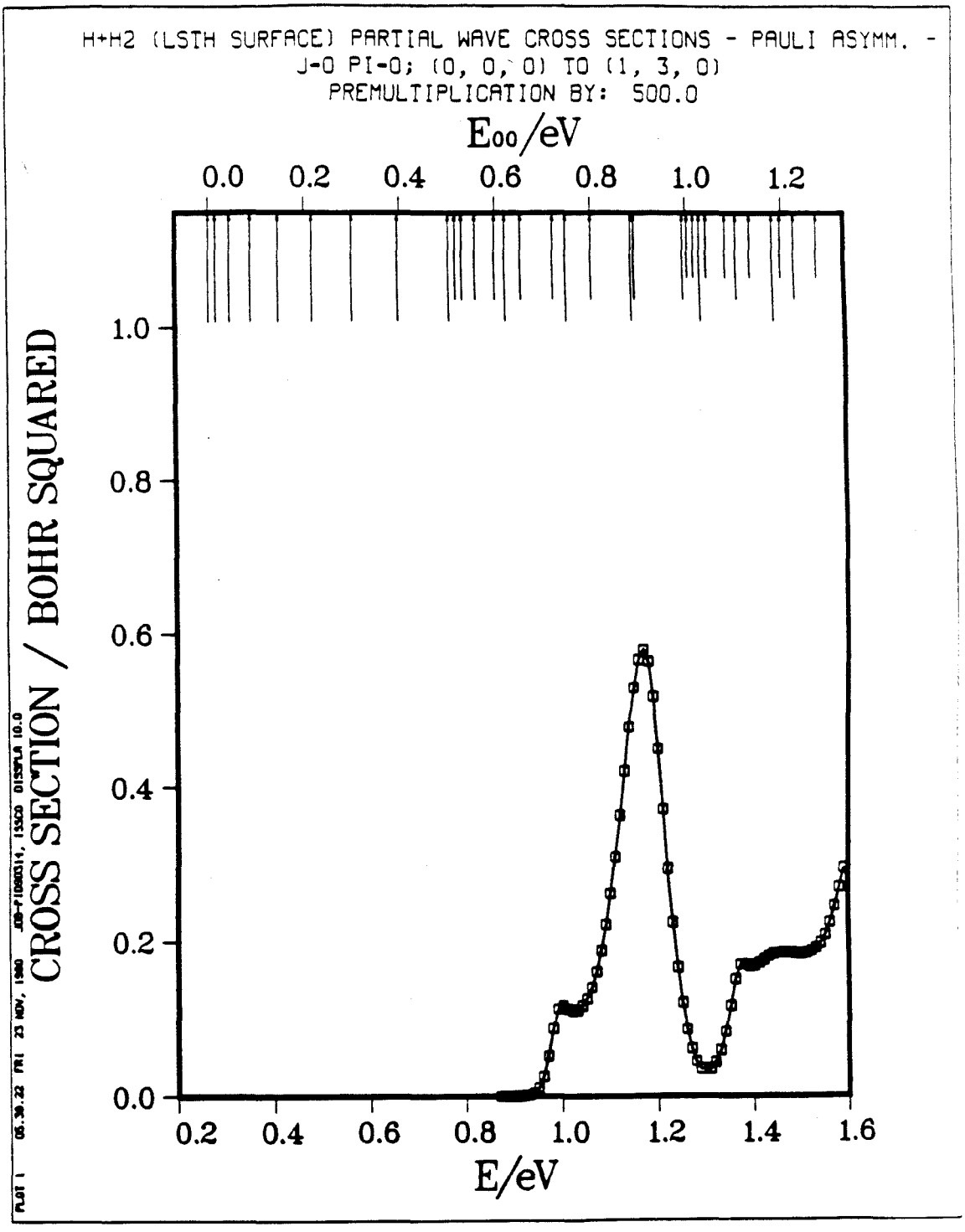
H+H2 (LSTH SURFACE) PARTIAL WAVE CROSS SECTIONS - PAULI ASYMM. -
J-0 PI-0; (0, 0, 0) TO (1, 3, 0)
PREMULTIPLICATION BY: 500.0
E00/eV
0.0
0.2
0.4
0.6
0.8
1.0
1.2
CROSS SECTION / BOHR SQUARED
0.0
0.2
0.4
0.6
0.8
1.0
0.2
0.4
0.6
0.8
1.0
1.2
1.4
1.6
E/eV

Fig. 7.25d

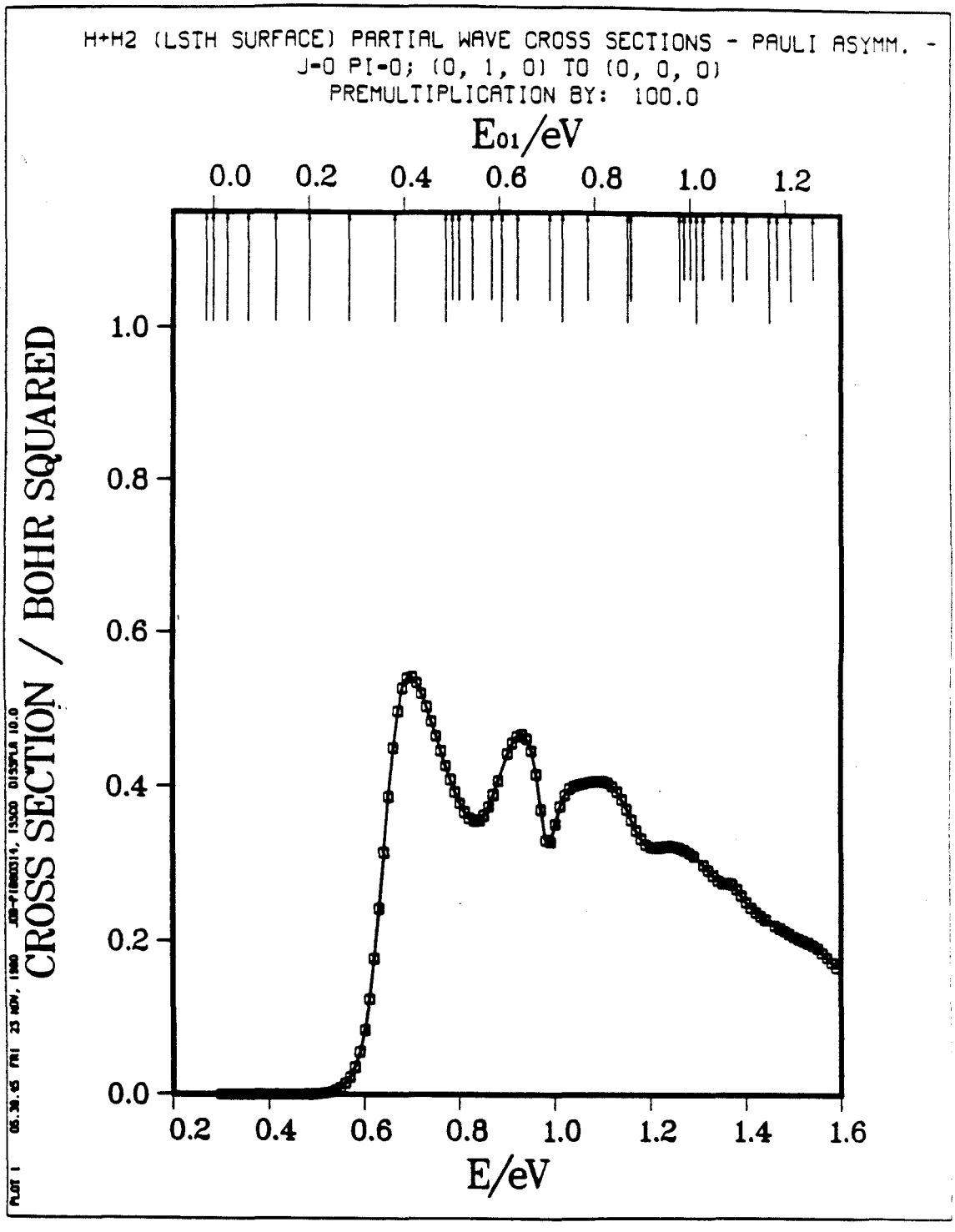
H+H2 (LSTH SURFACE) PARTIAL WAVE CROSS SECTIONS - PAULI ASYMM. -
J=0 PI=0; (0, 1, 0) TO (0, 0, 0)
PREMULTIPLICATION BY: 100.0
E01/eV
0.0
0.2
0.4
0.6
0.8
1.0
1.2
CROSS SECTION / BOHR SQUARED
0.0
0.2
0.4
0.6
0.8
1.0
0.2
0.4
0.6
0.8
1.0
1.2
1.4
1.6
E/eV

Fig. 7.26a

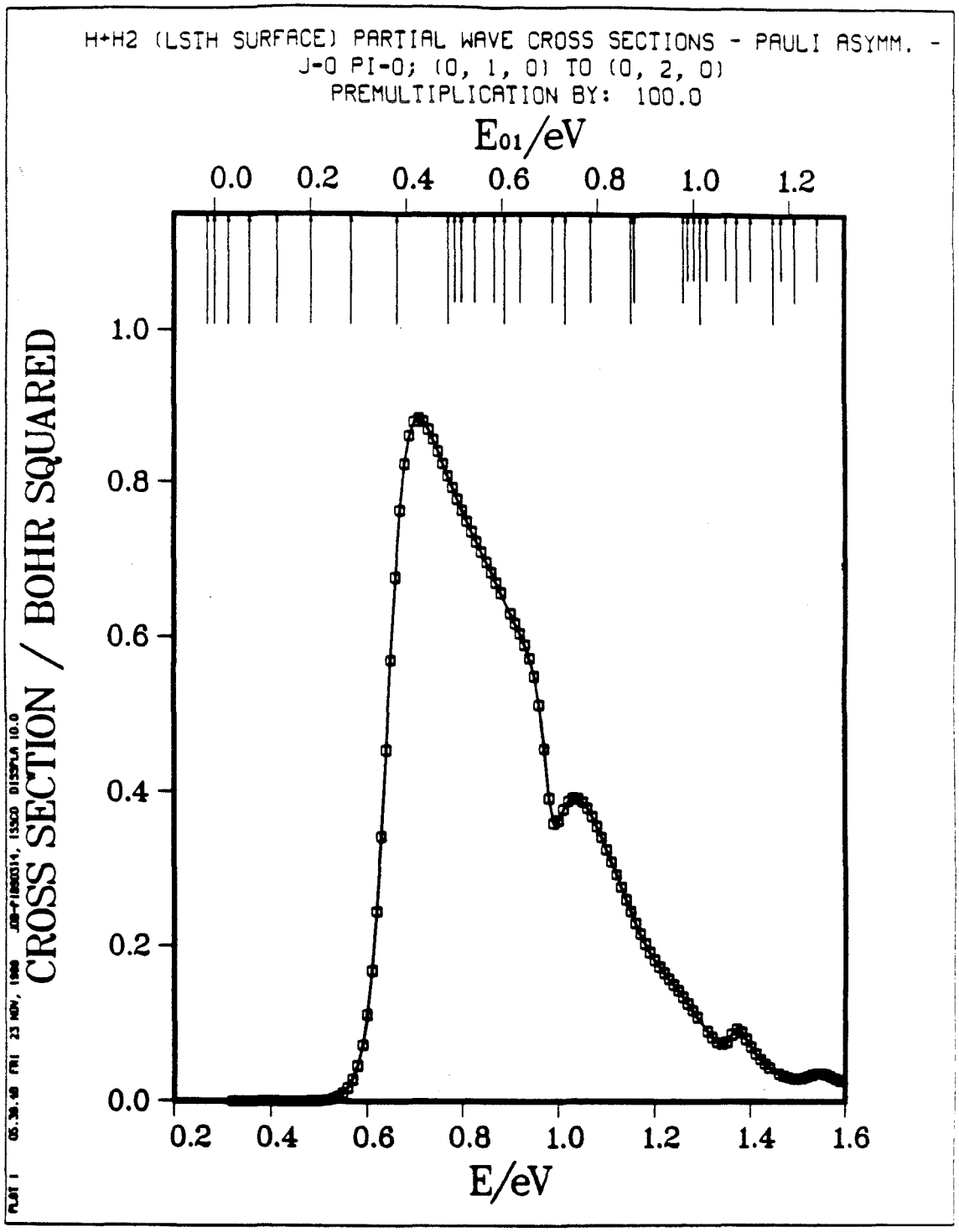
H+H2 (LSTH SURFACE) PARTIAL WAVE CROSS SECTIONS - PAULI ASYMM. -
J=0 PI=0; (0, 1, 0) TO (0, 2, 0)
PREMULTIPLICATION BY: 100.0
E01/eV
0.0
0.2
0.4
0.6
0.8
1.0
1.2
CROSS SECTION / BOHR SQUARED
0.0
0.2
0.4
0.6
0.8
1.0
0.2
0.4
0.6
0.8
1.0
1.2
1.4
1.6
E/eV

Fig. 7.26b

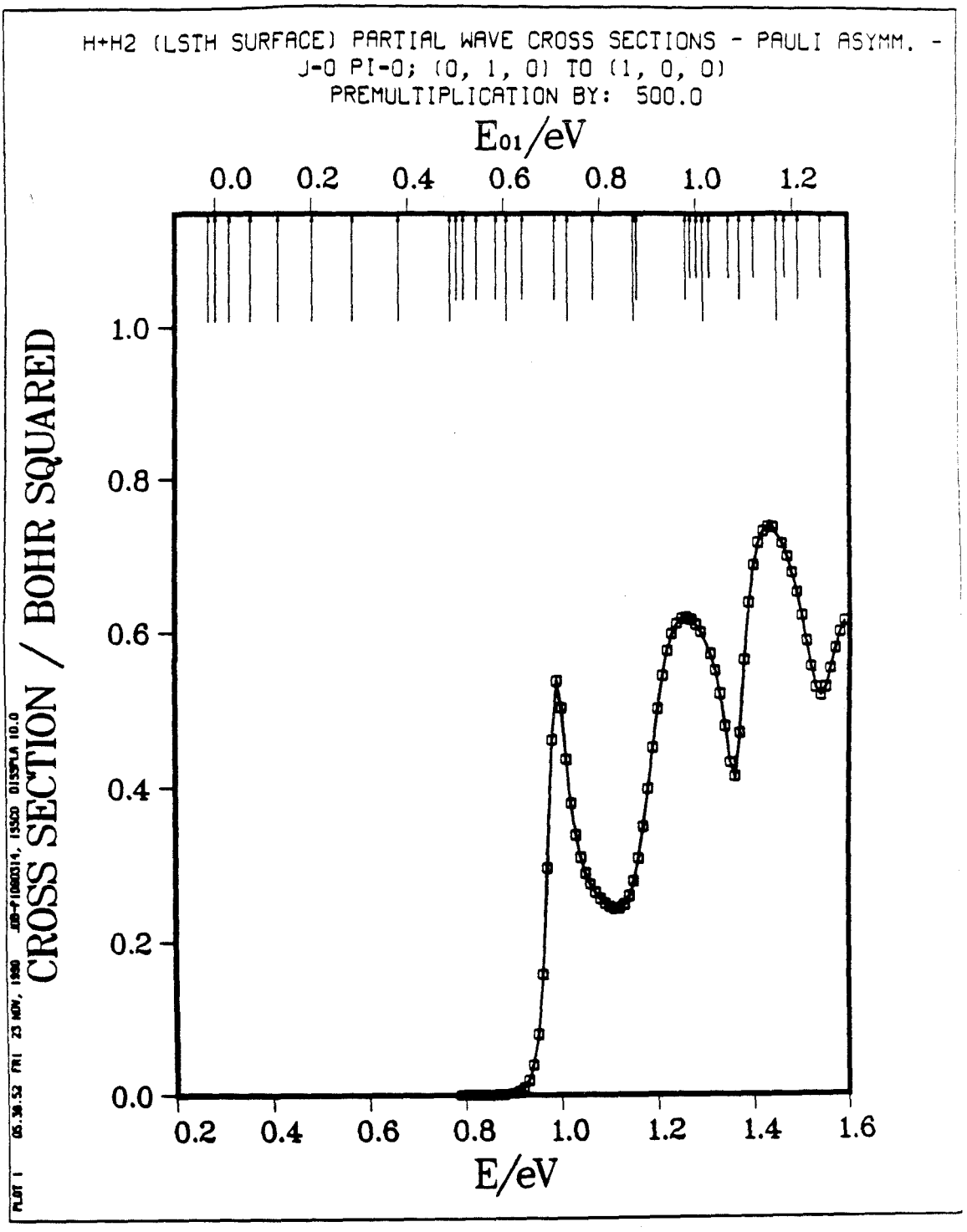
H+H2 (LSTH SURFACE) PARTIAL WAVE CROSS SECTIONS - PAULI ASYMM. -
J=0 PI=0; (0, 1, 0) TO (1, 0, 0)
PREMULTIPLICATION BY: 500.0
E01/eV
0.0
0.2
0.4
0.6
0.8
1.0
1.2
CROSS SECTION / BOHR SQUARED
0.0
0.2
0.4
0.6
0.8
1.0
0.2
0.4
0.6
0.8
1.0
1.2
1.4
1.6
E/eV

Fig. 7.26c

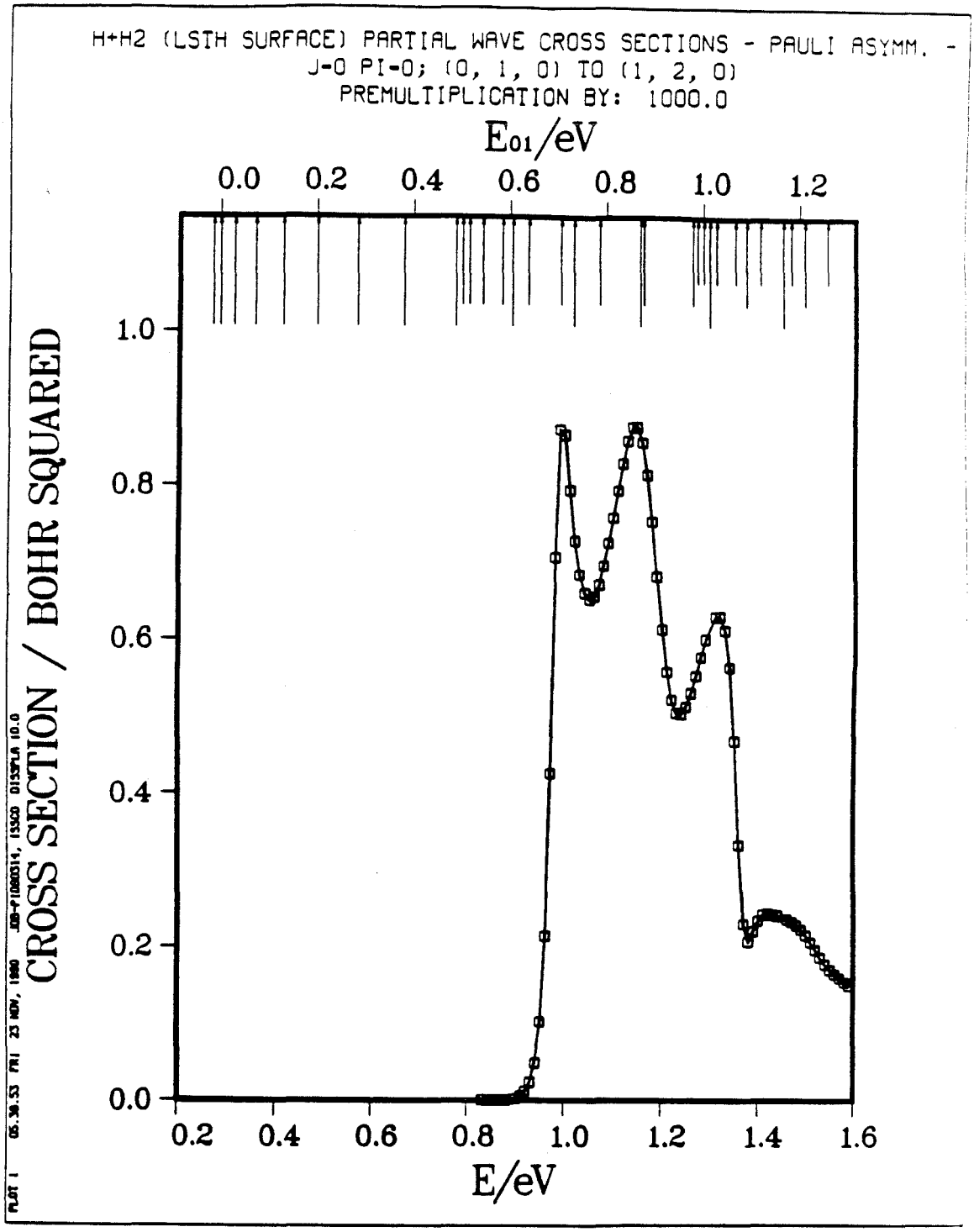
H+H2 (LSTH SURFACE) PARTIAL WAVE CROSS SECTIONS - PAULI ASYMM. -
J=0 PI=0; (0, 1, 0) TO (1, 2, 0)
PREMULTIPLICATION BY: 1000.0
E01/eV
0.0
0.2
0.4
0.6
0.8
1.0
1.2
CROSS SECTION / BOHR SQUARED
0.0
0.2
0.4
0.6
0.8
1.0
0.2
0.4
0.6
0.8
1.0
1.2
1.4
1.6
E/eV

Fig. 7.26d

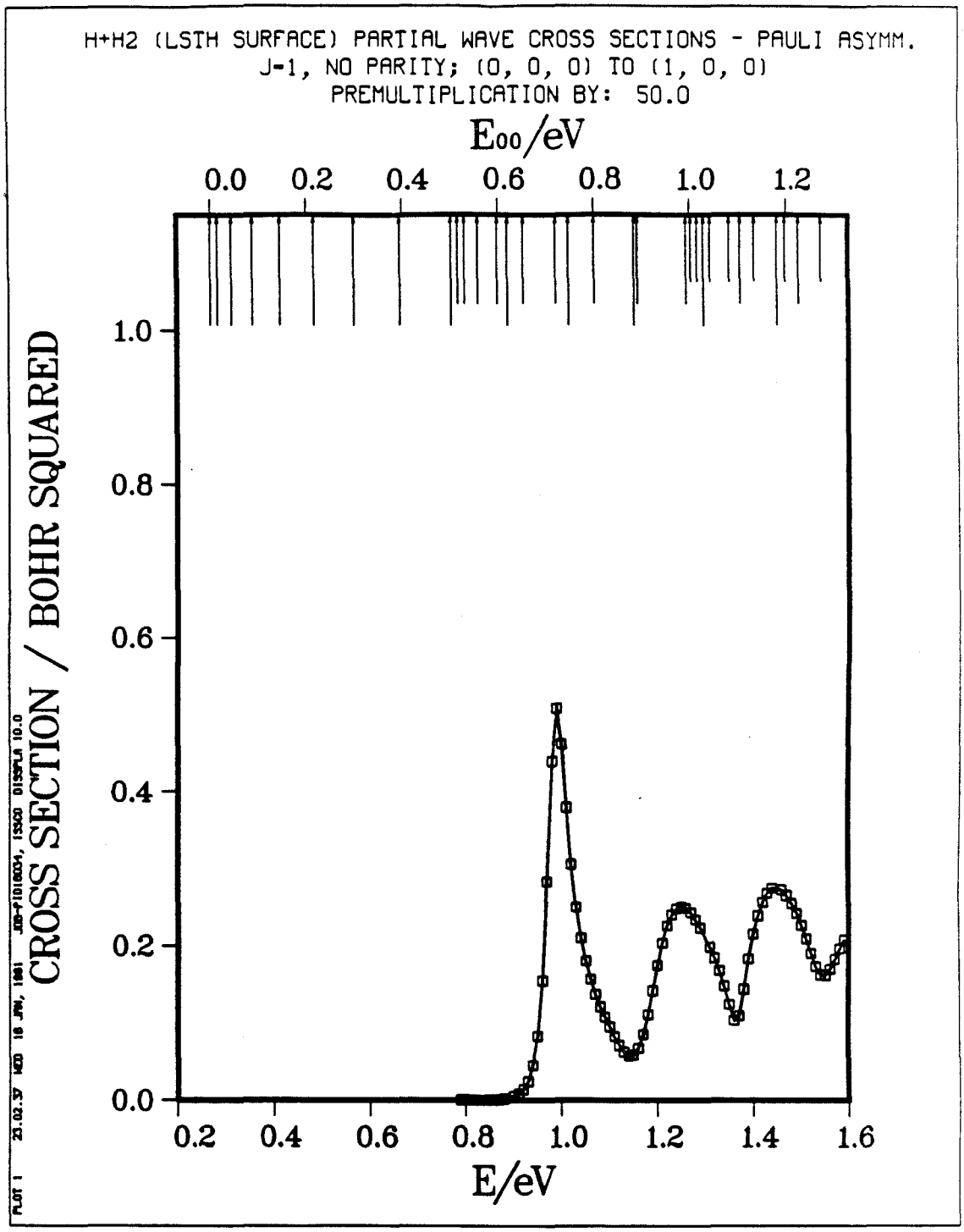
H+H2 (LSTH SURFACE) PARTIAL WAVE CROSS SECTIONS - PAULI ASYMM.
J-1, NO PARITY; (0, 0, 0) TO (1, 0, 0)
PREMULTIPLICATION BY: 50.0
E00/eV
0.0
0.2
0.4
0.6
0.8
1.0
1.2
CROSS SECTION / BOHR SQUARED
0.0
0.2
0.4
0.6
0.8
1.0
0.2
0.4
0.6
0.8
1.0
1.2
1.4
1.6
E/eV

Fig. 7.27a

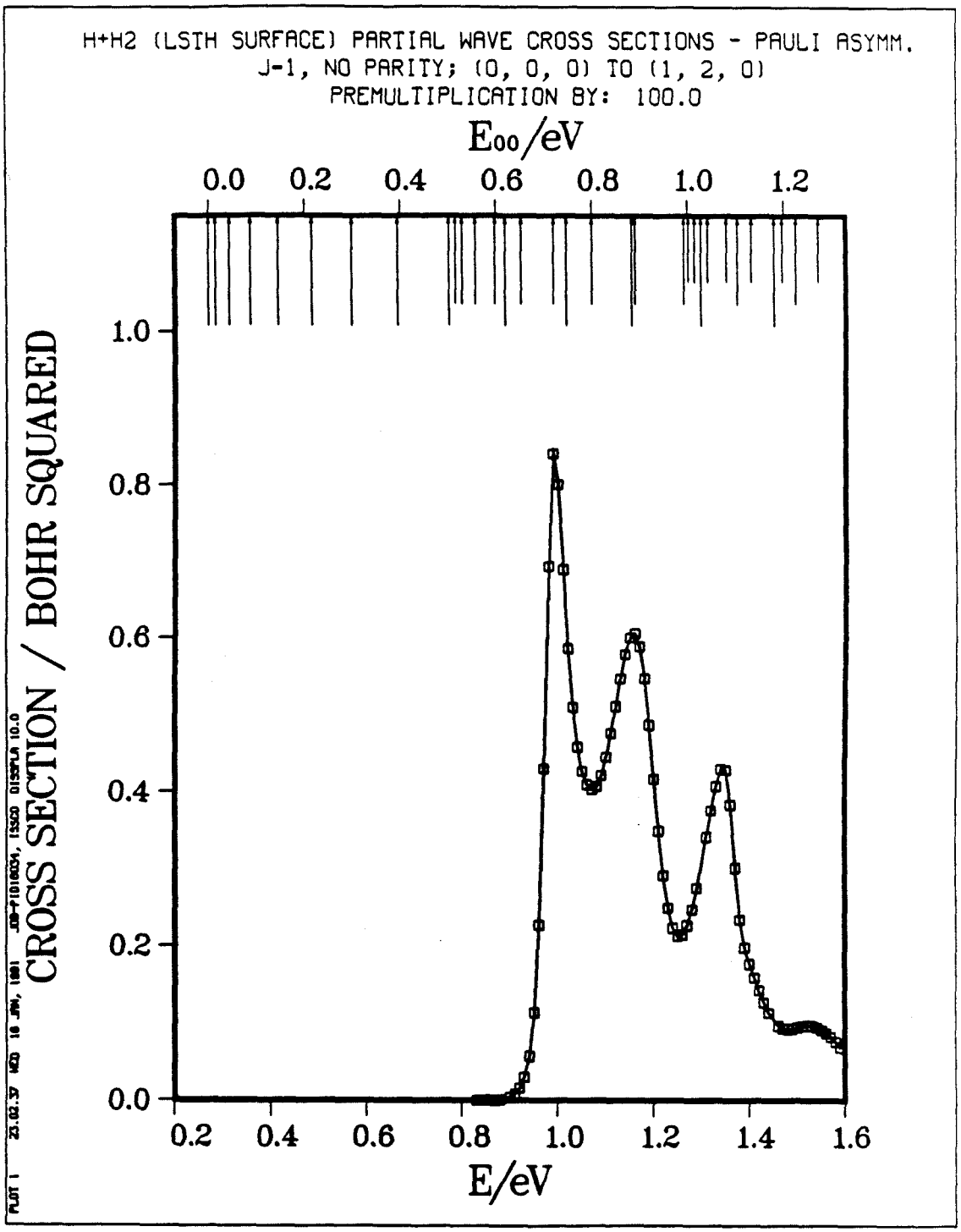
H+H2 (LSTH SURFACE) PARTIAL WAVE CROSS SECTIONS - PAULI ASYMM.
J-1, NO PARITY; (0, 0, 0) TO (1, 2, 0)
PREMULTIPLICATION BY: 100.0
E00/eV
0.0
0.2
0.4
0.6
0.8
1.0
1.2
CROSS SECTION / BOHR SQUARED
0.0
0.2
0.4
0.6
0.8
1.0
0.2
0.4
0.6
0.8
1.0
1.2
1.4
1.6
E/eV

Fig. 7.27b

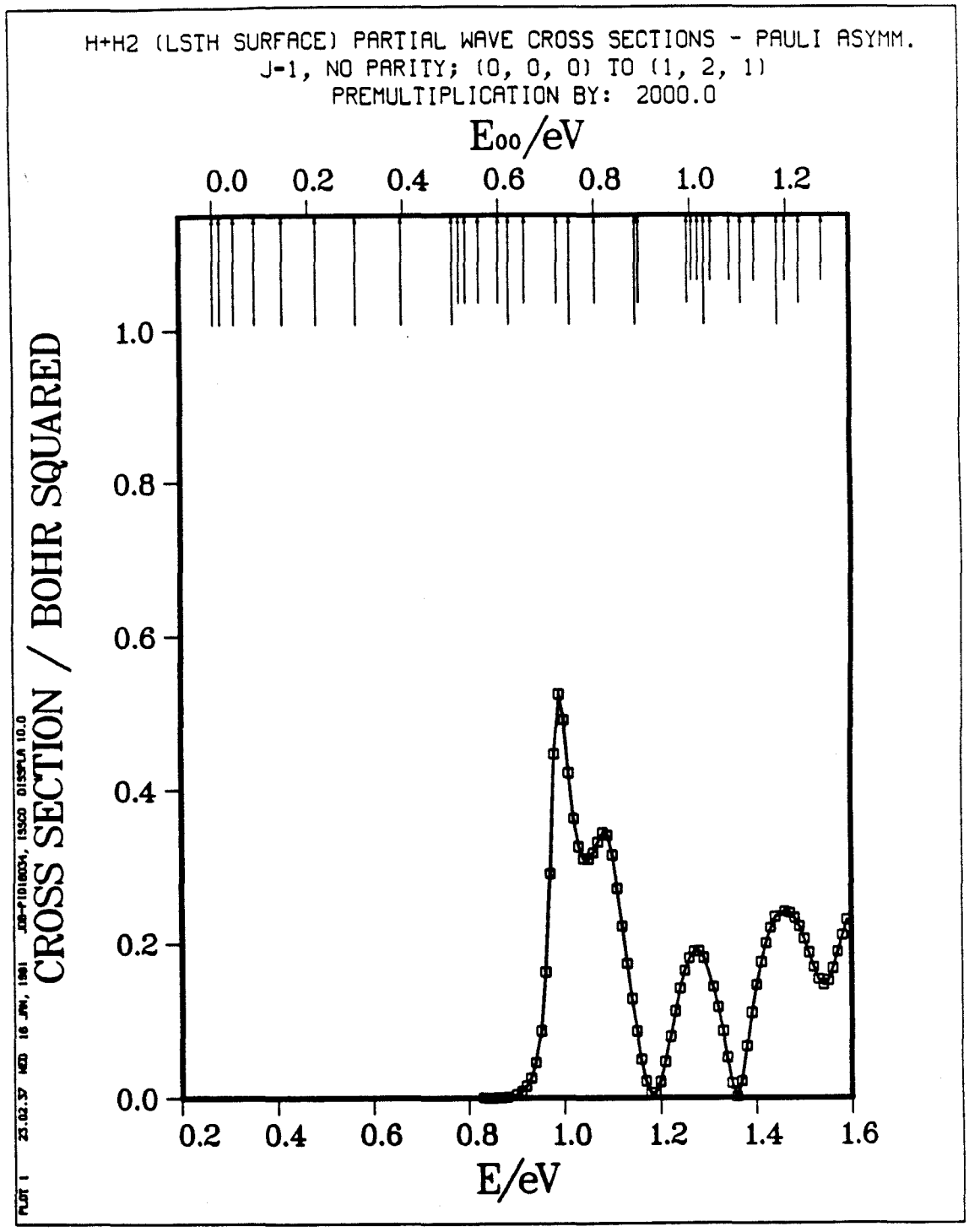
H+H2 (LSTH SURFACE) PARTIAL WAVE CROSS SECTIONS - PAULI ASYMM.
J=1, NO PARITY; (0, 0, 0) TO (1, 2, 1)
PREMULTIPLICATION BY: 2000.0
E00/eV
0.0
0.2
0.4
0.6
0.8
1.0
1.2
CROSS SECTION / BOHR SQUARED
0.0
0.2
0.4
0.6
0.8
1.0
0.2
0.4
0.6
0.8
1.0
1.2
1.4
1.6
E/eV
PLOT 1 25.02.97 WED 16 JAN, 1991 JOB=P1016034, 13SCO DISSPLA 10.0

Fig. 7.27c

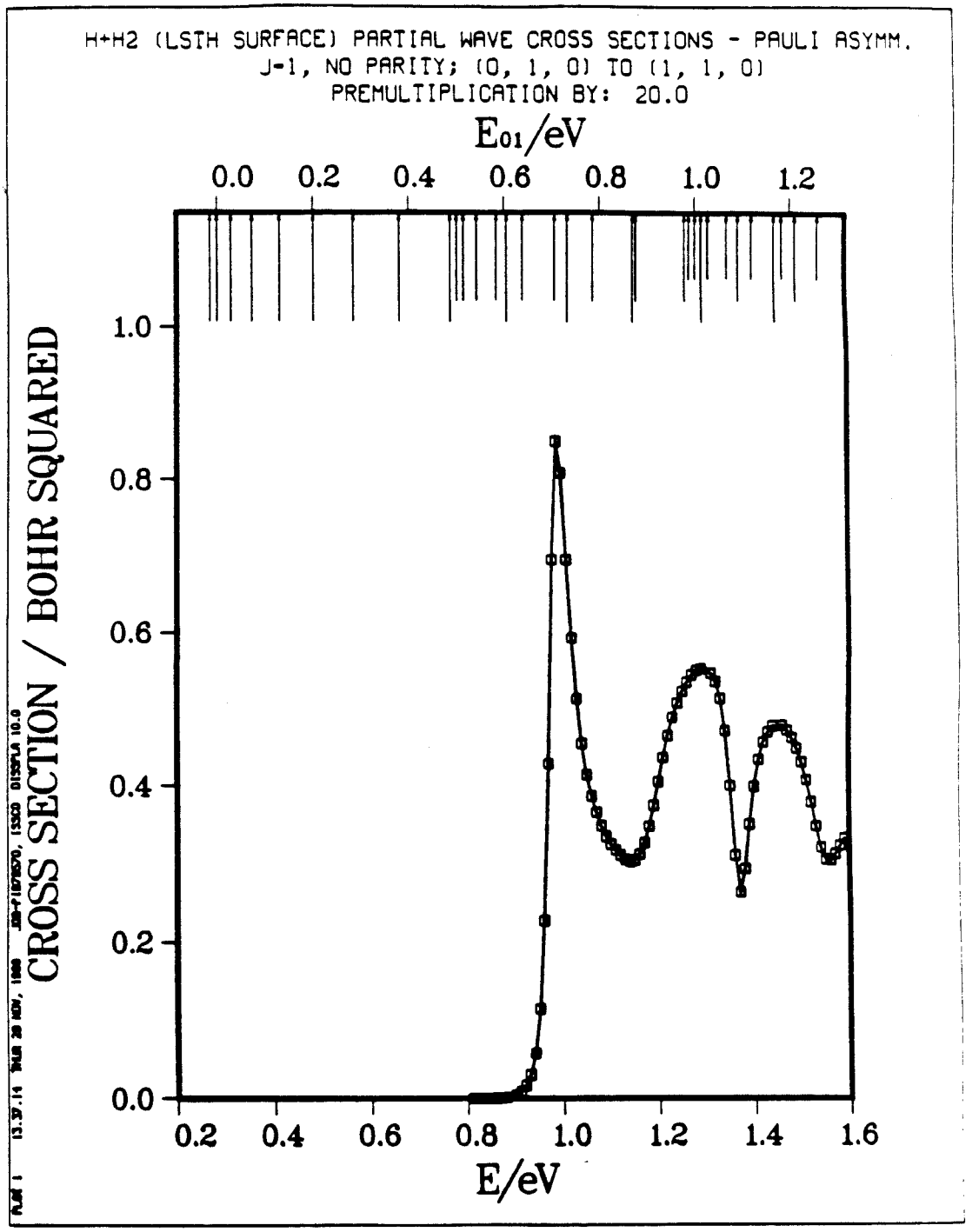
H+H2 (LSTH SURFACE) PARTIAL WAVE CROSS SECTIONS - PAULI ASYMM.
J=1, NO PARITY; (0, 1, 0) TO (1, 1, 0)
PREMULTIPLICATION BY: 20.0
E01/eV
0.0
0.2
0.4
0.6
0.8
1.0
1.2
CROSS SECTION / BOHR SQUARED
0.0
0.2
0.4
0.6
0.8
1.0
0.2
0.4
0.6
0.8
1.0
1.2
1.4
1.6
E/eV

Fig. 7.27d

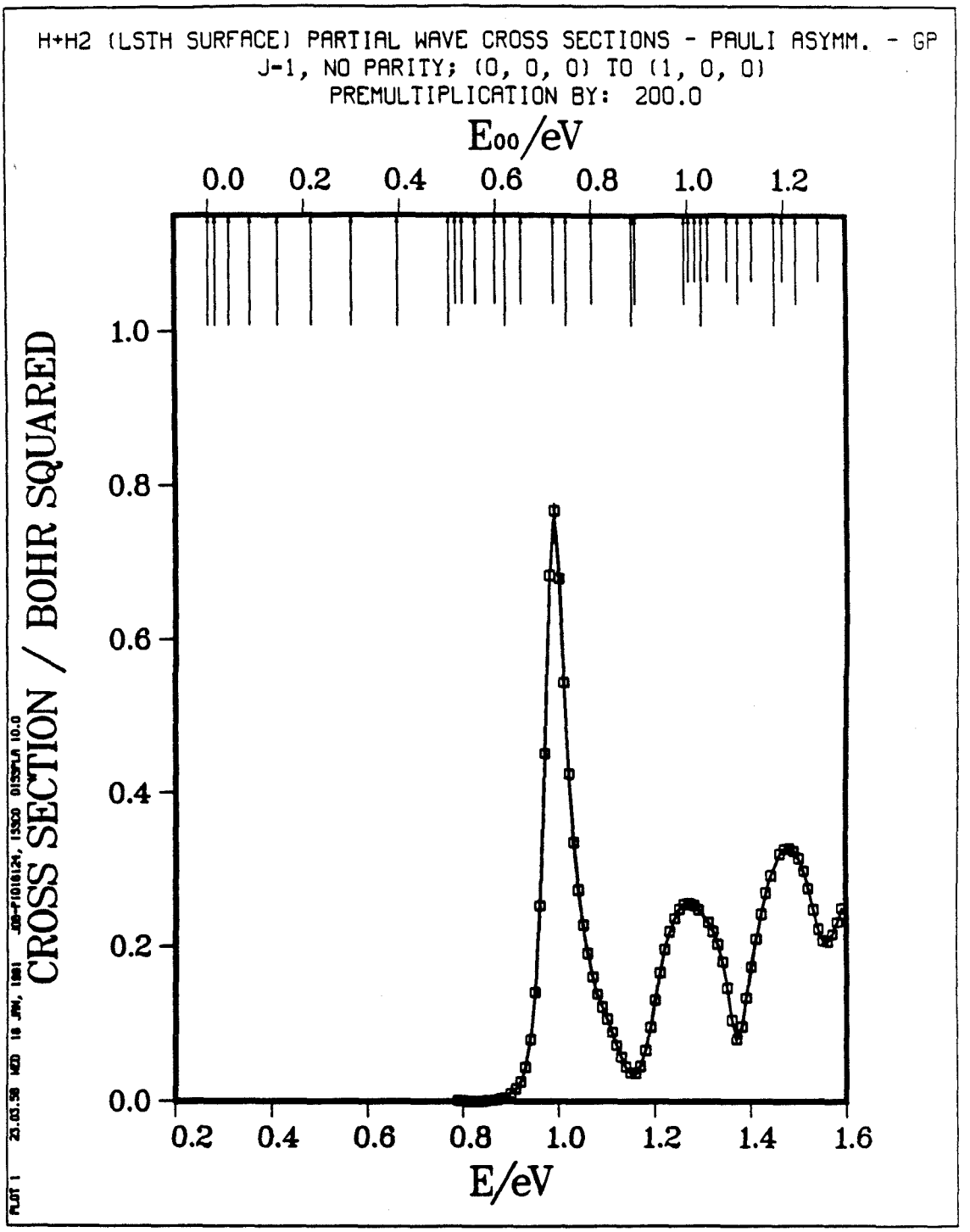
H+H2 (LSTH SURFACE) PARTIAL WAVE CROSS SECTIONS - PAULI ASYMM. - GP
J-1, NO PARITY; (0, 0, 0) TO (1, 0, 0)
PREMULTIPLICATION BY: 200.0
E00/eV
0.0
0.2
0.4
0.6
0.8
1.0
1.2
CROSS SECTION / BOHR SQUARED
0.0
0.2
0.4
0.6
0.8
1.0
0.2
0.4
0.6
0.8
1.0
1.2
1.4
1.6
E/eV

Fig. 7.28a

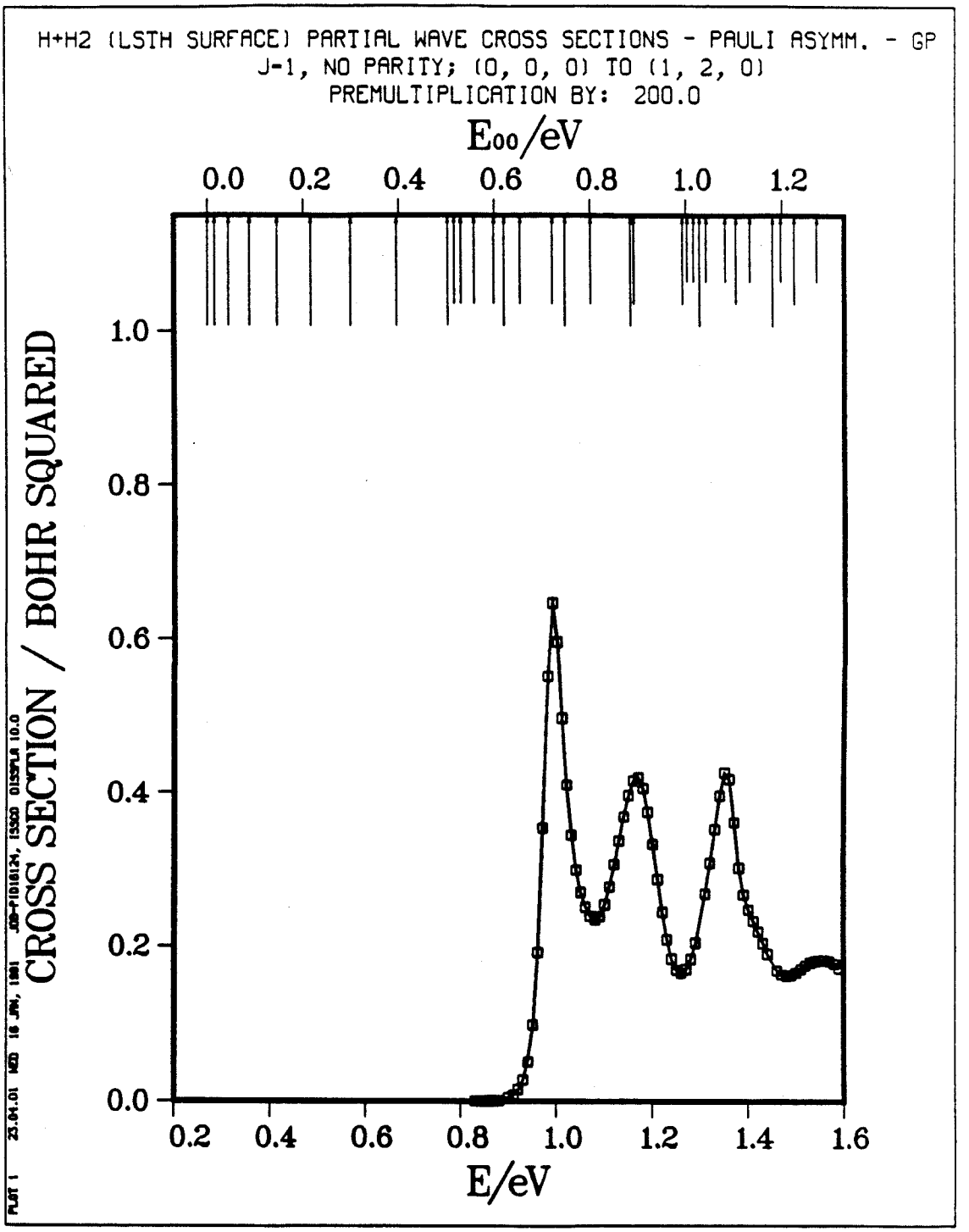
H+H2 (LSTH SURFACE) PARTIAL WAVE CROSS SECTIONS - PAULI ASYMM. - GP
J-1, NO PARITY; (0, 0, 0) TO (1, 2, 0)
PREMULTIPLICATION BY: 200.0
E00/eV
0.0
0.2
0.4
0.6
0.8
1.0
1.2
CROSS SECTION / BOHR SQUARED
0.0
0.2
0.4
0.6
0.8
1.0
0.2
0.4
0.6
0.8
1.0
1.2
1.4
1.6
E/eV

Fig. 7.28b

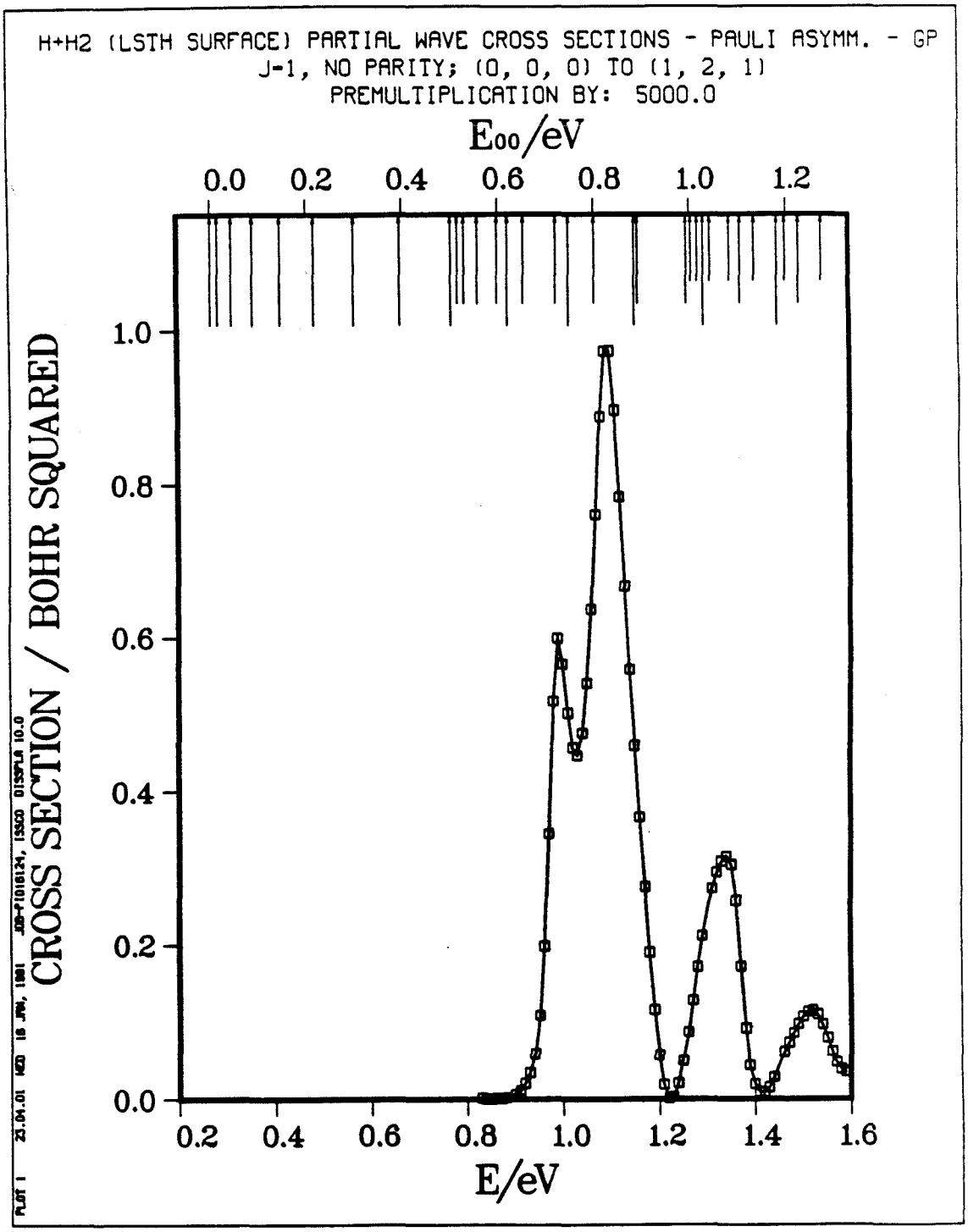
H+H2 (LSTH SURFACE) PARTIAL WAVE CROSS SECTIONS - PAULI ASYMM. - GP
J=1, NO PARITY; (0, 0, 0) TO (1, 2, 1)
PREMULTIPLICATION BY: 5000.0
E00/eV
0.0
0.2
0.4
0.6
0.8
1.0
1.2
CROSS SECTION / BOHR SQUARED
0.0
0.2
0.4
0.6
0.8
1.0
0.2
0.4
0.6
0.8
1.0
1.2
1.4
1.6
E/eV

Fig. 7.28c

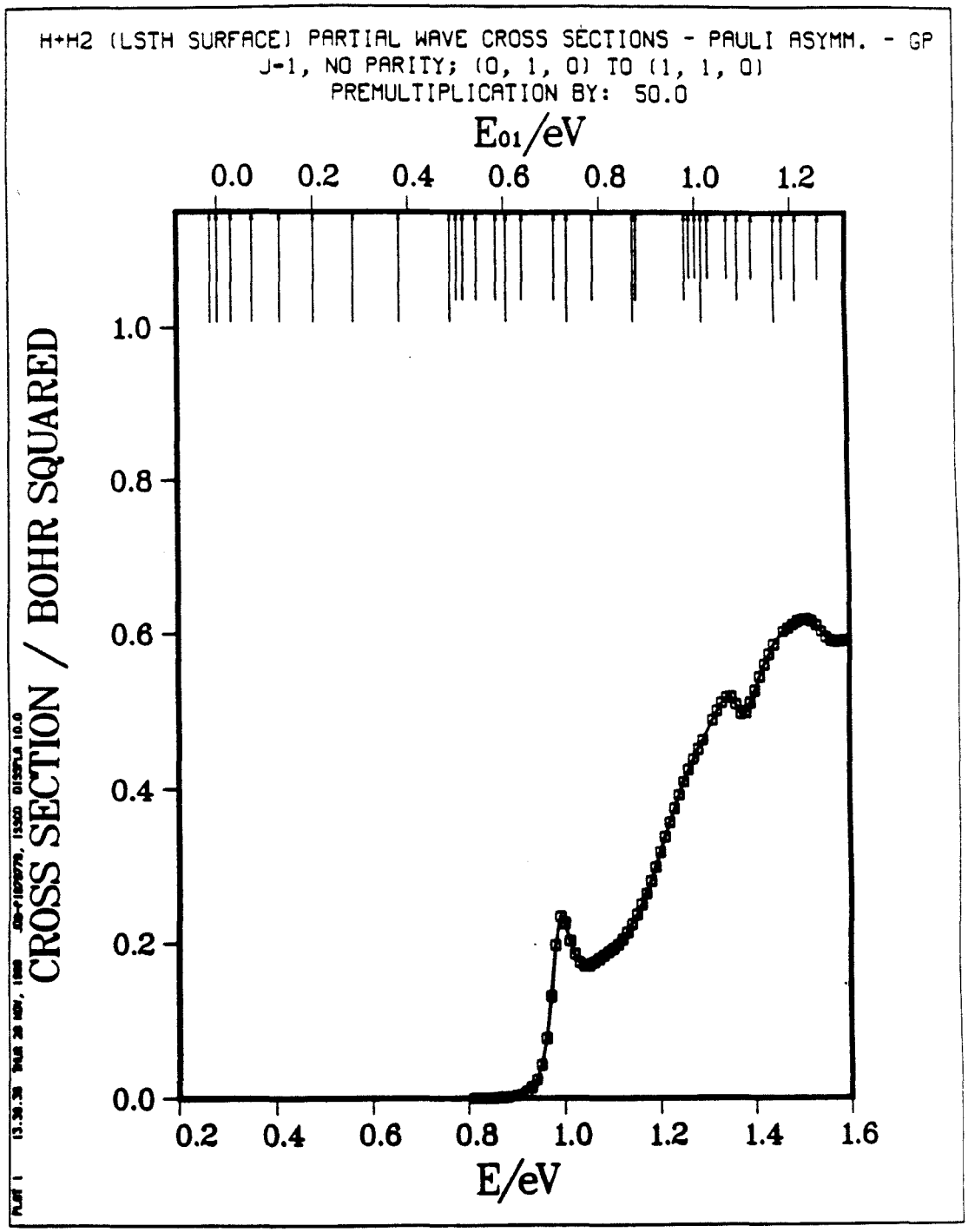
H+H2 (LSTH SURFACE) PARTIAL WAVE CROSS SECTIONS - PAULI ASYMM. - GP
J=1, NO PARITY; (0, 1, 0) TO (1, 1, 0)
PREMULTIPLICATION BY: 50.0
E01/eV
0.0
0.2
0.4
0.6
0.8
1.0
1.2
CROSS SECTION / BOHR SQUARED
0.0
0.2
0.4
0.6
0.8
1.0
0.2
0.4
0.6
0.8
1.0
1.2
1.4
1.6
E/eV

Fig. 7.28d

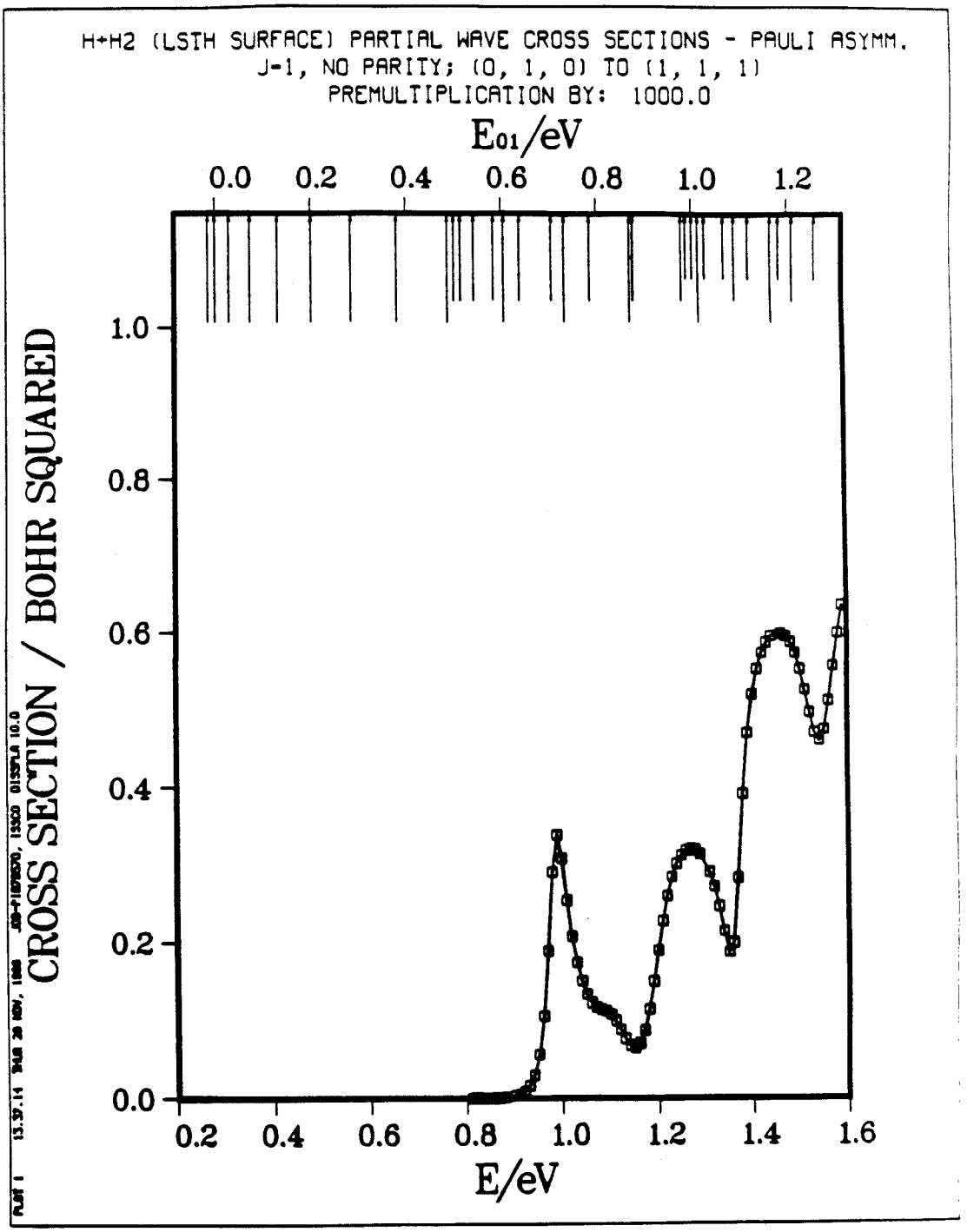
H+H2 (LSTH SURFACE) PARTIAL WAVE CROSS SECTIONS - PAULI ASYMM.
J=1, NO PARITY; (0, 1, 0) TO (1, 1, 1)
PREMULTIPLICATION BY: 1000.0
E01/eV
0.0
0.2
0.4
0.6
0.8
1.0
1.2
CROSS SECTION / BOHR SQUARED
0.0
0.2
0.4
0.6
0.8
1.0
0.2
0.4
0.6
0.8
1.0
1.2
1.4
1.6
E/eV

Fig. 7.29a

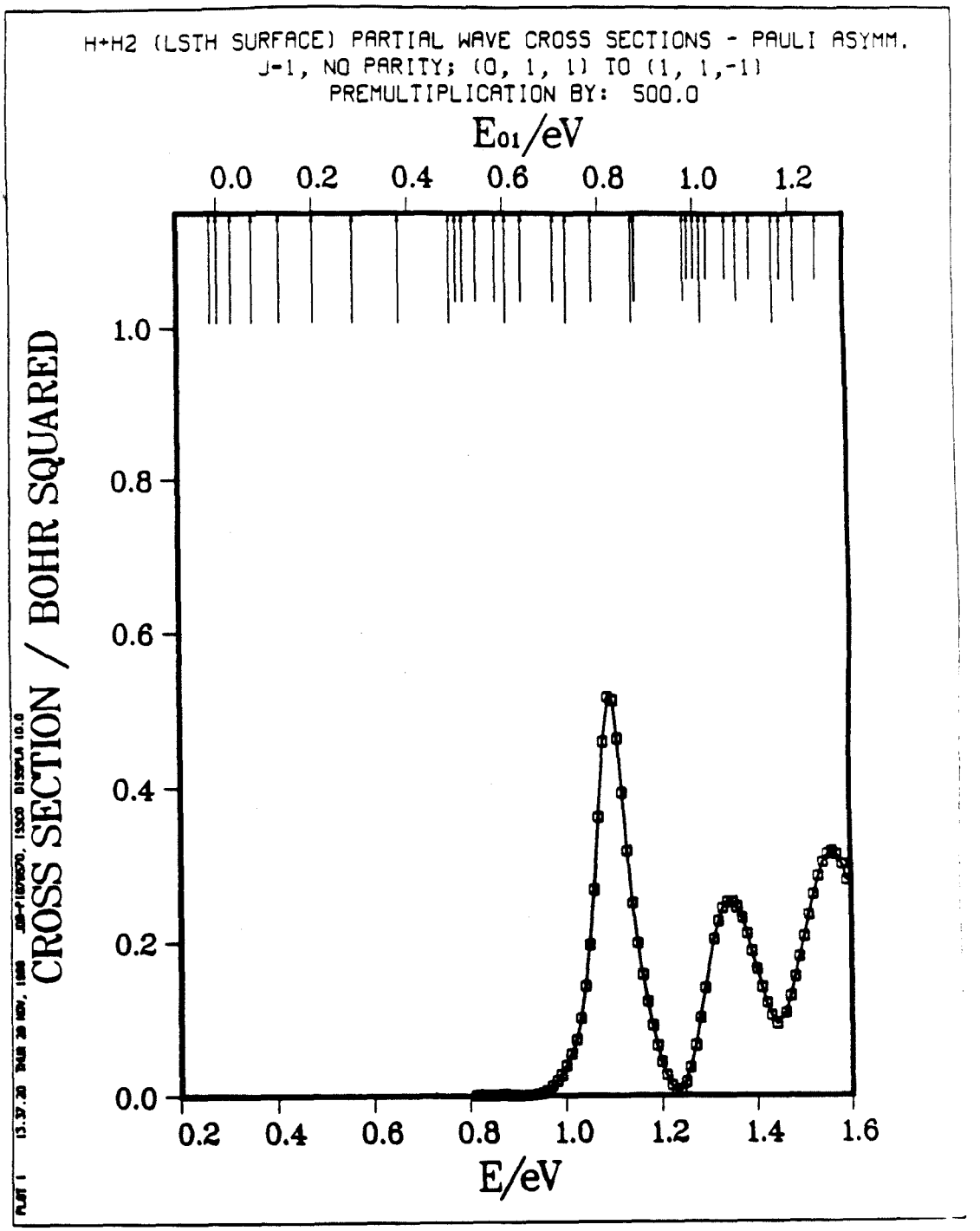
H+H2 (LSTH SURFACE) PARTIAL WAVE CROSS SECTIONS - PAULI ASYMM.
J=1, NO PARITY; (0, 1, 1) TO (1, 1,-1)
PREMULTIPLICATION BY: 500.0
E01/eV
0.0
0.2
0.4
0.6
0.8
1.0
1.2
CROSS SECTION / BOHR SQUARED
1.0
0.8
0.6
0.4
0.2
0.0
0.2
0.4
0.6
0.8
1.0
1.2
1.4
1.6
E/eV

Fig. 7.29b

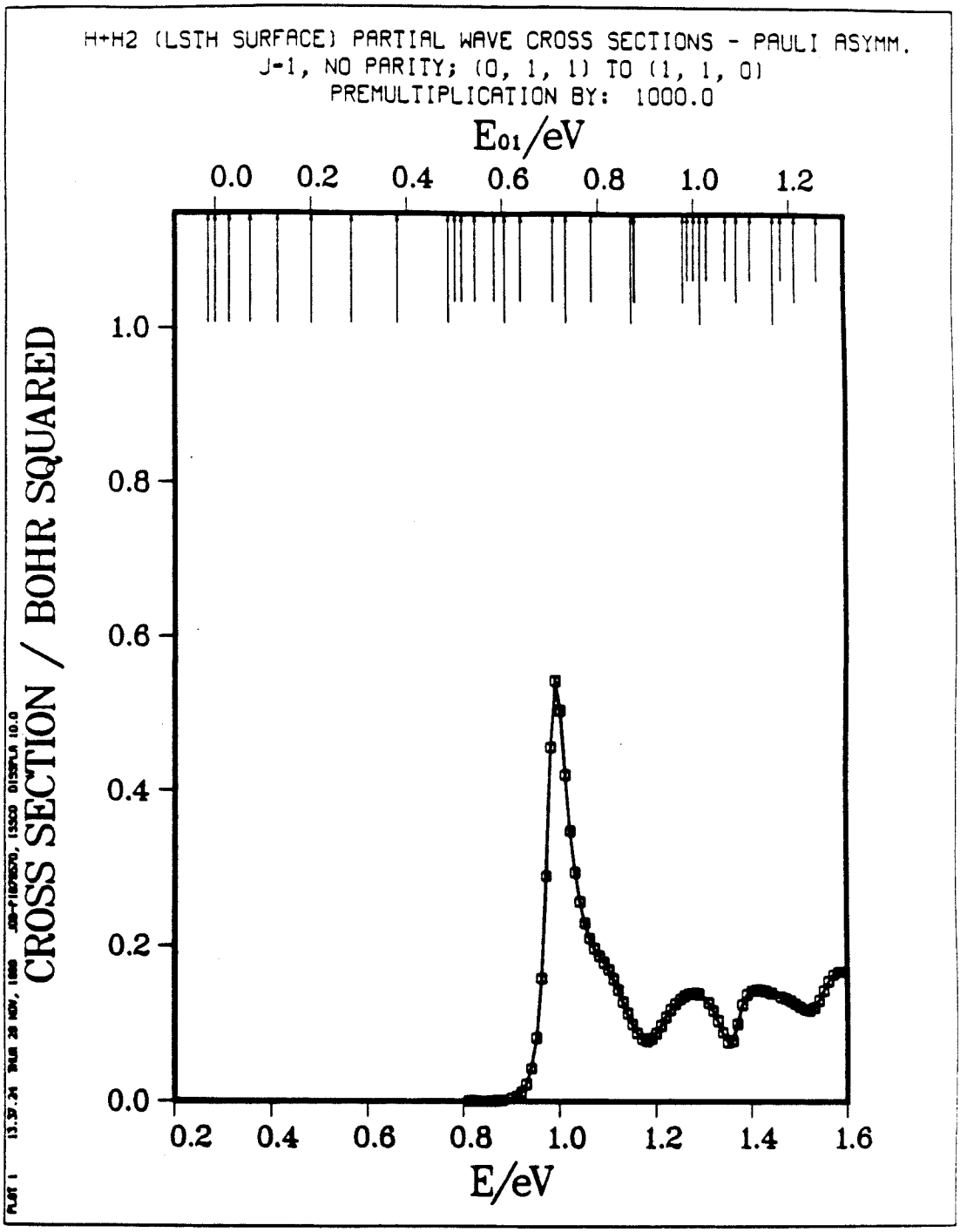
H+H2 (LSTH SURFACE) PARTIAL WAVE CROSS SECTIONS - PAULI ASYMM.
J=1, NO PARITY; (0, 1, 1) TO (1, 1, 0)
PREMULTIPLICATION BY: 1000.0
E01/eV
0.0
0.2
0.4
0.6
0.8
1.0
1.2
CROSS SECTION / BOHR SQUARED
0.0
0.2
0.4
0.6
0.8
1.0
E/eV
0.2
0.4
0.6
0.8
1.0
1.2
1.4
1.6

Fig. 7.29c

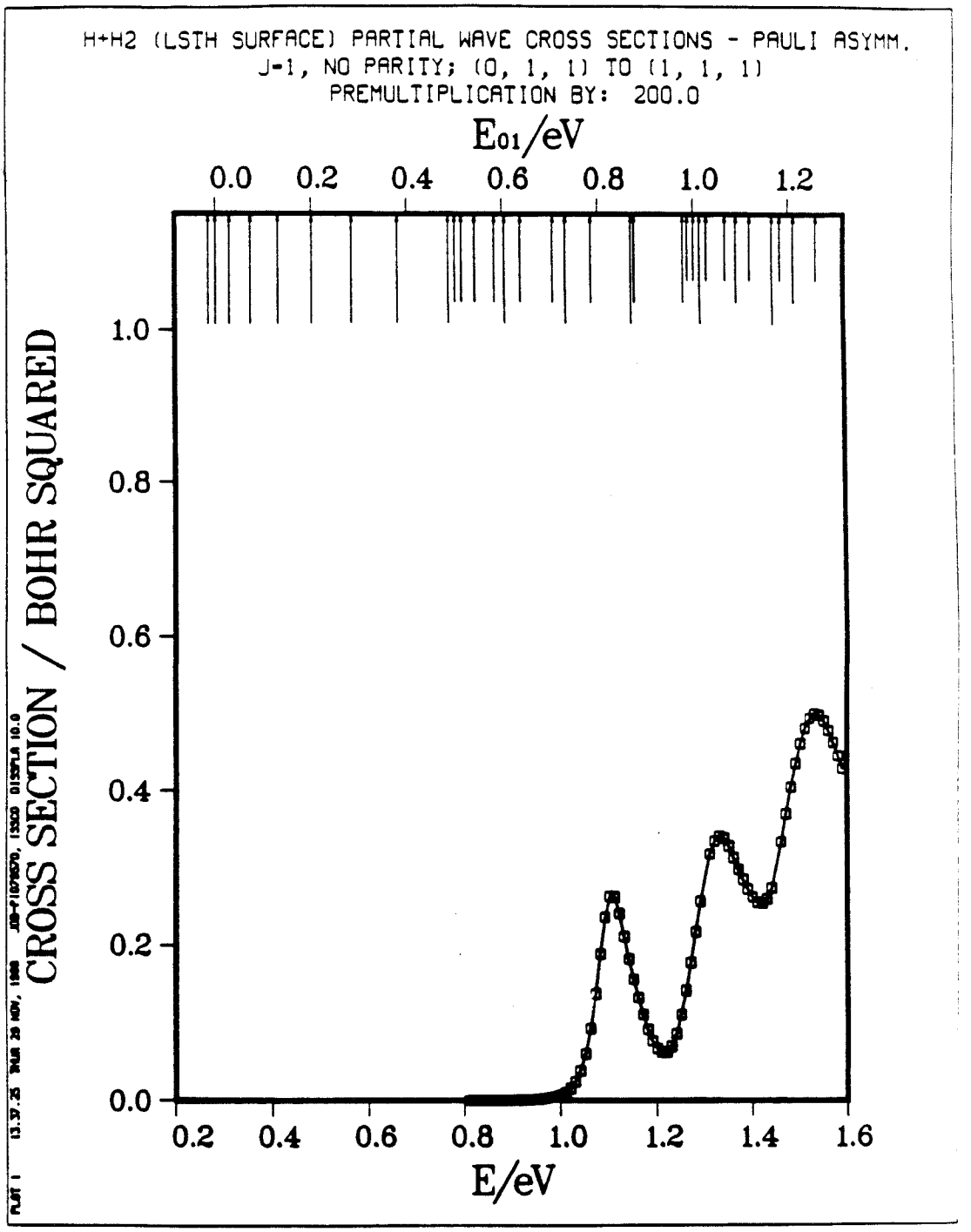
H+H2 (LSTH SURFACE) PARTIAL WAVE CROSS SECTIONS - PAULI ASYMM.
J=1, NO PARITY; (0, 1, 1) TO (1, 1, 1)
PREMULTIPLICATION BY: 200.0
E01/eV
0.0
0.2
0.4
0.6
0.8
1.0
1.2
CROSS SECTION / BOHR SQUARED
0.0
0.2
0.4
0.6
0.8
1.0
1.2
1.4
1.6
E/eV

Fig. 7.29d

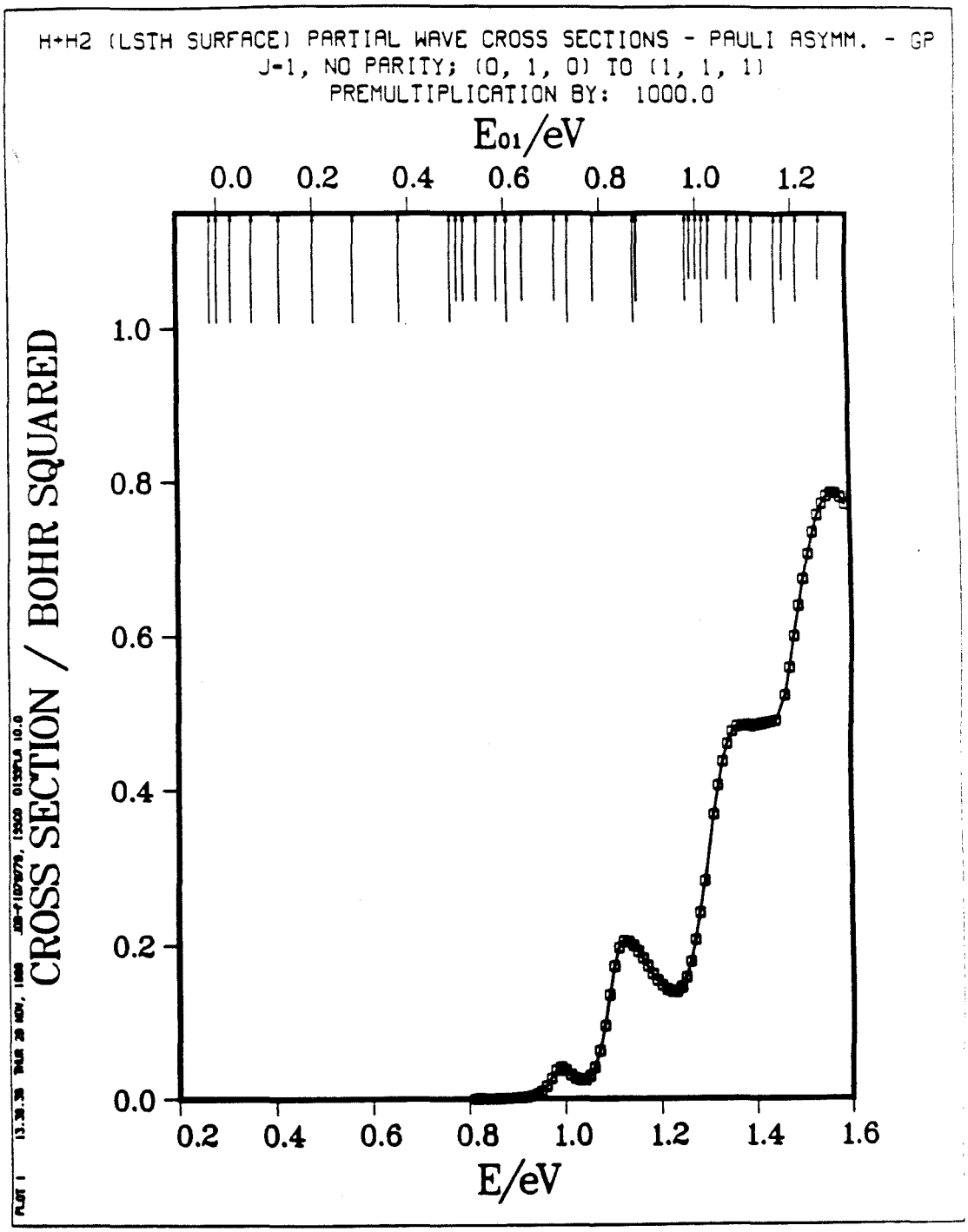
H+H2 (LSTH SURFACE) PARTIAL WAVE CROSS SECTIONS - PAULI ASYMM. - GP
J=1, NO PARITY; (0, 1, 0) TO (1, 1, 1)
PREMULTIPLICATION BY: 1000.0
E01/eV
0.0
0.2
0.4
0.6
0.8
1.0
1.2
CROSS SECTION / BOHR SQUARED
0.0
0.2
0.4
0.6
0.8
1.0
0.2
0.4
0.6
0.8
1.0
1.2
1.4
1.6
E/eV

Fig. 7.30a

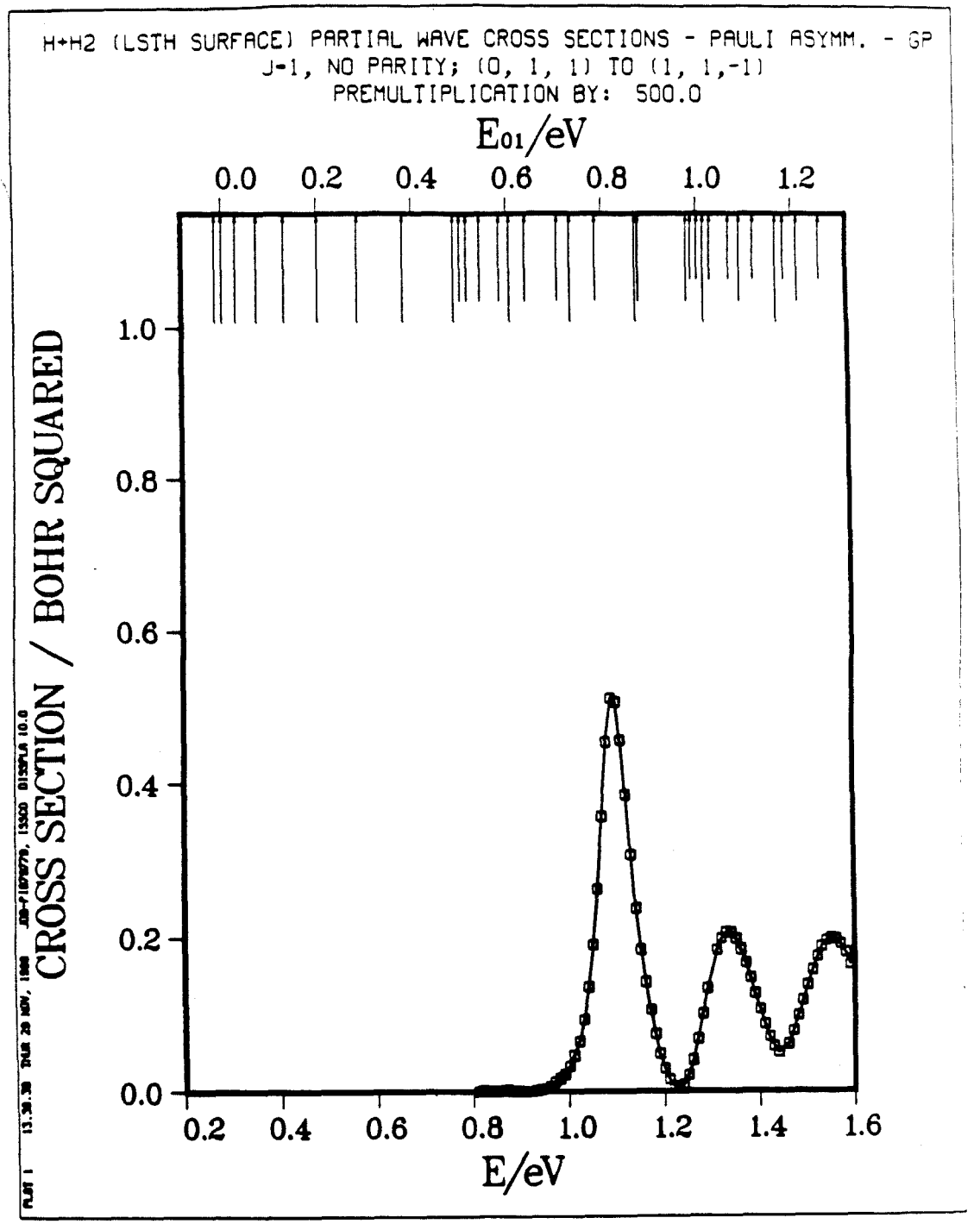
H+H2 (LSTH SURFACE) PARTIAL WAVE CROSS SECTIONS - PAULI ASYMM. - GP
J=1, NO PARITY; (0, 1, 1) TO (1, 1,-1)
PREMULTIPLICATION BY: 500.0
E01/eV
0.0
0.2
0.4
0.6
0.8
1.0
1.2
CROSS SECTION / BOHR SQUARED
1.0
0.8
0.6
0.4
0.2
0.0
0.2
0.4
0.6
0.8
1.0
1.2
1.4
1.6
E/eV

Fig. 7.30b

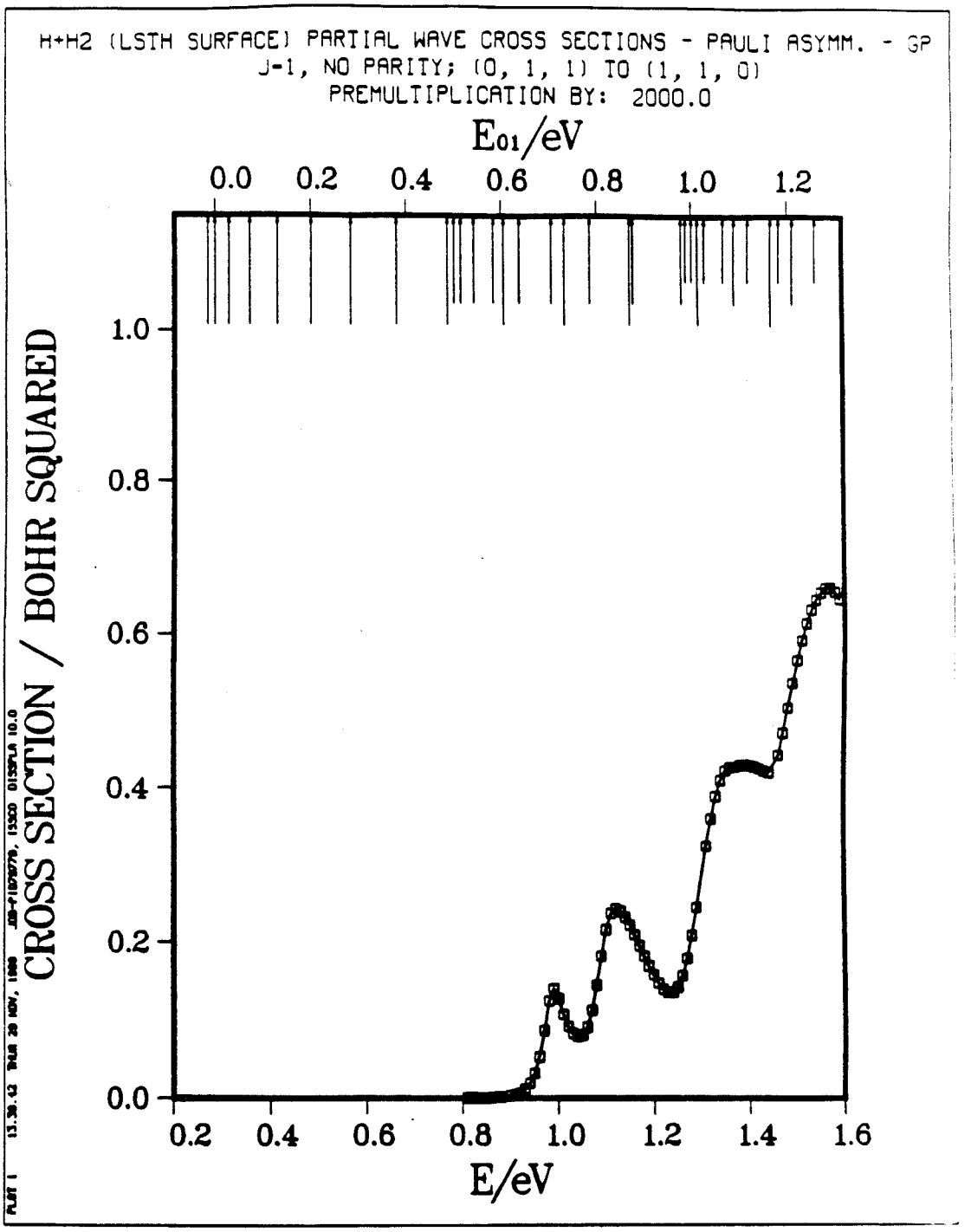
H+H2 (LSTH SURFACE) PARTIAL WAVE CROSS SECTIONS - PAULI ASYMM. - GP
J=1, NO PARITY; (0, 1, 1) TO (1, 1, 0)
PREMULTIPLICATION BY: 2000.0
E01/eV
0.0
0.2
0.4
0.6
0.8
1.0
1.2
CROSS SECTION / BOHR SQUARED
0.0
0.2
0.4
0.6
0.8
1.0
0.2
0.4
0.6
0.8
1.0
1.2
1.4
1.6
E/eV

Fig. 7.30c

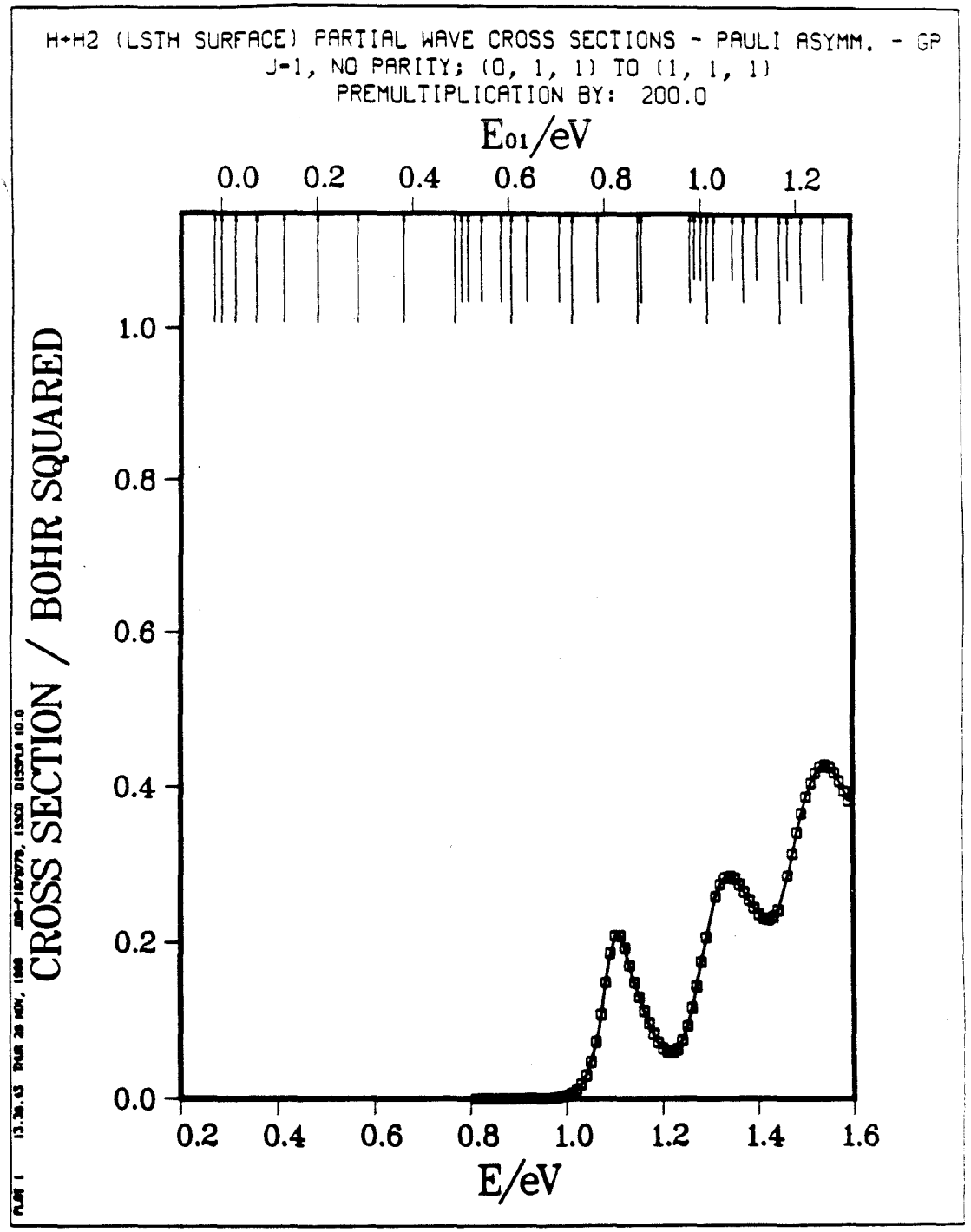
H+H2 (LSTH SURFACE) PARTIAL WAVE CROSS SECTIONS - PAULI ASYMM. - GP
J=1, NO PARITY; (0, 1, 1) TO (1, 1, 1)
PREMULTIPLICATION BY: 200.0
E01/eV
0.0
0.2
0.4
0.6
0.8
1.0
1.2
CROSS SECTION / BOHR SQUARED
0.0
0.2
0.4
0.6
0.8
1.0
0.2
0.4
0.6
0.8
1.0
1.2
1.4
1.6
E/eV

Fig. 7.30d

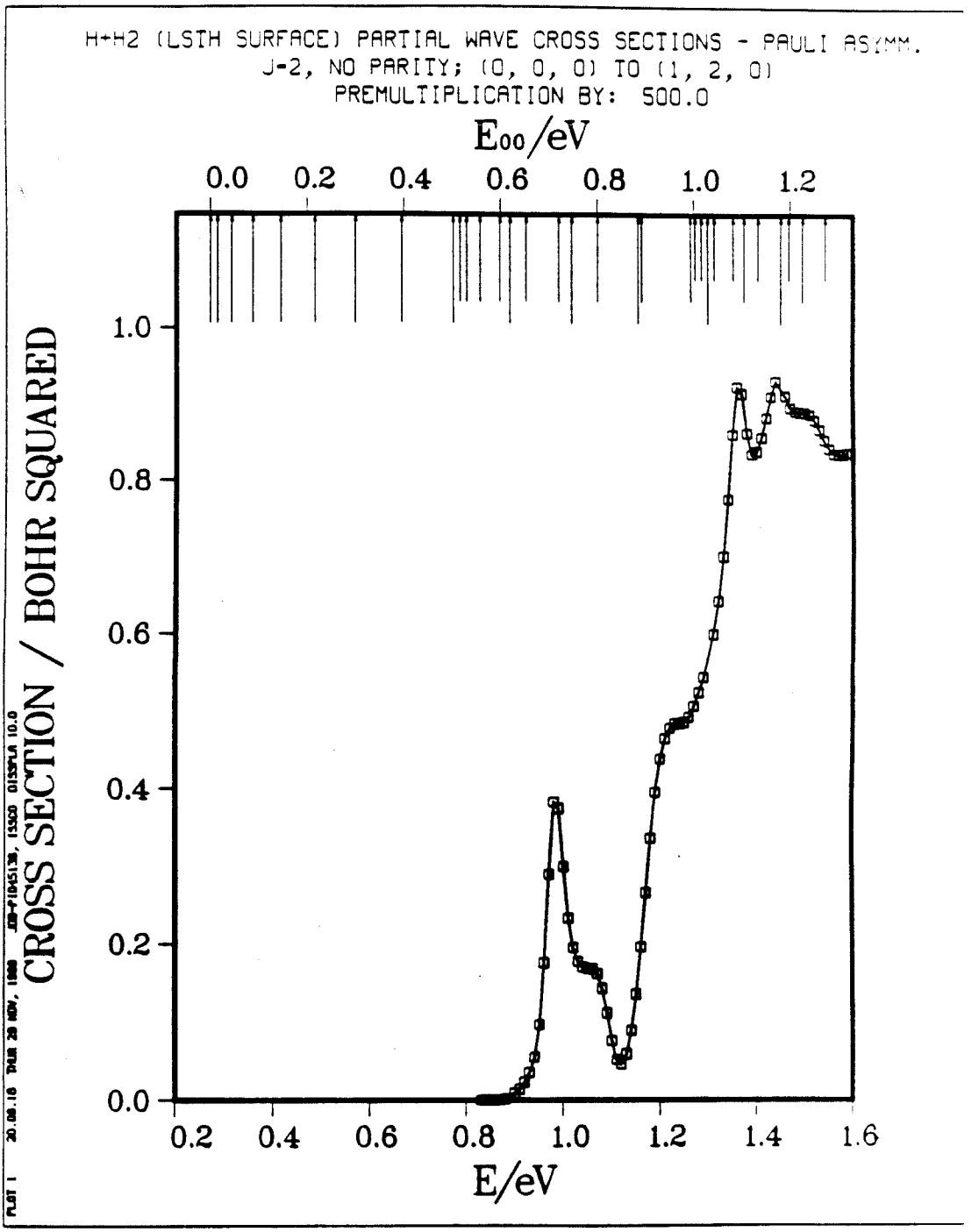
H+H2 (LSTH SURFACE) PARTIAL WAVE CROSS SECTIONS - PAULI ASYMM.
J=2, NO PARITY; (0, 0, 0) TO (1, 2, 0)
PREMULTIPLICATION BY: 500.0
E00/eV
0.0
0.2
0.4
0.6
0.8
1.0
1.2
CROSS SECTION / BOHR SQUARED
0.0
0.2
0.4
0.6
0.8
1.0
0.2
0.4
0.6
0.8
1.0
1.2
1.4
1.6
E/eV

Fig. 7.31a

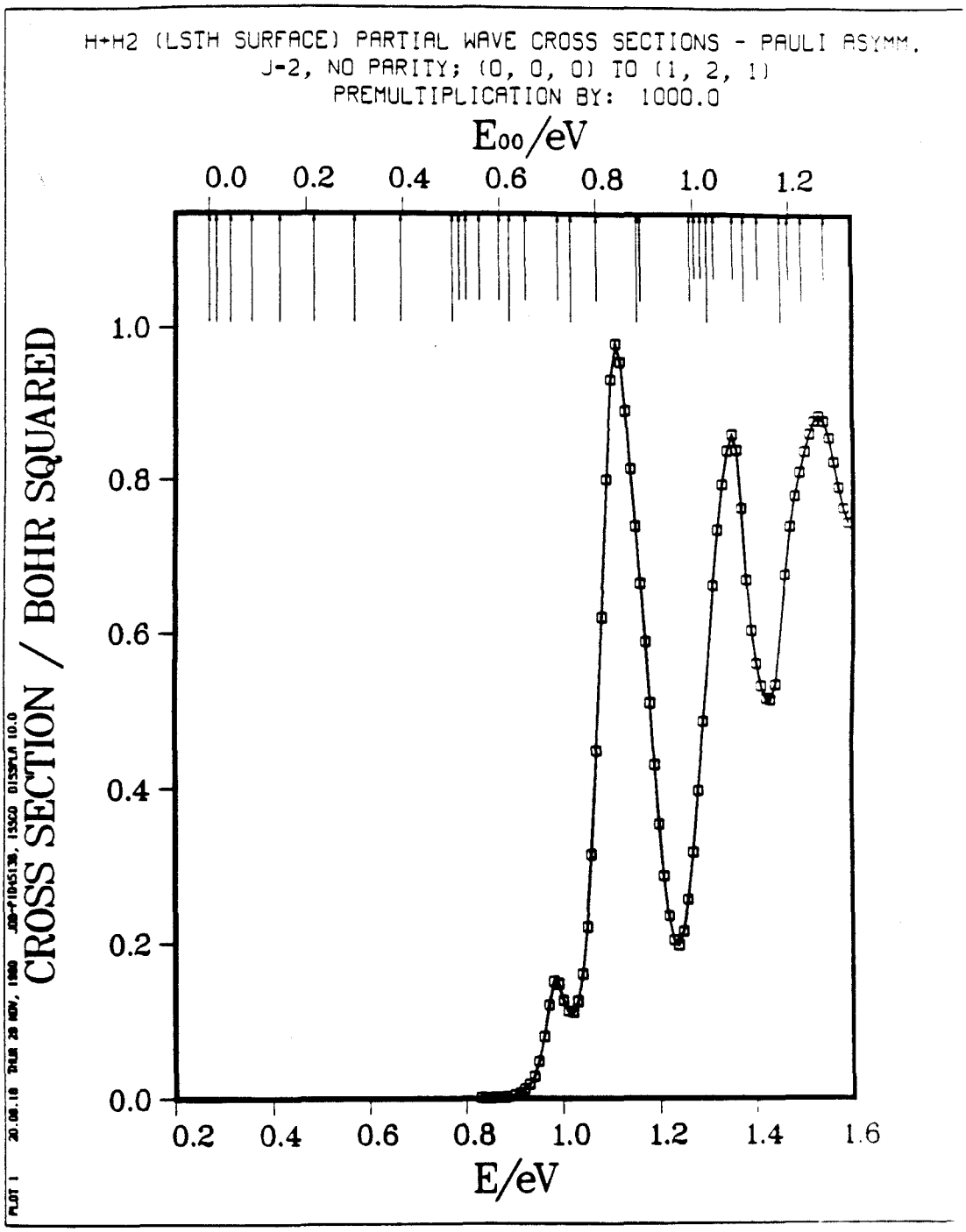
H+H2 (LSTH SURFACE) PARTIAL WAVE CROSS SECTIONS - PAULI ASYMM.
J=2, NO PARITY; (0, 0, 0) TO (1, 2, 1)
PREMULTIPLICATION BY: 1000.0
E00/eV
0.0
0.2
0.4
0.6
0.8
1.0
1.2
CROSS SECTION / BOHR SQUARED
0.0
0.2
0.4
0.6
0.8
1.0
0.2
0.4
0.6
0.8
1.0
1.2
1.4
1.6
E/eV

Fig. 7.31b

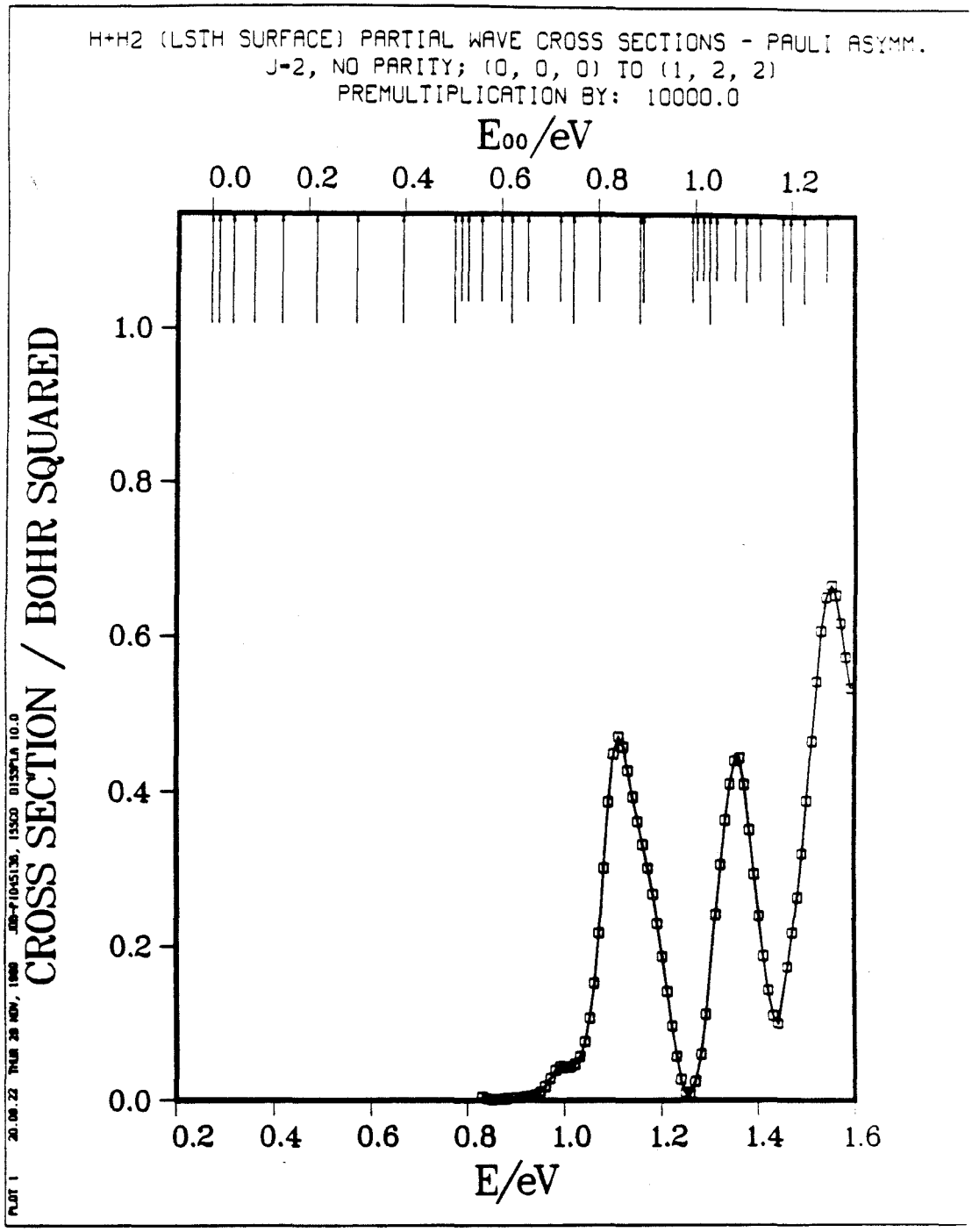
H+H2 (LSTH SURFACE) PARTIAL WAVE CROSS SECTIONS - PAULI ASYMM.
J=2, NO PARITY; (0, 0, 0) TO (1, 2, 2)
PREMULTIPLICATION BY: 10000.0
E00/eV
0.0
0.2
0.4
0.6
0.8
1.0
1.2
CROSS SECTION / BOHR SQUARED
0.0
0.2
0.4
0.6
0.8
1.0
0.2
0.4
0.6
0.8
1.0
1.2
1.4
1.6
E/eV

Fig. 7.31c

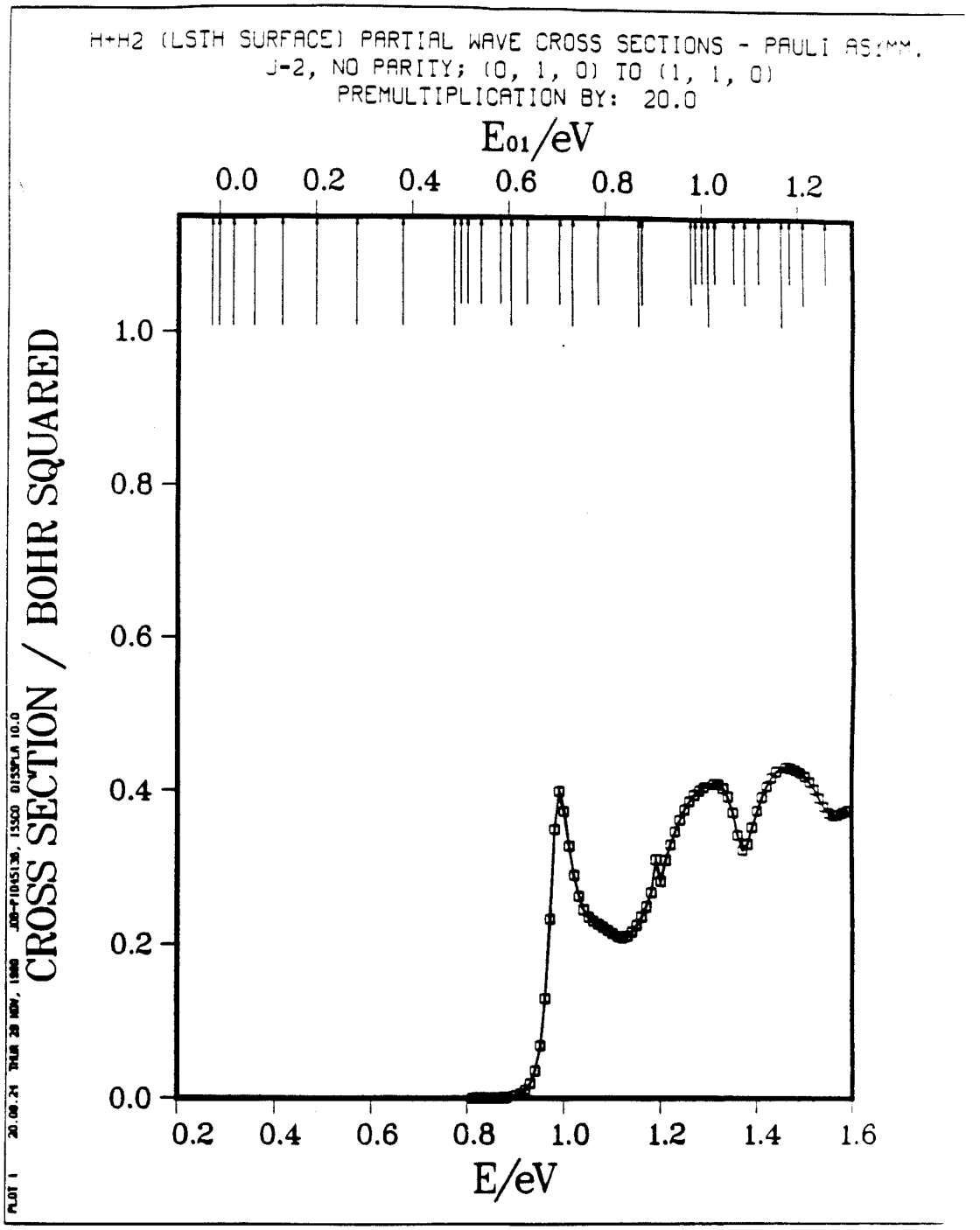
H+H2 (LSTH SURFACE) PARTIAL WAVE CROSS SECTIONS - PAULI ASYMM.
J=2, NO PARITY; (0, 1, 0) TO (1, 1, 0)
PREMULTIPLICATION BY: 20.0
E01/eV
0.0
0.2
0.4
0.6
0.8
1.0
1.2
CROSS SECTION / BOHR SQUARED
0.0
0.2
0.4
0.6
0.8
1.0
0.2
0.4
0.6
0.8
1.0
1.2
1.4
1.6
E/eV

Fig. 7.31d

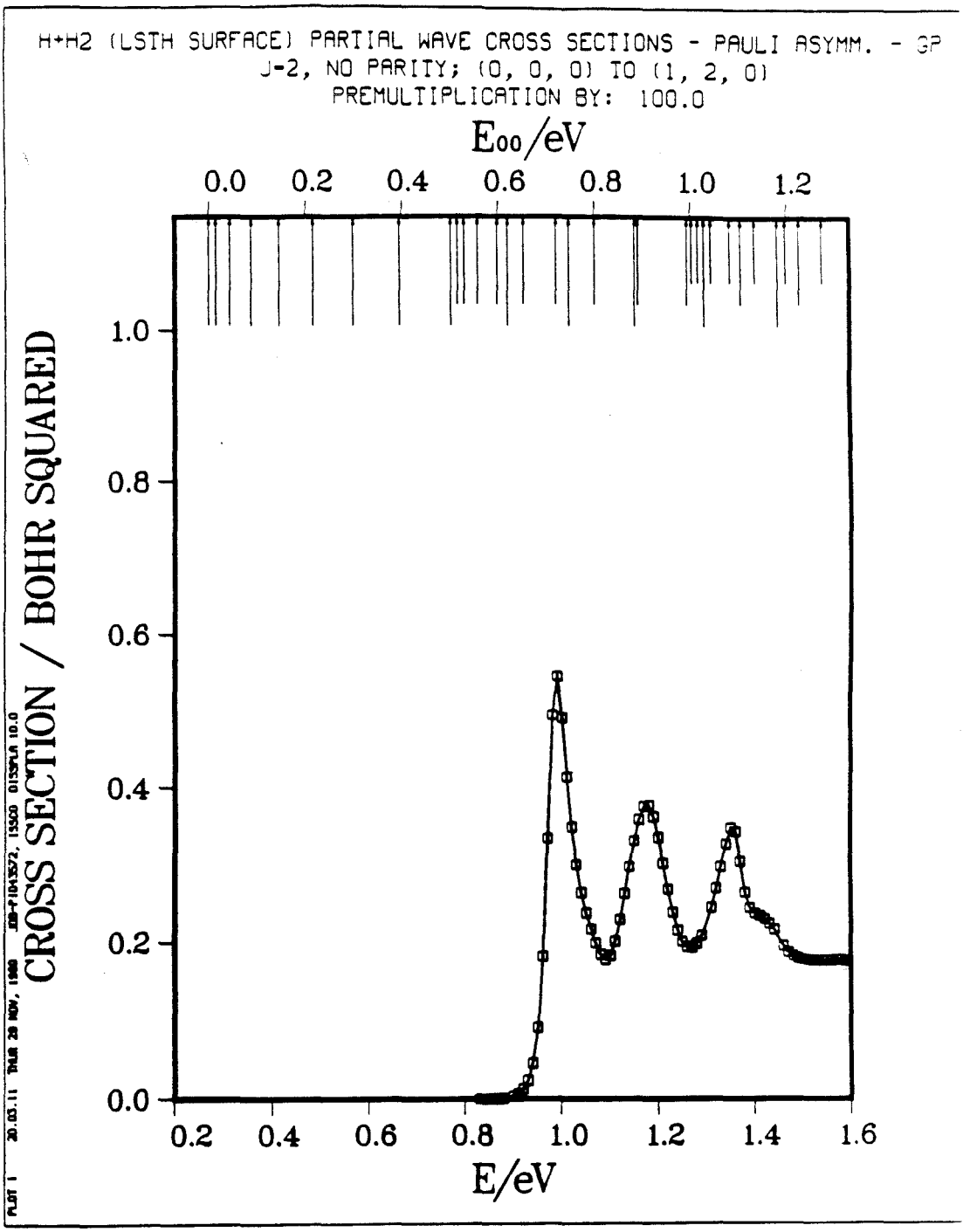
H+H2 (LSTH SURFACE) PARTIAL WAVE CROSS SECTIONS - PAULI ASYMM. - GP
J=2, NO PARITY; (0, 0, 0) TO (1, 2, 0)
PREMULTIPLICATION BY: 100.0
E00/eV
0.0
0.2
0.4
0.6
0.8
1.0
1.2
CROSS SECTION / BOHR SQUARED
0.0
0.2
0.4
0.6
0.8
1.0
0.2
0.4
0.6
0.8
1.0
1.2
1.4
1.6
E/eV

Fig. 7.32a

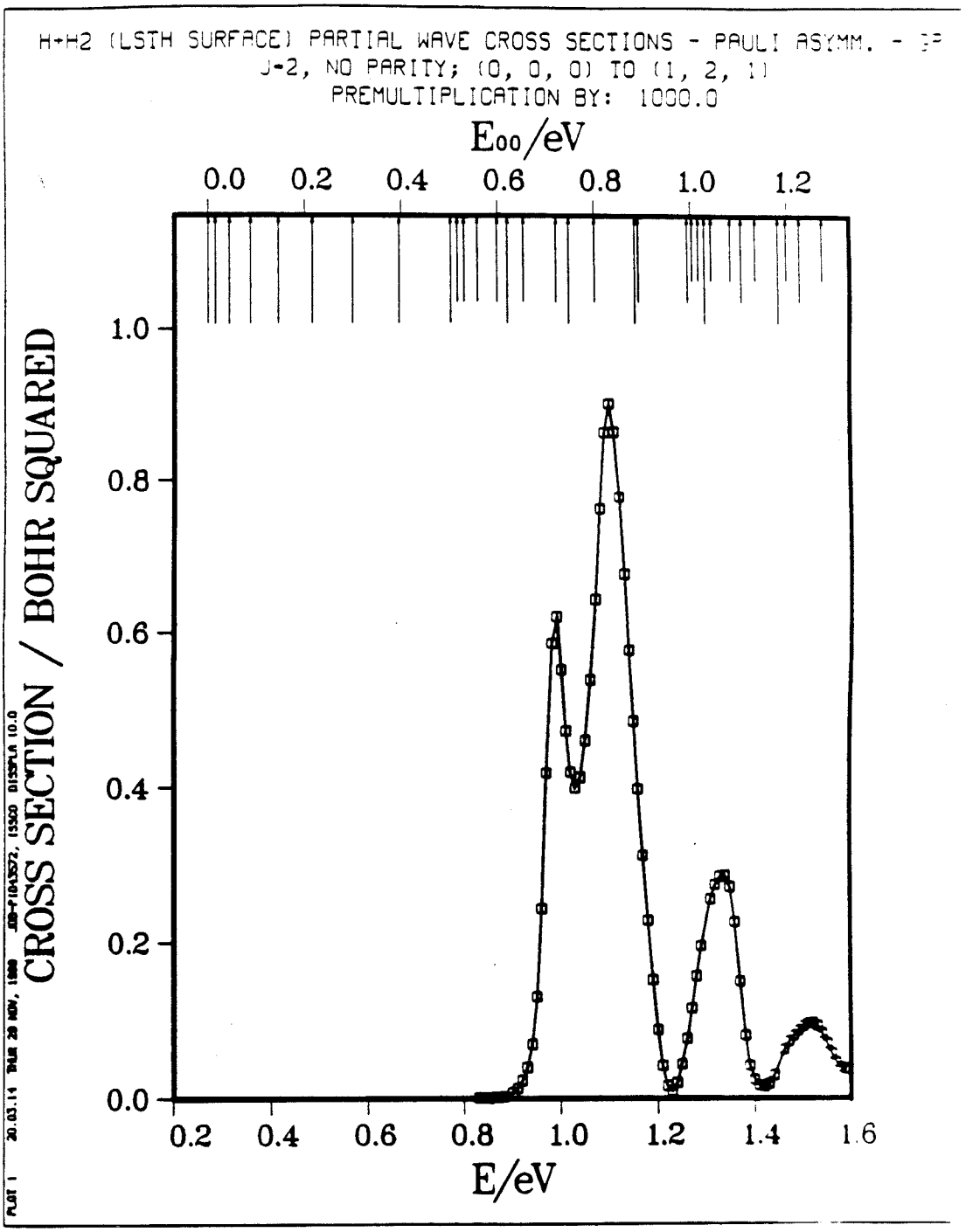
H+H2 (LSTH SURFACE) PARTIAL WAVE CROSS SECTIONS - PAULI ASYMM. - 3P
J=2, NO PARITY; (0, 0, 0) TO (1, 2, 1)
PREMULTIPLICATION BY: 1000.0
E00/eV
0.0
0.2
0.4
0.6
0.8
1.0
1.2
CROSS SECTION / BOHR SQUARED
0.0
0.2
0.4
0.6
0.8
1.0
0.2
0.4
0.6
0.8
1.0
1.2
1.4
1.6
E/eV

Fig. 7.32b

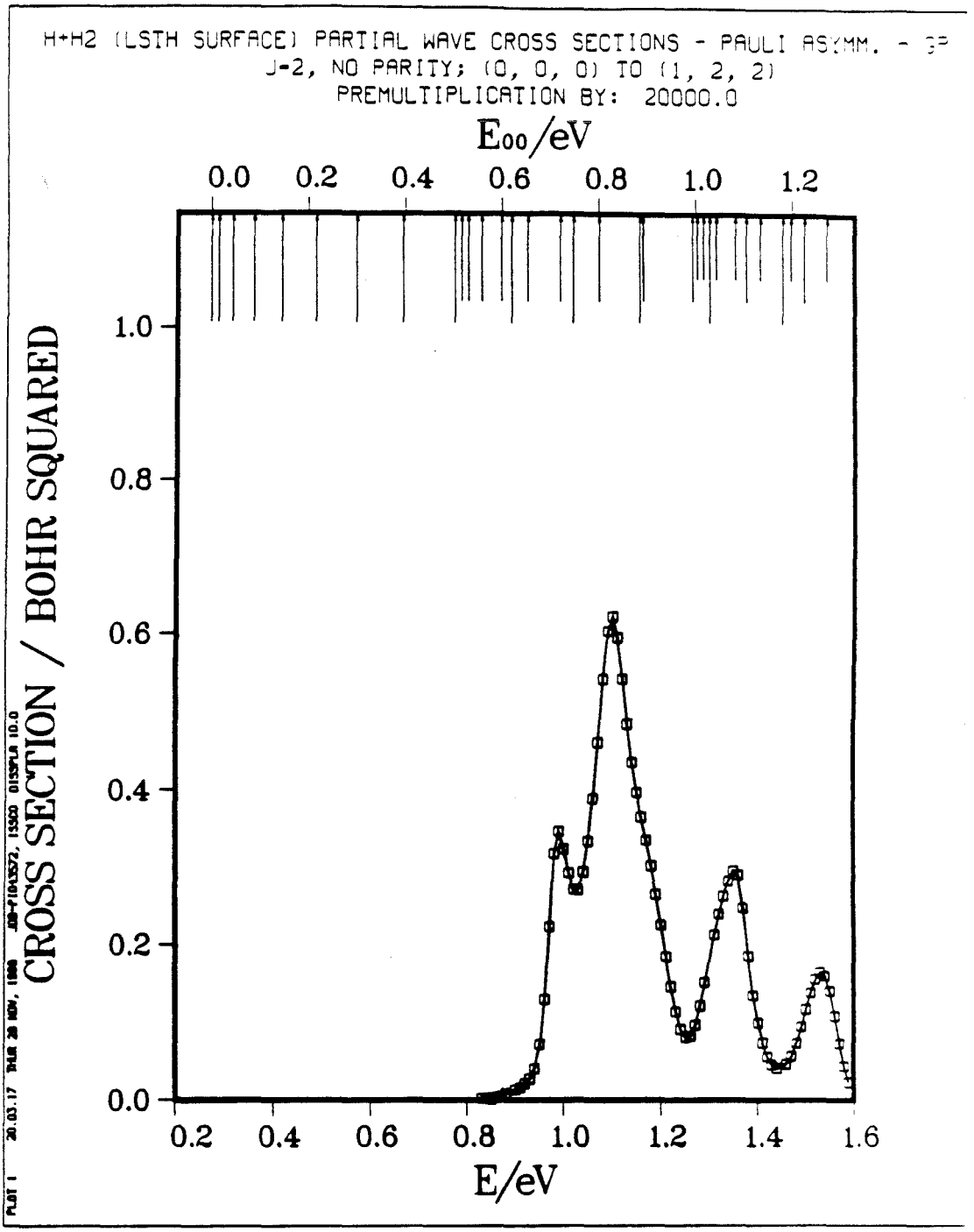
H+H2 (LSTH SURFACE) PARTIAL WAVE CROSS SECTIONS - PAULI ASYMM. - SP
J=2, NO PARITY; (0, 0, 0) TO (1, 2, 2)
PREMULTIPLICATION BY: 20000.0
E00/eV
0.0
0.2
0.4
0.6
0.8
1.0
1.2
CROSS SECTION / BOHR SQUARED
0.0
0.2
0.4
0.6
0.8
1.0
0.2
0.4
0.6
0.8
1.0
1.2
1.4
1.6
E/eV

Fig. 7.32c

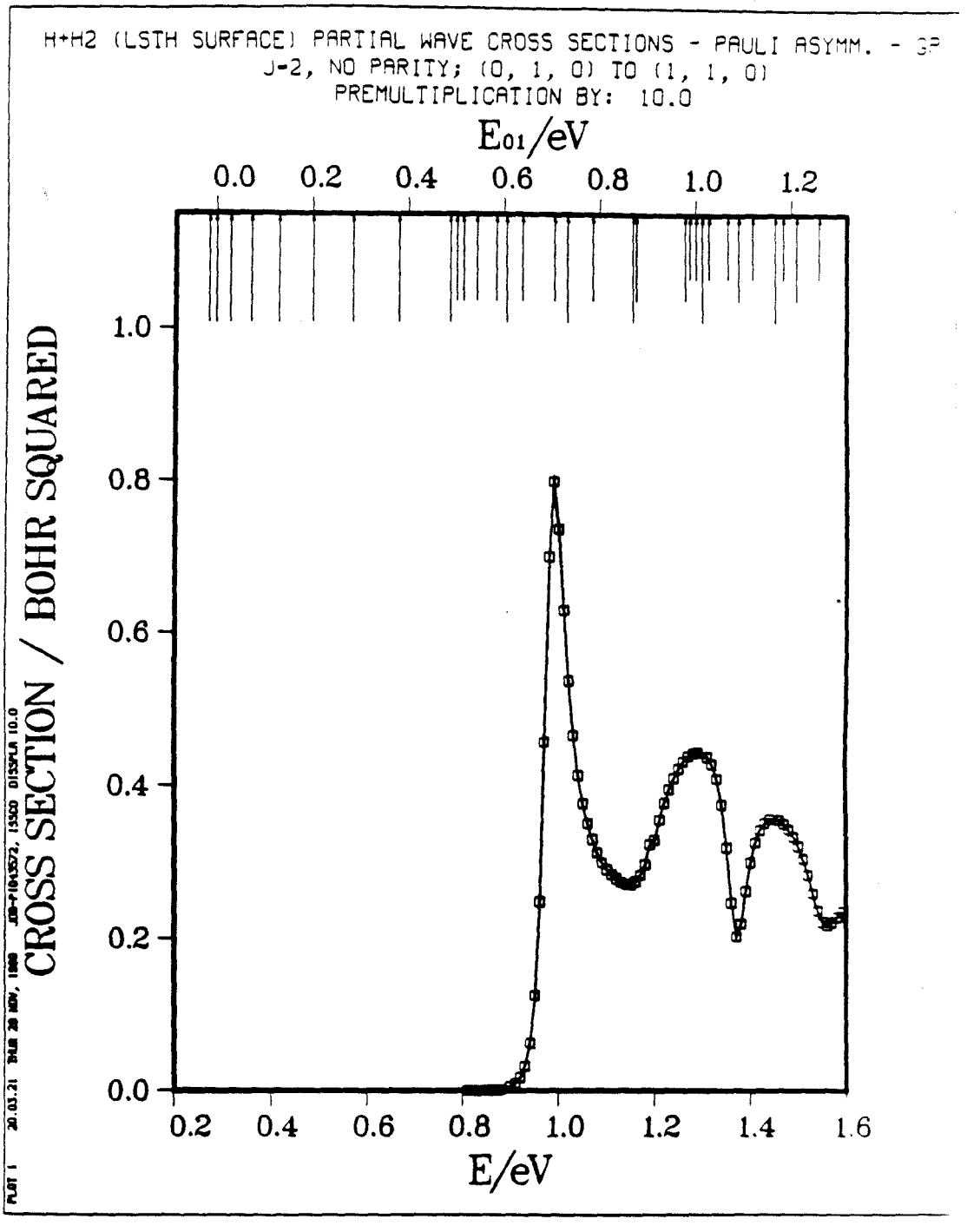
H+H2 (LSTH SURFACE) PARTIAL WAVE CROSS SECTIONS - PAULI ASYMM. - 3P
J=2, NO PARITY; (0, 1, 0) TO (1, 1, 0)
PREMULTIPLICATION BY: 10.0
E01/eV
0.0
0.2
0.4
0.6
0.8
1.0
1.2
CROSS SECTION / BOHR SQUARED
0.0
0.2
0.4
0.6
0.8
1.0
0.2
0.4
0.6
0.8
1.0
1.2
1.4
1.6
E/eV

Fig. 7.32d

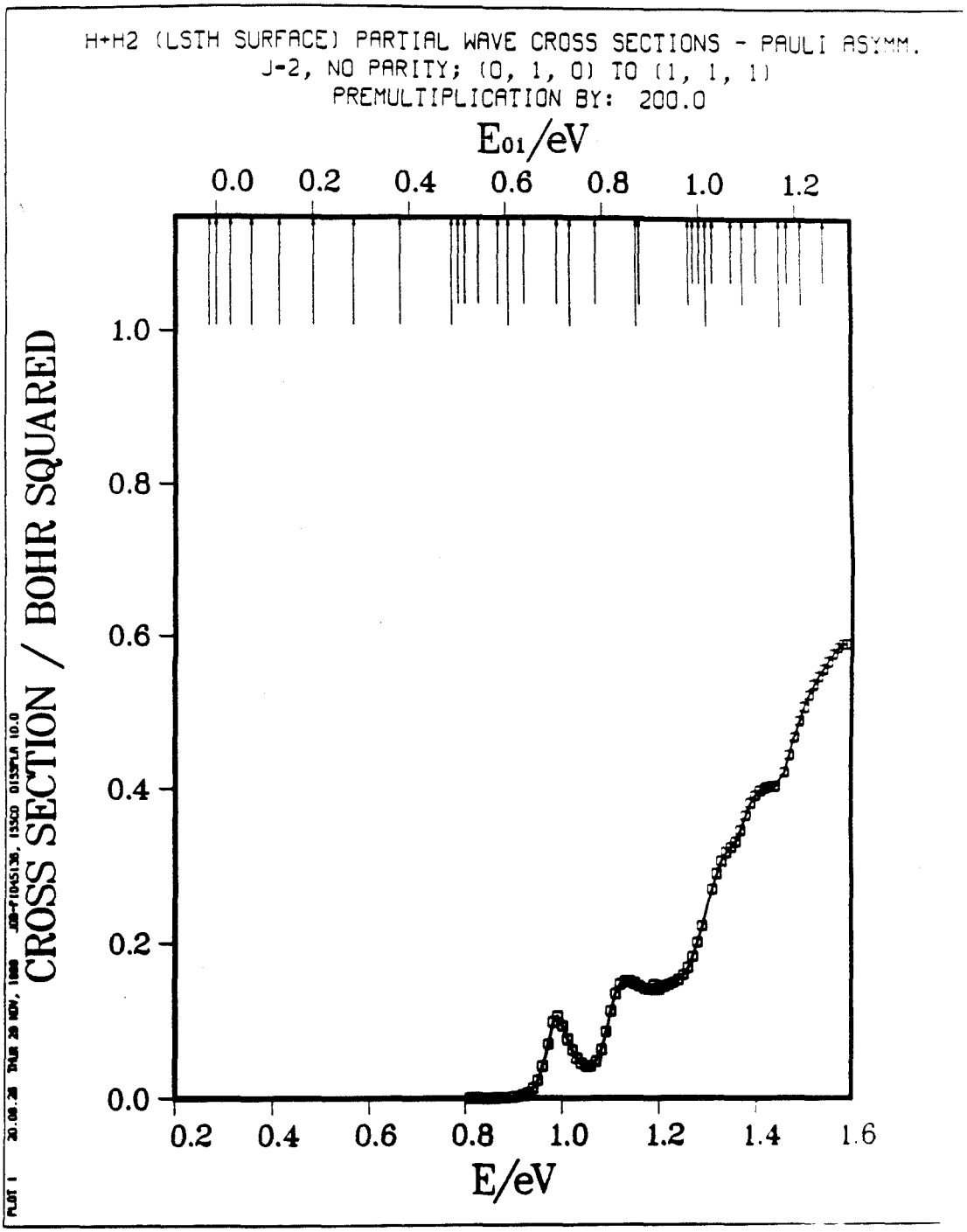
H+H2 (LSTH SURFACE) PARTIAL WAVE CROSS SECTIONS - PAULI ASYMM.
J=2, NO PARITY; (0, 1, 0) TO (1, 1, 1)
PREMULTIPLICATION BY: 200.0
E01/eV
0.0
0.2
0.4
0.6
0.8
1.0
1.2
CROSS SECTION / BOHR SQUARED
0.0
0.2
0.4
0.6
0.8
1.0
0.2
0.4
0.6
0.8
1.0
1.2
1.4
1.6
E/eV

Fig. 7.33a

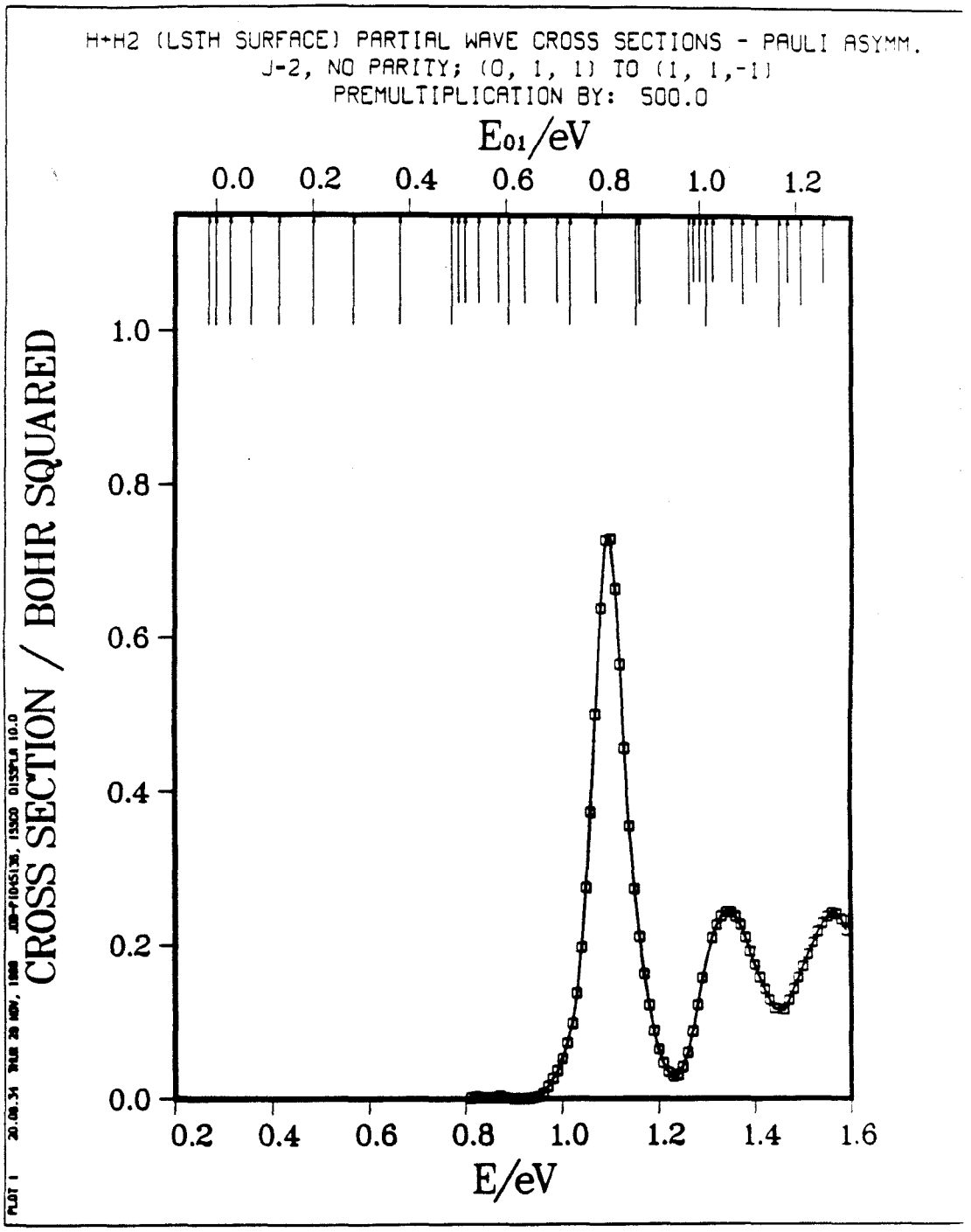
H+H2 (LSTH SURFACE) PARTIAL WAVE CROSS SECTIONS - PAULI ASYMM.
J=2, NO PARITY; (0, 1, 1) TO (1, 1,-1)
PREMULTIPLICATION BY: 500.0
E01/eV
0.0
0.2
0.4
0.6
0.8
1.0
1.2
CROSS SECTION / BOHR SQUARED
1.0
0.8
0.6
0.4
0.2
0.0
0.2
0.4
0.6
0.8
1.0
1.2
1.4
1.6
E/eV

Fig. 7.33b

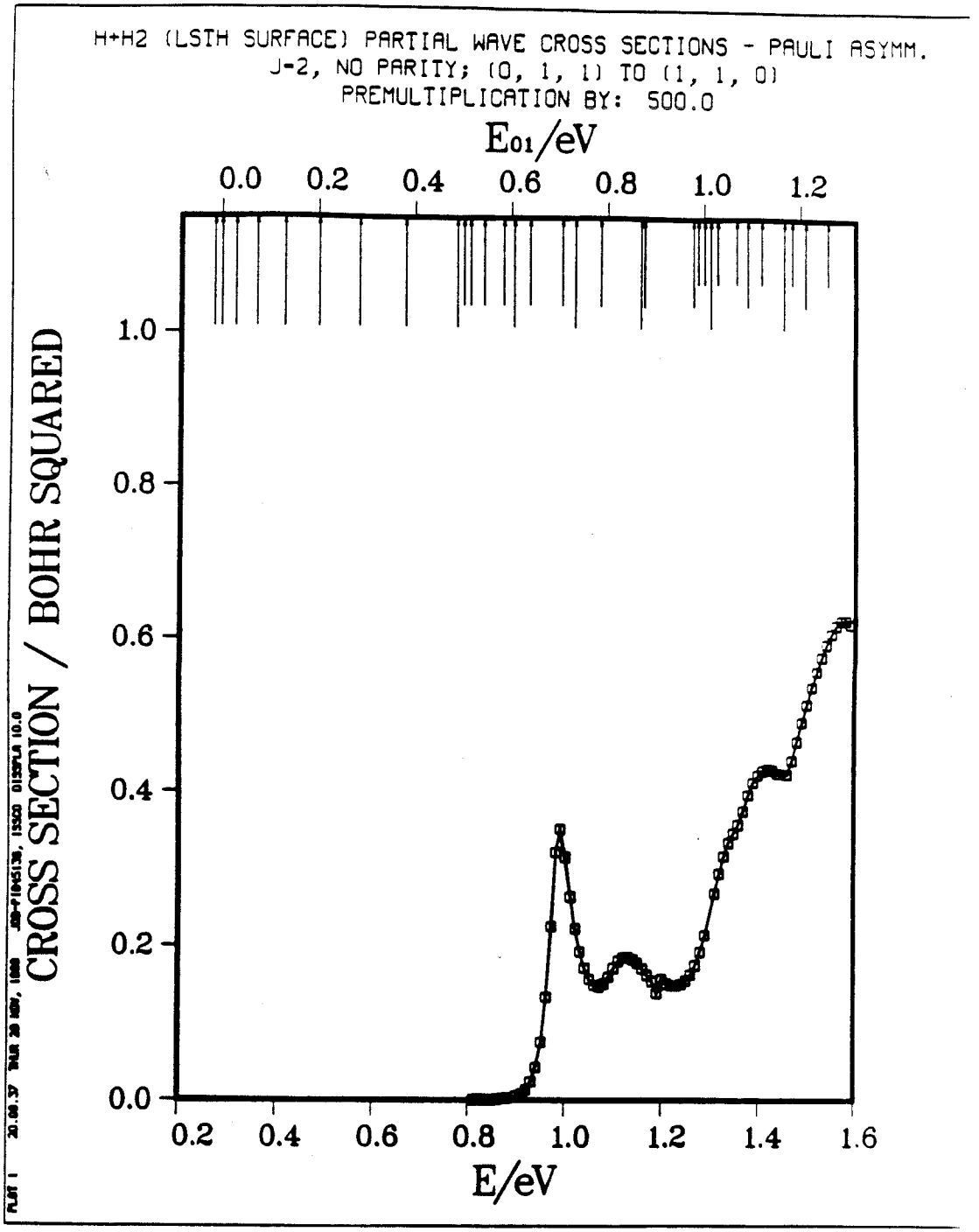
H+H2 (LSTH SURFACE) PARTIAL WAVE CROSS SECTIONS - PAULI ASYMM.
J=2, NO PARITY; (0, 1, 1) TO (1, 1, 0)
PREMULTIPLICATION BY: 500.0
E01/eV
0.0
0.2
0.4
0.6
0.8
1.0
1.2
CROSS SECTION / BOHR SQUARED
0.0
0.2
0.4
0.6
0.8
1.0
0.2
0.4
0.6
0.8
1.0
1.2
1.4
1.6
E/eV

Fig. 7.33c

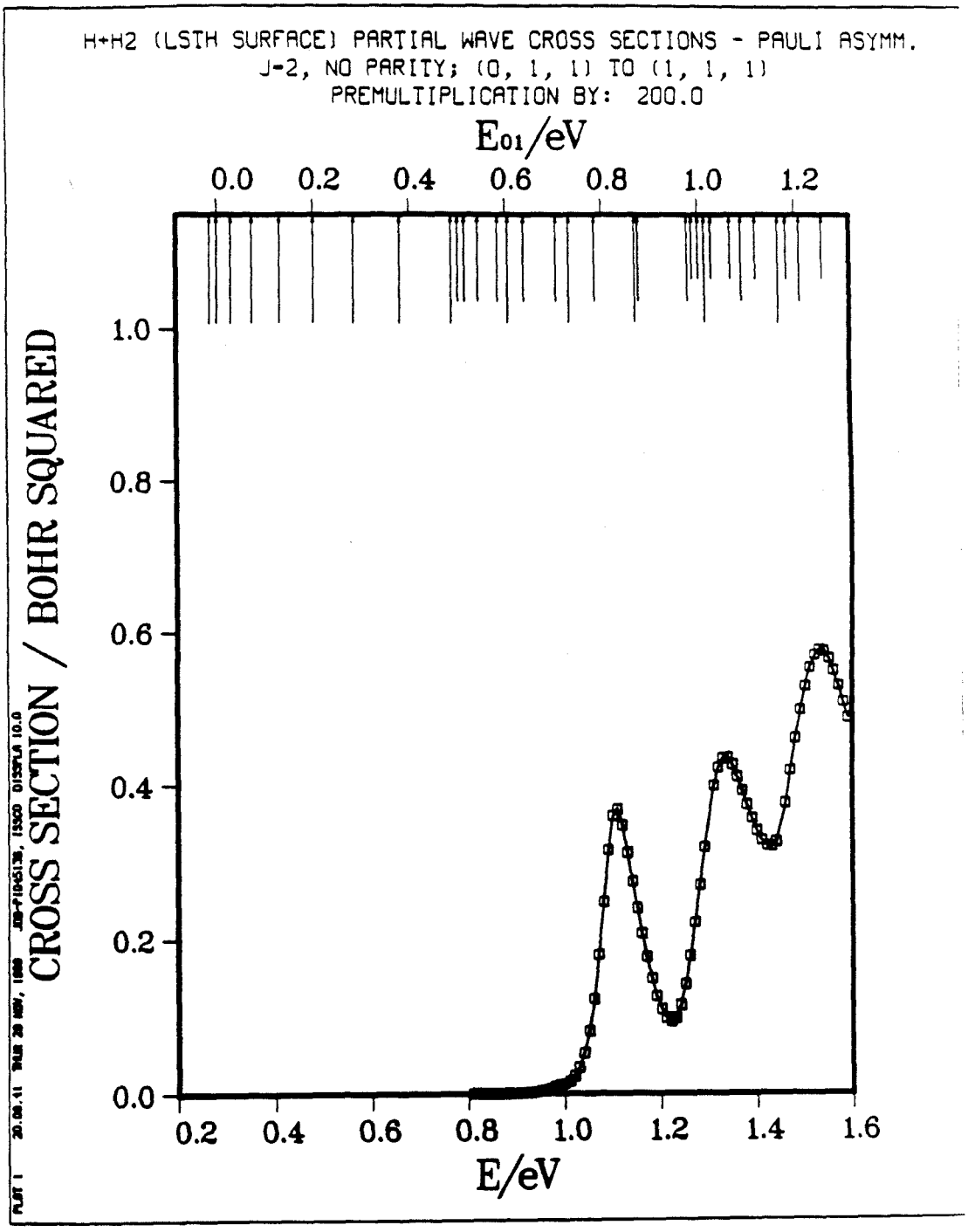
H+H2 (LSTH SURFACE) PARTIAL WAVE CROSS SECTIONS - PAULI ASYMM.
J=2, NO PARITY; (0, 1, 1) TO (1, 1, 1)
PREMULTIPLICATION BY: 200.0
E01/eV
0.0
0.2
0.4
0.6
0.8
1.0
1.2
CROSS SECTION / BOHR SQUARED
0.0
0.2
0.4
0.6
0.8
1.0
0.2
0.4
0.6
0.8
1.0
1.2
1.4
1.6
E/eV

Fig. 7.33d

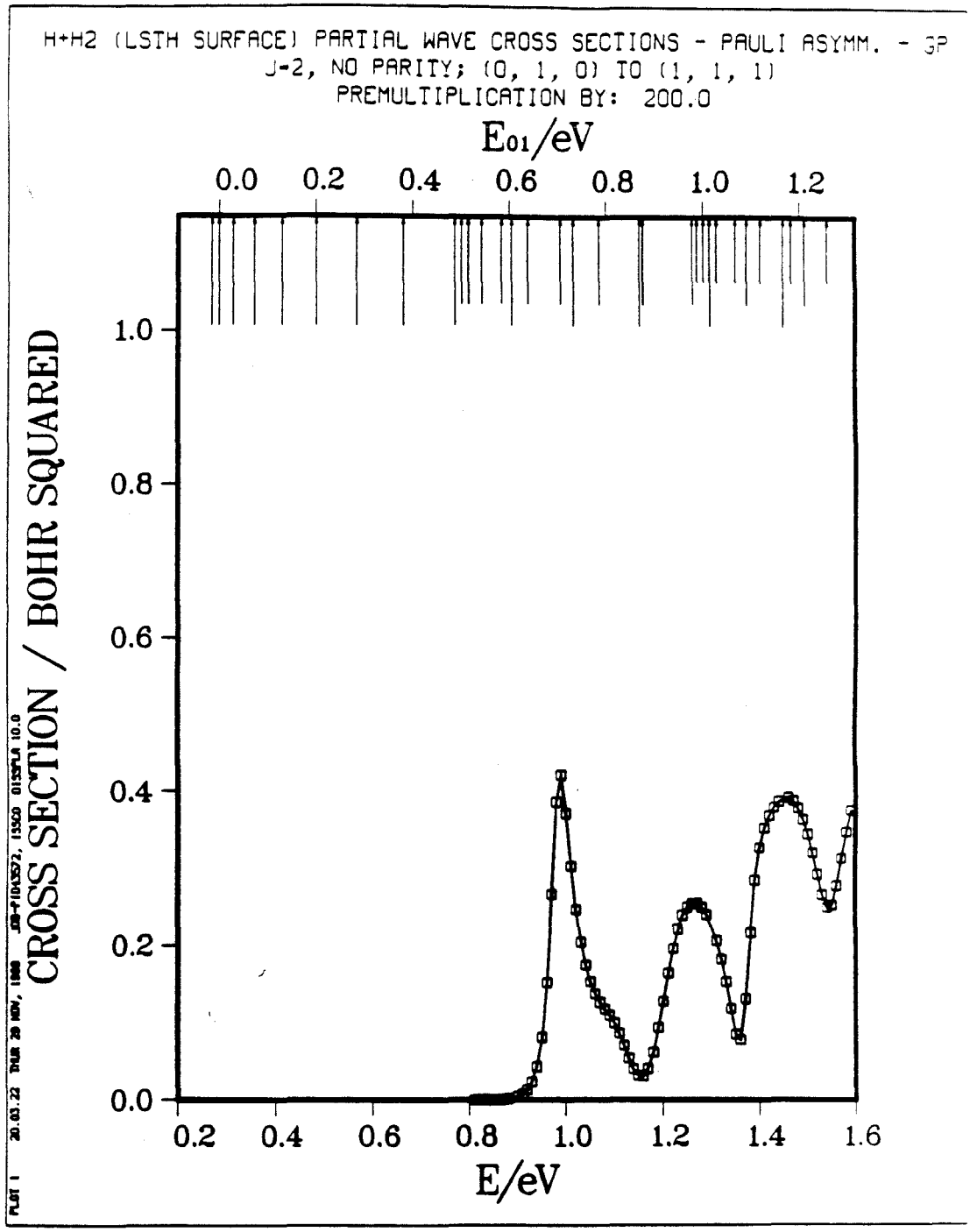
H+H2 (LSTH SURFACE) PARTIAL WAVE CROSS SECTIONS - PAULI ASYMM. - 3P
J=2, NO PARITY; (0, 1, 0) TO (1, 1, 1)
PREMULTIPLICATION BY: 200.0
E01/eV
0.0
0.2
0.4
0.6
0.8
1.0
1.2
CROSS SECTION / BOHR SQUARED
0.0
0.2
0.4
0.6
0.8
1.0
0.2
0.4
0.6
0.8
1.0
1.2
1.4
1.6
E/eV

Fig. 7.34a

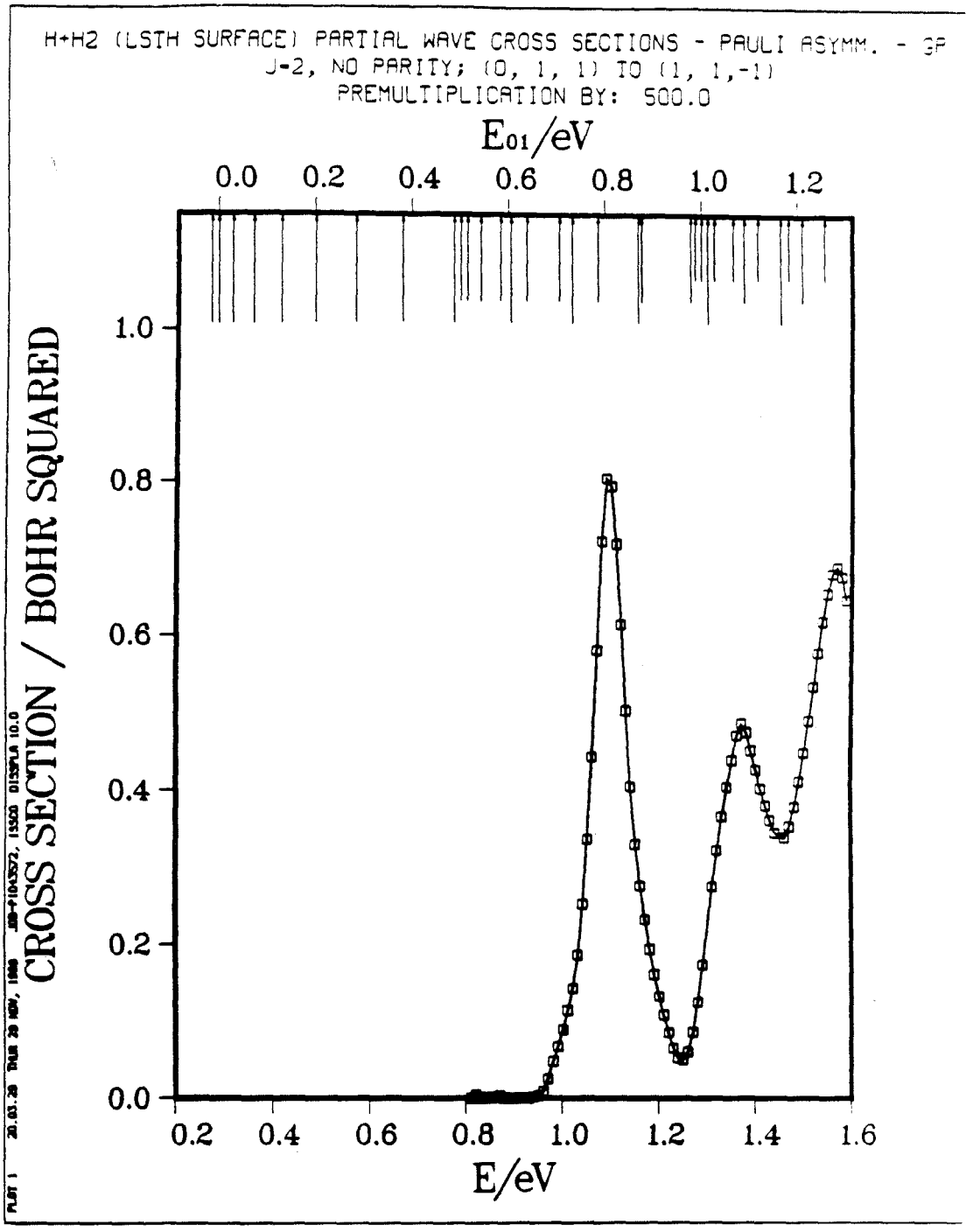
H+H2 (LSTH SURFACE) PARTIAL WAVE CROSS SECTIONS - PAULI ASYMM. - 3P
J=2, NO PARITY; (0, 1, 1) TO (1, 1,-1)
PREMULTIPLICATION BY: 500.0
E01/eV
0.0
0.2
0.4
0.6
0.8
1.0
1.2
CROSS SECTION / BOHR SQUARED
0.0
0.2
0.4
0.6
0.8
1.0
0.2
0.4
0.6
0.8
1.0
1.2
1.4
1.6
E/eV

Fig. 7.34b

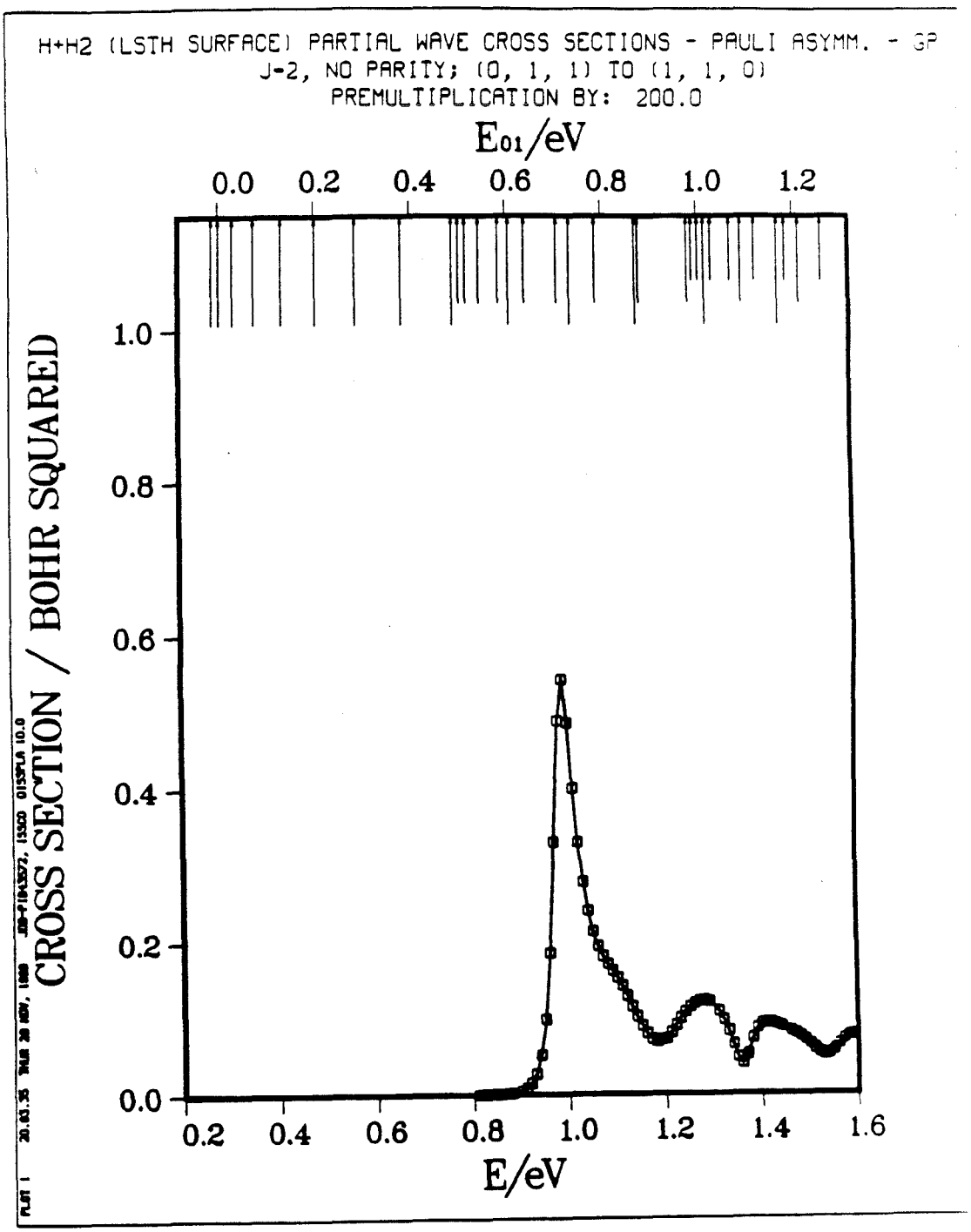
H+H2 (LSTH SURFACE) PARTIAL WAVE CROSS SECTIONS - PAULI ASYMM. - GP
J=2, NO PARITY; (0, 1, 1) TO (1, 1, 0)
PREMULTIPLICATION BY: 200.0
E01/eV
0.0
0.2
0.4
0.6
0.8
1.0
1.2
CROSS SECTION / BOHR SQUARED
0.0
0.2
0.4
0.6
0.8
1.0
0.2
0.4
0.6
0.8
1.0
1.2
1.4
1.6
E/eV

Fig. 7.34c

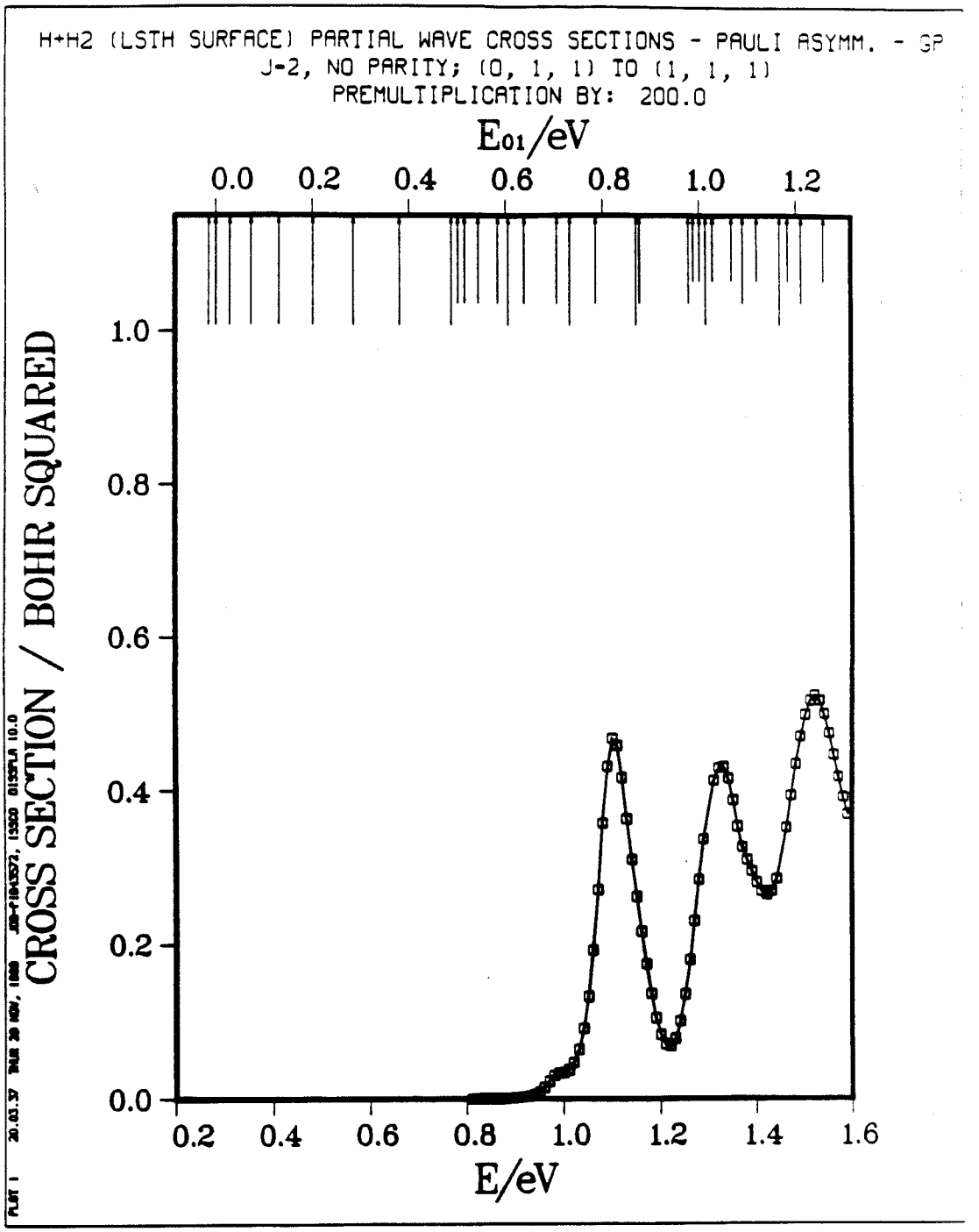
H+H2 (LSTH SURFACE) PARTIAL WAVE CROSS SECTIONS - PAULI ASYMM. - GP
J=2, NO PARITY; (0, 1, 1) TO (1, 1, 1)
PREMULTIPLICATION BY: 200.0
E01/eV
0.0
0.2
0.4
0.6
0.8
1.0
1.2
CROSS SECTION / BOHR SQUARED
0.0
0.2
0.4
0.6
0.8
1.0
0.2
0.4
0.6
0.8
1.0
1.2
1.4
1.6
E/eV

Fig. 7.34d

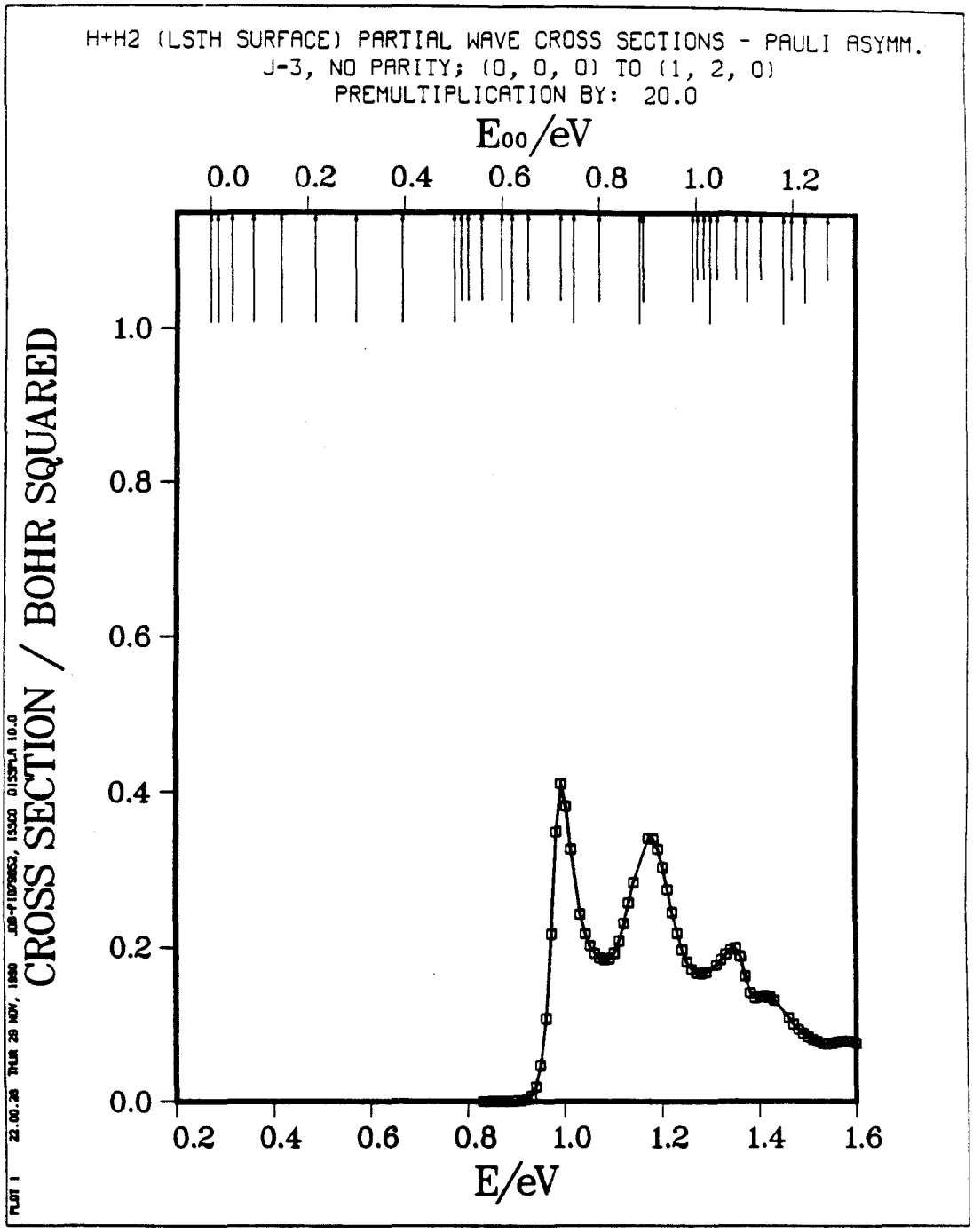
H+H2 (LSTH SURFACE) PARTIAL WAVE CROSS SECTIONS - PAULI ASYMM.
J=3, NO PARITY; (0, 0, 0) TO (1, 2, 0)
PREMULTIPLICATION BY: 20.0
E00/eV
0.0
0.2
0.4
0.6
0.8
1.0
1.2
CROSS SECTION / BOHR SQUARED
0.0
0.2
0.4
0.6
0.8
1.0
0.2
0.4
0.6
0.8
1.0
1.2
1.4
1.6
E/eV

Fig. 7.35a

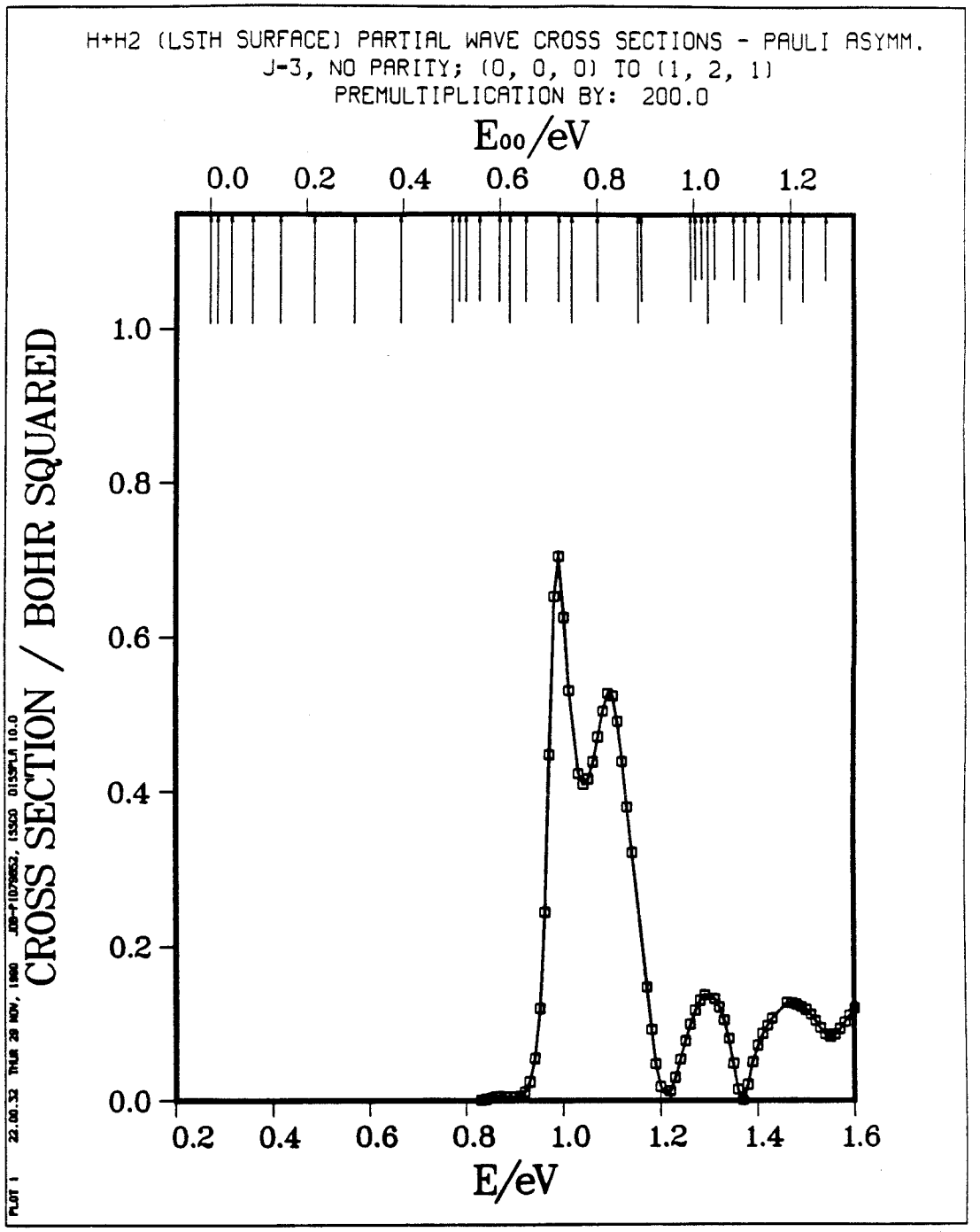
H+H2 (LSTH SURFACE) PARTIAL WAVE CROSS SECTIONS - PAULI ASYMM.
J-3, NO PARITY; (0, 0, 0) TO (1, 2, 1)
PREMULTIPLICATION BY: 200.0
E00/eV
0.0
0.2
0.4
0.6
0.8
1.0
1.2
CROSS SECTION / BOHR SQUARED
0.0
0.2
0.4
0.6
0.8
1.0
0.2
0.4
0.6
0.8
1.0
1.2
1.4
1.6
E/eV

Fig. 7.35b

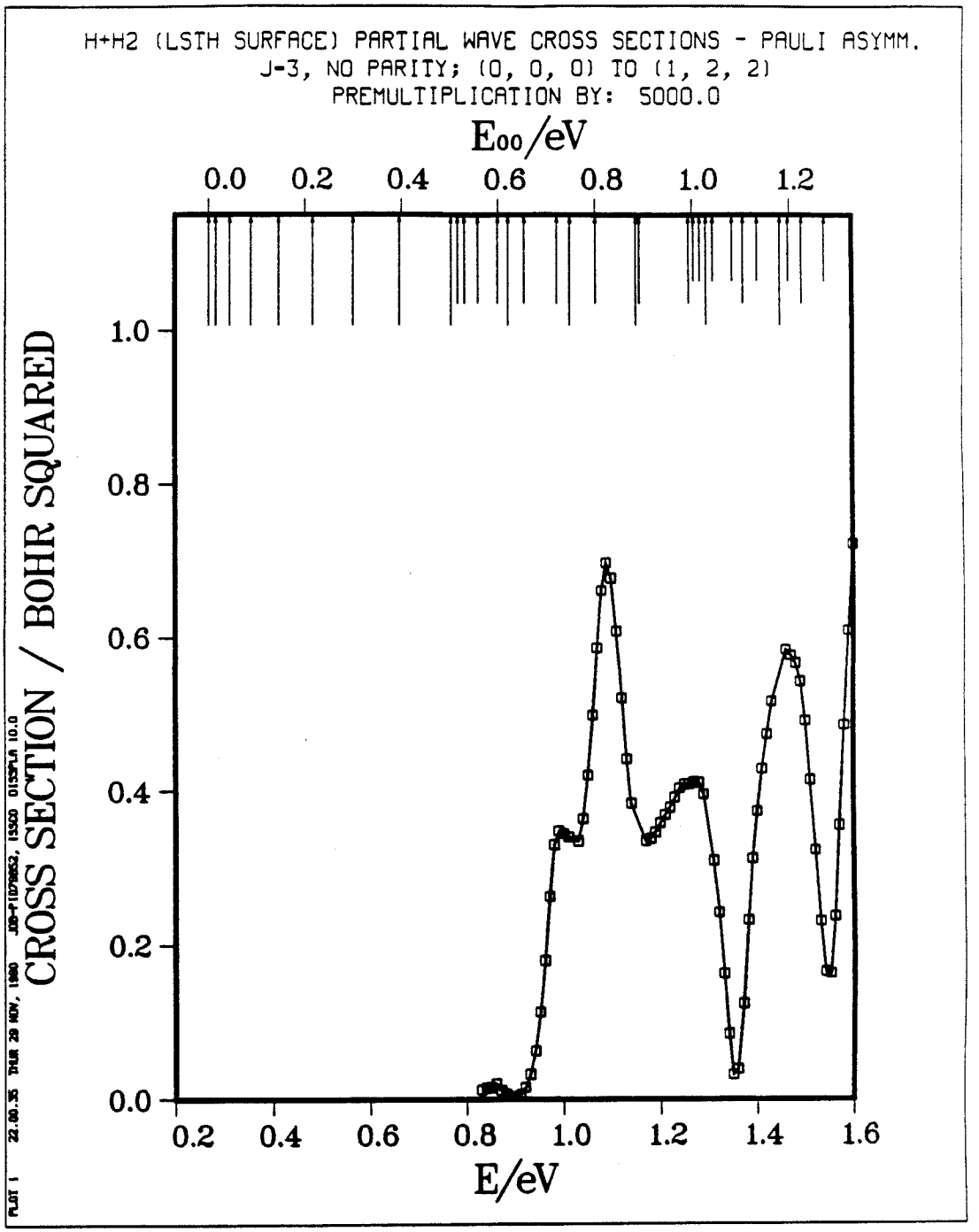
H+H2 (LSTH SURFACE) PARTIAL WAVE CROSS SECTIONS - PAULI ASYMM.
J-3, NO PARITY; (0, 0, 0) TO (1, 2, 2)
PREMULTIPLICATION BY: 5000.0
E00/eV
0.0
0.2
0.4
0.6
0.8
1.0
1.2
CROSS SECTION / BOHR SQUARED
0.0
0.2
0.4
0.6
0.8
1.0
0.2
0.4
0.6
0.8
1.0
1.2
1.4
1.6
E/eV

Fig. 7.35c

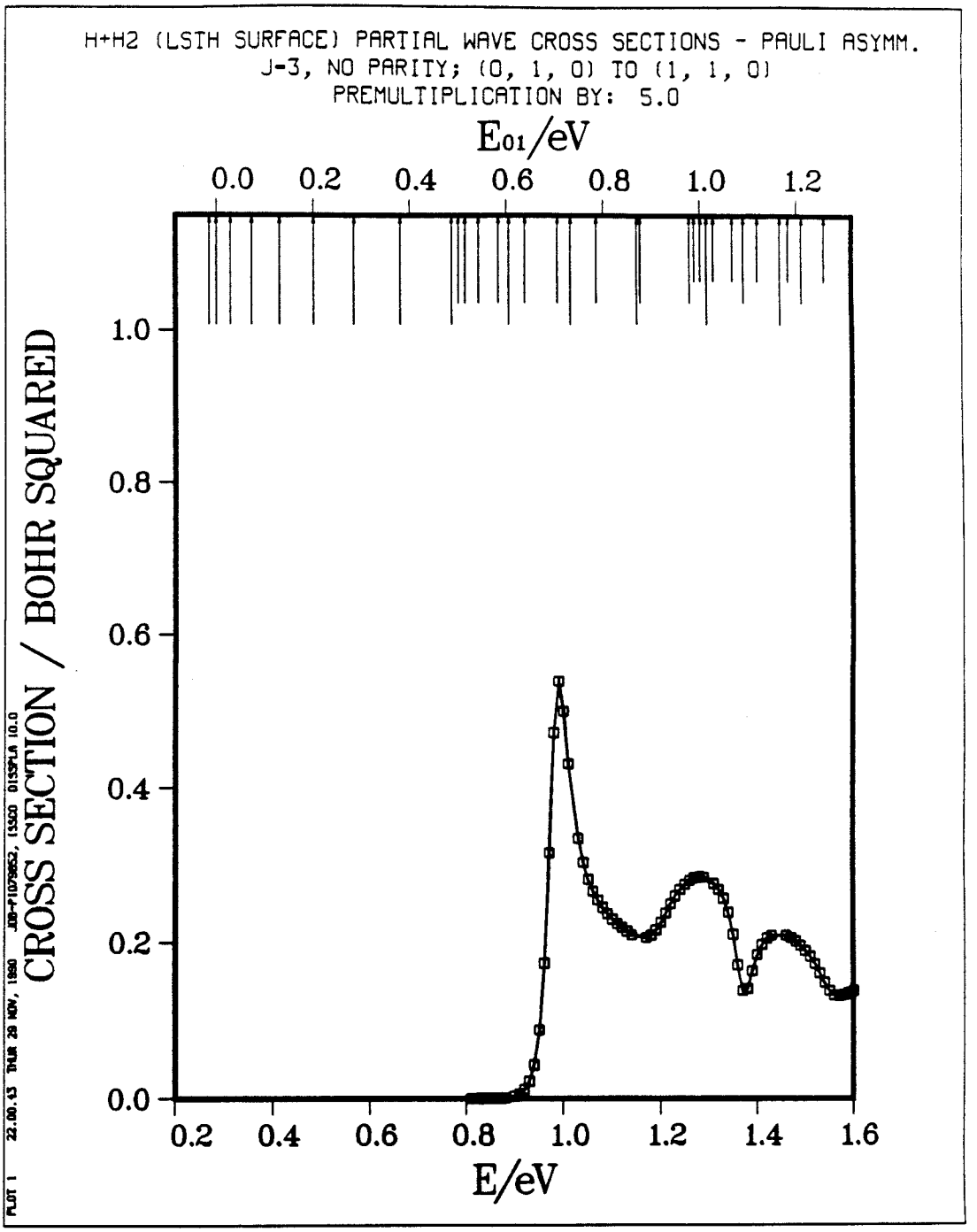
H+H2 (LSTH SURFACE) PARTIAL WAVE CROSS SECTIONS - PAULI ASYMM.
J-3, NO PARITY; (0, 1, 0) TO (1, 1, 0)
PREMULTIPLICATION BY: 5.0
E01/eV
0.0
0.2
0.4
0.6
0.8
1.0
1.2
CROSS SECTION / BOHR SQUARED
0.0
0.2
0.4
0.6
0.8
1.0
E/eV
0.2
0.4
0.6
0.8
1.0
1.2
1.4
1.6
PLOT 1 22.00.43 THUR 29 NOV, 1990 JOB-P1079852, 13300 0155PLA 10.0

Fig. 7.35d

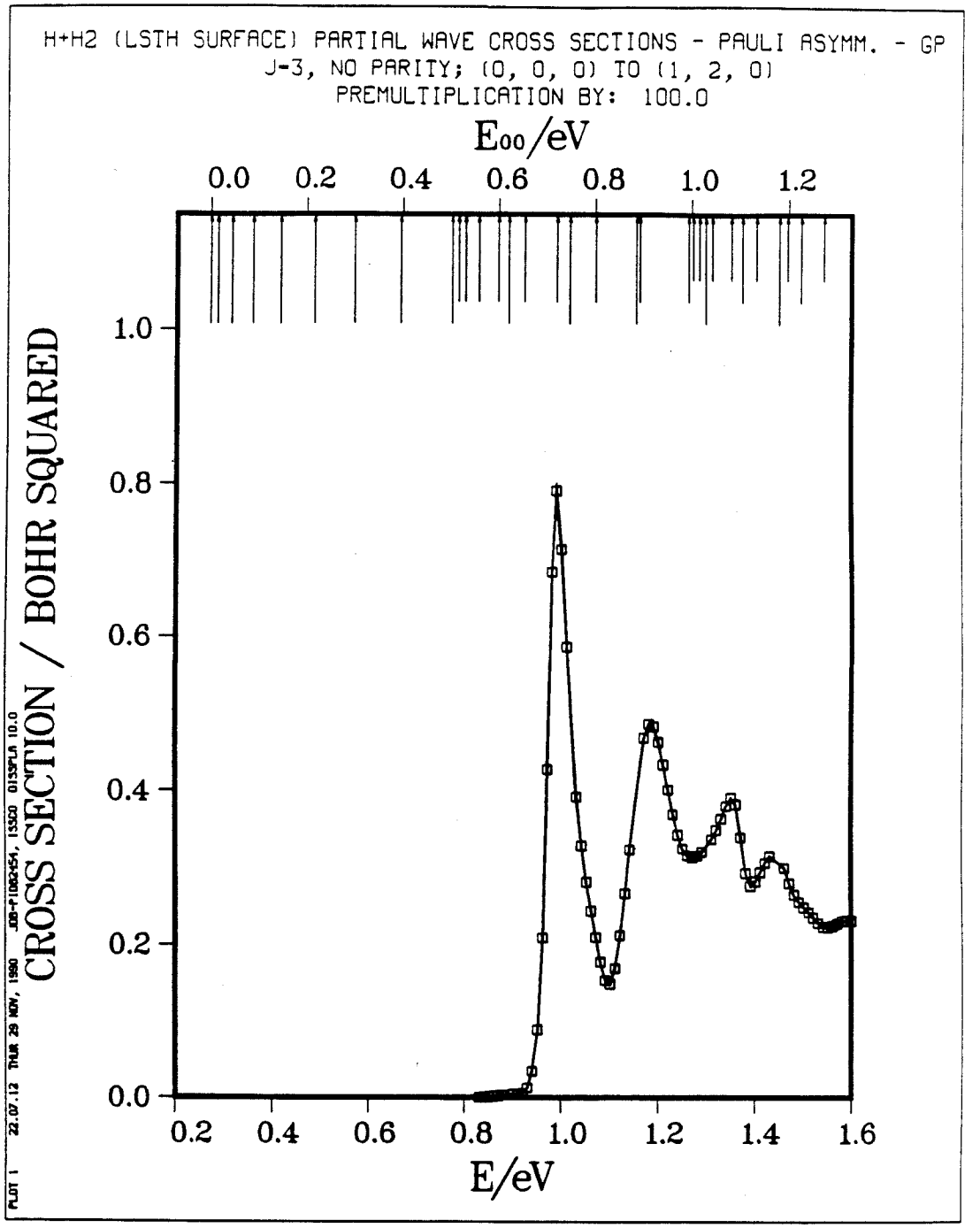
H+H2 (LSTH SURFACE) PARTIAL WAVE CROSS SECTIONS - PAULI ASYMM. - GP
J-3, NO PARITY; (0, 0, 0) TO (1, 2, 0)
PREMULTIPLICATION BY: 100.0
E00/eV
0.0
0.2
0.4
0.6
0.8
1.0
1.2
CROSS SECTION / BOHR SQUARED
0.0
0.2
0.4
0.6
0.8
1.0
0.2
0.4
0.6
0.8
1.0
1.2
1.4
1.6
E/eV
PLOT 1 22.07.12 THUR 29 NOV, 1990 JOB=F1D62454, 15300 0153PLA 10.0

Fig. 7.36a

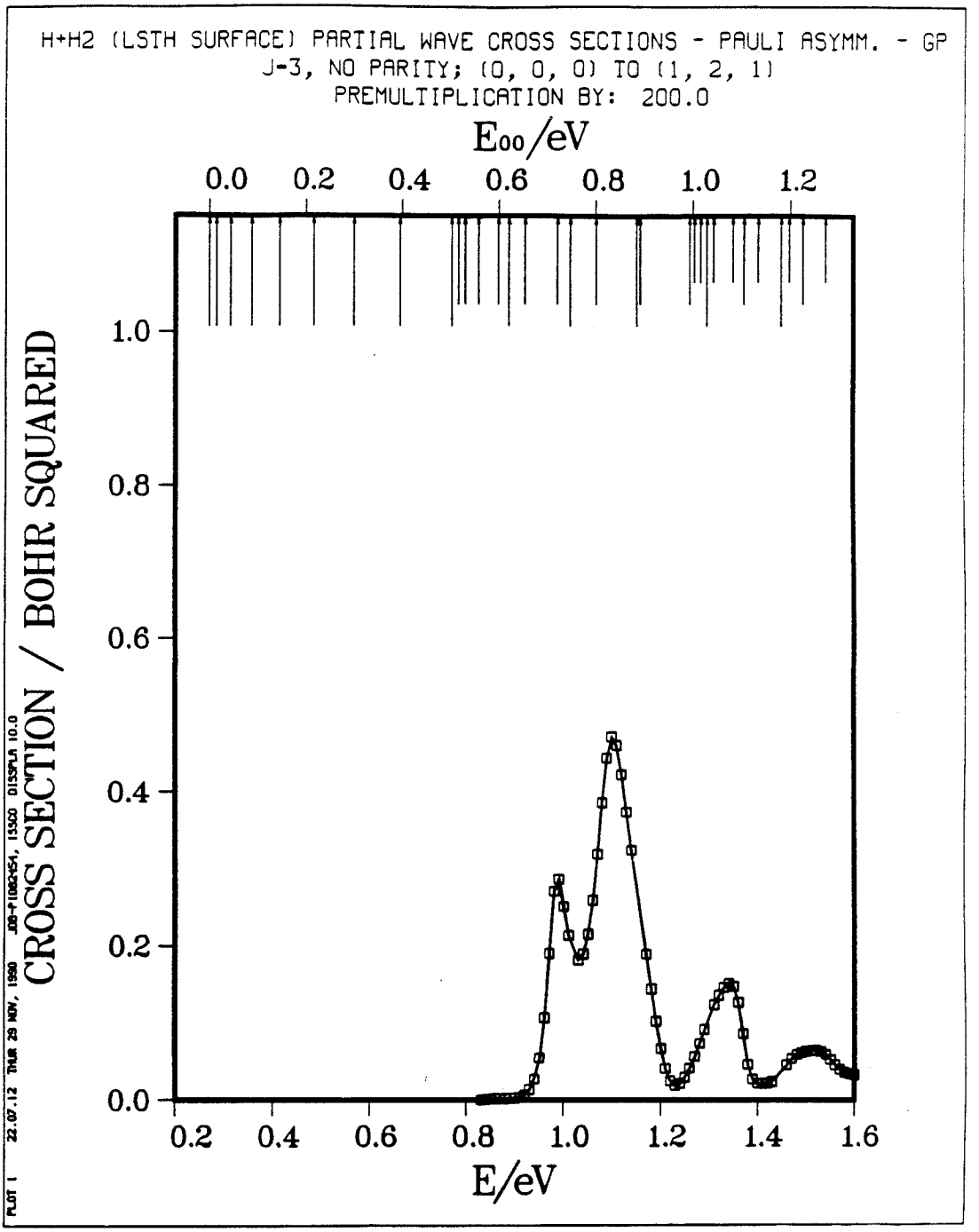
H+H2 (LSTH SURFACE) PARTIAL WAVE CROSS SECTIONS - PAULI ASYMM. - GP
J=3, NO PARITY; (0, 0, 0) TO (1, 2, 1)
PREMULTIPLICATION BY: 200.0
E00/eV
0.0
0.2
0.4
0.6
0.8
1.0
1.2
CROSS SECTION / BOHR SQUARED
0.0
0.2
0.4
0.6
0.8
1.0
0.2
0.4
0.6
0.8
1.0
1.2
1.4
1.6
E/eV
PLOT 1 22.07.12 THUR 29 NOV, 1990 JOB=T1082454, 15500 DISSPLA 10.0

Fig. 7.36b

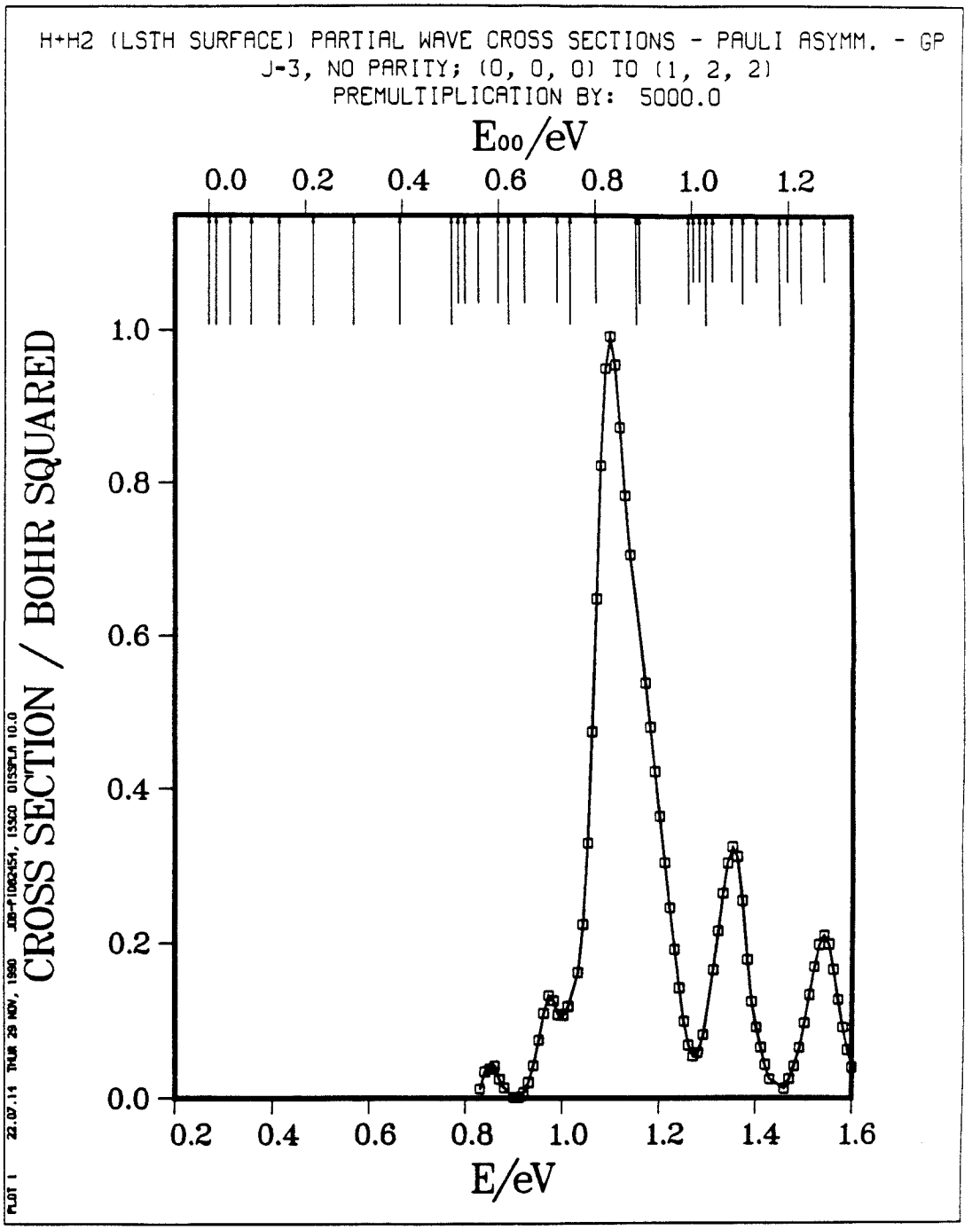
H+H2 (LSTH SURFACE) PARTIAL WAVE CROSS SECTIONS - PAULI ASYMM. - GP
J-3, NO PARITY; (0, 0, 0) TO (1, 2, 2)
PREMULTIPLICATION BY: 5000.0
E00/eV
0.0
0.2
0.4
0.6
0.8
1.0
1.2
CROSS SECTION / BOHR SQUARED
0.0
0.2
0.4
0.6
0.8
1.0
0.2
0.4
0.6
0.8
1.0
1.2
1.4
1.6
E/eV
PLOT 1 22.07.14 THUR 29 NOV, 1990 JOB=P1082454, 15SCO 01SPLA 10.0

Fig. 7.36c

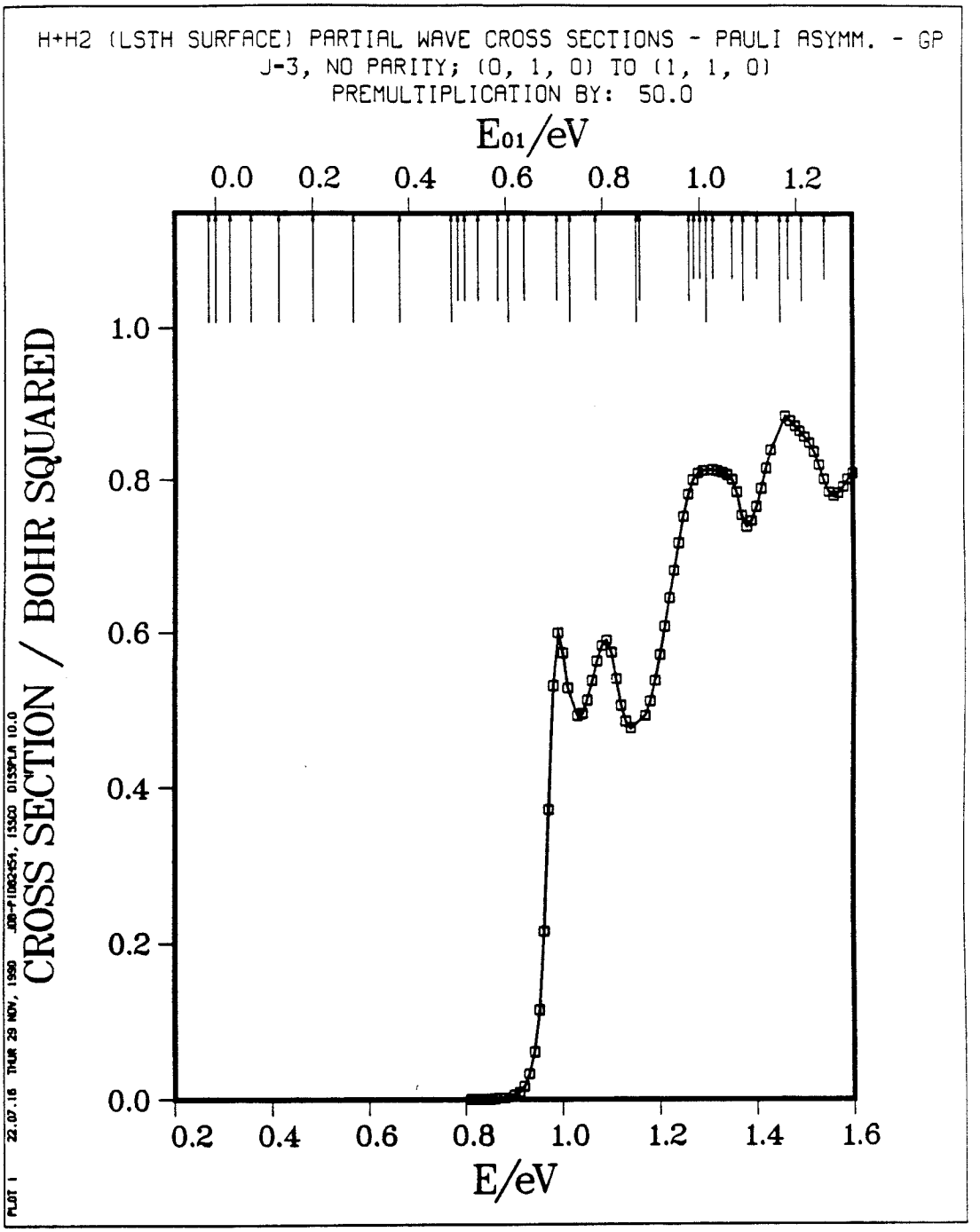
H+H2 (LSTH SURFACE) PARTIAL WAVE CROSS SECTIONS - PAULI ASYMM. - GP
J=3, NO PARITY; (0, 1, 0) TO (1, 1, 0)
PREMULTIPLICATION BY: 50.0
E01/eV
0.0
0.2
0.4
0.6
0.8
1.0
1.2
CROSS SECTION / BOHR SQUARED
0.0
0.2
0.4
0.6
0.8
1.0
0.2
0.4
0.6
0.8
1.0
1.2
1.4
1.6
E/eV
PLOT 1 22.07.16 THUR 29 NOV, 1990 JOB-P1062454, 13SEC DISSPLA 10.0

Fig. 7.36d

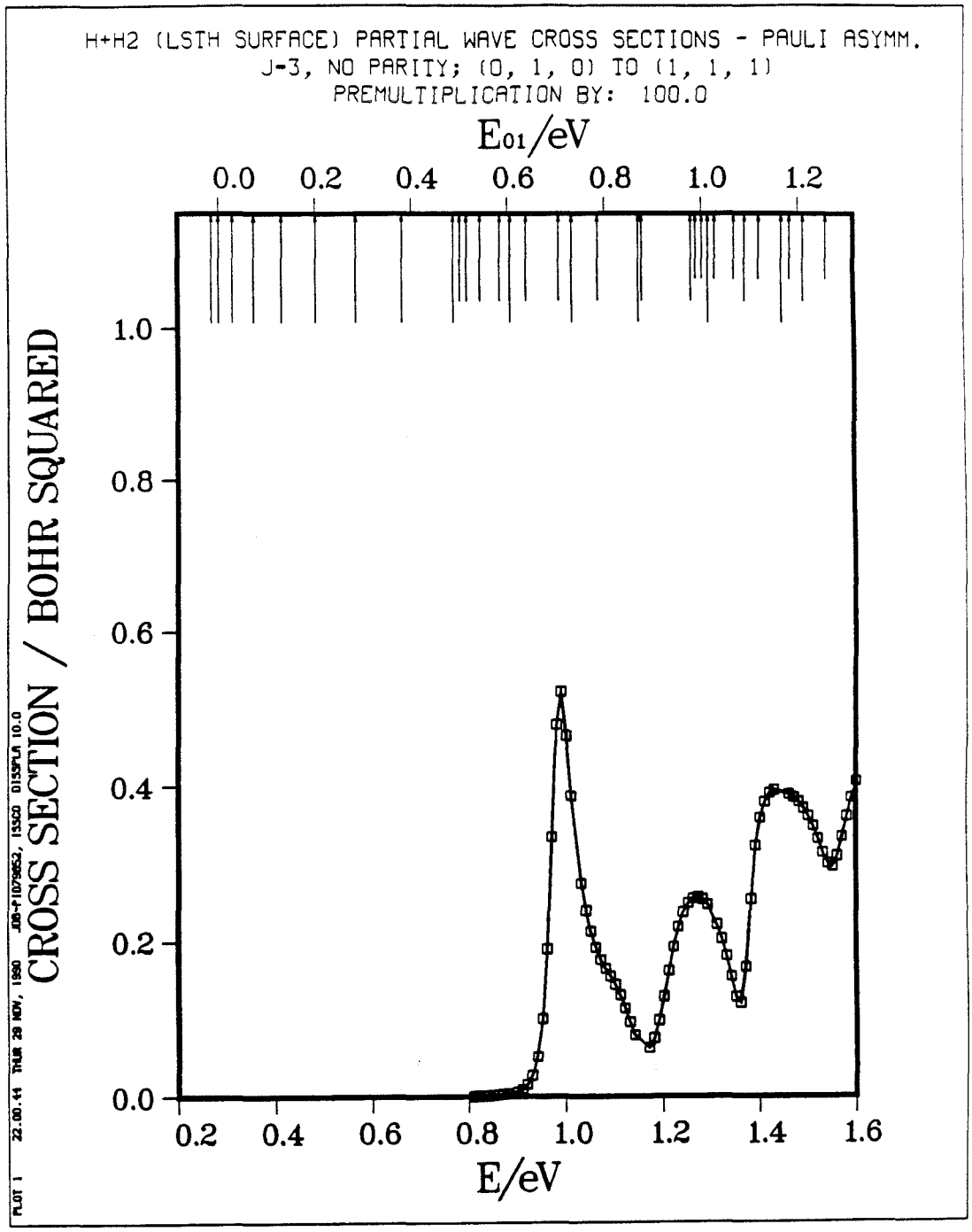
H+H2 (LSTH SURFACE) PARTIAL WAVE CROSS SECTIONS - PAULI ASYMM.
J=3, NO PARITY; (0, 1, 0) TO (1, 1, 1)
PREMULTIPLICATION BY: 100.0
E01/eV
0.0
0.2
0.4
0.6
0.8
1.0
1.2
CROSS SECTION / BOHR SQUARED
0.0
0.2
0.4
0.6
0.8
1.0
0.2
0.4
0.6
0.8
1.0
1.2
1.4
1.6
E/eV
PLOT 1 22.00.41 THUR 29 NOV, 1990 JOB=P1079652, 1350 DISSPLA 10.0

Fig. 7.37a

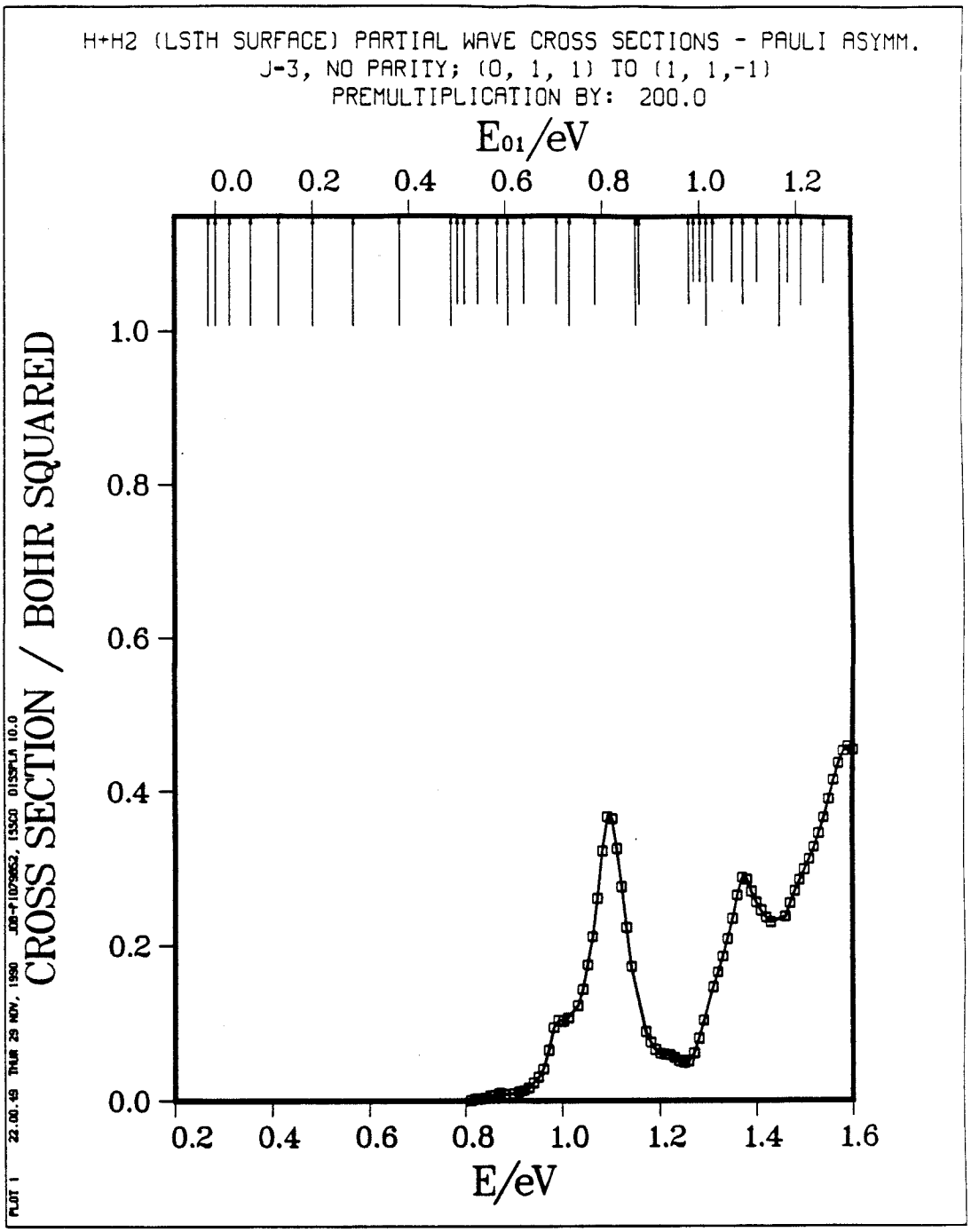
H+H2 (LSTH SURFACE) PARTIAL WAVE CROSS SECTIONS - PAULI ASYMM.
J-3, NO PARITY; (0, 1, 1) TO (1, 1,-1)
PREMULTIPLICATION BY: 200.0
E01/eV
0.0
0.2
0.4
0.6
0.8
1.0
1.2
CROSS SECTION / BOHR SQUARED
0.0
0.2
0.4
0.6
0.8
1.0
0.2
0.4
0.6
0.8
1.0
1.2
1.4
1.6
E/eV
PLOT 1 22.00.49 THUR 29 NOV, 1990 JOB-F1079852, 13SCO DISSPLA 10.0

Fig. 7.37b

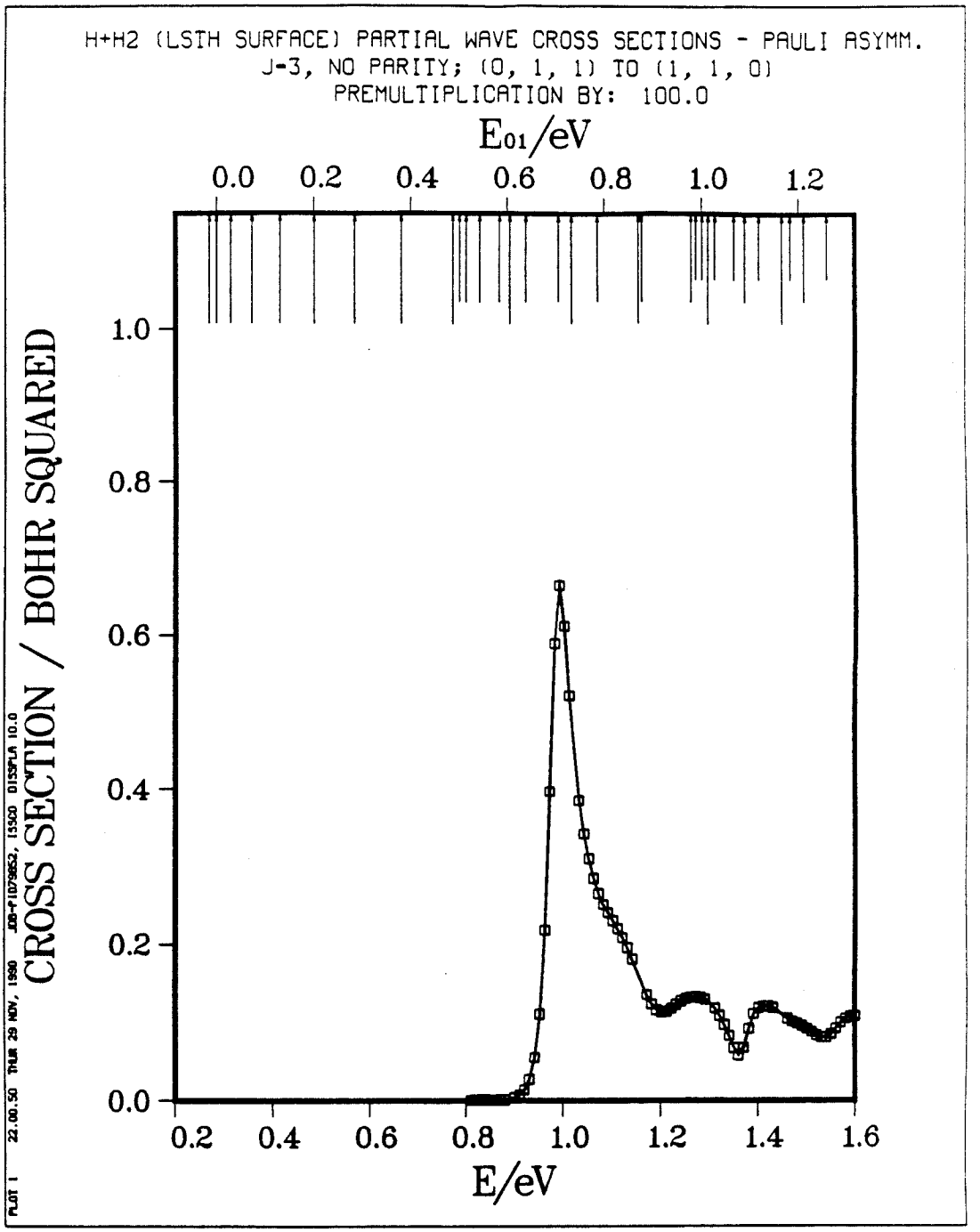
H+H2 (LSTH SURFACE) PARTIAL WAVE CROSS SECTIONS - PAULI ASYMM.
J=3, NO PARITY; (0, 1, 1) TO (1, 1, 0)
PREMULTIPLICATION BY: 100.0
E01/eV
0.0
0.2
0.4
0.6
0.8
1.0
1.2
CROSS SECTION / BOHR SQUARED
0.0
0.2
0.4
0.6
0.8
1.0
0.2
0.4
0.6
0.8
1.0
1.2
1.4
1.6
E/eV
PLOT 1 22.00.50 THUR 29 NOV, 1990 JOB=P1079852, 13520 DISSPLA 10.0

Fig. 7.37c

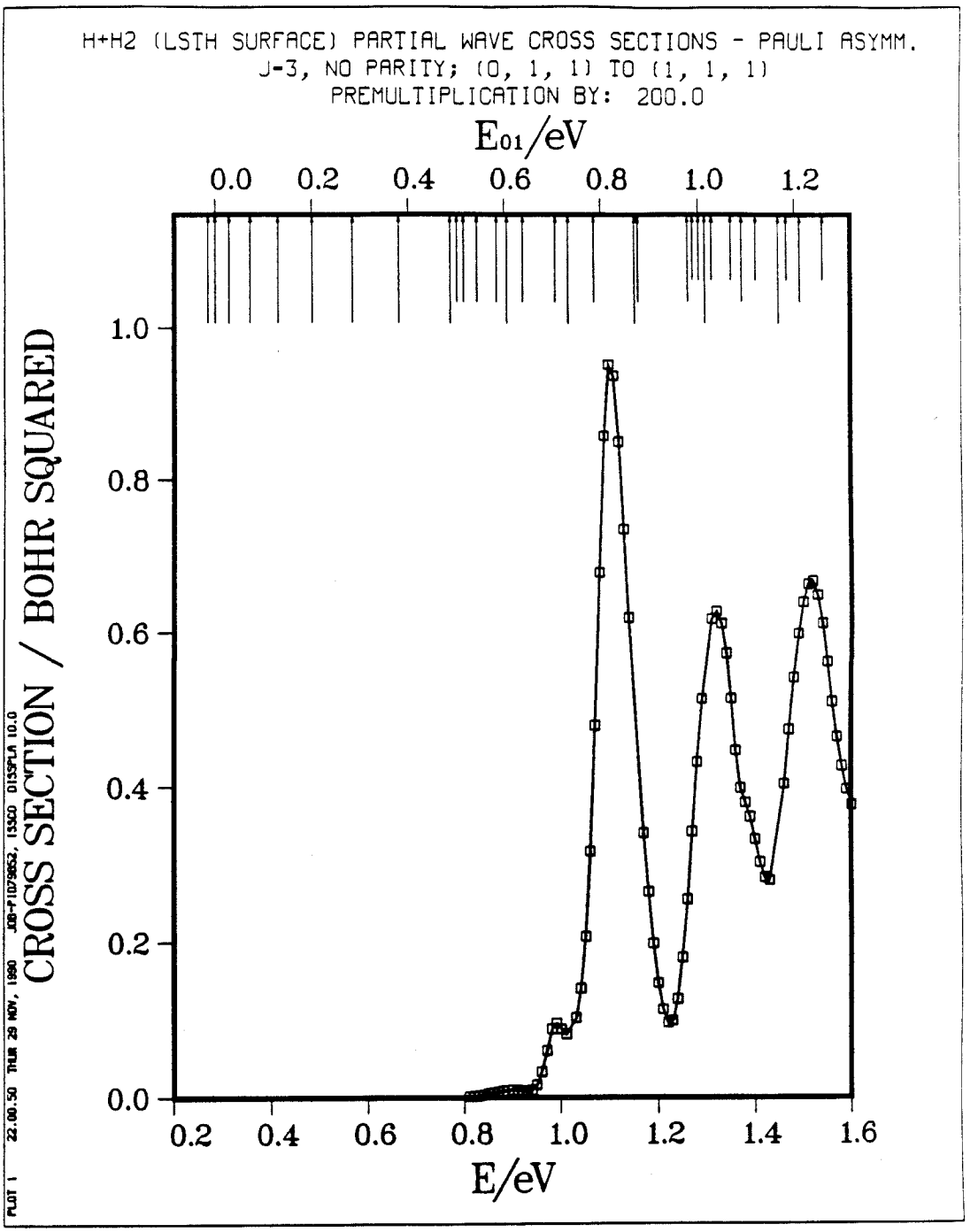
H+H2 (LSTH SURFACE) PARTIAL WAVE CROSS SECTIONS - PAULI ASYMM.
J=3, NO PARITY; (0, 1, 1) TO (1, 1, 1)
PREMULTIPLICATION BY: 200.0
E01/eV
0.0
0.2
0.4
0.6
0.8
1.0
1.2
CROSS SECTION / BOHR SQUARED
0.0
0.2
0.4
0.6
0.8
1.0
0.2
0.4
0.6
0.8
1.0
1.2
1.4
1.6
E/eV
PLOT 1 22.00.50 THUR 29 NOV, 1990 JOB=P1079652, 13SCO DISSPLA 10.0

Fig. 7.37d

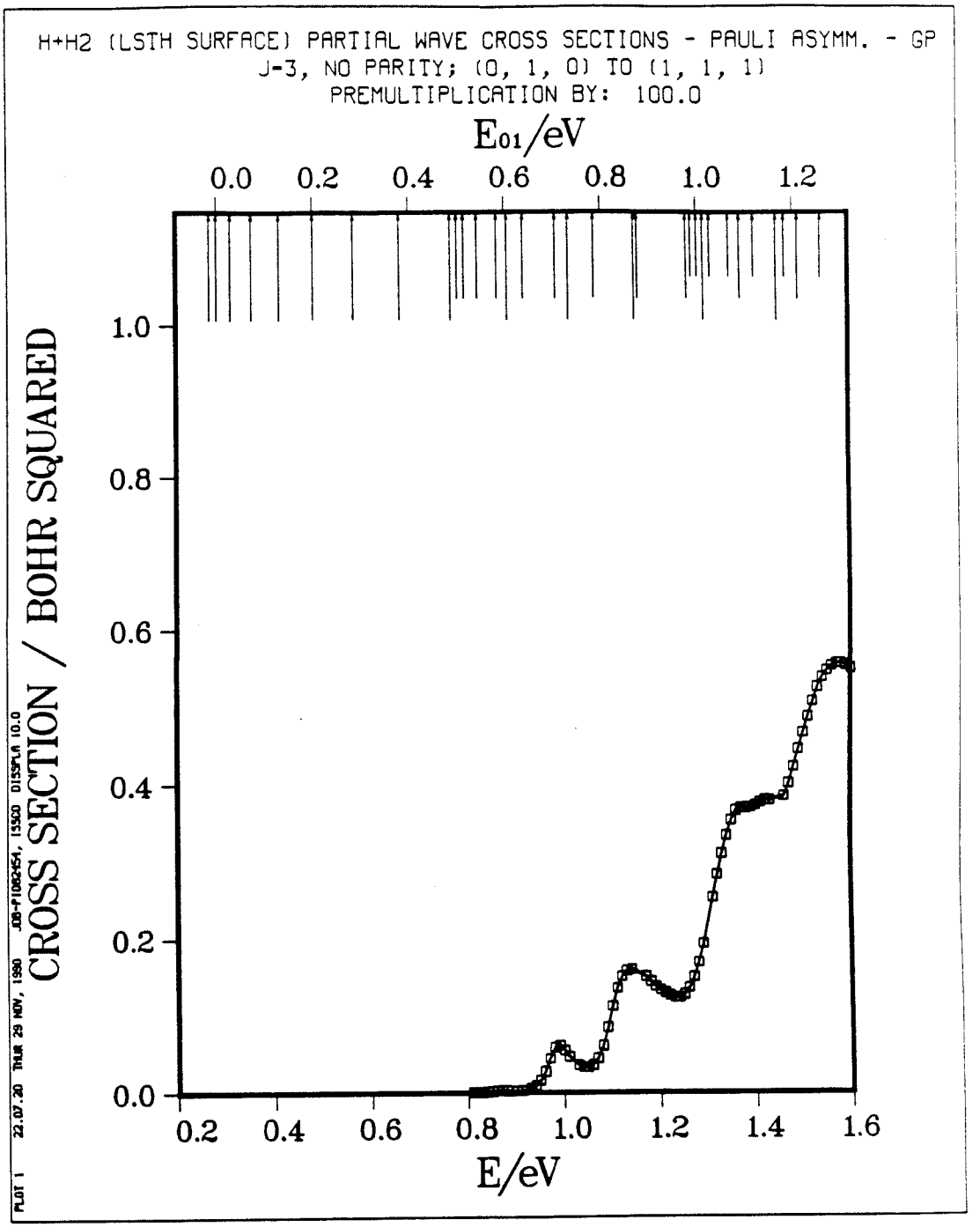
H+H2 (LSTH SURFACE) PARTIAL WAVE CROSS SECTIONS - PAULI ASYMM. - GP
J-3, NO PARITY; (0, 1, 0) TO (1, 1, 1)
PREMULTIPLICATION BY: 100.0
E01/eV
0.0
0.2
0.4
0.6
0.8
1.0
1.2
CROSS SECTION / BOHR SQUARED
0.0
0.2
0.4
0.6
0.8
1.0
0.2
0.4
0.6
0.8
1.0
1.2
1.4
1.6
E/eV
PLOT 1 22.07.20 THUR 29 NOV, 1990 JOB=P1002454, 13500 DISSPLA 10.0

Fig. 7.38a

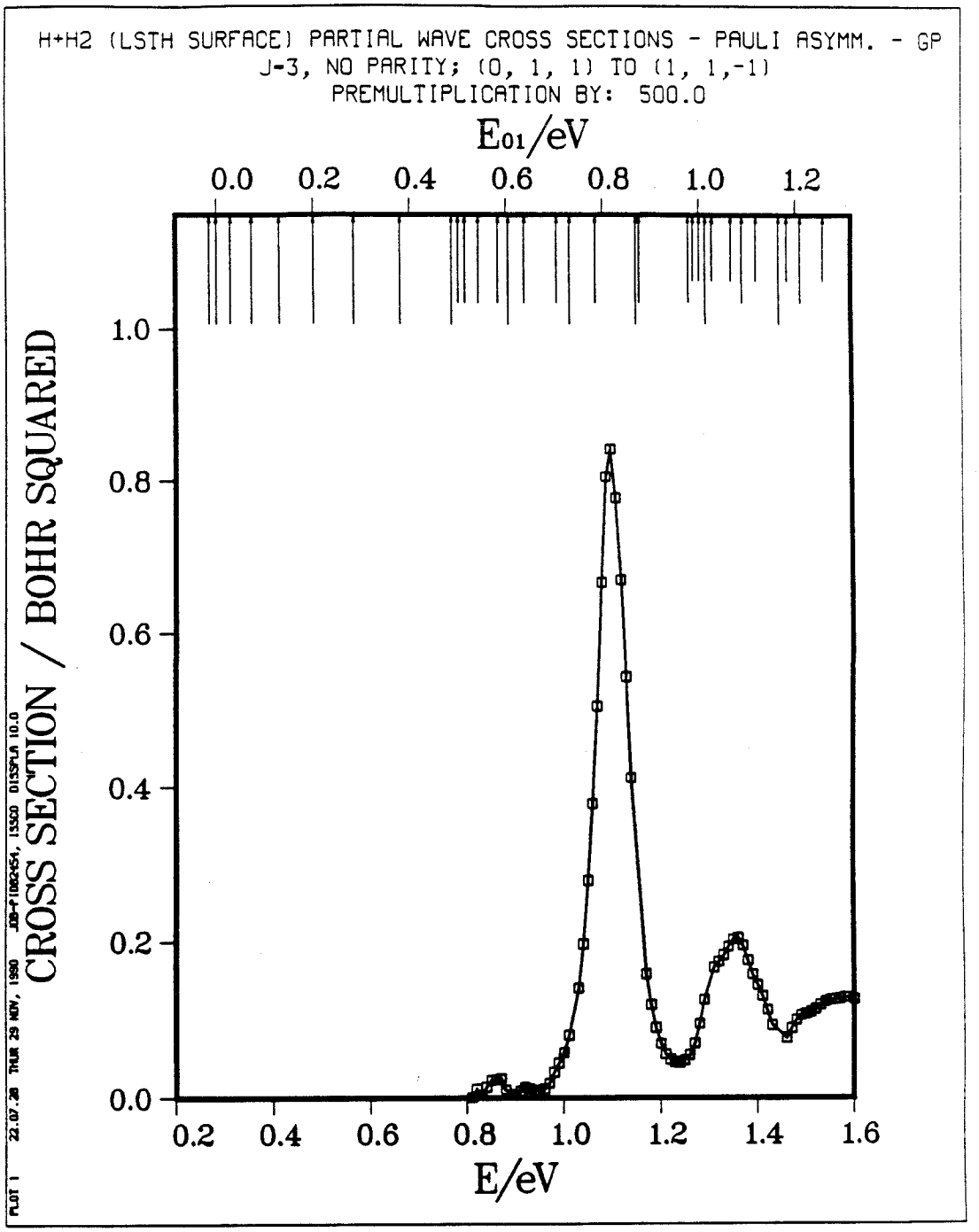
H+H2 (LSTH SURFACE) PARTIAL WAVE CROSS SECTIONS - PAULI ASYMM. - GP
J-3, NO PARITY; (0, 1, 1) TO (1, 1,-1)
PREMULTIPLICATION BY: 500.0
E01/eV
0.0
0.2
0.4
0.6
0.8
1.0
1.2
CROSS SECTION / BOHR SQUARED
0.0
0.2
0.4
0.6
0.8
1.0
0.2
0.4
0.6
0.8
1.0
1.2
1.4
1.6
E/eV
PLOT 1 22.07.28 THUR 29 NOV, 1990 JOB=P1062454, 13SCO DISSPLA 10.0

Fig. 7.38b

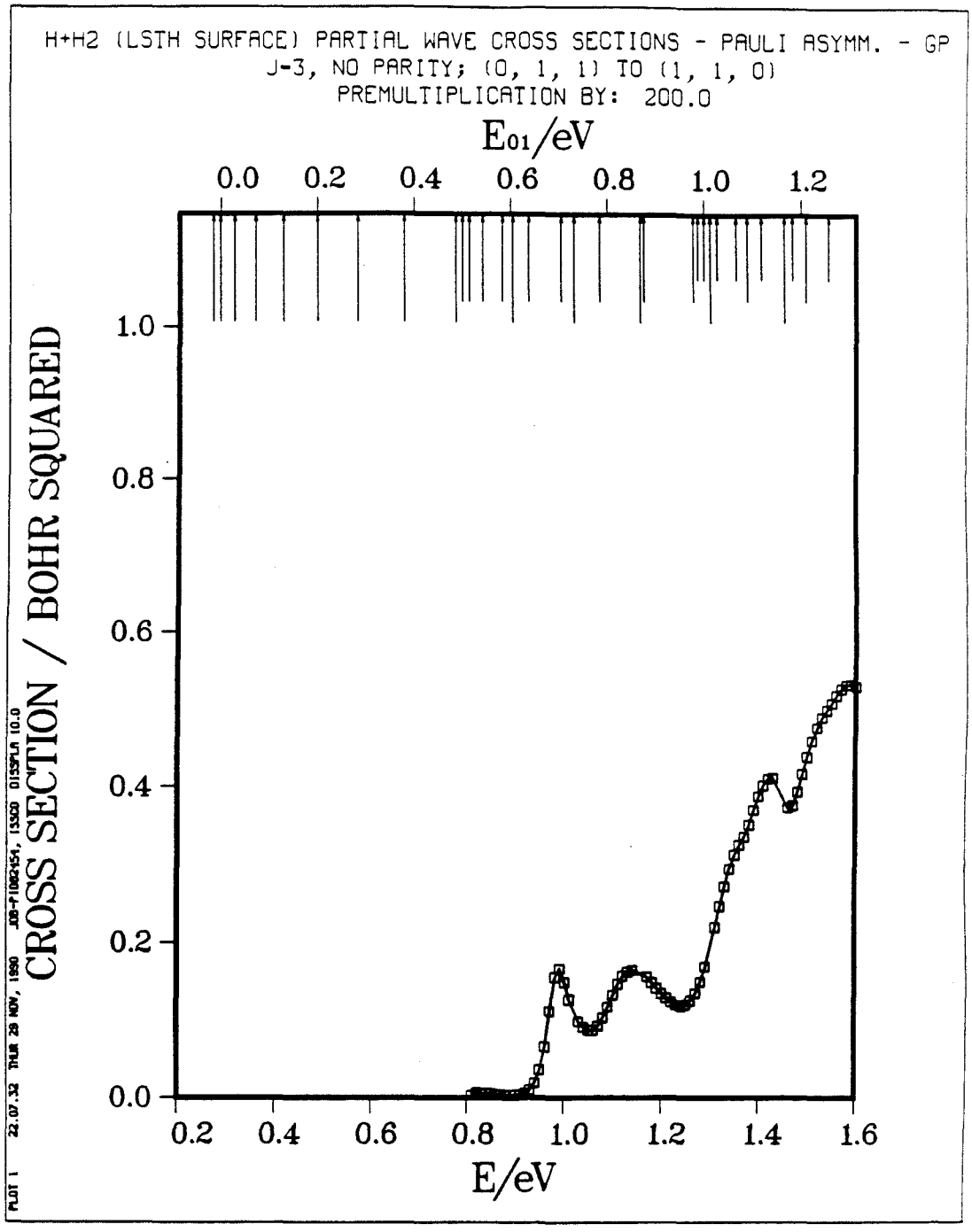
H+H2 (LSTH SURFACE) PARTIAL WAVE CROSS SECTIONS - PAULI ASYMM. - GP
J-3, NO PARITY; (0, 1, 1) TO (1, 1, 0)
PREMULTIPLICATION BY: 200.0
E01/eV
0.0
0.2
0.4
0.6
0.8
1.0
1.2
CROSS SECTION / BOHR SQUARED
0.0
0.2
0.4
0.6
0.8
1.0
0.2
0.4
0.6
0.8
1.0
1.2
1.4
1.6
E/eV
PLOT 1 22.07.32 THUR 28 NOV, 1990 JOB-P1080454, 15300 0153PLN 10.0

Fig. 7.38c

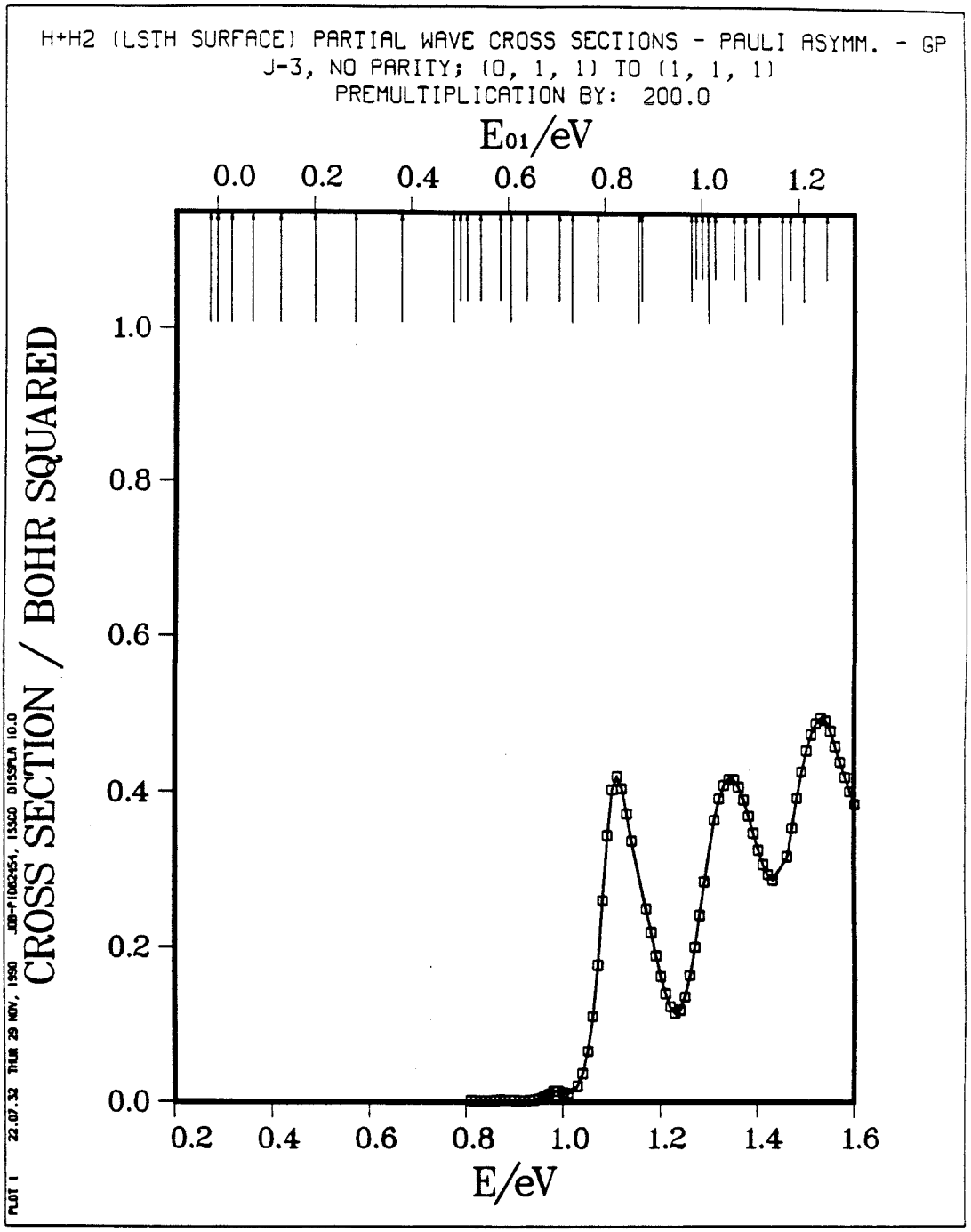
H+H2 (LSTH SURFACE) PARTIAL WAVE CROSS SECTIONS - PAULI ASYMM. - GP
J-3, NO PARITY; (0, 1, 1) TO (1, 1, 1)
PREMULTIPLICATION BY: 200.0
E01/eV
0.0
0.2
0.4
0.6
0.8
1.0
1.2
CROSS SECTION / BOHR SQUARED
0.0
0.2
0.4
0.6
0.8
1.0
0.2
0.4
0.6
0.8
1.0
1.2
1.4
1.6
E/eV
PLOT 1 22.07.32 THUR 29 NOV, 1990 JOB-P1002454, 13SCO DISSPLA 10.0

Fig. 7.38d

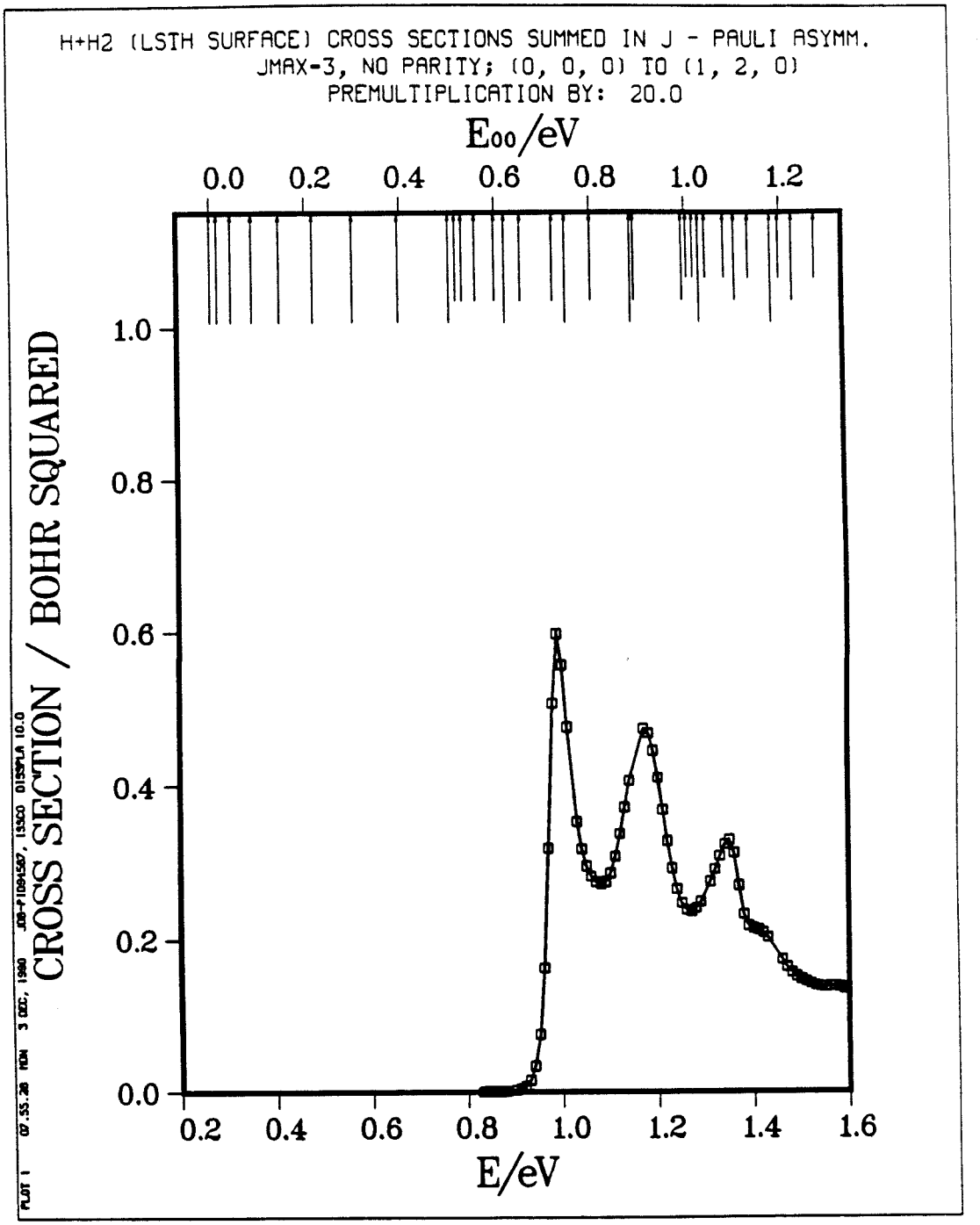
H+H2 (LSTH SURFACE) CROSS SECTIONS SUMMED IN J - PAULI ASYMM.
JMAX=3, NO PARITY; (0, 0, 0) TO (1, 2, 0)
PREMULTIPLICATION BY: 20.0
E00/eV
0.0
0.2
0.4
0.6
0.8
1.0
1.2
CROSS SECTION / BOHR SQUARED
0.0
0.2
0.4
0.6
0.8
1.0
0.2
0.4
0.6
0.8
1.0
1.2
1.4
1.6
E/eV

Fig. 7.39a

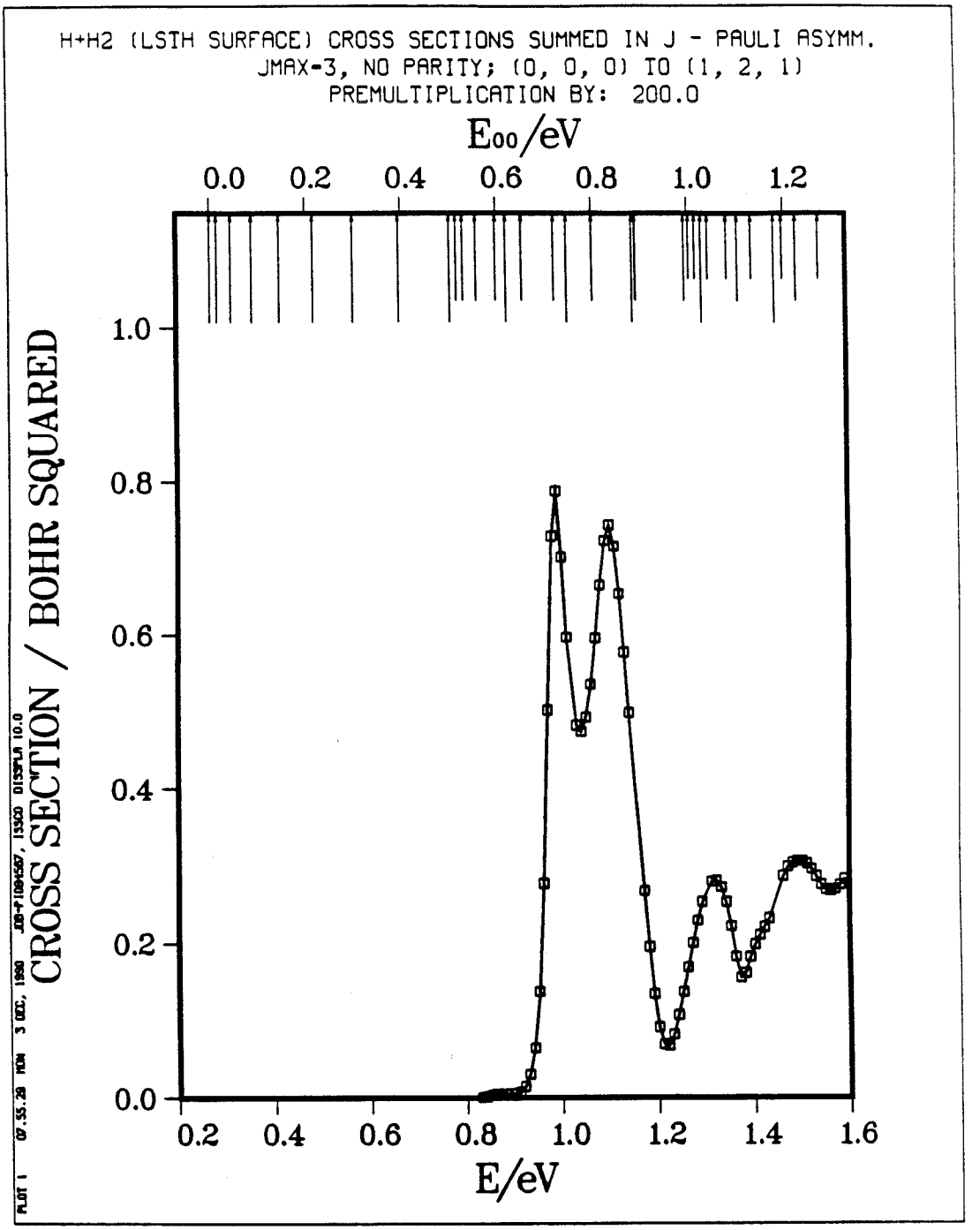
H+H2 (LSTH SURFACE) CROSS SECTIONS SUMMED IN J - PAULI ASYMM.
JMAX=3, NO PARITY; (0, 0, 0) TO (1, 2, 1)
PREMULTIPLICATION BY: 200.0
E00/eV
0.0
0.2
0.4
0.6
0.8
1.0
1.2
CROSS SECTION / BOHR SQUARED
0.0
0.2
0.4
0.6
0.8
1.0
0.2
0.4
0.6
0.8
1.0
1.2
1.4
1.6
E/eV

Fig. 7.39b

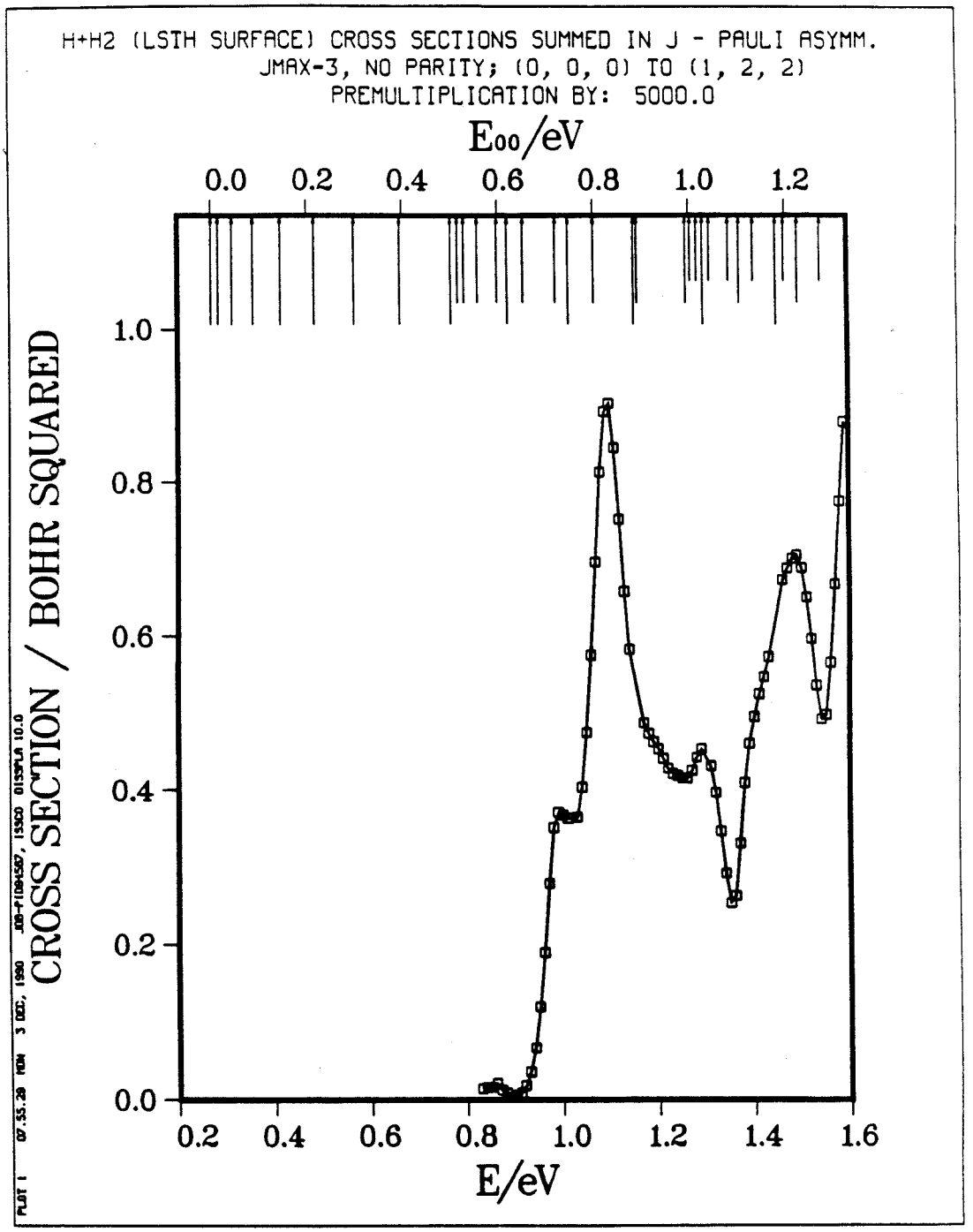
H+H2 (LSTH SURFACE) CROSS SECTIONS SUMMED IN J - PAULI ASYMM.
JMAX-3, NO PARITY; (0, 0, 0) TO (1, 2, 2)
PREMULTIPLICATION BY: 5000.0
E00/eV
0.0
0.2
0.4
0.6
0.8
1.0
1.2
CROSS SECTION / BOHR SQUARED
0.0
0.2
0.4
0.6
0.8
1.0
0.2
0.4
0.6
0.8
1.0
1.2
1.4
1.6
E/eV

Fig. 7.39c

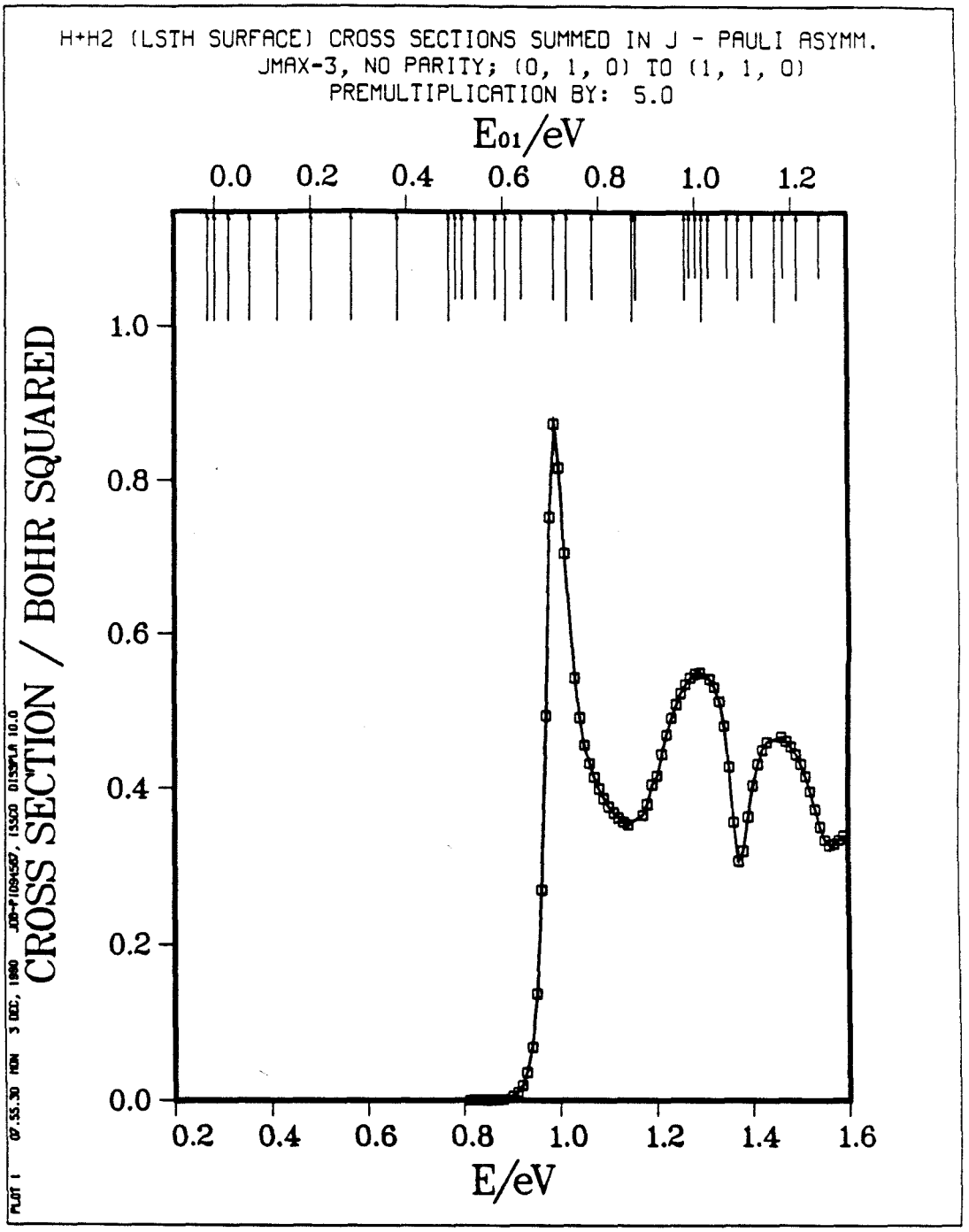
H+H2 (LSTH SURFACE) CROSS SECTIONS SUMMED IN J - PAULI ASYMM.
JMAX-3, NO PARITY; (0, 1, 0) TO (1, 1, 0)
PREMULTIPLICATION BY: 5.0
E01/eV
0.0
0.2
0.4
0.6
0.8
1.0
1.2
CROSS SECTION / BOHR SQUARED
0.0
0.2
0.4
0.6
0.8
1.0
0.2
0.4
0.6
0.8
1.0
1.2
1.4
1.6
E/eV

Fig. 7.39d

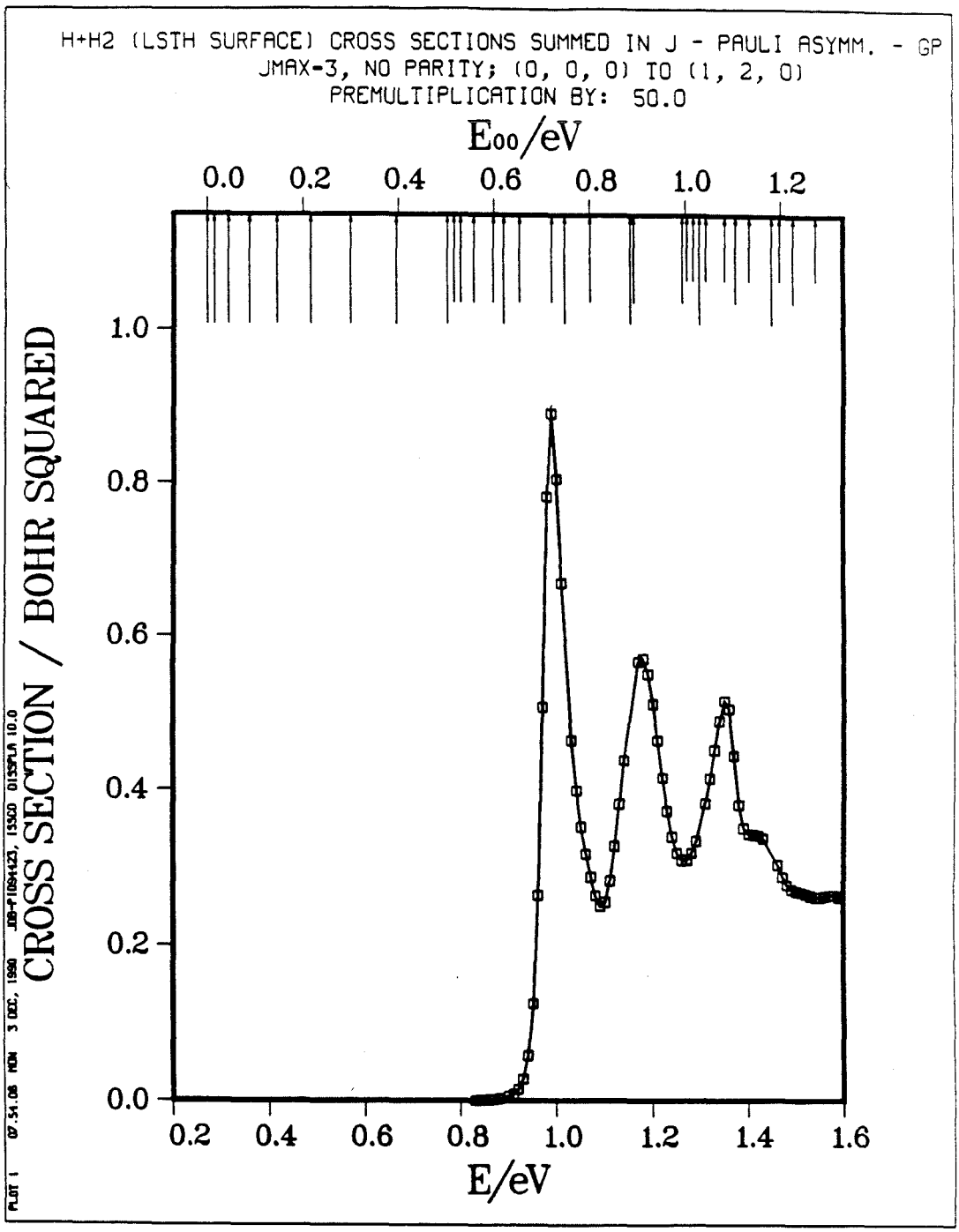
H+H2 (LSTH SURFACE) CROSS SECTIONS SUMMED IN J - PAULI ASYMM. - GP
JMAX=3, NO PARITY; (0, 0, 0) TO (1, 2, 0)
PREMULTIPLICATION BY: 50.0
E00/eV
0.0
0.2
0.4
0.6
0.8
1.0
1.2
CROSS SECTION / BOHR SQUARED
0.0
0.2
0.4
0.6
0.8
1.0
0.2
0.4
0.6
0.8
1.0
1.2
1.4
1.6
E/eV

Fig. 7.40a

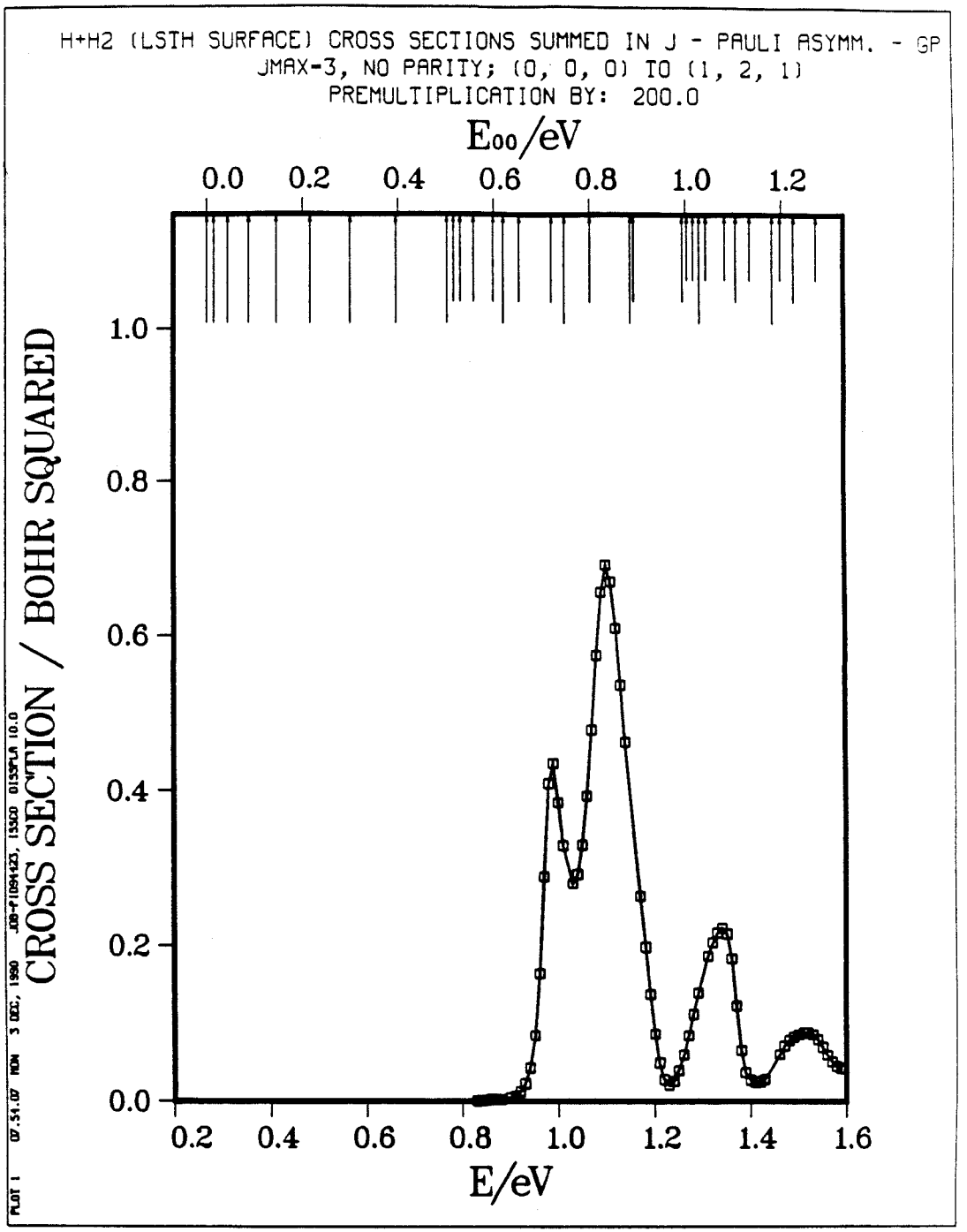
H+H2 (LSTH SURFACE) CROSS SECTIONS SUMMED IN J - PAULI ASYMM. - GP
JMAX=3, NO PARITY; (0, 0, 0) TO (1, 2, 1)
PREMULTIPLICATION BY: 200.0
E00/eV
0.0
0.2
0.4
0.6
0.8
1.0
1.2
CROSS SECTION / BOHR SQUARED
0.0
0.2
0.4
0.6
0.8
1.0
0.2
0.4
0.6
0.8
1.0
1.2
1.4
1.6
E/eV

Fig. 7.40b

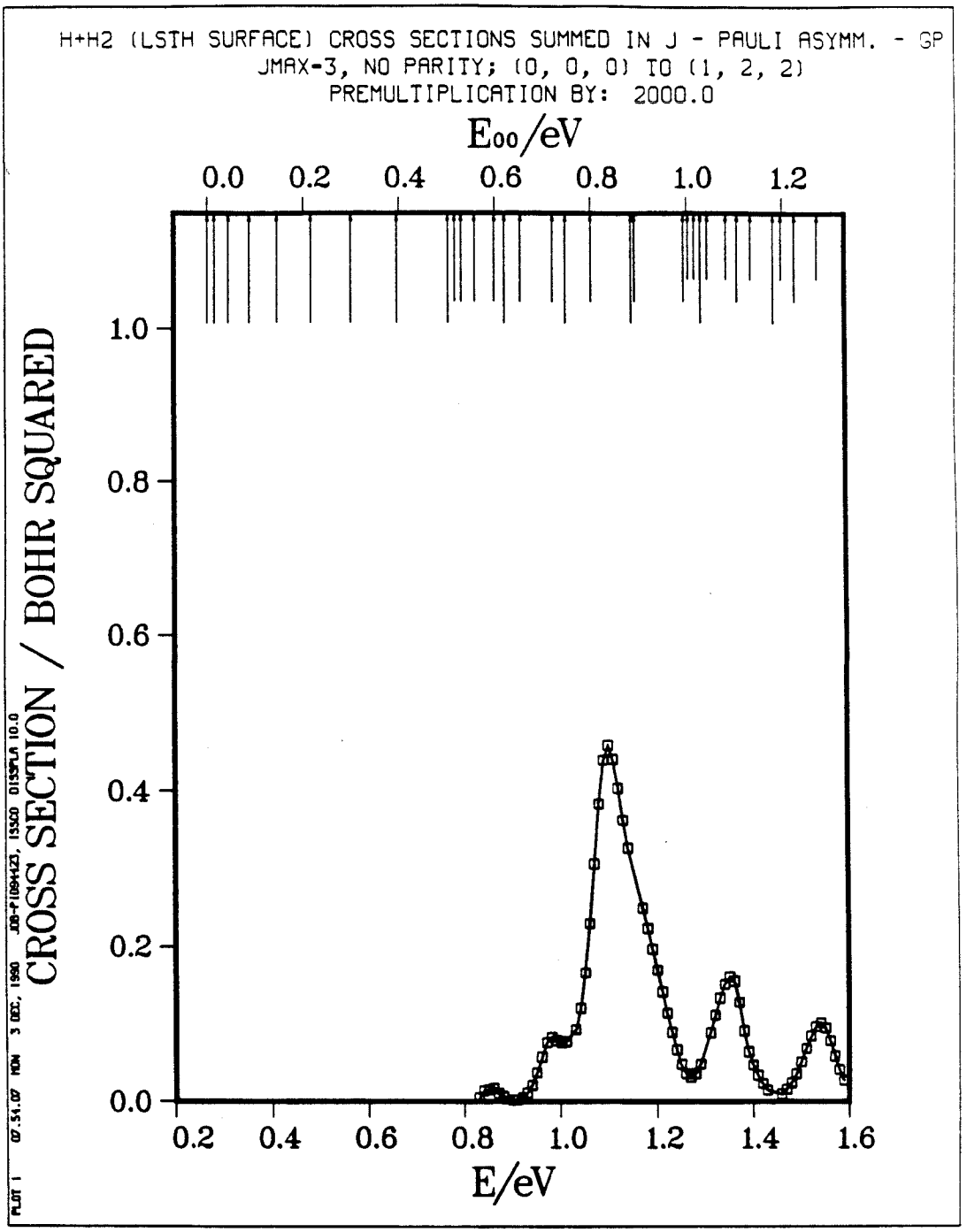
H+H2 (LSTH SURFACE) CROSS SECTIONS SUMMED IN J - PAULI ASYMM. - GP
JMAX=3, NO PARITY; (0, 0, 0) TO (1, 2, 2)
PREMULTIPLICATION BY: 2000.0
E00/eV
0.0
0.2
0.4
0.6
0.8
1.0
1.2
CROSS SECTION / BOHR SQUARED
0.0
0.2
0.4
0.6
0.8
1.0
0.2
0.4
0.6
0.8
1.0
1.2
1.4
1.6
E/eV
PLOT 1 07.54.07 MON 3 DEC, 1990 JOB=P1094423, 15SCO DISSPLA 10.0

Fig. 7.40c

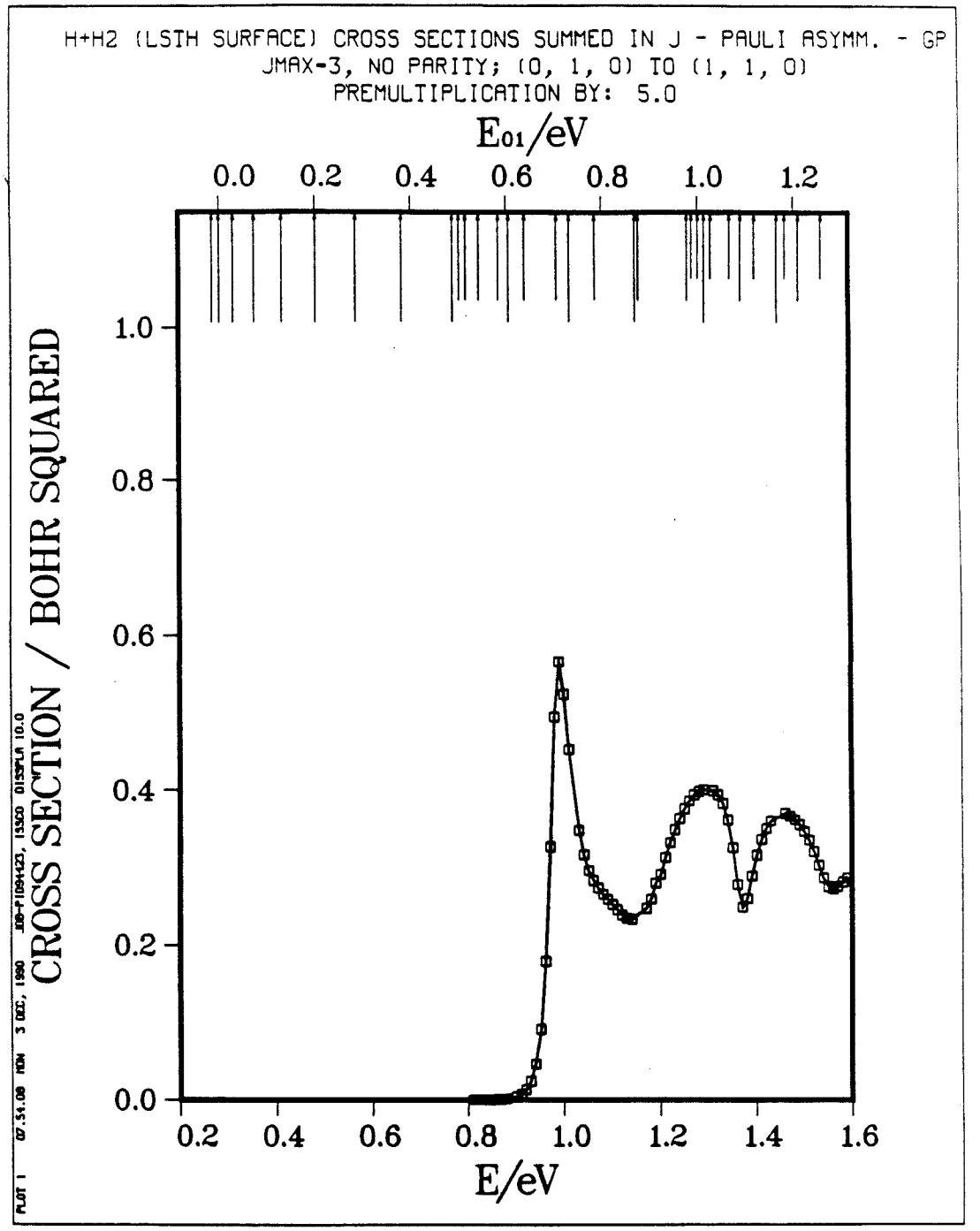
H+H2 (LSTH SURFACE) CROSS SECTIONS SUMMED IN J - PAULI ASYMM. - GP
JMAX=3, NO PARITY; (0, 1, 0) TO (1, 1, 0)
PREMULTIPLICATION BY: 5.0
E01/eV
0.0
0.2
0.4
0.6
0.8
1.0
1.2
CROSS SECTION / BOHR SQUARED
0.0
0.2
0.4
0.6
0.8
1.0
E/eV
0.2
0.4
0.6
0.8
1.0
1.2
1.4
1.6
PLOT 1 07.34.00 MON 5 DEC, 1988 JOB=P1094423, 13SCO 015SPLA 10.0

Fig. 7.40d

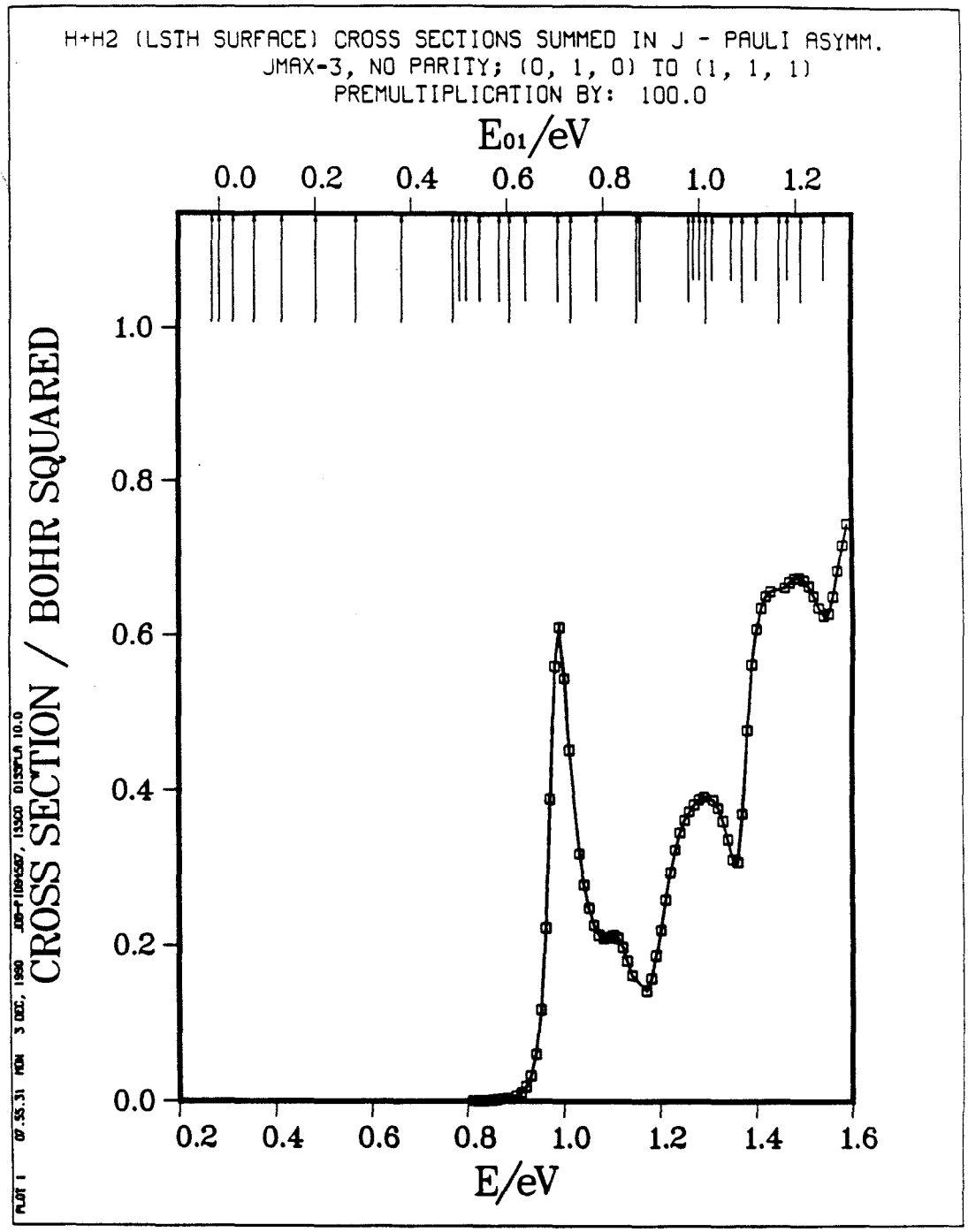
H+H2 (LSTH SURFACE) CROSS SECTIONS SUMMED IN J - PAULI ASYMM.
JMAX=3, NO PARITY; (0, 1, 0) TO (1, 1, 1)
PREMULTIPLICATION BY: 100.0
E01/eV
0.0
0.2
0.4
0.6
0.8
1.0
1.2
CROSS SECTION / BOHR SQUARED
0.0
0.2
0.4
0.6
0.8
1.0
0.2
0.4
0.6
0.8
1.0
1.2
1.4
1.6
E/eV

Fig. 7.41a

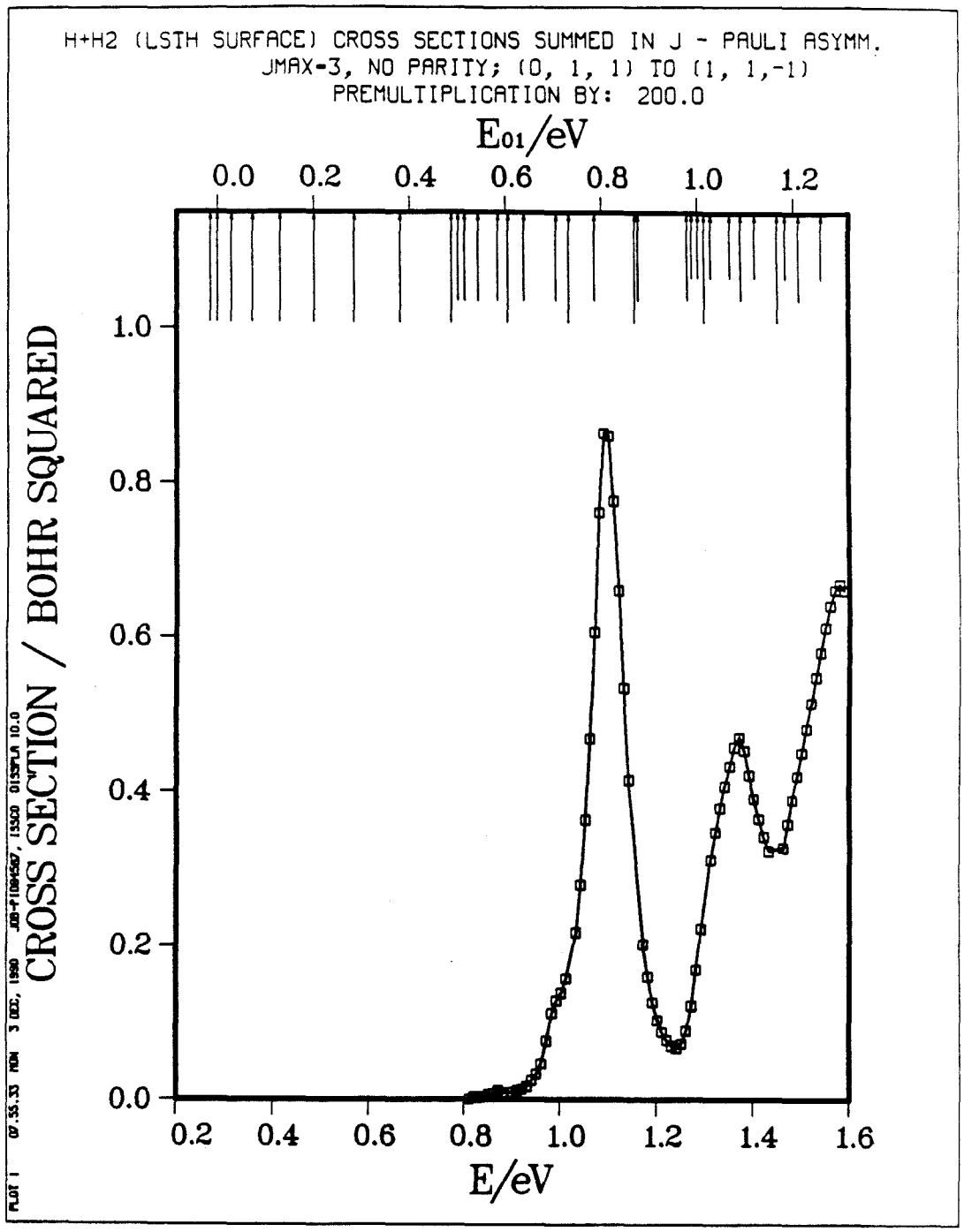
H+H2 (LSTH SURFACE) CROSS SECTIONS SUMMED IN J - PAULI ASYMM.
JMAX=3, NO PARITY; (0, 1, 1) TO (1, 1,-1)
PREMULTIPLICATION BY: 200.0
E01/eV
0.0
0.2
0.4
0.6
0.8
1.0
1.2
CROSS SECTION / BOHR SQUARED
0.0
0.2
0.4
0.6
0.8
1.0
0.2
0.4
0.6
0.8
1.0
1.2
1.4
1.6
E/eV

Fig. 7.41b

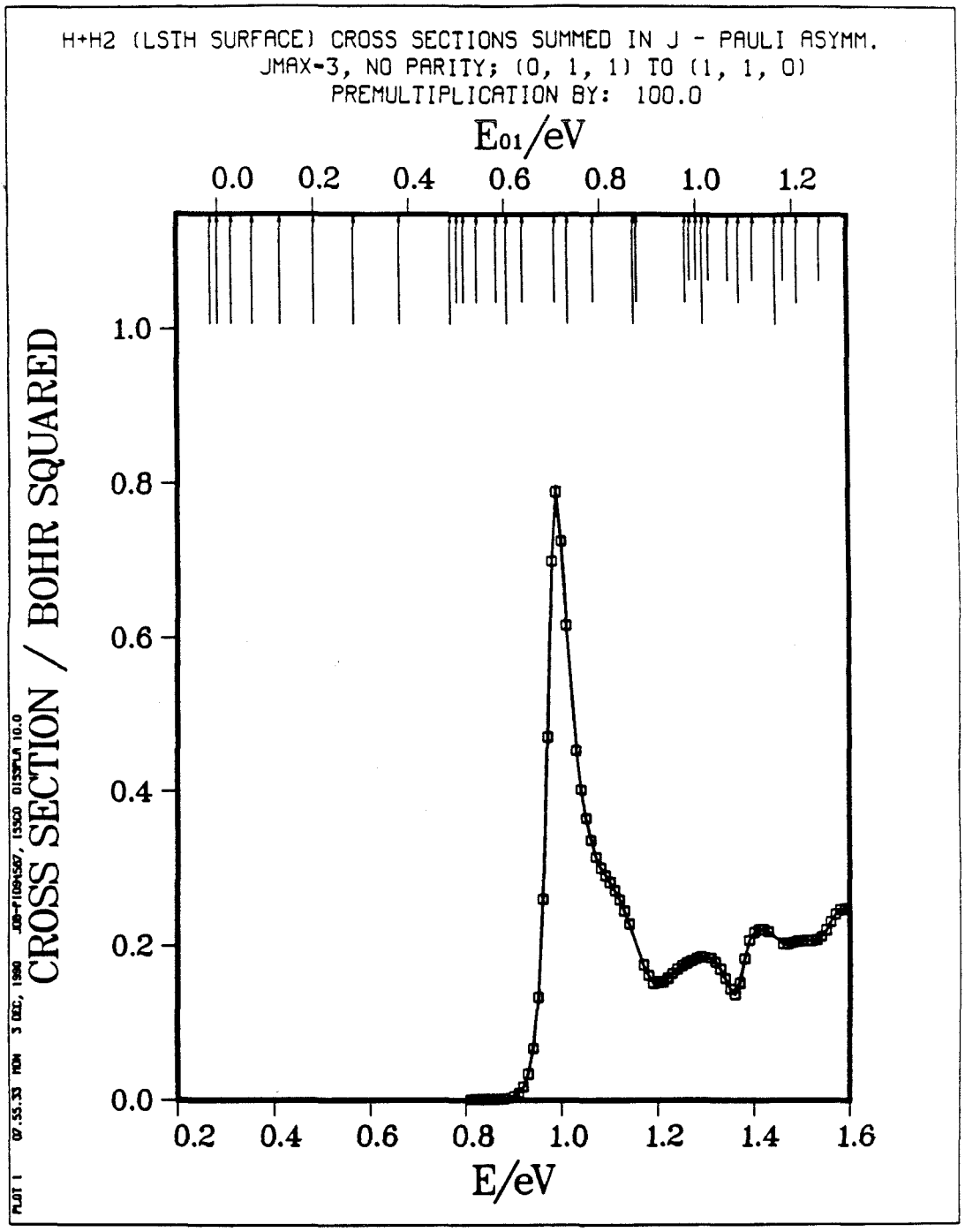
H+H2 (LSTH SURFACE) CROSS SECTIONS SUMMED IN J - PAULI ASYMM.
JMAX=3, NO PARITY; (0, 1, 1) TO (1, 1, 0)
PREMULTIPLICATION BY: 100.0
E01/eV
0.0
0.2
0.4
0.6
0.8
1.0
1.2
CROSS SECTION / BOHR SQUARED
0.0
0.2
0.4
0.6
0.8
1.0
0.2
0.4
0.6
0.8
1.0
1.2
1.4
1.6
E/eV

Fig. 7.41c

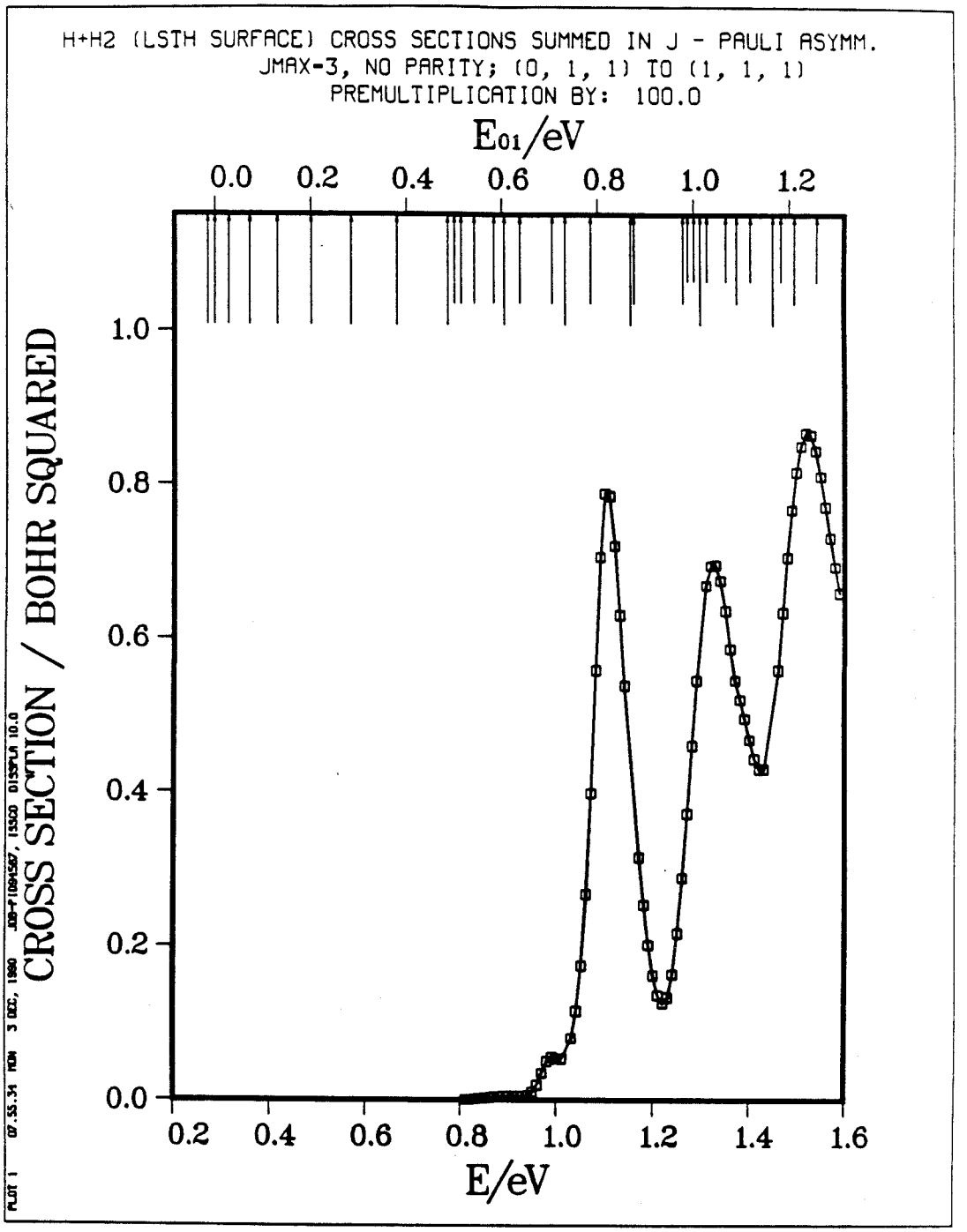
H+H2 (LSTH SURFACE) CROSS SECTIONS SUMMED IN J - PAULI ASYMM.
JMAX-3, NO PARITY; (0, 1, 1) TO (1, 1, 1)
PREMULTIPLICATION BY: 100.0
E01/eV
0.0
0.2
0.4
0.6
0.8
1.0
1.2
CROSS SECTION / BOHR SQUARED
0.0
0.2
0.4
0.6
0.8
1.0
E/eV
0.2
0.4
0.6
0.8
1.0
1.2
1.4
1.6

Fig. 7.41d

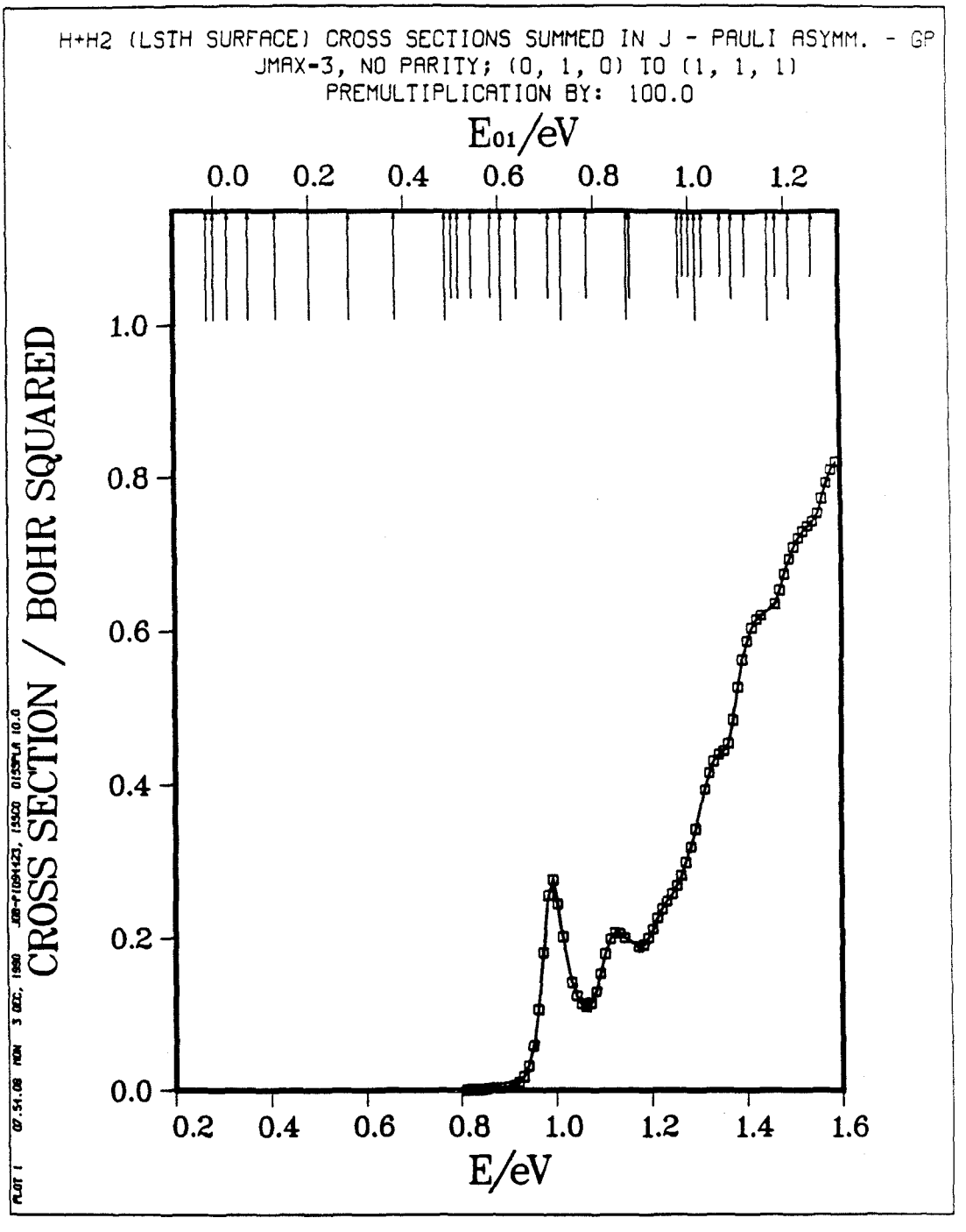
H+H2 (LSTH SURFACE) CROSS SECTIONS SUMMED IN J - PAULI ASYMM. - GP
JMAX=3, NO PARITY; (0, 1, 0) TO (1, 1, 1)
PREMULTIPLICATION BY: 100.0
E01/eV
0.0
0.2
0.4
0.6
0.8
1.0
1.2
CROSS SECTION / BOHR SQUARED
0.0
0.2
0.4
0.6
0.8
1.0
0.2
0.4
0.6
0.8
1.0
1.2
1.4
1.6
E/eV

Fig. 7.42a

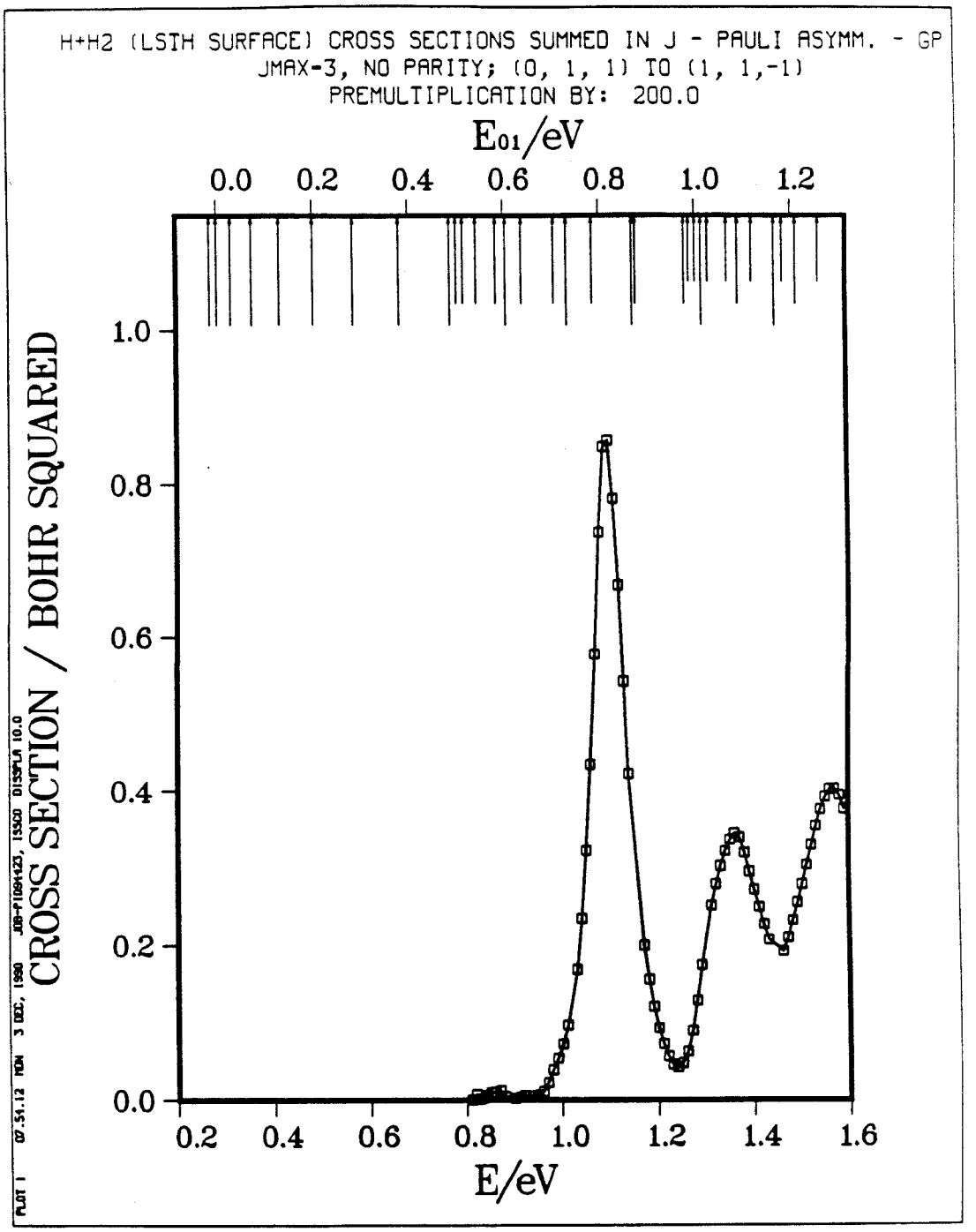
H+H2 (LSTH SURFACE) CROSS SECTIONS SUMMED IN J - PAULI ASYMM. - GP
JMAX-3, NO PARITY; (0, 1, 1) TO (1, 1,-1)
PREMULTIPLICATION BY: 200.0
E01/eV
0.0
0.2
0.4
0.6
0.8
1.0
1.2
CROSS SECTION / BOHR SQUARED
0.0
0.2
0.4
0.6
0.8
1.0
0.2
0.4
0.6
0.8
1.0
1.2
1.4
1.6
E/eV
PLOT 1 07.54.12 MON 3 DEC, 1990 JOB=P1094425, 15300 0139PLA 10.0

Fig. 7.42b

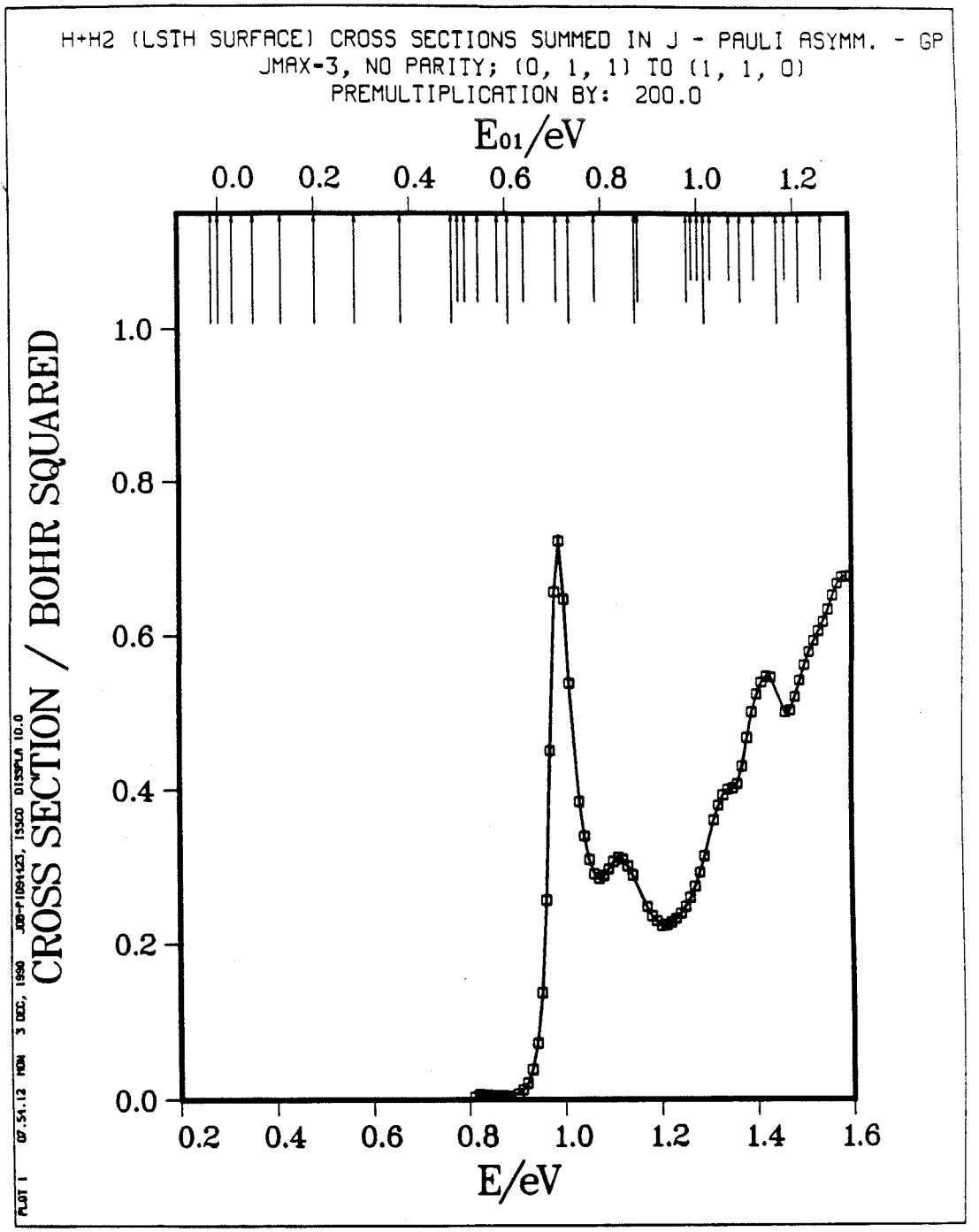
H+H2 (LSTH SURFACE) CROSS SECTIONS SUMMED IN J - PAULI ASYMM. - GP
JMAX=3, NO PARITY; (0, 1, 1) TO (1, 1, 0)
PREMULTIPLICATION BY: 200.0
E01/eV
0.0
0.2
0.4
0.6
0.8
1.0
1.2
CROSS SECTION / BOHR SQUARED
0.0
0.2
0.4
0.6
0.8
1.0
0.2
0.4
0.6
0.8
1.0
1.2
1.4
1.6
E/eV
PLOT 1 07.54.12 MON 3 DEC, 1990 JOB=P1069423, 13520 015SPLA 10.0

Fig. 7.42c

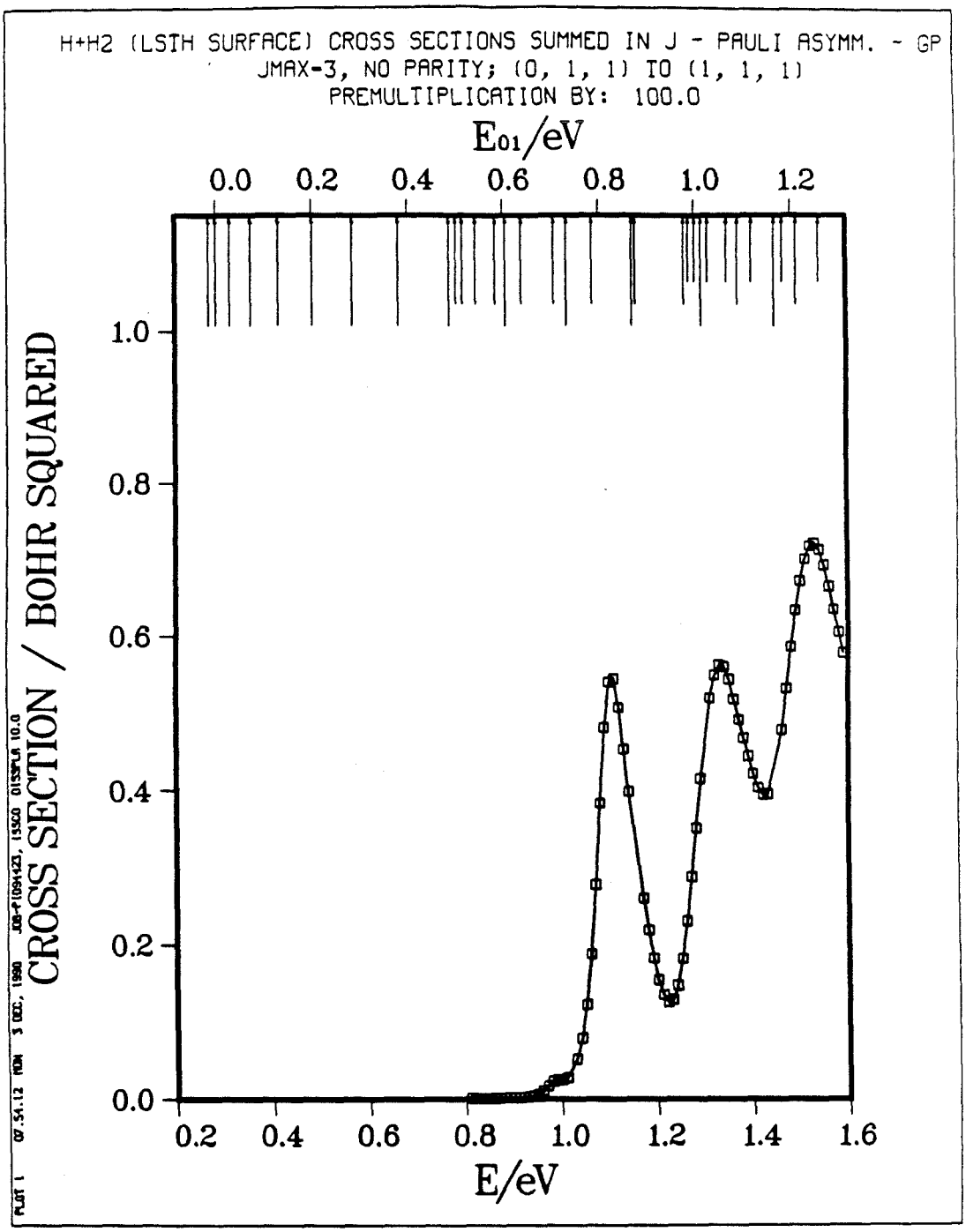
H+H2 (LSTH SURFACE) CROSS SECTIONS SUMMED IN J - PAULI ASYMM. - GP
JMAX=3, NO PARITY; (0, 1, 1) TO (1, 1, 1)
PREMULTIPLICATION BY: 100.0
E01/eV
0.0
0.2
0.4
0.6
0.8
1.0
1.2
CROSS SECTION / BOHR SQUARED
0.0
0.2
0.4
0.6
0.8
1.0
0.2
0.4
0.6
0.8
1.0
1.2
1.4
1.6
E/eV

Fig. 7.42d

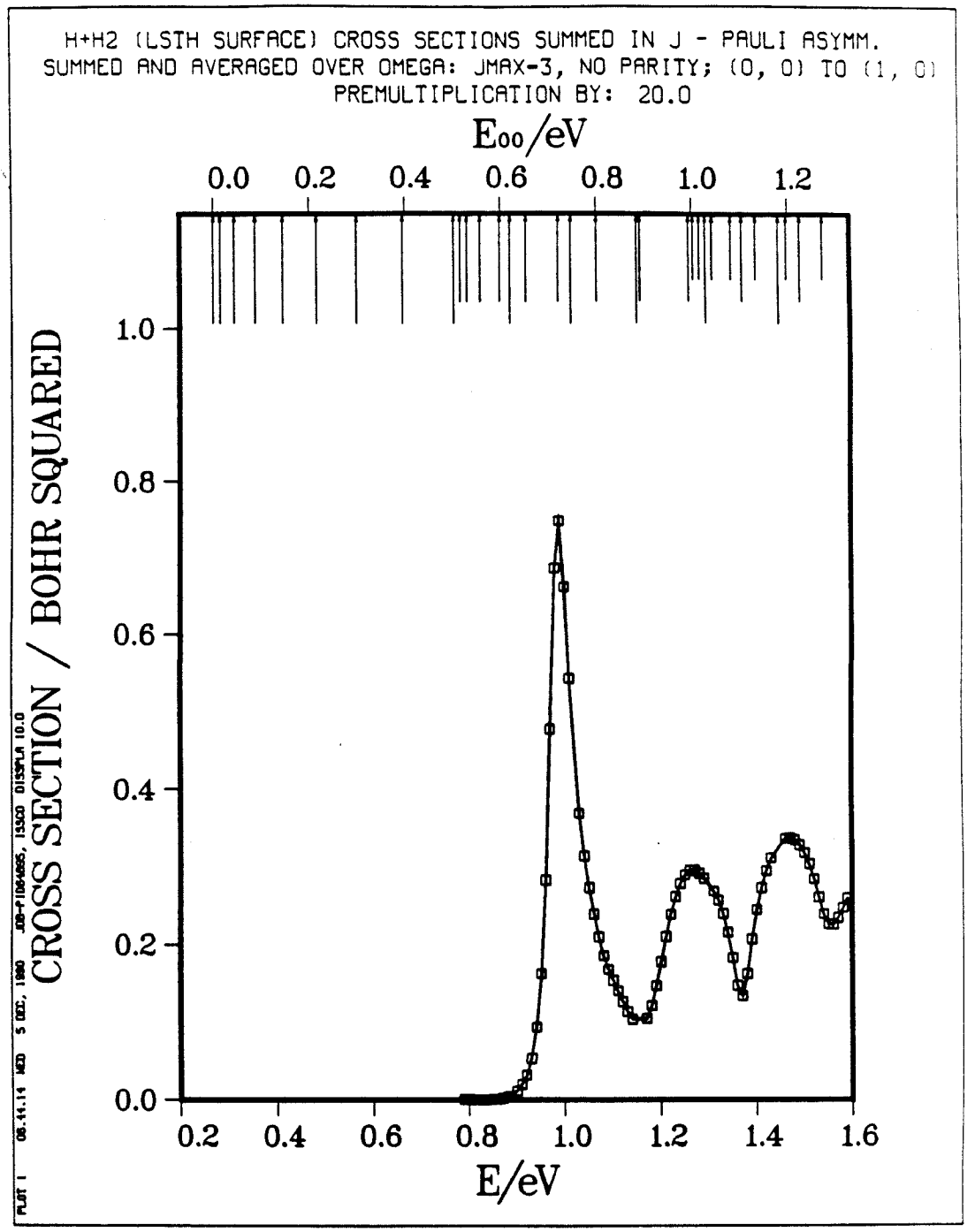
H+H2 (LSTH SURFACE) CROSS SECTIONS SUMMED IN J - PAULI ASYMM.
SUMMED AND AVERAGED OVER OMEGA: JMAX-3, NO PARITY; (0, 0) TO (1, 0)
PREMULTIPLICATION BY: 20.0
E00/eV
0.0
0.2
0.4
0.6
0.8
1.0
1.2
CROSS SECTION / BOHR SQUARED
0.0
0.2
0.4
0.6
0.8
1.0
1.2
1.4
1.6
E/eV

Fig. 7.43a

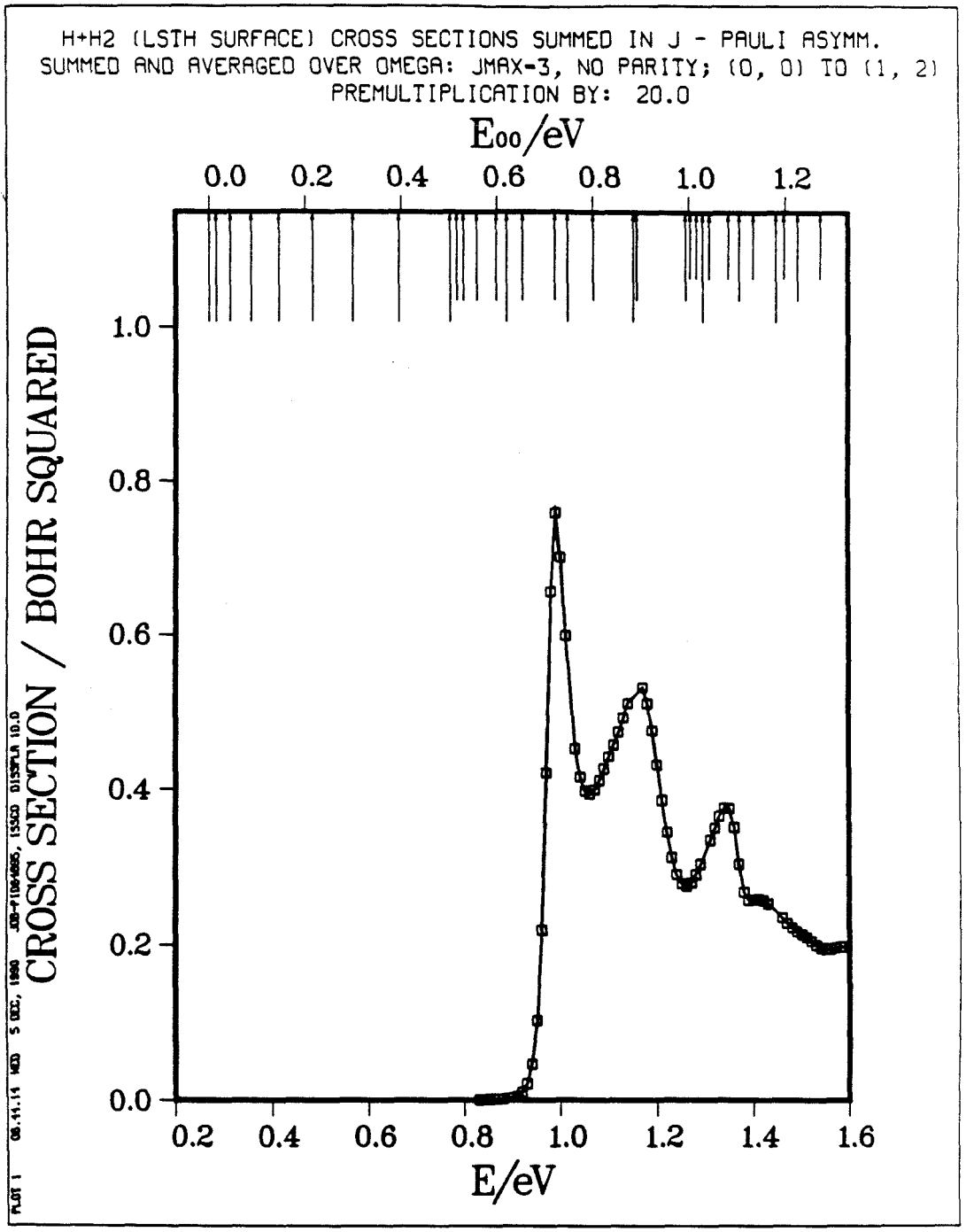
H+H2 (LSTH SURFACE) CROSS SECTIONS SUMMED IN J - PAULI ASYMM.
SUMMED AND AVERAGED OVER OMEGA: JMAX=3, NO PARITY; (0, 0) TO (1, 2)
PREMULTIPLICATION BY: 20.0
E00/eV
0.0
0.2
0.4
0.6
0.8
1.0
1.2
CROSS SECTION / BOHR SQUARED
0.0
0.2
0.4
0.6
0.8
1.0
0.2
0.4
0.6
0.8
1.0
1.2
1.4
1.6
E/eV

Fig. 7.43b

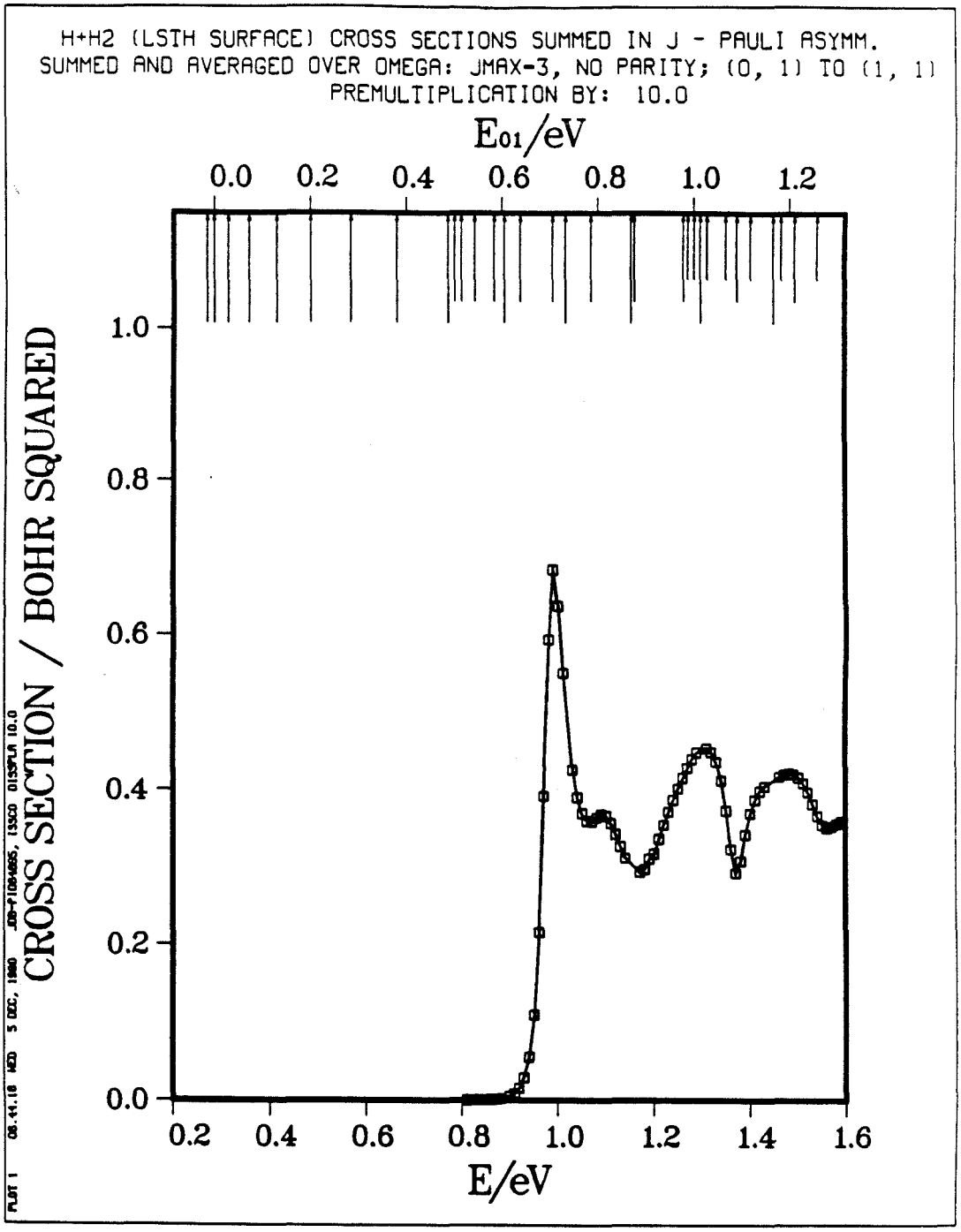
H+H2 (LSTH SURFACE) CROSS SECTIONS SUMMED IN J - PAULI ASYMM.
SUMMED AND AVERAGED OVER OMEGA: JMAX-3, NO PARITY; (0, 1) TO (1, 1)
PREMULTIPLICATION BY: 10.0
E01/eV
0.0
0.2
0.4
0.6
0.8
1.0
1.2
CROSS SECTION / BOHR SQUARED
0.0
0.2
0.4
0.6
0.8
1.0
0.2
0.4
0.6
0.8
1.0
1.2
1.4
1.6
E/eV

Fig. 7.43c

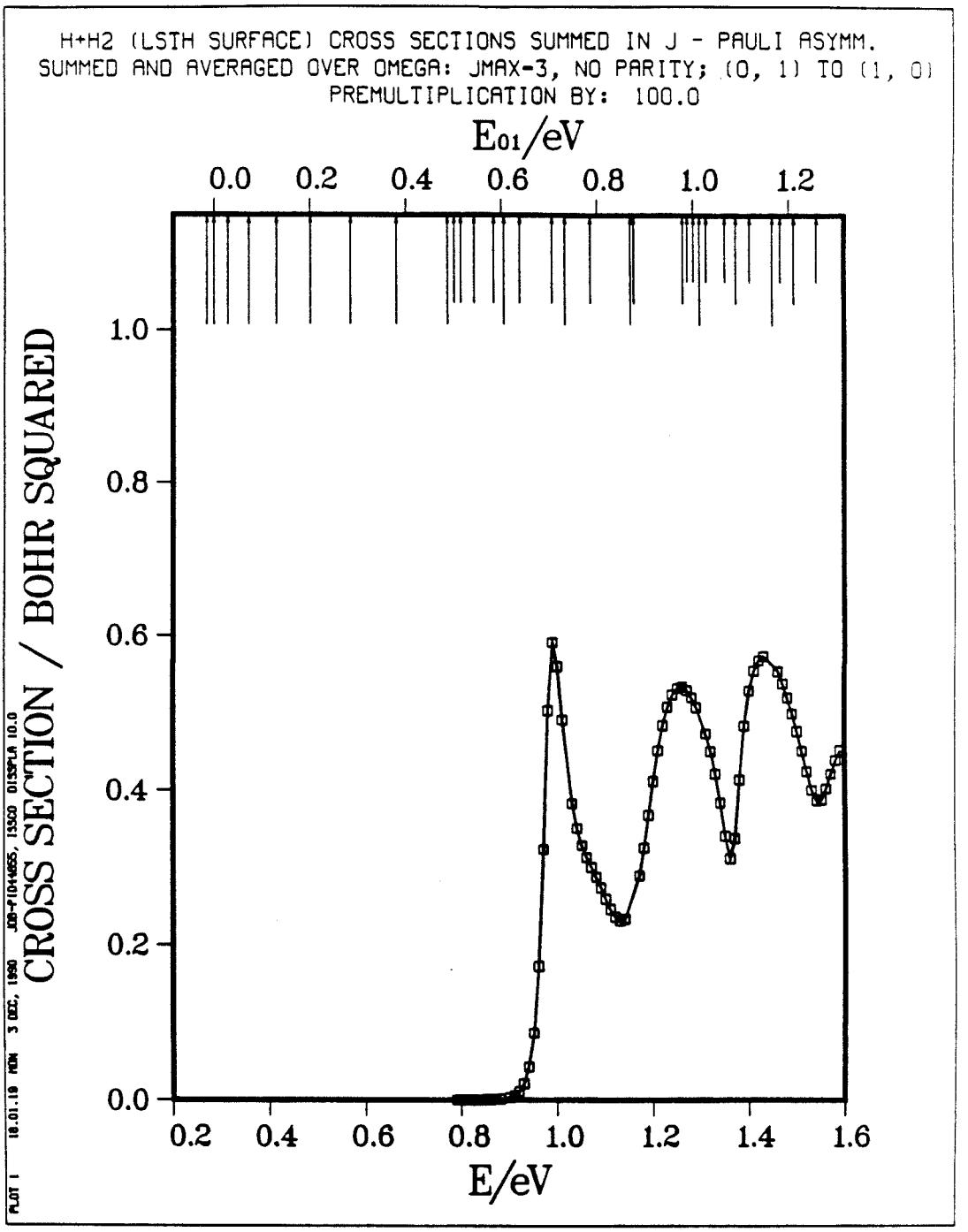
H+H2 (LSTH SURFACE) CROSS SECTIONS SUMMED IN J - PAULI ASYMM.
SUMMED AND AVERAGED OVER OMEGA: JMAX-3, NO PARITY; (0, 1) TO (1, 0)
PREMULTIPLICATION BY: 100.0
E01/eV
0.0
0.2
0.4
0.6
0.8
1.0
1.2
CROSS SECTION / BOHR SQUARED
0.0
0.2
0.4
0.6
0.8
1.0
0.2
0.4
0.6
0.8
1.0
1.2
1.4
1.6
E/eV
PLOT 1 16.01.19 MON 3 DEC, 1990 JOB-P1041655, 15SEC DISSPLA 10.0

Fig. 7.43d

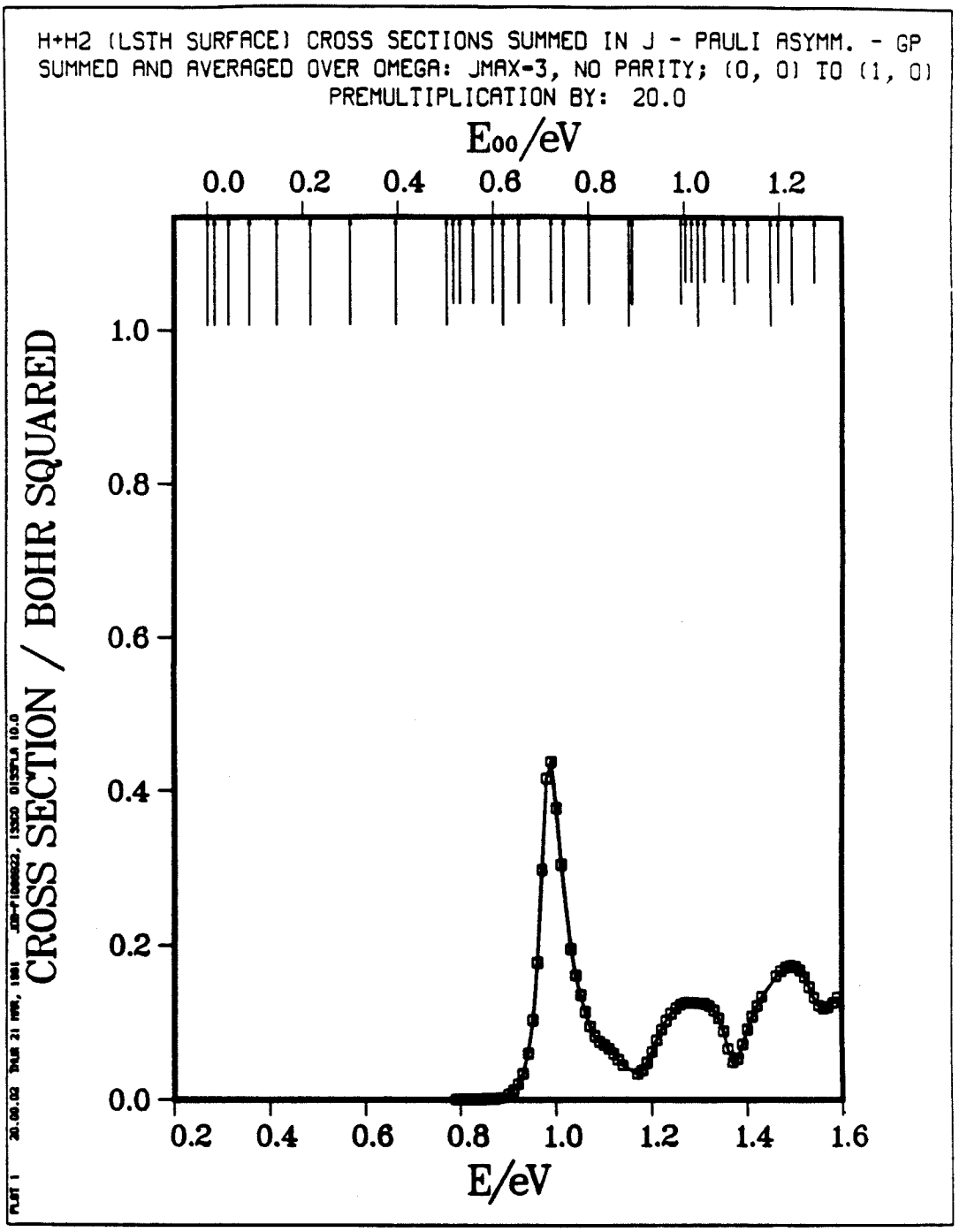
H+H2 (LSTH SURFACE) CROSS SECTIONS SUMMED IN J - PAULI ASYMM. - GP
SUMMED AND AVERAGED OVER OMEGA: JMAX=3, NO PARITY; (0, 0) TO (1, 0)
PREMULTIPLICATION BY: 20.0
E00/eV
0.0
0.2
0.4
0.6
0.8
1.0
1.2
CROSS SECTION / BOHR SQUARED
1.0
0.8
0.6
0.4
0.2
0.0
0.2
0.4
0.6
0.8
1.0
1.2
1.4
1.6
E/eV

Fig. 7.44a

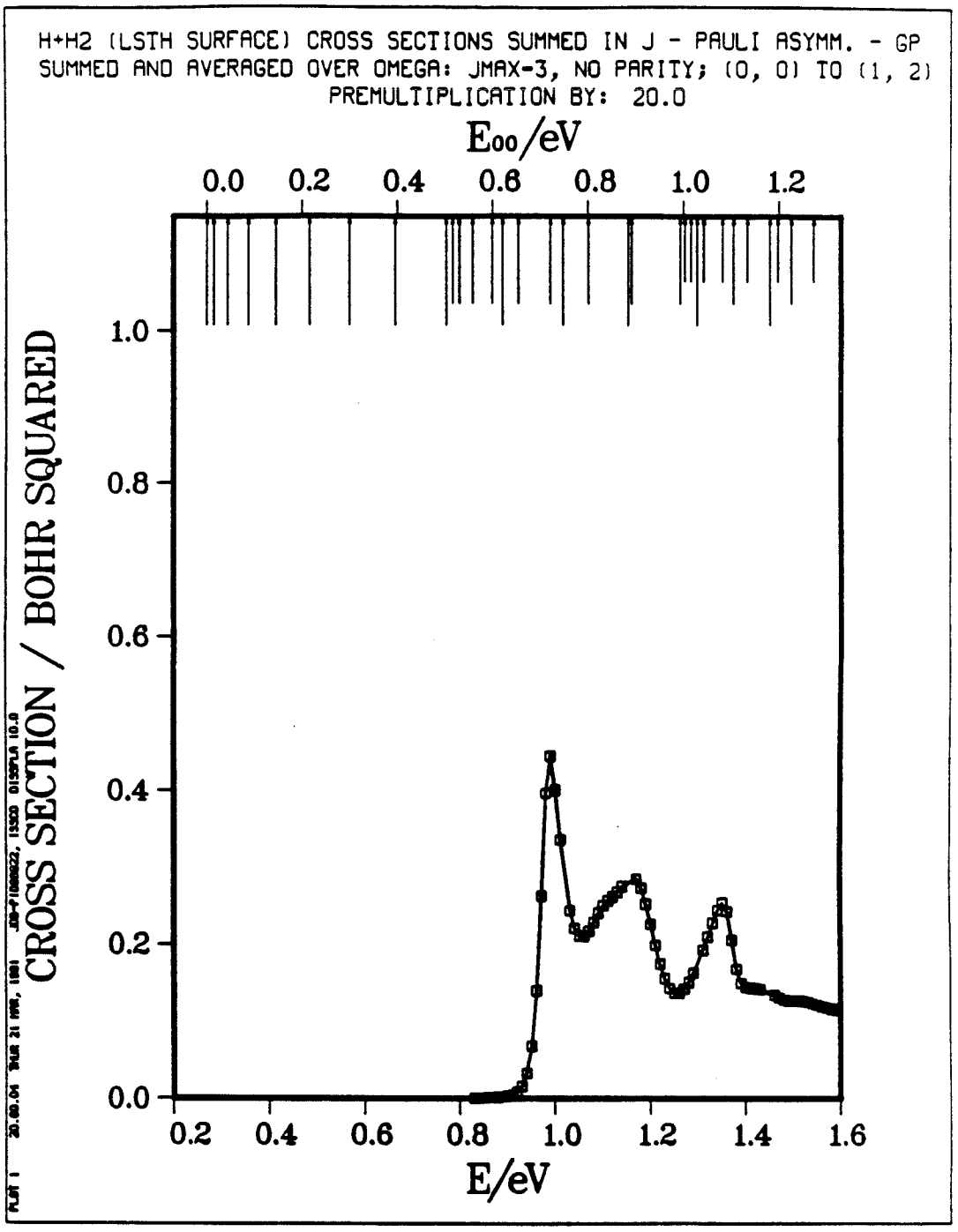
H+H2 (LSTH SURFACE) CROSS SECTIONS SUMMED IN J - PAULI ASYMM. - GP
SUMMED AND AVERAGED OVER OMEGA: JMAX-3, NO PARITY; (0, 0) TO (1, 2)
PREMULTIPLICATION BY: 20.0
E00/eV
0.0
0.2
0.4
0.6
0.8
1.0
1.2
CROSS SECTION / BOHR SQUARED
1.0
0.8
0.6
0.4
0.2
0.0
0.2
0.4
0.6
0.8
1.0
1.2
1.4
1.6
E/eV

Fig. 7.44b

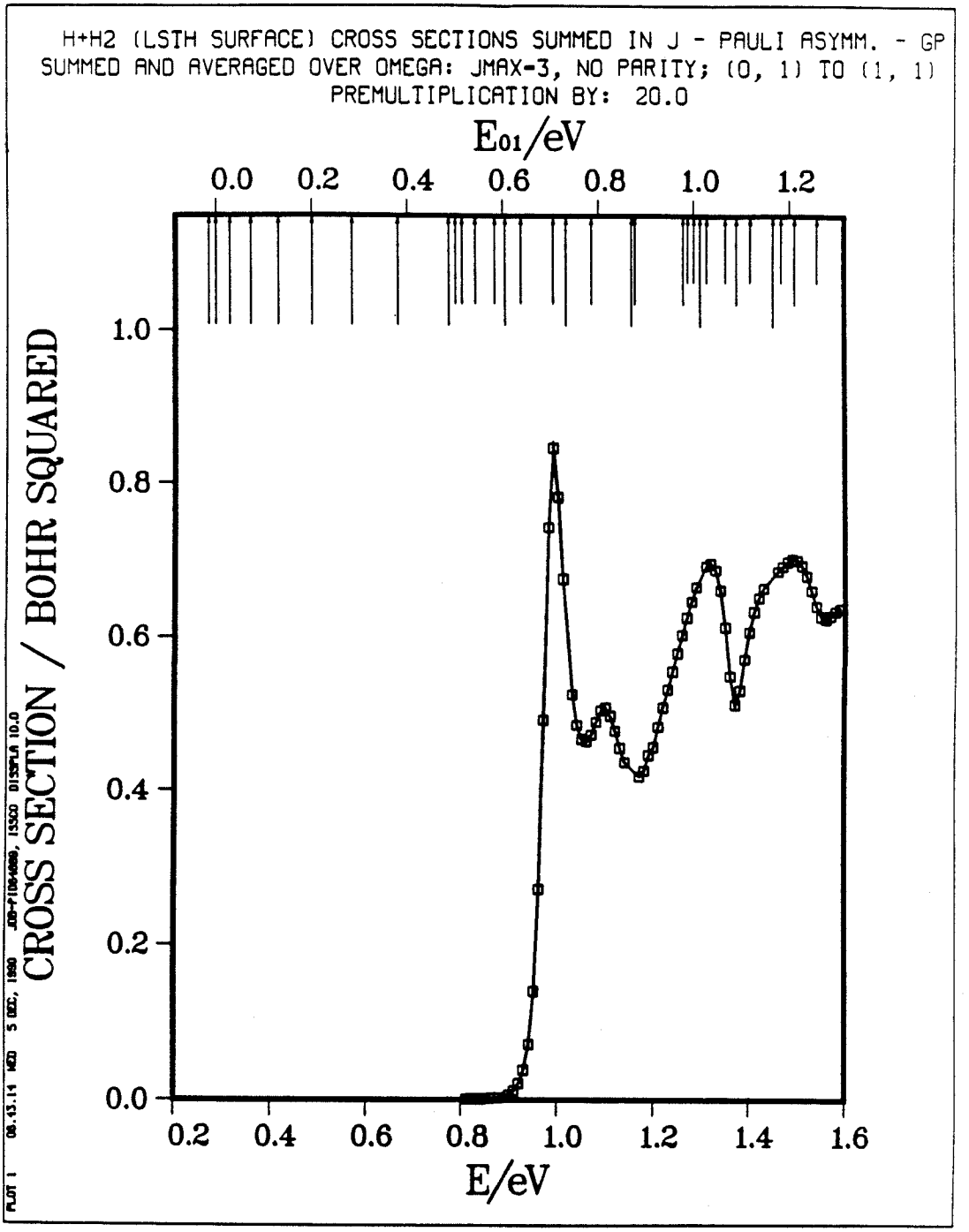
H+H2 (LSTH SURFACE) CROSS SECTIONS SUMMED IN J - PAULI ASYMM. - GP
SUMMED AND AVERAGED OVER OMEGA: JMAX-3, NO PARITY; (0, 1) TO (1, 1)
PREMULTIPLICATION BY: 20.0
E01/eV
0.0
0.2
0.4
0.6
0.8
1.0
1.2
CROSS SECTION / BOHR SQUARED
0.0
0.2
0.4
0.6
0.8
1.0
0.2
0.4
0.6
0.8
1.0
1.2
1.4
1.6
E/eV

Fig. 7.44c

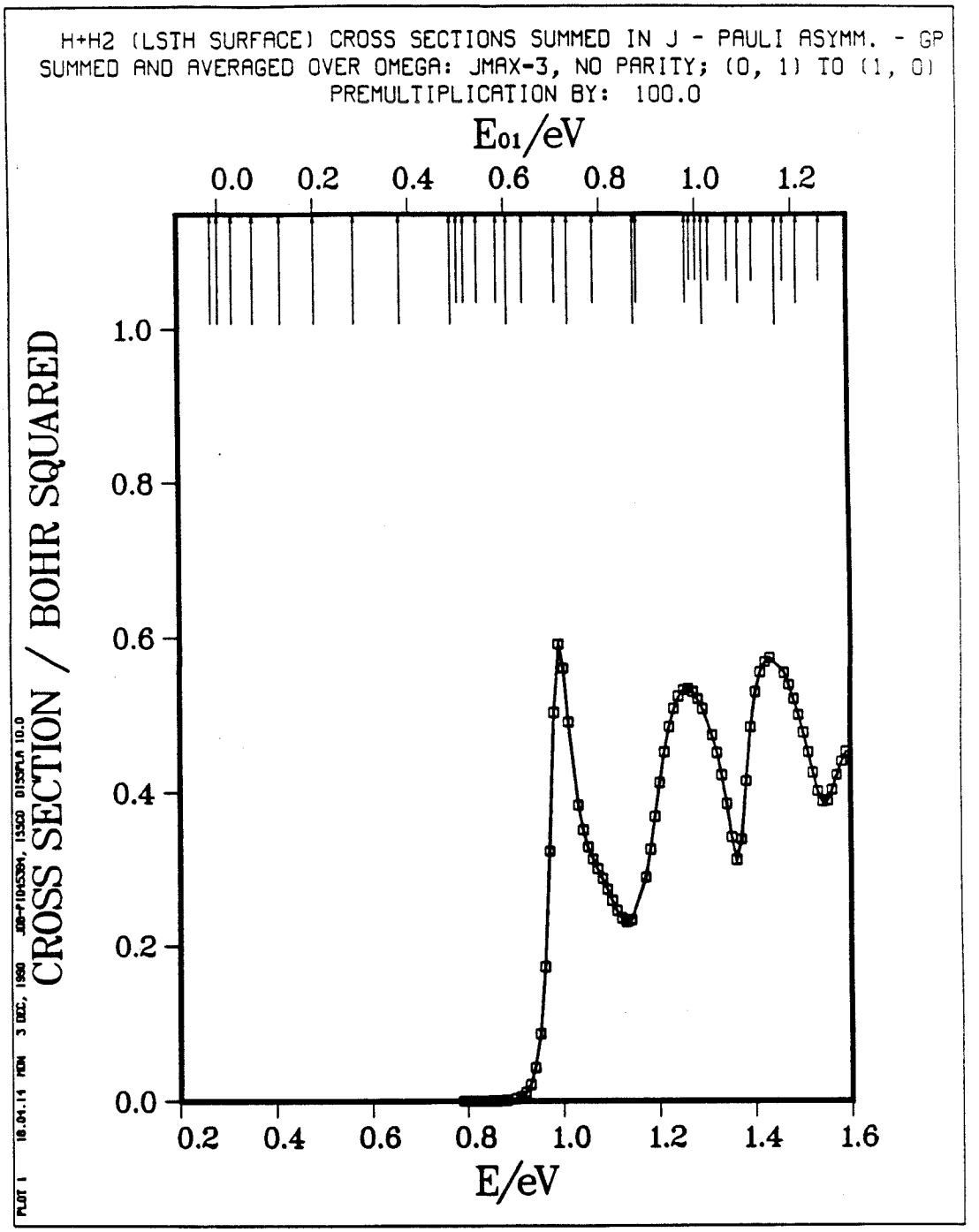
H+H2 (LSTH SURFACE) CROSS SECTIONS SUMMED IN J - PAULI ASYMM. - GP
SUMMED AND AVERAGED OVER OMEGA: JMAX=3, NO PARITY; (0, 1) TO (1, 0)
PREMULTIPLICATION BY: 100.0
E01/eV
0.0
0.2
0.4
0.6
0.8
1.0
1.2
CROSS SECTION / BOHR SQUARED
0.0
0.2
0.4
0.6
0.8
1.0
0.2
0.4
0.6
0.8
1.0
1.2
1.4
1.6
E/eV

Fig. 7.44d

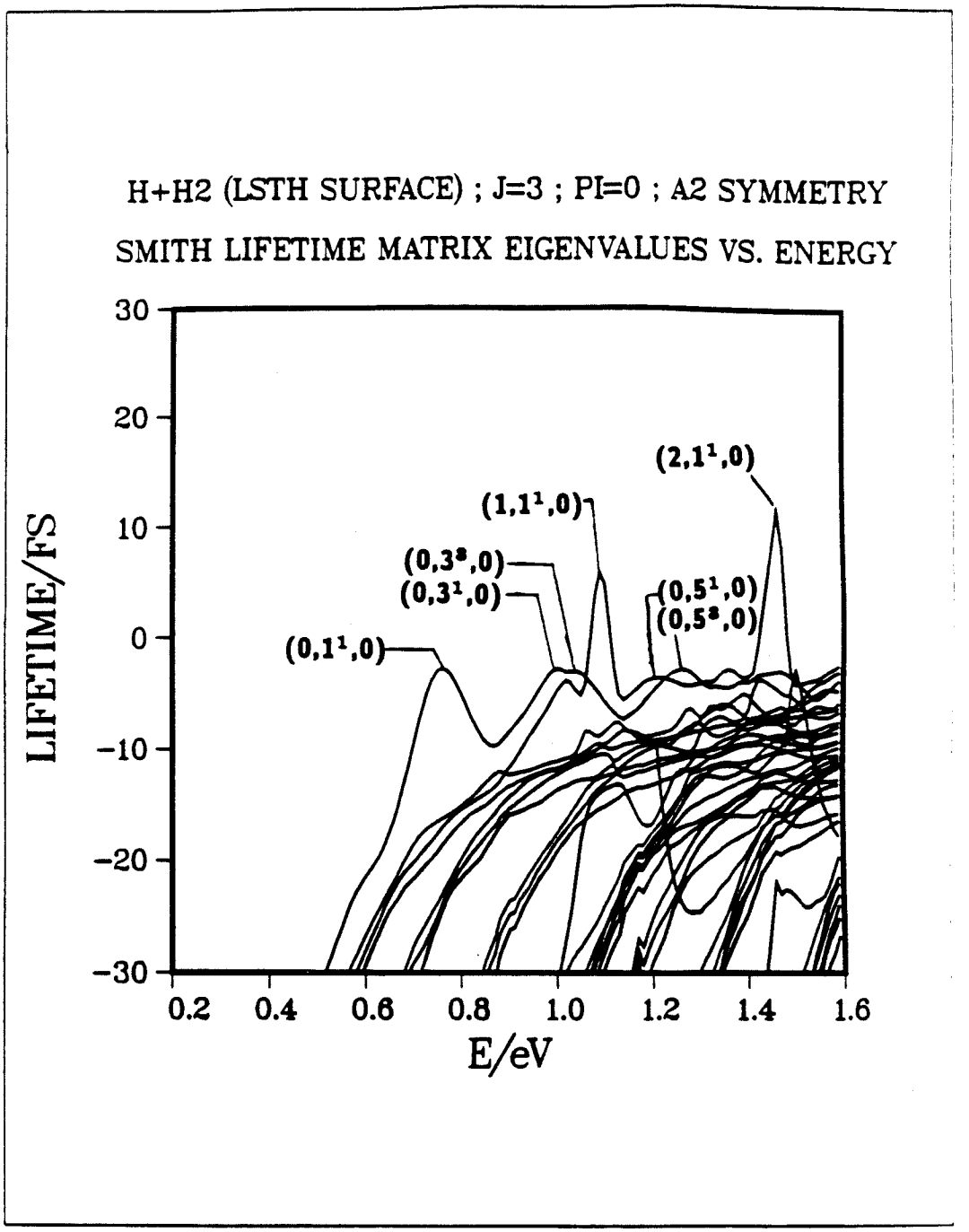
H+H2 (LSTH SURFACE) ; J=3 ; PI=0 ; A2 SYMMETRY
SMITH LIFETIME MATRIX EIGENVALUES VS. ENERGY
LIFETIME/FS
30
20
10
0
-10
-20
-30
0.2
0.4
0.6
0.8
1.0
1.2
1.4
1.6
E/eV
(2,1¹,0)
(1,1¹,0)
(0,3³,0)
(0,3¹,0)
(0,5¹,0)
(0,5³,0)
(0,1¹,0)

Fig. 7.45a

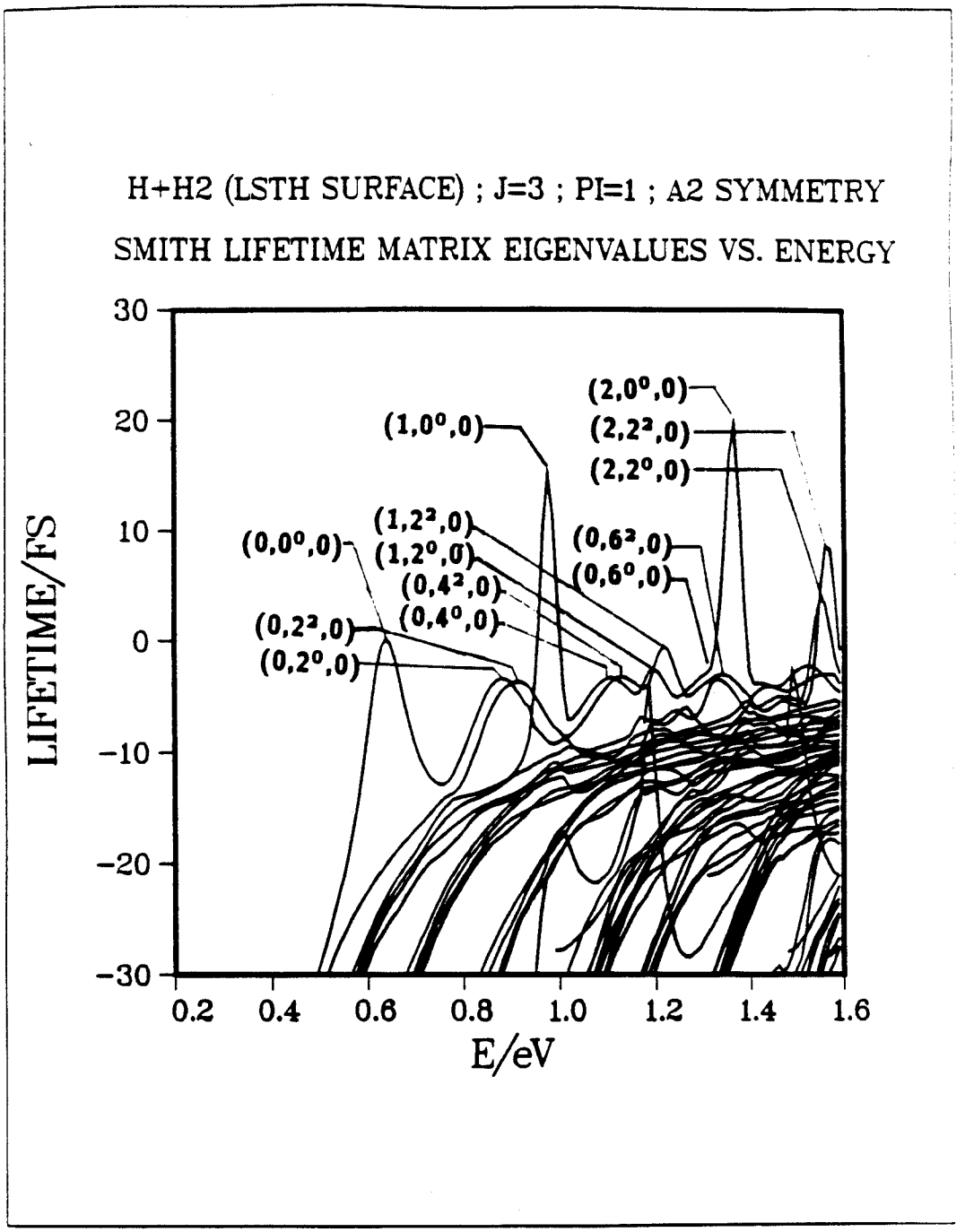
H+H2 (LSTH SURFACE) ; J=3 ; PI=1 ; A2 SYMMETRY
SMITH LIFETIME MATRIX EIGENVALUES VS. ENERGY
LIFETIME/FS
E/eV
30
20
10
0
-10
-20
-30
0.2
0.4
0.6
0.8
1.0
1.2
1.4
1.6
(2,0⁰,0)
(1,0⁰,0)
(2,2²,0)
(2,2⁰,0)
(1,2²,0)
(0,0⁰,0)
(1,2⁰,0)
(0,6²,0)
(0,6⁰,0)
(0,4²,0)
(0,4⁰,0)
(0,2²,0)
(0,2⁰,0)

Fig. 7.45b

Appendix A. Irreducible Representation Asymptotic Forms

Application of the projection operators to equation (3.1.1) yields the following result:

$$\hat{P}^{\Gamma}_{kk}\Psi^{\lambda' v'_{\lambda'} j'_{\lambda'} m'_{\lambda'}}_{\bar{\lambda}} \underset{R_{\bar{\lambda}}\to\infty}{\sim} \sum_{\lambda}\sum_{v_\lambda j_\lambda m_\lambda}\sum_{\lambda''} c^{\Gamma_k}_{\tau_\lambda \lambda'' j_\lambda}\left[e^{i\mathbf{k}_{\lambda v_\lambda j_\lambda}\cdot\mathbf{R}_{\lambda''}}\delta^{\lambda' v'_{\lambda'} j'_{\lambda'} m'_{\lambda'}}_{\lambda v_\lambda j_\lambda m_\lambda} + \hat{f}^{\lambda' v'_{\lambda'} j'_{\lambda'} m'_{\lambda'}}_{\lambda v_\lambda j_\lambda m_\lambda}(\theta_{\lambda''},\phi_{\lambda''})\frac{e^{ik_{\lambda v_\lambda j_\lambda} R_{\lambda''}}}{R_{\lambda''}}\right]\varphi^{\mathrm{sf}}_{\lambda v_\lambda j_\lambda m_\lambda}(\mathbf{r}_{\lambda''}) \tag{A.1}$$

where we will temporarily use τ_λ to denote the value of τ associated with the arrangement channel λ. (We will continue to use τ to represent an arbitrary type of channel.) Since the asymptotic diatom in all channels of type τ_λ are the same, we replace the λ label with τ_λ where appropriate (and likewise λ' with $\tau_{\lambda'}$) to get the expression

$$\hat{P}^{\Gamma}_{kk}\Psi^{\lambda' v'_{\tau_{\lambda'}} j'_{\tau_{\lambda'}} m'_{\tau_{\lambda'}}}_{\bar{\lambda}} \underset{R_{\bar{\lambda}}\to\infty}{\sim} \sum_{\lambda}\sum_{v_{\tau_\lambda} j_{\tau_\lambda} m_{\tau_\lambda}}\sum_{\lambda''} c^{\Gamma_k}_{\tau_\lambda \lambda'' j_{\tau_\lambda}}\left[e^{i\mathbf{k}_{\tau_\lambda v_{\tau_\lambda} j_{\tau_\lambda}}\cdot\mathbf{R}_{\lambda''}}\delta^{\lambda' v'_{\tau_{\lambda'}} j'_{\tau_{\lambda'}} m'_{\tau_{\lambda'}}}_{\lambda v_{\tau_\lambda} j_{\tau_\lambda} m_{\tau_\lambda}} + \hat{f}^{\lambda' v'_{\tau_{\lambda'}} j'_{\tau_{\lambda'}} m'_{\tau_{\lambda'}}}_{\lambda v_{\tau_\lambda} j_{\tau_\lambda} m_{\tau_\lambda}}(\theta_{\lambda''},\phi_{\lambda''})\frac{e^{ik_{\tau_\lambda v_{\tau_\lambda} j_{\tau_\lambda}} R_{\lambda''}}}{R_{\lambda''}}\right]\varphi^{\mathrm{sf}}_{\tau_\lambda v_{\tau_\lambda} j_{\tau_\lambda} m_{\tau_\lambda}}(\mathbf{r}_{\lambda''}) \tag{A.2}$$

The final form we want for the result involves a sum over τ replacing the sum over λ (followed by replacement of λ'' by λ). For the incoming wave this is simple to acheive; the sum over λ is completed, which replaces all instances of λ with λ', and then a sum over τ is added along with a term $\delta^{\tau_{\lambda'}}_{\tau}$ to yield

$$\sum_{\lambda}\sum_{v_{\tau_\lambda} j_{\tau_\lambda} m_{\tau_\lambda}}\sum_{\lambda''} c^{\Gamma_k}_{\tau_\lambda \lambda'' j_{\tau_\lambda}} e^{i\mathbf{k}_{\tau_\lambda v_{\tau_\lambda} j_{\tau_\lambda}}\cdot\mathbf{R}_{\lambda''}}\delta^{\lambda' v'_{\tau_{\lambda'}} j'_{\tau_{\lambda'}} m'_{\tau_{\lambda'}}}_{\lambda v_{\tau_\lambda} j_{\tau_\lambda} m_{\tau_\lambda}} = \sum_{\tau}\sum_{v_\tau j_\tau m_\tau}\sum_{\lambda''} c^{\Gamma_k}_{\tau \lambda'' j_\tau} e^{i\mathbf{k}_{\tau v_\tau j_\tau}\cdot\mathbf{R}_{\lambda''}}\delta^{\tau_{\lambda'} v'_{\tau_{\lambda'}} j'_{\tau_{\lambda'}} m'_{\tau_{\lambda'}}}_{\tau v_\tau j_\tau m_\tau} \tag{A.3}$$

The justification for the second term is more difficult, and will be done for each permutation group seperately.

In the case of P_1 symmetry (or an ABC system), the terms $c^{\Gamma_k}_{\tau_\lambda \lambda'' j_{\tau_\lambda}}$ are zero unless λ'' and τ_λ refer to the same arrangement channel, *i.e.*, $\lambda'' = \alpha$ and $\tau_\lambda = \mathrm{A}$

or $\lambda'' = \beta$ and $\tau_\lambda = \mathrm{B}$ or $\lambda'' = \gamma$ and $\tau_\lambda = \mathrm{C}$, in which case the coefficient term is 1. Therefore, we can write

$$P_1 : \quad \begin{aligned} &\sum_{\lambda} \sum_{v_{\tau_\lambda} j_{\tau_\lambda} m_{\tau_\lambda}} \sum_{\lambda''} c^{\Gamma_k}_{\tau_\lambda \lambda'' j_{\tau_\lambda}} \hat{f}^{\lambda' v'_{\tau_{\lambda'}} j'_{\tau_{\lambda'}} m'_{\tau_{\lambda'}}}_{\lambda v_{\tau_\lambda} j_{\tau_\lambda} m_{\tau_\lambda}} (\theta_{\lambda''}, \phi_{\lambda''}) \times \\ &\qquad \frac{e^{i k_{\tau_\lambda v_{\tau_\lambda} j_{\tau_\lambda}} R_{\lambda''}}}{R_{\lambda''}} \varphi^{\mathrm{sf}}_{\tau_\lambda v_{\tau_\lambda} j_{\tau_\lambda} m_{\tau_\lambda}} (\mathbf{r}_{\lambda''}) \\ &= \sum_{\lambda} \sum_{v_{\tau_\lambda} j_{\tau_\lambda} m_{\tau_\lambda}} \hat{f}^{\lambda' v'_{\tau_{\lambda'}} j'_{\tau_{\lambda'}} m'_{\tau_{\lambda'}}}_{\lambda v_{\tau_\lambda} j_{\tau_\lambda} m_{\tau_\lambda}} (\theta_\lambda, \phi_\lambda) \times \\ &\qquad \frac{e^{i k_{\tau_\lambda v_{\tau_\lambda} j_{\tau_\lambda}} R_\lambda}}{R_\lambda} \varphi^{\mathrm{sf}}_{\tau_\lambda v_{\tau_\lambda} j_{\tau_\lambda} m_{\tau_\lambda}} (\mathbf{r}_\lambda) \end{aligned} \tag{A.4}$$

Multiplication of each term in the sum over λ on the right side of this equation by $c^{\Gamma_k}_{\tau \lambda j_\tau}$ and summing over τ leaves the value of the expression unchanged, due to the form of these coefficients. This yields

$$P_1 : \quad \begin{aligned} &\sum_{\lambda} \sum_{v_{\tau_\lambda} j_{\tau_\lambda} m_{\tau_\lambda}} \sum_{\lambda''} c^{\Gamma_k}_{\tau_\lambda \lambda'' j_{\tau_\lambda}} \hat{f}^{\lambda' v'_{\tau_{\lambda'}} j'_{\tau_{\lambda'}} m'_{\tau_{\lambda'}}}_{\lambda v_{\tau_\lambda} j_{\tau_\lambda} m_{\tau_\lambda}} (\theta_{\lambda''}, \phi_{\lambda''}) \times \\ &\qquad \frac{e^{i k_{\tau_\lambda v_{\tau_\lambda} j_{\tau_\lambda}} R_{\lambda''}}}{R_{\lambda''}} \varphi^{\mathrm{sf}}_{\tau_\lambda v_{\tau_\lambda} j_{\tau_\lambda} m_{\tau_\lambda}} (\mathbf{r}_{\lambda''}) \\ &= \sum_{\tau} \sum_{\lambda} \sum_{v_\tau j_\tau m_\tau} \hat{f}^{\lambda' v'_{\tau_{\lambda'}} j'_{\tau_{\lambda'}} m'_{\tau_{\lambda'}}}_{\lambda v_\tau j_\tau m_\tau} (\theta_\lambda, \phi_\lambda) \frac{e^{i k_\tau R_\lambda}}{R_\lambda} \varphi^{\mathrm{sf}}_{\tau m_\tau} (\mathbf{r}_\lambda) \end{aligned} \tag{A.5}$$

For the P_3 symmetry case, all arrangement channels have the same value of τ; consequently, we may write the second term of equation (A.2) as

$$P_3 : \quad \begin{aligned} &\sum_{\lambda} \sum_{v_{\tau_\lambda} j_{\tau_\lambda} m_{\tau_\lambda}} \sum_{\lambda''} c^{\Gamma_k}_{\tau_\lambda \lambda'' j_{\tau_\lambda}} \hat{f}^{\lambda' v'_{\tau_{\lambda'}} j'_{\tau_{\lambda'}} m'_{\tau_{\lambda'}}}_{\lambda v_{\tau_\lambda} j_{\tau_\lambda} m_{\tau_\lambda}} (\theta_{\lambda''}, \phi_{\lambda''}) \times \\ &\qquad \frac{e^{i k_{\tau_\lambda v_{\tau_\lambda} j_{\tau_\lambda}} R_{\lambda''}}}{R_{\lambda''}} \varphi^{\mathrm{sf}}_{\tau_\lambda v_{\tau_\lambda} j_{\tau_\lambda} m_{\tau_\lambda}} (\mathbf{r}_{\lambda''}) \\ &= \sum_{\lambda} \sum_{vjm} \sum_{\lambda''} c^{\Gamma_k}_{\tau \lambda'' j} \hat{f}^{\lambda' v' j' m'}_{\lambda v j m} (\theta_{\lambda''}, \phi_{\lambda''}) \frac{e^{i k_{\tau v j} R_{\lambda''}}}{R_{\lambda''}} \varphi^{\mathrm{sf}}_{\tau v j m} (\mathbf{r}_{\lambda''}) \end{aligned} \tag{A.6}$$

Since the only term that depends on λ is the scattering amplitude, we can take that sum into a new expression; we can also freely add a sum over τ since it takes only

one value. We then get

$$P_3: \quad \sum_{\lambda} \sum_{v_{\tau_\lambda} j_{\tau_\lambda} m_{\tau_\lambda}} \sum_{\lambda''} c^{\Gamma_k}_{\tau_\lambda \lambda'' j_{\tau_\lambda}} \hat{f}^{\lambda' v'_{\tau_{\lambda'}} j'_{\tau_{\lambda'}} m'_{\tau_{\lambda'}}}_{\lambda v_{\tau_\lambda} j_{\tau_\lambda} m_{\tau_\lambda}} (\theta_{\lambda''}, \phi_{\lambda''}) \times \frac{e^{ik_{\tau_\lambda v_{\tau_\lambda} j_{\tau_\lambda}} R_{\lambda''}}}{R_{\lambda''}} \varphi^{\mathrm{sf}}_{\tau_\lambda v_{\tau_\lambda} j_{\tau_\lambda} m_{\tau_\lambda}} (\mathbf{r}_{\lambda''})$$

$$= \sum_{\tau} \sum_{vjm} \sum_{\lambda''} c^{\Gamma_k}_{\tau \lambda'' j} \left(\sum_{\lambda} \hat{f}^{\lambda' v' j' m'}_{\lambda v j m} (\theta_{\lambda''}, \phi_{\lambda''}) \right) \frac{e^{ik_{\tau v j} R_{\lambda''}}}{R_{\lambda''}} \varphi^{\mathrm{sf}}_{\tau v j m} (\mathbf{r}_{\lambda''}) \tag{A.6}$$

The P_2 case (for an AB_2 system) requires a combination of the above arguments for the P_1 and P_3 cases. We begin by seperation into the two different τ values, by explicitly substituting the channel indices for λ:

$$\begin{aligned} P_2: \quad & \sum_{\lambda} \sum_{v_{\tau_\lambda} j_{\tau_\lambda} m_{\tau_\lambda}} \sum_{\lambda''} c^{\Gamma_k}_{\tau_\lambda \lambda'' j_{\tau_\lambda}} \hat{f}^{\lambda' v'_{\tau_{\lambda'}} j'_{\tau_{\lambda'}} m'_{\tau_{\lambda'}}}_{\lambda v_{\tau_\lambda} j_{\tau_\lambda} m_{\tau_\lambda}} (\theta_{\lambda''}, \phi_{\lambda''}) \times \\ & \frac{e^{ik_{\tau_\lambda v_{\tau_\lambda} j_{\tau_\lambda}} R_{\lambda''}}}{R_{\lambda''}} \varphi^{\mathrm{sf}}_{\tau_\lambda v_{\tau_\lambda} j_{\tau_\lambda} m_{\tau_\lambda}} (\mathbf{r}_{\lambda''}) \\ & = \sum_{v_A j_A m_A} \sum_{\lambda''} c^{\Gamma_k}_{A \lambda'' j_A} \hat{f}^{\lambda' v'_{\tau_{\lambda'}} j'_{\tau_{\lambda'}} m'_{\tau_{\lambda'}}}_{\alpha v_A j_A m_A} (\theta_{\lambda''}, \phi_{\lambda''}) \times \\ & \frac{e^{ik_{A v_A j_A} R_{\lambda''}}}{R_{\lambda''}} \varphi^{\mathrm{sf}}_{A v_A j_A m_A} (\mathbf{r}_{\lambda''}) \\ & + \sum_{v_B j_B m_B} \sum_{\lambda''} c^{\Gamma_k}_{B \lambda'' j_B} \left(\hat{f}^{\lambda' v'_{\tau_{\lambda'}} j'_{\tau_{\lambda'}} m'_{\tau_{\lambda'}}}_{\beta v_B j_B m_B} (\theta_{\lambda''}, \phi_{\lambda''}) \right. \\ & \left. + \hat{f}^{\lambda' v'_{\tau_{\lambda'}} j'_{\tau_{\lambda'}} m'_{\tau_{\lambda'}}}_{\gamma v_B j_B m_B} (\theta_{\lambda''}, \phi_{\lambda''}) \right) \times \\ & \frac{e^{ik_{B v_B j_B} R_{\lambda''}}}{R_{\lambda''}} \varphi^{\mathrm{sf}}_{B v_B j_B m_B} (\mathbf{r}_{\lambda''}) \end{aligned} \tag{A.7}$$

In the first of the terms on the right side, the only nonzero term is for $\lambda'' = \alpha$, and in the second of these terms, $\lambda'' = \alpha$ is the only term which is explicitly zero. If we define

$$\hat{g}^{\lambda' v'_{\tau_{\lambda'}} j'_{\tau_{\lambda'}} m'_{\tau_{\lambda'}}}_{\tau v_\tau j_\tau m_\tau} (\theta_{\lambda''}, \phi_{\lambda''}) = \begin{cases} \hat{f}^{\lambda' v'_{\tau_{\lambda'}} j'_{\tau_{\lambda'}} m'_{\tau_{\lambda'}}}_{\alpha v_A j_A m_A} (\theta_{\lambda''}, \phi_{\lambda''}) & \tau = \mathrm{A} \\ \hat{f}^{\lambda' v'_{\tau_{\lambda'}} j'_{\tau_{\lambda'}} m'_{\tau_{\lambda'}}}_{\beta v_B j_B m_B} (\theta_{\lambda''}, \phi_{\lambda''}) + \hat{f}^{\lambda' v'_{\tau_{\lambda'}} j'_{\tau_{\lambda'}} m'_{\tau_{\lambda'}}}_{\gamma v_B j_B m_B} (\theta_{\lambda''}, \phi_{\lambda''}) & \tau = \mathrm{B} \end{cases} \tag{A.8}$$

we can rewrite $(A.7)$ as

$$P_2: \quad \begin{aligned} &\sum_{\lambda} \sum_{v_{\tau_\lambda} j_{\tau_\lambda} m_{\tau_\lambda}} \sum_{\lambda''} c^{\Gamma_k}_{\tau_\lambda \lambda'' j_{\tau_\lambda}} \hat{f}^{\lambda' v'_{\tau_{\lambda'}} j'_{\tau_{\lambda'}} m'_{\tau_{\lambda'}}}_{\lambda v_{\tau_\lambda} j_{\tau_\lambda} m_{\tau_\lambda}} (\theta_{\lambda''}, \phi_{\lambda''}) \times \\ &\qquad \frac{e^{ik_{\tau_\lambda} v_{\tau_\lambda} j_{\tau_\lambda} R_{\lambda''}}}{R_{\lambda''}} \varphi^{\mathrm{sf}}_{\tau_\lambda v_{\tau_\lambda} j_{\tau_\lambda} m_{\tau_\lambda}} (\mathbf{r}_{\lambda''}) \\ &= \sum_{\tau} \sum_{v_\tau j_\tau m_\tau} \sum_{\lambda''} c^{\Gamma_k}_{\tau \lambda'' j_\tau} \hat{g}^{\lambda' v'_{\tau_{\lambda'}} j'_{\tau_{\lambda'}} m'_{\tau_{\lambda'}}}_{\tau v_\tau j_\tau m_\tau} (\theta_{\lambda''}, \phi_{\lambda''}) \times \\ &\qquad \frac{e^{ik_{\vec{\tau}} R_{\lambda''}}}{R_{\lambda''}} \varphi^{\mathrm{sf}}_{\vec{\tau} m_\tau} (\mathbf{r}_{\lambda''}) \end{aligned} \tag{A.9}$$

Definitions similar to that of $(A.8)$ may be made in the P_1 and P_3 cases, in which case the overall form of the equation for the Γ irreducible representation wavefunction, obtained by application of the projection operators to equation (3.1.1), can be written as

$$\begin{aligned} \hat{P}^{\Gamma}_{kk} \Psi^{\lambda' v'_{\lambda'} j'_{\lambda'} m'_{\lambda'}}_{\bar{\lambda}} \underset{R_{\bar{\lambda}} \to \infty}{\sim} &\sum_{\tau} \sum_{v_\tau j_\tau m_\tau} \sum_{\lambda''} c^{\Gamma_k}_{\tau \lambda'' j_\tau} \left[e^{i\mathbf{k}_{\vec{\tau}} \cdot \mathbf{R}_{\lambda''}} \delta^{\tau' v'_{\tau'} j'_{\tau'} m'_{\tau'}}_{\tau v_\tau j_\tau m_\tau} \right. \\ &\left. + \hat{g}^{\lambda' v'_{\tau'} j'_{\tau'} m'_{\tau'}}_{\tau v_\tau j_\tau m_\tau} (\theta_{\lambda''}, \phi_{\lambda''}) \frac{e^{ik_{\vec{\tau}} R_{\lambda''}}}{R_{\lambda''}} \right] \varphi^{\mathrm{sf}}_{\vec{\tau} m_\lambda} (\mathbf{r}_{\lambda''}) \end{aligned} \tag{A.10}$$

By identification of $\tau_{\lambda'}$ with τ' and use of the symmetry properties for the scattering amplitudes given in the main text, equation (4.1.1) for the space-fixed representation may be derived. A brief examination of equation (3.1.3) will show that the same logic applies to the derivation of (4.1.2) for the helicity amplitudes.

Appendix B - Derivation of the Spin Statistics Equations

The unsymmetrized spin wavefunction for the nuclei can be represented as a product of the spin wavefunctions for each nucleus: $|s_1 m_1\rangle|s_2 m_2\rangle|s_3 m_3\rangle$. This wavefunction is an eigenfunction of the operators $\hat{s}_i^2$ and $\hat{s}_{Zi}$ $(i = 1, 2, 3)$:

$$\begin{aligned} \hat{s}_i^2|s_1 m_1\rangle|s_2 m_2\rangle|s_3 m_3\rangle &= \hbar^2 s_i(s_i+1)|s_1 m_1\rangle|s_2 m_2\rangle|s_3 m_3\rangle \\ \hat{s}_{Zi}|s_1 m_1\rangle|s_2 m_2\rangle|s_3 m_3\rangle &= \hbar m_i|s_1 m_1\rangle|s_2 m_2\rangle|s_3 m_3\rangle \end{aligned} \qquad (B.1)$$

When two or all three of the nuclei are identical (P_2 or P_3 symmetry, respectively), the indistinguishable nuclei must have the same spin, and symmetrized wavefunctions involving the permutation of the identical nuclei can be generated by application of the projection operators for the group.

In the case of P_2 symmetry, we can define a notation which implicitly takes account of the identical spins of the two indistinguishable particles (which will be assumed to be those labelled 2 and 3):

$$|s_1 m_1 s m_2 m_3\rangle = |s_1 m_1\rangle|s m_2\rangle|s m_3\rangle \qquad (B.2)$$

where we have set $s_2 = s_3 = s$. We can also write the wavefunction which is an eigenfunction of the operators for the total spin angular momentum $\hat{S}^2$ and projection of this angular momentum on the space-fixed **Z** axis $\hat{S}_Z$ for the identical particles:

$$|s_1 m_1 S M_S\rangle = |s_1 m_1\rangle \sum_m C(ssS; m, M_S - m, M_S)|s m\rangle|s(M_S - m)\rangle \qquad (B.3)$$

where $C(ssS; m, M_S - m, M_S)$ is a Clebsch-Gordon coefficient.[81] The functions so defined are also eigenfunctions of the projection operators for the P_2 group, since permutation of the two identical particles either leaves the function unchanged or

changes its sign:

$$\begin{aligned}\hat{P}_{23}|s_1 m_1 S M_S\rangle &= |s_1 m_1\rangle \sum_m C(ssS; m, M_S - m, M_S)|s(M_S - m)\rangle|sm\rangle \\ &= (-1)^{2s+S}|s_1 m_1\rangle \sum_m C(ssS; M_S - m, m, M_S)|sM_S - m\rangle|sm\rangle \\ &= (-1)^{2s+S}|s_1 m_1\rangle \sum_{m'} C(ssS; m', M_S - m', M_S)|sm'\rangle|s(M_S - m')\rangle \\ &= (-1)^{2s+S}|s_1 m_1 S M_S\rangle\end{aligned} \tag{B.4}$$

in which $m' = M_S - m$ and we have used the Clebsch-Gordon symmetry property[81]

$$C(j_1 j_2 J; m_1 m_2 M) = (-1)^{j_1+j_2-J} C(j_2 j_1 J; m_2 m_1 M) \tag{B.5}$$

Functions for which $2s + S$ is even will be symmetric with respect to this permutation and thus will have A' symmetry, and those for which $2s + S$ is odd will be antisymmetric and will have A'' symmetry. As noted in the text, the irreducible representation of the wavefunction is independent of M_S.

If the two identical nuclei have integer spin (bosons), then the quantity $2s$ is even; if they have half-odd integer spin (fermions), this quantity is odd. For bosons, the total nuclear wavefunction (spatial times spin) must have A' symmetry, and therefore the A' spatial wavefunction has only spin states with even S associated to it (since $(-1)^{S+2s} = (-1)^S$ in this case), and the A'' spatial wavefunction has only the odd S states. For fermions, the total nuclear wavefunction must have A'' symmetry; since in this case $(-1)^{2s+S} = -(-1)^S$, the same rules apply as for bosons.

To determine the numbers of states with even or odd values of S, we will examine seperately the cases of bosons and fermions. The maximum value of S is $2s$, and there are $2S + 1$ M_S states associated with each value of S, for a total of $(2s + 1)^2$ states. For integer s, the number of states for even and odd S are:

$$\begin{aligned}N_S^e &= 1 + 5 + 9 + \ldots + 4s + 1 = \frac{1}{2}(2s + 1)(2s + 2) \\ N_S^o &= 3 + 7 + 11 + \ldots + 4s - 1 = \frac{1}{2}(2s)(2s + 1)\end{aligned} \qquad s \text{ integer} \tag{B.6}$$

while for half-odd integer s the number of states for even and odd S are

$$\begin{aligned} N_S^e &= 1+5+9+\ldots+4s-1 = \frac{1}{2}(2s)(2s+1) \\ N_S^o &= 3+7+11+\ldots+4s+1 = \frac{1}{2}(2s+1)(2s+2) \end{aligned} \qquad s \text{ half}-\text{odd integer}; \tag{B.7}$$

Equations $(B.6)$ and $(B.7)$ may be combined into a single statement, using the fact that the sign of $(-1)^{2s}$ differs between the two, to yield

$$\begin{aligned} N_S^e &= \frac{1}{2}(2s+1)\left(2s+1+(-1)^{2s}\right) \\ N_S^o &= \frac{1}{2}(2s+1)\left(2s+1-(-1)^{2s}\right) \end{aligned} \tag{B.8}$$

as given in the text.

For the P_3 group, the three identical nuclei must have the same spin, and we can define the simpler notation

$$|sm_1m_2m_3\rangle \equiv |sm_1\rangle|sm_2\rangle|sm_3\rangle \tag{B.9}$$

We can define a symmetrized spin wavefunction by application of the projection operators for the P_3 group to the above wavefunction:[74]

$$|sm_1m_2m_3;\Gamma_{ij}\rangle = \hat{P}_{ij}^{\Gamma}|sm_1m_2m_3\rangle = \frac{n_\Gamma}{6}\sum_R d_{ij}^{\Gamma *}(R)\hat{O}_R|sm_1m_2m_3\rangle \tag{B.10}$$

The results of this are as follows: for $m_1 = m_2 = m_3 = m$ we find that

$$|smmm;A_1\rangle = |smmm\rangle; \qquad |smmm;A_2\rangle = |smmm;E_{ij}\rangle = 0 \tag{B.11}$$

and so for each of the $2s+1$ functions of this type a single A_1 IR function exists. If however only two are equal (so that $m_1 = m' \neq m_2 = m_3 = m$) the result is

$$\begin{aligned} |sm'mm;A_1\rangle &= \frac{1}{3}\left(|sm'mm\rangle + |smm'm\rangle + |smmm'\rangle\right); \\ |sm'mm;A_2\rangle &= |sm'mm;E_{21}\rangle = |sm'mm;E_{22}\rangle = 0 \\ |sm'mm;E_{11}\rangle &= \frac{1}{3}\left(2|sm'mm\rangle - |smm'm\rangle - |smmm'\rangle\right); \\ |sm'mm;E_{12}\rangle &= \frac{1}{\sqrt{3}}\left(|smmm'\rangle - |smm'm\rangle\right). \end{aligned} \tag{B.12}$$

(We have defined the E symmetry functions to be either symmetric or antisymmetric with respect to permutation of particles 2 and 3.) There are $2s(2s+1)$ different functions of type $|sm'mm\rangle$ (with m' taking on $2s+1$ possible values and m restricted in each case to the $2s$ remaining). There are also $2s(2s+1)$ functions of type $|smm'm\rangle$ and of type $|smmm'\rangle$; however, the A_1 functions generated by $|sm'mm\rangle$, $|smm'm\rangle$ and $|smmm'\rangle$ are identical and the E functions of one of these a linear combination of the E functions of another, and so there are only $2s(2s+1)$ distinct symmetrized functions of each symmetry. Finally, for all three m_i different, we get

$$
\begin{aligned}
|sm_1m_2m_3;A_1\rangle =& \frac{1}{6}\left(|sm_1m_2m_3\rangle + |sm_2m_3m_1\rangle + |sm_3m_1m_2\rangle\right.\\
&\left. +|sm_1m_3m_2\rangle + |sm_3m_2m_1\rangle + |sm_2m_1m_3\rangle\right)\\
|sm_1m_2m_3;A_2\rangle =& \frac{1}{6}\left(|sm_1m_2m_3\rangle + |sm_2m_3m_1\rangle + |sm_3m_1m_2\rangle\right.\\
&\left. -|sm_1m_3m_2\rangle - |sm_3m_2m_1\rangle - |sm_2m_1m_3\rangle\right)\\
|sm_1m_2m_3;E_{11}\rangle =& \frac{1}{3}\left(|sm_1m_2m_3\rangle - \frac{1}{2}|sm_2m_3m_1\rangle - \frac{1}{2}|sm_3m_1m_2\rangle\right.\\
&\left. +|sm_1m_3m_2\rangle - \frac{1}{2}|sm_3m_2m_1\rangle - \frac{1}{2}|sm_2m_1m_3\rangle\right)\\
|sm_1m_2m_3;E_{21}\rangle =& \frac{1}{2\sqrt{3}}\left(|sm_3m_2m_1\rangle + |sm_2m_1m_3\rangle - |sm_2m_3m_1\rangle - |sm_3m_1m_2\rangle\right)\\
|sm_1m_2m_3;E_{12}\rangle =& \frac{1}{2\sqrt{3}}\left(|sm_3m_2m_1\rangle - |sm_2m_1m_3\rangle + |sm_2m_3m_1\rangle - |sm_3m_1m_2\rangle\right)\\
|sm_1m_2m_3;E_{22}\rangle =& \frac{1}{3}\left(|sm_1m_2m_3\rangle - \frac{1}{2}|sm_2m_3m_1\rangle - \frac{1}{2}|sm_3m_1m_2\rangle\right.\\
&\left. -|sm_1m_3m_2\rangle + \frac{1}{2}|sm_3m_2m_1\rangle + \frac{1}{2}|sm_2m_1m_3\rangle\right)
\end{aligned}
\qquad (B.13)
$$

When all three values of m_i differ there are a total of $(2s-1)(2s)(2s+1)$ different unsymmetrized states, each of which can be decomposed into one A_1, one A_2 and two E states. However, any of the six permutations of the m_i quantum numbers in the symmetrized function $|sm_1m_2m_3\rangle$ generates the same A_1 and (within a sign change) A_2 symmetrized functions, and results in taking a linear combination of the E functions generated by a different permutation; therefore the the number of

distinct symmetrized functions generated from these states is $\frac{(2s-1)(2s)(2s+1)}{6}$ A_1 and A_2 states and $\frac{(2s-1)(2s)(2s+1)}{3}$ E states.

The equations (B.10) through (B.12) along with the analysis of the number of states generated are sufficient to determine the spin weighting for the irreducible representations of P_3. We may also want to determine the spin wavefunctions which are eigenfunctions of the square of the total spin angular momentum operator for all three identical particles and the projection of this quantity onto the space-fixed **Z** axis; these operators will be called $\hat{S}^2$ and $\hat{S}_Z$, but it should be noted that they are not the same as those so named for the P_2 case, as they operate on all three particles and not just two of them. There are three equally valid expressions for these functions, depending on which two spins are first coupled in the formalism; these are

$$|ss_{12};SM_S\rangle = \sum_{m_1}\sum_{m_{12}} C(sss_{12};m_1m_2m_{12})C(s_{12}sS;m_{12}m_3M_S)|sm_1m_2m_3\rangle \qquad (B.13a)$$

$$|ss_{13};SM_S\rangle = \sum_{m_1}\sum_{m_{13}} C(sss_{13};m_1m_3m_{13})C(s_{13}sS;m_{13}m_2M_S)|sm_1m_2m_3\rangle \qquad (B.13b)$$

$$|ss_{23};SM_S\rangle = \sum_{m_2}\sum_{m_{23}} C(sss_{23};m_2m_3m_{23})C(s_{23}sS;m_{23}m_1M_S)|sm_1m_2m_3\rangle \qquad (B.13c)$$

where s_{ij} is the result of coupling the spins s_i and s_j. The functions generated by (B.13a) and those generated by (B.13b) when s_{12} in the first expression and s_{13} in the second are equal are in general not the same; however, each of these expressions yields a complete basis set for functions with quantum numbers S and M_S if all possible values of s_{ij} are included in the basis. In keeping with the convention of equations (B.11) and (B.12), we will use expression (B.13c) which couples spins 2 and 3 first.

Since the operators for the spin angular momentum and the permutation operators commute, the expression for the symmetrized spin function which is an

eigenfunction of $\hat{S}^2$ and of $\hat{S}_Z$ can be written as

$$
\begin{aligned}
|ss_{23};\Gamma_{ij}SM_S\rangle &= \hat{P}^{\Gamma}_{ij}|ss_{23};SM_S\rangle \\
&= \sum_{m_2}\sum_{m_{23}} C(sss_{23};m_2m_3m_{23})C(s_{23}sS;m_{23}m_1M_S)\hat{P}^{\Gamma}_{ij}|sm_1m_2m_3\rangle \\
&= \sum_{m_2}\sum_{m_{23}} C(sss_{23};m_2m_3m_{23})C(s_{23}sS;m_{23}m_1M_S)|sm_1m_2m_3;\Gamma_{ij}\rangle
\end{aligned}
\tag{B.14}
$$

Volume 154, number 2 CHEMICAL PHYSICS LETTERS 13 January 1989

HYPER-SPHERICAL COORDINATE REACTIVE SCATTERING USING VARIATIONAL SURFACE FUNCTIONS

Steven A. CUCCARO [1], Paul G. HIPES [2] and Aron KUPPERMANN

Arthur Amos Noyes Laboratory of Chemical Physics, Division of Chemistry and Chemical Engineering [3], *California Institute of Technology, Pasadena, CA 91125, USA*

Received 3 October 1988; in final form 11 October 1988

An efficient numerical method of calculating surface functions for accurate quantum mechanical three-dimensional reactive scattering using symmetrized hyper-spherical coordinates has been developed. This method is at least 20 times faster than the finite-element method used previously and its accuracy is demonstrated for the $H+H_2$ system.

1. Introduction

Accurate quantum solutions for three-dimensional reactive scattering for triatomic systems were first calculated in the mid 1970s for the system $H+H_2$ [1–5]. The difficulty and computational expense of these calculations has, until recently, precluded extension to higher energies and more complex systems; however, the development of more efficient algorithms coupled with increased access to supercomputers has resulted in a resurgence of activity in this field [6–17]. In particular, the use of symmetrized hyper-spherical coordinates (SHC) and local hyper-spherical surface functions (LHSF) [18,19] is a very promising approach.

The first accurate calculations of 3D reactive scattering matrices using a hyper-spherical coordinate method were recently performed on the total angular momentum $J=0$ partial wave of the $H+H_2$ system [6]. This method, applied to the PK2 potential energy surface [20], involved the calculation of sets of LHSF using a two-dimensional finite-element (FE) approach. The FE method is accurate and reliable for this system, and has been used to extend the range of energies at which the corresponding $J=0$ partial wave scattering matrices have been calculated to 1.6 eV [11]; however, extension to higher values of J and to less symmetric systems requires an excessive increase in computational effort. As a consequence, there was a need to develop a more efficient method for calculating these LHSF.

In this paper we present a new variational method for calculating LHSF. The formalism is described in section 2. Section 3 discusses the numerical parameters used and section 4 compares the results of LHSF and scattering calculations for the $J=0$ partial wave on both the PK2 and LSTH [21,22] potential energy surfaces with those of previous calculations using a finite-element method [6,11,23] to obtain the surface functions. In addition, some comparison of the $J=1$ PK2 scattering results with those of the matching method [3] are made. A summary is given in section 5.

[1] Work performed in partial fulfillment of the requirements for the Ph.D. degree in Chemistry at the California Institute of Technology.

[2] Current address: 216 Synchrotron Laboratory 206-49, California Institute of Technology, Pasadena, CA 91125, USA.

[3] Contribution No. 7865.

Volume 154, number 2 CHEMICAL PHYSICS LETTERS 13 January 1989

2. Formalism of variational surface functions

The SHC coordinate system used in this calculation has been described previously [6,11,18,19]. Let A_α, A_β, A_γ be the atoms of a triatomic system and λ, ν, κ an arbitrary permutation of α, β, γ. The λ SHC for this system are

$$\rho=(r_\lambda^2+R_\lambda^2)^{1/2},\quad \omega_\lambda=2\arctan\frac{r_\lambda}{R_\lambda},\quad \gamma_\lambda=\arccos\frac{\boldsymbol{R}_\lambda\cdot\boldsymbol{r}_\lambda}{R_\lambda r_\lambda},\qquad 0\leqslant\omega_\lambda,\gamma_\lambda\leqslant\pi\,, \tag{1}$$

where $\boldsymbol{r}_\lambda$ is the mass-scaled [24,25] internuclear vector for the diatom $A_\nu A_\kappa$ and $\boldsymbol{R}_\lambda$ the position vector of the atom A_λ with respect to the center of mass of $A_\nu A_\kappa$. The orientation of the system in space is determined by the Euler angles θ_λ, ϕ_λ (the polar angles of $\boldsymbol{R}_\lambda$ with respect to a space-fixed OZ axis), and ψ_λ (the angle between the $\boldsymbol{R}_\lambda$,$\boldsymbol{r}_\lambda$ and $\boldsymbol{R}_\lambda$,OZ half-planes). In this coordinate system the Hamiltonian is expressed as

$$\hat{H}_\lambda=-\frac{\hbar^2}{2\mu}\rho^{-5/2}\frac{\partial^2}{\partial\rho^2}\rho^{5/2}+\frac{\hat{\Lambda}^2}{2\mu\rho^2}+V(\rho,\omega_\lambda,\gamma_\lambda)+\frac{15\hbar^2}{8\mu\rho^2}\,, \tag{2}$$

in which the global reduced mass μ is defined as $[m_\lambda m_\nu m_\kappa/(m_\lambda+m_\nu+m_\kappa)]^{1/2}$. The generalized or grand canonical angular momentum operator $\hat{\Lambda}^2$ is defined by

$$\hat{\Lambda}^2=\hat{L}_\lambda^2+\frac{\hat{l}_\lambda^2}{\cos^2(\frac{1}{2}\omega_\lambda)}+\frac{\hat{j}_\lambda^2}{\sin^2(\frac{1}{2}\omega_\lambda)}\,, \tag{3}$$

where $\hat{l}_\lambda^2$ and $\hat{j}_\lambda^2$ are the angular momentum operators associated with the vectors $\boldsymbol{R}_\lambda$ and $\boldsymbol{r}_\lambda$, respectively, and

$$\hat{L}_\lambda^2=\frac{-4\hbar^2}{\sin\omega_\lambda}\left(\frac{\partial^2}{\partial\omega_\lambda^2}+1\right)\sin\omega_\lambda \tag{4}$$

is an angular momentum associated with the hyper-angle ω_λ. The term $V(\rho,\omega_\lambda,\gamma_\lambda)$ is the potential energy function of the electronically adiabatic triatomic system.

The equation that defines the LHSF $\Phi_n^{JM\Pi\Gamma}$ with associated eigenvalues $\epsilon_n^{J\Pi\Gamma}$ is

$$\left(\frac{\hat{\Lambda}^2}{2\mu\rho^2}+V(\rho,\omega_\lambda,\gamma_\lambda)\right)\Phi_n^{JM\Pi\Gamma}(\zeta_\lambda;\rho)=\epsilon_n^{J\Pi\Gamma}(\rho)\,\Phi_n^{JM\Pi\Gamma}(\zeta_\lambda;\rho)\,, \tag{5}$$

in which ζ_λ stands for the set of five hyper-spherical angles $(\omega_\lambda,\gamma_\lambda,\theta_\lambda,\phi_\lambda,\psi_\lambda)$. The indices J, M, Π, Γ are, respectively, the quantum numbers of the total angular momentum of the system, its projection on the space-fixed OZ axis, the inversion parity of the triatomic system through its center of mass, and the irreducible representation of the surface function in the permutation group of the system (P_3 for $H+H_2$). The boundary conditions for eq. (5) are the usual "well-behavedness" ones (single valuedness, continuity, non-divergence, differentiability, etc.). The index n denotes a quantum number which, in addition to J, M, Π, Γ, uniquely labels the LHSF. A set of two-dimensional surface functions $\psi_{n\Omega}^{J\Pi\Gamma}(\omega_\lambda,\gamma_\lambda;\rho)$ independent of the orientation of the system in space can be defined by expansion of the LHSF in terms of Wigner rotation matrices $D_{M\Omega}^J(\phi_\lambda,\theta_\lambda,\psi_\lambda)$ [26]:

$$\Phi_n^{JM\Pi\Gamma}(\zeta_\lambda;\rho)=\sum_{\Omega=0}^{J}\mathcal{S}_{M\Omega}^{J\Pi}(\phi_\lambda,\theta_\lambda,\psi_\lambda)\,\psi_{n\Omega}^{J\Pi\Gamma}(\omega_\lambda,\gamma_\lambda;\rho)\,, \tag{6}$$

where

$$\mathcal{S}_{M\Omega}^{J\Pi}(\phi_\lambda,\theta_\lambda,\psi_\lambda)=N_{J\Omega}[D_{M\Omega}^J(\phi_\lambda,\theta_\lambda,\psi_\lambda)+(-1)^{J+\Pi+\Omega}D_{M,-\Omega}^J(\phi_\lambda,\theta_\lambda,\psi_\lambda)]$$

and $N_{J\Omega}$ is a normalization constant. $\mathcal{S}_{M\Omega}^{J\Pi}$ is even (odd) with respect to inversion of the system through its

center of mass for $\Pi=0$ (1), and in the case of $\Omega=0$ is zero when $J+\Pi$ is odd. The boundary conditions for the $\psi^{JM\Pi\Gamma}_{n\Omega}(\omega_\lambda, \gamma_\lambda; \rho)$ which result from the "well-behavedness" of the $\Phi^{JM\Pi\Gamma}_n$ are that

$$\psi^{JM\Pi\Gamma}_{n\Omega}(\omega_\lambda, \gamma_\lambda=\{0, \pi\}; \rho)=0 \qquad \text{for } \Omega\neq 0$$

and

$$\frac{\partial}{\partial\gamma_\lambda}[\psi^{JM\Pi\Gamma}_{n\Omega}(\omega_\lambda, \gamma_\lambda; \rho)]\,|_{\gamma_\lambda=\{0,\pi\}}=0 \qquad \text{for } \Omega=0\,.$$

Furthermore, the potential function $V(\rho, \omega_\lambda, \gamma_\lambda)$ has in general extrema at $\gamma_\lambda=\{0, \pi\}$ (corresponding to collinear configurations of the system). As a result of these considerations, the $\psi^{JM\Pi\Gamma}_{n\Omega}$ can be factored as a function of ω_λ times a normalized [2] associated Legendre function $\mathscr{P}^\Omega_j(\cos\gamma_\lambda)$ in the vicinity of $\gamma_\lambda=0$ and π. This makes it both convenient and desirable (because of the presence in eq. (3) of the operator $\hat{j}^2_\lambda$) to expand these $\psi^{JM\Pi\Gamma}_{n\Omega}$ according to

$$\psi^{JM\Pi\Gamma}_{n\Omega}(\omega_\lambda, \gamma_\lambda; \rho)=\sum_{j=\Omega}^{\infty}\mathscr{P}^\Omega_j(\cos\gamma_\lambda)\,\frac{\phi^{JM\Pi\Gamma}_{nj\Omega}(\omega_\lambda; \rho)}{\sin\omega_\lambda}\,, \tag{7}$$

where the coefficients $\phi^{JM\Pi\Gamma}_{nj\Omega}(\omega_\lambda; \rho)$ are called one-dimensional surface functions. Replacement of eqs. (7) and (6) into eq. (5) leads to the equation satisfied by these functions:

$$\frac{\hbar^2}{2\mu\rho^2}\left\{\left[-4\left(\frac{\partial^2}{\partial\omega_\lambda^2}+1\right)+\frac{J(J+1)+j(j+1)-2\Omega^2}{\cos^2(\frac{1}{2}\omega_\lambda)}+\frac{j(j+1)}{\sin^2(\frac{1}{2}\omega_\lambda)}\right]\phi^{JM\Pi\Gamma}_{nj\Omega}(\omega_\lambda; \rho)\right.$$

$$\left.-\frac{\hbar^2}{\cos^2(\frac{1}{2}\omega_\lambda)}\,[\xi_+(J, \Omega)\,\xi_+(j, \Omega)\,\phi^{JM\Pi\Gamma}_{nj,\Omega+1}(\omega_\lambda; \rho)+\xi_-(J, \Omega)\,\xi_-(j, \Omega)\,\phi^{JM\Pi\Gamma}_{nj\Omega-1|}(\omega_\lambda; \rho)]\right\}$$

$$+\sum_{j=\Omega}^{\infty}V^\Omega_{jj}(\rho, \omega_\lambda)\,\phi^{JM\Pi\Gamma}_{nj\Omega}(\omega_\lambda; \rho)=\epsilon^{JM\Pi\Gamma}_n(\rho)\,\phi^{JM\Pi\Gamma}_{nj\Omega}(\omega_\lambda; \rho)\,. \tag{8}$$

The multiplicative factor $(\sin\omega_\lambda)^{-1}$ has been introduced into eq. (7) because of the form of eq. (4). The presence of this term forces the boundary conditions $\phi^{JM\Pi\Gamma}_{nj\Omega}(\omega_\lambda=\{0, \pi\}; \rho)=0$ for eq. (8). These conditions are necessary for $\psi^{JM\Pi\Gamma}_{n\Omega}$ not to diverge at $\omega_\lambda=\{0, \pi\}$ but may not be sufficient; however, in practice they have indeed sufficed for $H+H_2$, and we do not anticipate problems with other systems. In eq. (8), $\xi_\pm(i, k)=[i(i+1)-k(k\pm1)]^{1/2}$ and the term V^Ω_{jj} is given by

$$V^\Omega_{jj}(\rho, \omega_\lambda)=\int_0^\pi\mathscr{P}^\Omega_j(\cos\gamma_\lambda)\,V(\rho, \omega_\lambda, \gamma_\lambda)\,\mathscr{P}^\Omega_j(\cos\gamma_\lambda)\sin\gamma_\lambda\,\mathrm{d}\gamma_\lambda\,. \tag{9}$$

It is important to note that for eq. (8) to be valid, the functions $\phi^{JM\Pi\Gamma}_{nj\Omega}$ with $\Omega=0$ must be defined to be identically equal to zero when $J+\Pi$ is odd. The set of equations (6), (7), and (8) are equivalent to eq. (5).

The variational basis set is suggested by the expansion equation (7) and by eq. (8). We define functions $t^{J\lambda}_{vj\Omega}(\omega_\lambda; \rho)$ with associated eigenvalues $e^J_{vj\Omega}(\rho)$ which satisfy the latter after the Ω and j coupling is removed:

$$\left[-\frac{2\hbar^2}{\mu\rho^2}\left(\frac{\partial}{\partial\omega_\lambda^2}+1-\frac{J(J+1)+j(j+1)-2\Omega^2}{4\cos^2(\frac{1}{2}\omega_\lambda)}-\frac{j(j+1)}{4\sin^2(\frac{1}{2}\omega_\lambda)}\right)+V^\Omega_{jj}\right]t^{J\lambda}_{vj\Omega}=e^J_{vj\Omega}\,t^{J\lambda}_{vj\Omega}\,. \tag{10}$$

These functions are required to satisfy the same boundary conditions as the $\phi^{JM\Pi\Gamma}_{nj\Omega}$: $t^{J\lambda}_{vj\Omega}(0; \rho)=t^{J\lambda}_{vj\Omega}(\pi, \rho)=0$. We now define a five-dimensional variational basis set by

$$F^{JM\Pi}_{\lambda vj\Omega}(\zeta_\lambda; \rho)=\mathscr{D}^{J\Pi}_{M\Omega}(\phi_\lambda, \theta_\lambda, \psi_\lambda)\,\mathscr{P}^\Omega_j(\cos\gamma_\lambda)\,f^{J\lambda}_{vj\Omega}(\omega_\lambda; \rho)\,, \tag{11}$$

where for notational convenience we have defined $f^{J\lambda}_{vj\Omega}(\omega_\lambda; \rho)=t^{J\lambda}_{vj\Omega}(\omega_\lambda; \rho)/\sin\omega_\lambda$. Since this basis set is con-

centrated in the λ arrangement channel region when ρ is sufficiently large, accurate representation of the surface functions concentrated in the ν and κ channels may require a large number of terms at such values of ρ. To overcome this difficulty, a new basis set is constructed which consists of the union of the basis sets $F^{JM\Pi}_{\lambda v j\Omega}$, $F^{JM\Pi}_{\nu v j\Omega}$ and $F^{JM\Pi}_{\kappa v j\Omega}$. Furthermore, for systems containing either two or three identical atoms we construct symmetrized basis sets which belong to irreducible representations Γ of the P_2 or P_3 permutation groups, respectively. For the three identical atom case, these symmetrized variational basis sets are given by

$$F^{JM\Pi\Gamma}_{vj\Omega}(\zeta_\lambda;\rho)=\sum_{\lambda'} c^{\Gamma}_{\lambda' j} F^{JM\Pi}_{\lambda' vj\Omega}(\zeta_{\lambda'};\rho)\,, \tag{12}$$

where the sum in λ' is over λ, ν and κ, the $c^{\Gamma}_{\lambda' j}$ are easily determined constants, and the sets of angles ζ_ν and ζ_κ are considered to be functions of ζ_λ. The functions $F^{JM\Pi\Gamma}_{vj\Omega}$ will be referred to as primitives to distinguish them from the unsymmetrized basis functions $F^{JM\Pi}_{\lambda vj\Omega}$. The five-dimensional LHSF are now expanded in terms of these primitives:

$$\Phi^{JM\Pi\Gamma}_{n}(\zeta_\lambda;\rho)=\sum_{vj\Omega} a^{J\Pi\Gamma}_{vj\Omega n}(\rho)\, F^{JM\Pi\Gamma}_{vj\Omega}(\zeta_\lambda;\rho)\,. \tag{13}$$

The primitive basis set is not orthogonal, since the variational basis sets with different λ' overlap; therefore, calculation of the $a^{J\Pi\Gamma}_{vj\Omega n}$ coefficients requires the determination of overlap integrals for the variational basis set as well as integrals involving the Hamiltonian. Integration over the three Euler angles θ_λ, ϕ_λ, and ψ_λ is analytic, leaving two-dimensional quadratures to be done numerically. These quadratures are the most expensive part of the entire computation. Any quadrature scheme may be employed; the one we used is discussed in section 3.

Once all of the necessary integrals have been calculated, the $a^{J\Pi\Gamma}_{vj\Omega n}$ coefficients are determined by a generalized eigenvalue–eigenvector procedure. With sufficienty large basis sets, the overlap matrix between the primitives becomes nearly singular as a consequence of near linear dependence; for this reason it was necessary to develop a method for dealing with this situation. The primitive overlap matrix is diagonalized, and eigenvectors corresponding to eigenvalues smaller than a tolerance parameter (for the calculations described below, this parameter was set to zero) are eliminated from consideration. The remaining set of eigenvectors is used to transform the Hamiltonian matrix to yield a new eigenvalue problem from which the linear dependence effects have been removed.

From eqs. (6), (12), and (13), the expansion of the two-dimensional surface functions $\psi^{J\Pi\Gamma}_{n\Omega}(\omega_\lambda,\gamma_\lambda;\rho)$ in terms of the one-dimensional functions $f^{J\lambda}_{vj\Omega}$ can be shown to be

$$\begin{aligned}\psi^{J\Pi\Gamma}_{n\Omega}(\omega_\lambda,\gamma_\lambda;\rho)=\sum_{vj\Omega'} a^{J\pi\Gamma}_{vj\Omega' n}\{&c^{\Gamma}_{\lambda j}\delta^{\Omega}_{\Omega'}[1+(-1)^{J+\Pi}\delta^{\Omega}_{0}]\mathscr{P}^{\Omega}_{J}(\cos\gamma_\lambda) f^{J\lambda}_{vj\Omega'}(\omega_\lambda;\rho)\\ &+c^{\Gamma}_{\nu j} d^{J\Pi}_{\Omega\Omega'}(\Delta_{\nu\lambda})\,\mathscr{P}^{\Omega'}_{J}(\cos\gamma_\nu) f^{J\nu}_{vj\Omega'}(\omega_\nu;\rho)+c^{\Gamma}_{\kappa j}(-1)^{\Omega+\Omega'} d^{J\Pi}_{\Omega\Omega'}(\Delta_{\lambda\kappa})\,\mathscr{P}^{\Omega'}_{J}(\cos\gamma_\kappa) f^{J\kappa}_{vj\Omega}(\omega_\kappa;\rho)\,.\end{aligned} \tag{14}$$

The functions $d^{J\Pi}_{\Omega\Omega'}(\Delta)=d^{J}_{\Omega\Omega'}(\Delta)+(-1)^{J+\Pi+\Omega'} d^{J}_{\Omega,-\Omega'}(\Delta)$, where $\mathbf{d}^J$ is the Wigner little d matrix [24]; they appear in eq. (14) because of the integration of products of two $\mathscr{D}^{J\Pi}_{M\Omega}$ functions depending on different Euler angles. The angles $\Delta_{\nu\lambda}$ between the vectors $\boldsymbol{R}_\lambda$ and $\boldsymbol{R}_\nu$ and $\Delta_{\lambda\kappa}$ between the vectors $\boldsymbol{R}_\kappa$ and $\boldsymbol{R}_\lambda$ are functions of ω_λ and γ_λ only.

The same formalism is used in determining the surface functions at values of ρ for which the surface function amplitude is negligible in regions of configuration space in the interstices between the arrangement channel regions. For such values of ρ, the overlap between $f^{J\lambda}_{vj\Omega}$ and $f^{J\nu}_{vj\Omega}$ vanishes, making the set of primitive functions be automatically orthogonal; this greatly reduces the numerical work necessary for the LHSF calculation, because the basis set includes only the λ basis functions.

The calculations of the six-dimensional scattering wavefunction $\Psi^{JM\Pi\Gamma}$ is done by expanding it in terms of the five-dimensional LHSF:

$$\Psi^{JM\Pi\Gamma}(\rho, \zeta_\lambda) = \sum_n b_n^{J\Pi\Gamma}(\rho; \bar{\rho})\, \Phi_n^{JM\Pi\Gamma}(\zeta_\lambda; \bar{\rho}) \,. \tag{15}$$

The $\Phi_n^{JM\Pi\Gamma}$ are determined at a set of discrete values of $\bar{\rho}$, labeled $\bar{\rho}_i$. Substituting eq. (15) into the (time-independent) Schrödinger equation corresponding to the Hamiltonian defined by eq. (2) and using eq. (5), the coefficients $b(\rho; \bar{\rho}_i)$ are found to satisfy

$$\left(-\frac{\hbar^2}{2\mu}\frac{1}{\rho^{5/2}}\frac{d^2}{d\rho^2}\rho^{5/2} + \frac{15\hbar^2}{8\mu\rho^2} + \left(\frac{\bar{\rho}_i}{\rho}\right)^2 \epsilon_n^{J\Pi\Gamma}(\bar{\rho}_i) - E\right)\delta_n^{n'} b_n^{J\Pi\Gamma}(\rho; \bar{\rho}_i) + \sum_{n'} b_{n'}^{J\Pi\Gamma}(\rho; \bar{\rho}_i)\,[\mathcal{S}^{J\Pi\Gamma}]_n^{n'}(\rho; \bar{\rho}_i) = 0 \,, \tag{16}$$

in which the interaction matrix $\mathcal{S}^{J\Pi\Gamma}$ is defined by

$$[\mathcal{S}^{J\Pi\Gamma}]_n^{n'}(\rho; \bar{\rho}_i) = \langle \Phi_n^{JM\Pi\Gamma}(\zeta_\lambda; \bar{\rho}_i) \,|\, \bar{V}(\rho, \omega_\lambda, \gamma_\lambda; \bar{\rho}_i) \,|\, \Phi_{n'}^{JM\Pi\Gamma}(\zeta_\lambda; \bar{\rho}_i) \rangle$$
$$= \sum_{vj\Omega} \sum_{v'j'\Omega'} a_{vj\Omega n}^{J\Pi\Gamma}(\bar{\rho}_i)\, a_{v'j'\Omega' n'}^{J\Pi\Gamma}(\bar{\rho}_i) \langle F_{vj\Omega}^{JM\Pi\Gamma}(\zeta_\lambda; \bar{\rho}_i) \,|\, \bar{V}(\rho, \omega_\lambda, \gamma_\lambda; \bar{\rho}_i) \,|\, F_{v'j'\Omega'}^{JM\Pi\Gamma}(\zeta_\lambda; \bar{\rho}_i) \rangle \,, \tag{17}$$

with $\bar{V}(\rho, \omega_\lambda, \gamma_\lambda; \bar{\rho}_i) = V(\rho, \omega_\lambda, \gamma_\lambda) - (\bar{\rho}_i/\rho)^2 V(\bar{\rho}_i, \omega_\lambda, \gamma_\lambda)$. The integrals in the right-most part of eq. (17) are obtained from linear combinations of related integrals involving the variational basis set (11).

The coefficients $b(\rho; \bar{\rho}_i)$ are calculated as a function of ρ in a region near $\bar{\rho}_i$ corresponding to a hyper-spherical shell. The smooth matching of the scattering wavefunction across the boundary $\rho_{i,i+1}$ of adjacent hyperspherical shells is accomplished by imposing the conditions

$$b_n^{J\Pi\Gamma}(\rho_{i,i+1}; \bar{\rho}_{i+1}) = \sum_{n'} b_{n'}^{J\Pi\Gamma}(\rho_{i,i+1}; \bar{\rho}_i)\,[\mathcal{O}^{J\Pi\Gamma}]_n^{n'}(\bar{\rho}_{i+1}, \bar{\rho}_i) \,, \tag{18}$$

$$\left(\frac{\partial b_n^{J\Pi\Gamma}(\rho; \bar{\rho}_{i+1})}{\partial \rho}\right)_{\rho \to \rho_{i,i+1}^{(+)}} = \sum_{n'} \left(\frac{\partial b_{n'}^{J\Pi\Gamma}(\rho; \bar{\rho}_i)}{\partial \rho}\right)_{\rho \to \rho_{i,i+1}^{(-)}} [\mathcal{O}^{J\Pi\Gamma}]_n^{n'}(\bar{\rho}_{i+1}, \bar{\rho}_i) \,, \tag{19}$$

in which the overlap matrices $\mathcal{O}^{J\Pi\Gamma}$ are defined by

$$[\mathcal{O}^{J\Pi\Gamma}]_n^{n'}(\bar{\rho}_{i+1}, \bar{\rho}_i) = \langle \Phi_n^{JM\Pi\Gamma}(\zeta_\lambda; \bar{\rho}_{i+1}) \,|\, \Phi_{n'}^{JM\Pi\Gamma}(\zeta_\lambda; \bar{\rho}_i) \rangle$$
$$= \sum_{vj\Omega} \sum_{v'j'\Omega'} a_{vj\Omega n}^{J\Pi\Gamma}(\bar{\rho}_{i+1})\, a_{v'j'\Omega' n'}^{J\Pi\Gamma}(\bar{\rho}_i) \langle F_{vj\Omega}^{JM\Pi\Gamma}(\zeta_\lambda; \bar{\rho}_{i+1}) \,|\, F_{v'j'\Omega'}^{JM\Pi\Gamma}(\zeta_\lambda; \bar{\rho}_i) \rangle \,. \tag{20}$$

The methodology described above is closely related in spirit to the method independently developed by Schatz [17], which was published after the present work was completed. The major differences are in the selection of reference potential for calculation of the ω_λ-dependent portion of the basis set and in the method for dealing with overcompleteness of the basis set. Our reference potential, denoted by the term V_{jj}^{Ω} in eq. (10), is the potential energy surface at fixed $\bar{\rho}$ averaged over the diatomic rotation; the choice of this reference potential naturally follows from the expression for the one-dimensional surface functions $\phi_{nj\Omega}^{J\Pi\Gamma}$ of eq. (8). We allow for the large amount of linear dependence which is produced by this reference potential at small values of $\bar{\rho}$ by the method for solution of the generalized eigenvalue problem described above. This does not increase the time required for the calculation. Schatz, on the other hand, chooses for his reference potential $V(\bar{\rho}, \omega_\lambda, \gamma_\lambda = \pi/2)$ for $\bar{\rho} \geq 3.3$ bohr and $V(\bar{\rho} = 3.3 \text{ bohr}, \omega_\lambda, \gamma_\lambda = \pi/2)$ for $\bar{\rho} < 3.3$ bohr; the change in the reference potential at small $\bar{\rho}$ avoids problems with linear dependence.

3. Numerical parameters

One of the most important parameters in the calculations performed is the number of primitives used to expand the surface functions. In addition to the indices J, M, Π and Γ which label the LHSF, the basis functions and the primitives formed from them are labelled by indices v, j, and Ω, which asymptotically correspond re-

spectively to the diatom vibrational, total rotational and helicity rotational projection quantum numbers [2,3]. The range of (v, j, Ω) included in the calculation of a desired set of LHSF is selected by preliminary calculations at a small subset of the values of $\bar{\rho}$ to be used in the full calculation. For these initial calculations, the basis set is deliberately chosen to be larger than necessary for the accuracy and number of surface functions desired. The number of accurate surface functions obtained by this method is determined by comparison of two such calculations with different size basis sets at each value of $\bar{\rho}$. Examination of the coefficients of the basis functions contributing to each surface function considered allows selection of a smaller basis set which can be used with minimal loss of accuracy. This method becomes complicated with larger variational basis sets, due to increasing linear dependence among some of the primitive functions; however, the overall pattern of important coefficients is still effective in optimizing the choice of basis sets for succeeding calculations. When this method of selection is used, the number of good surface functions of each symmetry which are produced is approximately one half the number of primitives of that symmetry used in the calculation.

To obtain the results presented below, the one-dimensional numerical functions $t^{J\lambda}_{v j\Omega}(\omega_\lambda; \rho)$ from eq. (10) are calculated on a grid of 450 ω_λ points using a one-dimensional finite element method. Each element is quadratic and uses two Gauss–Legendre points. The reference potential V^{Ω}_{jj} for these functions is determined by a Gauss–Legendre quadrature with 96 γ_λ points. The grid for the two-dimensional integrals is the direct product of these two independent quadrature grids. Convergence of the surface function energies with the fineness of the mesh is to four decimal places.

For the system $H + H_2$, the dependence of the basis functions eq. (11) in the ν and κ coordinates is the same as that for the λ channel functions, so it is not necessary to repeat the calculation for $t^{J\nu}_{v j\Omega}$ and $t^{J\kappa}_{v j\Omega}$. In addition, the integrals between products of functions in the λ and ν channels equal the integrals between the corresponding functions in the ν and κ channels, so the integration need only be done for λ, ν pairs to obtain the overlap integrals for all three regions.

LHSF are calculated every 0.2 bohr from $\bar{\rho}=2.0$ to 12.0 bohr, and interaction matrices $\mathcal{J}^{JnP}$ (see eqs. (16) and (17)) are determined at five evenly spaced values of ρ for every value of $\bar{\rho}_i$. One overlap matrix $\mathcal{O}^{JnP}$ (see eqs. (18)–(20)) is calculated between sets of the LHSF at each pair of adjacent $\bar{\rho}$ values. For $\bar{\rho} \geq 6.2$ bohr the variational basis functions in arrangement channel λ are orthogonal to those in ν and κ because we set the maximum value of ω_λ equal to the physically reasonable value $2\arcsin(3.0\,\text{bohr}/\bar{\rho})$, which at $\bar{\rho}=6.2$ bohr equals 57.9°. This value of ω_λ is deep in a classically forbidden region for all γ_λ for the total energies discussed below. As a result, the time needed for the surface function calculation in this region is small compared to that for the $\rho < 6.2$ bohr region. The initial value problem described by eq. (16) is solved using a logarithmic derivative propagator [27] with a step size of $\Delta\rho=0.025$ bohr and a constant-ρ projection [6,11,28] at 12.2 bohr. These parameters were chosen to achieve a calculation accuracy about equal to that described previously [6,11].

The five-dimensional basis functions are generated from the functions $f^{J\lambda}_{v j\Omega}$ according to eq. (11). For each of the potential energy surfaces and for $J=0$, a set of $(v, j, \Omega=0)$ quantum numbers was chosen to give a variational basis set of 152 functions. This set has a maximum of 12 vibrational functions for the value $j=0$, with monotonically decreasing number of vibrations for each succeeding value of j to the maximum of $j=23$ for which only one vibrational function is used. Symmetrization of this basis set yielded 76 A_1, 76 A_2 and 152 E primitives.

For the LSTH potential energy surface, the scattering results were obtained from 36 A_1, 35 A_2, and 69 E LHSF at each value of $\bar{\rho}$. The calculation of each LHSF (including the evaluation of all the associated overlap and interaction matrices for the solution of the propagation equation (16)) requires an average of 0.27 s on a Cray X-MP/48. The timings are very similar for the PK2 potential energy surface.

For $J=0$, the variational LHSF calculation is about a factor of 20 faster than the finite-element method one for equivalent accuracy [6,11]. We estimate that the numerical effort required for the finite-element calculation of the LHSF will increase with J as $(J+1)^a$ with $2 < a \leq 3$, whereas for the variational method $a \approx 2$; therefore, the speed of the variational LHSF calculation with respect to that of the finite-element one is expected to increase with increasing J.

Table 1
Comparison of surface function energies (in eV) for finite-element (FE) and variational (V) methods – $J=0$

$\bar{\rho}$ (a_0)	PK2								LSTH							
	A1			A2 [a]		E			A1			A2			E		
	n	FE	V	n	V	n	FE	V	n	FE	V	n	FE	V	n	FE	V
2.0	1	3.0031	3.0029	1	3.7612	1	3.1562	3.1558	1	3.1988	3.1987	1	4.0947	4.0937	1	3.3938	3.3935
	5	4.5951	4.5586	5	5.8307	10	5.2093	5.1996	5	4.7962	4.7918	5	6.1193	6.1104	10	5.4317	5.4247
	10	5.8126	5.7980	10	7.1675	20	6.5485	6.5309	10	6.0898	6.0795	10	7.6127	7.5981	20	6.8744	6.8608
	15	6.8547	6.8247	15	8.5371	30	7.7914	7.7361	15	7.2700	7.2574	15	9.1025	9.0699	30	8.1385	8.1159
	20	7.9175	7.8703	20	9.5651	40	8.9223	8.8574	20	8.3031	8.2787	20	10.137	10.088	40	9.3596	9.3065
3.0	1	0.61272	0.61267	1	0.80296	1	0.61277	0.61272	1	0.72438	0.72435	1	0.96023	0.96011	1	0.72440	0.72437
	5	1.1472	1.1463	5	1.3912	10	1.3210	1.3192	5	1.2819	1.2814	5	1.5368	1.5357	10	1.4473	1.4464
	10	1.6735	1.6679	10	2.0120	20	1.8613	1.8573	10	1.7585	1.7550	10	2.1531	2.1463	20	1.9919	1.9877
	15	2.0847	2.0788	15	2.5986	30	2.3244	2.3082	15	2.2466	2.2432	15	2.7673	2.7604	30	2.4375	2.4328
	20	2.5316	2.5219	20	3.0725	40	2.8049	2.7933	20	2.6695	2.6638	20	3.2483	3.2368	40	2.9494	2.9377
4.0	1	0.41158	0.41118	1	0.41563	1	0.41169	0.41129	1	0.43738	0.43713	1	0.44677	0.44658	1	0.43753	0.43728
	5	0.88557	0.88426	5	0.89775	10	0.89821	0.89670	5	0.87687	0.87631	5	0.90314	0.90240	10	0.90160	0.90082
	10	1.2436	1.2413	10	1.3507	20	1.3192	1.3158	10	1.2080	1.2068	10	1.3431	1.3410	20	1.2916	1.2895
	15	1.5936	1.5868	15	1.7777	30	1.6246	1.6193	15	1.5617	1.5583	15	1.7631	1.7583	30	1.6026	1.5994
	20	1.8317	1.8234	20	2.0267	40	1.9527	1.9428	20	1.8025	1.7976	20	1.9981	1.9925	40	1.9166	1.9110
5.0	1	0.32308	0.32230	1	0.33328	1	0.32308	0.32230	1	0.29753	0.29702	1	0.31150	0.31112	1	0.29753	0.29702
	5	0.83267	0.82921	5	0.83878	10	0.84158	0.83878	5	0.79821	0.79600	5	0.80894	0.80723	10	0.80894	0.80723
	10	1.1443	1.1394	10	1.2899	20	1.2973	1.2899	10	1.1107	1.1069	10	1.2614	1.2562	20	1.2614	1.2562
	15	1.4603	1.4506	15	1.6199	30	1.6060	1.5974	15	1.4218	1.4149	15	1.5910	1.5821	30	1.5579	1.5526
	20	1.8092	1.7972	20	1.9166	40	1.8322	1.8190	20	1.7572	1.7510	20	1.8734	1.8665	40	1.7837	1.7756

[a] For PK2 A2 there are no FE data available.

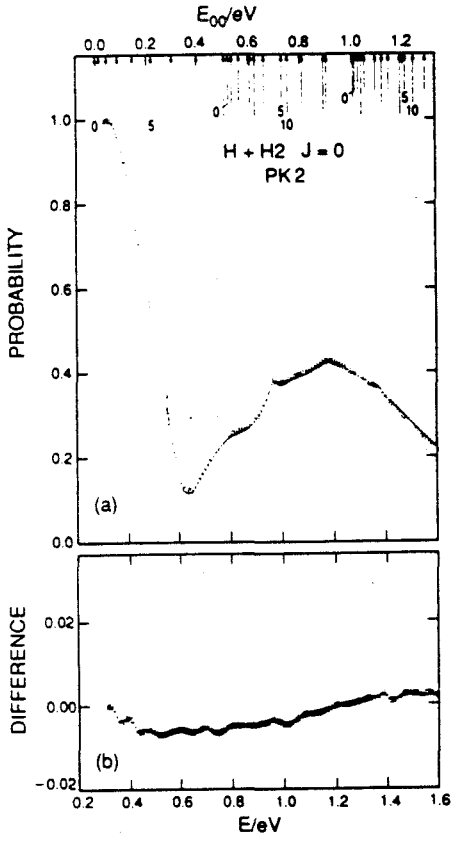

Fig. 1. Probabilities (a) and probability differences (b) as a function of total energy E (lower abscissa) and initial relative translational energy E_{00} (upper abscissa) for the $J=0$ (0, 0, 0+) → (0, 0, 0) E symmetry transition in $H+H_2$ collisions on the PK2 potential energy surface. The symbol (v, j, Ω) labels an asymptotic state of the $H+H_2$ system in which v, j and Ω are the quantum numbers of the initial or final H_2 states as defined in the text. The vertical arrows on the upper abscissa denote the energies at which the corresponding $H_2(v, j)$ states open up. The length of those arrows decreases as v spans the values 0, 1, and 2, and the numbers 0, 5, and 10 associated with the arrows define a labelling for the value of j. The square symbols in (a) are the current variational surface function results and the solid line are the FE results [11]. The differences between the former and the latter are plotted in (b).

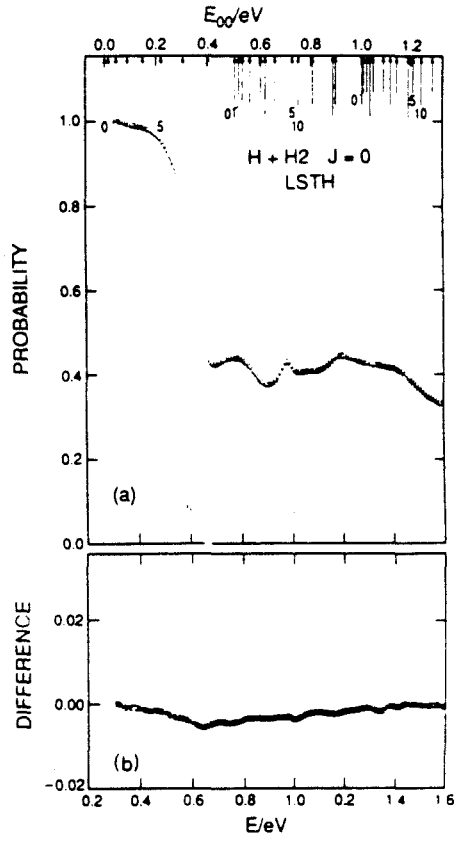

Fig. 2. Same as for fig. 1 for the LSTH potential energy surface. The FE results are taken from ref. [22].

4. Results and discussion

As can be seen in table 1, the present variational (V) LHSF energies consistently fall below those calculated by the finite-element method (FE) [11,23], with a maximum reduction of about 65 meV for the higher energy LHSF. As both methods obey a minimum principle, this implies better quality of the LHSF in the current method.

Flux is conserved for the PK2 surface to better than 1% for energies less than 1.55 eV for the scattering calculations using FE LHSF [11] and for energies below 1.74 eV for the current calculations. For the LSTH surface, flux is conserved to better than 2% below 1.55 eV for the FE results [23] and, for the current results, to better than 1% below 1.68 eV and to better than 2% between 1.68 and 1.74 eV. Examination of the scattering matrices produced by each method shows good agreement between the two below the first resonance at 0.97 eV, with a difference which is usually no greater than 2% for probabilities greater than 10^{-2}. Above this energy the agreement between the results for the $v=0$ to $v'=0$ state transitions remains equally good; however, the agreement for $v=1$ to $v'=1$ transitions is not as good, with a difference usually no greater than 4% in the probabilities greater than 10^{-2} for these transitions. On the basis of the lower LHSF energies and the better scattering matrix unitarities of the current method, we believe that the current scattering calculations are more accurate than the ones using FE LHSF. A comparison of $J=0$ probability curves generated by the two methods is plotted in fig. 1 for the PK2 surface and in fig. 2 for the LSTH surface, together with the difference of the results of the two methods. The relative differences for the probabilities of these figures never exceed 6% for the PK2 or 2% for the LSTH potential energy surface; the greater maximum relative difference for the former is due to the smaller minimum value of the probability itself rather than to a greater difference between the results.

The scattering results calculated from the variational LHSF are converged with respect to number of surface functions used in the propagation to 2% in the probabilities greater than 0.1 and 1.5° in the corresponding scattering matrix element phases. The energies of the LHSF corresponding to asymptotically open states are converged to 0.5% with respect to size of the basis set used in their calculation, and thus the scattering results are also well converged with respect to this parameter.

Calculations were also performed for both parities of the $J=1$ partial wave and are of similar quality. $J=1$ probabilities in excess of 0.1 generally agree with the matching method ones [3] (which were obtained up to 0.7 eV only) to better than about 3%. In none of these calculations have we encountered the difficulties previously predicted [10]. A detailed analysis of the $J=1$ results, up to 1.75 eV, and of the corresponding resonances will be the subject of a separate publication.

5. Summary

A new general variational method for calculating local LHSF was described. It is about a factor of 20 more efficient than the finite-element method for the $J=0$ partial wave of $H+H_2$; this relative efficiency is expected to increase with increasing J. The results of the two methods agree well at the LHSF level, and at the scattering matrix level agree well for energies below 0.97 eV and moderately well for higher energies; the variational ones are believed to be the more accurate ones.

Acknowledgement

The work described in this paper was supported in part by DOE grant DE-AS03-83ER and AFAL contract F04611-86-K-0067. One of the authors (SAC) also thanks NSF for a Graduate Fellowship. Most of the calculations were performed on the Cray X-MP/48 and SCS-40 machines at the NSF San Diego Supercomputing Center.

References

[1] A. Kuppermann and G.C. Schatz, J. Chem. Phys. 62 (1975) 2502;
A. Kuppermann, G.C. Schatz and M. Baer, J. Chem. Phys. 65 (1976) 4596;
G.C. Schatz and A. Kuppermann, J. Chem. Phys. 65 (1976) 4624.
[2] G.C. Schatz and A. Kuppermann, J. Chem. Phys. 65 (1976) 4642.
[3] G.C. Schatz and A. Kuppermann, J. Chem. Phys. 65 (1976) 4668.
[4] A.B. Elkowitz and R.E. Wyatt, J. Chem. Phys. 62 (1975) 2504; 63 (1975) 702.
[5] R.B. Walker, E.B. Stechel and J.C. Light, J. Chem. Phys. 69 (1978) 2922.
[6] A. Kuppermann and P.G. Hipes, J. Chem. Phys. 84 (1986) 5962.
[7] F. Webster and J.C. Light, J. Chem. Phys. 85 (1986) 4744.
[8] G.C. Schatz, in: Theory of chemical reactions dynamics, ed. D.C. Clary (Reidel, Dordrecht, 1986) p. 1
[9] M. Baer, J. Phys. Chem. 91 (1987) 5846.
[10] G.A. Parker, R.T Pack, B.J. Archer and R.B. Walker, Chem. Phys. Letters 137 (1987) 564;
R.T Pack and G.A. Parker, J. Chem. Phys. 87 (1987) 3888.
[11] P.G. Hipes and A. Kuppermann, Chem. Phys. Letters 133 (1987) 1.
[12] J. Linderberg and B. Vessal, Intern. J. Quantum Chem. 31 (1987) 65.
[13] D.W. Schwenke, K. Haug, D.G. Truhlar, Y. Sun, J.Z.H. Zhang and D.J. Kouri, J. Phys. Chem. 91 (1987) 6080.
[14] J.Z.H. Zhang and W.H. Miller, Chem. Phys. Letters 140 (1987) 329;
J.Z.H. Zhang, S.-I. Chu and W.H. Miller, J. Chem. Phys. 88 (1988) 4549.
[15] J.Z.H. Zhang, D.J. Kouri, K. Haug, D.W. Schwenke, Y. Shima and D.G. Truhlar, J. Chem. Phys. 88 (1988) 2492.
[16] M. Mladenovic, M. Zhao, D.G. Truhlar, D.W. Schwenke, Y. Sun and D.J. Kouri, Chem. Phys. Letters 146 (1988) 358.
[17] G.C. Schatz, Chem. Phys. Letters 150 (1988) 92.
[18] A. Kuppermann, Chem. Phys. Letters 32 (1975) 374.
[19] R.T. Ling and A. Kuppermann, in: Electronic and Atomic Collisons, Abstracts of Papers of the 9th International Conference on the Physics of Electronic and Atomic Collisions, Seattle, Washington, 24–30 July 1975, Vol. 1, eds. J.S. Risley and R. Geballe (Univ Washington Press, Seattle, 1975) pp. 353, 354.
[20] R.N. Porter and M. Karplus, J. Chem. Phys. 40 (1964) 1105.
[21] B. Liu, J. Chem. Phys. 58 (1973) 1925;
P. Siegbahn and B. Liu, J. Chem. Phys. 68 (1978) 2457.
[22] D.G. Truhlar and C.J. Horowitz, J. Chem. Phys. 68 (1978) 2468; 71 (1979) 1514 (E).
[23] P.G. Hipes and A. Kuppermann, unpublished results.
[24] L.M. Delves, Nucl. Phys. 9 (1959) 391; 20 (1960) 275.
[25] A. Kuppermann, in: Theoretical chemistry – theory of scattering: papers in honor of Henry Eyring, Vol. 6, part A, ed. D. Henderson (Academic Press, New York, 1981) ch. 2, pp. 70–164.
[26] A.S. Davydov, Quantum mechanics, 2nd Ed. (Pergamon Press, Oxford, 1976) pp. 151–161.
[27] B.R. Johnson, J. Compl. Phys. 49 (1973) 23; J. Chem. Phys. 67 (1977) 4086; NRCC Workshop, Lawrence Berkeley Laboratory Report No. LBL-9501 (1979).
[28] D.M. Hood and A. Kuppermann, in: Theory of chemical reaction dynamics, ed. D.C. Clary (Reidel, Dordrecht, 1986) pp. 193–214; unpublished results.

Volume 157, number 5 CHEMICAL PHYSICS LETTERS 19 May 1989

SYMMETRY ANALYSIS OF ACCURATE H+H_2 RESONANCES FOR LOW PARTIAL WAVES

Steven A. CUCCARO [1], Paul G. HIPES [2] and Aron KUPPERMANN
Arthur Amos Noyes Laboratory of Chemical Physics, Division of Chemistry and Chemical Engineering [3], California Institute of Technology, Pasadena, CA 91125, USA

Received 20 January 1989; in final form 28 February 1989

We have performed accurate quantum mechanical three-dimensional reactive scattering calculations for both parities of the $J=1$ partial wave of the H+H_2 system up to total energies of 1.75 eV. The collision lifetime resonance spectra for both $J=0$ and $J=1$ are discussed in terms of the characteristics of the system's potential energy surface and of a simple physical model involving its symmetry properties.

1. Introduction

We have recently developed a new variational technique [1] for calculating the local hyperspherical surface functions (LHSF) necessary for performing three-dimensional (3D) quantum mechanical reactive scattering calculations by the symmetrized hyperspherical coordinate method. We have shown that this technique produces results of similar quality as the finite element (FE) one previously used [2,3], with significantly less numerical effort. Using the LHSF generated by this variational method, we have performed 3D reactive scattering calculations for the H+H_2 system on the PK2 [4] and LSTH [5,6] potential energy surfaces for the $J=0$ and both parities of the $J=1$ partial waves. The calculations are of sufficiently high quality for resonance analysis using the collision lifetime matrix formalism [7]. We briefly describe the parameters used in the calculation, and follow with a presentation and analysis of the results. Other recent hyperspherical calculations for $J=1$ H+H_2 have been published by Schatz [8] and by Pack, Parker and coworkers [9], over a more limited energy range. In addition, results using different methods have been obtained by Mladenovic et al. [10] and by Zang and Miller [11].

2. Method

The details of the partial wave methodology for arbitrary J and the parameters used for the $J=0$ calculation have been presented previously [1]; therefore, only a few relevant points will be mentioned here. The $J=0$ and $J=1$ calculations use the same values for many numerical parameters: the choice of grid is the same, as are the number and location of the sets of LHSF. The basis set for $J=0$ is formed from a choice of quantum numbers (v, j, $\Omega=0$) [1,12], yielding a total of 152 functions. This basis is symmetrized according to the irreducible representations of the P_3 symmetry group of H+H_2, to give 76 A_1, 76 A_2, and 152 E "primitive" functions. These are used as a variational basis for calculation of the LHSF of the corresponding symmetry. The same set of v and j quantum numbers is used for the $J=1$ calculations; in addition, making Ω equal to both 0 and 1 produces a variational basis set of 292 functions. From these, a primitive basis set is generated consisting of 64 A_1, 76 A_2 and 140 E primitives for the even parity $\Pi=0$ (which for $J=1$ contains only

Work performed in partial fulfillment of the requirements for the Ph.D. Degree in Chemistry at the California Institute of Technology.

[2] Current address: Mail code 206-49, California Institute of Technology, Pasadena, CA 91125, USA.

[3] Contribution No. 7909.

0 009-2614/89/$ 03.50

$\Omega=1$ functions) and another with 140 A_1, 152 A_2 and 292 E primitives for the odd parity $\Pi=1$ (containing both $\Omega=0$ and $\Omega=1$ functions).

The $J=1$ scattering results on the PK2 surface were obtained from 31 A_1, 31 A_2, and 64 E LHSF for $\Pi=0$ and 67 A_1, 62 A_2, and 133 E LHSF for $\Pi=1$. The calculation of each $J=1$ LHSF and all associated matrices used in the logarithmic derivative propagation [13] required an average of 13.1 s on an SCS-40 minisupercomputer, as compared to 6.9 s for $J=0$. Similarly, the $J=1$ scattering calculations for the LSTH surface used 32 A_1, 32 A_2 and 64 E LHSF for $\Pi=0$ and 74 A_1, 70 A_2, and 127 E LHSF for $\Pi=1$, with an average time of 12.5 s per LHSF, compared to 6.6 s for $J=0$. The corresponding maximum deviation from flux conservation is never greater than 1% for the PK2 and 2% for the LSTH surface.

3. Results and discussion

From our irreducible representation scattering matrices we have calculated distinguishable atom $J=1$ state-to-state reaction probabilities over the energy range 0.3 to 1.73 eV for the PK2 potential energy surface. The coupled channel (CC) results published by Schatz at 0.5 and 0.6 eV [8] and ours agree to within 10%, which is reasonable since he used a much smaller basis set than ours. Schatz also made calculations based on the coupled states (CS) approximation using a larger basis set than in this CC method. These CS probabilities are closer to our highly converged values than the CC ones, indicating that the CS approximation for his larger basis set is more accurate than the CC results using his smaller basis set. Our $J=1$ results agree with the LSTH calculations of Zhang and Miller [11] at 1.14 eV to about 2% or better.

We performed lifetime matrix analysis [3,7,14] of each of the matrices $\mathbf{S}^{J\Pi\Gamma}$ for $\Gamma=A_1$, A_2, E, $\Pi=0$, 1, and $J=0$, 1. We label the resonances obtained by the notation appropriate for vibrational states of linear triatomic molecules, (v_1, v_2^K, v_3), where v_1, v_2, and v_3 denote respectively the quantum numbers for the symmetric, bend and asymmetric vibrations and K is the quantum number of the vibrational angular momentum [15][#1]. For the resonance state, v_1, v_2 and v_3 denote approximate constants of the motion; their values are chosen on the basis of the energy spacing of the resonances. In the present paper, as well as in all previous ones using this labeling, it has been customary to set $v_3=0$ [3,16,17], implying that such resonances have no asymmetric stretch character. However, modeling of collinear H_3 resonances (for which only v_1 and v_3 are defined) has shown that they may have significant asymmetric as well as symmetric stretch character. The vibrationally adiabatic model suggests that the lowest collinear H_3 resonance be assigned the quantum numbers $v_1=1$, $v_3=0$ [18], whereas the hyperspherically adiabatic model leads to the assignment $v_1=0$, $v_3=2$ [19,20], corresponding to the second excited state of the asymmetric stretch and asymptotically correlating to the $v=1$ state of the isolated diatom. Therefore, the nodal structures of the corresponding model wavefunctions are completely different, and neither should be assumed correct without further comparison with the accurate resonance wavefunction. The assignment $v_3=0$ used in this paper corresponds to a vibrationally adiabatic description, but is a matter of notation rather than of physical validity.

Lifetime matrix analyses of the $J=0$ scattering matrices for the PK2 surface were previously performed up to 1.6 eV using the FE method for calculating the LHSF [3]. They were recalculated using the variational LHSF approach, and the results are comparable. The resonant time delays and resonance positions found for scattering matrices generated from both FE and variational LHSF are listed in table 1; the lifetime matrix eigenvalues for the current variational LHSF calculation are plotted versus energy in fig. 1. The main difference between the two calculations is the appearance of two weak reso-

[#1] In a previous paper [3] we used Ω to denote the vibrational angular momentum quantum number, in analogy to the notation of refs. [16,17]. However, we have also used Ω [1,3] to denote the quantum number for the component of the system's total angular momentum along the direction of the vector which connects the center of mass of a pair of the system's atoms to the third atom (and asymptotically corresponds to the helicity rotational quantum number). Since these two angular momentum components are in general distinct, we shall for clarity use the symbol K in this paper to denote the first one (i.e. the vibrational angular momentum component), while continuing to use Ω for the second.

Table 1
Resonance characteristics for PK2 [a] potential energy surface

J	Assignment	Current results			FE [b] lifetime (fs)	RPO [c] E (eV)
		E (eV)	lifetime (fs)	E (eV)		
0, 1	(0, 0^0, 0)	0.61	7	0.61		0.655
1	(0, 1^1, 0)	0.74	6			
0, 1	(0, 2^0, 0)	0.85	3	0.847		0.934
0, 1	(1, 0^0, 0)	0.97	41	0.971	42	0.975
1	(0, 3^1, 0)	0.97	6			
0, 1	(0, 4^0, 0)	1.07	2			
1	(1, 1^1, 0)	1.08	18			
0, 1	(1, 2^0, 0)	1.17	7	1.170		1.175
0, 1	(2, 0^0, 0)	1.38	46	1.382	50	1.366
1	(2, 1^1, 0)	1.47	35			
0	?	1.51	7			1.542
0, 1	(2, 2^0, 0)	1.56	20	1.56		
1	(2, 3^1, 0)	1.65	5			

[a] Ref. [4].
[b] Finite element results, ref. [3].
[c] Resonant periodic orbit results, ref. [21].

nances at energies of 1.07 and 1.51 eV, which were not previously reported. The first is assigned the label (0, 4^0, 0); however, the resonance at 1.51 eV, indicated by an unlabeled arrow in fig. 1, does not seem to correspond to the energy of an expected state of metastable linear H_3 and as such will remain unlabeled. The lifetimes of these resonances vary greatly; the long-lived ones at 0.969, 1.381, and 1.56 eV correspond to Feshbach resonances and have lifetimes of 41, 46, and 20 fs, respectively, while the weaker peaks correspond to shape or barrier resonances [21] and have an average lifetime of 6 fs. In both calculations, the A_1 and E symmetries show the same resonance energies and lifetimes, with more numerical noise present in the E calculation due to the larger number of states, and no resonance structure is found in the A_2 symmetry.

The $J=0$ LSTH surface resonance energy and lifetimes from the current calculations and the previous FE calculations are listed in table 2, and the present lifetime matrix eigenvalues are displayed in fig. 2. The assignment of these states is the same as for those found for the PK2 surface. In addition, there is a high energy resonance at 1.72 eV, which corresponds to (2, 4^0, 0); however, the lifetime analysis near this energy is obscured by numerical noise, so this energy is less reliable than the other resonance energies.

The energy spacings of each of the $v_2=0$, $v_2=2$ and $v_2=4$ series of resonances suggest that a resonance with assignment (1, 4^0, 0) should exist, for the LSTH surface, at the position indicated in fig. 2. So far, this resonance has not been found. By analogy, an equivalent resonance should exist (but is not found) for PK2, as indicated in fig. 1. The latter cannot correspond to the unlabeled resonance at 1.51 eV, because of the insufficiently large spacing between the (0, 4^0, 0) and (2, 4^0, 0) resonances for the LSTH surface.

The $J=1$ partial wave includes resonance states with $K=1$ in addition to $K=0$. Interestingly, the lifetime matrix analysis of the $J=1$, $\Pi=1$, A_2 symmetry yields the same resonance energies as those found for the $J=0$, A_1 symmetry for both the PK2 and LSTH surfaces, with one exception; we therefore interpret these resonances as $K=0$ states. The exception is that there is no visible A_2 resonance at 1.51 eV for either surface, but it is possible that numerical noise interferes with its detection. The absence of a discernable energy shift due to the increase in J is consistent with the approximate rotational constants for linear H_3 [23]; estimates of the magnitude of the shift in going from $J=0$ to $J=1$ yields a value of about 0.002 eV, which is small compared with the accuracy to which we have determined the resonance energies.

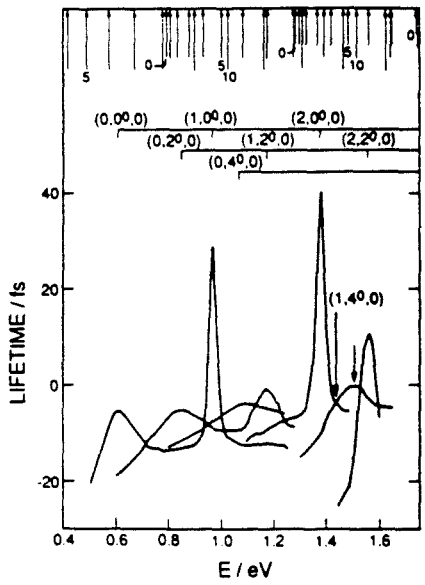

Fig. 1. Resonant lifetime as a function of energy for the A_1 symmetry of the $J=0$ partial wave of $H+H_2$ (PK2 surface). The abcissa E is the total energy and the ordinate represents the resonant eigenvalue of the collision lifetime matrix. The vertical arrows on the upper abcissa denote the energies of the $H_2(v,j)$ states. The length of these arrows decreases as v spans the values 0 through 3. The numbers 0, 5, and 10 define a labeling for the value of j. The energy grid used for these lifetime calculations was 0.001 eV in the neighborhood of the two strongest resonances $(1, 0^0, 0)$ and $(2, 0^0, 0)$ and 0.01 eV elsewhere. The labeling of the resonances at the top of the panel is described in the text. The downward pointing unlabeled vertical arrow at 1.51 eV indicates an unassigned resonance. The downward pointing arrow labeled $(1, 4^0, 0)$ corresponds to a resonance expected on the basis of energy spacings (see text) but not found in the present calculations.

Additional resonances appear in the $J=1$, $\Pi=1$, A_1 and $J=1$, $\Pi=0$, A_2 partial waves. For the PK2 surface, they occur at 0.74, 0.97, 1.08, 1.47, and 1.65 eV (fig. 3). The assignments and lifetimes are given in table 1. The v_1 and v_2 assignments are done on the basis of the energy spacings, and the K assignment on the basis of the restrictions imposed by the values of J and v_2 and the evenness of v_2 [3,25]. The corresponding values for the LSTH surface are listed in table 2 and displayed in fig. 4; they have energies of 0.77, 1.00, 1.09, 1.22, 1.45, and 1.63 eV. The strong resonances $(1, 1^1, 0)$, $(2, 1^1, 0)$ and $(2, 3^1, 0)$ were found previously with approximate models using the LSTH surface [16,17,23,24]; these results are also given in table 2 for comparison. The remaining peaks in the lifetime analysis are weak and have not been reported before. No resonances were found for the $J=1$, $\Pi=0$, A_1 symmetry on either surface. All resonances seen in the $J=1$ A_1 and A_2 symmetries with a particular parity are also seen in the $J=1$ E symmetry of the same parity. Again, the E results are of lower accuracy because of the larger number of states.

Calculations for collinear triatomic systems have previously given strong indications [19] that the characteristics of resonance spectra are closely related to the geometry of potential energy surfaces in the strong interaction region of configuration space, and that it may be possible to infer such geometry from experimentally observed resonance spectra. We will now try to obtain such relation with the $J=0$, 1 resonance at hand. Examination of the energy spacings between consecutive resonances in each of the series $(0, v_2^K, 0)$, $(1, v_2^K, 0)$, and $(2, v_2^K, 0)$ shows them to be nearly constant with respect to v_1 and v_2 and having global averages of 0.104 ± 0.013 and 0.103 ± 0.015 eV for the LSTH and PK2 surfaces, respectively. This correlates very well with the spacings of 0.11 and 0.12 eV predicted from the corresponding bending force constants [6,26] and a harmonic model.

Examining the series $(v_1, 0^0, 0)$ for $v_1 = 0$, 1, 2 furnishes consecutive resonance energy differences of 0.33 and 0.38 eV for LSTH and 0.36 and 0.41 eV for PK2, whereas a harmonic model based on the symmetric stretch force constant predicts constant spacing of 0.26 eV for LSTH and 0.47 eV for PK2. Not surprisingly, a symmetric stretch static model does not fit the resonance spectra well.

The energy shift between the $(0, 0^0, 0)$ LSTH and PK2 resonances should depend in part on the difference of 0.029 eV between the corresponding saddle point energies [4,6]. The observed downward shift of 0.04 eV can be totally accounted for by the difference in zero point bend energies and saddle point heights; this method of accounting does not seem to be physically reasonable, since the difference in the symmetric and/or asymmetric stretching characteristics of the potential energy surfaces should also contribute to this shift.

We conclude that bending mode force constants in the saddle point region of this system can easily be obtained from the corresponding resonance level spacings, but that static characteristics of the sur-

Volume 157, number 5 CHEMICAL PHYSICS LETTERS 19 May 1989

Table 2
Resonance characteristics for LSTH [a] potential energy surface

J	Assignment	Current results			FE [b] lifetime (fs)	RPO [c] E (eV)	SCSA [d] E (eV)	CEQB [e] E (eV)	CS [f] E (eV)
		E (eV)	lifetime (fs)	E (eV)					
0, 1	$(0, 0^0, 0)$	0.65	11	0.65	11				
1	$(0, 1^1, 0)$	0.77	9						
0, 1	$(0, 2^0, 0)$	0.88	10	0.880	10				
0, 1	$(1, 0^0, 0)$	0.98	28	0.981	28	0.981	0.98	0.97	
1	$(0, 3^1, 0)$	1.00	8						
1	$(1, 1^1, 0)$	1.09	29			1.085	1.09	1.09	1.10
0, 1	$(0, 4^0, 0)$	1.10	5						
0, 1	$(1, 2^0, 0)$	1.19	8	1.191		1.186		1.20	1.20
1	$(0, 5^1, 0)$	1.22	6						
0, 1	$(2, 0^0, 0)$	1.36	30	1.364	31	1.374	1.24	1.35	
1	$(2, 1^1, 0)$	1.45	38			1.461	1.35		
0	?	1.50	4						
0, 1	$(2, 2^0, 0)$	1.54	12	1.55±0.03		1.545	1.46		
1	$(2, 3^1, 0)$	1.63	8			1.641			
0, 1	$(2, 4^0, 0)$	1.72 [g]	5			1 734			

[a] Refs. [5,6]. [b] Ref. [22]
[c] Resonant periodic orbit results, ref. [23].
[d] Small curvature semiclassical adiabatic results, ref. [24].
[e] Collinear exact quantum with adiabatic bend results, ref. [17].
[f] Coupled state results, ref. [16].
[g] This resonance energy is less accurate than the rest. See text for details.

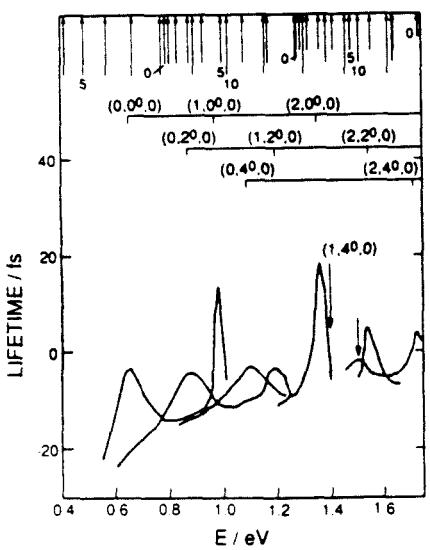

Fig. 2. Same as fig. 1 but for the LSTH surface; a constant energy grid of 0.01 eV was used throughout.

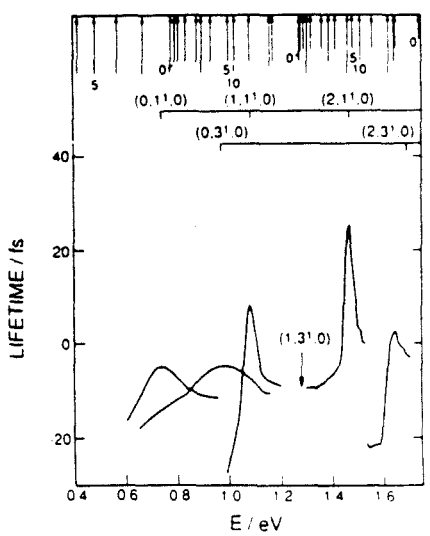

Fig. 3. Resonant lifetime as a function of energy for the A_1 symmetry of the $J=1$, $\Pi=0$ partial wave of $H+H_2$ (PK2 surface). The abcissa and ordinate are as given in fig. 1; the energy grid is 0.01 eV throughout. The downward pointing labeled arrows have similar meanings to the ones in figs. 1 and 2.

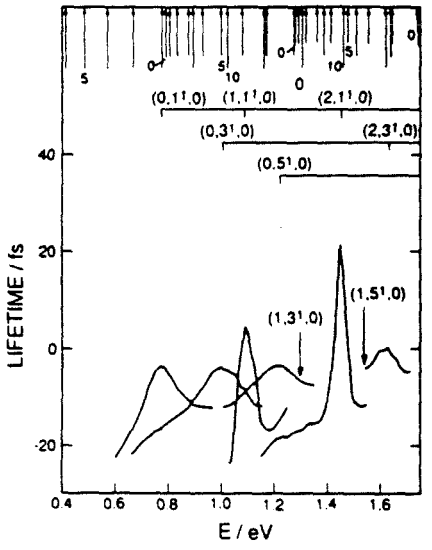

Fig. 4. Same as fig. 3 but for the LSTH surface.

Table 3
Empirical resonance selection rules

J	Π	K	A_1	A_2	E
0	0	0	yes	no	yes
1	0	1	no	yes	yes
1	1	0	no	yes	yes
1	1	1	yes	no	yes

faces are inadequate to understand the stretch motion features of the resonance spectra.

The presence or absence of resonances in each of the partial waves examined is summarized in table 3. An empirical selection rule, satisfied by the results of that table, is that resonances are present in the $\Gamma = E$ symmetry for all allowed values of K, and in $\Gamma = A_1$, A_2 when the quantity $(-1)^{\Pi+K}$ equals X_Γ, where $X_\Gamma = 1$ (-1) for $\Gamma = A_1$ (A_2). This result can be derived from a simple model. According to it, no resonances in the J, Π, Γ partial wave can exist if the scattering wavefunction vanishes identically for all configurations of the system in the vicinity of the saddle point for which the distances of the two end atoms to the central atom are equal. This is physically reasonable since we expect the resonance scattering wavefunction to have large density for symmetric displacements of the system around the saddle point.

Let us now show how this model leads to the empirical rule just mentioned. Let ABC be a linear triatom for which atoms A and C are identical. Consider a bent configuration of this system in which the distances AB and BC are equal. Let X_Γ be the eigenvalue of the operator which permutes A and C, which is equal to 1 for $\Gamma = A_1$ and to -1 for $\Gamma = A_2$. This permutation is equivalent to the product of the inversion operator and a rotation by π around the system's principle axis of inertia, and therefore application of these operations multiplies the triatom wavefunction by $(-1)^\Pi$ and $(-1)^K$, respectively. Since the wavefunction of the initial symmetric configuration cannot by assumption vanish identically if a resonance is to exist, we must have $X_\Gamma = (-1)^{\Pi+K}$, QED. For a system in which all three atoms are identical, neither of the two degenerate E symmetry wavefunctions is necessarily even or odd with respect to two-atom permutations, and when one of these wavefunctions is subjected to this permutation the result is a linear combination of both; thus the E symmetry should display the resonances found in both the A_1 and A_2 symmetry results of the same parity, as we have indeed observed.

The existence of resonances seems also to require the presence of minima in adiabatic curves as a function of an appropriate reaction coordinate [18–20,27–33]. In the particular case of hyperspherical coordinates, one examines LHSF energies including adiabatic correction terms as a function of ρ; these correction terms are large for the $H + H_2$ system. Plots of LSHF energies for the $J = 0$, 1 partial waves of each parity and symmetry do indeed show minima (even without corrections) for the symmetry–parity combinations which support resonances, but not for those combinations which have shown no resonances. A physical interpretation of the resonances depends, in addition to the symmetry arguments given above, on an explanation as to why these particular combinations of irreducible representation and inversion parity yield adiabatic energy versus ρ curves with minima.

4. Summary

Application of the variational method for calculation of LHSF to the $J = 1$ partial wave of $H + H_2$

yields results of sufficient quality for lifetime matrix analysis to give accurate resonance energies and lifetimes. The dependence of resonance energies on the bending mode characteristics of the system's potential energy surface is explained by a simple harmonic model, and the existence of patterns of resonant behavior in terms of the irreducible representations of the P_3 permutation group is interpreted using a simple physical picture.

Acknowledgement

The work described in this paper was supported in part by DOE grant DE-AS03-83ER and AFAL contract F04611-86-K-0067. One of the authors (SAC) also thanks NSF for a Graduate Fellowship. Most of the calculations were performed on the Cray X-MP/48 and SCS-40 machines at the NSF San Diego Supercomputing Center.

References

[1] S.A. Cuccaro, P.G. Hipes and A. Kuppermann, Chem. Phys. Letters 154 (1989) 155.
[2] A. Kuppermann and P.G. Hipes, J. Chem. Phys. 84 (1986) 5962.
[3] P.G. Hipes and A. Kuppermann, Chem. Phys. Letters 133 (1987) 1.
[4] R.N. Porter and M. Karplus, J. Chem. Phys. 40 (1964) 1105.
[5] B. Liu, J. Chem. Phys. 58 (1973) 1925;
P. Siegbahn and B. Liu, J. Chem. Phys. 68 (1978) 2457.
[6] D.G. Truhlar and C.J. Horowitz, J. Chem. Phys. 68 (1978) 2468; 71 (1979) 1514 (E).
[7] F.T. Smith, Phys. Rev. 118 (1960) 349.
[8] G.C. Schatz, Chem. Phys. Letters 150 (1988) 92.
[9] G.A. Parker, R.T Pack, B.J. Archer and R.B. Walker, Chem. Phys. Letters 137 (1987) 564;
R.T Pack and G.A. Parker, J. Chem. Phys. 87 (1987) 3888.
[10] M. Mladenovic, M. Zhao, D.G. Truhlar, D.W. Schwenke, Y. Sun and D.J. Kouri, Chem. Phys. Letters 146 (1988) 358.
[11] J.Z.H. Zhang and W.H. Miller, Chem. Phys. Letters 153 (1988) 465.
[12] G.C. Schatz and A. Kuppermann, J. Chem. Phys. 65 (1976) 4642; 4668.
[13] B.R. Johnson, J. Compl. Phys. 49 (1973) 23.
[14] D.M. Hood and A. Kuppermann, in: Theory of chemical reaction dynamics, ed. D.C. Clary (Reidel, Dordrecht, 1986) pp. 193–204; unpublished results.
[15] G. Herzberg, Infrared and Raman spectra of polyatomic molecules (Van Nostrand, Princeton, 1945) p. 272.
[16] M.C. Colton and G.C. Schatz, Chem. Phys. Letters 124 (1986) 256.
[17] J.M. Bowman, Chem. Phys. Letters 124 (1986) 260.
[18] B.C. Garrett and D.G. Truhlar, J. Phys. Chem. 86 (1982) 1136.
[19] A. Kuppermann, Reactive scattering resonances and their physical interpretation, in: potential energy surfaces and dynamics calculations, ed. D.G. Truhlar (Plenum Press, New York, 1981) ch. 16.
[20] J. Römelt, J. Chem. Phys. 79 (1983) 197.
[21] E. Pollak, Chem. Phys. Letters 137 (1987) 171.
[22] P.G. Hipes, Three-Dimensional Atom–Diatom Reactive Scattering Calculations Using Symmetrized Hyperspherical Coordinates, Ph.D. Thesis, California Institute of Technology (1988); unpublished results.
[23] E. Pollak, J. Phys. Chem. 90 (1986) 3619.
[24] B.C. Garrett, D.W. Schwenke, R.T. Skodje, D. Thirumalai, T.C. Thompson and D.G. Truhlar, Bimolecular reactive collisions, adiabatic and nonadiabatic methods for energies, lifetimes, and branching probabilities, in: Resonances, ACS Symp. Ser. Vol. 263 (Am. Chem. Soc., Washington, 1984) p. 375.
[25] G. Herzberg, Infrared and Raman spectra of polyatomic molecules (Van Nostrand, Princeton, 1945) p. 80.
[26] A.B. Elkowitz and R.E. Wyatt, J. Chem. Phys. 62 (1975) 2504; 63 (1975) 702.
[27] A. Kuppermann and J.P. Dwyer, in: Electronic and atomic collisions, Abstract of Contributed Papers, XIth International Conference on the Physics of Electronic and Atomic Collisions, eds. K. Takayanagi and N. Oda (Society for Atomic Collision Research, Japan, 1979) pp. 888, 889.
[28] G. Hauke, J. Manz and J. Römelt, J. Chem. Phys. 73 (1980) 5040.
[29] J.A. Kaye and A. Kuppermann, Chem. Phys. Letters 77 (1981) 573.
[30] V.K. Babamov and R.A. Marcus, J. Chem. Phys. 74 (1981) 1790.
[31] J.M. Launay and B. Lepetit, Chem. Phys. Letters 144 (1988) 346.
[32] J.M. Launay and M. Le Dourneuf, J. Phys. B 15 (1982) L455.
[33] B. Lepetit, M. Le Dourneuf, J.M. Launay and F.X. Gadea, Chem. Phys. Letters 135 (1987) 377.